

به نام خدا



# مرکز دانلود رایگان مهندسی متالورژی و مواد

[www.Iran-mavad.com](http://www.Iran-mavad.com)



# Carbon Nanotubes

## Properties and Applications

Edited by

Michael J. O'Connell, Ph.D.

*Senior Research Scientist, Theranos, Inc.  
Menlo Park, California*



**Taylor & Francis**

Taylor & Francis Group  
Boca Raton London New York

---

CRC is an imprint of the Taylor & Francis Group,  
an informa business

[www.iran-mavad.com](http://www.iran-mavad.com)

مرجع دانشجویان و مهندسين مواد

© 2006 by Taylor & Francis Group, LLC

Published in 2006 by  
CRC Press  
Taylor & Francis Group  
6000 Broken Sound Parkway NW, Suite 300  
Boca Raton, FL 33487-2742

© 2006 by Taylor & Francis Group, LLC  
CRC Press is an imprint of Taylor & Francis Group

No claim to original U.S. Government works  
Printed in the United States of America on acid-free paper  
10 9 8 7 6 5 4 3 2 1

International Standard Book Number-10: 0-8493-2748-2 (Hardcover)  
International Standard Book Number-13: 978-0-8493-2748-3 (Hardcover)  
Library of Congress Card Number 2005036354

This book contains information obtained from authentic and highly regarded sources. Reprinted material is quoted with permission, and sources are indicated. A wide variety of references are listed. Reasonable efforts have been made to publish reliable data and information, but the author and the publisher cannot assume responsibility for the validity of all materials or for the consequences of their use.

No part of this book may be reprinted, reproduced, transmitted, or utilized in any form by any electronic, mechanical, or other means, now known or hereafter invented, including photocopying, microfilming, and recording, or in any information storage or retrieval system, without written permission from the publishers.

For permission to photocopy or use material electronically from this work, please access [www.copyright.com](http://www.copyright.com) (<http://www.copyright.com/>) or contact the Copyright Clearance Center, Inc. (CCC) 222 Rosewood Drive, Danvers, MA 01923, 978-750-8400. CCC is a not-for-profit organization that provides licenses and registration for a variety of users. For organizations that have been granted a photocopy license by the CCC, a separate system of payment has been arranged.

**Trademark Notice:** Product or corporate names may be trademarks or registered trademarks, and are used only for identification and explanation without intent to infringe.

---

#### Library of Congress Cataloging-in-Publication Data

---

Carbon nanotubes : properties and applications / editor Michael  
O'Connell.

p. cm.

Includes bibliographical references and index.

ISBN-13: 978-0-8493-2748-3 (hardcover)

ISBN-10: 0-8493-2748-2 (hardcover)

1. Carbon. 2. Nanostructured materials. 3. Tubes. I. O'Connell, Michael (Michael J.)

TA455.C3C374 2006

620.1'93--dc22

2005036354

---

**informa**

Taylor & Francis Group  
is the Academic Division of Informa plc.

Visit the Taylor & Francis Web site at  
<http://www.taylorandfrancis.com>

and the CRC Press Web site at  
<http://www.crcpress.com>

[www.iran-mavad.com](http://www.iran-mavad.com)

مرجع دانشجویان و مهندسين مواد

© 2006 by Taylor & Francis Group, LLC

---

# Preface

In 1985, a molecule called buckminsterfullerene was discovered by a group of researchers at Rice University. This molecule consisted of 60 carbon atoms in  $sp^2$  hybridized bonds arranged in a surprisingly symmetric fashion. The Nobel Prize was awarded to Richard Smalley, Robert Curl, and Harry Kroto for their discovery of this new allotrope of carbon. This discovery was groundbreaking for the now vibrant field of carbon nanotechnology.

Carbon nanotubes, discovered in 1991 by Sumio Iijima, are members of the fullerene family. Their morphology is considered equivalent to a graphene sheet rolled into a seamless tube capped on both ends. Single-walled carbon nanotubes (SWNTs) have diameters on the order of single-digit nanometers, and their lengths can range from tens of nanometers to several centimeters. SWNTs also exhibit extraordinary mechanical properties ideal for applications in reinforced composite materials and nanoelectromechanical systems (NEMS): Young's modulus is over 1 TPa and the tensile strength is an estimated 200 GPa. Additionally, SWNTs have very interesting band structures. Depending on the atomic arrangement of the carbon atoms making up the nanotube (chirality), the electronic properties can be metallic or semiconducting in nature, making it possible to create nanoelectronic devices, circuits, and computers using SWNTs.

This book introduces carbon nanotubes and the science used to investigate them. The field is progressing at staggering rates, with thousands of publications appearing in the literature each year. The current progress and the applications SWNTs have found use in are particularly impressive, since the existence of the fullerenes has only been known for 20 years. This book is a great resource for anyone new to carbon nanotube research. It can also introduce the experienced researcher to subjects outside his or her area of study. The book assumes that the reader has a basic understanding of chemistry and physics. I hope that high school students and undergraduates may stumble upon this book, find the inspiration to study science, and pursue a career in nanotechnology research.

This book was written by many expert carbon nanotube researchers. The book does not build information sequentially, but rather each chapter can be read as a mini-book of its particular subject. I encourage the reader to explore this book in the order of subject matter interest.



This book begins with an introduction and history of carbon nanotubes. The introduction was written by Frank Hennrich, Candace Chan, Valerie Moore, Marco Rolandi, and Mike O'Connell. Frank Hennrich received his Ph.D. in physical chemistry from Karlsruhe University based on his work on the producing and characterizing of fullerenes and SWNTs. His main interests at his current position in the Institute of Nanotechnology (Research Center Karlsruhe) include Raman spectroscopy, nanotube separations, and nanotube electronic devices. Candace Chan received a B.S. in chemistry from Rice University, where she worked on SWNT cutting and functionalization. She is currently pursuing a Ph.D. at Stanford University as a National Science Foundation Fellow and Stanford Graduate Fellow in the departments of chemistry and materials science and engineering. Her current research interests are synthesizing new nanowire materials and incorporating them into memory, electronic, and sensor devices. Valerie Moore recently completed her Ph.D. in chemistry at Rice University in the areas of characterization and application of colloidal SWNT suspensions and novel methods toward (n, m)-selective SWNT growth. She holds a B.S. in chemistry from Centenary College of Louisiana, where she was able to conduct undergraduate research at NASA Glenn Research Center on carbon nanotube growth in flames. Marco Rolandi recently received his Ph.D. in applied physics from Stanford University, where he characterized carbon nanotubes using Raman spectroscopy. He also holds an M.Sci. in physics from Queen Mary and Westfield College, University of London.

Following the introduction is a discussion on the various ways to synthesize carbon nanotubes, written by David Mann and Mike O'Connell. While SWNTs had been discovered as a by-product in 1991, they were not controllably synthesized until 1993. David Mann is busy completing a Ph.D. in applied physics from Stanford University, where he conducts research on nanotubes covering a wide variety of topics, including novel synthesis methods as well as electrical and thermal characterization. He received a B.S. in physics from Harvey Mudd College.

The next chapter is about another type of nanotube material synthesis. Satishkumar B. Chikkannanavar, Brian W. Smith, and David E. Luzzi look at the carbon nanotube as a volume of space capable of transporting or containing other materials inside. These amazing structures, commonly known as peapods, have interesting properties and great potential in many useful applications. Satishkumar B. Chikkannanavar finished his undergraduate from Karnataka University and Ph.D. at Indian Institute of Science, Bangalore. He did his postdoctoral research at the University of Pennsylvania, working on carbon nanotubes and fullerene hybrid materials, and currently he is at the Los Alamos National Laboratory. His research interests include near-infrared optical characteristics of carbon nanotubes, optical sensing of biomolecules, and device applications. Brian W. Smith received his Ph.D. in materials science from the University of Pennsylvania, where he was instrumental in the discovery, synthesis, and characterization of carbon nanotube peapod materials. He is currently a member of the technical

staff at the Fox Chase Cancer Center (Philadelphia). His research program is focused on applications of nanotechnology in cancer treatment, specifically in the area of radioimmunotherapy. David E. Luzzi received his Ph.D. in materials science and engineering from Northwestern University in 1986. His Luzzi Research Group at the University of Pennsylvania synthesizes novel nanoscale materials based primarily on SWNTs, and his research interest includes structure and properties of carbon nanotubes, interface in structural materials, and mechanical properties of Laves phases.

The next few chapters discuss the properties of SWNTs. Marcus Freitag begins with the description of the electronic properties and band structure of nanotubes, and then moves on to the electronic properties of devices made with SWNTs. Marcus Freitag is a research staff member at the IBM T.J. Watson Research Center in Yorktown Heights, New York. He received his Diplom degree at the University of Tuebingen, Germany, his M.S. at the University of Massachusetts, and his Ph.D. in physics at the University of Pennsylvania. He joined IBM's research division in 2004 after 2 years of postdoctoral work with Carbon Nanotechnologies. His research is focused on electronic transport and electro-optic interactions in carbon nanotubes.

Carbon nanotubes can be paramagnetic or diamagnetic depending on their chirality. Junichiro Kono and Stephan Roche cover the magnetic properties of nanotubes. Junichiro Kono currently serves as an associate professor of electrical and computer engineering at Rice University. His research interests include optical studies of low-dimensional solids and nanostructures; spintronics, opto-spintronics, and optical quantum information processing; nonlinear, ultrafast, and quantum optics in solids; physical phenomena in ultrahigh magnetic fields; and physics and applications of terahertz phenomena in semiconductors. He holds a Ph.D. in physics from the State University of New York–Buffalo and an M.S. and B.S. in applied physics from the University of Tokyo. Stephan Roche completed his Ph.D. at French CNRS in 1996. He worked as an EU research fellow in the department of applied physics at Tokyo University, Japan, and in the department of theoretical physics at Valladolid University, Spain, before being appointed as assistant professor at the University of Grenoble. He is now research staff of the Commissariat à l'Energie Atomique in Grenoble, focusing on charge transport in nanoelectronics and mesoscopic systems from a theoretical perspective.

The next chapter discusses using Raman spectroscopy to probe the electronic and chemical behavior of SWNTs. This chapter was written by Stephen K. Doorn, Daniel Heller, Monica Usrey, Paul Barone, and Michael S. Strano. Stephen K. Doorn received his B.S. in chemistry (with honors) from the University of Wisconsin and holds a Ph.D. in physical chemistry from Northwestern University. He is currently a technical staff member in the chemistry division at Los Alamos National Laboratory. His research efforts are focused on spectroscopic materials characterization and fundamental studies and biosensor applications of nanoparticle assemblies. His specific interests in carbon nanotubes include fundamental spectroscopy, separations, redox chemistry,

and sensors. Daniel Heller is a graduate student in the department of chemistry at the University of Illinois–Urbana/Champaign in the laboratory of Michael S. Strano. He studies the chemistry and physics of nanoscale materials and their interactions with biological systems. Monica Usrey is a graduate student in the department of chemical and biomolecular engineering at the University of Illinois–Urbana/Champaign working with Michael S. Strano. She works with the functionalization of single-walled carbon nanotubes with diazonium salts, with emphasis on electronic structure separation. She holds a B.S. in chemical engineering from the University of Louisville. Paul Barone is completing work for a Ph.D. in chemical and biomolecular engineering at the University of Illinois–Urbana/Champaign. He studies the photophysics of single-walled carbon nanotube/protein systems. He received his B.S. in chemical engineering from the University of Missouri–Columbia. Michael S. Strano is an assistant professor in the department of chemical and biomolecular engineering at the University of Illinois–Urbana/Champaign. His research focuses on the chemistry of nanotube and nanowire systems and the photophysics of such systems. Daniel Heller, Monica Usrey, Paul Barone, and Michael S. Strano also include a discussion on the optical properties of nanotubes and separations.

Next, Randal J. Grow discusses some of the electromechanical properties of SWNTs and their applications in NEMS devices. Randal J. Grow recently completed a Ph.D. in applied physics from Stanford University, where he conducted research on the electromechanical properties of carbon nanotubes and germanium nanowires, among other things. He also holds a B.A. in physics from Colorado College.

Carbon nanotubes are the strongest material known. In their chapter, Han Gi Chae, Jing Liu, and Satish Kumar discuss the mechanical properties of SWNTs spun into fibers. Han Gi Chae is working toward his Ph.D. degree in polymeric materials at the Georgia Institute of Technology, where he conducts research on polymer/nanotubes composite fibers. Prior to joining Georgia Tech, he conducted research on high-performance polymer hybrids at Korea Institute of Science and Technology, Seoul, Korea. He received his B.S. and M.S. in polymer engineering from Hanyang University, Korea. Jing Liu is working toward her Ph.D. degree in polymeric materials at Georgia Institute of Technology, where she conducts research on carbon nanotubes/polymer composites and novel structured materials by electrospinning. She received her M.E. degree in polymer materials from Zhejiang University, China. Satish Kumar is a professor in the School of Polymer, Textile and Fiber Engineering at the Georgia Institute of Technology. His research interests are structure, processing, and properties of polymers, fibers, and composites. His current research focus includes carbon nanotube composites, electrospinning, and electrochemical supercapacitors.

Covalent sidewall functionalization opens new doors for nanotube research. Christopher A. Dyke and James M. Tour include their chapter on the synthesis and applications of covalently modified SWNTs. Christopher A. Dyke is currently the chief scientific officer of NanoComposites, Inc.

(NCI). NCI employs carbon nanotube functionalization technology for the enhancement of polymeric materials. He received his Ph.D. in synthetic organic chemistry from the University of South Carolina with postdoctoral research at Rice University, where he worked on carbon nanotube technology. James M. Tour is the chair professor of chemistry, professor of computer science, and professor of mechanical engineering and materials science at Rice University's Center for Nanoscale Science and Technology. He received his B.S. in chemistry from Syracuse University and his Ph.D. from Purdue University, with postdoctoral research at the University of Wisconsin and Stanford University. He presently works on carbon nanotubes and composites, molecular electronics, and nanomachines.

C. Patrick Collier's chapter discusses the use of SWNTs as tips for scanning probe microscopy. He includes the fabrication of these tips, the properties of the SWNTs on the tips, and applications in biosensing. C. Patrick Collier is an assistant professor of chemistry at the California Institute of Technology. His research interests include single-molecule spectroscopy, scanning probe microscopy using carbon nanotube tips, and nanolithography. He obtained his Ph.D. from the University of California–Berkeley, where he was involved in the discovery of a reversible metal–insulator transition in ordered two-dimensional superlattices of silver quantum dots under ambient conditions. In his postdoctoral work at University of California–Los Angeles and Hewlett-Packard Labs, he was involved in some of the first demonstrations of defect-tolerant computation in molecular electronics. He received a B.A. in chemistry and a B.Mus. from Oberlin College.

---

# *Acknowledgments*

I am sincerely thankful for the time and effort put in by all of the authors. I also acknowledge the Director of Central Intelligence Fellowship Program for its support during my postdoctoral fellowships at Los Alamos National Laboratory and Stanford University, and Theranos, Inc., for my current support. Finally, I honor my Ph.D. advisor at Rice University, the recently departed Rick Smalley. Rick was a good friend and mentor to me. He shared his vision for the success of carbon nanotechnology with so many people around the world. His passion for science helped to make carbon nanotechnology the vibrant research field it is today. He is gone, but not forgotten. Rick left behind in many, including myself, a deep fascination and respect for the curious molecules known as carbon nanotubes.

---

## About the Editor



**Dr. Michael J. O'Connell** graduated with a B.S. in biochemistry and molecular biology from the University of California in 1998 and developed an interest in the emerging field of nanotechnology. He went on to Rice University and received his Ph.D. in physical chemistry in 2002 for research with Richard E. Smalley on aqueous phase suspensions of carbon nanotubes. O'Connell then joined Los Alamos National Laboratory in 2003 as a postdoctoral researcher with Stephen K. Doorn, working on carbon nanotube spectroscopy and sensors. In 2004 he transferred as a postdoctoral fellow to Stanford University to work with Hongjie Dai on biological applications of carbon nanotubes. He has numerous patents and publications in the nanotech field. He is now leading a team of nanotech researchers at Theranos to create future generation products.

O'Connell's many accomplishments include the Director of Central Intelligence Postdoctoral Fellowship from 2003 to 2005. He also wrote "4-Centimeter-Long Carbon Nanotubes" for *Nanotech Briefs* that won the Nano 50 Award in 2005. He has been a Los Alamos National Laboratory Director's Postdoctoral Fellow in 2003, a Los Alamos National Laboratory Postdoctoral Fellow in 2003, a Welch Fellow of Rice University from 2000 to 2002, and a President's Undergraduate Fellow of the University of California–Santa Cruz from 1997 to 1998. O'Connell was honored with the College Eight Research Award from the University of California–Santa Cruz from 1997 to 1998 and is a member of the Phi Lambda Upsilon Honor Society.



---

# Contributors

**Paul Barone**

Department of Chemical and  
Biomolecular Engineering  
University of Illinois–Urbana/  
Champaign  
Urbana, Illinois

**Han Gi Chae**

School of Polymer, Textile, and Fiber  
Engineering  
Georgia Institute of Technology  
Atlanta, Georgia

**Candace Chan**

Departments of Chemistry and  
Materials Science and Engineering  
Stanford University  
Stanford, California

**Satishkumar B. Chikkannanavar**  
Chemical Sciences and Engineering  
Los Alamos National Laboratory  
Los Alamos, New Mexico

**C. Patrick Collier**

Division of Chemistry and  
Chemical Engineering  
California Institute of Technology  
Pasadena, California

**Stephen K. Doorn**

Chemistry Division  
Los Alamos National Laboratory  
Los Alamos, New Mexico

**Christopher A. Dyke**

Corporate Development  
Laboratory  
NanoComposites, Inc.  
Houston, Texas

**Marcus Freitag**

Watson Research Center  
IBM Corporation  
Yorktown Heights, New York

**Randal J. Grow**

Department of Applied Physics  
Stanford University  
Stanford, California

**Daniel Heller**

Department of Chemistry  
University of Illinois–Urbana/  
Champaign  
Urbana, Illinois

**Frank Hennrich**

Institut für Nanotechnologie  
Karlsruhe, Germany

**Junichiro Kono**

Department of Electrical and  
Computer Engineering  
Rice University  
Houston, Texas

**Satish Kumar**

School of Polymer, Textile, and Fiber  
Engineering  
Georgia Institute of Technology  
Atlanta, Georgia

**Jing Liu**

School of Polymer, Textile, and Fiber  
Engineering  
Georgia Institute of Technology  
Atlanta, Georgia

**David E. Luzzi**

Department of Materials Science  
and Engineering  
Laboratory for Research on  
Structure of Matter  
University of Pennsylvania  
Philadelphia, Pennsylvania

**David Mann**

Geballe Laboratory for Advanced  
Materials and  
Department of Applied Physics  
Stanford University  
Stanford, California

**Valerie Moore**

Center for Nanoscale Science and  
Technology  
Rice University  
Houston, Texas

**Mike O'Connell**

Theranos, Inc.  
Menlo Park, California

**Stephan Roche**

Commissariat à l'Énergie Atomique  
Grenoble, France

**Marco Rolandi**

Department of Chemistry and  
Laboratory for Advanced  
Materials  
Stanford University  
Stanford, California

**Brian W. Smith**

Department of Materials Science  
and Engineering  
Laboratory for Research on  
Structure of Matter  
University of Pennsylvania  
Philadelphia, Pennsylvania  
and  
Department of Medical Oncology  
Fox Chase Cancer Center  
Philadelphia, Pennsylvania

**Michael S. Strano**

Department of Chemical and  
Biomolecular Engineering  
University of Illinois–Urbana/  
Champaign  
Urbana, Illinois

**James M. Tour**

Departments of Chemistry,  
Mechanical Engineering, and  
Materials Science, and Center for  
Nanoscale Science and Technology  
Rice University  
Houston, Texas

**Monica Usrey**

Department of Chemical and  
Biomolecular Engineering  
University of Illinois–Urbana/  
Champaign  
Urbana, Illinois



---

# Contents

<b>Chapter 1 The element carbon</b> .....	<b>1</b>
<i>Frank Hennrich, Candace Chan, Valerie Moore, Marco Rolandi, and Mike O'Connell</i>	
<b>Chapter 2 Synthesis of carbon nanotubes</b> .....	<b>19</b>
<i>David Mann</i>	
<b>Chapter 3 Carbon nanotube peapod materials</b> .....	<b>51</b>
<i>Satishkumar B. Chikkannanavar, Brian W. Smith, and David E. Luzzi</i>	
<b>Chapter 4 Carbon nanotube electronics and devices</b> .....	<b>83</b>
<i>Marcus Freitag</i>	
<b>Chapter 5 Magnetic properties</b> .....	<b>119</b>
<i>Junichiro Kono and Stephan Roche</i>	
<b>Chapter 6 Raman spectroscopy of single-walled carbon nanotubes: probing electronic and chemical behavior</b> .....	<b>153</b>
<i>Stephen K. Doorn, Daniel Heller, Monica Usrey, Paul Barone, and Michael S. Strano</i>	
<b>Chapter 7 Electromechanical properties and applications of carbon nanotubes</b> .....	<b>187</b>
<i>Randal J. Grow</i>	
<b>Chapter 8 Carbon nanotube-enabled materials</b> .....	<b>213</b>
<i>Han Gi Chae, Jing Liu, and Satish Kumar</i>	
<b>Chapter 9 Functionalized carbon nanotubes in composites</b> .....	<b>275</b>
<i>Christopher A. Dyke and James M. Tour</i>	
<b>Chapter 10 Carbon nanotube tips for scanning probe microscopy</b> .....	<b>295</b>
<i>C. Patrick Collier</i>	

## *chapter one*

---

# *The element carbon*

*Frank Hennrich*

*Institut für Nanotechnologie*

*Candace Chan*

*Stanford University*

*Valerie Moore*

*Rice University*

*Marco Rolandi*

*Stanford University*

*Mike O'Connell*

*Theranos, Inc.*

## *Contents*

1.1 Allotropes of carbon.....	2
1.2 History .....	3
1.3 Structure .....	6
1.4 Progress of single-walled carbon nanotube research .....	8
References.....	16

Carbon is the most versatile element in the periodic table, owing to the type, strength, and number of bonds it can form with many different elements. The diversity of bonds and their corresponding geometries enable the existence of structural isomers, geometric isomers, and enantiomers. These are found in large, complex, and diverse structures and allow for an endless variety of organic molecules.

The properties of carbon are a direct consequence of the arrangement of electrons around the nucleus of the atom. There are six electrons in a carbon atom, shared evenly between the 1s, 2s, and 2p orbitals. Since the 2p atomic orbitals can hold up to six electrons, carbon can make up to four bonds;

however, the valence electrons, involved in chemical bonding, occupy both the 2s and 2p orbitals.

Covalent bonds are formed by promotion of the 2s electrons to one or more 2p orbitals; the resulting hybridized orbitals are the sum of the original orbitals. Depending on how many p orbitals are involved, this can happen in three different ways. In the first type of hybridization, the 2s orbital pairs with one of the 2p orbitals, forming two hybridized  $sp^1$  orbitals in a linear geometry, separated by an angle of  $180^\circ$ . The second type of hybridization involves the 2s orbital hybridizing with two 2p orbitals; as a result, three  $sp^2$  orbitals are formed. These are on the same plane separated by an angle of  $120^\circ$ . In the third hybridization, one 2s orbital hybridizes with the three 2p orbitals, yielding four  $sp^3$  orbitals separated by an angle of  $109.5^\circ$ .  $sp^3$  hybridization yields the characteristic tetrahedral arrangements of the bonds. In all three cases, the energy required to hybridize the atomic orbitals is given by the free energy of forming chemical bonds with other atoms.

Carbon can bind in a sigma ( $\sigma$ ) bond and a pi ( $\pi$ ) bond while forming a molecule; the final molecular structure depends on the level of hybridization of the carbon orbitals. An  $sp^1$  hybridized carbon atom can make two  $\sigma$  bonds and two  $\pi$  bonds,  $sp^2$  hybridized carbon forms three  $\sigma$  bonds and one  $\pi$  bond, and an  $sp^3$  hybridized carbon atom forms four  $\sigma$  bonds. The number and nature of the bonds determine the geometry and properties of carbon allotropes.

## 1.1 Allotropes of carbon

Carbon in the solid phase can exist in three allotropic forms: graphite, diamond, and buckminsterfullerene (Figure 1.1). Diamond has a crystalline structure where each  $sp^3$  hybridized carbon atom is bonded to four others

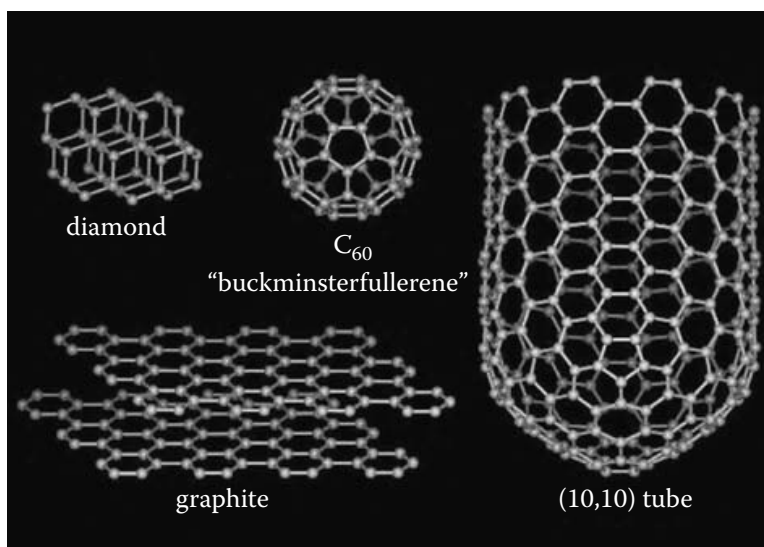


**Figure 1.1** The three allotropes of carbon. (From [http://smalley.rice.edu/smalley.cfm?doc\\_id=4866](http://smalley.rice.edu/smalley.cfm?doc_id=4866).)

in a tetrahedral arrangement. The crystalline network gives diamond its hardness (it is the hardest substance known) and excellent heat conduction properties (about five times better than copper).<sup>1</sup> The  $sp^3$  hybridized bonds account for its electrically insulating property and optical transparency. Graphite is made by layered planar sheets of  $sp^2$  hybridized carbon atoms bonded together in a hexagonal network. The different geometry of the chemical bonds makes graphite soft, slippery, opaque, and electrically conductive. In contrast to diamond, each carbon atom in a graphite sheet is bonded to only three other atoms; electrons can move freely from an unhybridized p orbital to another, forming an endless delocalized  $\pi$  bond network that gives rise to the electrical conductivity.

Buckminsterfullerenes, or fullerenes, are the third allotrope of carbon and consist of a family of spheroidal or cylindrical molecules with all the carbon atoms  $sp^2$  hybridized. The tubular form of the fullerenes, nanotubes, will be the subject of this book, and a detailed description of their history, properties, and challenges will be given in the next section.

## 1.2 History

Fullerenes were discovered in 1985 by Rick Smalley and coworkers.<sup>2</sup>  $C_{60}$  was the first fullerene to be discovered.  $C_{60}$ , or “bucky ball,” is a soccer ball (icosahedral)-shaped molecule with 60 carbon atoms bonded together in pentagons and hexagons. The carbon atoms are  $sp^2$  hybridized, but in contrast to graphite, they are not arranged on a plane. The geometry of  $C_{60}$  strains the bonds of the  $sp^2$  hybridized carbon atoms, creating new properties for  $C_{60}$ . Graphite is a semimetal, whereas  $C_{60}$  is a semiconductor.

The discovery of  $C_{60}$  was, like many other scientific breakthroughs, an accident. It started because Kroto was interested in interstellar dust, the long-chain polyynes formed by red giant stars. Smalley and Curl developed a technique to analyze atom clusters produced by laser vaporization with time-of-flight mass spectrometry, which caught Kroto’s attention. When they used a graphite target, they could produce and analyze the long chain polyynes (Figure 1.2a). In September of 1985, the collaborators experimented with the carbon plasma, confirming the formation of polyynes. They observed two mysterious peaks at mass 720 and, to a lesser extent, 840, corresponding to 60 and 70 carbon atoms, respectively (Figure 1.2b). Further reactivity experiments determined a most likely spherical structure, leading to the conclusion that  $C_{60}$  is made of 12 pentagons and 20 hexagons arranged to form a truncated icosahedron<sup>2,3</sup> (Figure 1.3).

In 1990, at a carbon-carbon composites workshop, Rick Smalley proposed the existence of a tubular fullerene.<sup>4</sup> He envisioned a bucky tube that could be made by elongating a  $C_{60}$  molecule. In August of 1991, Dresselhaus followed up in an oral presentation in Philadelphia at a fullerene workshop on the symmetry proposed for carbon nanotubes capped at either end by fullerene hemispheres.<sup>5</sup> Experimental evidence of the existence of carbon nanotubes came in 1991 when Iijima imaged multiwalled carbon nanotubes

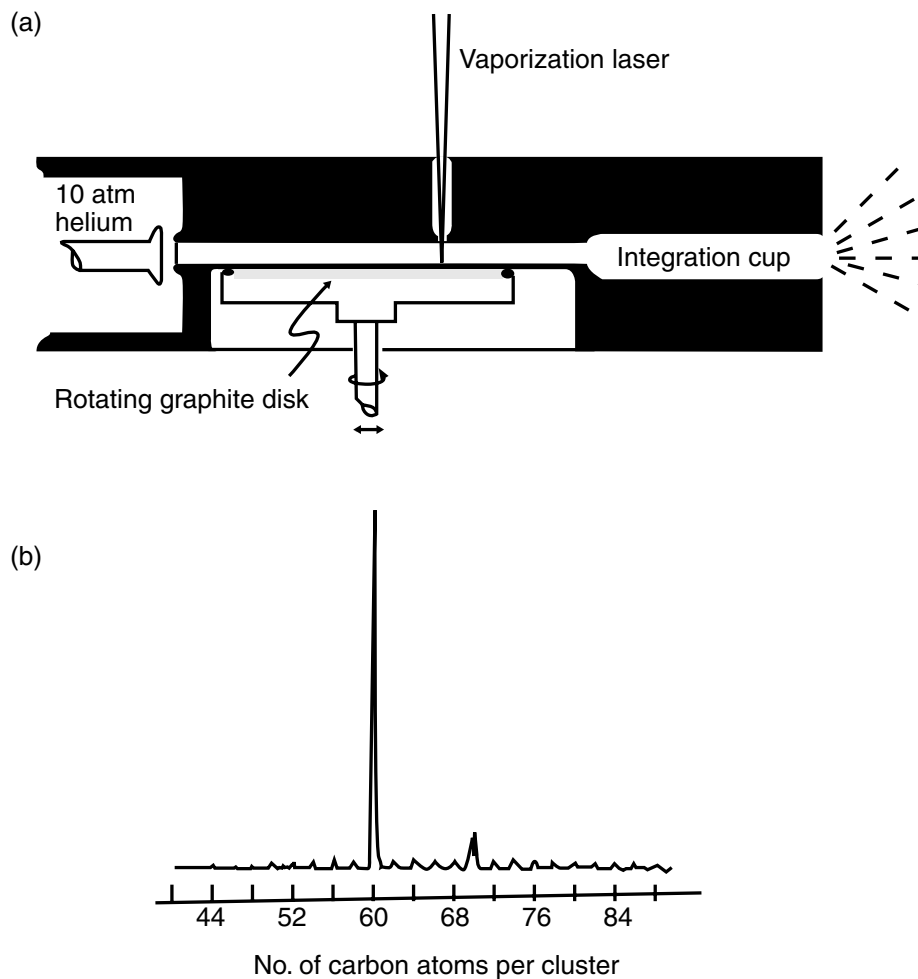


**Figure 1.2** (a) Schematic of the pulsed supersonic nozzle used to generate carbon cluster beams. (b) Time-of-flight mass spectra of carbon clusters prepared by laser vaporization of graphite. (From H.W. Kroto, J.R. Heath, S.C. Obrien, R.F. Curl, and R.E. Smalley. C-60-Buckminsterfullerene, *Nature*, 318, 162–163, 1985.)

(MWNTs) using a transmission electron microscope<sup>6</sup> (Figure 1.4). Two years after his first observation of MWNTs, Iijima and coworkers<sup>7</sup> and Bethune and coworkers<sup>8</sup> simultaneously and independently observed single walled carbon nanotubes (SWNTs).

Although Iijima is credited with their official discovery, carbon nanotubes were probably already observed thirty years earlier from Bacon at Union Carbide in Parma, OH. Bacon began carbon arc research in 1956 to investigate the properties of carbon fibers. He was studying the melting of graphite under high temperatures and pressures and probably found carbon nanotubes in his samples. In his paper, published in 1960, he presented the observation of carbon nanowhiskers under SEM investigation of his material<sup>9</sup> and he proposed a scroll like-structure. Nanotubes were also produced and imaged directly by Endo in the 1970's via high resolution transmission electron microscopy (HRTEM) when he explored the production of carbon fibers by pyrolysis of benzene and ferrocene at 1000°C.<sup>10</sup> He observed carbon fibers with a hollow core and a catalytic particle at the end. He later

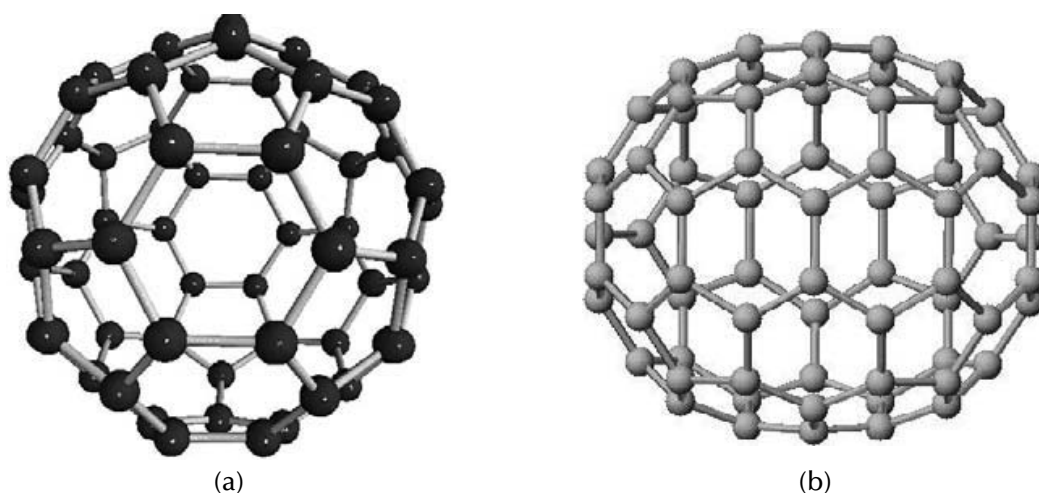


Figure 1.3 Models of the first fullerenes discovered,  $C_{60}$  and  $C_{70}$ .

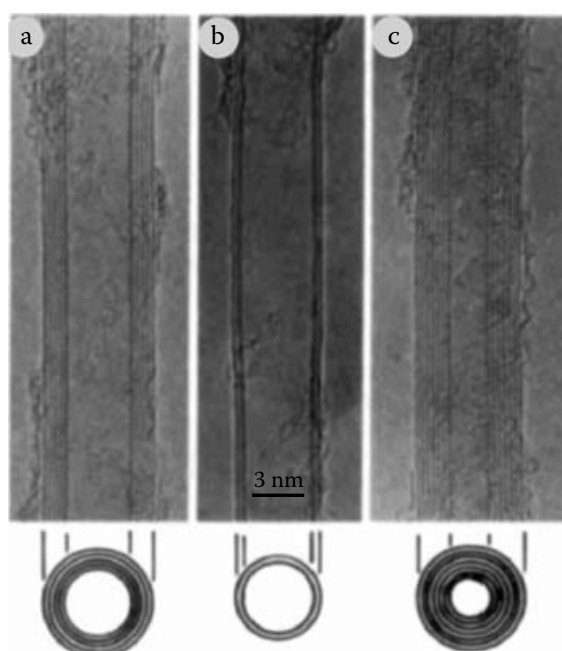


Figure 1.4 Transmission electron micrographs (TEMs) of the first observed multi-walled carbon nanotubes (MWNTs) reported by Iijima in 1991. (From S. Iijima. Helical microtubules of graphitic carbon, *Nature*, 354, 56–58, 1991.)

discovered that the particle was iron oxide from sand paper. Iron oxide is now well-known as a catalyst in the modern production of carbon nanotubes.

Although carbon nanotubes were observed four decades ago, it was not until the discovery of  $C_{60}$  and theoretical studies of possible other fullerene structures that the scientific community realized their importance. Since this pioneering work, carbon nanotube research has developed into a leading area in nanotechnology expanding at an extremely fast pace. Only 9 papers containing the words “carbon nanotube” were published in 1992 and over 5000 publications were printed in 2004. All this interest in this new form of



material was triggered by its unique properties and numerous potential applications, which will be described in the next sections.

### 1.3 Structure

Iijima was first to recognize that nanotubes were concentrically rolled graphene sheets with a large number of potential helicities and chiralities rather than a graphene sheet rolled up like a scroll as originally proposed by Bacon. Iijima initially observed only MWNTs with between 2 and 20 layers, but in a subsequent publication in 1993, he confirmed the existence of SWNTs single-walled carbon nanotubes and elucidated their structure.<sup>7</sup>

A SWNT is a rolled graphene sheet. Although the growth mechanism does not suggest a carbon nanotube is actually formed like a sushi roll, the way the graphene sheet is rolled determines the fundamental properties of the tube.

In order to describe such a fundamental characteristic of the nanotube, two vectors,  $C_h$  and  $T$ , whose rectangle defines the unit cell (Figure 1.5), can be introduced.  $C_h$  is the vector that defines the circumference on the surface of the tube connecting two equivalent carbon atoms,  $C_h = n\hat{a}_1 + m\hat{a}_2$ , where

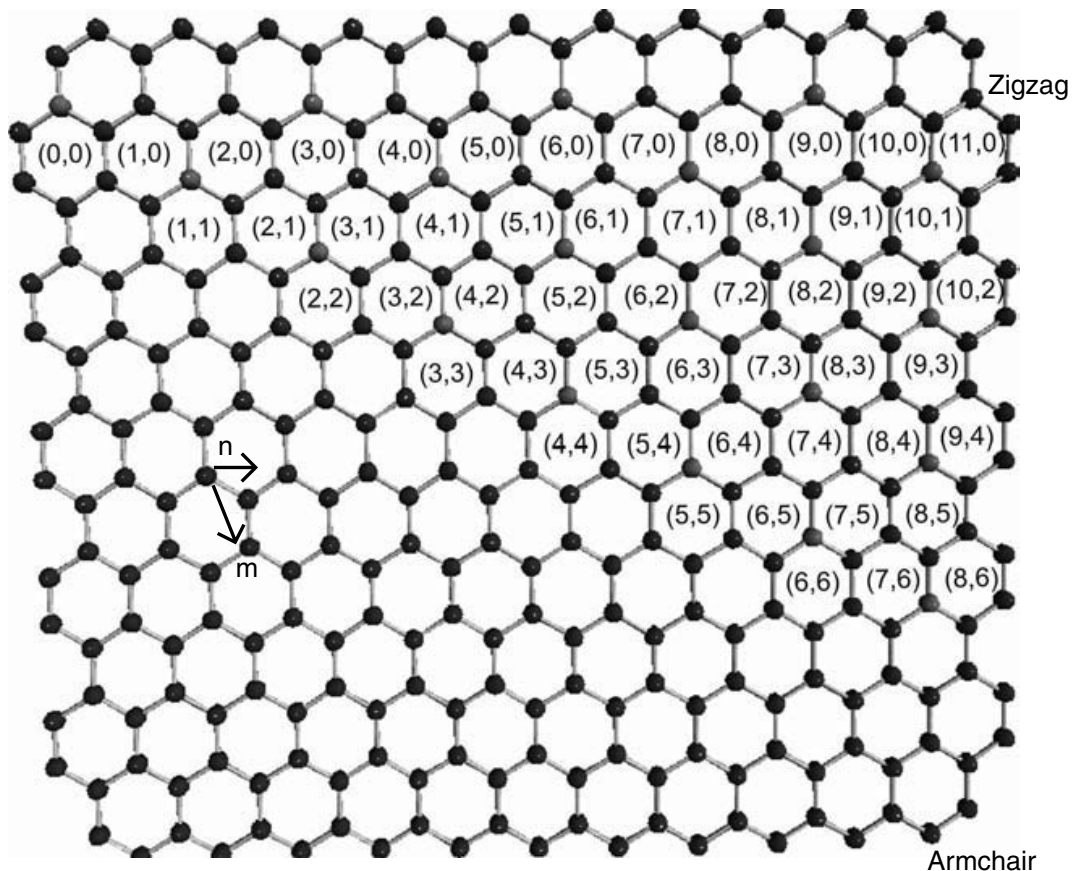


**Figure 1.5** The graphene sheet labeled with the integers  $(n, m)$ . The diameter, chiral angle, and type can be determined by knowing the integers  $(n, m)$ .

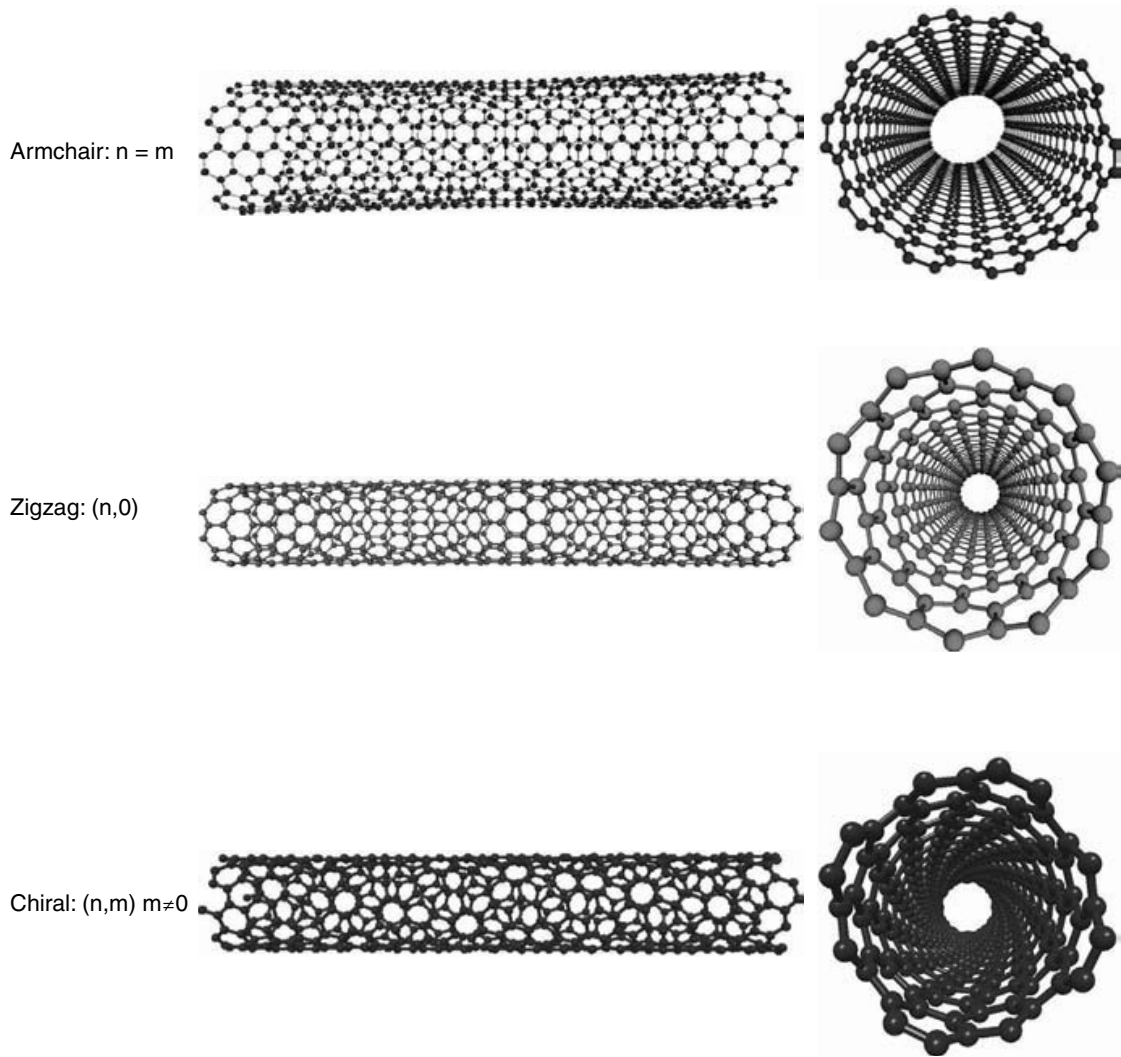


**Figure 1.6** Examples of the three types of SWNTs identified by the integers  $(n, m)$ .

$\hat{a}_1$  and  $\hat{a}_2$  are the two basis vectors of graphite and  $n$  and  $m$  are integers.  $n$  and  $m$  are also called indexes and determine the chiral angle  $\theta = \tan^{-1}[\sqrt{3}(n/(2m + n))]$ .

The chiral angle is used to separate carbon nanotubes into three classes differentiated by their electronic properties: armchair ( $n = m, \theta = 30^\circ$ ), zig-zag ( $m = 0, n > 0, \theta = 0^\circ$ ), and chiral ( $0 < |m| < n, 0 < \theta < 30^\circ$ ) (Figure 1.6). Armchair carbon nanotubes are metallic (a degenerate semimetal with zero band gap). Zig-zag and chiral nanotubes can be semimetals with a finite band gap if  $n - m/3 = i$  ( $i$  being an integer and  $m \neq n$ ) or semiconductors in all other cases. The band gap<sup>11</sup> (Figure 1.7a) for the semimetallic and semiconductor nanotubes scales approximately with the inverse of the tube diameter,<sup>12</sup> giving each nanotube a unique electronic behavior (Figure 1.7b).

The diameter of the nanotube can be expressed as

$$d_t = \sqrt{3}[a_{c-c}(m^2 + mn + n^2)^{1/2}/\pi] = C_h/\pi \quad (1.1)$$



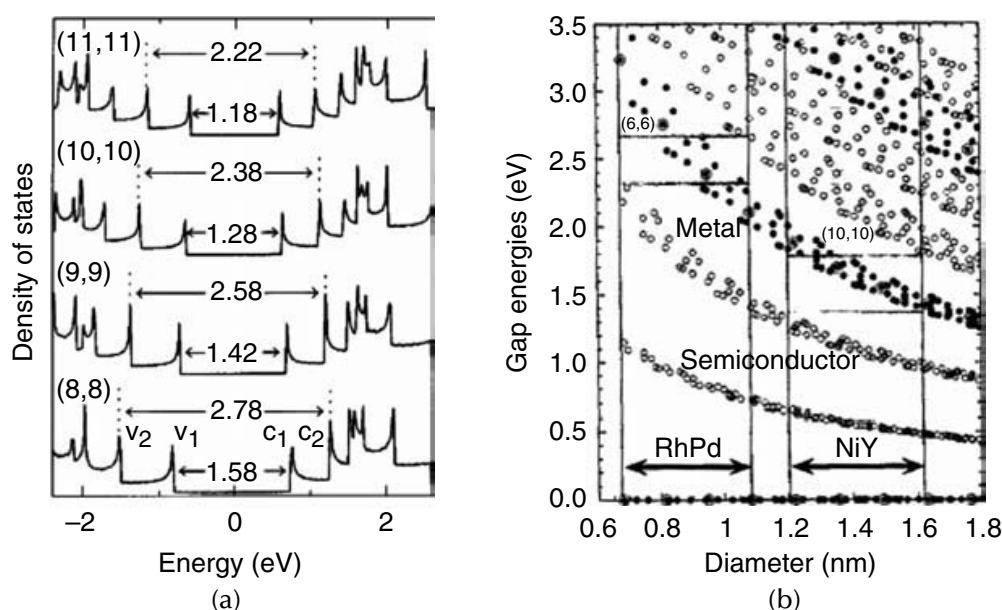


**Figure 1.7** (a) Electronic density of states (DOSs) calculated with a tight binding model for (8, 8), (9, 9), (10, 10), and (11, 11) armchair nanotubes. The Fermi energy is located at 0 eV. Wave vector-conserving optical transitions can occur between mirror-image spikes, that is,  $v_1 \rightarrow c_1$  and  $v_2 \rightarrow c_2$ . (From A.M. Rao, E. Richter, S. Bandow, B. Chase, P.C. Eklund, K.A. Williams, S. Fang, K.R. Subbaswamy, M. Menon, A. Tess, R.E. Smalley, G. Dresselhaus, and M.S. Dresselhaus. Diameter-selective raman scattering from vibrational modes in carbon nanotubes, *Science*, 275, 187, 1997. Copyright AAAS.) (b) Band gap energies between mirror-image spikes in DOSs calculated for  $\gamma = 2.75$  eV. Semiconductor SWNTs are open circles; metallic SWNTs are solid circles with the armchair SWNTs as double circles. (From H. Kataura, Y. Kumazawa, Y. Maniwa, I. Umez, S. Suzuki, Y. Ohtsuka and Y. Achiba. Optical properties of single-wall carbon nanotubes, *Synthetic Metals*, 103, 2555–2558, 1999. With permission from Elsevier.)

where  $C_h$  is the length of  $C_h$ , and  $a_{c-c}$  is the C-C bond length (1.42 Å). Combining different diameters and chiralities results in several hundred individual nanotubes, each with its own distinct mechanical, electrical, piezoelectric, and optical properties that will be discussed in this book.

## 1.4 Progress of single-walled carbon nanotube research

SWNTs are a distinctive class of molecules that exhibit unique properties. Since the discovery of carbon nanotubes (CNTs), numerous ideas for applications have arose in a wide variety of scientific disciplines, including (1) electronics (wires, transistors, switches, interconnects, memory storage devices); (2) opto-electronics (light-emitting diodes, lasers); (3) sensors; (4) field emission devices (displays, scanning and electron probes/microscopes); (5) batteries/fuel cells; (6) fibers, reinforced composites; (7) medicine/biology (fluorescent markers for cancer treatment, biological labels, drug delivery carriers); (8) catalysis; and (9) gas storage. This section presents a brief timeline of some of the most significant findings.

In computer chip circuits, transistors and wires are produced by lithography. Moore's law has predicted an exponential enhancement of computer power over several decades, but achieving this rate of progress will become more difficult in the next few years due to the limitations in the materials involved. Smaller and cheaper circuitry may be feasible from using molecular nanostructures. CNTs as quasi one-dimensional (1D) molecular nanostructures are perfect applicants for nanoscale transistors or wires.

In terms of transport, the 1D nature of CNTs severely reduces the phase space for scattering, allowing CNTs to realize maximum possible bulk mobility of this material. The low scattering probability and high mobility are responsible for high ON current (in excess of 1 mA/ $\mu\text{m}$ ) in semiconductor CNT transistors. Furthermore, the chemical stability and perfection of the CNT structure suggest that the carrier mobility at high gate fields may not be affected by processing and roughness scattering, as in the conventional semiconductor channel. Similarly, in metallic CNTs, low scattering, together with the strong chemical bonding and extraordinary thermal conductivity, allows them to withstand extremely high current densities (up to  $\sim 10^9 \text{ A/cm}^2$ ).

Additionally, because CNTs can be both metallic and semiconducting, an all-nanotube electronic device can be envisioned. In this case, metallic CNTs could act as high current carrying local interconnects, while semiconducting CNTs would form the active devices.

In 1997, researchers from Delft University of Technology in The Netherlands and Rice University in Texas were the first to show individual SWNTs act as genuine quantum wires.<sup>13</sup> Their measurement of the electrical transport properties of SWNTs confirmed the theoretical prediction that a SWNT behaves electrically as a single molecule. In 1998, two groups<sup>14,15</sup> from Delft University of Technology demonstrated the first molecular transistor using a carbon nanotube. They contacted a semiconducting nanotube on a  $\text{SiO}_2$  surface and modulated its conductance using a back gate. The device demonstrated the possibility of making nanoscale transistors work at room temperature and opened the exciting and rapidly growing field of nanotube electronics. Later, in 2001, SWNTs were integrated into logic circuits by researchers at IBM.<sup>16</sup> By applying current through a SWNT bundle, the metallic SWNTs can be selectively oxidized leaving only semiconducting tubes behind in the device. The same year, Javey et al.<sup>17</sup> demonstrated the first ballistic transistor using a carbon nanotube. They used palladium, a high work function metal, to contact the tube, eliminating Schottky barriers at the contacts and obtaining complete transparency for charge injection. Defect-free short devices showed no scattering in the p-channel at low temperature with the conductance reaching the theoretical limit of  $4e^2/h$ . Also in 2001, Kociak et al.<sup>18</sup> reported that ropes of SWNTs are intrinsically superconducting below 0.55 K, which was the first observation of superconductivity in a system with such a small number of conduction channels.

The promising characteristics of individual carbon nanotube field effect transistors (CNT-FETs) have led to initial attempts at integration of these

devices into useful structures of several CNT-FETs that can perform a logic operation, functioning as memory devices. In 2000, Charles Lieber's research group at Harvard University used SWNTs to construct nonvolatile random access memory and logic function tables at an integration level approaching  $10^{12}$  elements/cm<sup>2</sup> and an element operation frequency in excess of 100 GHz.<sup>19</sup>

Nanosensor platforms based on CNTs-FETs have also been developed. Adsorption of species to the surface perturbs the electronic states of the SWNT and causes depletion or accumulation of carriers, effectively gating the channel. Thus, detection of the analyte is observed as a change in conductance between source and drain electrodes. Carbon nanotubes have been heavily explored for their use in gas, biological and chemical sensors because of their very small diameters and their unique property that all of the atoms are on the surface of the tube. This high surface area and quantum wire nature of SWNTs make the conductance very sensitive to the local environment since any local charge could dramatically decrease the carrier concentration along the 1D wire axis. The surface of the nanotube may be modified or functionalized for selectivity or improved sensitivity for the analyte. Preliminary studies on SWNT-sensors were based on detecting changes in conductance in CNT-FETs due to adsorption of gases to the sidewall of the nanotube. Nitrogen dioxide (NO<sub>2</sub>) and ammonia (NH<sub>3</sub>) were the first gases detected by Hongjie Dai's research group at Stanford University.<sup>20</sup> Further research has found that modifying the nanotube with a polymer coating or target/receptor pair can greatly increase sensitivity and selectivity of these nanosensors. The small diameter of nanotubes has also been exploited in biosensors since sizes of 10-100 nm are on the order of the sizes of biological macromolecules. Thus, single-molecule detection may be possible using nanotube sensors.

While the injection of minority charge carriers at the drain contact can make a CNT-FET inoperable as a transistor, it allows for the injection of holes and electrons into the CNT at the same time. By operating the CNT-FET in the OFF state, one can achieve equal amounts of hole and electron current in the nanotube. If the applied drain voltage is further above the turn-on voltage of the transistor, high electron and hole currents are achieved. Electrons that are injected at the source contact can recombine with holes injected at the drain contact, resulting in the emission of a photon. Experimentally, Misewich et al. recently demonstrated that biasing a CNT-FET in the OFF state indeed leads to the emission of polarized infrared light.<sup>21</sup>

Field emission (FE) is a process allowing a device to emit electrons as a result of the application of an electrical field. The extremely sharp geometry of the tube tips makes carbon nanotubes an excellent candidate. In 1995, deHeer and coworkers<sup>22</sup> demonstrated field emission from carbon nanotubes vertically grown on a surface with current densities up to 0.1 mA/cm<sup>2</sup> and a field enhancement factor two orders of magnitude higher than for other materials by applying a few hundred volts. The relatively low voltages needed for FE in CNTs is an advantage in many applications. FE is important

in several areas of industry including lighting and displays. Electron sources may be industrially the most promising application; the field is nearly within reach of practical uses like flat-panel displays and scanning electron displays. In 1999, Choi and coworkers fabricated a fully sealed field emission display 4.5 inches in size using SWNTs.<sup>23</sup>

The mechanical resistance of CNTs is due to one of the strongest bonds in nature. Because of their flexibility, CNTs can be bent repeatedly up to 90° without breaking or damaging them. The exceptional mechanical properties, tensile strength, low density, and high aspect ratio of CNTs find two different applications: the strengthening of fibers in high-performance composite materials, replacing standard C fibers, Kevlar, and glass fibers; and as probes for scanning tunneling microscopes (STMs) and atomic force microscopy (AFM). One of the main challenges is to achieve good adhesion between the CNTs and the matrix, which can be accomplished through covalent coupling. This can be achieved by introducing functional groups to the tube walls, but one has to find an optimum density of functional groups in order to have a sufficient number of connections to the matrix without weakening the stability of the tubes.

Covalent functionalization of SWNTs involves introducing  $sp^3$  hybridized carbon atoms to the graphene sheet. Functionalization occurs at defect sites along the sidewalls and tube ends, which are also easily oxidized to form open tubes. The addition of functional groups such as fluorine,<sup>24</sup> carboxylates,<sup>25</sup> and various organic groups<sup>26</sup> has allowed for improved solubility of SWNTs in different solvents and processability in composite materials. Covalent functionalization may distort or even destroy the unique properties of the perfect  $sp^2$  hybridized graphene sheet, so noncovalent functionalization using polymer wrapping<sup>27</sup> and complexation with surfactants<sup>28</sup> have also been used.

Fibers and yarns are among the most promising forms for using nanotubes on a macroscopic scale, mainly because, in analogy to high-performance polymer fibers, they allow nanotubes to be aligned and then weaved into textile structures or used as cables. In 2000, Vigolo et al.<sup>29</sup> reported a simple method of flow-induced alignment to assemble SWNTs into infinitely long ribbons and fibers. Forcing a SWNT/polyvinyl alcohol (PVA) mixture through a syringe needle achieves the flow-induced alignment. The fibers and ribbons produced had an elastic modulus 10 times higher than the modulus of high-quality bucky paper. These fibers show rather good alignment (Figure 1.8a and b) and can be tied into knots without breaking (Figure 1.8c).

AFM evolved to be one of the most important tools for analyzing surfaces, with the use of CNTs as tips an advancement regarding lateral resolution. The huge aspect ratio allows investigation of samples with deep holes or trenches. Furthermore, due to their elasticity, CNTs allow more gentle investigations of surfaces than standard tips. In 1995, Hongjie Dai and coworkers<sup>30</sup> reported the first example of carbon nanotubes as scanning probe tips. They manually attached MWNTs and ropes of individual SWNTs



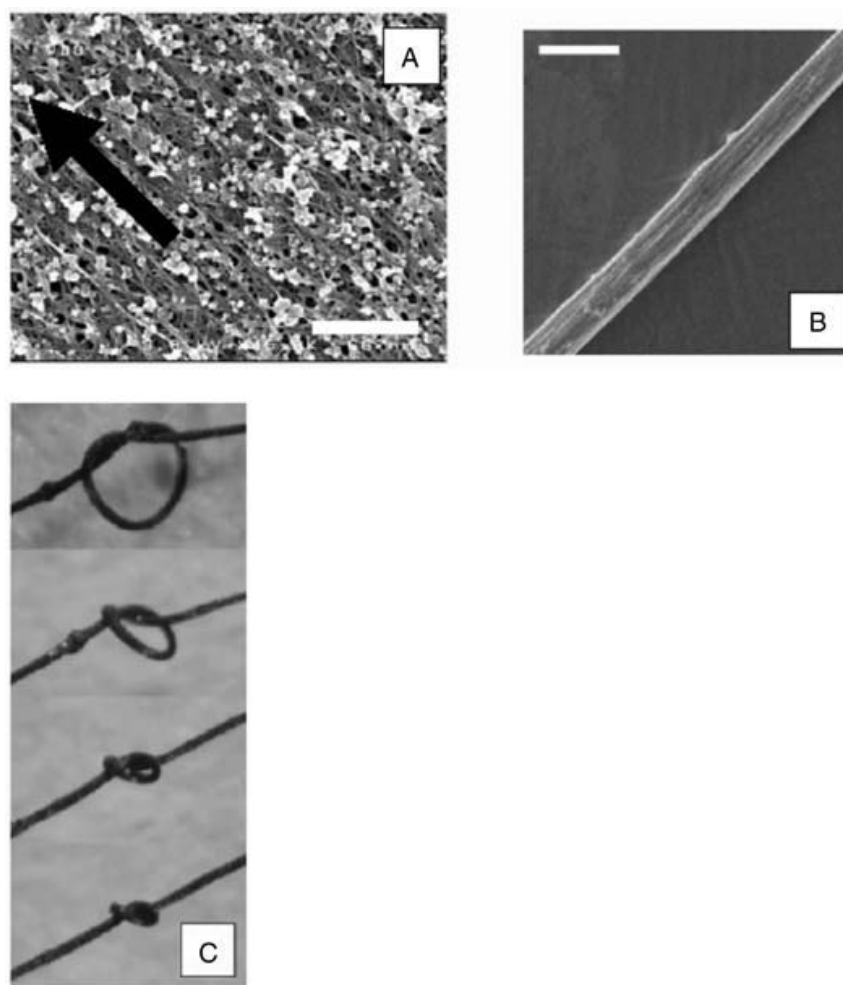


**Figure 1.8** Scanning electron micrographs (SEMs) of a SWNT ribbon (scale bar = 667 nm) (a) and a SWNT fiber (scale bar = 25  $\mu\text{m}$ ) (b), each showing the alignment of the SWNTs within the structure. (c) An optical micrograph of a SWNT fiber tied in a knot showing the high flexibility and resistance to torsion (fiber diameter = 15  $\mu\text{m}$ ). (From B. Vigolo, A. Pénicaud, C. Coulon, C. Sauder, R. Pailler, C. Journet, P. Bernier, and P. Poulin. Macroscopic fibers and ribbons of oriented carbon nanotubes, *Science*, 290, 1331–1334, 2000. Copyright AAAS.)

to the apex of silicon pyramidal tips using tape adhesive and a micromanipulator under an optical microscope.

In 2002, a procedure for suspending individual SWNTs in aqueous/surfactant media was reported by O'Connell et al.<sup>31</sup> Because the noncovalent functionalization separated the SWNTs from each other, fluorescence was observed across the band gap of semiconducting nanotubes (Figure 1.9). This created a new technique for analyzing SWNT samples and opened the door to nanotube applications involving individually dispersed SWNTs in water and various attempts to sort tubes by length, diameter, and electronic properties. The discovery of nanotube fluorescence in the near-infrared (NIR) spectrum also created a potential application for SWNT-based optical sensors. In 2005, Barone et.al. developed a nanotube fluorescence-based sensor for  $\beta$ -D-glucose using the adsorption of specific biomolecules to modulate

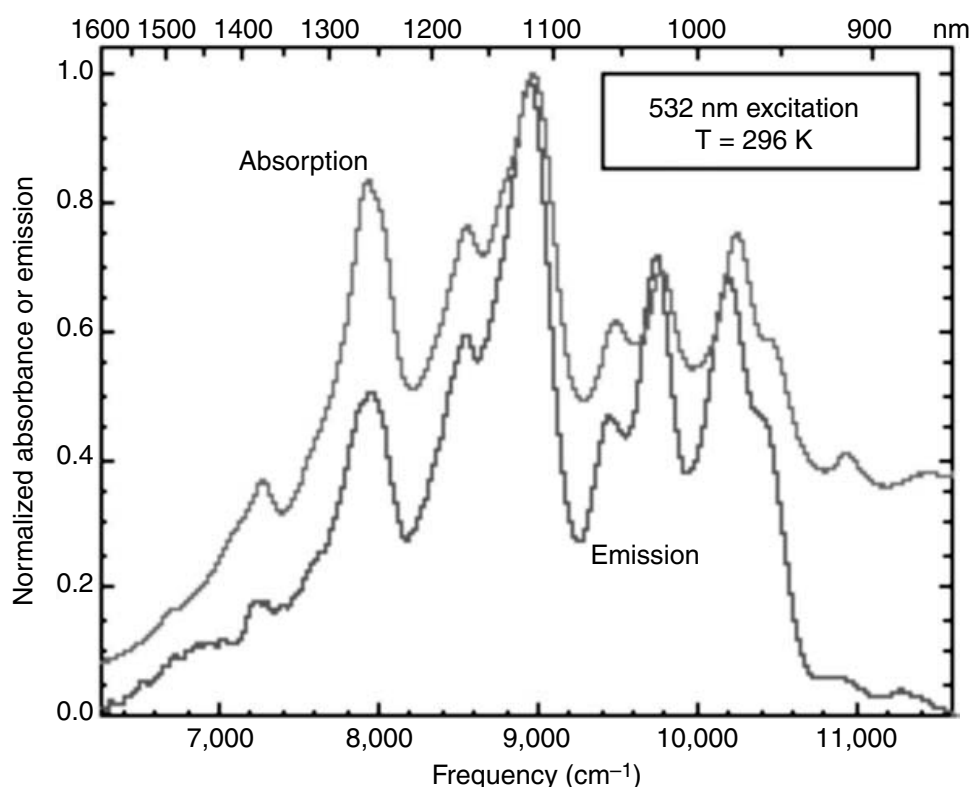


**Figure 1.9** Absorption and emission spectra of the same of individually suspended SWNTs in SDS/D<sub>2</sub>O in the first van Hove transition region. The correspondence demonstrates that the photoluminescence is indeed band gap emission. (From M.J. O'Connell, S.M. Bachilo, C.B. Huffman, V.C. Moore, M.S. Strano, E.H. Haroz, K.L. Rialon, P.J. Boul, W.H. Noon, C. Kittrell, J. Ma, R.H. Hauge, R. Bruce Weisman, and R.E. Smalley. Band gap fluorescence from individual single-walled carbon nanotubes, *Science*, 297, 593–596, 2002.)

the SWNT emission.<sup>32</sup> Recently, Dai and coworkers<sup>33</sup> used the optical absorbance properties of SWNTs to demonstrate the selective destruction of cancer cells. Cancer cells have many surface receptors for folate, so by noncovalently functionalizing SWNTs with folate, SWNTs were able to enter cancerous cells but not the receptor-free healthy ones. Normally, NIR light is harmless to the body, but with radiation from a NIR laser, the cells that internalized SWNTs heated up to 70°C in two minutes and resulted in cell death.

Because of their intrinsic optical properties, nanotubes have been considered potential candidates for drug delivery carriers. The capped ends of nanotubes may be opened up by oxidation, allowing for the insertion of molecules of interest inside the nanotube. Smith et al.<sup>34</sup> observed peapods, SWNTs filled with C<sub>60</sub>, via high-resolution transmission electron microscopy (HRTEM) on samples of purified nanotube material produced by pulsed laser vaporization (Figure 1.10). They also observed coalescence of the end-ofullerenes with extended exposure to the 100-kilovolt electron beam. That these peapods can form suggests that nanotubes may serve as carriers for other encapsulated molecules such as drugs or imaging reagents.

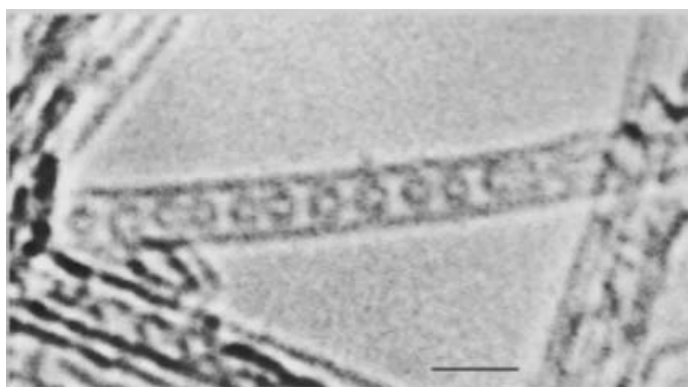


**Figure 1.10** The first published transmission electron micrograph (TEM) of a peapod SWNT filled with C<sub>60</sub> (scale bar = 2 nm). (From B.W. Smith, M. Monthieux, and D.E. Luzzi. Encapsulated C<sub>60</sub> in carbon nanotubes, *Nature*, 396, 323–324, 1998.)

CNTs also have potential for use in energy applications. For heterogenic catalysis, activated coal is very often used as a catalyst carrier substance because it has a high specific surface. Using CNTs as a carrier substance has the advantage that the morphology and the chemical composition of the CNTs are better defined; therefore the covalent connection of the catalyst is better controlled. The potential of using CNTs as catalyst supports has already been investigated. An industrial interest exists in the area of fuel cell electrodes or supported catalysts for fluid phase reactions.

The strong capillarity of CNTs due to their tubular shape, together with their high surface/weight ratio, make CNTs ideal for gas adsorption, and hence for fuel cell applications. There is great interest in small and lightweight hydrogen storage materials. The reports on hydrogen storage in CNTs are still very controversial, and the reversible hydrogen content on the pristine SWNT does not yet satisfy the Department of Energy (DOE) target of 6.5 wt%.

Despite all the progress made on various uses for CNTs, a great deal of research is still focused on fundamental problems that inhibit the use of CNTs for applications. For many applications, the availability of ensembles of CNTs with uniform diameters, length, and electronic properties is important. For example, for electric leads, metallic CNTs are needed, but transistors require semiconducting tubes. To date there is no existing CNT synthesis method that sufficiently allows the control over length, diameter, or the electronic properties of the CNTs. The synthesis products are always a mixture of tubes with a certain length and diameter distribution, and always a mixture of metallic and semiconducting CNTs. Chemical vapor deposition (CVD) proceeds by decomposing carbonaceous gas (hydrocarbons, CO, etc.) on a finely dispersed catalyst. This is the most controllable method for producing CNTs (especially insofar as patterning and alignment are concerned) suitable for mass production and large-area deposition. Thus, CVD yields the most important technique for potential industrial applications.

Postsynthesis separation methods have been developed to try to isolate the correct CNT type for the application at hand. Separating metallic from

semiconducting SWNTs, starting from individual tube suspensions, was first done via dielectrophoresis.<sup>35</sup> The physical method makes use of the different polarizabilities of metallic and semiconducting SWNTs induced by an alternating current (AC) electrical field. Theoretically, it was expected that the dielectric constant of semiconducting SWNTs is of the order of  $5 \cdot \epsilon_0$ , compared to  $80 \cdot \epsilon_0$  for aqueous surfactant solution. For metallic SWNTs, the dielectric constant should be at least of the order of  $1000 \cdot \epsilon_0$ . The dielectric constants of semiconducting and metallic SWNTs, being smaller and larger than that of water, respectively, give access to separating the two tube types by exposing them to a strong and inhomogeneous electrical field. The interaction of the induced dipole moment with the inhomogeneous external field leads to a movement of the metallic tubes toward the high field region, whereas the semiconducting tubes move in the opposite direction, toward the low field region.

More easily scalable would be a chemical access to separate metallic from semiconducting SWNTs. Indeed, Strano and coworkers reported that diazonium reagents, under carefully controlled conditions, primarily react with metallic SWNTs.<sup>36</sup> The metallic tubes are not yet separated from the semiconducting ones, but have been modified chemically. Having found a chemistry that appears to be selective toward primarily metallic SWNTs, it is now the challenge to extract the metallic tubes from the still-mixed suspension.

After solving serious problems like the above mentioned, there are still remaining questions concerning manipulating individual CNTs. A major problem in the realization of electronic circuits is the difficulty to wire up carbon nanotubes, i.e., to position and contact them in a controlled way. To overcome these problems, several attempts have been tried, including dielectrophoresis (controlled deposition of individual tubes with alternating current fields), catalytic growth of CNTs (a CVD synthesis where CNTs are grown on silicon from predeposited catalyst islands), and self-assembling on chemically modified surfaces (a process using chemically modified silicon surfaces for the selective deposition of carbon nanotubes). The most elegant way would be to selectively grow tubes at the location desired, with controllable length and diameter. In 2003, Huang et al.<sup>37</sup> reported millimeters-long, horizontally aligned growth of SWNTs on silicon oxide surfaces with no external force like electric or magnetic fields. This growth method involves rapidly inserting a sample of catalyst on a room temperature surface into a hot oven. The catalyst lifts off the surface and grows in the gas phase, which aligns the tubes horizontally and allows for long growth. This is a major step toward controlling the arrangement of SWNTs for the fabrication of nanotube devices. Most recently in 2004, Hata et al.<sup>38</sup> reported the aligned, vertical growth of SWNTs up to 2.5 mm tall (Figure 1.11).

Carbon nanotube research has progressed at an amazing rate considering the existence of these molecules has not been known for very long. Carbon nanotechnology has captured the interest of the world with its unique and interesting properties and broad range of applications. The following



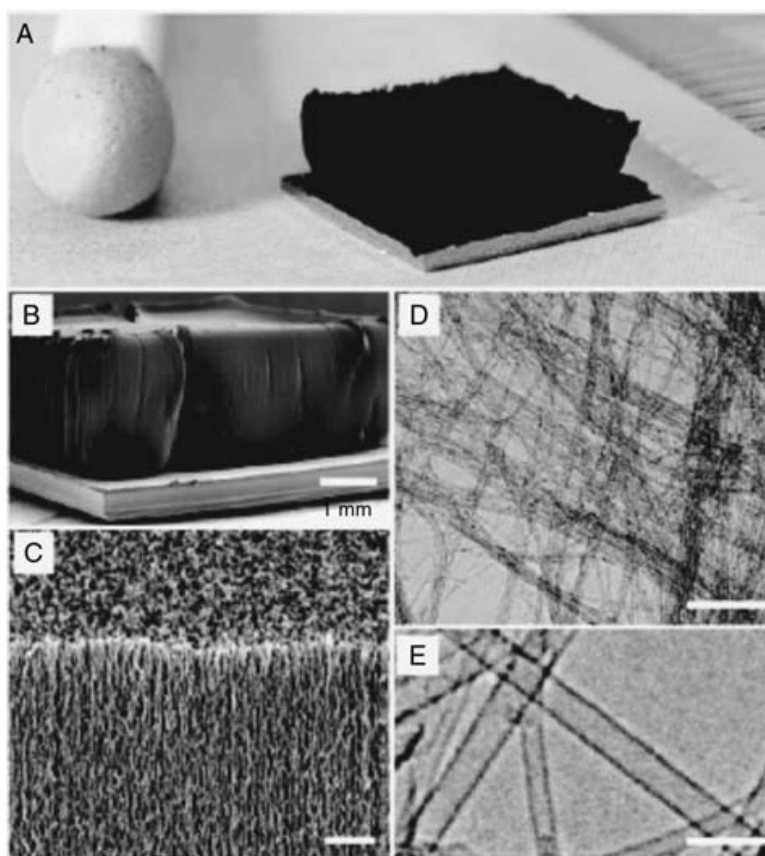


**Figure 1.11** (a) SWNT forest grown with water-assisted CVD. Picture of a 2.5-mm-tall SWNT forest on a  $7 \times 7$  mm silicon wafer. A matchstick on the left and ruler in millimeter markings on the right are for size references. (b) Scanning electron microscopy (SEM) image of the same SWNT forest. Scale bar, 1 mm. (c) SEM image of the SWNT forest ledge. Scale bar,  $1 \mu\text{m}$ . (d) Low-resolution TEM image of the nanotubes. Scale bar, 100 nm. (e) High-resolution TEM image of the SWNTs. Scale bar, 5 nm. (From K. Hata, D.N. Futaba, K. Mizuno, T. Namai, M. Yumura, and S. Iijima. Water-assisted highly efficient synthesis of impurity-free single-walled carbon nanotubes, *Science*, 306, 1362–1364, 2004. Copyright AAAS.)

chapters in this book discuss in more detail some of the topics reviewed in this introductory chapter.

## References

1. [http://smalley.rice.edu/smalley.cfm?doc\\_id=4866](http://smalley.rice.edu/smalley.cfm?doc_id=4866)
2. H. W. Kroto, J. R. Heath, S. C. O'Brien, R. F. Curl, and R. E. Smalley. C-60-Buckminsterfullerene, *Nature*, 318, 162–163, 1985.
3. M. S. Dresselhaus, G. Dresselhaus, and R. Saito. Physics of carbon nanotubes, *Carbon*, 33, 883–91, 1995.
4. R. E. Smalley. Formation and properties of  $\text{C}_{60}$  and the fullerenes, National Institute of Standards and Technology, Dec. 6–7, 1990.
5. M. S. Dresselhaus. Oral presentation at fullerene workshop, University of Pennsylvania, 1991.

6. S. Iijima. Helical microtubules of graphitic carbon, *Nature*, 354, 56–58, 1991.
7. S. Iijima and T. Ichihashi. Single-shell carbon nanotubes of 1-nm diameter, *Nature*, 363, 603–605, 1993.
8. D. S. Bethune, C. H. Klang, M. S. de Vries, G. Gorman, R. Savoy, J. Vazquez, and R. Beyers. Cobalt-catalysed growth of carbon nanotubes with single-atomic-layer walls, *Nature*, 363, 605–607, 1993.
9. R. Bacon. Growth, structure, and properties of graphite whiskers, *Journal of Applied Physics*, 31, 283–290, 1960.
10. A. Oberlin, M. Endo, and T. Koyama. Filamentous growth of carbon through benzene decomposition, *Journal of Crystal Growth*, 32, 335–349, 1976.
11. A. M. Rao, E. Richter, S. Bandow, B. Chase, P. C. Eklund, K. A. Williams, S. Fang, K. R. Subbaswamy, M. Menon, A. Thess, R. E. Smalley, G. Dresselhaus, and M. S. Dresselhaus. Diameter-selective raman scattering from vibrational modes in carbon nanotubes, *Science*, 275, 187–191, 1997.
12. H. Kataura, Y. Kumazawa, Y. Maniwa, I. Umez, S. Suzuki, Y. Ohtsuka and Y. Achiba. Optical properties of single-wall carbon nanotubes, *Synthetic Metals*, 103, 2555–2558, 1991.
13. S. J. Tans, M. H. Devoret, H. Dai, A. Thess, R. E. Smalley, L. J. Geerligs, and C. Dekker. Individual single-wall carbon nanotubes as quantum wires, *Nature*, 386, 474–477, 1997.
14. S. J. Tans, A. R. M. Verschueren, and C. Dekker. Room-temperature transistor based on a single carbon nanotube, *Nature*, 393, 49–52, 1998.
15. R. Martel, T. Schmidt, H. R. Shea, T. Hertel, and P. Avouris. Single- and multi-wall carbon nanotube field-effect transistors, *Applied Physics Letters*, 73, 2447–2449, 1998.
16. P. G. Collins, M. S. Arnold, and P. Avouris. Engineering carbon nanotubes and nanotube circuits using electrical breakdown, *Science*, 292, 706–709, 2001.
17. A. Javey, J. Guo, Q. Wang, M. Lundstrom, and H. Dai. Ballistic carbon nanotube field-effect transistors, *Nature*, 424, 654–657, 2003.
18. M. Kociak, A. Yu. Kasumov, S. Guéron, B. Reulet, I. I. Khodos, Yu. B. Gorbatov, V. T. Volkov, L. Vaccarini, and H. Bouchiat. Superconductivity in ropes of single-walled carbon nanotubes, *Physical Review Letters*, 86, 2416–2419, 2001.
19. T. Rueckes, K. Kim, E. Joselevich, G. Y. Tseng, C. L. Cheung, and C. M. Lieber. Carbon nanotube-based nonvolatile random access memory for molecular computing, *Science*, 289, 94, 2000.
20. J. Kong, N. R. Franklin, C. W. Zhou, M. G. Chapline, S. Peng, K. J. Cho, and H. J. Dai. Nanotube molecular wires as chemical sensors, *Science*, 287, 622, 2000.
21. J. Misewich, R. Martel, P. Avouris, J. C. Tsang, S. Heinze, and J. Tersoff. Electrically induced optical emission from a carbon nanotube FET, *Science*, 300, 783, 2003.
22. W. A. de Heer, A. Châtelain, and D. Ugarte. A carbon nanotube field-emission electron source, *Science*, 270, 1179–1180, 1995.
23. W. B. Choi, D. S. Chung, J. H. Kang, H. Y. Kim, Y. W. Jin, I. T. Han, Y. H. Lee, J. E. Jung, N. S. Lee, G. S. Park, and J. M. Kim. Fully sealed, high-brightness carbon nanotube field-emission display, *Applied Physics Letters*, 75, 3129–3131, 1999.
24. E. T. Mickelson, C. B. Huffman, A. G. Rinzler, R. E. Smalley, R. H. Hauge, and J. L. Margrave. Fluorination of single-wall carbon nanotubes, *Chemical Physics Letters*, 296, 188–194, 1998.

25. H. Peng, L. B. Alemany, J. L. Margrave, and V. N. Khabashesku. Sidewall carboxylic acid functionalization of single-walled carbon nanotubes, *Journal of the American Chemical Society*, 125, 15174–15182, 2003.
26. Dyke, C. A. and Tour, J. M. Feature Article: Covalent Functionalization of Single-Walled Carbon Nanotubes for Materials Applications, *J. Phys. Chem. A.*, 108, 11151–11159, 2004.
27. M. J. O'Connell, P. Boul, L. M. Ericson, C. Huffman, Y. H. Wang, E. Haroz, C. Kuper, J. Tour, K. D. Ausman, and R. E. Smalley. Reversible water-solubilization of single-walled carbon nanotubes by polymer wrapping, *Chemical Physics Letters*, 342, 265–271, 2001.
28. V. C. Moore, M. S. Strano, E. H. Haroz, R. H. Hauge, R. E. Smalley, J. Schmidt, and Y. Talmon. Individually suspended single-walled carbon nanotubes in various surfactants, *Nano Letters*, 3, 1379–1382, 2003.
29. B. Vigolo, A. Pénicaud, C. Coulon, C. Sauder, R. Pailler, C. Journet, P. Bernier, and P. Poulin. Macroscopic fibers and ribbons of oriented carbon nanotubes, *Science*, 290, 1331–1334, 2000.
30. H. Dai, J. H. Hafner, A. G. Rinzler, D. T. Colbert, R. E. Smalley. Nanotubes as nanoprobe in scanning probe microscopy, *Nature*, 384, 147–150, 1996.
31. M. J. O'Connell, S. M. Bachilo, C. B. Huffman, V. C. Moore, M. S. Strano, E. H. Haroz, K. L. Rialon, P. J. Boul, W. H. Noon, C. Kittrell, J. Ma, R. H. Hauge, R. Bruce Weisman, and R. E. Smalley. Band gap fluorescence from individual single-walled carbon nanotubes, *Science*, 297, 593–596, 2002.
32. P. W. Barone, S. Baik, D. A. Heller, and M. S. Strano. Near-infrared optical sensors based on single-walled carbon nanotubes, *Nature Materials*, 4, 86–92, 2005.
33. N. W. S. Kam, M. O'Connell, J. A. Wisdom, and H. Dai. Carbon nanotubes as multifunctional biological transporters and near-infrared agents for selective cancer cell destruction, *Proceedings of the National Academy of Sciences of the USA*, 102, 11600, 2005.
34. B. W. Smith, M. Monthieux, and D. E. Luzzi. Encapsulated C<sub>60</sub> in carbon nanotubes, *Nature*, 396, 323–324, 1998.
35. R. Krupke, F. Hennrich, H. v. Löhneysen, and M. M. Kappes. Separation of metallic from semiconducting single-walled carbon nanotubes, *Science*, 301, 344, 2003.
36. M. S. Strano, C. A. Dyke, M. L. Usrey, P. W. Barone, M. J. Allen, H. W. Shan, C. Kittrell, R. H. Hauge, J. M. Tour, and R. E. Smalley. Electronic structure control of single-walled carbon nanotube functionalization, *Science*, 301, 1519, 2003.
37. S. Huang, X. Cai, and J. Liu. Growth of millimeter-long and horizontally aligned single-walled carbon nanotubes on flat substrates, *Journal of the American Chemical Society*, 125, 5636–5637, 2003.
38. K. Hata, D. N. Futaba, K. Mizuno, T. Namai, M. Yumura, and S. Iijima. Water-assisted highly efficient synthesis of impurity-free single-walled carbon nanotubes, *Science*, 306, 1362–1364, 2004.

## *chapter two*

---

# *Synthesis of carbon nanotubes*

*David Mann*  
*Stanford University*

### *Contents*

2.1	Introduction .....	20
2.2	CNT synthesis methods overview .....	23
2.2.1	Arc discharge synthesis.....	23
2.2.2	Laser ablation synthesis .....	26
2.2.3	Thermal synthesis .....	27
2.2.3.1	Chemical vapor deposition.....	27
2.2.3.2	High-pressure carbon monoxide synthesis.....	28
2.2.3.3	Flame synthesis.....	28
2.2.4	PECVD synthesis.....	29
2.3	Specifics of CVD growth method .....	30
2.3.1	Growth mechanics .....	30
2.3.2	Carbon feedstock.....	33
2.3.3	Catalyst .....	34
2.3.3.1	Unsupported catalyst.....	35
2.3.3.2	Supported catalyst.....	35
2.3.3.3	Vapor phase catalyst .....	36
2.4	Recent advances in SWCNT growth control.....	37
2.4.1	Location and orientation control .....	37
2.4.1.1	Catalyst patterning .....	37
2.4.1.2	Suspended aligned SWCNTs.....	38
2.4.1.3	Aligned SWCNTs on substrates.....	39
2.4.2	Growth of ultralong SWCNTs.....	39
2.4.3	Water-assisted high-yield growth of SWCNTs.....	40
2.4.4	Diameter and chirality control.....	40

2.4.4.1	Nanoparticle production for narrow-diameter SWCNTs .....	41
2.4.4.2	CoMoCAT: chirality selectivity in bulk production of SWCNTs .....	41
2.4.4.3	PECVD production of narrow-diameter and chirality SWCNTs .....	42
2.5	Conclusion.....	42
	References.....	42

## 2.1 Introduction

There have been numerous reviews on the synthesis of carbon nanotubes, which are members of the fullerene family.<sup>1-4</sup> This chapter is meant to update and distill the information from these reviews and the newest synthesis-related papers.

Since their discovery, carbon nanotubes have been of great interest, both for the elucidation of fundamental one-dimensional science and for a wide variety of potential applications. Though Iijima was credited for recognizing carbon nanotubes in 1991,<sup>5</sup> the first nanotubes were produced much earlier, possibly as a result of Roger Bacon's work studying carbon whiskers in 1960.<sup>6</sup> Nanotubes were probably first observed directly by Endo in the 1970s via high-resolution transmission electron microscopy (HRTEM) when he was exploring the production of carbon fibers by pyrolysis of benzene and ferrocene at 1000°C,<sup>7,8</sup> and Tibbetts also imaged some nanotube-like material in 1984.<sup>9</sup> However, Iijima was first to recognize that nanotubes were made up of concentric rolled graphene sheets with a large number of potential helicities and chiralities, rather than a graphene sheet rolled up like a scroll, as originally proposed by Bacon. Iijima and Ichihashi initially observed only multiwalled carbon nanotubes (MWCNTs) (Figure 2.1) with between 2 and 20 layers, but in a subsequent publication he confirmed the existence of single-walled carbon nanotubes (SWCNTs) (Figure 2.2) in 1993,<sup>10</sup> where he describes the varying chiralities of different individual SWCNTs (Figure 2.3).<sup>\*</sup> SWCNTs were independently observed by Bethune et al. in the same issue of *Nature*.<sup>11</sup>

Most early mechanical, thermal, and electrical measurements were carried out on MWCNTs long before SWCNTs. This is in part because MWCNTs proved themselves far easier to manufacture in large scale than SWCNTs, and are thus farther along in terms of material development. In fact, the first mass production of MWCNTs was reported less than a year after Iijima's 1991 publication by Ebbesen and Ajayan.<sup>12</sup> They tuned the arc discharge synthesis method used by Bacon and Iijima to produce several grams of

\* Chirality refers to the rolling axis of the graphite sheet, which has a profound effect on the electrical properties of the SWCNT, and is discussed in detail in the introduction and in the chapter on SWCNT devices. Assuming a random chirality distribution, ~67% of SWCNTs are semiconductors and 33% are semimetal or metallic.



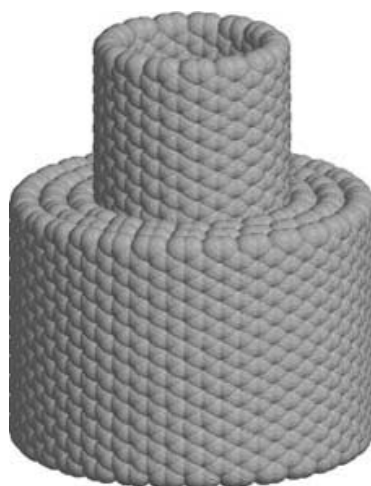


**Figure 2.1** Cartoon of a multiwalled nanotube.

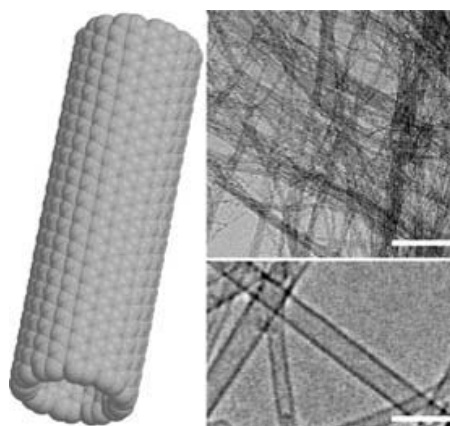


**Figure 2.2** Cartoon of a single-walled nanotube and two TEM images of SWCNTs. Scale bar of top image is 100 nm, bottom image is 5 nm. (Reprinted with permission of Hata, K. et al., Water-assisted highly efficient synthesis of impurity-free single-walled carbon nanotubes, *Science* 306, 1362–1364, 2004.)

~75% pure MWCNTs. This production advance opened the door to wide-scale study of this remarkable material, and it was discovered that MWCNTs outperform conventional materials in many fields, most notably in their field emission properties.<sup>13</sup> Currently, Motorola, as well as a few other companies, have a prototype MWCNT-based television display. MWCNTs in bulk have already been used to strengthen many polymers and materials more effectively and at lower concentrations than the carbon fibers that preceded them. There are literally hundreds of publications about various nanotube composites, and there are many extensive review articles on the topic, including, though not limited to, the ones referenced here.<sup>14–16</sup> The cost of bulk MWCNT material is fairly low, and they can be purchased from many chemical companies. One can also purchase vertical MWCNT forests for field emission applications on a variety of substrates. Thus, in many ways, MWCNTs are already well on their way to mass production and

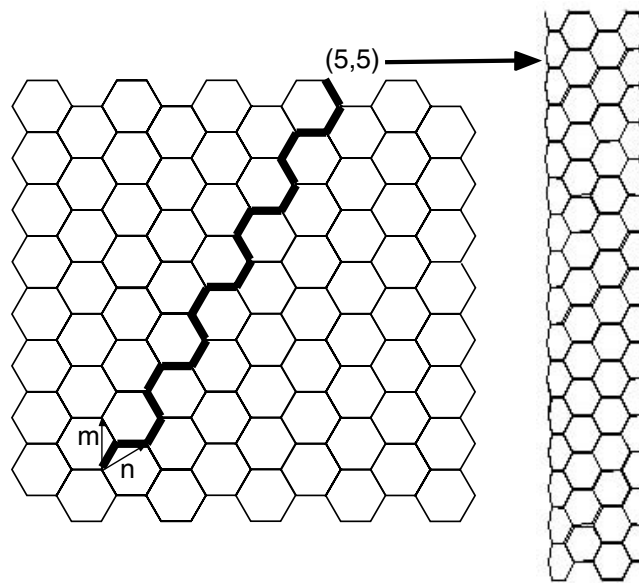


**Figure 2.3** Graphene sheet with chiral vectors  $n$  and  $m$ . All single-walled nanotube chiralities can be defined by these two chiral vectors. The electrical properties of each can be determined by the chirality. For example, when  $m = n$ , the SWCNT is an armchair tube, and when  $n = 0$ , the SWCNT is a zigzag tube (so named for the shape of the end). All other tubes are termed chiral. If  $m - n = 3q$ , where  $q$  is an integer, then the nanotube is metallic (this includes armchair tubes where  $m = n$ ). In all other cases, the nanotube is semiconducting with a band gap that varies as  $1/\text{diameter}$ .

utilization for a wide variety of applications. It should be noted that even contemporary MWCNT material still has a fairly high defect density, and any crystalline improvements will only serve to heighten the utility of MWCNTs.

Currently the vast majority of research is being carried out on SWCNTs, since ultimately SWCNTs can be produced with a much higher crystalline quality than MWCNTs. The resulting material approaches the theoretical predictions for mechanical strength and thermal and electrical conductivity. Recently, freestanding vertical forests of SWCNTs have been produced, leading to the possibility of even better field emission than MWCNTs.<sup>17,18</sup> The primary obstacle for large-scale use as thermal and mechanical enhancers is cost. Even with numerous advances in the last 10 years, purified SWCNTs remain significantly more expensive than MWCNTs ( $\sim \$500/\text{g}$  of SWCNT vs.  $\sim \$10/\text{g}$  of MWCNT). As growth methods improve and yields and purity increase, this cost difference can be expected to decrease. Smalley at Rice University has recently built a large high-pressure carbon monoxide (HiPco) reactor that can produce several grams an hour of fluffy black powder consisting of  $\sim 90\%$  pure SWCNT. Continuous SWCNT “yarn” can now be spun directly from a specially designed vertical reactor.<sup>19</sup> A recent advance by Hata et al.<sup>17</sup> may lower the cost of bulk SWCNTs several times, producing 99.97% SWCNTs using a simple chemical vapor deposition (CVD) reactor. Integration of these extremely efficient and high-quality growths with

specialized reactors designed for continual output promises to make bulk SWCNTs a mainstream industrial material.

SWCNTs also have extraordinary, and widely varying, individual properties, which have led to the demonstration of ultrafast electronics<sup>20,21</sup> and highly sensitive chemical and biological sensors.<sup>22–24</sup> In order to bring these impressive proofs of concept to market, it is vital to be able to precisely control the synthesis of SWCNTs in several ways, or develop a suitable aftergrowth purification method that is selective for certain types of SWCNTs. In terms of increased growth-related control, CVD is considered to be the most promising form of CNT synthesis. CVD allows the production of nanotubes to occur at predetermined locations via patterning,<sup>25</sup> and well-oriented arrays are possible through gas flow or electric field alignment.<sup>26–28</sup> While this is an attractive start, many electronic and sensor applications require specific diameters and chirality of SWCNTs. Though there have been numerous inroads in the production of narrow diameters of SWCNTs, only one synthesis method<sup>29</sup> has thus far resulted in a nonrandom distribution of chiralities (90% vs. ~67% semiconducting SWCNTs).

## 2.2 CNT synthesis methods overview

CNT synthesis has been shown to occur in a wide range of environments. Whether near the focus of a high-powered laser,<sup>30</sup> in between two arcing graphite electrodes,<sup>5</sup> in a hot furnace full of hydrocarbon gas,<sup>31</sup> or even in the middle of a flame,<sup>32</sup> nanotubes form, given the right conditions (Table 2.1). The basic prerequisites for the formation of SWCNTs are an active catalyst, a source of carbon, and adequate energy.

### 2.2.1 Arc discharge synthesis

Arc discharge was the first recognized method for producing both SWCNTs and MWCNTs, and has been optimized to be able to produce gram quantities of either. The method is similar to the Kratschmer–Huffman method of generating fullerenes and the procedure to make carbon whiskers developed by Roger Bacon over 30 years ago (Figure 2.4).<sup>6</sup> Arc discharge synthesis uses a low-voltage (~12 to 25 V), high-current (50 to 120 amps) power supply (an arc welder can be used). An arc is produced across a 1-mm gap between two graphite electrodes 5 to 20 mm in diameter. An inert gas such as He or Ar is used as the atmosphere for the reaction, at a pressure of 100 to 1000 torr. Iijima produced the first MWCNTs by this method.<sup>5</sup> He found that nanotubes formed on the cathode, along with soot and fullerenes. Iijima and Ichihashi and Bethune et al. were the first to report on the production of SWCNTs.<sup>10,11</sup> Both Iijima and Bethune found that SWCNTs could only form by adding metal catalyst to the anode; specifically, Iijima used an Fe:C anode in a methane:argon environment, while Bethune utilized a Co:C anode with a He environment. There are several variations one can make to tailor the arc discharge process. Currently, most growth is carried out in an Ar:He gas



**Table 2.1** List of Notable Accomplishments in SWCNT Synthesis

Date	Authors	Method	Conditions	Temperature (Celsius)	Catalyst	Comments
1993	Iijima <sup>10</sup> Bethune <sup>11</sup>	Arc discharge	50–500 Torr CH <sub>4</sub> /Ar or He	>2500	Fe or Co in carbon	First confirmed SWCNT production
1996	Thess et al. <sup>30</sup>	Laser ablation	500 Torr Ar	Furnace @ 1200 (target at >2500)	Ni/Co in Carbon	First laser ablation, high yield
1996	Dai et al. <sup>31</sup>	CVD	CO @ 1.1 atm	1200	Mo, Co/Ni	First SWCNT CVD growth
1998	Kong et al. <sup>25,99</sup>	CVD	CH <sub>4</sub> @ 1.25-atm inlet	1000	Fe/Al <sub>2</sub> O <sub>3</sub>	First patterned-substrate growth
1999	Cassell et al. <sup>69</sup>	CVD	CH <sub>4</sub> @ 1.25-atm inlet	900–1000	Fe/Mo/Al <sub>2</sub> O <sub>3</sub>	First large-scale bulk CVD synthesis of SWCNT
1999	Nikolaev et al. <sup>37</sup>	CVD (HiPco)	CO @ 10 atm	1200	Fe(CO) <sub>5</sub> vapor	Demonstration of HiPco SWCNTs (later P ~ 30–50 atm)
2000	Vander Wal et al. <sup>41,100</sup>	Flame	N <sub>2</sub> /Ar/air + C <sub>2</sub> H <sub>2</sub> or C <sub>2</sub> H <sub>4</sub>	900–1400 in flame	Metallocene	First flame synthesis of SWCNTs
2000	Kitiyanan et al. <sup>67</sup> Bachilo et al. <sup>94</sup>	CVD	CO @ 1 atm	700	Co/Mo/silica	Demonstration of CoMoCAT: diameter control in bulk catalyst
2001	Li et al. <sup>52</sup>	CVD	CH <sub>4</sub> @ 1 atm	900	Fe/Ferritin	Diameter-selective substrate synthesis from predefined nanoparticles
2001	Ural et al. <sup>27</sup> Zhang et al. <sup>28</sup>	CVD	CH <sub>4</sub> + H <sub>2</sub> @ 1 atm	900	Fe/Mo/silica	First aligned SWCNT growth: E-field alignment (substrate aligned in 2002)

2002	Maruyama et al. <sup>63</sup>	CVD	$C_2H_5OH$ or $CH_3OH$ @ 5–10 Torr	550–900	Fe/Co (Co/ Mo)	First growth from alcohol; low temperature; first proposition of amorphous carbon etchant (OH) during growth First ultralong SWCNTs (>400 $\mu m$ ) Aligned SWCNTs from gas flow utilizing fast heating and tip growth (>1 mm) First PECVD of SWCNTs
2002	Kim et al. <sup>61</sup>	CVD	$CH_4 + H_2 + C_2H_4$ @ 1 atm	900	Fe/Ferritin	
2003	Huang et al. <sup>26</sup>	CVD	$CO + H_2$ @ 1 atm	900	Fe/Mo	
2003	Kato et al. <sup>48</sup>	PECVD	$CH_4 + H_2$ @ 500 mT	550–850	Fe/Co/ zeolite	
2004	Li et al. <sup>29</sup>	Remote PECVD	$CH_4 + Ar$ in plasma @ 500 mT	550–750	Fe	Preferential low T growth of semiconducting SWCNTs in PECVD
2004	Murakami et al. <sup>18</sup>	CVD	$C_2H_5OH$ in Ar/ $H_2$	800	Co/Mo	First vertical SWCNT films (<15 $\mu m$ tall)
2004	Hata et al. <sup>17</sup>	CVD	$C_2H_4 + Ar + H_2O$ @ 1 atm	750	Fe, Co/Mo, Fe/Mo	2.5-mm vertical SWCNT growth; ultrahigh yield; controlled use of $H_2O$ as amorphous carbon etchant

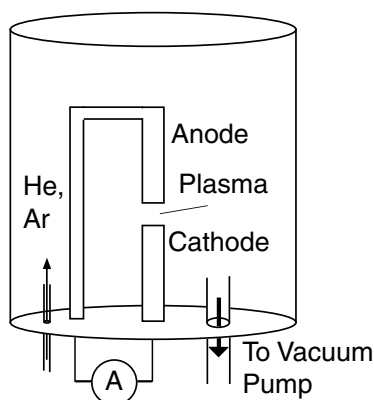


Figure 2.4 Schematic of an arc discharge chamber.

mixture. By tailoring the Ar:He gas ratio, the diameter of the SWCNTs formed can be controlled, with greater Ar yielding smaller diameters.<sup>33</sup> The anode–cathode distance can be changed to vary the strength of the plasma formed in between. The overall gas pressure has been shown to affect the weight percent yield of SWCNTs.<sup>34</sup> Several metal catalyst compositions produce SWCNTs, but the current standard widely used for SWCNT production is a Y:Ni mixture that has been shown to yield up to 90% SWCNT, with an average diameter of 1.2 to 1.4 nm.<sup>35</sup> In general, the nanotubes produced by this synthesis method need extensive purification before use. On the other hand, both SWCNTs and MWCNTs made from this process are now commercially available relatively inexpensively, and have been for several years.

### 2.2.2 Laser ablation synthesis

The first large-scale (gram quantities) production of SWCNTs was achieved in 1996 by the Smalley group at Rice University (Figure 2.5).<sup>30</sup> The laser ablation technique uses a 1.2 at. % of cobalt/nickel with 98.8 at.% of graphite composite target that is placed in a 1200°C quartz tube furnace with an inert atmosphere of ~500 Torr of Ar or He and vaporized with a laser pulse. A pulsed- or continuous-wave laser can be used. Nanometer-size metal catalyst particles are formed in the plume of vaporized graphite. The metal particles catalyze the growth of SWCNTs in the plasma plume, but many by-products are formed at the same time. The nanotubes and by-products are collected via condensation on a cold finger downstream from the target. The yield

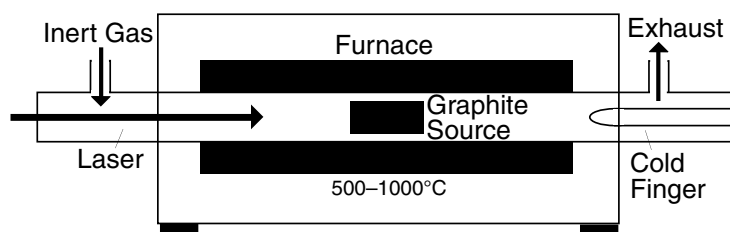


Figure 2.5 Schematic of a laser ablation furnace.

varies from 20 to 80% of SWCNTs by weight. The by-products of this synthesis are graphitic and amorphous carbon, “bucky onions” (concentric fulleroid spheres) surrounding metal catalyst particles and small fullerenes (C<sub>60</sub>, C<sub>70</sub>, etc.). In principle, arc discharge and laser ablation are similar methods, as both use a metal-impregnated graphite target (or anode) to produce SWCNTs, and both produce MWCNT and fullerenes when pure graphite is used instead. The diameter distribution of SWCNTs made by this method is roughly between 1.0 and 1.6 nm.

### 2.2.3 Thermal synthesis

Thermal synthesis is considered a “medium temperature” method, since the hot zone of the reaction never reaches above 1200°C. Fundamentally different from plasma-based synthesis, thermal synthesis relies on only thermal energy and, in almost all cases, on active catalytic species such as Fe, Ni, and Co to break down carbon feedstock and produce CNTs. Depending on the carbon feedstock, Mo and Ru are sometimes added as promoters to render the feedstock more active for the formation of CNTs. CVD, HiPco, and flame synthesis are considered thermal CNT synthesis methods.

#### 2.2.3.1 Chemical vapor deposition

CVD was first reported to produce defective MWCNTs in 1993 by Endo et al.<sup>36</sup> In 1996 Dai in Smalley’s group successfully adapted CO-based CVD to produce SWCNT at Rice University.<sup>32</sup> The CVD process encompasses a wide range of synthesis techniques, from the gram-quantity bulk formation of nanotube material to the formation of individual aligned SWCNTs on SiO<sub>2</sub> substrates for use in electronics. CVD can also produce aligned vertical MWCNTs for use as high-performance field emitters.<sup>13</sup> Additionally, CVD in its various forms produces SWCNT material of higher atomic quality and higher percent yield than the other methods currently available and, as such, represents a significant advance in SWCNT production. The majority of SWCNT production methods developed lately have been direct descendents of basic CVD. Simply put, gaseous carbon feedstock is flowed over transition metal nanoparticles at medium to high temperature (550 to 1200°C) and reacts with the nanoparticles to produce SWCNTs (Figure 2.6). With CVD,

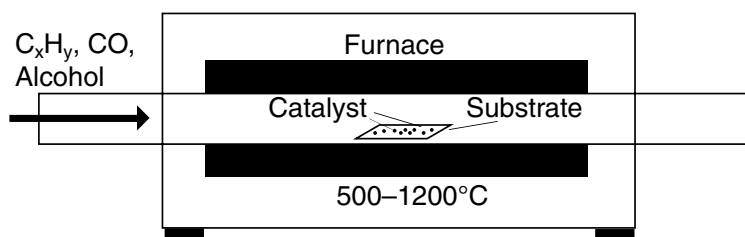
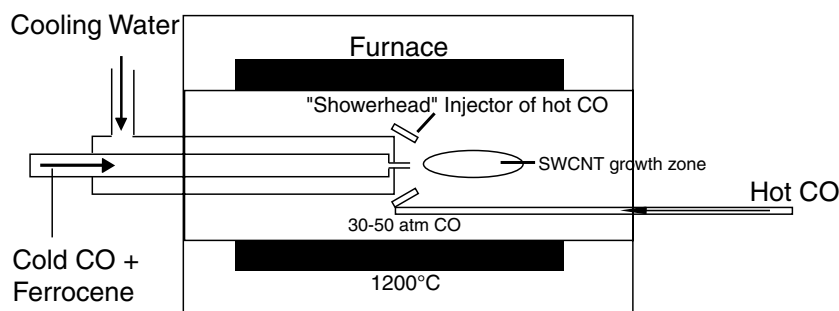


Figure 2.6 Schematic of a CVD furnace.



**Figure 2.7** Schematic of a HiPco furnace. The CO gas + catalyst precursor is injected cold into the hot zone of the furnace, while excess CO gas is “showered” on it from all sides. Empirically this leads to the highest yield and longest individual nanotubes formed by this process.

SWCNTs anywhere from 0.4 to 5 nm can be readily produced, and depending on the conditions, feedstock, and catalyst, the yield can exceed 99% (weight percent of final material) and the final product can be completely free of amorphous carbon. Due to its promise and its breadth, the remaining sections (Sections 2.3 and 2.4) of this chapter will be devoted to CVD synthesis.

### 2.2.3.2 High-pressure carbon monoxide synthesis

One of the recent methods for producing SWCNTs in gram to kilogram quantities is the HiPco process (Figure 2.7).<sup>37,38</sup> Though related to CVD synthesis, HiPco deserves a separate mention, since in recent years it has become a source of high-quality, narrow-diameter distribution SWCNTs around the world. The metal catalyst is formed *in situ* when  $\text{Fe}(\text{CO})_5$  or  $\text{Ni}(\text{CO})_4$  is injected into the reactor along with a stream of carbon monoxide (CO) gas at 900 to 1100°C and at a pressure of 30 to 50 atm. The reaction to make SWCNTs is the disproportionation of CO by nanometer-size metal catalyst particles. Yields of SWCNT material are claimed to be up to 97% atomic purity. The SWCNTs made by this process have diameters between 0.7 and 1.1 nm. By tuning the pressure in the reactor and the catalyst composition, it is possible to tune the diameter range of the nanotubes produced.<sup>39</sup>

### 2.2.3.3 Flame synthesis

Though still not a viable method for the production of high-quality SWCNTs, so-called flame synthesis has the potential to become an extremely cheap and simple way to produce nanotubes. Flames have been shown to produce MWCNTs since the early 1990s.<sup>40</sup> First exhibited for the production of SWCNTs by Vander Wal et al., a hydrocarbon flame composed of ~10% ethylene or acetylene with Fe or Co (cobaltacene, ferrocene, cobalt acetylacetonate) particles interspersed and diluted in  $\text{H}_2$  and either He or Ar was ignited by the researchers. Since then, many groups have been able to produce SWCNTs,<sup>41–46,101</sup> and there has been a brief review written by Height et al. on the specifics of various methods for both MWCNT and SWCNT production.<sup>32</sup> The current yields are low, but it is extremely attractive and



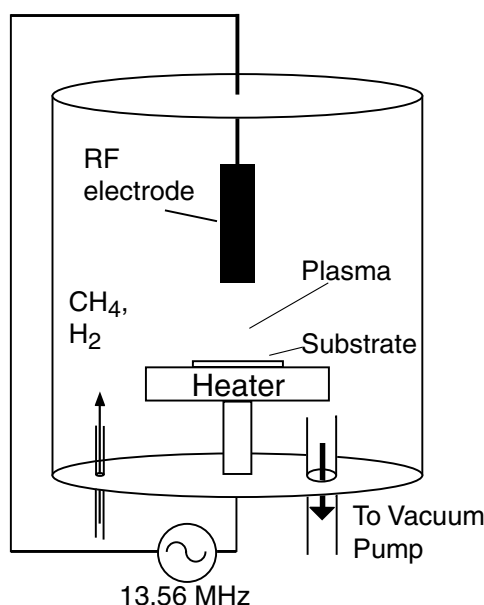


Figure 2.8 Schematic of a direct radiofrequency PECVD system.

potentially very cheap to be able to produce nanotubes with technology no more complicated than fire.

#### 2.2.4 PECVD synthesis

Plasma-enhanced chemical vapor deposition (PECVD) systems have been used to produce both SWCNTs and MWCNTs. PECVD is a general term, encompassing several differing synthesis methods. Direct PECVD systems can be used for the production of MWCNT field emitter towers<sup>47</sup> and some SWCNTs<sup>48</sup> (Figure 2.8). A remote PECVD can also be used to produce both MWCNTs and SWCNTs<sup>29</sup> (Figure 2.9). For SWCNT synthesis in the direct PECVD system, the researchers heated the substrate up to 550 to 850°C, utilized a  $\text{CH}_4/\text{H}_2$  gas mixture at 500 mT, and applied 900 W of plasma power as well as an externally applied magnetic field. The remote PECVD system utilized by Li et al. used  $\text{CH}_4/\text{Ar}$  held at 500 mT, with only 50 to 75 W of plasma power.<sup>29</sup> To grow SWCNT by hot-wire CVD (HWCVD), hydrocarbons with dissolved Fe-containing molecules are passed over an

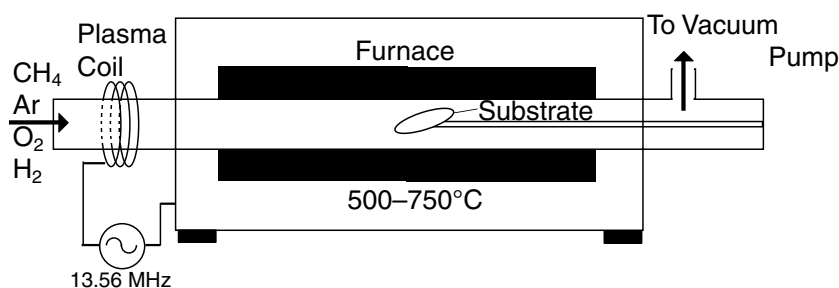


Figure 2.9 Schematic of a remote radiofrequency PECVD system.

extremely hot filament near the furnace entrance to facilitate a plasma-induced breakdown of hydrocarbons and nucleation of nanotube growth. By initiating growth in the vapor phase, a substrate can be placed downstream in a cooler area of the furnace ( $\sim 450^\circ\text{C}$ ) so that the nanotubes can deposit from the vapor phase onto the substrate.<sup>49</sup> This is useful because by lowering the substrate temperature, the variety of substrates on which SWCNTs can be synthesized is widened. As such, PECVD and HWCVD are essentially a crossover between plasma-based growth and CVD synthesis. In contrast to arc discharge, laser ablation, and solar furnace, the carbon for PECVD synthesis comes from feedstock gases such as  $\text{CH}_4$  and  $\text{CO}$ , so there is no need for a solid graphite source. The argon-assisted plasma is used to break down the feedstock gases into  $\text{C}_2$ ,  $\text{CH}$ , and other reactive carbon species ( $\text{C}_x\text{H}_y$ ) to facilitate growth at low temperature and pressure.

## 2.3 Specifics of CVD growth method

Chemical vapor deposition of SWCNTs encompasses a phenomenal number of methods and theories. There are literally thousands of publications over the last 10 years on CVD of single-walled nanotubes, all describing distinct growth conditions, catalysts, substrates, and resulting quality, yield, and diameters. There are a huge number of variables that make the difference between the production of grams of pristine SWCNTs and random amorphous carbon deposition. By separating CVD growth into three separate parts — growth mechanics, carbon feedstock, and catalyst — hopefully some semblance of order will result. It is important to note that these three attributes are interdependent, and this compilation is by no means comprehensive.

### 2.3.1 Growth mechanics

Since the growth of the first confirmed SWCNTs from CVD,<sup>31</sup> experimentalists and theorists have proposed numerous growth mechanisms. For a detailed review of the myriad growth mechanisms on the atomistic scale, it is instructive to look at Charlier and Iijima's treatment from 2001.<sup>50</sup> To begin with, it should be noted that there will be a few simplifying assumptions made here that have been borne out by numerous experiments and appear in most theories of formation of SWCNTs in CVD synthesis: (1) an active catalyst nanoparticle (Fe, Ni, Co, etc.) and ready access to carbon feedstock are essential to the efficient formation of SWCNT; (2) ideally, once a nanotube begins to grow, the diameter is set and will not change as growth continues; (3) at the onset of growth, the catalyst particle and the resultant nanotube are of similar size,<sup>51,52</sup> which leads to the assumption that (4) one particle leads to only one nanotube during a single growth step. There are (sometimes glaring) exceptions to each of these assumptions. For the first assumption, it should be noted that nanotubes can be produced from nanoparticles of graphitic carbon heated up to high temperature without the need for catalyst, though the applications for this approach are fairly limited.<sup>53</sup> Second, there

are cases in which long nanotubes have been shown to change chirality (though not significant diameter change) along their length, but this is due to a defect during growth and should be considered a (common) exception rather than a rule.<sup>54</sup> Further, though assumptions 3 and 4 have been observed directly, a common alternate situation is where the formation of bundles of small-diameter nanotubes (1 to 3 nm) from a 10- to 20-nm catalyst particle has been reported and explained,<sup>55</sup> and in fact is the primary mode of production in laser ablation.<sup>30</sup> However, diameter control from the latter growth mechanism is problematic at best, and bundles of nanotubes have limited uses, so only the one-to-one formation mechanism from small, discrete nanoparticles (0.4 to 5 nm) will be discussed.

CNT growth in CVD can be split into two basic types depending on the location of the catalyst, so-called gas phase growth, and substrate growth. Both of these growth pathways can in turn be split into bulk carbon diffusion and surface carbon diffusion models. In gas phase growth, the catalyst formation and nanotube growth occur literally in mid-air. In substrate growth, catalyst nanoparticles or metal precursors are deposited either on a substrate such as SiO<sub>2</sub> or on a high-surface-area powder before growth. The underlying chemistry for both methods that leads to the formation of nanotubes from nanoparticles is similar, and both can usually be classed into surface carbon diffusion and bulk carbon diffusion:

1. Surface carbon diffusion: The metal particle remains a solid, the “cracked” carbon diffuses around the surface, and carbon nanotube nucleates on the side of the metal particle. Since carbon continually breaks down on the particle, the tube continues to grow. This is a common mechanism used to explain low-temperature growth, notably with Ni catalyst nanoparticles.<sup>56</sup>
2. Bulk carbon diffusion: The carbon feedstock is “cracked” or broken down on the surface of the metal particle, similar to above. The metal nanoparticle dissolves the carbon until it reaches saturation, at which point a CNT with one or more walls grows from the outer surface. In this situation, the metal can either remain as a solid or become a liquid nanodroplet. In the case where it becomes a liquid, it is instructive to imagine the droplet dissolving carbon until it becomes saturated. At this point, a nanotube begins to extrude and the continued dissolution of carbon provides fuel for the process of hydrocarbon vapor → metal-carbon-liquid → crystalline carbon solid (vapor-liquid-solid model). This model was proposed originally to explain the formation of silicon and germanium whiskers in the 1960s<sup>57,58</sup> and was extended to explain nanotube formation by Saito et al.<sup>59</sup>

Both mechanisms have been indirectly observed via high-resolution transmission electron microscopy (HRTEM), where the specific favored mechanism by a particular growth method depends on the temperature, the type of metal catalyst, and the carbon feedstock used.

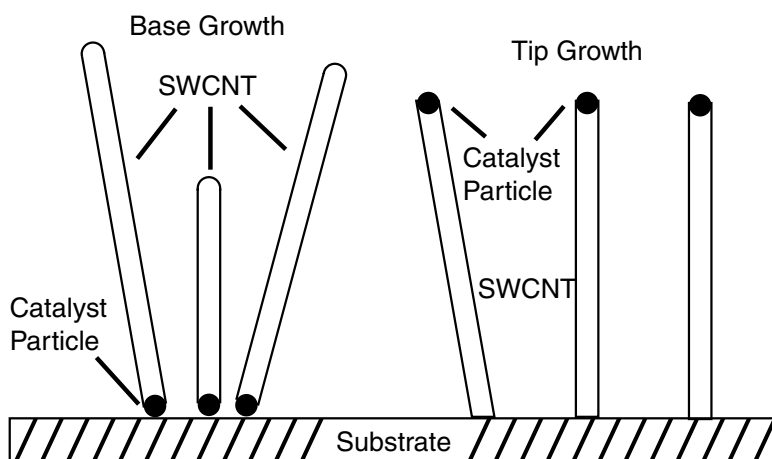


**Figure 2.10** Schematic of both tip growth and base growth of nanotubes on a substrate.

In substrate growth, once the nanotube begins to grow by either surface or bulk carbon diffusion, the CNT will undergo either base growth or tip growth (Figure 2.10). In base growth the catalyst particle remains attached to the surface and the nanotube is extruded into the air or along the surface. During tip growth, the end of the nanotube remains stuck to the surface and the catalyst particle shoots into the air at the opposite end of the extruding nanotube. These two mechanisms have been proposed and indirectly observed for growth of carbon fibers, MWCNT, and SWCNT, depending on the catalyst type, hydrocarbon source, and growth temperature. Tip growth is considered the dominant mechanism for MWCNT growth, and base growth is dominant for SWCNT growth. Whether catalyst particles will result in tip or base growth depends largely on the stiction of the nanoparticle to the substrate or support material. For instance, Huang et al. utilize a fast-heating method that reduces the stiction of the nanoparticle to the substrate.<sup>60</sup> As a result, they believe the nanoparticle leaps off the substrate as the CNT grows, leading to a tip growth situation. If the same sample is heated up slowly, the particle remains stuck to the surface and the tube grows out from it, an example of base growth. Further study into how to manipulate growth conditions and catalysts to favor one or the other continues to be an important topic of research.

For a catalyst particle of unchanging size, the growth of CNTs should continue until the hydrocarbon is shut off, either by removing the feedstock from the reaction area or by amorphous or graphitic carbon fully coating the particle, blocking the gas. Additionally, in the case of base growth, growth may slow down or stop due to slow diffusion of hydrocarbons down to the nanoparticle at the bottom of the CNT. If nothing impedes the source of carbon to the nanoparticle, and nothing impedes the nanotube extrusion, the growth should be continuous. In reality, there are competing reactions at the nanoparticle site, such as the formation of graphitic shells and the deposition of amorphous carbon. As a result, in suboptimal growth conditions, amorphous carbon can coat the nanoparticle, preventing feedstock

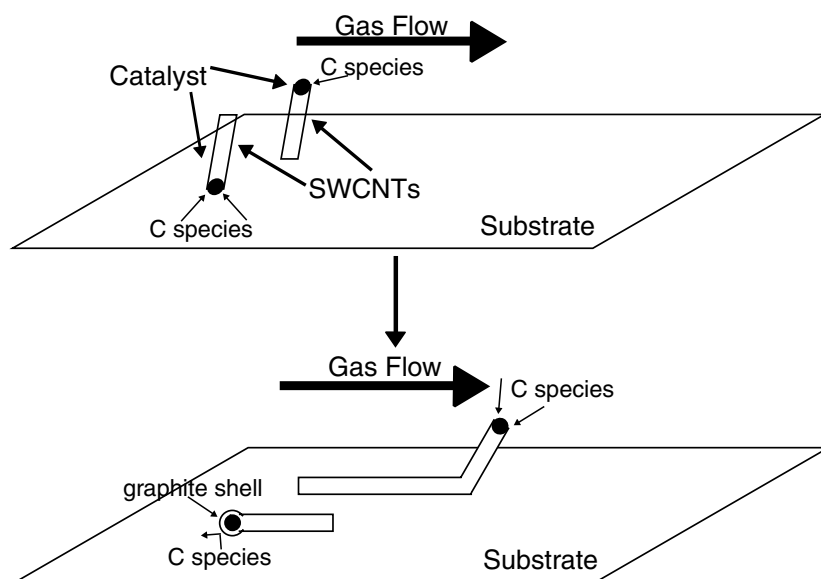


**Figure 2.11** Schematic drawing of tip growth mechanism of ultralong aligned nanotubes put forward by J. Liu (see reference 61), also known as kite growth. The upper catalyst particles float in the gas flow, continually extruding nanotube while remaining suspended in the gas. In this way, the growth can continue unabated as the nanotube's length increases, even if the rest of the nanotube contacts the substrate surface. In contrast, the base growth particle inhibits growth since the energy required to produce the nanotube increases suddenly once the nanotube contacts the surface (the nanotube will resist movement across the substrate), possibly leading to the formation of a graphitic carbon shell and subsequent termination of access to the growth gas (C species).

from reacting with the particle and cutting off the carbon source, terminating the growth. Alternatively, if the nanotube exiting the particle encounters an excessive external force, the energy for forming a nanotube might exceed the energy necessary to form a graphitic carbon shell, at which point the nanoparticle will coat itself with a carbon shell, cutting itself off from the carbon feedstock (Figure 2.11).

### 2.3.2 Carbon feedstock

The first SWCNT synthesis performed with CVD utilized carbon monoxide (CO) as a feedstock.<sup>31</sup> Since then, methane,<sup>25,100</sup> ethylene,<sup>61</sup> acetylene,<sup>62</sup> ethanol, methanol,<sup>63</sup> and benzene,<sup>64</sup> as well as others, have been used successfully to make SWCNT at various temperatures and using several catalytic metals. Since much of the growth dynamics is not well understood, there is no feedstock that provides a clear advantage over others, though there are many particular applications in which one or another feedstock excel. One of the obvious variations in feedstock choice is reactivity. For instance,  $\text{CH}_4$  is much less reactive than ethylene ( $\text{C}_2\text{H}_4$ ) or acetylene ( $\text{C}_2\text{H}_2$ ). As a result, SWCNTs have been grown from  $\text{C}_2\text{H}_4$  at temperatures as low as  $550^\circ\text{C}$ ,<sup>65</sup> whereas  $\text{CH}_4$  synthesis is not reported below  $680^\circ\text{C}$ .<sup>66</sup> Additionally, the oxygen content of the feedstock may have an effect on growth quality and yield. Many growth



methods, such as HiPco<sup>37</sup> and CoMoCAT,<sup>67</sup> utilize CO as a feedstock to much success, yielding high-quality SWCNTs that are smaller in diameter (0.7 to 1.5 nm) than those from most other conventional hydrocarbon methods (1 to 5 nm). As mentioned earlier, the presence of a controlled amount of oxygen, OH, or H<sub>2</sub>O may have a cleansing effect by preventing the formation of amorphous carbon (which is more reactive than its graphitic cousin, and thus more sensitive to small amounts of oxidizers). To this end, ethanol (C<sub>2</sub>H<sub>5</sub>OH) has proven to be a highly useful feedstock, yielding the longest single tubes ever observed,<sup>68</sup> as well as a number of high-yield growths, revealing yields of close to one SWCNT per catalyst particle (previously, in most synthesis not all catalyst nanoparticles successfully produced tubes, often lower than 10%). Virtually all growth methods dilute the active carbon species in argon, hydrogen, nitrogen, helium, or some mixture of these four, which provides yet another degree of freedom. Recently, the use of C<sub>2</sub>H<sub>4</sub> mixed with a small and measured amount of H<sub>2</sub>O has been successfully utilized for highly efficient and clean growths.<sup>17</sup> The use of etching gases, such as H<sub>2</sub>O, OH, or O<sub>2</sub>, to improve growth properties is still in its infancy and is doubtless to be the next major step toward cheap and reliable production of SWCNTs.

### 2.3.3 Catalyst

A wide variety of catalytic species can be used to produce SWCNTs in CVD growth. It is important at this point to note that the word *catalyst* is used somewhat indiscriminately in nanotube science, whether or not the “catalyst” actually remains in its original form after making a nanotube. In fact, several catalytic species, such as Fe and Co, in many cases actually form metal carbides when they produce nanotubes, and remain carbides after growth. Regardless of feedstock, it has been found that Fe, Co, and Ni nanoparticles are all able to form SWCNTs. The use of bimetallic or trimetallic mixtures of Fe, Co, and Ni with elements such as Y, Mo, Ru, and Pt has led to massive increases in yield under certain conditions.<sup>69,70</sup> These results are empirical, and there is little generally accepted theory for why this is, though there are literally hundreds of experimental and theoretical papers that analyze the effects on yield of differing concentrations of elements using a particular growth condition. Specific catalyst mixtures, such as Fe/Mo and Co/Mo,<sup>67,71,72</sup> have been analyzed in depth, though usually with only one feedstock gas. Interestingly, work by Mizuno et al. shows that while a typical Co/Mo-based catalyst is highly active in ethanol growth while having relatively low SWCNT yield in CH<sub>4</sub> growth, a common Fe/Mo catalyst has high yield in CH<sub>4</sub> growth and low yield in ethanol.<sup>73</sup> This observation is one of many that make it clear that the catalyst–growth dynamics–feedstock picture is not yet complete, and there is much more to learn. Regardless of the catalyst metals chosen for growth, catalyst material can take any of three basic forms, depending on the type of samples desired: unsupported, supported, and vapor phase.

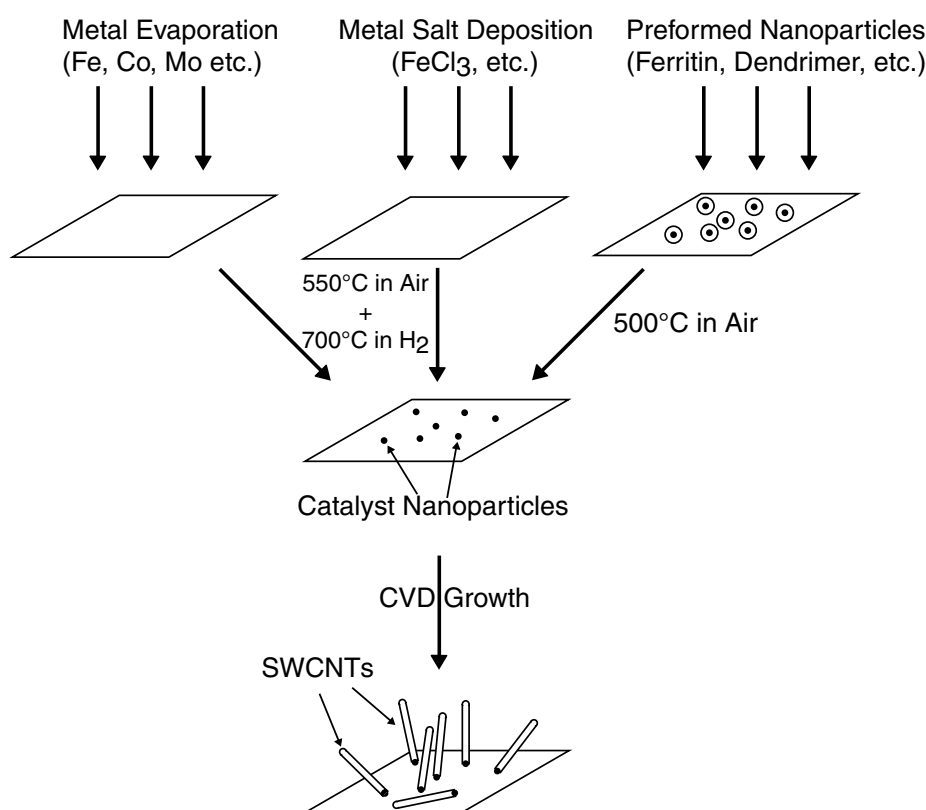


**Figure 2.12** Schematic of the production of unsupported catalyst particles on a substrate. As shown in the schematic, in the case of evaporated films (sputtered, ebeam, or thermal evaporation) and metal salts, it is optimal to first calcine the sample in air to fully oxidize the metal, and then reduce the film (in  $H_2$ ) at high temperature to cause uniform aggregation of nanoparticles before growth.

### 2.3.3.1 Unsupported catalyst

Unsupported catalyst is prepared such that discrete catalyst nanoparticles lie directly on the growth substrates to individually nucleate nanotube growth (Figure 2.12). This can be done in a variety of ways, such as by depositing via high-vacuum thermal evaporation a primary thin film of Fe or Co, possibly followed by a film of Mo, or by soaking the growth substrate in Fe, Co, or Mo nitrate, chloride, or acetate salt and then drying the sample. Spin coating and drop drying of the various solutions or suspensions are also common. Most of these methods can be easily patterned via photolithography to afford discrete catalyst islands from which nanotubes grow. These catalysts range from extremely simple catalysts that produce a wide range of diameters (such as the deposition of thin films or the soaking of substrates in salt solutions)<sup>63</sup> to complex and specialized, such as Fe-cored ferritin proteins,<sup>52</sup> dendrimers,<sup>51</sup> or Fe-cored di-block copolymer micelles.<sup>74</sup>

### 2.3.3.2 Supported catalyst

Supported catalysts were originally designed in the late 1990s to improve the yield per growth of CVD by providing an extremely high surface area per gram for bulk growth (Figure 2.13). The surface area of many of these

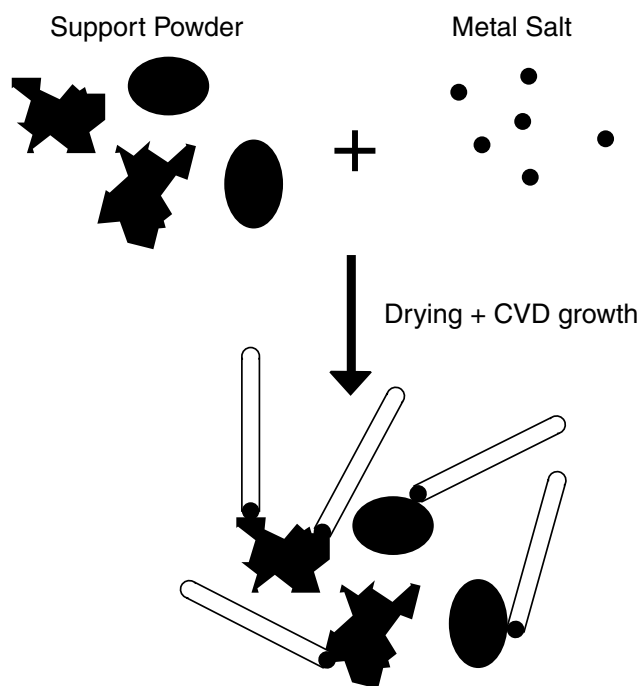


**Figure 2.13** Schematic of the formation and use of supported catalysts. In actuality, the surface area of a supported catalyst can be extremely large, leading to the formation of numerous catalyst nanoparticles per particle of support, leading to very high yields. Also, mesoporous supports can be utilized and can lead to diameter control via the diameter of the pores.

materials is quite high,  $>300 \text{ m}^2/\text{g}$ , leading to very high yields of SWCNTs in a relatively small sample batch, for example, with yields of  $>500 \text{ wt.}\%$  of SWCNTs over the metallic precursors using ethylene feedstock and Fe/Mo on an MgO support.<sup>70</sup> The catalyst is generally prepared by impregnating support material such as silica,<sup>67,69</sup> zeolite,<sup>63,75</sup> alumina,<sup>69</sup> or  $\text{MgO}$ <sup>76–78</sup> via wet chemical reaction or simply drying a stirred mixture of support and catalyst salt. In addition to bulk growth, the catalysts can be deposited in photolithographically patterned islands or via other lithographic techniques, resulting in well-defined SWCNT growth sites across a substrate. The use of three-dimensional meso-structured supports made of silica and alumina can also lead to diameter control. In one case,  $\text{AlPO}_4$  zeolites have been used to produce 4-Å-diameter SWCNTs,<sup>75</sup> which are the smallest possible SWCNT predicted by simulation. Also, the use of support can allow the production of tubes on substrates that are considered unfriendly to nanotube growth, such as Si, W, Pt, or Au.

### 2.3.3.3 Vapor phase catalyst

Vapor phase catalysts are utilized in many of the latest CVD-based bulk growth types, such as HiPco,<sup>37,38</sup> or vertical EtOH vapor systems<sup>19</sup> (Figure 2.14). In these systems, a volatile Fe- or Ni-containing compound, such as iron pentacarbonyl ( $\text{Fe}(\text{CO})_5$ ), ferrocene ( $\text{Fe}(\text{C}_5\text{H}_5)_2$ ), or nickelocene ( $\text{Ni}(\text{C}_5\text{H}_5)_2$ ), is vaporized and released into a furnace at 900 to 1200°C along

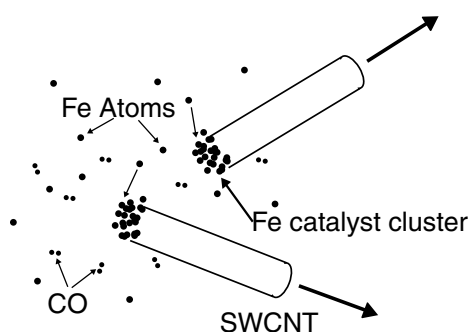


**Figure 2.14** Schematic of the Boudouard process wherein a catalyst particle aggregates while simultaneously producing a nanotube. Growth terminates after the particle grows too large.

with feedstock gas. The nanotubes form in the vapor phase and condense out onto cold surfaces. Gas phase or float-zone growth has been proposed to follow the Boudouard process, wherein catalyst particles are continually aggregating in the hot zone of the furnace, while simultaneously producing nanotubes.<sup>37,38</sup>

## 2.4 Recent advances in SWCNT growth control

In order to fully realize the scientific and commercial applications of SWCNTs, it is essential to be able to precisely control the result of each growth. True deterministic synthesis remains the last obstacle to the large-scale use of SWCNT-based devices and materials. Depending on the context, deterministic growth can mean precise positioning, orientation, length, diameter, chirality, or yield. There has been considerable progress in realizing each of these goals. Examples are illustrated next.

### 2.4.1 Location and orientation control

For all electronic and sensing applications, the precise placement and orientation of SWCNTs is critical. There is always the possibility of growing SWCNTs in bulk, suspending them in solution, and then depositing them on a substrate. However, for large-scale high-performance and reproducible device production, it is advantageous to be able to grow the SWCNTs in areas of choice, without the need for postgrowth manipulation. To that end, there have been several advances in the control of position and orientation, and the realization of well-oriented arrays of SWCNTs has been achieved.

#### 2.4.1.1 Catalyst patterning

Substrate-based growth was pioneered in 1998 by Kong in Dai's group at Stanford University<sup>25</sup> (Figure 2.15). This approach represented the first major step away from the bulk production of nanotube powders toward the deterministic growth of individual SWCNTs for use as field effect transistors (FETs), interconnects, or chemical, biological, and mechanical sensors. Before

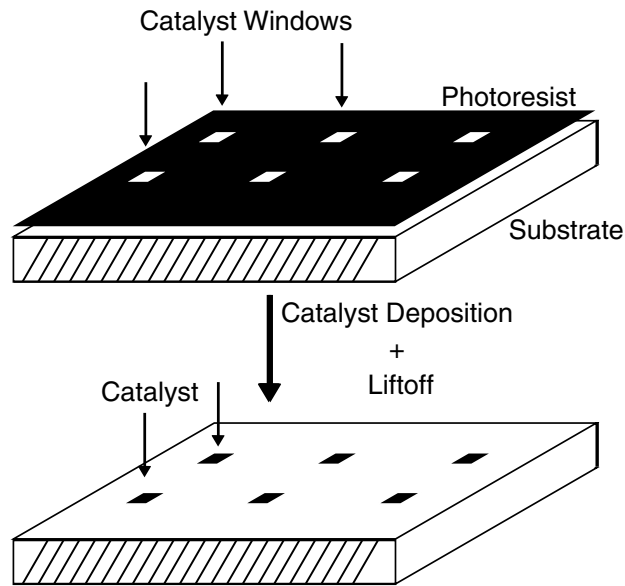


**Figure 2.15** Schematic of the catalyst patterning process. Photolithography or ebeam lithography is used to pattern small openings in a resist layer. Catalyst is then deposited by spin coating, evaporation, or simple drying. The resist is lifted off, leaving well-defined catalyst islands from which nanotubes grow.

this advance, any electronic device assembled using nanotubes required the suspension and deposition of SWCNT from bulk material, which increased the risk of bundle and defect formation as a result of the purification and suspension processes.

In substrate-based growth, standard lithographic methods (electron beam or photolithography) are used to pattern well-defined holes in the resist in which supported or unsupported catalyst is deposited. The resist is lifted off, leaving isolated catalyst islands. Growth is then performed on the substrate, producing nanotubes only from the predefined islands. By discerning the position of the as-grown nanotubes, it becomes possible to reliably fabricate nanotube-based devices on the wafer scale.

#### 2.4.1.2 Suspended aligned SWCNTs

For certain applications such as interconnects, oscillators, and antennas, tubes suspended between pillars or electrical contacts are practical and useful. To that end, Cassell<sup>79</sup> et al., and Franklin and Dai<sup>80</sup> produced quasi-oriented SWCNT growth between silicon pillars. Contact printing was used to selectively place the liquid-based alumina-supported Fe/Mo catalyst on top of the pillars. During CVD growth, the SWCNTs formed bridges between the tops of adjacent pillars. Since the nanotubes grow via the base growth method from this particular catalyst, the nanotubes grew out from the pillars and remained suspended in space until they attached to another pillar. This type of suspended SWCNT is not obtainable using any other type of known synthesis method. Dai's group also successfully produced aligned suspended SWCNTs between electrical contacts through the use of an electric field of up to 1 V/ $\mu\text{m}$ .<sup>28</sup> The alignment is due to the large polarizability of



SWCNTs; in the electric field the SWCNT acts as a strong dipole, experiencing a strong tendency to align with the field. These achievements resulted in the first examples of aligned, long SWCNTs.

### 2.4.1.3 Aligned SWCNTs on substrates

Alignment of nanotubes on a substrate improves upon the patterned growth mentioned above. In directionless patterned growth, the nanotubes grow out in random directions from the catalyst island. With patterned alignment, both the origin and the precise orientation of the tube can be known.

The electric field alignment method also works for SWCNTs grown on a substrate, which allowed Ural et al. to produce large numbers of long and highly aligned nanotubes<sup>27</sup> (Figure 2.16). The production of aligned nanotubes without electric field was recently achieved by Liu at Duke University via a fast-heating method, wherein the substrate was plunged into a hot furnace. They hypothesized that the catalyst particles leap off the surface and enter the laminar flow of growth gases, producing SWCNTs as they travel. The nanotube adheres to the substrate via van der Waals interaction, producing long and aligned nanotubes<sup>20</sup> (Figure 2.11). Since Liu's publication there have been several papers reporting alignment from growth gases, some of which do not require the fast-heating step<sup>68,81–83</sup> (Figure 2.17).

### 2.4.2 Growth of ultralong SWCNTs

CVD is also capable of producing extremely long nanotubes (>4 cm so far, with longer unofficially reported). The first report of an ultralong nanotube was by Kim et al., who reported tube growth of up to 400  $\mu\text{m}$  from ferritin-derived Fe catalyst particles utilizing  $\text{CH}_4/\text{C}_2\text{H}_4/\text{H}_2$  CVD growth at 900°C.<sup>61</sup> This showed the potential for catalyst particles in CVD to remain active for long periods, facilitating extremely long nanotubes. The current confirmed record length of 4 cm for a SWCNT was produced by Zheng et al. at Los Alamos National Laboratory using ethanol CVD.<sup>68</sup> The length was actually limited by the substrate size, as the longest nanotube they measured

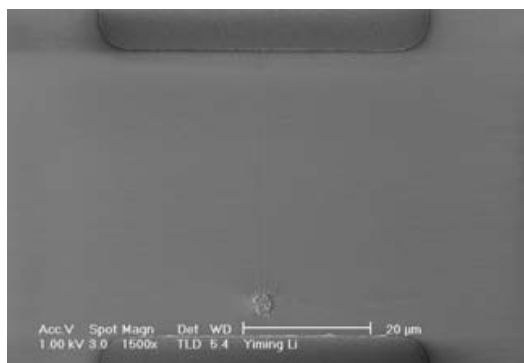


**Figure 2.16** Scanning electron microscope (SEM) image of a SWCNT aligned by electric field. (Courtesy of Yiming Li.)

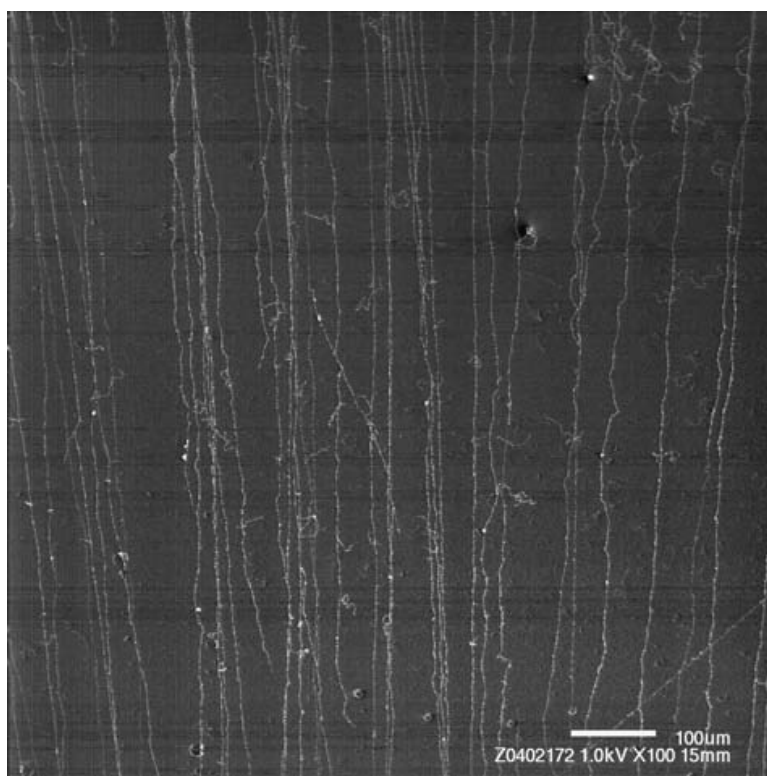


**Figure 2.17** SEM image of dozens of SWCNTs aligned by gas flow in ethanol CVD synthesis using  $\text{FeCl}_3$  salt as a catalyst. (Courtesy of Lianxi Zheng.)

grew to the edge of the substrate. By optimizing the carrier gas concentrations, temperature, and catalyst choice, it seems that nanotubes may potentially be grown to any desired length and at any density. As mentioned earlier, every publication that discusses long aligned SWCNT growth cites tip growth as the mechanism.

### 2.4.3 Water-assisted high-yield growth of SWCNTs

As mentioned previously, by adding a small and measured amount of  $\text{H}_2\text{O}$  to standard ethylene/argon CVD growth, Hata et al. have achieved up to 2.5-mm vertical growth of dense SWCNTs<sup>17</sup> (Figure 2.18). They justify the success of this approach by running a series of control experiments that demonstrate that  $\text{H}_2\text{O}$  at these concentrations effectively etches amorphous carbon without etching SWCNTs at  $750^\circ\text{C}$ . As a result, by using water as a selective oxidizer, they achieved a growth situation where the catalyst particles are never inactivated by a coating of amorphous carbon. At the best condition found thus far, water-assisted growth yields up to 99.98% pure SWCNT samples. This is by far more pure than any other growth method currently in existence.

### 2.4.4 Diameter and chirality control

Diameter control has always been a challenge for CVD synthesis. In contrast to competing synthesis methods such as arc discharge and HiPco, which



**Figure 2.18** Shown are 2.5-mm-tall SWCNTs made by water-assisted ethylene CVD. A matchstick on the left-hand side of the picture shows the height of the nanotubes. The nanotubes have individual diameters of 1 to 3 nm and have grown to reach an aspect ratio of  $10^6$ , virtually unheard of for crystalline materials. (Reprinted with the permission of Hata, K. et al., Water-assisted highly efficient synthesis of impurity-free single-walled carbon nanotubes, *Science* 306, 1362–1364, 2004.)

produce tubes in a fairly small diameter range, CVD historically produces SWCNTs anywhere from 0.4 to 5 nm. Much has been done to narrow that range: rational catalyst design, deterministic single-nanoparticle formation, and fine-tuning of growth conditions. The selection of chirality is still more difficult, since several semiconducting and metallic chiralities have almost precisely the same diameters. Much has been done in postsynthesis separation,<sup>84–93</sup> and it remains to be seen whether postgrowth processing or a suitable synthesis method will adequately address this problem first.

#### 2.4.4.1 Nanoparticle production for narrow-diameter SWCNTs

There have been several attempts to directly engineer unsupported individual nanoparticles, based on the premise that if one can control the precise diameter of the nanoparticle, the resultant nanotube diameter will be similarly controlled. As an example, Li et al. utilized ferritin,<sup>52</sup> an Fe-containing protein, to produce narrow-diameter particles. They started with apo-ferritin, which is ferritin with the Fe stripped from it, and then manually loaded Fe atoms into the ferritin. By decanting ferritins at various levels of concentration, they were capable of producing nanotubes with differing diameter ranges. Ferritins with roughly 300 atoms of Fe loaded produced SWCNTs from 0.8 to 1.5 nm, and ferritins with roughly 1200 atoms of Fe produced SWCNTs from 1 to 3 nm. The next year, Choi et al. developed a second method for deterministic particle formation using dendrimers as the Fe trapping agent, which yielded a diameter range of only 1 to 2 nm.<sup>51</sup>

#### 2.4.4.2 CoMoCAT: chirality selectivity in bulk production of SWCNTs

Bachilo et al. have developed a very promising bulk supported catalyst, which is referred to as CoMoCAT. It is based on a mesoporous silica support with a varying ratio of Co and Mo utilizing CO as the feedstock gas. From fluorescence measurements, it appears that only one or two semiconducting chiralities are present.<sup>94</sup> The researchers in this group have studied the

interaction of cobalt, molybdenum, and carbon in depth in order to achieve a catalyst that produces high yield with highly uniform catalyst particles.<sup>67,71,95,96</sup> The method is so successful for the production of nanotubes that Resasco has started a company, Southwest Nano, based on the production of SWCNT materials derived from this process.

#### 2.4.4.3 PECVD production of narrow-diameter and chirality SWCNTs

Another approach to tight-diameter distribution is the engineering of the growth method itself. It is well known that plasma-based growth methods such as arc discharge and laser ablation result in nanotubes of small diameter and a relatively narrow diameter range of ~0.8 to 1.6 nm. By modifying a remote plasma-enhanced CVD system and using ferritin-derived catalyst particles, Li et al. were able to produce very narrow-diameter SWCNTs (0.8 to 1.5 nm).<sup>29</sup> As an added bonus, from electrical transport data it is evident that the percentage of semiconducting tubes is ~90%. This is a significant deviation from what is expected from a random chirality distribution (67%). However, it is unclear as to why there is some preference toward semiconducting tubes. Density functional theory calculations reveal that large-band-gap nanotubes of small diameter take less energy to form than metallic nanotubes.<sup>97</sup> It is possible that the small diameter coupled with the low thermal budget leads to a growth situation that favors large-band-gap nanotubes. It is also possible that any H<sup>\*</sup> in the plasma may selectively etch metallic SWCNTs, as shown by Hassanien et al.<sup>98</sup> PECVD also allows for very low growth temperature; for SWCNTs, the use of PECVD has allowed for the production of nanotubes directly on substrates at as low as 550°C.<sup>97</sup>

## 2.5 Conclusion

In conclusion, there have been tremendous advances in nanotube synthesis since 1991. Some of the hurdles separating SWCNTs from commercial usage, such as yield, purity, and alignment, have recently been satisfactorily addressed. Yet, there still remain challenges for chirality and diameter control. For many applications, such as biological and chemical sensors, the current level of control may be nearly sufficient for commercial deployment. However, in order to realize the more ambitious goals of nanotube-based electronics using nanotube FETs and nanotube interconnects, to take full advantage of the remarkable properties of nanotubes, more work remains to be done.

## References

1. Terrones, M., Carbon nanotubes: synthesis and properties, electronic devices, and other emerging applications, *International Materials Reviews* 49, 325–377, 2004.

2. Dai, H.J., Carbon nanotubes: synthesis, integration, and properties, *Accounts of Chemical Research* 35, 1035–1044, 2002.
3. Dai, H.J., Nanotube growth and characterization, *Carbon Nanotubes* 80, 29–53, 2001.
4. Liu, J., Fan, S.S., and Dai, H.J., Recent advances in methods of forming carbon nanotubes, *MRS Bulletin* 29, 244–250, 2004.
5. Iijima, S., Helical microtubules of graphitic carbon, *Nature* 354, 56–58, 1991.
6. Bacon, R., Growth, structure, and properties of graphite whiskers, *Journal of Applied Physics* 31, 283–290, 1960.
7. Oberlin, A., Endo, M., and Koyama, T., High resolution electron microscope observations of graphitized carbon fibers, *Carbon* 14, 133–135, 1976.
8. Oberlin, A., Endo, M., and Koyama, T., Filamentous growth of carbon through benzene decomposition, *Journal of Crystal Growth* 32, 335–349, 1976.
9. Tibbetts, G.G., Why are carbon filaments tubular?, *Journal of Crystal Growth* 66, 632–638, 1984.
10. Iijima, S. and Ichihashi, T., Single-shell carbon nanotubes of 1-nm diameter, *Nature* 363, 603–615, 1993.
11. Bethune, D.S., Kiang, C.H., de Vries, M.S., Gorman, G., Savoy, R., Vazquez, J., and Beyers, R., Cobalt-catalysed growth of carbon nanotubes with single-atomic-layer walls, *Nature* 363, 605–607, 1993.
12. Ebbesen, T.W. and Ajayan, P.M., Large-scale synthesis of carbon nanotubes, *Nature* 358, 220–222, 1992.
13. Fan, S.S., Chapline, M.G., Franklin, N.R., Tomblor, T.W., Cassell, A.M., and Dai, H.J., Self-oriented regular arrays of carbon nanotubes and their field emission properties, *Science* 283, 512–514, 1999.
14. Harris, P.J.F., Carbon nanotube composites, *International Materials Reviews* 49, 31–43, 2004.
15. Lau, K.T. and Hui, D., The revolutionary creation of new advanced materials: carbon nanotube composites, *Composites Part B: Engineering* 33, 263–277, 2002.
16. Breuer, O. and Sundararaj, U., Big returns from small fibers: a review of polymer/carbon nanotube composites, *Polymer Composites* 25, 630–645, 2004.
17. Hata, K., Futaba, D.N., Mizuno, K., Namai, T., Yumura, M., and Iijima, S., Water-assisted highly efficient synthesis of impurity-free single-walled carbon nanotubes, *Science* 306, 1362–1364, 2004.
18. Murakami, Y., Chiashi, S., Miyauchi, Y., Hu, M.H., Ogura, M., Okubo, T., and Maruyama, S., Growth of vertically aligned single-walled carbon nanotube films on quartz substrates and their optical anisotropy, *Chemical Physics Letters* 385, 298–303, 2004.
19. Li, Y.L., Kinloch, I.A., and Windle, A.H., Direct spinning of carbon nanotube fibers from chemical vapor deposition synthesis, *Science* 304, 276–278, 2004.
20. Burke, P.J., AC performance of nanoelectronics: towards a ballistic THz nanotube transistor, *Solid-State Electronics* 48, 1981, 2004.
21. Javey, A., Guo, J., Wang, Q., Lundstrom, M., and Dai, H.J., Ballistic carbon nanotube field-effect transistors, *Nature* 424, 654–657, 2003.
22. Wang, J., Nanomaterial-based electrochemical biosensors, *Analyst* 130, 421, 2005.



23. Pengfei, Q.F., Vermesh, O., Grecu, M., Javey, A., Wang, O., Dai, H.J., Peng, S., and Cho, K.J., Toward large arrays of multiplex functionalized carbon nanotube sensors for highly sensitive and selective molecular detection, *Nano Letters* 3, 347, 2003.
24. Kong, J., Franklin, N.R., Zhou, C.W., Chapline, M.G., Peng, S., Cho, K.J., and Dai, H.J., Nanotube molecular wires as chemical sensors, *Science (Washington D.C.)* 287, 622, 2000.
25. Kong, J., Soh, H.T., Cassell, A.M., Quate, C.F., and Dai, H.J., Synthesis of individual single-walled carbon nanotubes on patterned silicon wafers, *Nature* 395, 878–881, 1998.
26. Huang, S.M., Cai, X.Y., and Liu, J., Growth of millimeter-long and horizontally aligned single-walled carbon nanotubes on flat substrates, *Journal of the American Chemical Society* 125, 5636–5637, 2003.
27. Ural, A., Li, Y.M., and Dai, H.J., Electric-field-aligned growth of single-walled carbon nanotubes on surfaces, *Applied Physics Letters* 81, 3464–3466, 2002.
28. Zhang, Y.G., Chang, A.L., Cao, J., Wang, Q., Kim, W., Li, Y.M., Morris, N., Yenilmez, E., Kong, J., and Dai, H.J., Electric-field-directed growth of aligned single-walled carbon nanotubes, *Applied Physics Letters* 79, 3155–3157, 2001.
29. Li, Y.M., Mann, D., Rolandi, M., Kim, W., Ural, A., Hung, S., Javey, A., Cao, J., Wang, D.W., Yenilmez, E., Wang, Q., Gibbons, J.F., Nishi, Y., and Dai, H.J., Preferential growth of semiconducting single-walled carbon nanotubes by a plasma enhanced CVD method, *Nano Letters* 4, 317–321, 2004.
30. Thess, A., Lee, R., Nikolaev, P., Dai, H.J., Petit, P., Robert, J., Xu, C.H., Lee, Y.H., Kim, S.G., Rinzler, A.G., Colbert, D.T., Scuseria, G.E., Tomanek, D., Fischer, J.E., and Smalley, R.E., Crystalline ropes of metallic carbon nanotubes, *Science* 273, 483–487, 1996.
31. Dai, H., Rinzler, A.G., Nikolaev, P., Thess, A., Colbert, D.T., and Smalley, R.E., Single-wall nanotubes produced by metal-catalyzed disproportionation of carbon monoxide, *Chemical Physics Letters* 260, 471–475, 1996.
32. Height, M.J., Howard, J.B., Tester, J.W., and Sande, J.B.V., Flame synthesis of single-walled carbon nanotubes, *Carbon* 42, 2295, 2004.
33. Farhat, S., de La Chapelle, M.L., Loiseau, A., Scott, C.D., Lefrant, S., Journet, C., and Bernier, P., Diameter control of single-walled carbon nanotubes using argon-helium mixture gases, *Journal of Chemical Physics* 115, 6752–6759, 2001.
34. Waldorff, E.I., Waas, A.M., Friedmann, P.P., and Keidar, M., Characterization of carbon nanotubes produced by arc discharge: effect of the background pressure, *Journal of Applied Physics* 95, 2749–2754, 2004.
35. Journet, C., Maser, W.K., Bernier, P., Loiseau, A., delaChapelle, M.L., Lefrant, S., Deniard, P., Lee, R., and Fischer, J.E., Large-scale production of single-walled carbon nanotubes by the electric-arc technique, *Nature* 388, 756–758, 1997.
36. Endo, M., Takeuchi, K., Igarashi, S., Kobori, K., Shiraishi, M., and Kroto, H.W., The production and structure of pyrolytic carbon nanotubes (PCNTs), *Journal of the Physics and Chemistry of Solids* 54, 1841–1848, 1993.
37. Nikolaev, P., Bronikowski, M.J., Bradley, R.K., Rohmund, F., Colbert, D.T., Smith, K.A., and Smalley, R.E., Gas-phase catalytic growth of single-walled carbon nanotubes from carbon monoxide, *Chemical Physics Letters* 313, 91–97, 1999.

38. Bronikowski, M.J., Willis, P.A., Colbert, D.T., Smith, K.A., and Smalley, R.E., Gas-phase production of carbon single-walled nanotubes from carbon monoxide via the HiPco process: a parametric study, *Journal of Vacuum Science and Technology A: Vacuum, Surfaces, and Films* 19, 1800–1802, 2001.
39. O'Connell, M.J., Bachilo, S.M., Huffman, C.B., Moore, V.C., Strano, M.S., Haroz, E.H., Rialon, K.L., Boul, P.J., Noon, W.H., Kittrell, C., Ma, J.P., Hauge, R.H., Weisman, R.B., and Smalley, R.E., Band gap fluorescence from individual single-walled carbon nanotubes, *Science* 297, 593–596, 2002.
40. Richter, H., Hernadi, K., Caudano, R., Fonseca, A., Migeon, H.N., Nagy, J.B., Schneider, S., Vandooren, J., and VanTiggelen, P.J., Formation of nanotubes in low pressure hydrocarbon flames, *Carbon* 34, 427, 1996.
41. Vander Wal, R.L., Ticich, T.M., and Curtis, V.E., Diffusion flame synthesis of single-walled carbon nanotubes, *Chemical Physics Letters* 323, 217, 2000.
42. Yuan, L.M., Saito, K., Hu, W.C., and Chen, Z., Ethylene flame synthesis of well-aligned multi-walled carbon nanotubes, *Chemical Physics Letters* 346, 23, 2001.
43. Vander Wal, R.L., Fe-catalyzed single-walled carbon nanotube synthesis within a flame environment, *Combustion and Flame* 130, 37, 2002.
44. Merchan-Merchan, W., Saveliev, A., Kennedy, L.A., and Fridman, A., Formation of carbon nanotubes in counter-flow, oxy-methane diffusion flames without catalysts, *Chemical Physics Letters* 354, 20, 2002.
45. Yuan, L.M., Saito, K., Pan, C.X., Williams, F.A., and Gordon, A.S., Nanotubes from methane flames, *Chemical Physics Letters* 340, 237, 2001.
46. Diener, M.D., Nicholson, N., and Alford, J.M., Synthesis of single walled carbon nanotubes in flames, *Journal of Physical Chemistry B* 104, 9615, 2000.
47. Meyyappan, M., Delzeit, L., Cassell, A., and Hash, D., Carbon nanotube growth by PECVD: a review, *Plasma Sources, Science and Technology* 12, 205–216, 2003.
48. Kato, T., Jeong, G., Hirata, T., Hatakeyama, R., Tohji, K., and Motomiya, K., Single-walled carbon nanotubes produced by plasma-enhanced chemical vapor deposition, *Chemical Physics Letters* 381, 422–426, 2003.
49. Mahan, A.H., Alleman, J.L., Heben, M.J., Parilla, P.A., Jones, K.M., and Dillon, A.C., Hot wire chemical vapor deposition of isolated carbon single-walled nanotubes, *Applied Physics Letters* 81, 4061, 2002.
50. Charlier, J.C. and Iijima, S., Growth mechanisms of carbon nanotubes, *Carbon Nanotubes* 80, 55, 2001.
51. Choi, H.C., Kim, W., Wang, D.W., and Dai, H.J., Delivery of catalytic metal species onto surfaces with dendrimer carriers for the synthesis of carbon nanotubes with narrow diameter distribution, *Journal of Physical Chemistry B* 106, 12361–12365, 2002.
52. Li, Y.M., Kim, W., Zhang, Y.G., Rolandi, M., Wang, D.W., and Dai, H.J., Growth of single-walled carbon nanotubes from discrete catalytic nanoparticles of various sizes, *Journal of Physical Chemistry B* 105, 11424–11431, 2001.
53. Botti, S., Ciardi, R., Terranova, M.L., Piccirillo, S., Sessa, V., Rossi, M., and Vittori-Antisari, M., Self-assembled carbon nanotubes grown without catalyst from nanosized carbon particles adsorbed on silicon, *Applied Physics Letters* 80, 1441, 2002.

54. Doorn, S.K., O'Connell, M.J., Zheng, L.X., Zhu, Y.T.T., Huang, S.M., and Liu, J., Raman spectral imaging of a carbon nanotube intramolecular junction, *Physical Review Letters* 94, 016802, 2005.
55. Gavillet, J., Loiseau, A., Journet, C., Willaime, F., Ducastelle, F., and Charlier, J.C., Root-growth mechanism for single-wall carbon nanotubes, *Physical Review Letters* 87, 275504, 2001.
56. Seidel, R., Duesberg, G.S., Unger, E., Graham, A.P., Liebau, M., and Kreupl, F., Chemical vapor deposition growth of single-walled carbon nanotubes at 600°C and a simple growth model, *Journal of Physical Chemistry B* 108, 1888, 2004.
57. Wagner, R.S. and Ellis, W.C., Vapor-liquid-solid mechanism of single crystal growth (new method growth catalysis from impurity whisker epitaxial + large crystals SI E), *Applied Physics Letters* 4, 89, 1964.
58. Wagner, R.S., Doherty, C.J., and Ellis, W.C., Preparation + morphology of crystals of silicon + germanium grown by vapor-liquid-solid mechanism, *Jom — Journal of Metals* 16, 761, 1964.
59. Saito, Y., Okuda, M., Tomita, M., and Hayashi, T., Extrusion of single-wall carbon nanotubes via formation of small particles condensed near an arc evaporation source, *Chemical Physics Letters* 236, 419, 1995.
60. Huang, S., Woodson, M., Smalley, R., and Liu, J., Growth mechanism of oriented long single walled carbon nanotubes using “fast-heating” chemical vapor deposition process, *Nano Letters* 4, 1025–1028, 2004.
61. Kim, W., Choi, H.C., Shim, M., Li, Y.M., Wang, D.W., and Dai, H.J., Synthesis of ultralong and high percentage of semiconducting single-walled carbon nanotubes, *Nano Letters* 2, 703–708, 2002.
62. Satishkumar, B.C., Govindaraj, A., Sen, R., and Rao, C.N.R., Single-walled nanotubes by the pyrolysis of acetylene-organometallic mixtures, *Chemical Physics Letters* 293, 47, 1998.
63. Maruyama, S., Kojima, R., Miyauchi, Y., Chiashi, S., and Kohno, M., Low-temperature synthesis of high-purity single-walled carbon nanotubes from alcohol, *Chemical Physics Letters* 360, 229–234, 2002.
64. Bai, S., Li, F., Yang, Q.H., Cheng, H.M., and Bai, J., Influence of ferrocene/benzene mole ratio on the synthesis of carbon nanostructures, *Chemical Physics Letters* 376, 83, 2003.
65. Liao, H.W. and Hafner, J.H., Low-temperature single-wall carbon nanotube synthesis by thermal chemical vapor deposition, *Journal of Physical Chemistry B* 108, 6941, 2004.
66. Harutyunyan, A.R., Pradhan, B.K., Kim, U.J., Chen, G.G., and Eklund, P.C., CVD synthesis of single wall carbon nanotubes under “soft” conditions, *Nano Letters* 2, 525, 2002.
67. Kitiyanan, B., Alvarez, W.E., Harwell, J.H., and Resasco, D.E., Controlled production of single-wall carbon nanotubes by catalytic decomposition of CO on bimetallic Co-Mo catalysts, *Chemical Physics Letters* 317, 497–503, 2000.
68. Zheng, L.X., O'Connell, M.J., Doorn, S.K., Liao, X.Z., Zhao, Y.H., Akhadow, E.A., Hoffbauer, M.A., Roop, B.J., Jia, Q.X., Dye, R.C., Peterson, D.E., Huang, S.M., Liu, J., and Zhu, Y.T., Ultralong single-wall carbon nanotubes, *Nature Materials* 3, 673–676, 2004.

69. Cassell, A.M., Raymakers, J.A., Kong, J., and Dai, H.J., Large scale CVD synthesis of single-walled carbon nanotubes, *Journal of Physical Chemistry B* 103, 6484–6492, 1999.
70. Lyu, S.C., Liu, B.C., Lee, S.H., Park, C.Y., Kang, H.K., Yang, C.W., and Lee, C.J., Large-scale synthesis of high-quality single-walled carbon nanotubes by catalytic decomposition of ethylene, *Journal of Physical Chemistry B* 108, 1613, 2004.
71. Herrera, J.E. and Resasco, D.E., Loss of single-walled carbon nanotubes selectivity by disruption of the Co-Mo interaction in the catalyst, *Journal of Catalysis* 221, 354–364, 2004.
72. Alvarez, W.E., Pompeo, F., Herrera, J.E., Balzano, L., and Resasco, D.E., Characterization of single-walled carbon nanotubes (SWNTs) produced by CO disproportionation on Co-Mo catalysts, *Chemistry of Materials* 14, 1853–1858, 2002.
73. Mizuno, K., Hata, K., Saito, T., Ohshima, S., Yumura, M., and Iijima, S., Selective matching of catalyst element and carbon source in single-walled carbon nanotube synthesis on silicon substrates, *Journal of Physical Chemistry B* 109, 2632–2637, 2005.
74. Fu, Q., Huang, S.M., and Liu, J., Chemical vapor depositions of single-walled carbon nanotubes catalyzed by uniform Fe<sub>2</sub>O<sub>3</sub> nanoclusters synthesized using diblock copolymer micelles, *Journal of Physical Chemistry B* 108, 6124, 2004.
75. Li, Z.M., Zhai, J.P., Liu, H.J., Li, I.L., Chan, C.T., Sheng, P., and Tang, Z.K., Synthesis of 4 Å single-walled carbon nanotubes in catalytic Si-substituted AlPO<sub>4</sub>-5 molecular sieves, *Applied Physics Letters* 85, 1253–1255, 2004.
76. Hu, P.A., Wang, X.B., Liu, Y.Q., Wang, B., and Zhu, D.B., Synthesis of single-walled carbon nanotubes using MgO as a catalyst support, *Synthetic Metals* 135, 833, 2003.
77. Ulla, M.A., Spretz, R., Lombardo, E., Daniell, W., and Knozinger, H., Catalytic combustion of methane on Co/MgO: characterization of active cobalt sites, *Applied Catalysis B: Environmental* 29, 217, 2001.
78. Tang, S., Zhong, Z., Xiong, Z., Sun, L., Liu, L., Lin, J., Shen, Z.X., and Tan, K.L., Controlled growth of single-walled carbon nanotubes by catalytic decomposition of CH<sub>4</sub> over Mo/Co/MgO catalysts, *Chemical Physics Letters* 350, 19, 2001.
79. Cassell, A.M., Franklin, N.R., Tomblor, T.W., Chan, E.M., Han, J., and Dai, H.J., Directed growth of free-standing single-walled carbon nanotubes, *Journal of the American Chemical Society* 121, 7975–7976, 1999.
80. Franklin, N.R. and Dai, H.J., An enhanced CVD approach to extensive nanotube networks with directionality, *Advanced Materials* 12, 890–894, 2000.
81. Yu, Z., Li, S.D., and Burke, P.J., Synthesis of aligned arrays of millimeter long, straight single-walled carbon nanotubes, *Chemistry of Materials* 16, 3414–3416, 2004.
82. Durkop, T., Getty, S.A., Cobas, E., and Fuhrer, M.S., Extraordinary mobility in semiconducting carbon nanotubes, *Nano Letters* 4, 35–39, 2004.
83. Li, S.D., Yu, Z., Rutherglen, C., and Burke, P.J., Electrical properties of 0.4 cm long single-walled carbon nanotubes, *Nano Letters* 4, 2003–2007, 2004.

84. Krupke, R., Hennrich, F., Kappes, M.M., and Lohneysen, H.V., Surface conductance induced dielectrophoresis of semiconducting single-walled carbon nanotubes, *Nano Letters* 4, 1395, 2004.
85. Chen, Z., Wu, Z., Sippel, J., Rinzler, A.G., Metallic/semiconducting nanotube separation and ultra-thin, transparent nanotube films, *AIP Conference Proceedings*, 723, 69–74, 2004.
86. Dyke, C.A., Stewart, M.P., and Tour, J.M., Separation of single-walled carbon nanotubes on silica gel. Materials morphology and Raman excitation wavelength affect data interpretation, *Journal of the American Chemical Society* 127, 4497, 2005.
87. Zheng, M., Jagota, A., Strano, M.S., Santos, A.P., Barone, P., Chou, S.G., Diner, B.A., Dresselhaus, M.S., McLean, R.S., Onoa, G.B., Samsonidze, G.G., Semke, E.D., Usrey, M., and Walls, D.J., Structure-based carbon nanotube sorting by sequence-dependent DNA assembly, *Science* 302, 1545, 2003.
88. Krupke, R. and Hennrich, F., Separation techniques for carbon nanotubes, *Advanced Engineering Materials* 7, 111, 2005.
89. Brar, V.W., Samsonidze, G.G., Santos, A.P., Chou, S.G., Chattopadhyay, D., Kim, S.N., Papadimitrakopoulos, F., Zheng, M., Jagota, A., Onoa, G.B., Swan, A.K., Unlu, M.S., Goldberg, B.B., Dresselhaus, G., and Dresselhaus, M.S., Resonance Raman spectroscopy characterization of single-wall carbon nanotube separation by their metallicity and diameter, *Journal of Nanoscience and Nanotechnology* 5, 209, 2005.
90. Strano, M.S., Probing chiral selective reactions using a revised Kataura plot for the interpretation of single-walled carbon nanotube spectroscopy, *Journal of the American Chemical Society* 125, 16148, 2003.
91. Park, N., Miyamoto, Y., Lee, K., Choi, W.I., Ihm, J., Yu, J.J., and Han, S.W., Band gap sensitivity of bromine adsorption at carbon nanotubes, *Chemical Physics Letters* 403, 135, 2005.
92. An, K.H., Park, J.S., Yang, C.M., Jeong, S.Y., Lim, S.C., Kang, C., Son, J.H., Jeong, M.S., and Lee, Y.H., A diameter-selective attack of metallic carbon nanotubes by nitronium ions, *Journal of the American Chemical Society* 127, 5196, 2005.
93. An, L., Fu, Q.A., Lu, C.G., and Liu, J., A simple chemical route to selectively eliminate metallic carbon nanotubes in nanotube network devices, *Journal of the American Chemical Society* 126, 10520, 2004.
94. Bachilo, S.M., Balzano, L., Herrera, J.E., Pompeo, F., Resasco, D.E., and Weisman, R.B., Narrow (n,m)-distribution of single-walled carbon nanotubes grown using a solid supported catalyst, *Journal of the American Chemical Society* 125, 11186–11187, 2003.
95. Alvarez, W.E., Kitiyanan, B., Borgna, A., and Resasco, D.E., Synergism of Co and Mo in the catalytic production of single-wall carbon nanotubes by decomposition of CO, *Carbon* 39, 547–558, 2001.
96. Resasco, D.E., Alvarez, W.E., Pompeo, F., Balzano, L., Herrera, J.E., Kitiyanan, B., and Borgna, A., A scalable process for production of single-walled carbon nanotubes (SWNTs) by catalytic disproportionation of CO on a solid catalyst, *Journal of Nanoparticle Research* 4, 131–136, 2002.



97. Li, Y.M., Peng, S., Mann, D., Cao, J., Tu, R., Cho, K.J., and Dai, H.J., On the origin of preferential growth of semiconducting single-walled carbon nanotubes, *Journal of Physical Chemistry B* 109, 6968, 2005.
98. Hassanien, A., Tokumoto, M., Umek, P., Vrbancic, D., Mozetic, M., Mihailovic, D., Venturini, P., and Pejovnik, S., Selective etching of metallic single-wall carbon nanotubes with hydrogen plasma, *Nanotechnology* 16, 278, 2005.
99. Kong, J., Cassell, A.M., and Dai, H.J., Chemical vapor deposition of methane for single-walled carbon nanotubes, *Chemical Physics Letters* 292, 567–574, 1998.
100. Vander Wal, R.L., Ticich, T.M., and Curtis, V.E., Flame synthesis of metal-catalyzed single-wall carbon nanotubes, *Journal of Physical Chemistry A* 104, 7209, 2000.



## chapter three

---

# Carbon nanotube peapod materials

Satishkumar B. Chikkannanavar,\* Brian W. Smith,\*\*  
David E. Luzzi  
University of Pennsylvania

### Contents

3.1	Introduction and historical perspective .....	53
3.2	C <sub>60</sub> @SWNT .....	53
3.2.1	Mechanism of formation.....	54
3.2.2	Structural characterization of peapods.....	57
3.2.2.1	Electron diffraction.....	57
3.2.2.2	EELS spectroscopy.....	57
3.2.2.3	X-ray diffraction.....	58
3.2.2.4	Raman spectroscopy .....	58
3.2.3	Properties of peapods.....	59
3.2.3.1	Band structure.....	59
3.2.3.2	Electrical and thermal conduction.....	62
3.2.3.3	Optical properties .....	62
3.2.4	Transformations of peapods.....	63
3.2.4.1	Effects of doping.....	63
3.2.4.2	High-pressure transformations .....	65
3.2.4.3	Irradiation-induced and thermally induced coalescence .....	65
3.3	Beyond C <sub>60</sub> : other hierarchical nanotube materials .....	66
3.3.1	Alternate synthesis methods.....	66

\* Satishkumar B. Chikkannanavar's present address: C-CSE, Chemical Sciences and Engineering, Los Alamos National Laboratory, MS:J563, Los Alamos, New Mexico.

\*\* Brian W. Smith's present address: Department of Medical Oncology, Fox Chase Cancer Center, Philadelphia, Pennsylvania.

3.3.2	Peapods of metallofullerenes .....	67
3.3.3	Peapods of fullerene adducts .....	69
3.3.4	Heterostructures from nonfullerene materials .....	70
3.4	Ordered phases of fullerenes in larger nanotubes .....	73
3.5	Double-wall carbon nanotubes .....	74
3.6	Conclusions and future prospects .....	75
	Acknowledgments .....	77
	References .....	77

**Abstract** The remarkable electronic and mechanical properties of carbon nanotubes are widely acclaimed, but these molecules also have a unique structure that encapsulates a one-dimensional volume of space. The promise afforded by this structure is often overlooked. Carbon nanotubes have the capability to contain or transport other atoms, molecules, or crystalline materials inside. The constrained lumen of a nanotube could be a novel reaction chamber, catalyzing the synthesis of new compounds by forcing reactants and products to adopt specific conformations. Perhaps most importantly, the intrinsic properties of nanotubes could be modified by filling with species that have opportune magnetic, electronic charge transfer, absorption, mechanical, catalytic, or thermal characteristics. Such nanoscale heterostructures could have broadly tunable properties, but the components are noncovalently associated, so the chemistry and mechanical integrity of the underlying nanotube is preserved. Because of this potential, filling methods are certain to play a critical role in the evolution of carbon nanotubes as engineering materials.

Initial efforts to create nanotube heterostructures were focused on filling multiwall carbon nanotubes (MWNTs) with metal salts and low-surface-tension melts by capillarity. However, this approach has proven limited in terms of yield, homogeneity of filling, and the types of materials that can be encapsulated. More recently, the 1998 discovery of a new class of supramolecular materials based on single-wall carbon nanotubes (SWNTs) introduced new methods for efficient filling. The first of these materials, descriptively called a peapod, was a one-dimensional crystal of  $C_{60}$  molecules assembled inside a SWNT, and was obtained by a vapor phase process. Syntheses of many other peapod materials have been enabled by this discovery. SWNTs have been filled with various fullerenes and metallofullerenes, fullerene adducts, metal complexes, and other small molecules. This growing area of research is rapidly expanding the scope of nanotube-based materials. In this review, we discuss advances in the creation of nanotube heterostructures. Specifically, we will explore the synthesis of these one-dimensional materials and how their structures are manifest in their unique properties. In addition, we will discuss recent advances in the synthesis and characterization of related double-wall carbon nanotube materials.

### 3.1 Introduction and historical perspective

The deceptively simple one-dimensional structure of a carbon nanotube gives rise to a host of fascinating mechanical, electrical, field emission, and optical properties.<sup>1–3</sup> Among carbon nanotubes,<sup>4,5</sup> single-wall nanotubes have been the most extensively studied because a direct comparison can often be made between theoretical properties and experimental measurements. As nanotubes encompass a lumen in their structure, they afford a rich reaction space for nanoscale experiments, such as insertion and manipulation of atomic, ionic, or molecular species. This has afforded the potential of tuning the intrinsic properties of carbon nanotubes.

Initial efforts to create hierarchical nanotube materials focused on filling multiwall carbon nanotubes (MWNTs) with metal complexes and related species.<sup>6–9</sup> Following the discovery of single-wall carbon nanotubes (SWNTs) and their bulk synthesis, various attempts were made to fill them with metal chloride and metal species by capillarity.<sup>10–13</sup> However, these attempts suffered from heterogeneity and limited yield. Thus, it was somewhat surprising when a new class of filled nanotube materials based instead on encapsulated fullerenes was discovered in 1998.<sup>14</sup> The canonical structure was referred to as a peapod ( $C_{60}@SWNT$ ) and consisted of  $C_{60}$  molecules self-assembled inside the lumen of a single-wall nanotube, obtained by a vapor phase filling process.<sup>15</sup> Since then, various molecular species have been considered for filling and modifying SWNTs, yielding myriad new hybrid materials with unique structural characteristics and interesting phenomenological properties. In this chapter we discuss the advances in this nascent field and the potential implications for applications of nanotechnology.

### 3.2 $C_{60}@SWNT$

The first peapods, depicted in Figure 3.1a and b, were discovered by transmission electron microscopy (TEM) as self-assembled  $C_{60}$  molecules inside SWNTs produced by laser vaporization and processed by chemical etching and annealing.<sup>14</sup> The fullerene molecules were co-formed during the laser vaporization process along with the nanotubes and assembled during the vacuum annealing process. This novel material is termed  $C_{60}@SWNT$ , where @ is read “contained by” by analogy to the naming convention used in metallofullerene chemistry. The structure is a remarkable serendipity of nature: the most abundant nanotubes produced under the tested conditions are 1.4 nm in diameter, which is precisely the right size to encapsulate 0.7-nm-diameter  $C_{60}$  molecules while maintaining the energetically preferred van der Waals distance between the two molecules. An example of a fullerene-filled rope illustrating the characteristic peapod contrast is shown in Figure 3.1c. Following the initial discovery, chemical characterization corroborated that the discrete molecules inside the SWNTs were indeed  $C_{60}$  fullerenes.<sup>15</sup> However, experiments to characterize the structure and property

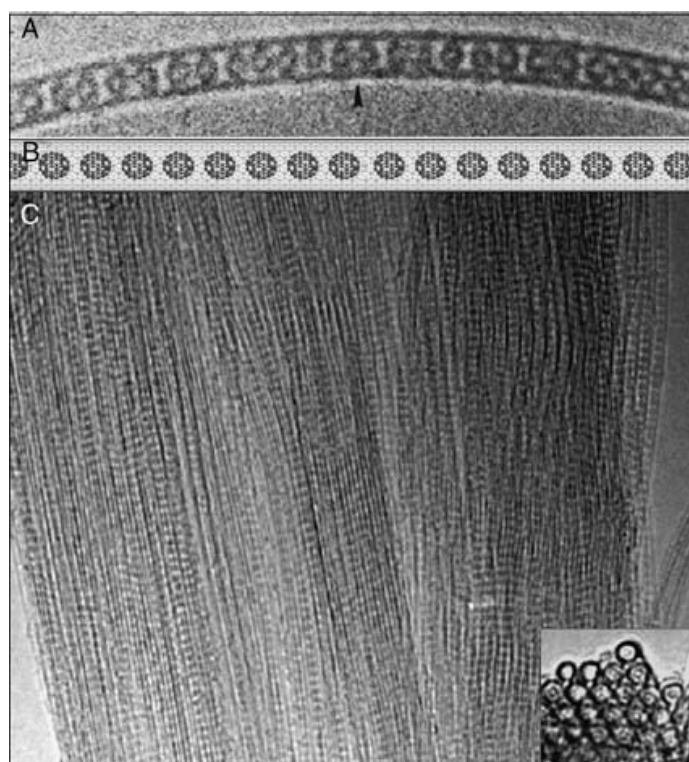


**Figure 3.1** (a) High-resolution transmission electron microscopy (HRTEM) micrograph of isolated peapod illustrating the one-dimensional array of fullerene  $C_{60}$  molecules filled inside a SWNT. (b) The molecular model of the peapod structure showing the spherical molecules of  $C_{60}$  of 0.7 nm diameter encapsulated inside a  $\sim 1.4$ -nm (10, 10) nanotube. (c) Illustrates the TEM micrograph of a SWNT rope filled with  $C_{60}$  molecules showing characteristic image contrast.

of peapods would require bulk samples. A thorough understanding of the mechanism of peapod formation was needed.

### 3.2.1 Mechanism of formation

To determine the mechanism of peapod formation, Smith and Luzzi performed a novel *in situ* experiment involving the exposure of a nanotube bucky paper sample to a fullerene vapor generated *in situ* during TEM imaging.<sup>16</sup> As the temperature of the stage was ramped to about 325°C, corresponding to the sublimation temperature of  $C_{60}$  at the microscope column pressure, impurity  $C_{60}$  fullerenes present in the sample vaporized and bombarded the surfaces of SWNTs via dynamic adsorption and desorption. It was proposed that diffusion of the fullerenes along the nanotubes facilitated access to the nanotubes' interiors through defective regions, e.g., open caps or sidewall defects. The micrographs illustrating the successive events during this experiment are shown in Figure 3.2. The molecules are seen to be mobile in successive frames, and they ostensibly fill the nanotubes once they encounter openings. Once the fullerenes are encapsulated by a nanotube, they evidently self-assemble into a linear chain, which has been found to be the energetically favored configuration.

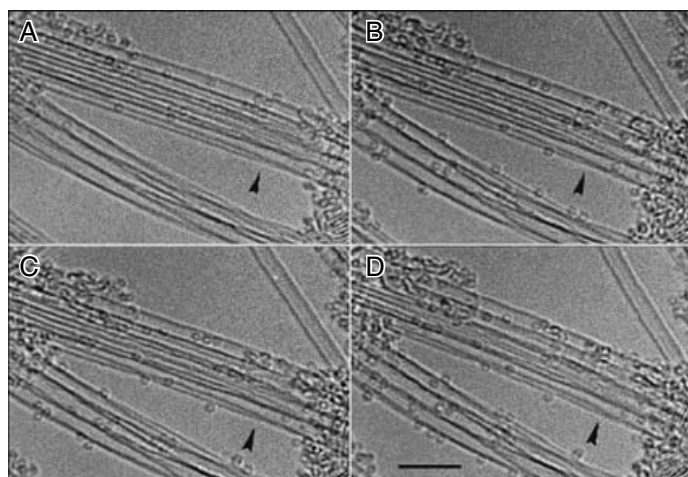


**Figure 3.2** (a–d) Successive micrographs taken during the *in situ* annealing of nanotubes' bucky paper material at 350°C. The sequence shows the mobility of exterior C<sub>60</sub> molecules on the surface of SWNTs, which appear as circles 0.7 nm in diameter. A fixed position is indicated with an arrow to infer the mobility of molecules. Scale bar is 5 nm. (From Smith, B.W. and Luzzi, D.E., *Chem. Phys. Lett.*, 321, 169, 2000. With permission.)

Theoretical studies have supported this proposed mechanism of fullerene encapsulation. Calculations have been based on the intermolecular binding potentials for graphitic materials and other related experimental parameters, such as filling temperature, vapor pressure, and process kinetics. Using a continuum model with a Lennard–Jones potential, Girifalco et al.<sup>17</sup> have calculated that the binding energy of C<sub>60</sub> molecules inside a (10, 10) nanotube is six times higher than that of C<sub>60</sub> on the exterior of the nanotube. Thus, any C<sub>60</sub> molecule physisorbed to the surface of a SWNT near an opening to the interior will be drawn down a potential gradient and into the tube. A C<sub>60</sub> molecule physisorbed on the exterior of a SWNT can diffuse along the surface very easily at the relevant temperatures, as the energy barrier for sliding is only ~0.1% of the binding energy to the wall.<sup>17</sup>

Berber et al.<sup>18</sup> carried out molecular dynamics calculations using an electronic Hamiltonian to study the mechanism of peapod encapsulation. In their model they predicted a barrierless filling process and an optimal filling temperature of ~400°C. Encapsulation occurred predominantly through wall defects and open ends of nanotubes. A more quantitative treatment of the filling mechanism was proposed by Ulbricht and Hertel,<sup>19</sup> who experimentally deduced the interaction potential of fullerene molecules on a graphite surface through temperature-programmed thermal desorption (TPD) spectroscopy. Using molecular mechanics and molecular dynamics, the authors further described a system where fullerene molecules were allowed to fill inside a rope comprising three open-ended nanotubes, with one of the tubes having a wall defect (Figure 3.3). Potential energy calculations for various filling geometries indicated a lip barrier at the entrance of an open tube (groove, position 2), while encapsulation through open ends and defects



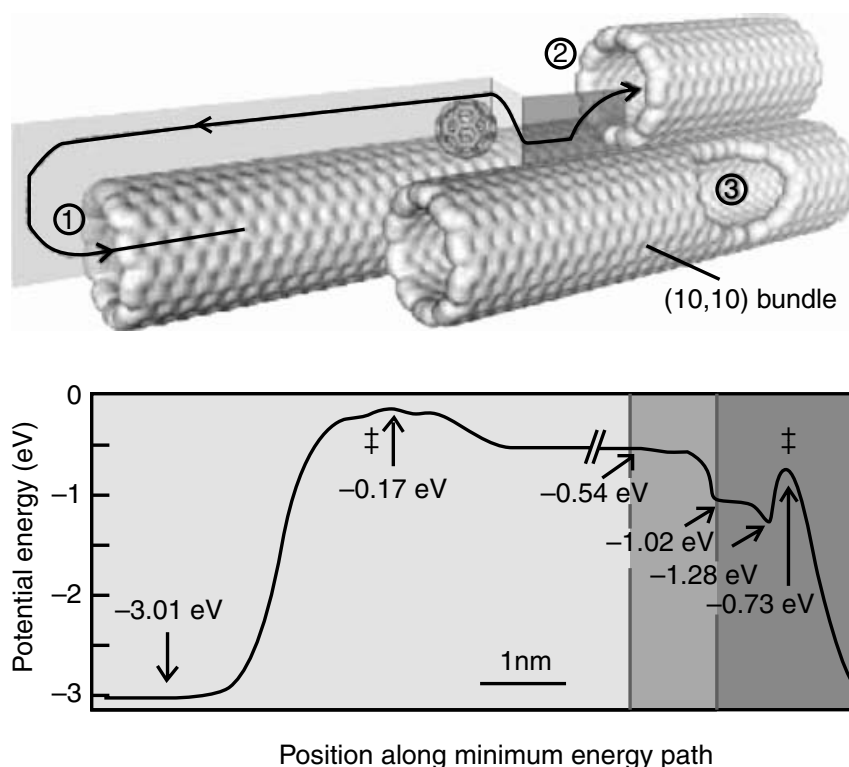


**Figure 3.3** A cut through the three-dimensional potential energy surface of a small (10, 10) tube bundle with three defect positions, which facilitate the filling of fullerene molecules. Calculations show that encapsulation is most efficient via the head-on approach along the reaction path labeled (2) than the other two positions due to the coordination. Double cross indicates the transition states. (From Ulbricht, H. and Hertel, T., *J. Phys. Chem.*, 107, 14185, 2003. With permission.)

(positions 1 and 3) was barrier-free. The successful encapsulation rates estimated by the authors for filling through these three sites (isolated end, groove, and wall defect) were respectively  $10^5 \text{ sec}^{-1}$ ,  $10^7 \text{ sec}^{-1}$ , and  $10^3 \text{ sec}^{-1}$ . It may soon become possible to investigate these findings experimentally by filling isolated nanotubes with carefully controlled defects.

This understanding of the fundamental mechanism of  $\text{C}_{60}$  encapsulation enabled the development of methods for milligram-scale peapod synthesis. Efficient processing schemes were necessary to remove amorphous carbon (a-C) coverage from the starting nanotube material and to introduce openings in the nanotube structure. Treatment with acids or oxidizers, and particularly treatment with peroxide ( $\text{H}_2\text{O}_2$ ) followed by HCl suspension, has yielded the best results for filling experiments.<sup>20,21</sup> This has been attributed to the efficient decomposition and solubilization of overcoated a-C by aqueous peroxide and the concomitant oxidation of nanotubes resulting in open end caps and sidewall defects. It is also necessary to select temperature–pressure conditions that balance the  $\text{C}_{60}$  vapor pressure and the surface diffusivity to optimize encapsulation probability. Good yields are generally obtained when syntheses are performed under an inert, static  $\text{C}_{60}$  atmosphere around  $400^\circ\text{C}$ . Under these conditions, the fullerene molecules can efficiently access the lumens of nanotubes through defect sites.



### 3.2.2 Structural characterization of peapods

#### 3.2.2.1 Electron diffraction

Because of the initial unavailability of bulk material, the first quantitative investigations of peapod structure utilized electron diffraction. Smith et al.<sup>21</sup> performed electron diffraction studies on individual ropes containing C<sub>60</sub> peapods at 94 K. The obtained patterns showed characteristic broken streaks oriented parallel to the rope lattice reflections and perpendicular to the real space direction of the bundle axis. These features corresponded to the intersection of the Ewald sphere with the form factor of a one-dimensional lattice of C<sub>60</sub>. The spacing of the streaks indicated a real space center-to-center distance of ~10 Å, which is similar to the nearest-neighbor separation in face-centered cubic (fcc) C<sub>60</sub>, 10.01 Å. These measurements were performed using an internal calibration standard such that any tilt of the rope out of the imaging plane would not affect the determined lattice parameter, and they were validated by simulation. Similar studies by other investigators<sup>22</sup> have concluded that the lattice parameter is 9.7 Å, which is slightly less than the bulk <110> separation. This discrepancy has never been reconciled but could be due to differences in experimental conditions, sample material, or measurement error.

Hirahara et al.<sup>22</sup> characterized one-dimensional crystals of a variety of larger fullerenes encapsulated in SWNTs using high-resolution transmission electron microscopy (HRTEM) and electron diffraction. They concluded that the intermolecular distances of various fullerenes in SWNTs are considerably smaller than those for bulk fullerene crystals, suggesting an effect of confinement in the one-dimensional channels inside SWNTs.

#### 3.2.2.2 EELS spectroscopy

Microscopy is a local probe that cannot provide an accurate assessment of bulk filling fraction. A *quantitative* measurement of yield was first obtained by Liu et al. using electron energy loss spectroscopy (EELS).<sup>23,24</sup> Studies were performed to compare the energy loss spectra of peapod and reference (empty nanotube) samples. The C1s core level excitation spectra for both samples show features at 285.4 and 292 eV, corresponding to transitions into unoccupied  $\pi^*$  and  $\sigma^*$  states. However, the spectrum from the peapod sample showed an additional fine structure that was attributed to the presence of the encapsulated fullerenes. The difference spectrum obtained after normalization of the peapod and reference spectra by the C1s edge jump was then compared to C1s spectra for fcc and polymerized C<sub>60</sub> (Figure 3.4). From these data, it was possible to determine that the filling fraction in the peapod sample was ~60%. Notably, this study also concluded that the electronic and optical properties of encapsulated fullerene molecules were similar to those for fcc C<sub>60</sub>, except for small changes in the relative intensities of the  $\pi^*$ -derived molecular orbitals.

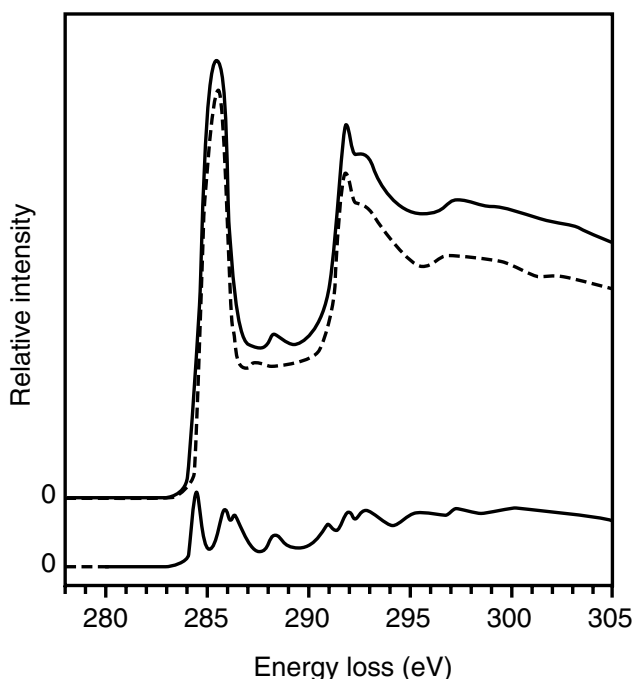


**Figure 3.4** C1s core-level excitation spectra of peapods (solid line) and reference empty SWNTs (dashed line). The difference spectrum at the bottom is the resulting response of the C<sub>60</sub> peas. (From Liu, X. et al., *Phys. Rev. B*, 65, 045419, 2002.)

### 3.2.2.3 X-ray diffraction

X-ray diffraction is typically applied to SWNTs to determine the crystalline ordering of nanotube bundles. For 1.4-nm-diameter SWNTs, the bundles are packed in a two-dimensional triangular lattice with a parameter of 17.4 Å, yielding an intense (1, 0) rope lattice reflection at 0.42 Å<sup>-1</sup>.<sup>25,26</sup> The intensity of this reflection is strongly attenuated by the presence of encapsulated C<sub>60</sub> due to the destructive interference of the form factors of the two component molecules.<sup>27,28</sup> Therefore, the attenuation of this peak can be used as a metric to quantify the filling yield. Zhou et al.<sup>26</sup> analyzed x-ray scattering from peapod samples using a two-dimensional detector and measured the filling fraction by this method to be 60 to 85%. **Figure 3.5** shows the x-ray diffraction patterns of peapod and control (empty) samples. The control sample shows the intense first-order peak due to the crystalline lattice of nanotubes. For the peapod sample, this reflection is weak in intensity due to the diminished overall form factor.

### 3.2.2.4 Raman spectroscopy

Raman spectroscopy has proven to be a key technique in the study of SWNTs<sup>29</sup> and peapods.<sup>30,31</sup> In the case of C<sub>60</sub>, two modes with A<sub>g</sub> symmetry and eight modes with H<sub>g</sub> symmetry are Raman active. Most prominent is the pentagonal pinch mode A<sub>g</sub>(2), located at 1469 cm<sup>-1</sup> at room temperature. Low-temperature Raman spectroscopy characterization of peapods using laser excitations in the range 1.24 to 3.0 eV was reported by Pfeiffer et al.<sup>30</sup> The peapod spectra (**Figure 3.6**) show slight downshifts of the radial

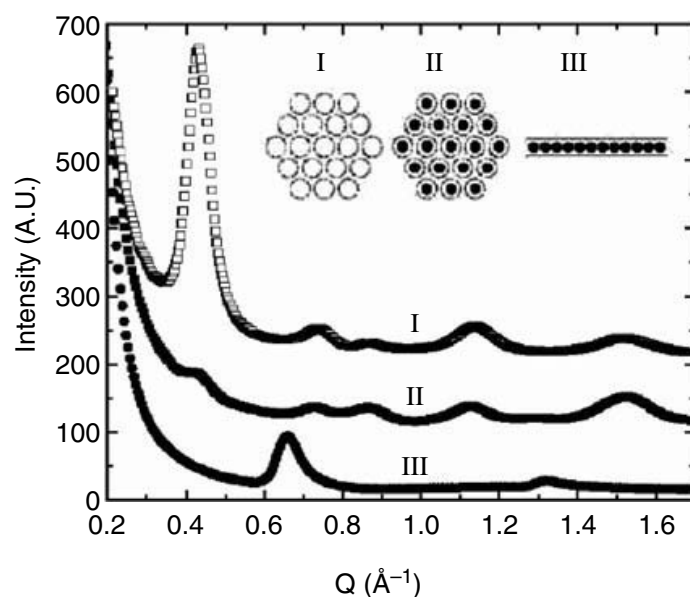


**Figure 3.5** X-ray diffraction patterns from the starting SWNT film (control sample) and C<sub>60</sub>@SWNT film (peapod sample). Note the filling of C<sub>60</sub> molecules into nanotubes significantly changes the diffraction profile. The (001) and (002) peaks from the C<sub>60</sub> chains are easily detected. (From Zhou, W. et al., *Appl. Phys. Lett.*, 84, 2172, 2004.)

breathing modes relative to the empty samples. This was attributed to an expansion of individual nanotubes upon filling, resulting in slightly larger diameters and lower-frequency resonances. The peapod spectra also show an unusual splitting of the C<sub>60</sub> A<sub>g</sub>(2) mode into component peaks at 1466 and 1474 cm<sup>-1</sup>. The relative intensity of these two peaks changes as a function of the excitation energy. To determine the origin of this splitting, Pfeiffer et al.<sup>31</sup> further considered the symmetry, nanotube polarization effects, and motion of the constituent molecules. Using molecular dynamics calculations to account for interactions between the peas (C<sub>60</sub> molecules) and the pod (nanotube), the authors interpreted the peak splitting as a consequence of the motion of encapsulated C<sub>60</sub> molecules within, and their mechanical coupling to, the host nanotubes.

### 3.2.3 Properties of peapods

#### 3.2.3.1 Band structure

One prospect afforded by the ability to encapsulate heteromolecules within a nanotube is the possibility to modify that SWNT's intrinsic electronic structure. Interactions between the component molecules result in a mixed band structure that differs from that of either isolated species. As we describe below, this has been experimentally verified primarily by scanning tunneling microscopy (STM) studies of individual peapods performed at low temperature and ultrahigh vacuum.<sup>32</sup>

Theoretical models of a one-dimensional chain of C<sub>60</sub> molecules inside a semiconducting SWNT have predicted hybridization of the C<sub>60</sub> lowest unoccupied molecular orbital (LUMO) with the conduction band of the

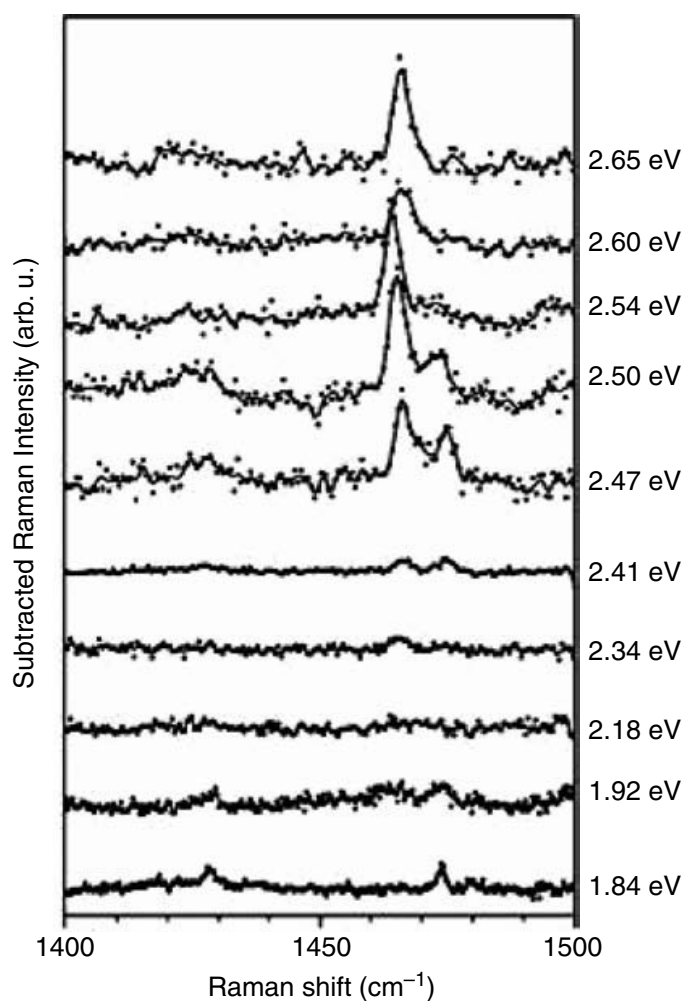


**Figure 3.6** Raman response of the  $A_g(2)$  pinch mode of the encapsulated  $C_{60}$  peas for different laser lines at 80 K after subtracting the Raman signal of the empty reference SWNTs. Notice the splitting of the pinch mode due to the encapsulation process. (From Pfeiffer, R. et al., *Diamond Rel. Mater.*, 11, 957, 2002.)

nanotube.<sup>33,34</sup> Even though no electron charge transfer is predicted (which, independently, would result in a rigid shift of the relevant Fermi levels), this partial mixing leads to new states that are not present in the band structure of either component. This prediction was empirically verified by Hornbaker et al.,<sup>32</sup> who studied individual peapods by STM and found that these assemblies can be distinguished from empty nanotubes by a characteristic periodic modulation. This modulation, present only for peapod structures at certain bias voltages, was superimposed on the usual honeycomb lattice image of the SWNT cage and showed a characteristic spacing of  $\sim 10$  Å, which is very close to the experimental lattice spacing observed in TEM and diffraction studies.<sup>21,22,27,28</sup>

This study also generated detailed information about the spatially resolved density of states (DOS) by obtaining differential conductance ( $dI/dV$ ) spectra at the STM junction as a function of the bias voltage (V) while moving the tip along the peapod. The authors observed that the occupied electronic states (imaged at negative sample bias) were equivalent to those

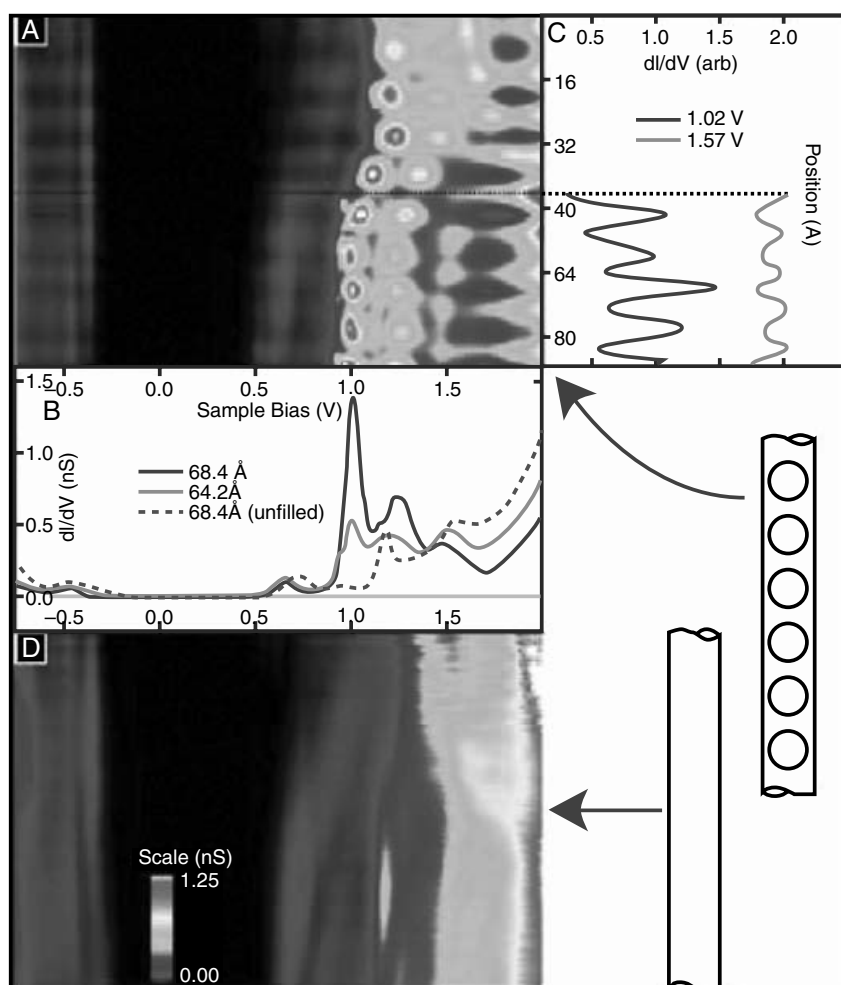


**Figure 3.7** Differential conductance spectra of a  $C_{60}$  peapod. (a) Conductance vs. position ( $\text{\AA}$ ) and sample bias (V) for the peapod. Spatially localized modulations are observed only for positive sample bias, i.e., in the unoccupied density of states. The periodicity of these modulations matches the periodicity of the encapsulated fullerenes. (b, c) Conductance at constant position and at constant sample bias. (d) Conductance vs. position for the same location on the SWNT after the  $C_{60}$  molecules have been shuttled into an empty part of the tube by manipulation with the STM tip. No periodic modulations are observed. (From Hornbaker, D.J. et al., *Science*, 295, 828, 2002.)

expected for an unfilled semiconducting SWNT (Figure 3.7). However, the unoccupied states (imaged at positive sample bias) showed a strong periodic modulation in the bias range of 1.0 to 1.25 eV (Figure 3.7) that corresponded to the features detected in the lattice images. Calculations suggested that these modulations appeared *between* the  $C_{60}$  molecules, i.e., out of phase with the peas. The observation of energy-dependent periodic variations in the unoccupied DOS suggests that  $C_{60}$ @SWNT should have significantly different conduction properties than an empty SWNT.

Okada et al.<sup>33</sup> used a total energy approach to predict the electronic band structure for peapods derived from various armchair nanotubes. Calculations showed that encapsulation was exothermic into (10, 10) SWNTs but



endothermic into the slightly smaller (9, 9) and (8, 8) structures. Peapods based on (10, 10) tubes showed a unique band structure having additional free electron states near the Fermi level of the unperturbed SWNT.

### 3.2.3.2 *Electrical and thermal conduction*

Initial progress toward measurement of the electrical and thermal properties of peapods was slow due to the relative unavailability of bulk samples. However, transport measurements have been successfully performed on bucky paper materials in which a significant fraction of the SWNTs are filled with  $C_{60}$  molecules. Four probe resistivity measurements<sup>35</sup> of such samples have shown decreased resistivity at low temperature with respect to control samples of unfilled nanotubes. This has been attributed to availability of additional conduction channels afforded by the one-dimensional  $C_{60}$  chains (as described in the previous section). It is not likely that the lower resistivity is due to charge transfer, as is known to occur with ion-doped nanotube samples.<sup>36</sup>

Despite this consistent finding, there have been conflicting reports of the electrical transport properties of  $C_{60}$ @SWNT.<sup>37</sup> Figure 3.8a and b show four probe measurements performed on two peapod samples designated A and 24 by the study authors.<sup>20,21</sup> The reported filling fractions for samples A and 24 are 23 and 60%, respectively. Curiously, sample A shows a lower resistivity than empty nanotubes across the measured temperature range (Figure 3.8a), while the opposite trend emerges for sample 24 (Figure 3.8b). The first case is again in agreement with theoretical calculations by Okada et al.,<sup>33</sup> who predicted additional conduction channels contributed by the unoccupied electronic states from the fullerene molecules. Since both samples have mean SWNT diameters of about 1.4 nm, which are predominantly armchair, a decrease in resistivity would be expected upon filling with fullerene molecules. The observed discrepancies are potentially attributable to different sample processing histories. It is well documented that the specifics of acid treatment, exposure to  $C_{60}$  vapor, thermal anneal, etc., are important in determining the resulting material structure and properties. Further discussion of these factors can be found in reports on transport measurements by Vavro et al.<sup>35,37</sup>

### 3.2.3.3 *Optical properties*

Optical absorption characterization of thin films of nanotubes and peapods has been carried out by Kataura et al.<sup>25</sup> There are no literature reports evidencing distinct, unique optical characteristics for peapods in comparison to nanotubes. However, it has been recently shown that individual semiconducting nanotubes can be isolated from bundles in surfactant micelles and show characteristic signatures in UV-vis absorption and fluorescence spectra.<sup>38,39</sup> Efforts to isolate peapod samples for optical characterization are still in progress, so the effect of filling on optical behavior of individual nanotubes remains unknown.



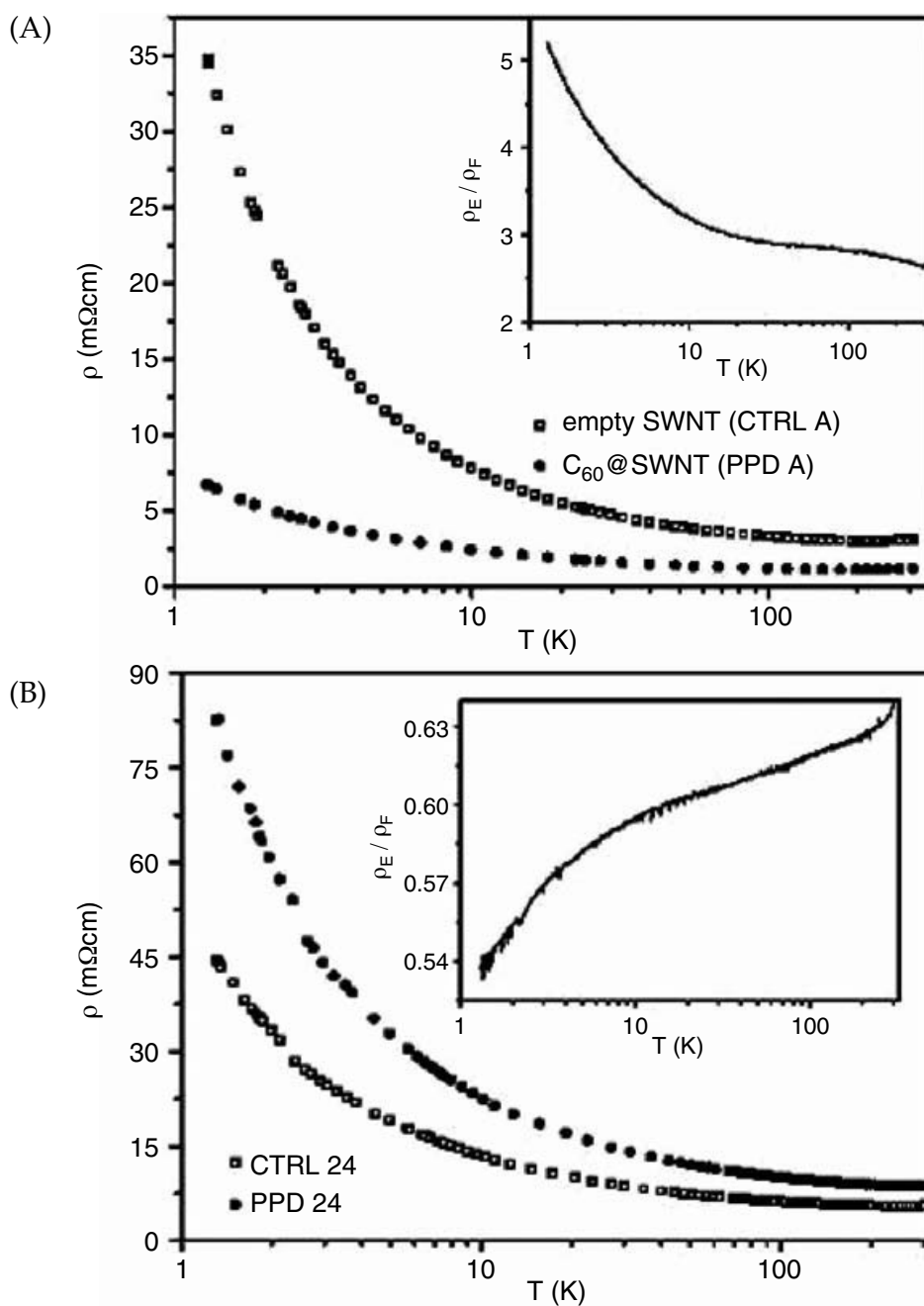


**Figure 3.8** (a) Four-point resistivity vs.  $T$  for  $C_{60}$ @SWNT PPD-A (filled circles) and empty CTRL-A sample (open squares); the ratio of empty to filled is shown in the inset. (b) Temperature dependence of resistivity for  $C_{60}$ @SWNT sample 24 (filled circles) and empty reference 24 (open squares). (Courtesy of Dr. J. E. Fischer and Dr. J. Vavro.)

### 3.2.4 Transformations of peapods

#### 3.2.4.1 Effects of doping

Chemical doping has afforded a means of further modification of the electrical properties of  $C_{60}$ @SWNT. Using Raman and resistivity measurements, Pichler et al.<sup>40</sup> characterized peapods that were  $n$ -doped with potassium ions. The authors observed that the doping is competitive between the peas and

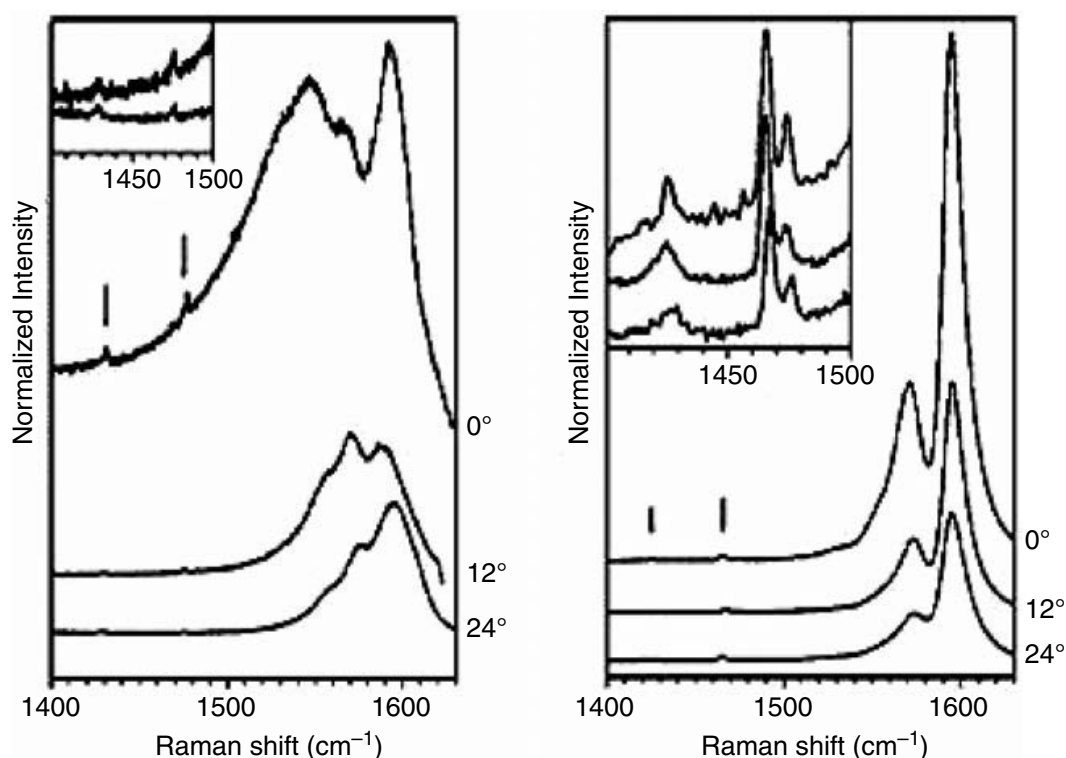


**Figure 3.9** Raman spectra of  $C_{60}$  peapods in the range of the G lines for two different levels of  $FeCl_3$  intercalation, as indicated by the intercalation time in hours. Two different excitation energies were used: left panel, 1.84 eV (red laser), and right panel, 2.5 eV (green laser). The inset shows blown-up spectra for the  $A_g$  pinch mode and the  $H_g(7)$  mode, as indicated by the arrows. (From Pichler, T. et al., *Phys. Rev. B*, 67, 125416, 2003.)

the pods: initial doping occurs in the SWNTs, and the fullerenes are doped only upon heavy potassium uptake. The radial breathing modes measured by Raman showed broadening upon doping, which was interpreted as a loss of resonance due to chemical reaction between the dopants and the fullerenes, yielding polymeric metallic phases.

Pichler et al.<sup>41</sup> also studied the effect of *p*-doping with  $FeCl_3$ . The Raman spectra of the *p*-doped peapods (Figure 3.9) exhibited intensity changes in the G-band region. When excited with a red laser (1.84 eV), the characteristic lower-frequency Fano resonance due to the metallic nanotubes showed a drastic bleaching with increasing doping (left panel). By comparison, when excited with a green laser (2.54 eV), higher-frequency features from the semiconducting nanotubes decreased more gradually in peak intensity (right panel). These results relate to the initial relative doping level of metallic vs. semiconducting SWNTs. The spectra do not show changes in the fullerene molecules upon doping, as seen for the  $A_g(2)$  pinch mode and  $H_g(7)$  modes upon doping (insets). The authors concluded that the *p*-dopant transfers charge initially to the host nanotubes, as was observed for *n*-type doping. Raman measurements performed at saturation doping indicated a charge transfer of 0.05 e/C atom to nanotubes and 6 e/ $C_{60}$  molecule.

### 3.2.4.2 High-pressure transformations

The low dimensionality of a peapod makes it an interesting model for testing material response to hydrostatic pressure. Hodak and Girifalco<sup>42</sup> have computed the cohesive properties of SWNT ropes composed of either (10, 10) tubes or peapods using Lennard–Jones potentials. The calculations predict a 15% greater cohesive energy for peapod ropes than for ropes of empty SWNTs. This suggests that peapods are more resistant to applied external pressure.

Rafailov et al.<sup>43</sup> empirically studied the transformation of C<sub>60</sub>@SWNT and C<sub>70</sub>@SWNT under hydrostatic pressure using a diamond anvil cell and Raman characterization. Both materials showed a linear pressure-induced hardening of all the relevant Raman modes. A linear hardening of the C<sub>60</sub> A<sub>g</sub>(2) mode was observed for C<sub>60</sub>@SWNT, indicating no pressure-induced structural transformation of the C<sub>60</sub> molecules. However, for C<sub>70</sub>@SWNT an abrupt discontinuity was observed at 1.5 GPa in the pressure dependence of modes in the range 1440 to 1490 cm<sup>-1</sup>. This was interpreted as a change in the orientation of the elliptical C<sub>70</sub> molecules, from a perpendicular to a parallel orientation of the fullerene's long axis with respect to the SWNT axis. Obviously, no such transformation could occur in the case of the spheroidal C<sub>60</sub> molecule.

### 3.2.4.3 Irradiation-induced and thermally induced coalescence

C<sub>60</sub>@SWNT experiences a unique coalescence transformation when irradiated with an electron beam or vacuum annealed at moderately high temperatures. The energy imparted by these processes is sufficient to cause a structural rearrangement of the sterically confined C<sub>60</sub> molecules into coaxial capsules having a larger average radius of curvature and lower overall strain energy. TEM studies of peapods by Luzzi and Smith<sup>44</sup> indicated that knock-on ejections occur more rapidly to the C<sub>60</sub> molecules than to the surrounding SWNTs because of differences in bond strain. Any dangling bonds appearing in the C<sub>60</sub> cages can be satisfied only by the fusion of adjacent C<sub>60</sub> molecules into larger, irregularly shaped fullerenes. Smith and Luzzi reported (Figure 3.10) the thermally induced conversion of C<sub>60</sub>@SWNT into extended segments of uniform double-wall nanotubes (DWNTs).<sup>44</sup> Bandow et al.<sup>45</sup> performed a rigorous study of this phenomenon, demonstrating the complete transformation of peapods into DWNTs by vacuum annealing at ~1200°C. The authors examined the coalescence process by Raman spectroscopy and found that the transformation begins at temperatures as low as 800°C. The final product was generally determined by the diameter of the host SWNT; i.e., the coalesced structure always filled the available lumen, leaving only the graphitic van der Waals separation between the two components.

Continued studies<sup>46–48</sup> of these structures have generated more information about the mechanism of formation. Hernandez et al.<sup>49</sup> studied the coalescence mechanism of encapsulated C<sub>60</sub> with tight-binding molecular

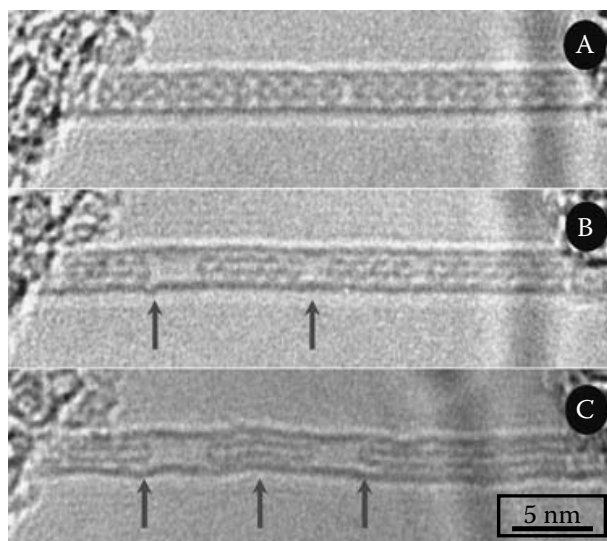


**Figure 3.10** HRTEM micrographs of sequence of coalescence events in peapods. (a) Starting peapod showing the linear chain of fullerene molecules inside a SWNT. The peapod shows the coalescence of peas and shrinkage of resultant partial tube-like structures (b) and shows the coaxial tubes formed inside the starting nanotubes (c).

dynamics simulations. They observed that the process proceeds through two distinct steps: polymerization of adjacent fullerene molecules into corrugated tube-like structures, followed by surface reconstruction to yield concentric double-wall nanotubes.

### 3.3 Beyond $C_{60}$ : other hierarchical nanotube materials

#### 3.3.1 Alternate synthesis methods

The ability to fill SWNTs with  $C_{60}$  molecules is facilitated by the low sublimation temperature of  $C_{60}$ . It is relatively easy to attain high vapor pressures at temperatures that are well below the threshold for decomposition. However, most materials do not possess this characteristic, and most molecular solids and liquids decompose or react before adequate vapor pressures can be attained for reasonable filling kinetics. For this reason, extension of the peapod synthesis scheme to other types of encapsulated species may require an alternate approach.

In principle, liquid solutions can be used to deliver  $C_{60}$  and other molecules to openings in processed SWNTs. The energetics of encapsulation remain much the same, but in this case there is an activation barrier associated with the solvation energy of the fill molecule by the solvent. In this method, the SWNT effectively acts as a thermodynamic sieve to remove the fill molecule from solution. There are several examples of successful solution-based filling. Yudasaka et al.<sup>50</sup> employed a low-temperature reflux of  $C_{60}$  and SWNTs in ethanol and reported a high filling yield.

Using an alkali–fullerene plasma technique, Jeong et al.<sup>51</sup> succeeded at filling SWNTs with  $C_{60}$  molecules. The method is based on a plasma synthesis

in which vaporized fullerene molecules are carried by charged alkali ions under the influence of applied voltage. Upon contact with SWNT ropes, the molecules are encapsulated.

### 3.3.2 Peapods of metallofullerenes

Methods for encapsulating  $C_{60}$  in SWNTs are most logically extended to the metallofullerene family of molecules.<sup>52</sup> Initially, metallofullerene filling was explored because the heavy metal ions contained by the fullerene cages are exogenous to nanotube material. Therefore, the detection of these strongly electron-scattering heteroatoms inside SWNTs proved that extrinsic molecules could be inserted into the tubes under controlled conditions. Unfortunately, the relatively low yields and difficult chromatographic purification of metallofullerene molecules have slowed progress in this area.<sup>52</sup>

Smith et al.<sup>53</sup> reported the first successful encapsulation of metallofullerenes in SWNTs. The authors synthesized  $La_2@C_{80}$  metallofullerene peapods by evaporating a toluene solution of  $La_2@C_{80}$  onto a bucky paper sample, and then annealing the sample *in situ* at  $\sim 600^\circ\text{C}$  during TEM imaging. The authors observed a discontinuous ratcheting motion of the La atoms inside the fullerene cages, which was not expected based upon published nuclear magnetic resonance (NMR) data. It was hypothesized that this behavior was due to intermolecular charge transfer. Similarly, Hirahara et al.<sup>54</sup> studied the encapsulation of  $Gd@C_{82}$  in SWNTs and characterized the resulting structures by electron diffraction, measuring a one-dimensional metallofullerene lattice parameter of  $\sim 1.1$  nm. The authors also performed electrical resistance measurements on bulk samples of fullerene and metallofullerene peapods, which showed higher resistivity than an unfilled nanotube control.<sup>54</sup> This was explained as a manifestation of charge carrier scattering by the local electrostatic potential of the encapsulated molecules.

The tremendous spatial resolution that can be attained by HRTEM and EELS has proven essential to the characterization of these novel hierarchical nanostructures. For instance, Suenaga et al.<sup>55</sup> were able to image single Gd atoms in the structure  $Gd@C_{82}@SWNT$  using energy-filtered TEM. Based upon scattering cross sections as well as the relative intensities of the Gd and C edges in the EELS spectrum, the authors estimated a metal atom concentration that correlated well with the imaging data. Figure 3.11 shows the relevant TEM image, schematic model, and EELS spectrum from this study.

Metallofullerene peapods have made it possible to glean further insight into reactions that can occur inside the constrained environment of a SWNT. Okazaki et al.<sup>56</sup> empirically followed the coalescence mechanism of  $Sm@C_{82}$  inside SWNTs using a combination of TEM imaging and EELS analysis. The individual metallofullerenes were seen to coalesce during electron irradiation such that the chemical environment of the metal atoms is perturbed and discrete metal clusters are formed. This process was quantified by a change in the fine structure in the Sm energy loss spectrum.



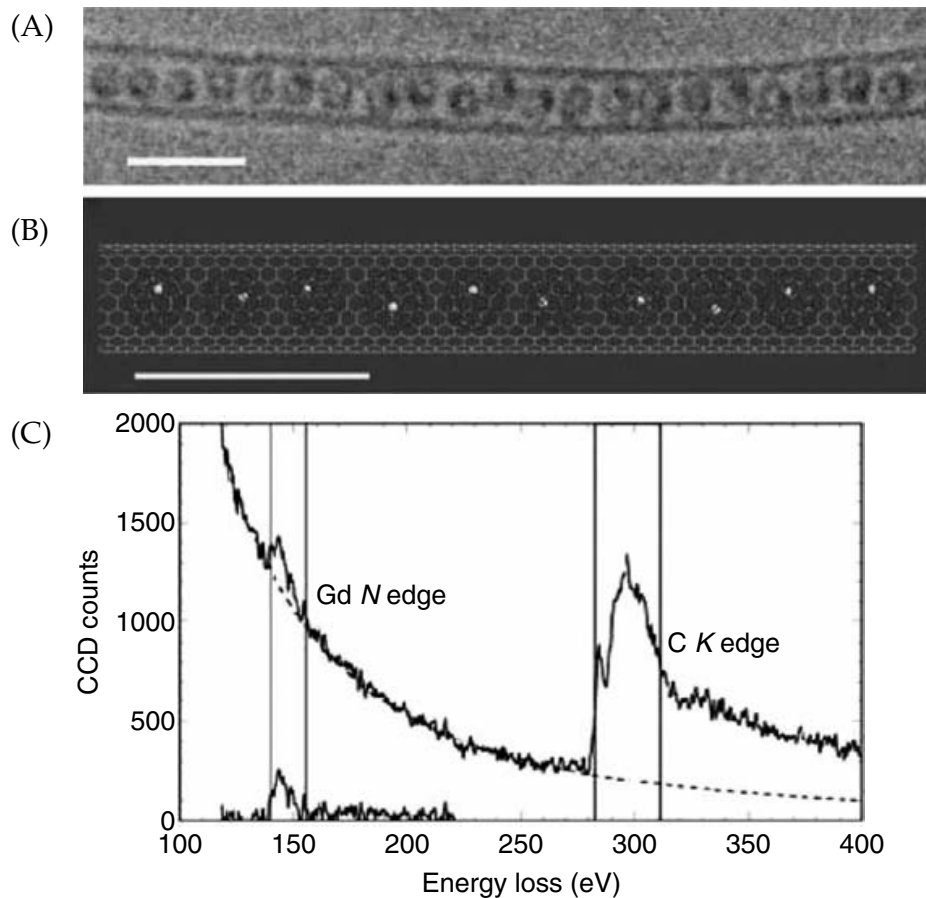


**Figure 3.11** (a) A conventional high-resolution image and (b) a schematic presentation of a similar structure. A chain of endohedral Gd-metallofullerenes (Gd@C<sub>82</sub>) is encapsulated in a SWNT. The Gd atoms are shown in yellow in (b). Scale bars, 3 nm. (c) A typical EELS spectrum showing the Gd N edge and carbon K edge (chosen at the central pixel of a Gd atom). The background-stripped Gd N edge is crucial with respect to the noise level and implies that one (or two) Gd atom(s) are involved. (From Suenaga, K. et al., *Science*, 290, 2280, 2000.)

Interactions between metallofullerenes and SWNTs have been implicated in modifying the intrinsic SWNT electronic band gap. Using low-temperature scanning tunneling microscopy, Lee et al.<sup>57</sup> observed a spatial modulation of the band gap in semiconducting nanotubes due to the encapsulation of metallofullerenes. The authors found a band gap reduction from 0.5 to ~0.1 eV at the metallofullerene sites, possibly due to intermolecular charge transfer. This phenomenon was alternatively attributed to elastic strain arising from the encapsulation, but this is unlikely given the fact that local strains are also induced by the measurement process itself.

Shimada et al.<sup>58</sup> have characterized the low-temperature transport properties of isolated ropes of C<sub>60</sub>@SWNT and Gd@C<sub>82</sub>@SWNT on SiO/Si substrates. The fullerene peapods showed *p*-type characteristics, while the metallofullerene peapods showed both *p*-type and *n*-type characteristics, indicative of ambipolar field effect behavior. This effect is apparent in the



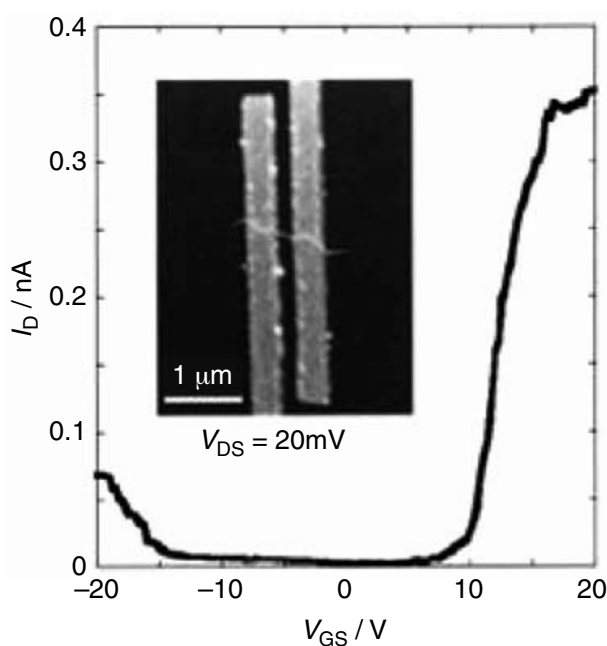


**Figure 3.12**  $I_D$ - $V_{GS}$  curve for Gd@C<sub>82</sub> metallofullerene peapods ( $V_{DS}$  520 mV). The inset is an atomic force microscopy (AFM) image of the Gd@C<sub>82</sub> peapods — a field effect transistor (FET) was used in the measurement. (From Shimada, T. et al., *Appl. Phys. Lett.*, 81, 4067, 2002.)

data of Figure 3.12, which shows the current–voltage characteristics of a device made from a metallofullerene-filled rope.

The related endohedral species N@C<sub>60</sub> has also been explored as a candidate for filling SWNTs.<sup>59</sup> When encapsulated inside a fullerene cage, nitrogen has unpaired electrons and high spin angular momentum, making N@C<sub>60</sub> useful as a spin probe. Simon et al.<sup>59</sup> inserted N@C<sub>60</sub> into SWNTs using a low-temperature process and characterized the resulting peapods using Raman spectroscopy and electron spin resonance (ESR).

### 3.3.3 Peapods of fullerene adducts

Fullerene adducts or organic derivatives of fullerene molecules<sup>60</sup> are the ideal candidates for application in peapod syntheses to create advanced materials. For example, a C<sub>60</sub> molecule could serve as a vector to enable a second, covalently conjugated molecule to be encapsulated inside a SWNT. This approach could facilitate the assembly of molecular “packages” wrapped in a protective SWNT for the purpose of drug delivery. Unfortunately, fullerene adducts typically decompose at relatively low temperatures, necessitating mild filling conditions using solutions<sup>50</sup> or supercritical fluids. Britz et al.<sup>61</sup> have succeeded in filling fullerene C<sub>60</sub> adducts using supercritical CO<sub>2</sub> at 50°C and 150 bar to obtain the adduct peapods C<sub>61</sub>(COOC<sub>2</sub>H<sub>5</sub>)<sub>2</sub>@SWNT and C<sub>61</sub>(COOH)<sub>2</sub>@SWNT. By contrast to other encapsulated fullerenes, the adducts did not form ordered one-dimensional lattices due to the steric effects of the distal functional groups. Based upon the nature of these ligands,

adducts potentially can be tailored to have a strong thermodynamic preference for the interior space of a SWNT over the exterior surface.

### 3.3.4 Heterostructures from nonfullerene materials

The novel peapod structures build upon a rich legacy of other nanotube heterostructures. In fact, it was not long after the discovery of MWNTs that methods for filling their comparatively large luminal cavities were developed. There has been a substantial effort to fill MWNTs with low-surface-tension liquids by capillarity.<sup>6–9,62–71</sup> This was first accomplished by a one-step process, in which capped MWNTs were opened and filled with an unidentified lead compound by annealing MWNTs decorated with evaporated Pb particles in air at 400°C (above  $T_m$  for Pb) for 30 min.<sup>7</sup> Other one-step processes have relied upon wet chemical methods, in which acids or precursors of the filling medium were reacted directly with MWNTs for a number of hours.<sup>6</sup> MWNTs have also been filled by a two-step process, in which tubes were first opened by annealing at 700 to 850°C in air<sup>62,70</sup> or under flowing  $\text{CO}_2$ ,<sup>63</sup> and the open tubes were then filled by direct immersion in a liquid or molten filling medium.<sup>66–69</sup>

These techniques have in common the opening of MWNTs, either by air oxidation (possibly catalyzed by the metal in the case of the one-step process) or chemical oxidation, and the subsequent uptake of a liquid. Dujardin et al.<sup>64</sup> and Ebbesen<sup>65</sup> have independently determined an upper limit of 100 to 200 mN/m for the surface tension of the filling medium above which capillary filling will not occur, although this value is greatly affected by the actual diameter of the MWNT cavity.<sup>70</sup> For these reasons, capillary-based filling is limited to those compounds having low melting points and low surface tensions. A typical example of filled MWNT is shown in the high-resolution transmission electron microscope image in Figure 3.13.

Success has been realized using a broad range of fill materials. Examples of filled or coated MWNTs include those containing Ag, Au,<sup>67,68</sup> Bi,<sup>62</sup> Pd, and Re metals,<sup>68</sup>  $\text{V}_2\text{O}_5$ ,<sup>66</sup>  $\text{SiO}_2$ ,  $\text{Al}_2\text{O}_3$ ,<sup>71</sup>  $\text{ZrO}_2$ ,<sup>72</sup>  $\text{WO}_3$ ,  $\text{MoO}_3$ ,  $\text{Sb}_2\text{O}_5$ ,  $\text{MoO}_2$ ,  $\text{RuO}_2$  and  $\text{IrO}_2$ ,<sup>73</sup>  $\text{La}_2\text{O}_3$ ,  $\text{Pr}_2\text{O}_3$ ,  $\text{CeO}_2$ ,  $\text{Y}_2\text{O}_3$ ,  $\text{Nd}_2\text{O}_3$ ,  $\text{Sm}_2\text{O}_3$ ,<sup>68</sup> and various other Ni,

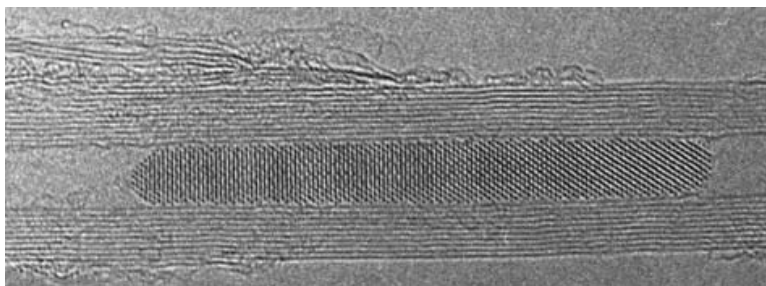


**Figure 3.13** Transmission electron micrograph of a MWNT filled with  $\text{Sm}_2\text{O}_3$ . The interlayer separation in the MWNT is ca. 0.34 nm. Lattice planes in the oxide are clearly seen. (From Chen, Y.K. et al., *J. Mater. Chem.*, 7, 545, 1997.)

Co, Fe, and U oxides,<sup>63</sup> AgNO<sub>3</sub>, CoNO<sub>3</sub>, CuNO<sub>3</sub>,<sup>70</sup> AuCl,<sup>67</sup> and various other nitrate and chloride salts, and the eutectic systems KCl-CuCl<sub>2</sub><sup>68</sup> and KCl-UCl<sub>4</sub>.<sup>69</sup> Certain proteins have been introduced into MWNTs by a similar solution-based method,<sup>8,74</sup> although only in aggregate form. In the case of crystalline filling media, it is sometimes possible to reduce the medium by hydrogen gas flow<sup>9-12</sup> and to remove the MWNT template,<sup>66,71-73</sup> yielding freestanding nanowires.

Reactor-based techniques have also been developed for synthesizing MWNTs filled with various poly- and monocrystalline transition metal (Cr, Ni), rare earth (Dy, Gd, La, Sm, Yb), and covalent (Ge, S, Sb, Se) compounds<sup>75</sup> and carbides.<sup>76,77</sup> In this case, nanotubes were produced by the usual carbon arc evaporation process; only the graphite anode was drilled and packed with the filling medium or its corresponding precursor, and filled MWNTs were collected from the resulting cathode deposit. Alternately, Kyotani et al.<sup>78</sup> and Pradhan et al.<sup>79</sup> synthesized Pt nanowires inside MWNTs using a template carbonization method. Gao and Bando<sup>80</sup> utilized a modified approach of carbon vaporization and synthesized Ga-filled MWNTs using Ga<sub>2</sub>O<sub>3</sub> and amorphous carbon. The encapsulated liquid metal column showed expansion under the thermal effect, which may find application as a thermometer for nanoscale experiments. Using hydrothermal synthesis, Gogotsi et al.<sup>81</sup> synthesized MWNTs that were filled with discrete water columns. The encapsulated water has been shown to exhibit unique physical characteristics due to confinement inside the nanochannels of tubes.<sup>82-85</sup>

Extension of these filling methods to SWNTs has proven difficult because the small lumen diameter does not permit efficient capillary uptake, resulting in preferential wetting of the exterior surfaces by the fill medium. However, a limited number of compounds have been successfully encapsulated in SWNTs, including compositions from the KCl-UCl<sub>4</sub> and AgCl-AgBr systems,<sup>11</sup> Au, Ag, Pt, Pd,<sup>12</sup> Ho, Gd,<sup>86</sup> and KI.<sup>13,87</sup> This last material was studied quantitatively by TEM and lattice image simulation, whereby the authors discovered that the encapsulated 2 × 2 halide nanostructure had a reduced coordination in comparison to the bulk crystal (Figure 3.14). This is yet another example of how the confined nanometer-scale environment inside a SWNT can facilitate the synthesis of an entirely new material. Using scanning transmission electron microscope (STEM) imaging and x-ray energy-dispersive spectroscopy (XEDS), the chemical characteristics of rare earth metal (Ho, Gd) chloride and metal nanowires have been characterized.<sup>86</sup> Figure 3.15 shows the STEM bright-field and dark-field images of Ho nanowires (left panel) filled inside SWNTs, and the XEDS spectra (right panel) of Gd-chloride and Gd nanowires shows the chemical composition of the nanowires. These studies have established beyond doubt the chemical nature of the nanowires inside the nanotubes and their transformation following encapsulation in nanotubes.

This array of methods is beginning to prove useful in the creation and study of nonfullerene peapod materials. Morgan et al.<sup>88</sup> have encapsulated icosahedral *o*-carborane molecules in SWNTs by a vapor phase process.

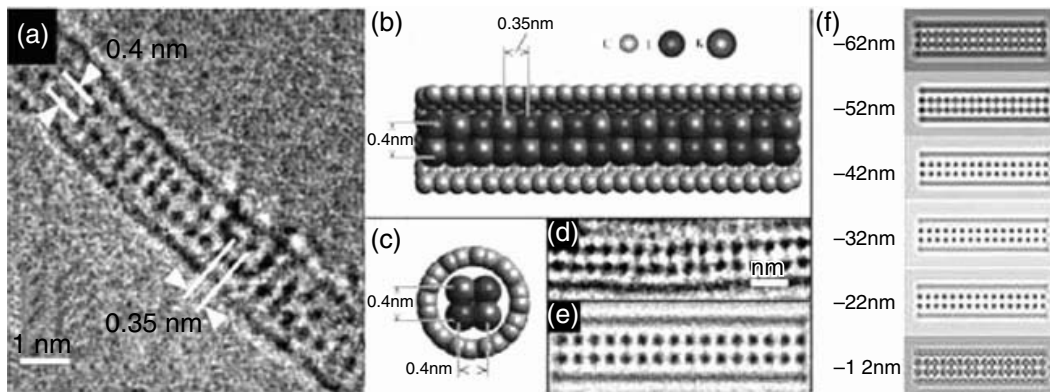


**Figure 3.14** (a) Conventional HRTEM image of a  $2 \times 2$  KI crystal formed within a 1.4-nm-diameter SWNT. (b, c) Side-on and end-on structural representations of the  $2 \times 2$  KI crystal within a (10, 10) SWNT showing measured lattice distortions. (d–f) HRTEM image: calculated Scherzer focus image and calculated through focal series corresponding to (b) and (c). (From Sloan, J. et al., *Chem. Commun.*, 1319, 2002.)

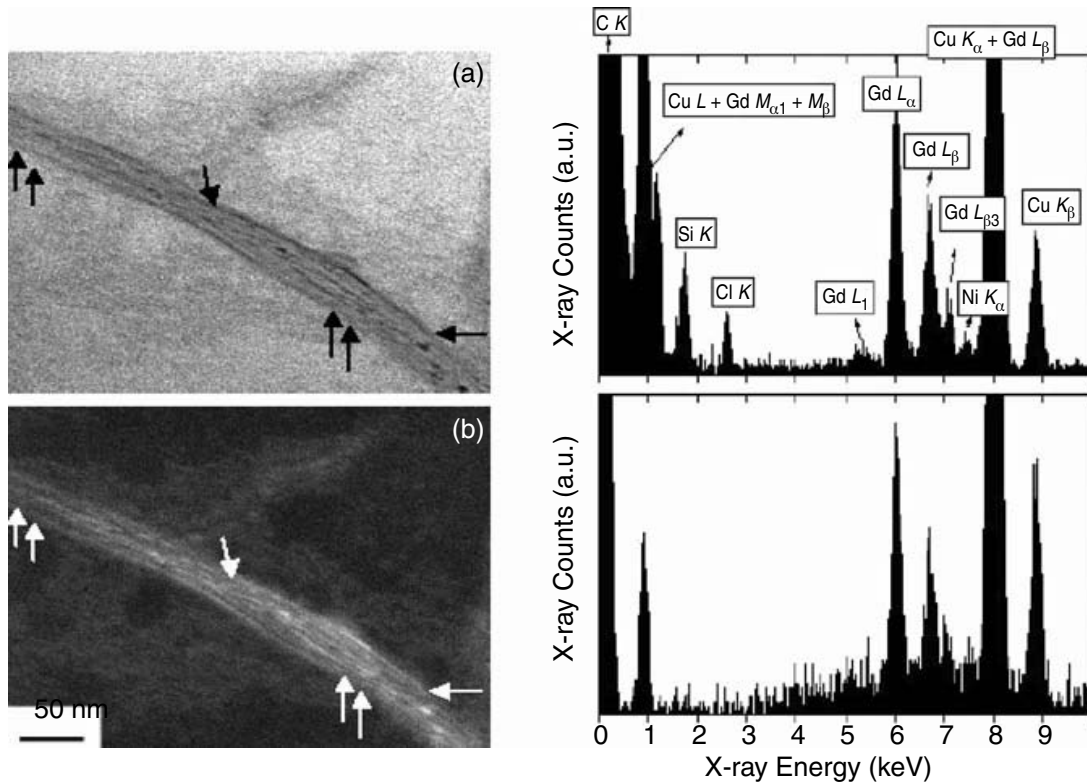


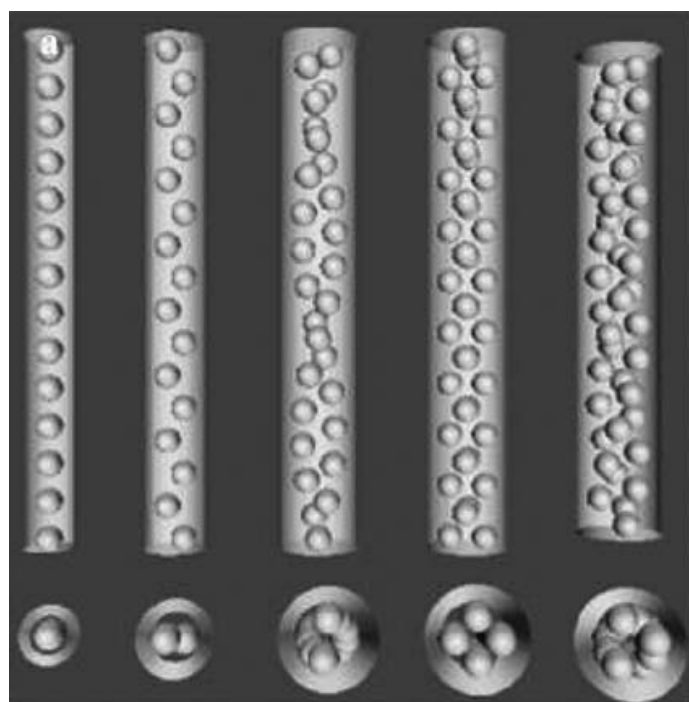
**Figure 3.15** STEM bright-field (a) and high-angle (b) annular dark-field image pair of a Ho-filled SWNT rope. Two of the many metal nanowires present in the images are indicated as lying between the single and double arrows, respectively. XEDS spectra recorded on SWNT ropes for  $\text{GdCl}_3$  (top) and Gd (bottom) nanowires. The analyzed sample area for the spectrum was  $1 \mu\text{m}$ . The Ni K line is due to the catalyst particles. (From Satishkumar, B.C. et al., *J. Nanosci. Nanotech.*, 3, 159, 2003.)



Takenobu et al.<sup>89</sup> have reported filling SWNTs with molecules that have either strong electron affinity or high ionization potential. The authors measured intermolecular charge transfer using a combination of Raman spectroscopy and optical absorption. Jishi et al.<sup>90</sup> have modeled the structures of selenium atoms encapsulated in C, boron-nitrogen (BN), and boron-carbon-nitrogen (BCN) nanotubes using density functional calculations.

### 3.4 Ordered phases of fullerenes in larger nanotubes

The interior space of a SWNT is so small that encapsulated C<sub>60</sub> molecules are constrained to be co-linear, resulting in the formation of ordered one-dimensional arrays. However, it is possible that other quasi-one-dimensional phases could result in tubes with larger-diameter lumens. Hodak and Girifalco<sup>91</sup> modeled this scenario, using a simulated annealing method to predict the minimum energy configurations of C<sub>60</sub> arrays inside nanotubes of various diameters. As the tube diameter was expanded beyond 1.4 nm, the preferred arrangement changed from co-linear to zigzag, double-helical, two-layered, and finally triple-helical arrays. Figure 3.16a shows these various structures modeled inside armchair nanotubes. Different properties are predicted for each of these hierarchical nanostructures.<sup>92</sup>



(a)

**Figure 3.16** (a) Ordered phases of C<sub>60</sub> molecules: the single-chain phase inside (10, 10) tube, the zigzag phase inside (13, 13) tube, the double-helix phase (tube with radius 10.96 Å), the phase of two-molecule layers (tube with radius 11.33 Å), and the triple helix for (17, 17) tube. (From Hodak, M. and Girifalco, L.A., *Phys. Rev. B*, 67, 075419, 2003.)



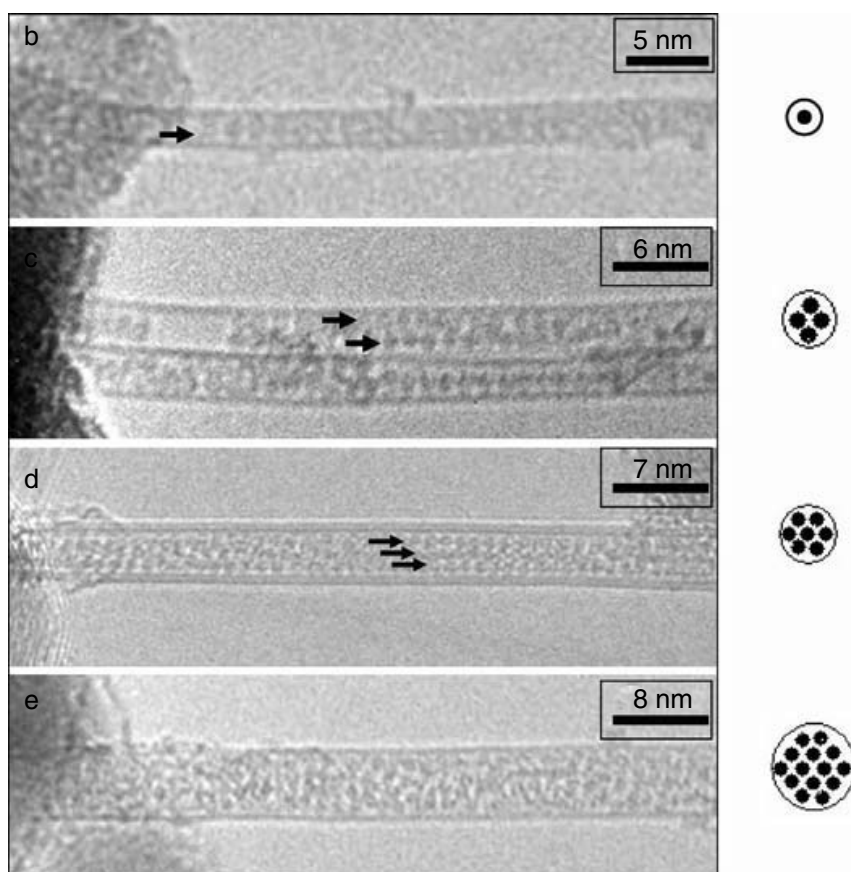


**Figure 3.16** (b–e) HRTEM images of nanotubes showing linear, triangular (one-dimensional), and multilayered arrays of  $C_{60}$  molecules. (From Chikkannanavar, S.B. et al., *Nano Lett.*, 5, 151, 2004.)

There is some experimental evidence to support the aforementioned models. Chikkannanavar et al.<sup>93</sup> have observed ordered phases of  $C_{60}$  inside larger, CVD-produced single- and double-wall nanotubes grown on a substrate (Figure 3.16b to e). Khlobystov et al.<sup>94</sup> have discovered similar zigzag and helical phases inside double-wall nanotubes, and Mickelson et al.<sup>95</sup> have reported multilayered arrangements of  $C_{60}$  inside multiwall BN nanotubes.

### 3.5 Double-wall carbon nanotubes

DWNTs represent structural intermediates between SWNTs and MWNTs. We have already discussed how  $C_{60}@SWNT$  and other peapod materials can be transformed by thermal annealing to create extended segments of DWNTs by coalescing the encapsulated fullerenes.<sup>44–49</sup> However, the potentially interesting electronic properties of these nested graphene cylinders has motivated the search for a direct and scalable synthesis route.

Perhaps the easiest methods for the production of MWNTs and SWNTs are chemical vapor deposition or catalytic decomposition.<sup>1,2,96–103</sup> In CVD, the product is formed by the catalysis of hydrocarbon gas by a metal nanoparticle supported on a mesoporous substrate like alumina. By contrast, catalytic

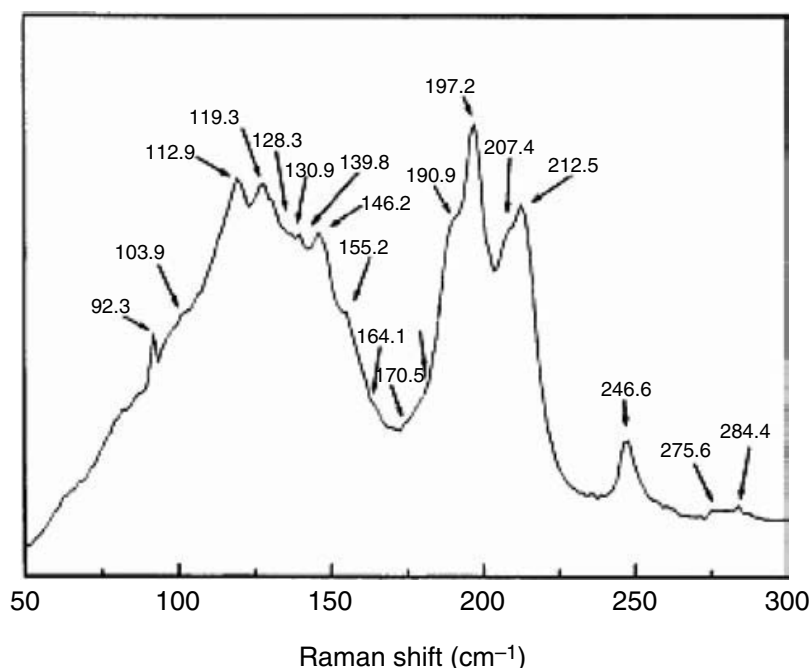


**Figure 3.17** Raman spectrum of CVD-grown DWNTs showing the radial breathing modes of the nanotubes. (From Ren, W. et al., *Chem. Phys. Lett.*, 359, 196, 2002.)

decomposition involves the thermal decomposition of an organometallic precursor to form both the catalyst and the carbon feedstock. These methods share the property that the size of the catalyst particle is generally correlated to the type of nanotube produced, suggesting that careful control of catalyst size could enable the preferential production of DWNTs. Flahaut et al.<sup>104</sup> synthesized a mixture of SWNTs, DWNTs, and MWNTs by CVD over Co-MgO composite powders, but precise control over catalyst size was not possible by this method. Ren et al.<sup>105</sup> subsequently used ferrocene, thiophene, and methane at 1100°C to synthesize ropes of DWNTs. The corresponding Raman spectrum in the radial breathing mode region is shown in Figure 3.17, and the derived nanotube diameters are summarized in Table 3.1. Zhu et al.<sup>106</sup> succeeded at producing DWNTs in high yield by a CVD method, and Cumings et al.<sup>107</sup> prepared DWNTs over a catalyst generated from iron salts deposited in fumed alumina. More recently, it has proven possible to grow DWNTs on a patterned substrate. Chikkannanavar et al.<sup>93</sup> synthesized isolated DWNTs on Si<sub>3</sub>N<sub>4</sub>/Si substrates (Figure 3.18) using an iron catalyst. The ability to produce these structures in the presence of patterned leads could enable further measurement and elucidation of their transport properties.

### 3.6 Conclusions and future prospects

The nanotube provides the special structural feature of a lumen, a characteristic through which this material is imbued with a clearly defined inside. For the case of a single-wall nanotube, nature has provided us with the fascinating structure in which the inside and the outside are separated by a

**Table 3.1** Raman Peak Positions and Calculated Diameters of CVD-Synthesized DWNTs

Outer diameter of the as-prepared DWNTs, $\lambda(d_t)$ cm <sup>-1</sup> (nm)	Inner diameter of the as-prepared DWNTs, $\lambda(d_t)$ cm <sup>-1</sup> (nm)
92.3 (2.75)	128.3 (1.98)
	130.9 (1.94)
103.9 (2.44)	146.2 (1.74)
	155.2 (1.64)
112.9 (2.25)	164.1 (1.55)
	170.5 (1.49)
	175.6 (1.45)
119.3 (2.13)	190.9 (1.33)
	197.2 (1.29)
128.3 (1.98)	197.2 (1.29)
	207.4 (1.22)
	212.5 (1.20)
130.9 (1.94)	207.4 (1.22)
	212.5 (1.20)
139.8 (1.82)	246.6 (1.03)
146.2 (1.74)	275.6 (0.92)
	284.4 (0.89)

Source: Ren, W. et al., *Chem. Phys. Lett.*, 359, 196, 2002.

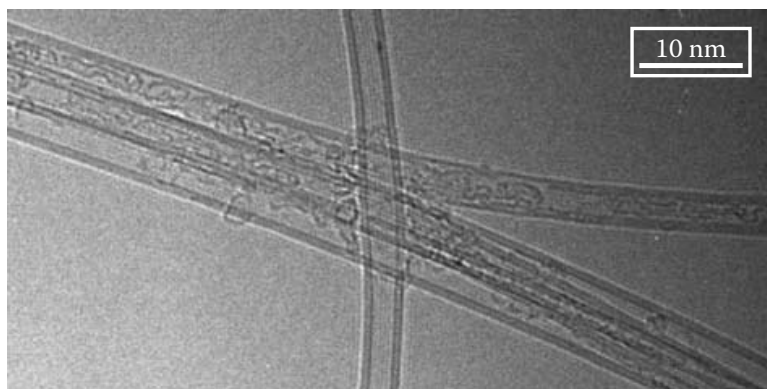


**Figure 3.18** HRTEM micrograph of DWNTs synthesized by CVD using Fe as a catalyst and CH<sub>4</sub>/C<sub>2</sub>H<sub>4</sub> as a precursor at 900°C. (Courtesy of Dr. A.T. Johnson and Dr. S. Paulson.)

stable, single atomic sheet. Through scientific research, methods have been devised to controllably open nanotubes, and to fill these structures with a variety of materials. Although this research is still in a fairly early stage, it has been proven that controlled filling can be used as a means to modify the electronic and mechanical properties of the nanotube. Work has also shown that the confined nanoscale dimensions of the interior of the nanotube can be used to control the product of a chemical reaction that occurs within the

lumen. Recent progress also indicates that it will only be a short time before it is proven that modifications to optical and magnetic properties also can be produced. Further work is needed before it is known whether filled nanotubes can be used for catalysis or other applications in which interior species of a filled nanotube are used to modify the exterior environment. Promising indications of this possibility have been recorded through experiments in which electron transfer through the nanotube wall onto molecules within a nanotube has been achieved.

A one-dimensional structure with a lumen can be otherwise described as a pipe. In much the same way as pipes are used for material transport at the macroscale, it is hoped that nanotubes can be used to transport material at the nanoscale. It takes only a small imagination to conceive of a wide variety of potential applications of such a capability in electromechanical, chemical, and biomedical devices. Research has proven that mass transport can occur, even in nanotubes with an interior diameter under 1 nm. Researchers have shown that mass transport can be driven in single-wall and larger multiwall carbon nanotubes, although complete control of this mass transport remains a challenge for future work.

Work on the use of the inside of nanotubes is only in the early stages. Due to the enormous number of potential filling materials, there is a high probability that many exciting scientific discoveries about filled systems and technological inventions using the lumen of the nanotube lie in our future. When this uncommon aspect of the nanotube, that it is a nanoscale one-dimensional material with an inside, is considered together with the other stellar properties of the nanotube, it is clear that the level of attention devoted to this fascinating material by the scientific community, and increasingly the emerging technology business community, is not only justified, but perhaps too conservative.

## Acknowledgments

The authors acknowledge support from the Office of Naval Research through grant N00014-00-1-0482 (BCS), the Commonwealth of Pennsylvania Nanotechnology Institute (BWS), and the National Science Foundation through grant DMR-0100273 (DEL).

## References

1. Dresselhaus, M.S., Dresselhaus, G., and Avouris, P., *Carbon Nanotubes: Synthesis, Structure, Properties, and Applications*, Springer, New York, 2001.
2. Rao, C.N.R., Satishkumar, B.C., Govindaraj, A., and Nath, M., Nanotubes, *ChemPhysChem*, 2, 78, 2001.
3. Dai, H.J., Carbon nanotubes: opportunities and challenges, *Surf. Sci.*, 500, 218, 2002.
4. Iijima, S., Helical microtubules of graphitic carbon, *Nature*, 354, 56, 1991.

5. Bethune, D.S. et al., Cobalt-catalysed growth of carbon nanotubes with single-atomic-layer walls, *Nature*, 363, 605, 1993.
6. Tsang, S.C. et al., A simple chemical method of opening and filling carbon nanotubes, *Nature*, 372, 159, 1994.
7. Ajayan, P.M. and Iijima, S., Capillarity-induced filling of carbon nanotubes, *Nature*, 361, 333, 1993.
8. Tsang, S.C. et al., Immobilization of small proteins in carbon nanotubes: high resolution transmission electron microscopy study and catalytic activity, *J. Chem. Soc. Chem. Commun.*, 2579, 1995.
9. Satishkumar, B.C. et al., Novel experiments with carbon nanotubes: opening, filling, closing and functionalizing the nanotubes, *J. Phys. B Atom. Mol. Opt. Phys.*, 9, 4925, 1996.
10. Sloan, J. et al., The opening and filling of single walled carbon nanotubes, *Chem. Commun.*, 347, 1998.
11. Sloan, J. et al., Capillarity and silver nanowire formation observed in single walled carbon nanotubes, *Chem. Commun.*, 699, 1999.
12. Govindaraj, A. et al., Metal nanowires and intercalated metal layers in single-walled carbon nanotube bundles, *Chem. Mater.*, 12, 202, 2000.
13. Sloan, J. et al., Integral atomic layer architectures of 1D crystals inserted into single walled carbon nanotubes, *Chem. Commun.*, 1319, 2002.
14. Smith, B.W., Monthieux, M., and Luzzi, D.E., Encapsulated C<sub>60</sub> in carbon nanotubes, *Nature*, 396, 323, 1998.
15. Burteaux, B. et al., Abundance of encapsulated C<sub>60</sub> in single-wall carbon nanotubes, *Chem. Phys. Lett.*, 310, 21, 1999.
16. Smith, B.W. and Luzzi, D.E., Formation mechanism of fullerene peapods and coaxial tubes: a path to large scale synthesis, *Chem. Phys. Lett.*, 321, 169, 2000.
17. Girifalco, L.A., Hodak, M., and Lee, R.S., Carbon nanotubes, bucky balls, ropes, and a universal graphitic potential, *Phys. Rev. B*, 62, 13104, 2000.
18. Berber, S., Kwon Y.-K., and Tománek, D., Microscopic formation mechanism of nanotube peapods, *Phys. Rev. Lett.*, 88, 185502, 2002.
19. Ulbricht, H. and Hertel, T., Dynamics of C<sub>60</sub> encapsulation into single-wall carbon nanotubes, *J. Phys. Chem.*, 107, 14185, 2003.
20. Kataura H. et al., High yield fullerene encapsulation in single wall carbon nanotubes, *Synth. Met.*, 121, 1195, 2001.
21. Smith, B.W. et al., High-yield synthesis and one-dimensional structure of C<sub>60</sub> encapsulated in single-wall carbon nanotubes, *J. Appl. Phys.*, 91, 9333, 2002.
22. Hirahara, K. et al., Electron diffraction study of one-dimensional crystals of fullerenes, *Phys. Rev. B*, 64, 115420, 2001.
23. Liu, X. et al., Determination of the filling factor of C<sub>60</sub> peapods by electron energy loss spectroscopy in transmission, *Synth. Met.*, 135, 715, 2003.
24. Liu, X. et al., Filling factors, structural, and electronic properties of C<sub>60</sub> molecules in single-wall carbon nanotubes, *Phys. Rev. B*, 65, 045419, 2002.
25. Thess, A. et al., Crystalline ropes of metallic carbon nanotubes, *Science*, 273, 483, 1996.
26. Journet, C. et al., Large-scale production of single-walled carbon nanotubes by the electric-arc technique, *Nature*, 388, 756, 1997.
27. Kataura, H. et al. Optical properties of fullerene and non-fullerene peapods, *Appl. Phys. A*, 74, 349, 2002.
28. Zhou, W. et al., Out-of-plane mosaic of single-wall carbon nanotube films, *Appl. Phys. Lett.*, 84, 2172, 2004.



29. Rao, A.M. et al., Diameter-selective Raman scattering from vibrational modes in carbon nanotubes, *Science*, 275, 187, 1997.
30. Pfeiffer, R. et al., Spectroscopic analysis of single-wall carbon nanotubes and carbon nanotube peapods, *Diamond Rel. Mater.*, 11, 957, 2002.
31. Pfeiffer, R. et al., Electronic and mechanical coupling between guest and host in carbon peapods, *Phys. Rev. B*, 69, 035404, 2004.
32. Hornbaker, D.J. et al., Mapping the one-dimensional electronic states of nanotube peapod structures, *Science*, 295, 828, 2002.
33. Okada, S., Saito, S., and Oshiyama, A., Energetics and electronic structures of encapsulated  $C_{60}$  in a carbon nanotube, *Phys. Rev. Lett.*, 86, 3835, 2001.
34. Kane, C.L. et al., Theory of scanning tunneling spectroscopy of fullerene peapods, *Phys. Rev. B*, 66, 235423, 2002.
35. Vavro, J. et al., Electrical and thermal properties of  $C_{60}$ -filled single-wall carbon nanotubes, *Appl. Phys. Lett.*, 80, 1450, 2002.
36. Lee, R.S. et al., Transport properties of a potassium-doped single-wall carbon nanotube rope, *Phys. Rev. B*, 61, 4526, 2000.
37. Vavro, J., Transport Properties of Single-Wall Carbon Nanotubes, Ph.D. thesis, University of Pennsylvania, Philadelphia, 2004.
38. O'Connell, M.J. et al., Band gap fluorescence from individual single-walled carbon nanotubes, *Science*, 297, 593, 2002.
39. Bachilo, S.M. et al., Structure-assigned optical spectra of single-walled carbon nanotubes, *Science*, 298, 2361, 2002.
40. Pichler, T. et al., Metallic polymers of  $C_{60}$  inside single-walled carbon nanotubes, *Phys. Rev. Lett.*, 87, 267401, 2001.
41. Pichler, T. et al., Quasicontinuous electron and hole doping of  $C_{60}$  peapods, *Phys. Rev. B*, 67, 125416, 2003.
42. Hodak, M. and Girifalco, L.A., Cohesive properties of fullerene-filled nanotube ropes, *Chem. Phys. Lett.*, 363, 93, 2002.
43. Rafailov, P.M., Thomsen, C., and Kataura, H., Resonance and high-pressure Raman studies on carbon peapods, *Phys. Rev. B*, 68, 193411, 2003.
44. Luzzi, D.E. and Smith, B.W., Carbon cage structures in single wall carbon nanotubes: a new class of materials, *Carbon*, 38, 1751, 2000.
45. Bandow, S. et al., Raman scattering study of double-wall carbon nanotubes derived from chains of fullerenes in single-wall carbon nanotubes, *Chem. Phys. Lett.*, 337, 48, 2001.
46. Bandow, S. et al., Diameter-selective resonant Raman scattering in double-wall carbon nanotubes, *Phys. Rev. B*, 66, 075416, 2002.
47. Abe, M. et al., Structural transformation from single-wall to double-wall carbon nanotube bundles, *Phys. Rev. B*, 68, 041405, 2003.
48. Bandow, S. et al., Raman scattering study on fullerene derived intermediates formed within single-wall carbon nanotube: from peapod to double-wall carbon nanotube, *Chem. Phys. Lett.*, 384, 320, 2004.
49. Hernandez, E. et al., Fullerene coalescence in nanopeapods: a path to novel tubular carbon, *Nano Lett.*, 3, 1037, 2003.
50. Yudasaka, M. et al., Nano-extraction and nano-condensation for  $C_{60}$  incorporation into single-wall carbon nanotubes in liquid phases, *Chem. Phys. Lett.*, 380, 42, 2003.
51. Jeong, G.H. et al.,  $C_{60}$  encapsulation inside single-walled carbon nanotubes using alkali-fullerene plasma method, *Carbon*, 40, 2247, 2002.
52. Shinohara, H., Endohedral metallofullerenes, *Rep. Prog. Phys.*, 63, 843, 2000.

53. Smith, B.W., Luzzi, D.E., and Achiba, Y., Tumbling atoms and evidence for charge transfer in  $\text{La}_2\text{C}_{80}\text{@SWNT}$ , *Chem. Phys. Lett.*, 331, 137, 2000.
54. Hirahara, K. et al., One-dimensional metallofullerene crystal generated inside single-walled carbon nanotubes, *Phys. Rev. Lett.*, 85, 5384, 2000.
55. Suenaga, K. et al., Element-selective single atom imaging, *Science*, 290, 2280, 2000.
56. Okazaki, T. et al., Real time reaction dynamics in carbon nanotubes, *J. Am. Chem. Soc.*, 123, 9673, 2001.
57. Lee, J. et al., Band gap modulation of carbon nanotubes by encapsulated metallofullerenes, *Nature*, 415, 1005, 2002.
58. Shimada, T. et al., Ambipolar field-effect transistor behavior of  $\text{Gd@C}_{82}$  metallofullerene peapods, *Appl. Phys. Lett.*, 81, 4067, 2002.
59. Simon, F. et al., Low temperature fullerene encapsulation in single wall carbon nanotubes: synthesis of  $\text{N@C}_{60}\text{@SWCNT}$ , *Chem. Phys. Lett.*, 383, 362, 2004.
60. Kadish, K.M. and Ruoff, R.S., Eds., *Fullerenes: Chemistry, Physics and Technology*, Wiley, New York, 2000.
61. Britz, D.A. et al., Selective host-guest interaction of single-walled carbon nanotubes with functionalised fullerenes, *Chem. Commun.*, 176, 2004.
62. Ajayan, P.M. et al., Opening carbon nanotubes with oxygen and implications for filling, *Nature*, 362, 522, 1993.
63. Tsang, S.C., Harris, P.J.F., and Green, M.L.H., Thinning and opening of carbon nanotubes by oxidation using carbon dioxide, *Nature*, 362, 520, 1993.
64. Dujardin, E. et al., Capillarity and wetting of carbon nanotubes, *Science*, 265, 1850, 1994.
65. Ebbesen, T.W., Wetting, filling, and decorating carbon nanotubes, *J. Phys. Chem. Solids*, 57, 951, 1996.
66. Ajayan, P.M., Stephan, O., Redlich, P., and Colliex, C., Carbon nanotubes as removable templates for metal oxide nanocomposites and nanostructures, *Nature*, 375, 564, 1995.
67. Chu, A. et al., Filling of carbon nanotubes with silver, gold, and gold chloride, *Chem. Mater.*, 8, 2751, 1996.
68. Chen, Y.K. et al., Synthesis of carbon nanotubes containing metal oxides and metals of the d-block and f-block transition metals and related studies, *J. Mater. Chem.*, 7, 545, 1997.
69. Sloan, J. et al., Selective deposition of  $\text{UCl}_4$  and  $(\text{KCl})_x(\text{UCl}_4)_y$  inside carbon nanotubes using eutectic and noneutectic mixtures of  $\text{UCl}_4$  with KCl, *J. Sol. St. Chem.*, 140, 83, 1998.
70. Ugarte, D. et al., Filling carbon nanotubes, *Appl. Phys. A*, 67, 101, 1998.
71. Satishkumar, B.C. et al., Oxide nanotubes prepared using carbon nanotubes as templates, *J. Mater. Res.*, 12, 604, 1997.
72. Rao, C.N.R., Govindaraj, A., and Satishkumar, B.C., Zirconia nanotubes, *Chem. Commun.*, 1581, 1997.
73. Satishkumar, B.C., Govindaraj, A., Nath, M., and Rao, C.N.R., Synthesis of metal oxide nanorods using carbon nanotubes as templates, *J. Mater. Chem.*, 10, 2115, 2000.
74. Davis, J.J. et al., The immobilisation of proteins in carbon nanotubes, *Inorg. Chim. Acta*, 272, 261, 1998.
75. Demoncey, N. et al., Filling carbon nanotubes with metals by the arc-discharge method; the key role of sulfur, *Eur. Phys. J. B*, 4, 147, 1998.

76. Liu, M. and Cowley, J.M., Encapsulation of lanthanum carbide in carbon nanotubes and carbon nanoparticles, *Carbon*, 33, 225, 1995.
77. Terrones, M. et al., Advances in the creation of filled nanotubes and novel nanowires, *MRS Bull.*, 24, 43, 1999.
78. Kyotani, T., Tsai, L., and Tomita, A., Formation of platinum nanorods and nanoparticles in uniform carbon nanotubes prepared by a template carbonization method, *Chem. Commun.*, 701, 1997.
79. Pradhan, B.K. et al., Inclusion of crystalline iron oxide nanoparticles in uniform carbon nanotubes prepared by a template carbonization method, *Chem. Mater.*, 10, 2510, 1998.
80. Gao, Y. and Bando, Y., Carbon nanothermometer containing gallium, *Nature*, 415, 599, 2002.
81. Gogotsi, Y., Libera, J.A., and Yoshimura, M., Hydrothermal synthesis of multiwall carbon nanotubes, *J. Mater. Res.*, 15, 2591, 2000.
82. Ye, H.H. et al., Wall structure and surface chemistry of hydrothermal carbon nanofibres, *Nanotechnology*, 15, 232, 2004.
83. Naguib, N. et al., Observation of water confined in nanometer channels of closed carbon nanotubes, *Nano Lett.*, 4, 2237, 2004.
84. Koga, K., Gao, G.T., Tanaka, H., and Zeng, X.C., Formation of ordered ice nanotubes inside carbon nanotubes, *Nature*, 402, 802, 2001.
85. Maniwa, Y. et al., Phase transition in confined water inside carbon nanotubes, *J. Phys. Soc. Jpn.*, 71, 2863, 2002.
86. Satishkumar, B.C., Taubert, A., and Luzzi, D.E., Filling single-wall carbon nanotubes with d- and f-metal chloride and metal nanowires, *J. Nanosci. Nanotech.*, 3, 159, 2003.
87. Meyer, R.R. et al., Discrete atom imaging of one-dimensional crystals formed within single-walled carbon nanotubes, *Science*, 289, 1324, 2000.
88. Morgan, D.A., Sloan, J., and Green, M.L.H., Direct imaging of o-carborane molecules within single walled carbon nanotubes, *Chem. Commun.*, 2442, 2002.
89. Takenobu, T. et al., Stable and controlled amphoteric doping by encapsulation of organic molecules inside carbon nanotubes, *Nat. Mater.*, 2, 683, 2003.
90. Jishi, A., White, C.T., and Mintmire, J.W., Endohedral selenium chains in carbon, boron nitride, and  $\text{BC}_2\text{N}$  nanotubes, *Int. J. Quant. Chem.*, 80, 480, 2000.
91. Hodak, M. and Girifalco, L.A., Ordered phases of fullerene molecules formed inside carbon nanotubes, *Phys. Rev. B*, 67, 075419, 2003.
92. Hodak, M. and Girifalco, L.A., Systems of  $\text{C}_{60}$  molecules inside (10,10) and (15,15) nanotube: a Monte Carlo study, *Phys. Rev. B*, 68, 085405, 2003.
93. Chikkannanavar, S.B., Luzzi, D.E., Paulson, S., and Johnson, A.T., Synthesis of peapods using substrate grown SWNTs and DWNTs: an enabling step towards peapod devices, *Nano Lett.*, 5, 151, 2004.
94. Khlobystov, A.N. et al., Observation of ordered phases of fullerenes in carbon nanotubes, *Phys. Rev. Lett.*, 92, 245507, 2004.
95. Mickelson, W. et al., Packing  $\text{C}_{60}$  in boron nitride nanotubes, *Science*, 300, 467, 2003.
96. Rao, C.N.R. et al., Synthesis of multi-walled and single-walled nanotubes, aligned-nanotube bundles and nanorods by employing organometallic precursors, *Mater. Res. Innov.*, 2, 128, 1998.
97. Satishkumar, B.C. et al., Single-walled nanotubes by the pyrolysis of acetylene-organometallic mixtures, *Chem. Phys. Lett.*, 293, 47, 1998.

98. Zhu, H.W. et al., Direct synthesis of long single-walled carbon nanotube strands, *Science*, 286, 884, 2002.
99. Huang, S., Cai, X., and Liu, J., Growth of millimeter-long and horizontally aligned single-walled carbon nanotubes on flat substrates, *J. Am. Chem. Soc.*, 125, 5636, 2003.
100. Colomer, J.-F. et al., Large-scale synthesis of single-wall carbon nanotubes by catalytic chemical vapor deposition (CCVD) method, *Chem. Phys. Lett.*, 317, 83, 2000.
101. Kitiyanan, B. et al., Controlled production of single-wall carbon nanotubes by catalytic decomposition of CO on bimetallic Co–Mo catalysts, *Chem. Phys. Lett.*, 317, 417, 2000.
102. Cheung, C.L. et al., Diameter-controlled synthesis of carbon nanotubes, *J. Phys. Chem. B*, 106, 2429, 2002.
103. Kim, W. et al., Synthesis of ultralong and high percentage of semiconducting single-walled carbon nanotubes, *Nano Lett.*, 2, 704, 2002.
104. Flahaut, E. et al., Synthesis of single-walled carbon nanotubes Co-MgO composite powders and extraction of the nanotubes, *J. Mater. Chem.*, 10, 249, 2000.
105. Ren, W. et al., Morphology, diameter distribution and Raman scattering measurements of double-walled carbon nanotubes synthesized by catalytic decomposition of methane, *Chem. Phys. Lett.*, 359, 196, 2002.
106. Zhu, J., Yudasaka, M., and Iijima, S., A catalytic chemical vapor deposition synthesis of double-walled carbon nanotubes over metal catalysts supported on a mesoporous material, *Chem. Phys. Lett.*, 380, 496, 2003.
107. Cumings, J., Mickelson, W., and Zettl, A., Simplified synthesis of double-wall carbon nanotubes, *Solid State Commun.*, 126, 359, 2003.

## *chapter four*

---

# *Carbon nanotube electronics and devices*

*Marcus Freitag*

*Watson Research Center, IBM Corporation*

### *Contents*

4.1	Metallic carbon nanotubes .....	84
4.1.1	Ballistic transport .....	85
4.1.2	Resonant scattering centers and resonant tunneling .....	87
4.1.3	Current-carrying capacity, current saturation .....	88
4.2	Semiconducting carbon nanotubes .....	90
4.2.1	Review of the silicon MOSFET .....	90
4.2.2	Nanotube field effect transistor .....	93
4.2.3	Schottky barriers .....	96
4.2.4	Gate-oxide scaling .....	99
4.2.5	Ambipolar transistor .....	100
4.2.6	High-performance FETs .....	102
4.2.7	Doping .....	102
4.2.8	Logic gates .....	104
4.2.9	Infrared emitters .....	107
4.2.10	Photodetectors .....	111
4.3	Outlook and challenges .....	113
	References .....	114

Depending on the exact way carbon nanotubes (CNTs) are wrapped, they are either metallic (Figure 4.1a) or semiconducting (Figure 4.1b). In the first part of this chapter, we address the electronic properties of metallic carbon nanotubes, and in the second part, we discuss the most important device made from a semiconducting nanotube, the carbon nanotube field effect transistor and its applications.



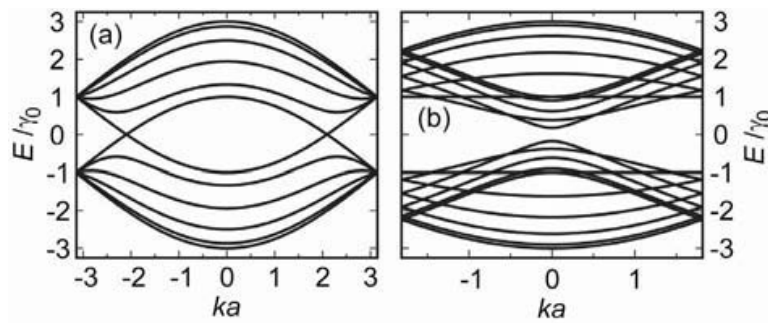


**Figure 4.1** Band structure of (a) a metallic (5, 5) CNT and (b) a semiconducting (10, 0) nanotube. The wavevector  $k$  is plotted in units of  $1/a$ , where  $a = 0.249$  nm is the graphene lattice constant. Energy  $E$  is plotted in units of  $\gamma_0 \sim 2.5$  eV, the carbon–carbon hopping matrix element in graphene. The low-energy band structure of metallic CNTs consists of two pairs of crossing bands right at the Fermi level. In semiconducting nanotubes a band gap on the order of 1 eV opens up at  $k = 0$ .

Low-bias transport in metallic carbon nanotubes is ballistic over length scales that can reach micrometers. This is possible because acoustic phonon scattering is exceptionally weak in this one-dimensional conductor, and only few defects that act as resonant scattering centers are present. At high bias, however, electrons strongly excite optical phonons, which leads to energy dissipation in the tube and current saturation.

The carbon nanotube field effect transistor, which utilizes a semiconducting carbon nanotube to switch, is a device that may have the potential to become technologically important for the semiconductor industry. It has very desirable properties, such as high carrier mobility, high current density, good switching characteristics, and scalability. It is compatible with the established silicon technology and allows the building of complementary devices for logic. We emphasize the differences between Schottky barrier devices and bulk-switching devices and show how doping can be used to build high-performance transistors and logic from carbon nanotubes. Ambipolar field effect transistors and their electro-optic properties are addressed at the end of this chapter.

## 4.1 Metallic carbon nanotubes

The mere fact that metallic behavior is observed in tubes 1 nm in diameter is not trivial. Most one-dimensional materials exhibit a Peierls instability that opens an energy gap and the material undergoes a metal-to-insulator transition.<sup>1</sup> The Peierls instability occurs because the total energy of a one-dimensional chain can often be reduced by doubling the unit cell. For example, two neighboring atoms move closer together, while the next pair moves farther apart. Carbon nanotubes do not show a Peierls instability even at the lowest measured temperatures, because of the enormous strength of the carbon–carbon bond in graphitic materials and the cylindrical — rather than chain-like — arrangement of carbon atoms.

From tight-binding calculations one finds that all achiral ( $m = n$ ) carbon nanotubes, such as the one depicted in Figure 4.1a, are truly metallic. Their band structure consists of two sets of linear bands that cross right at the Fermi level. Among the chiral tubes, about 2/3 are semiconducting [ $(m - n) \bmod 3 = 1$  or 2], while the remainder [ $(m - n) \bmod 3 = 0$ ] exhibit a small band gap on the order of a few meV. We include the small-gap semiconductors in this section on metallic carbon nanotubes because at room temperature ( $k_b T = 26$  meV) the effects related to the small band gaps are not very prominent.

### 4.1.1 Ballistic transport

The resistance of short one-dimensional conductors is independent of their composition or the length of the conductor, and only a function of the number of available conduction channels (i.e., one-dimensional subbands) and the transmission at the contacts.<sup>2</sup> For a single conduction channel with 100% transparent contacts, the quantum resistance is a universal constant, given by

$$R_Q = h/e^2 \approx 26 \text{ K}\Omega. \quad (4.1)$$

This behavior is often called ballistic conduction, since electrons travel between two terminals without any scattering event (Figure 4.2a). Note that the resistance of a ballistic conductor is *not* zero, even though there is no scattering in the conduction channel and no backscattering for electrons

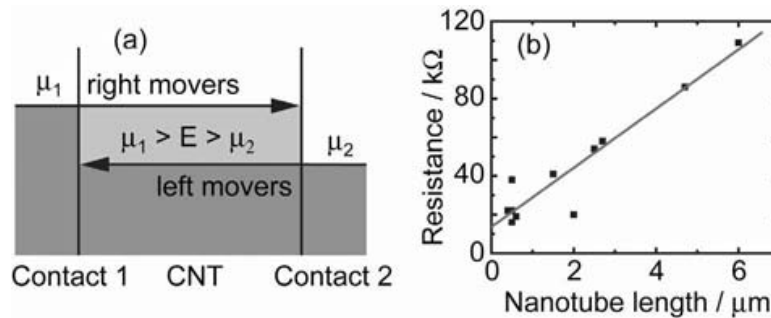


**Figure 4.2** (a) Illustration of ballistic transport in a system such as a short metallic carbon nanotube. (Energy is plotted as a function of position.) Carriers are injected into the CNT from contact 1 with energies up to  $\mu_1$  and from contact 2 with energies up to  $\mu_2$ . There is no scattering in the CNT, and carriers that are injected at certain energy  $E$  traverse the tube without any energy loss. The electrochemical potential equilibrates inside the macroscopic leads. The net current is carried by carriers with energy between  $\mu_1$  and  $\mu_2$  that travel from contact 1 to contact 2. (b) Low-bias resistance vs. nanotube length for 11 metallic chemical vapor deposition (CVD) tubes after 10. Two kilohms for the resistance of the leads has been subtracted for all data points. The solid line is a linear fit to the data with slope  $15 \text{ k}\Omega/\mu\text{m}$  and y-axis intercept of  $14 \text{ k}\Omega$ . The y-axis intercept suggests transmission coefficients of  $t_i = 0.5$  and the slope an electron mean free path of  $0.4 \mu\text{m}$ .

exiting the conductor. The quantum resistance (or contact resistance, as it is sometimes called) originates from the mismatch between the large number of modes in the macroscopic contacts that the current is distributed over, and the few electronic modes (one-dimensional subbands) available in the one-dimensional conductor. The interested reader can find an excellent introduction to Landauer–Büttiker formalism in Datta's book on electronic transport in mesoscopic systems.<sup>3</sup>

Equation 4.1 can be generalized to include  $M$  conduction channels and contacts with nonunity transmission coefficient  $t_i$ :

$$G = e^2/h \cdot \sum_{i=1}^M t_i(E_F) . \quad (4.2)$$

$G = 1/R_Q$  is the quantum conductance and  $E_F$  is the Fermi energy. Equation 4.2 is called the Landauer formula for a ballistic conductor. For 100% transparent contacts the conductance is simply  $M \times e^2/h$ . As one goes to a large number of conduction channels, such as in a macroscopic system, the quantum resistance (or contact resistance) goes to zero.

The Landauer formula can be further generalized to include scattering in the conduction channel by introducing an electron mean-free path (momentum scattering length  $l_m$ ):

$$R = R_Q \cdot L/l_m. \quad (4.3)$$

Here  $L$  is the length of the conductor and  $R_Q = 1/G$  is the quantum resistance. In this form, the classical length dependence of the resistance is recovered.

The low-energy band structure of a metallic carbon nanotube consists of four linear bands that cross at two distinct K-points (Figure 4.1a).<sup>4</sup> In each K-point, one band carries the forward-moving electrons, while the other carries the backward movers. Furthermore, each band is spin degenerate, so that there are a total of four forward-moving conduction channels in a metallic carbon nanotube. The theoretical limit for the conductance through an individual single-wall carbon nanotube is therefore  $G = 4 \times e^2/h$ , which corresponds to a resistance of 6.5 k $\Omega$ . Experimentally, one finds values for the carbon nanotube low-bias resistance between 10 k $\Omega$ <sup>5</sup> and several 100 k $\Omega$ ,<sup>6</sup> suggesting transmission coefficients (Equation 4.2) between 75 and 1%. Palladium contacts on chemical vapor deposition (CVD)-grown tubes were found to make the best contacts with almost unity transmission.<sup>7,8</sup>

According to Equation 4.3, the length dependence of the low-bias resistance can be used to extract the mean-free path. In carbon nanotubes, this has been done by contacting a tube with one lithographic contact as well as one movable scanned probe,<sup>9</sup> and also by comparing the resistances of many similarly fabricated two-terminal devices with varying nanotube lengths (Figure 4.2b).<sup>10</sup> Both methods yield a room temperature mean-free path on

the order of  $l_m \sim 500$  nm, much larger than typical values, around 10 nm in most other materials. In carbon nanotubes, scattering is suppressed because of the perfect lattice without localized surface states and the large momentum transfer that is required for backscattering. (Cumulative small-angle scattering that adds up to  $180^\circ$  is impossible in a one-dimensional system.) The two most prominent sources of scattering in metallic carbon nanotubes in the low-bias regime are acoustic phonon scattering<sup>11,12</sup> and elastic scattering from defects.<sup>13</sup> Acoustic phonon scattering usually dominates at room temperature, whereas elastic scattering from defects becomes important at low temperatures, where the mean-free path can be as long as several micrometers.

#### 4.1.2 Resonant scattering centers and resonant tunneling

By nature of their constant density of states, metallic carbon nanotubes are not expected to show any response to changing gate voltages (e.g., applied at the silicon substrate, which is separated from the carbon nanotube by an  $\text{SiO}_2$  layer). In some devices, however, one finds a moderate (up to a factor of 2) gate voltage dependence of the current. Scanning gate microscopy (SGM) (Figure 4.3a) can be used to show that these variations are due to localized scatterers in the carbon nanotube.<sup>13</sup> For this a conductive atomic force microscopy (AFM) tip is scanned above the device, close enough for the tip to act as an additional gate, but far enough to prevent a tunnel current

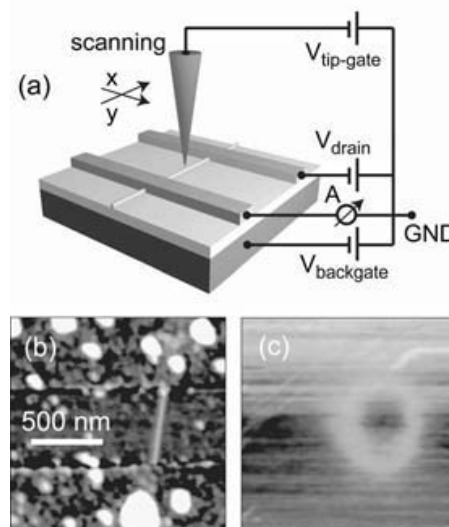


**Figure 4.3** (a) Schematic of scanning gate microscopy (SGM). A conductive AFM tip is scanned at constant height above a device and the source–drain current is measured as a function of the tip position. The potential on the tip acts as a local gate for the transport through the carbon nanotube. (b) AFM image of a metallic carbon nanotube contacted by metal leads. (c) Scanning gate microscopy image during the scan of (b) with  $V_{tip} = -5$  V. White corresponds to enhanced conductivity. The ring structure indicates resonant tunneling at a defect located in the center of the ring.

through the tip. The tip gate changes the potential of localized defect states, so that the defect energy levels move in and out of resonance with the nanotube Fermi level. The position of the defect energy levels depends on both the voltage on the tip and the distance between the tip and the defect. For fixed tip voltage, a defect state is in resonance at fixed tip to defect distance, so that scanning gate images show rings of reduced transport current, centered at the defect site. One typically finds about one such resonant scattering center in a micron-long tube segment.<sup>13</sup> The microscopic origin of defects has not been established yet. Bond rotation defects,<sup>14</sup> vacancies, chemically bonded species, and something adsorbed inside or outside the nanotube are all distinct possibilities.

Figure 4.3b shows the AFM image of a metallic carbon nanotube in between two contacts, and Figure 4.3c shows a scanning gate image of the transport current through the tube that exhibits a ring structure similar to the one described before. In this example, however, the current is enhanced in the ring, whereas usually it is reduced, suggesting a defect that acts as a resonant tunneling center rather than a resonant scattering center in this carbon nanotube.<sup>10</sup>

### 4.1.3 Current-carrying capacity, current saturation

A single carbon nanotube can carry up to 25  $\mu\text{A}$  of current. This corresponds to an extraordinarily high current density of  $10^9 \text{ A/cm}^2$ . In Figure 4.4, a typical I-V characteristic for a metallic carbon nanotube is shown.<sup>5</sup> The current increases linearly at low bias (the ballistic regime), but then rolls over and saturates at high bias. In the inset to the figure, the data are plotted in a different way, namely, resistance  $R \equiv V/I$  as a function of bias voltage. Above a few 100 mV the resistance increases linearly with voltage. A simple

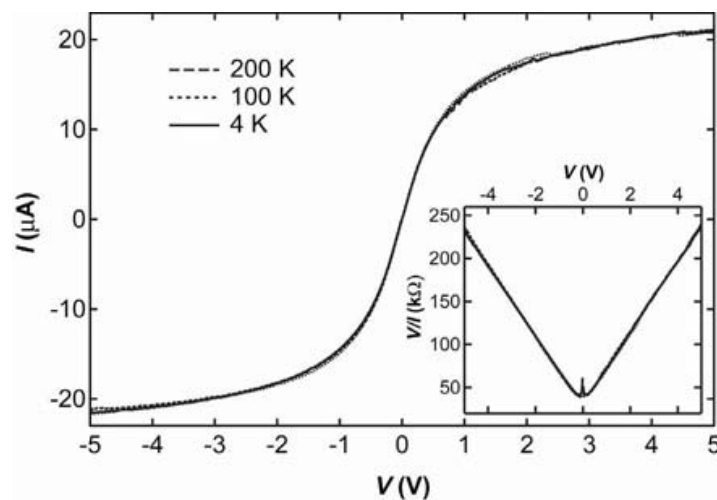


**Figure 4.4** Current saturation in a metallic carbon nanotube. Main image: current voltage characteristics showing current saturation at high bias. Inset: resistance  $R \equiv V/I$  vs. bias voltage. (Reprinted from Yao, Z. et al., *Phys. Rev. Lett.*, 84, 2941, 2000. With permission. Copyright © 2000 by the American Physical Society.)



model<sup>5</sup> that includes phonon excitation can explain the linear increase in resistance and correctly predicts the value for the saturation current around 25  $\mu\text{A}$ . Two important assumptions are made in the model: there is an energy threshold  $eV = \hbar\Omega$ , below which excitation of phonons is impossible and the transmission is ballistic. ( $V$  is the bias voltage and  $\hbar\Omega$  is the energy of the phonon.) We will later identify the threshold with the energy of the optical or zone boundary phonon in carbon nanotubes. Of course, there are acoustic phonons with arbitrarily low energy, but the coupling of electrons to these phonons is weak in carbon nanotubes.<sup>11,12</sup> The second assumption states that once the electron gains enough excess energy to excite the optical phonon, it does so instantaneously. The process of acceleration in the applied electric field and optical phonon excitation is repeated until the electron reaches the opposite contact.

We can use the Landauer formula (Equation 4.3) and Matthiessen's rule to combine the scattering mechanisms,

$$R = \frac{h}{4e^2} \left( \frac{L}{l_m} + \frac{L}{l_\Omega} \right), \quad (4.4)$$

where  $L$  is the length of the carbon nanotube,  $l_m$  is the low-bias mean-free path that may include elastic defect scattering and acoustic phonon scattering, and  $l_\Omega = \hbar\Omega L / eV$  is the length it takes an electron in the applied electric field to gain the optical/zone boundary phonon energy  $\hbar\Omega$ . Comparison with the functional form  $R = R_0 + V/I_0$  of the experimental data yields the low-bias

resistance  $R_0 = \frac{h}{4e^2} \frac{L}{l_m}$  and saturation current  $I_0 = \frac{4e}{h} \hbar\Omega$ . With  $L = 0.5 \mu\text{m}$

and  $R_0 = 40\text{K}\Omega$  the low-bias mean-free path for the device in Figure 4.4 becomes  $l_m \sim 100 \text{ nm}$ . This value is a lower limit because of likely nonunity transmission at the contacts. More importantly, the saturation current of  $I_0 \sim 25 \mu\text{A}$  suggests a phonon energy of  $\hbar\Omega \sim 0.16 \text{ eV}$ , which is right in the ballpark for zone boundary or optical phonons in carbon nanotubes.

The second assumption made before is justified as long as the electron-phonon scattering length for optical/zone boundary phonons,  $l_{op}$ , is much shorter than  $l_\Omega$ . Conversely, experimentally observed deviations from the current saturation at 25  $\mu\text{A}$  can be used to infer  $l_{op}$ . This is very significant because devices that are smaller than the electron-phonon scattering length will remain ballistic even at high bias. Two very recent experiments confirmed that the current does not saturate in short devices of  $\leq 100 \text{ nm}$ ,<sup>9,15</sup> and instead reaches values as high as 60  $\mu\text{A}$  with no sign of saturation before breakdown. Javey et al.<sup>15</sup> used electron beam lithography to fabricate carbon nanotube devices with lengths down to 10 nm and derived optical/zone boundary phonon scattering lengths between 11 and 15 nm. Park et al.<sup>9</sup> used a mobile scanned probe as an electronic contact and obtained  $l_{op} = 10 \text{ nm}$ .

## 4.2 Semiconducting carbon nanotubes

Semiconducting carbon nanotubes (Figure 4.1b) have a band gap that scales inversely with tube diameter,  $E_g \approx 0.84\text{eV}/d[\text{nm}]$ . Conduction through semiconducting tubes is dependent on the exact position of the Fermi level with respect to the band edges, and chemical or electrostatic doping can be used to change the conductivity significantly. Highly doped, for example, deep into the valence band, they conduct almost as good as metallic tubes, as they also have four available channels: two quasi-degenerate valence bands, each of which can carry spin up or down. The low-bias conduction is ballistic over 100-nm-length scales, and the maximal achievable currents with optimized contacts are  $\sim 20\text{ }\mu\text{A}$ , similar to what is observed in metallic tubes.

The strong dependence of the conductivity on the electrochemical potential in the carbon nanotube can be utilized to make a device that acts like a switch. It conducts current when the potential on a capacitively coupled gate moves the Fermi level into the valence — or conduction — band and acts as an insulator when the Fermi level is in the band gap. This kind of device is well known in the semiconductor industry and called a field effect transistor (FET). The silicon metal-oxide semiconductor field effect transistor (MOSFET)<sup>16,17</sup> is of immense technological importance. Essentially all modern computer chips are based on MOS logic. Fortunately, this device is the most straightforward to replicate with a semiconducting carbon nanotube in the channel instead of silicon (Figure 4.5).<sup>18,19</sup> Before addressing the carbon nanotube field effect transistor in detail, we introduce the silicon MOSFET in the next section. This gives us the opportunity to clarify some nomenclature and concepts that will be very helpful in understanding the operation of the carbon nanotube FET.

### 4.2.1 Review of the silicon MOSFET

An  $n$ -channel silicon MOSFET consists of a  $p$ -type substrate with two  $n^+$ -doped regions that serve as source and drain contacts (Figure 4.5a). The substrate (the semiconductor in the acronym MOS) is capped with a double

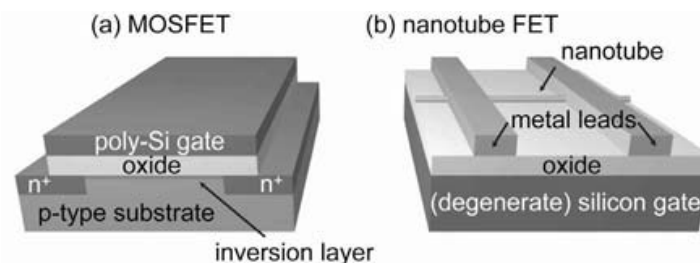


**Figure 4.5** Schematic of (a) a silicon MOSFET and (b) a carbon nanotube FET. The channel in the case of the MOSFET is an  $n$ -type inversion layer in the  $p$ -type substrate close to the interface with the silicon oxide. In the nanotube FET, the inversion layer is replaced by the carbon nanotube.

layer of SiO<sub>2</sub> (the oxide) and poly-Si (which is usually used instead of a real metal). The gate couples capacitively to the substrate, thus the term *field effect transistor* (FET). When a sufficiently positive gate voltage is applied, a thin (10- to 20-nm) inversion layer of electrons forms below the gate oxide in the *p*-doped silicon and connects the *n*<sup>+</sup>-doped reservoirs. Otherwise, the source-to-drain path is blocked by a depletion layer between the *p*-type substrate and the contact regions. Unlike a bipolar transistor, the MOSFET is unipolar in the sense that the current is carried by only one type of carrier (in our example by electrons). Simply inverting all the dopants (*n*-type substrate and *p*<sup>+</sup>-doped contacts) produces a unipolar device with complementary characteristics, where the current is carried by holes, and which turns on for negative gate voltages. The availability of both *n*- and *p*-type transistors in the same technology is very important for integration purposes in complementary logic (complementary metal-oxide semiconductor, or CMOS).

The subtleties of MOSFET technology can fill a whole book, and the interested reader is referred to a rich literature.<sup>20–23</sup> The idealized I-V characteristics for long-channel MOSFETs are given by

$$I = \mu C_{ox} \frac{W}{L} \left( (V_g - V_{th}) V_d - \frac{V_d^2}{2} \right) \quad (4.5)$$

(Figure 4.6d). Here  $\mu$  is the mobility,  $C_{ox}$  is the gate capacitance,  $W$  and  $L$  are the width and length of the channel,  $V_g$  is the gate voltage,  $V_{th}$  is the threshold voltage, and  $V_d$  is the drain voltage. At low bias the inversion layer is uniform over the entire length of the channel (Figure 4.6a), and the channel conductance is constant, leading to a linear regime in  $I$  vs.  $V_d$ . The gate controls the charge in the inversion layer and thus the resistance. At higher drain voltage, the inversion layer becomes thinner close to the drain contact and the current follows a parabolic form, until “pinch-off,” where the channel at the drain vanishes altogether and Equation 4.5 is no longer valid (Figure 4.6b).<sup>21</sup> The pinch-off point can be thought of as a singularity where the electric field along the channel direction goes to infinity, and after which the carriers are no longer confined to two dimensions. If the MOSFET is operated with a drain voltage above this value,  $V_{sat}$ , the pinch-off point moves toward the source (Figure 4.6c), an effect called *channel length modulation*, and the inversion layer becomes shorter than the physical length of the device. The voltage at the pinch-off point, however, stays  $V_{sat}$ , independent of bias voltage, and the current saturates (Figure 4.6d). The saturation current  $I_{sat}$  is a quadratic function of the gate voltage.

The most important feature of a field effect transistor is the modulation of the source–drain current by a gate voltage. Equation 4.5 shows that the ideal MOSFET turns on at a gate voltage  $V_g = V_{th}$ , the so-called threshold voltage. At this voltage, the inversion layer below the gate oxide that connects source and drain with a current path is formed. However, in reality,

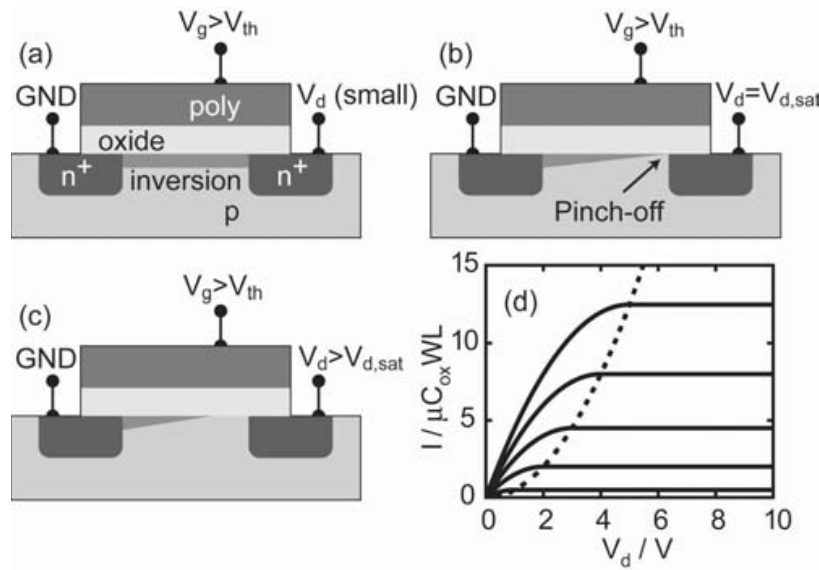


**Figure 4.6** Pinch-off in a MOSFET. (a–c) Schematic of the charge in a MOSFET for different drain voltages. (a) Linear response region. (b) Pinch-off. (c) Channel length modulation. (d) MOSFET idealized drain voltage characteristics for various gate voltages (bottom to top:  $V_g - V_{th} = 1, 2, \dots, 5$  V). The dotted line marks the onset of saturation.

the turn-on at  $V_g = V_{th}$  is not instantaneous because even below the threshold voltage, thermally excited carriers can carry a diffusion current. This subthreshold current is especially important for logic devices, since it limits the switching speed of the transistor. One finds that the current in the subthreshold region depends exponentially on the gate voltage and decays below  $V_{th}$  with a rate that is mainly dependent on temperature. In general, a finite *depletion layer capacitance*  $C_D$  in series with the *geometric capacitance*  $C_{ox}$  of the gate oxide decreases the rate with which the device turns off slightly. Because of the exponential gate voltage dependence of the current, the inverse subthreshold slope, defined as  $S \equiv [d(\log I)/dV_G]^{-1}$ , is a convenient measure for the switching:

$$S = (k_b T / e) \ln 10 \times (1 + C_D / C_{ox}). \quad (4.6)$$

$S$  can be easily determined graphically when the current as a function of the gate voltage is plotted on a log scale. At room temperature the subthreshold slope is typically between 70 and 100 mV/decade. The theoretical limit at room temperature is 60 mV/decade.<sup>21</sup>

Over the past decades progress in silicon technology has occurred mainly through simultaneous scaling of critical MOSFET dimensions and voltages.<sup>20</sup> This helps retain the favorable long-channel MOSFET characteristics, while making the devices switch faster and occupy less space, so there is more room for devices on a given die. As a rule of thumb, scaling devices by a factor  $\kappa$  means altering the device parameters as follows: channel length  $L/\kappa$ , channel width  $w/\kappa$ , oxide thickness  $t_{ox}/\kappa$ , doping level  $N_A \cdot \kappa$ ,  $N_D \cdot \kappa$ , and

all supply voltages  $V/\kappa$ . The threshold voltage then becomes  $V_{th}/\kappa$ , the number of devices that fit on a chip are  $N \cdot \kappa^2$ , the transit time reduces to  $t_{trans}/\kappa$ , and the power consumption per device is  $P/\kappa^2$ . Parameters that do not scale are, for example, the silicon band gap  $E_g$  and the subthreshold slope  $S$  (because both capacitances  $C_{ox}$  and  $C_D$  scale the same way as  $C/\kappa$ ). These scaling rules should not be considered a rigorous requirement, though. For example, one can focus on a few of these parameters that are easier to scale than others, as has been done in the past with the oxide thickness  $t_{ox}$ . In future MOSFET generations, however, it will become difficult to scale this parameter further, because around  $t_{ox} \sim 1$  nm the leakage current from the gate to the channel increases sharply due to tunneling, and power consumption and heat generation become unacceptably large. (Modern MOSFETs have gate-oxide thicknesses of only 1.5 nm.) This problem explains the interest of the semiconductor industry in high-k dielectrics as a replacement of  $\text{SiO}_2$ , because these deliver similar capacitive coupling at larger oxide thickness, and thus reduce the gate leakage.

#### 4.2.2 Nanotube field effect transistor

In 1998 the first carbon nanotube field effect transistors (CN-FETs) were demonstrated at Delft and at IBM (see schematic in Figure 4.5b).<sup>18,19</sup> Both groups used laser ablation-grown carbon nanotubes<sup>24</sup> that were dispersed in a solvent, separated from bundles by ultrasonic agitation, and deposited onto a Si/SiO<sub>2</sub> surface with prefabricated noble metal electrodes. A few of the semiconducting nanotubes would bridge two electrodes and define a conducting channel between them. Modulation of the channel conduction, and thus FET action, was achieved by means of the silicon back gate. CN-FETs fabricated in this fashion behaved like *p*-types, with on/off ratios exceeding several orders of magnitude. However, they showed high resistances in the ON state, in excess of 1 MΩ (i.e., much higher than  $h/4e^2$ ), and because of the thick (140- to 300-nm) gate dielectrics that were used, they also required large gate voltages for switching.

Figure 4.7a and b show the drain and gate voltage characteristics of a CN-FET with metal contacts on top of the carbon nanotube, as depicted in Figure 4.5b. The ON current is on the order of 1 μA, and the on/off ratio is in excess of 10<sup>5</sup> (Figure 4.7b). The transconductance is around  $g_m \sim 100$  nS for a typical source drain bias around 1 V. In contrast to the silicon MOSFET, no current saturation is observed. It is also apparent that the subthreshold slope  $S \sim 500$  mV/decade is much larger than the thermal limit for MOSFETs. We will see further below that there are fundamental differences between CN-FETs and silicon MOSFETs that are responsible for the discrepancies.

Thermal treatment of the CN-FET can reduce the contact resistance to below 100 kΩ in the case of titanium contacts, where it was proposed that abrupt TiC/nanotube contacts formed upon annealing.<sup>25</sup> It also seems that nanotubes, grown directly on the substrate such as by chemical vapor



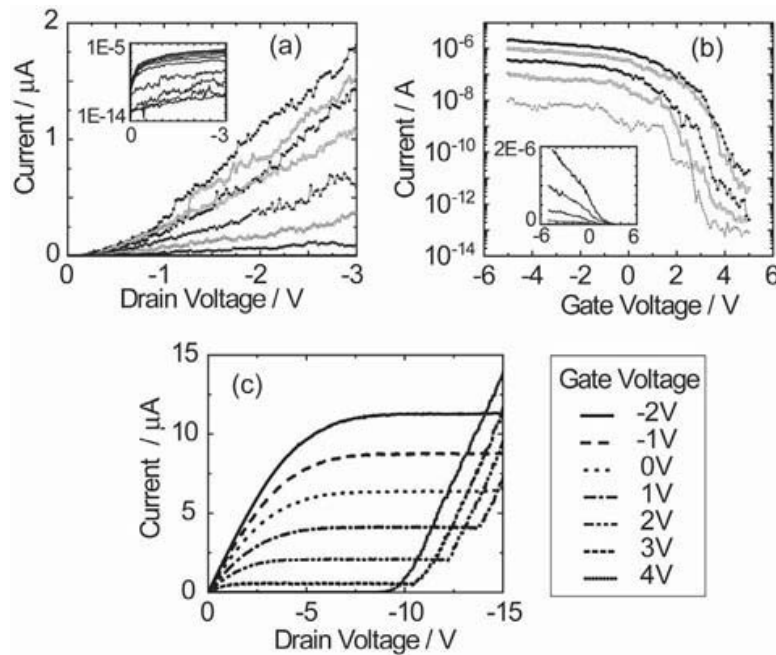


**Figure 4.7** Electronic characteristics of basic *p*-type CN-FETs. (a, b) Device with source–drain distance of 500 nm, oxide thickness of 100 nm, and top contacts made of titanium. (a)  $I$ - $V_d$  characteristics for  $V_g = -5$  (top) to 5 V (bottom) in 1-V steps. No current saturation is observed. Inset: same data on  $\log$  scale. (b)  $I$ - $V_g$  characteristics for  $V_d = -0.2, -0.6, -1.2, -2.0$ , and  $-3.0$  V (from bottom to top). The subthreshold slope is  $\sim 500$  mV/decade. Inset: same data on linear scale. (c) Drain voltage characteristics of an ultra-long-channel CN-FET with 60- $\mu\text{m}$  source–drain distance. (The nanotube is CVD grown. Top contacts are made of Pd with a 0.5-nm adhesion layer of Ti. The silicon-oxide thickness is 50 nm.) Current saturation is observed. Starting at  $\sim 10$  V, the current rises again and ambipolar conduction manifests itself in crossing in the  $I$ - $V$  for different  $V_g$ .

deposition, form better contacts than tubes that are deposited from solution, possibly due to residue on the nanotubes in the latter case. A metal with good wetting properties such as Pd in combination with nanotubes of diameter in excess of 2 nm seems to produce the best contacts, with nearly unity transmission for holes in the ON state.<sup>7</sup> Nanotubes with diameters well below 2 nm have band gaps that approach 1 eV, which makes the formation of Schottky barriers at the contacts more likely. We will review the effects of Schottky barriers on transport through CN-FETs extensively below.

Another avenue to improve the performance of CN-FETs is to optimize the gate stack. In this respect, carbon nanotubes are much more versatile than silicon, because the carbon nanotube surface has no dangling bonds. Surface roughness scattering is therefore not an issue. Several high- $k$  dielectrics have already proven successful in CN-FETs:  $\text{Al}_2\text{O}_3$ ,<sup>26</sup>  $\text{HfO}_2$ ,<sup>27</sup>  $\text{ZrO}_2$ ,<sup>28</sup> and  $\text{SrTiO}_3$ .<sup>29</sup> The omnipresent dielectric  $\text{SiO}_2$  is used in most published work on carbon nanotubes, mainly because it is readily available in the form of oxidized silicon wafers. For silicon MOSFETs, on the other hand,  $\text{SiO}_2$  is so far the only serious contender because MOSFETs rely on the nearly perfect interface that forms between silicon and its oxide. Most

high- $k$  dielectrics are accompanied by unacceptable mobility degradation in silicon MOSFETs.

Nanotubes that are dispersed in a solution may be deposited at any stage in the FET fabrication process as long as the solvent can be tolerated. On the other hand, it might be of advantage to also grow nanotubes by a CVD process on the chip at a time when some of the metallic leads, such as buried metal gates or contact pads, are already in place. The metal then needs to withstand the elevated temperatures of the growth process. Two ways of solving this problem have been found recently: the CVD growth temperature for single-wall carbon nanotubes can be reduced to 600°C, a value that most metals can withstand, by using methanol as the feedstock gas,<sup>30</sup> or by using plasma-enhanced CVD of methane.<sup>31</sup> A second solution is the use of metals that can withstand the usual growth temperatures around 800 to 900°C and still make a good contact to carbon nanotubes. Molybdenum and tungsten-platinum have been found to do just this.<sup>32,33</sup>

Even though MOSFETs and CN-FETs look quite similar in a schematic (Figure 4.5), the scaling rules for CN-FETs turn out to be very different from the ones previously discussed in MOSFETs: by nature of their small diameter, carbon nanotubes are already ultra-thin-body FETs. Silicon MOSFETs cannot be expected to provide this kind of confinement even in future technological generations. Quantum size effects are also evident in the number of channels that contribute to conduction in semiconducting carbon nanotubes (four), which means that current levels are far below present-day MOSFETs. On the other hand, typical current densities ( $\sim 10^8$  A/cm<sup>2</sup>) are significantly higher than in silicon MOSFETs. The low current levels should be acceptable in the future when only small capacitances (such as other CN-FETs) need to be charged. If one thinks of silicon-carbon nanotube hybrid structures, on the other hand, higher current drives would be required that could be delivered by arrays of closely spaced carbon nanotubes in parallel.

Similar to metallic carbon nanotubes but unlike silicon, semiconducting carbon nanotubes are ballistic at low bias and length scales below hundreds of nanometers.<sup>7</sup> Reducing the channel length below this value will not result in any change in resistance. Due to time-of-flight considerations, however, the device will still switch faster. On the other hand, CN-FETs with very long channel lengths, above 10  $\mu\text{m}$  (Figure 4.7c), behave more like bulk-switching MOSFETs (Figure 4.6d); i.e., they show current saturation, because the channel resistance gets larger than the resistance of the contact barriers. In these nanotubes transport is dominated by drift of carriers in a charge gradient that builds up inside the nanotube channel. It then makes sense to use a geometric capacitance to model conduction<sup>34</sup> and extract material quantities such as mobility. Fuhrer et al.<sup>35,36</sup> found a low-bias mobility,  $\mu \sim 100,000$  cm<sup>2</sup>/Vs, that exceeds any other known semiconductor mobility. The eventual breakdown of saturation in Figure 4.7c and the crossings in the various  $I$ - $V$  curves are due to the opening of an electron channel for conduction in addition to the prevalent hole conduction, and will be discussed in the section about ambipolar transistors. Due to the cylindrical

geometry of carbon nanotubes, the gate capacitance in long-channel devices scales with the inverse logarithm of the oxide thickness  $C_{ox} \sim 1/\ln(t_{ox})$ , rather than inversely, as in the planar MOSFET geometry.

A carbon nanotube is fully depleted so the depletion capacitance  $C_D = 0$  and the subthreshold slope  $S$  should be a constant 60 mV/decade at room temperature, according to MOSFET modeling. This is not generally observed in CN-FETs. Instead,  $S$  decreases for decreasing oxide thickness — from 1 V/decade in the early devices to 60 mV/decade in state-of-the-art CN-FETs. As we will see later, the dependence of  $S$  on  $t_{ox}$  is one of the manifestations of Schottky barriers in CN-FETs. In addition to improving  $S$ , gate-oxide scaling also enables low-voltage operation in CN-FETs. When  $t_{ox}$  is scaled aggressively, the Schottky barriers become extremely thin due to the one-dimensional nature of the carbon nanotube. This enables tunneling through the barrier and ambipolar conduction in the device.

Finally, the band gap of carbon nanotubes can in principle be “tuned” by synthesis of nanotubes with the appropriate diameter. In MOSFETs, the band gap is a quantity that does not scale.

### 4.2.3 Schottky barriers

Much of the difference in scaling between a MOSFET and a CN-FET can be explained with the presence of one-dimensional Schottky barriers at the contacts to the semiconducting nanotube.<sup>27,37–42</sup> Interestingly, during the first few years, CN-FETs were analyzed either like MOSFETs<sup>19</sup> or barrier injection transit time (BARITT) diodes.<sup>18</sup> Schottky barriers were experimentally confirmed in carbon nanotube cross-junctions made of one semiconducting and one metallic carbon nanotube.<sup>43</sup> Soon afterwards, they were also observed in CN-FETs by scanning gate microscopy<sup>44</sup> and by transport measurements.<sup>25,27,40,41,45</sup> Note that the contact issue is not limited to carbon nanotubes and is observed in all kinds of molecular electronic systems. It absolutely dominates transport through small molecules (see Lang and Avouris<sup>46</sup> and Hips<sup>47</sup> and references therein).

When a semiconducting and a metallic material are brought into contact, the Fermi level of the metal usually lines up inside the semiconducting band gap or occasionally in the conduction — or valence — bands. In the first case, a Schottky barrier forms (Figure 4.8a), whereas in the latter cases, there is no or only a highly penetrable barrier (Figure 4.8b and c). Note that an exact lineup of the metal Fermi level with the valence band (Figure 4.8b) does not mean that the device is fully ohmic, because there is still a triangular barrier present. A truly ohmic contact results only when the metal Fermi level lies well below the valence band edge (Figure 4.8c).

Schottky barriers in one dimension differ in one crucial aspect from Schottky barriers in three dimensions: they are much thinner (on the nanometer scale), and tunneling or thermally activated tunneling through the barrier is more important than thermal emission over the barrier.<sup>27,40,42</sup> This has important consequences for the switching behavior of CN-FETs and also

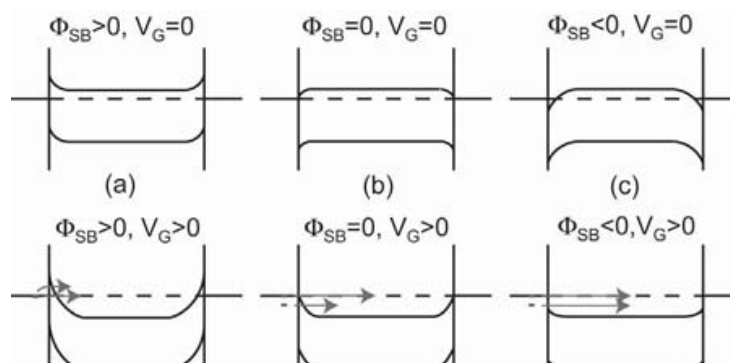


**Figure 4.8** Schematic of (a) a Schottky barrier FET, (b) a FET with zero Schottky barrier, and (c) a FET with truly ohmic contact for holes.

their scaling properties. We will discuss these issues extensively in the next section.

It is tempting to estimate the band lineup using the values for the electron affinity of the semiconductor and the work function of the metal. This can be problematic even in three-dimensional materials, where metal-induced gap states appear in the semiconductor that behave similar to surface states and pin the Fermi level of the metal close to the middle of the semiconducting band gap.<sup>20,48,49</sup> In a one-dimensional metal–semiconductor system, Fermi-level pinning due to metal-induced gap states is not as effective because their effect is limited to length scales on the order of the wire diameter (1 nm in the case of carbon nanotubes), a length that can easily be tunneled through.<sup>38</sup> On the other hand, dipoles on the metal surface due to the exposure to ambient gases or other molecular or atomic species can change the effective work function of the metal, and therefore the expected band lineup, significantly. One of these systems is oxygen on gold. Adsorbed oxygen increases the gold work function and makes the band lineup more *p*-type.<sup>50,51</sup> Another interesting case is hydrogen in connection with palladium. Here the dissolved hydrogen lowers the work function of palladium and makes the contact less *p*-type.<sup>7</sup> Note that in MOSFETs the contacts are made of the same semiconducting material as the channel (silicon). They are merely doped differently and the contact behaves in an ohmic manner.

Nanotubes with large diameters (~3 nm), as present in CVD-grown samples, have small band gaps (~0.5 eV), and no matter what contact material is used, the Schottky barrier for one kind of carrier is always small (<250 meV) or even negative. In addition, the effective mass of both electrons and holes is small in these nanotubes, enhancing tunneling through barriers.

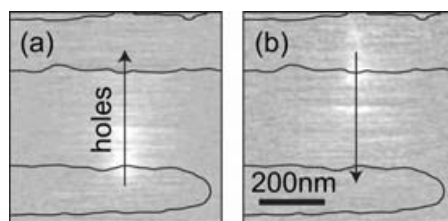


**Figure 4.9** Scanning gate microscopy images (transport current as a function of tip gate position) showing enhanced current at the Schottky barrier where holes are injected. The full color scale corresponds to a range of 0 to 700 pA (black to white). The contours of the leads are shown as an overlay to the SGM image. The arrows mark the position of the tube that is deposited on top of the contacts. (a) Top contact, genetic neutrally different alloy (GND), 0V; bottom contact, +1 V; tip voltage,  $-1.5$  V. (b) Top contact, +1 V; bottom contact, GND, 0V; tip voltage,  $-1.5$  V.

It is in these kinds of devices that extremely high ON currents of around  $25\ \mu\text{A}$  have been measured.<sup>7</sup> On the other hand, laser ablation-grown nanotubes around  $1.3\ \text{nm}$  in diameter have band gaps just short of  $1\ \text{eV}$  with significant Schottky barriers for both electrons and holes.<sup>25</sup>

The Schottky barriers in one-dimensional materials can be imaged with SGM, a technique described before (Figure 4.3a).<sup>44</sup> A bias is applied between source and drain while the back gate is grounded. For  $p$ -type transistors (as for most CN-FETs in air) the tip is biased negatively to turn on the conduction through a current-limiting Schottky barrier. The experiments show that the source barrier, where holes are injected into the carbon nanotube, limits the current through the CN-FET (Figure 4.9). Switching source and drain allows the other contact to be imaged. When a positive tip voltage is used, this pronounced dependence on the sign of the current is not observed, and instead defects along the length of the tube can be imaged by depleting the tube locally.<sup>52</sup> The SGM technique also indicates that for larger-diameter nanotubes ( $\sim 3\ \text{nm}$ ), the Schottky barriers become less important in switching the current.<sup>53</sup>

So why would anyone still want to work with small-diameter nanotubes that usually have Schottky barriers and low drive current? The short answer is that the ON current is only one of the key performance parameters a circuit designer is interested in. At least equally important is the OFF current that flows when the device is idle, and which increases power consumption and chip heating. It turns out that in terms of OFF current, the large-diameter tubes fare worse, because their small band gaps facilitate ambipolar conduction<sup>25,41</sup> and a Zener type of breakdown.<sup>54</sup> We will extensively discuss the ambipolar character of the conduction in carbon nanotubes later on. For now it should suffice that both Schottky barriers, the one for electrons at the drain and the one for holes at the source, can be overcome in these devices. The nanotube then acts as an electron channel for large positive gate voltages and a hole channel for large negative gate voltages, and the OFF state is limited to a small gate voltage range in between the two extremes.<sup>25,41</sup> At high drain voltages, this OFF state deteriorates and the devices develop a



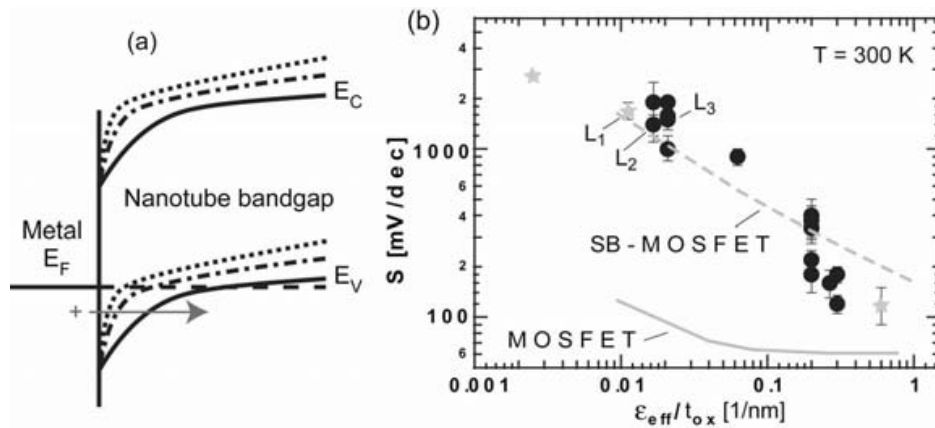


**Figure 4.10** (a) Schematic of switching a one-dimensional Schottky barrier FET. (After Heinze et al.<sup>40</sup>) The conduction and valence bands are shown for increasingly negative gate voltage (solid lines through dotted lines). (b) Subthreshold slope as a function of oxide thickness. The CN-FET data are taken from several different papers, as described in Appenzeller et al.<sup>27</sup> (Reprinted from Appenzeller, J. et al., *Phys. Rev. Lett.*, 89, 126801, 2002. With permission. Copyright © 2002 by the American Physical Society.)

bipolar state, where both electrons and holes are present in the channel at the same time.<sup>55</sup>

#### 4.2.4 Gate-oxide scaling

In MOSFETs, the subthreshold current is determined mainly by thermal activation over a bulk barrier. This leads to a subthreshold slope near  $S \sim 60$  mV/decade at room temperature (Equation 4.6), with a weak dependence on the depletion capacitance. In the case of CN-FETs, on the other hand, the Schottky barriers at the contacts are responsible for switching as they become thin enough for thermally assisted tunneling.<sup>27,40,42</sup> The subthreshold slope is then determined by the change in barrier thickness as a function of gate voltage (Figure 4.10a<sup>40</sup>), and not just by the thermal distribution of the carriers.

It is very instructive to look at the variation in the values of the subthreshold slope for devices with different gate-oxide thicknesses or dielectric constants.<sup>27,56</sup> Figure 4.10b shows a spread of almost two orders of magnitude in the subthreshold slope for those devices, but the data also show a clear trend when  $S$  is plotted as a function of the inverse effective oxide thickness  $\epsilon_{eff}/t_{ox}$ . ( $\epsilon_{eff}$  is the effective dielectric function of the gate oxide, taking into account that usually the tubes are not fully embedded in the oxide.) In a bulk-switching device such as a silicon MOSFET, the gate-oxide thickness affects the charge in the channel through the gate capacitance, and thus the conductance in the ON state, but the subthreshold slope  $S$  stays independent of the gate-oxide thickness (as long as the device remains in the long-channel limit). In a Schottky barrier transistor, on the other hand, the gate-oxide thickness defines the length scale over which the bands bend at the contacts, and thus  $t_{ox}$  is the single most important parameter to influence the Schottky

barrier width and the current in the subthreshold region. As a rule of thumb, the Schottky barrier width is on the order of  $t_{ox}$ .<sup>40</sup>

Heinze et al.<sup>40,57</sup> have modeled the carbon nanotube FET in various geometries, such as single or double gate, thin leads, thick leads, and needle-like leads, and found that the exact contact geometry does make a difference. Therefore, there is no universal scaling rule for the subthreshold slope with respect to  $t_{ox}$ . For thin leads with thickness  $\tau \sim t_{ox}$  one finds a square root dependence,  $S \sim t_{ox}^{1/2}$ , whereas for infinitely thick leads,  $S \sim t_{ox}^{2/3}$ . For needle-like contact geometries to a carbon nanotube, one would achieve the strongest field enhancement at the contact, and thus the highest ON currents and steepest subthreshold slopes. The above relations are valid in the thick oxide limit as long as  $t_{ox} > 10$  nm. For very thin oxides the Schottky barriers also become extremely thin and the subthreshold slope approaches the bulk-switching limit of  $S \sim 60$  mV/decade.

#### 4.2.5 Ambipolar transistor

In Schottky barrier CN-FETs with ultimately scaled gate-dielectric thickness, the subthreshold slope is pretty close to the thermal limit because the source Schottky barrier is highly penetrable. If this would be the only effect of gate-oxide scaling we would be in business, but unfortunately another problem arises in these devices. There are two Schottky barriers, one for holes at the source and one for electrons at the drain, and both can become so thin that they pose almost no barrier for transport (Figure 4.11a).<sup>40,41,55</sup> Therefore, a large leakage current flows in the transistor OFF state. In devices with a *p*-type band lineup, for example, this leakage current is carried by electrons that are injected at the drain when the drain voltage significantly exceeds the gate voltage. A similar phenomenon is observed even for thick oxides when the band lineup is close to mid-gap<sup>25</sup> (Figure 4.11b to d), or in large-diameter tubes where both Schottky barrier heights are small due to a small band gap (Figure 4.7c). Note that the first experiments on nanotube FETs<sup>18,19</sup> (Figure 4.7b) showed the nice unipolar behavior only because the devices were fabricated with small-diameter tubes on very thick oxides and the Schottky barrier heights for electrons and holes were quite dissimilar. For electronic purposes, ambipolar transport, as it is commonly called, is undesirable. High-performance FETs therefore require some inventive engineering to achieve both fast switching and low OFF currents.

The gate voltage characteristics of ambipolar devices show a pronounced V shape on a logarithmic plot (Figure 4.11c and d) with a minimum near  $V_g = 1/2 V_d$ .<sup>25,40,56</sup> (In devices with thick gate oxides, this minimum can be shifted considerably due to trapped charges in the oxide.) At the minimum, equal hole and electron currents are injected at the source and drain, respectively (the corresponding band bending is depicted in the solid curve in Figure 4.11a). For increasing drain voltages, the minimum rises exponentially with drain voltage (Figure 4.11c and d).<sup>55</sup> At highest drain voltages, the minimum can become almost as large as the ON current and the transistor

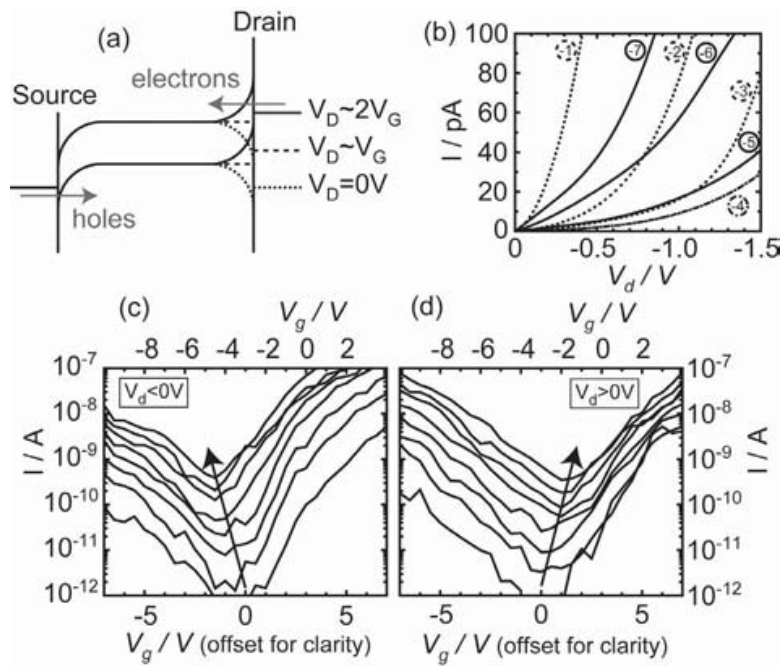


**Figure 4.11** Ambipolar characteristics. (a) Schematic of ambipolar conduction in Schottky barrier FETs. The channel is assumed to be ballistic. Dotted,  $V_d = 0$  V; dashed,  $V_d \sim V_g$ ; solid,  $V_d \sim 2V_g$ . (b) Drain voltage characteristic in a CN-FET with near mid-gap band lineup for various gate voltages  $V_g/V$  as indicated in the figure. (c) Gate voltage characteristic for various drain voltages:  $V_d = -0.2, -0.6, -1.0, \dots, -3.0$  V. The gate voltage scale at the bottom of both figures is offset by 3 V to account for trapped charges in the oxide. (d) Gate voltage characteristics with positive drain voltages:  $V_d = +0.2, +0.6, +1.0, \dots, +3.0$  V.

does not switch OFF any more. As the drain voltage increases, the minimum also shifts in gate voltage according to  $V_{g,min} = 1/2 V_d$  because at this gate voltage the potential in the carbon nanotube is positioned halfway between the source and drain potentials. Note that the direction in which the minimum moves only depends on the sign of the drain voltage (negative shift for negative  $V_d$  and positive shift for positive  $V_d$ ).

Plots of the current vs. drain voltage at different gate voltages show characteristic crossings in ambipolar CN-FETs (Figure 4.7c and Figure 4.11b). Consider a negative gate voltage where the CN-FET is initially a pure hole conductor with low low-bias resistance. The current starts to rise first with increasing  $|V_d|$ , but then moderates because the drain voltage does not act efficiently on the source Schottky barrier where holes are injected. In long-channel CN-FETs true current saturation is observed in this regime (Figure 4.7c), while in short-channel devices a rise in current is still present (Figure 4.11b). However, at some point electrons start to be injected at the drain and the current turns up sharply with increasing  $|V_d|$ . For less negative gate voltage  $V_g$ , the hole current is smaller because the source barrier is less transparent than before. On the other hand, the electron injection occurs earlier since the effective gate voltage that the electrons at the drain “see” is  $V_g - V_d$ . The corresponding  $I - V_d$  curve will then cross the curve

for more negative gate voltage. This can be seen in Figure 4.7c and also in Figure 4.11b, where the dotted curves cross the solid curves at high  $|V_d|$ .

#### 4.2.6 High-performance FETs

For ultimate performance in scaled devices, the ambipolar character of the conduction through the carbon nanotube needs to be suppressed. One way to do this is by electrostatic engineering, where the coupling of the gate to one Schottky barrier is made strong, while it is intentionally made weak at the other contact.<sup>57</sup> Indeed, selective etching of the gate oxide at one Schottky barrier has been used to decrease the gate coupling at that contact and the device becomes unipolar.<sup>58</sup>

An approach to suppress ambipolar conduction that does not rely on weakly gated tube segments is a modulation-doped *p-i-p* or *n-i-n* structure on a single tube (Figure 4.12b).<sup>59–62</sup> The CN-FET then behaves as a bulk-switching device with degenerately doped tube segments acting as extensions of the source and drain contacts and the intrinsic middle section acting as the channel. There are several advantages to this design: (1) The ON current is enhanced because the Schottky barriers to the leads are suppressed due to heavy doping. (2) In the *p-i-p* structure there is no barrier for holes between the doped and intrinsic tube segments, so the intrinsic segment can act like the channel in a bulk-switching device. (The same is true for electrons in the *n-i-n* structure.) Therefore, the subthreshold slope is steeper than in Schottky barrier transistors and approaches the theoretical limit of 60 mV/decade, independent of oxide thickness. (3) The barrier to inject the opposite kind of carrier into the intrinsic nanotube segment is maximized by using the full nanotube band gap  $E_g$ , and ambipolar conduction is suppressed.

Figure 4.12c and d show the schematic and electronic characteristics of an electrostatically doped CN-FET.<sup>62</sup> The nanotube segments close to the contacts are doped *p*-type by a negative back-gate voltage. The aluminum finger gate in the middle of the device is used to switch the middle section of the nanotube as shown by the shaded area of Figure 4.12b. The CN-FET now acts as a bulk-switching device and has a minimized subthreshold slope of 63 meV/decade. This compares to a subthreshold slope of 100 mV/decade when the two gates are used in unison to switch the Schottky barrier FET. Note that for insufficient back-gate voltages, the nanotube segments close to the contacts are depleted, and the device stays off for any kind of voltage on the aluminum finger gate. A similar *p-i-p* structure was recently also demonstrated by selective chemical doping of the nanotube segments close to the contacts.<sup>63</sup>

#### 4.2.7 Doping

In order to build logic circuits, it is of great advantage to employ both *n*- and *p*-type field effect transistors in a technology called complementary MOS

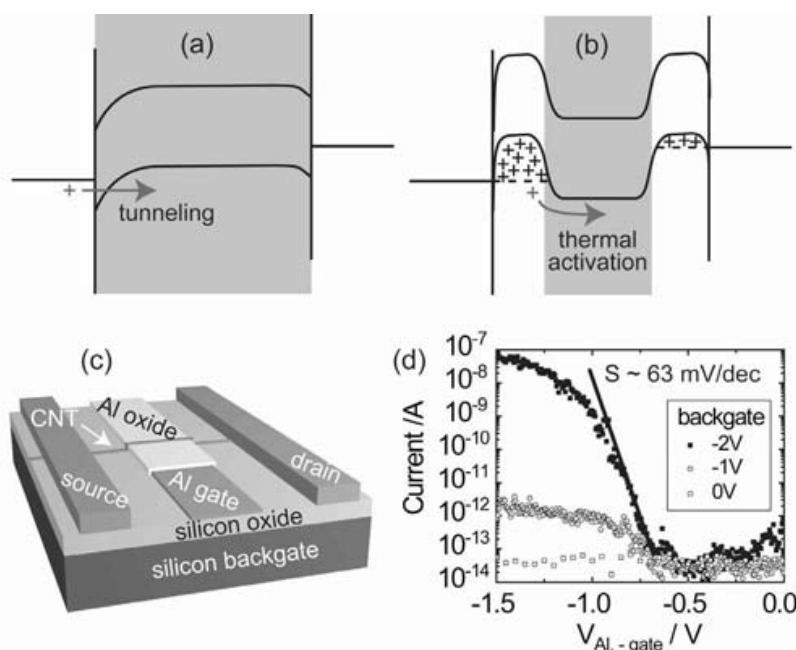


**Figure 4.12** Band bending in (a) a Schottky barrier CN-FET and (b) a *p-i-p*-doped carbon nanotube that acts as a bulk-switching CN-FET. (c) Schematic of an electrostatically defined *n-i-n/p-i-p* structure. The silicon back gate is used to dope the nanotube segments close to the contacts degenerately *n*- or *p*-type. The aluminum gate with an  $\text{Al}_2\text{O}_3$  dielectric switches the intrinsic middle segment of the nanotube. (d) Characteristic of the device. (Courtesy of Yu-ming Lin.)

logic, or just CMOS. In principle, one type of transistor integrated with resistors can also be used to perform logic operations, but the performance is lower in two crucial aspects: (1) power dissipation and (2) high-output impedance.<sup>64</sup> While power dissipation in CMOS is limited to the instant when the gate switches, transistor-resistor logic draws current continuously in the ON state. If one tries to reduce power consumption by increasing the resistance, one ends up with larger-output resistance. This is bad in terms of both switching speed and noise pickup. For carbon nanotubes to offer a viable alternative to silicon, there needs to be a way of making both *n*- and *p*-type devices on the same chip.

From tight-binding calculations one expects that undoped carbon nanotubes are intrinsic semiconductors.<sup>4</sup> There have been efforts with very limited success to substitutionally dope carbon nanotubes with either boron or nitrogen, two elements with roughly the same size, but one valence electron less or more than carbon.<sup>65</sup> One finds that addition of these species during growth leads to significant defects, bamboo-like growth, or the preferred growth of multiwalled nanotubes over single-walled tubes. Therefore, only pure carbon nanotubes have been seriously considered for electronic purposes so far.

A more versatile way of doping carbon nanotubes that are *n*- or *p*-type is by charge transfer from adsorbed atoms or molecules that are deposited on the surface after the growth process is completed. In practice, devices are assembled, including all the contacts, and in a final step the nanotube is



exposed to the dopant. Doping by adsorption benefits from the fact that the nanotube is all surface, and thus quite susceptible to the environment. The first example of doping a single carbon nanotube in this fashion was achieved with potassium, a strong electron donor.<sup>66</sup> Involuntary doping also happens in air when carbon nanotubes are exposed to oxygen and become *p*-type.<sup>50,51</sup> In vacuum they tend to turn ambipolar or even *n*-type, especially after annealing at elevated temperatures, a process that promotes desorption of molecular oxygen. Note that a third way of doping a carbon nanotube could be accomplished by incorporating atoms or molecules *inside* the hollow nanotube.<sup>67–69</sup>

There are two distinct locations along the channel of a CN-FET where dopants act quite differently: at the bulk of the carbon nanotube and at the interface between the nanotube and the metal. When the bulk of a *p*-type carbon nanotube is doped, for example, by evaporated potassium, the effect is a threshold voltage shift, rather than a *p*-to-*n* conversion.<sup>40,45</sup> Elevating the temperature allows the potassium to diffuse to the nanotube–metal contact area. At this location, the dopant acts as a dipole that shifts the band lineup between the contact metal and the carbon nanotube. The Schottky barrier height for holes is then increased while the one for electrons is decreased, which leads to a suppression of the *p*-branch and an increase of the *n*-branch.<sup>70</sup>

Potassium, other alkaline metals, and ammonia (NH<sub>3</sub>)<sup>71</sup> are good *n*-dopants for carbon nanotubes, but they are unstable under ambient conditions. Polyethyleneimine (PEI),<sup>72,73</sup> and hydrazine<sup>74</sup> have been shown to work similarly well without being as reactive in air. Often, doped devices not only achieve *p*-to-*n* conversion, but also provide better transistor performance than the as-fabricated unintentionally *p*-doped ones, because the band lineup is closer to the conduction band edge than it previously was to the valence band edge. The contact barrier is smaller and the devices show improved ON states, OFF states, and subthreshold swings over the original *p*-type devices. It can therefore even make sense to dope the as-fabricated *p*-type devices with stronger *p*-dopants. This has been done so far with (C<sub>2</sub>H<sub>4</sub>)<sub>3</sub>O<sup>+</sup>SbCl<sub>6</sub><sup>–</sup>,<sup>63</sup> NO<sub>2</sub>,<sup>75</sup> and various acids.<sup>74</sup>

#### 4.2.8 Logic gates

Field effect transistors constitute the basic building blocks of modern computer chips. To achieve functionality, they are interconnected in ways so that simple logic, arithmetic, or memory functions are performed. We have already talked about the advantage of using both *n*- and *p*-type transistors for this purpose. Another requirement for the transistors in any kind of integrated circuit is individual addressability. The common back gate, as is state of the art in CN-FETs, can usually not be used. (A single inverter or “NOT” gate is an exception to this rule, as it is built out of two FETs that use a common gate.) Therefore, CN-FETs with individual gates, either below the nanotube<sup>26</sup> or on top of it,<sup>76</sup> have been fabricated.

With the basic devices in place, it should be just a matter of wiring them up to make simple logic gates.

This, however, is easier said than done. One has to appreciate that nanotubes are not lithographically defined structures. As of now, they are deposited rather randomly or grown with poorly controlled yield on the substrate. There is also no control over the type of nanotube (semiconducting or metallic) that is grown, let alone the specific nanotube chirality. This makes it very hard to fabricate logic gates in an automated fashion on a small area. Most published work on simple integration of carbon nanotubes to perform logic therefore relies on locating working CN-FETs and wiring them up, sometimes with rather crude methods, such as makroscopic cables. Nevertheless, these examples can be seen as an encouraging proof of principle, and with increasing control over the nanotube material and its placement, integration will become a less daunting task over time.

The first demonstration of logic performed with CN-FETs was the inverter or NOT gate, implemented on a single carbon nanotube (Figure 4.13).<sup>77</sup> A NOT gate can be built out of only two FETs, one *p*-type and one *n*-type, that use a common gate as input and share one common electrode as output. The positive and negative supply voltages are applied at the two remaining contacts of the *p*- and *n*-FETs, respectively. An inverter can therefore be realized on a single carbon nanotube with three lithographic contacts and a single back gate that switches both FETs simultaneously. In Derycke et al.<sup>77</sup> two CN-FETs on the same tube were initially both *p*-type. One of

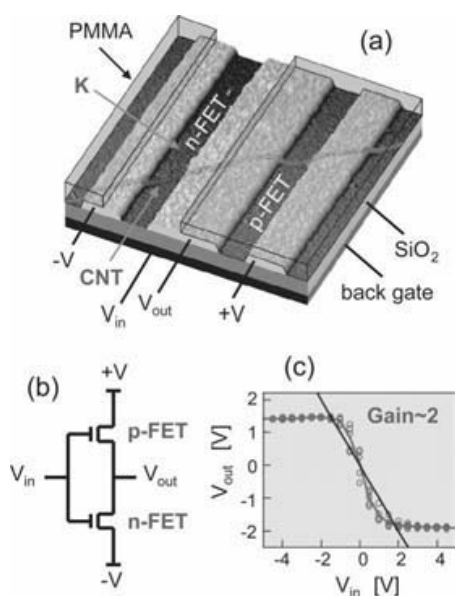


**Figure 4.13** Single carbon nanotube inverter. (a) Two CN-FETs that share a common electrode and the back gate are fabricated on a single carbon nanotube. One of the initially *p*-type CN-FETs is converted to *n*-type by potassium doping. (b) Wiring schematic of the inverter. (c) Output characteristics of the nanotube inverter. (Reprinted from Derycke, V. et al., *Nano Lett.*, 1, 453, 2001. With permission. Copyright © 2001 American Chemical Society.)

them was protected with polymer before the chip was exposed to potassium, which rendered the unprotected CN-FET *n*-type. (A second approach in the same reference<sup>77</sup> made use of desorption of molecular oxygen upon annealing to convert one CN-FET *n*-type.)

One can easily understand the inverting action of a NOT gate by considering the voltage divider that the two FETs in series form (Figure 4.13b). When a positive voltage is applied at the gates, the *p*-FET turns off while the *n*-FET turns on, and the output voltage is close to the (negative) voltage applied at the *n*-FET. Conversely, when a negative voltage is applied at the gates, the *p*-FET turns on while the *n*-FET turns off, and the output is pulled to the (positive) supply voltage at the *p*-FET. A practical inverter also requires gain if its output is to be used to drive further stages of logic. Figure 4.13c shows the characteristics of this nanotube inverter with a gain of  $>1$ , which is very encouraging given the advances that have been made with individual CN-FETs henceforth.

After this initial demonstration of logic with a carbon nanotube, more complex gates were fabricated. Bachtold et al. introduced individually switching CN-FETs with aluminum bottom gates and  $\text{Al}_2\text{O}_3$  gate dielectrics.<sup>26</sup> The *p*-FETs were then wired up with external resistors to form resistor–transistor logic devices, such as NOT-OR (NOR) gates, static memory (SRAM) cells, and a three-stage ring oscillator. Javey et al. combined local embedded metal gates for each FET with electrically induced local vacuum annealing to make *n*-FETs.<sup>78</sup> The complementary CN-FETs were then wired up to form NOR, OR, NOT-AND (NAND), and AND gates, as well as ring oscillators (each gate containing four to six individual FETs). The technique also produced an inverter with a gain of 8.

It is interesting to note that both ring oscillators demonstrated in Bachtold et al.<sup>26</sup> and Javey et al.<sup>78</sup> were totally dominated by the parasitic capacitances of the cables used to wire the devices up. They were therefore oscillating with frequencies of only 5 and 200 Hz, respectively. The intrinsic speed of nanotube devices is expected to be much higher than that, and it is clear that the true performance of nanotube logic can only be assessed with a more appropriate wiring strategy to reduce parasitic capacitances.

First advances in measuring the high-frequency performance of CN-FETs have been made recently with an ingenious method to overcome the problems associated with the low current drive of single nanotubes.<sup>79</sup> For this, an alternating current (AC) signal was applied at the source contact of the CN-FET, while a direct current (DC) bias was applied simultaneously at the gate and drain. The DC through the tube was then measured as a function of both the AC oscillation amplitude and the AC frequency. Owing to the strong nonlinearity of the CN-FET in the subthreshold region, the AC signal should have a strong effect on the DC whenever the device is DC biased close to the threshold voltage. Frank and Appenzeller<sup>79</sup> found that indeed the DC is a strong function of the AC amplitude in the subthreshold region, whereas it is utterly independent of the AC frequency up to the experimental limit of 250 MHz, given by the capacitance of their contact

pads (11 pF) and the output impedance of the AC voltage source (50  $\Omega$ ). The value of 250 MHz is therefore only a lower limit, and it is left to future experiments to determine the intrinsic response time of nanotube field effect transistors.

#### 4.2.9 Infrared emitters

We have shown before that for electronic purposes, ambipolar conduction in field effect transistors is undesirable, and in high-performance devices, the injection of carriers from the drain needs to be suppressed. On the other hand, for electro-optic applications, ambipolar conduction can be very welcome, because it allows electronically pumping a CN-FET with electrons *and* holes that are injected at opposite contacts into an intrinsic carbon nanotube.<sup>80</sup> The carriers can then recombine in the nanotube and emit infrared light. It should be emphasized here that the carbon nanotube is not chemically doped, such as a *p-n* light-emitting diode would be. In the CN-FET it is possible to inject the two carriers at the same time because there are two highly penetrable Schottky barriers, one for electrons and one for holes.

In electroluminescent CN-FETs the infrared emission happens predominantly at energies in the vicinity of the nanotube band gap ( $E_{11}$  transitions, Figure 4.14b). However, the spectrum shows a bias-dependent width with a strongly broadened peak when high source–drain fields are applied (Figure 4.14a).<sup>81</sup> The situation is similar to the previously discussed current saturation, where electrons can accelerate in the applied field until they gain sufficient energy for optical phonon emission.<sup>5,9,15,82</sup> In ambipolar FETs the same happens for holes and the maximum energy available for radiative recombination is expected to be about 360 meV (i.e., twice the optical phonon energy) above the nanotube band gap. Experimentally, one finds a spectral peak with a width around 100 to 200 meV and a significant hot energy tail

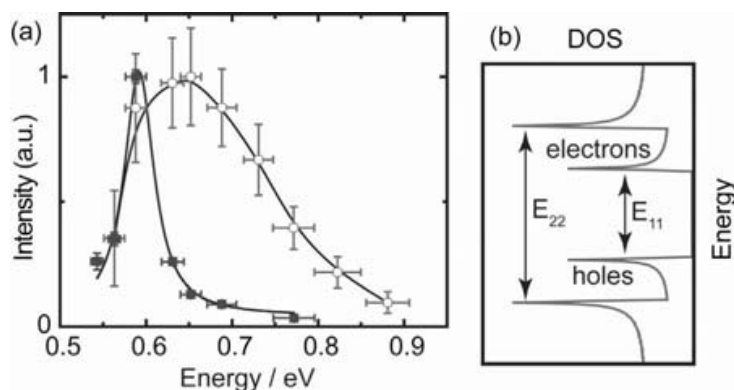


**Figure 4.14** Electroluminescence in ambipolar CN-FETs. (a) Infrared spectra for two ambipolar CN-FETs. The sharp peak is from a long tube, biased with low drain voltage, while the broad spectrum is from a short tube with high  $V_d$ . (b) Schematic of the density of states of semiconducting carbon nanotubes, depicting the one-dimensional van Hove singularities and the allowed optical transitions. The spectral peaks in electroluminescence correspond to the  $E_{11}$  transition.

at high bias (Figure 4.14a).<sup>81</sup> Light emission from carbon nanotubes is linearly polarized along the nanotube axis.<sup>80</sup>

The efficiency of electroluminescence in carbon nanotubes has been measured to be around  $\eta = 10^{-6} - 10^{-7}$  photons per injected electron-hole pair.<sup>81</sup> This is a rather low value for a direct-gap material. Typical efficiencies in nanotube photoluminescence are around  $10^{-4}$ .<sup>83,84</sup> There seems to be some additional quenching of radiative transitions in photoluminescence when the tubes are deposited on substrates,<sup>85</sup> as is the case in CN-FETs. However, even an efficiency of  $10^{-4}$  seems quite low, and the reason is still an open question. The strong coupling of electrons with the optical/zone boundary phonons in carbon nanotubes could be responsible, because their large energy might allow nonradiative decay by few-phonon excitation processes to compete with the optical transition across the rather small band gap. Decay to dark exciton states has been proposed as a possible answer as well.<sup>86,87</sup> They might trap the electron-hole pair in a state that cannot decay radiatively. Finally, Auger effects are likely to play a role, especially in the case of high currents, where many carriers are present at the same time and an electron-hole pair can recombine by giving its energy to another electron, hole, or electron-hole pair. Note that because of the nanoscale volumes of carbon nanotubes, current densities are naturally high, favoring Auger.

In typical CN-FETs it is not possible to determine exactly where in the carbon nanotube electron-hole recombination takes place, because the wavelength of the emitted light is on the order of  $2\ \mu\text{m}$ , i.e., much longer than the channel length.<sup>80</sup> Near-field measurements could be valuable here, but they are plagued by very low detection efficiencies when the aperture is considerably smaller than the detected wavelength. Long-channel CN-FETs, on the other hand, allow measuring the spatially resolved infrared emission by conventional far-field methods. In these FETs the emission is found to be localized in a spot on the order of a micrometer in length.<sup>88</sup> This suggests that the recombination is fast compared to carrier transit times of several 10 psec in long-channel CN-FETs. On the other hand, for CN-FETs with the more typical channel lengths around 500 nm, this means that a large fraction of the electrons and holes will actually reach the opposite contact without recombination.

So where is recombination taking place in long-enough ambipolar CN-FETs, which utilize intrinsic carbon nanotubes without any chemically defined  $p$ - $n$  junction? It turns out that the emission spot can be positioned anywhere along the length of the nanotube by simply changing biasing conditions (Figure 4.15a).<sup>88</sup> In other words, the nanotube infrared emitter acts as a voltage-translatable light source on a single carbon nanotube. There is no equivalent for this in three dimensions. The factors that make this flexibility possible in an ambipolar CN-FET are the Schottky barrier contacts that allow electron and hole injection from opposite electrodes into the undoped nanotube, and the presence of a back gate in close proximity to the carbon nanotube along its whole length.



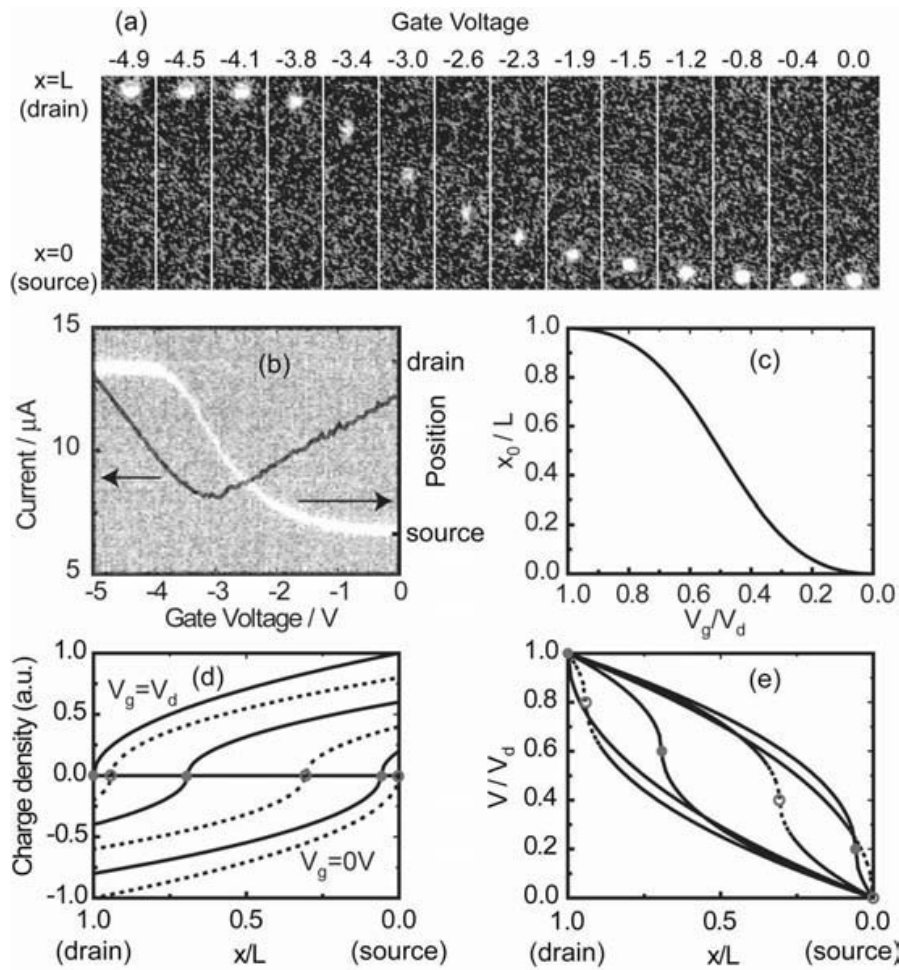


**Figure 4.15** Spatially resolved infrared emission in a long-channel CN-FET. (a) Individual frames of a video of the infrared emission during a gate voltage sweep. The nanotube is oriented vertically and the source–drain distance is 50 μm. The drain voltage is –15 V. (b) Gate voltage characteristics for the nanotube in (a) (left axis) and corresponding movement of the spot (right axis). (c) Modeling of the spot movement as a function of gate voltage (scaled by the drain voltage). (d) Charge density along the length of the tube for gate voltages  $V_g = 1.0V_d, 0.8V_d, 0.6V_d, 0.4V_d, 0.2V_d, 0$  V (top to bottom). (e) Potential (scaled by  $V_d$ ) along the length of the tube for the same set of gate voltages.

In the long-channel limit, where the channel length is much larger than both the carrier mean free path and the oxide thickness, conduction through the carbon nanotube can be treated classically in a drift model.<sup>34</sup> A charge gradient builds up along the nanotube and the current is sustained by the associated local electric field, rather than the externally applied field. (The source and drain fields are screened effectively by the back gate and the applied bias simply sets the boundary conditions for the conduction.)

$$I = -m \cdot \eta(x) \frac{dV(x)}{dx} \quad (4.7)$$

$m$  is the mobility,  $\eta(x) = \eta_e(x) + \eta_h(x)$  is the number density (the sum of electron and hole densities), and  $V(x)$  is the potential in the tube at position  $x$ . The back gate couples capacitively to the carbon nanotube, so

$$V(x) = V_g + C^{-1} \rho(x) \quad (4.8)$$

$C$  is the geometric capacitance of the carbon nanotube and  $\rho(x) = \eta_h(x) - \eta_e(x)$  is the charge density.

In the center of the recombination spot, electron and hole densities are the same, so  $\rho(x) = 0$ , which means that the potential at that spot is given by the gate potential (Equation 4.8). From this it is already clear that a change in gate voltage will move the recombination region to a different spot. Since electrons and holes annihilate in the recombination region, the number density of carriers is small there. Current continuity along the whole length of the tube requires the remaining charges to move faster. Therefore, a large electric field develops at the recombination spot, which explains the broad emission spectrum from hot carrier recombination that is observed when high currents are forced through the tube.<sup>81</sup>

To model the spot movement in ultra-long-channel CN-FETs,<sup>34</sup> the electron-hole recombination length can be neglected. The effect of Schottky barriers is also greatly reduced because the channel resistance becomes comparable or larger than the resistance of the contact barriers. Assuming open contacts, one expects that the spot moves between source and drain for gate voltages between  $0V < V_g < V_d$ . The effect of a voltage drop  $V_C$  at the contacts is analogous to a threshold voltage and mainly limits the range over which the spot moves to  $V_C < V_g < (V_d - V_C)$ . For example, in Figure 4.15a the spot moves from drain to source during a 3-V change in gate voltage. The applied drain voltage is  $-15$  V, so the voltage drop at the contacts is around  $V_C = 6$  V, consistent with typical Schottky barrier threshold voltages for devices with thick gate oxides around 100 nm.<sup>18,19</sup> Figure 4.15c shows the model's prediction for the movement of the spot. The spot is expected to move faster in the middle of the device than at the contacts, which is exactly what is observed in the experiment (Figure 4.15b, right axis).

For the current, the model predicts a quadratic dependence on gate voltage, which is reasonably well reproduced in Figure 4.15b (left axis). In the electron conduction regime to the right of the current minimum, one finds that the increase is less than predicted. This is mainly due to trapping and de-trapping of electrons in the gate oxide and at oxide surface states. These charges act like an additional negative gate voltage and lead to a hysteresis.<sup>35,89,90</sup> The higher noise in the data in this regime is probably also associated with electron trapping and de-trapping. Figure 4.15d shows the calculated square root dependence for the charge density, and Figure 4.15e the potential along the carbon nanotube. The circles in (d) and (e) mark the recombination spot. When the spot moves, most of the voltage drop in the device moves along.

#### 4.2.10 Photodetectors

In addition to emitting infrared light, carbon nanotubes have also proven to be very photosensitive.<sup>91–94</sup> When illuminated with UV light, a slow response on the order of seconds is observed.<sup>92</sup> Recovery to the original current level happens in air within several minutes, but in vacuum the change is permanent. Originally *p*-type devices become ambipolar or *n*-type, similar to when the devices are heated up in vacuum. Photodesorption of molecular oxygen, which is responsible for the *p*-type character of CN-FETs in air, is the main reason for photosensitivity in the UV spectral range.

In contrast to UV light, the effect of infrared illumination on adsorbed oxygen is negligible, and intrinsic effects to the carbon nanotube can be studied. In the previously discussed carbon nanotube infrared emitter, electrons and holes were electrically injected into a carbon nanotube and allowed to recombine radiatively. In photoconductivity, on the other hand, incident infrared light excites an electron from the nanotube valence band into the conduction band, and the photogenerated electron as well as the hole left back in the valence band are collected at the source and drain contacts.<sup>94</sup> Photoconductivity thus relies on two contributions that are equally important: (1) the absorption of the photon by the carbon nanotube and (2) the effective separation of the photogenerated electron–hole pair in an internal or externally applied electric field.

Figure 4.16a shows the gate voltage characteristic of an ambipolar CN-FET without and with infrared laser illumination.\* There is an overall shift in the gate voltage characteristic due to a photovoltage generated at the interface between the silicon back gate and the dielectric SiO<sub>2</sub>, an effect unrelated to the properties of the carbon nanotube.<sup>94</sup> The increase in OFF current that is observed under infrared (IR) illumination, however, is intrinsic to the carbon nanotube. This is shown in Figure 4.16b and c, where the dependence on the incident IR polarization angle and wavelength is depicted. Maximal photocurrent is observed at linear polarization along the axis of the carbon nanotube and at a wavelength that corresponds to one of the one-dimensional van Hove singularities in the nanotube density of states. Under these conditions, absorption of the light by the carbon nanotube is expected to be maximized. The CN-FET thus acts as a wavelength- and polarization-sensitive photodetector.

The widths of the photoconductivity peaks are on the order of 100 meV, which is slightly higher than what is observed in fluorescence excitation spectra. Some broadening might be due to the presence of the metal electrodes, inhomogeneous electric fields in the CN-FET, or lifetime broadening. The photocurrent is found to depend linearly on both the photon flux and the bias voltage.<sup>94</sup> The absence of saturation suggests that not all of the

\* Note that in contrast to electroluminescence, photoconductivity does not necessarily require ambipolar devices because the carriers are generated in the nanotube and there is no barrier for them at the contacts, neither in ambipolar nor in unipolar devices. In fact, unipolar devices might be of advantage because the dark current can be kept smaller in the transistor OFF state.

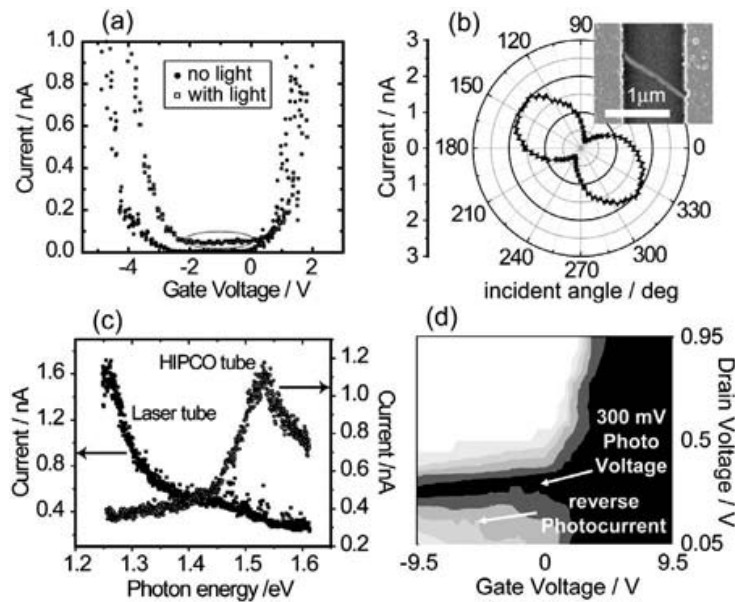


**Figure 4.16** Photoconductivity in CN-FETs. (Data taken from several different devices.) (a) Ambipolar CN-FET with and without IR laser illumination. In the marked range between  $-2$  and  $0$  V, the current is dominated by photogenerated electron–hole pairs that are collected by an applied drain voltage ( $-0.5$  V). (b) Dependence of the photocurrent on the incident polarization. (c) Dependence of the photocurrent on the incident photon energy for  $\sim 1.3$ -nm-diameter (laser) and  $1.1$ -nm-diameter (high-pressure carbon monoxide, or HiPco) tubes. (d) Photovoltage in a CN-FET. Color scale (black to white):  $0$  to  $>100$  pA.

photogenerated carriers can be separated by the applied electric field before they recombine again. The absence of photobleaching even at the highest photon flux is expected for excitation near the  $E_{22}$  transition, given the rapid (subpicosecond) relaxation of carriers to the bottom of the conduction band and top of the valence band, respectively.<sup>95</sup>

The absorption cross section can be estimated in a model that treats the carbon nanotube as a dielectric cylinder.<sup>94</sup> For an incident power density of  $1 \text{ kW/cm}^2$ , one finds an absorbed power on the order of  $1 \text{ nW}$ . This means that about 1 of 10 photons incident on the geometric area of the carbon nanotube is absorbed. Comparing the photocurrent with the number of absorbed photons, one finds a collection efficiency of photogenerated electron–hole pairs of  $\eta \sim 10\%$ .<sup>94</sup>

In the previous examples, an applied bias voltage provided the electric field that separates the photogenerated electron–hole pairs. In a Schottky barrier transistor there are also internal fields associated with the band bending near the contacts in which carriers are separated. In the case of a symmetric device, however, the two Schottky barriers counteract because their fields are directed opposite of each other. When the light is focused to a spot smaller than the nanotube channel length and only one Schottky barrier is illuminated at a time, this limitation is overcome and a measurable photocurrent is generated even without applied bias.<sup>96</sup>



In the case of two dissimilar Schottky barriers, collection of electrons at one contact and holes at the other can be favored and the device acts as a photovoltaic cell.<sup>94</sup> Figure 4.16d shows a three-dimensional plot of the gate and drain voltage characteristics of such a device, where the current is color coded. At low drain voltage the photocurrent flows in the reverse direction, and around 300 mV the drain voltage is just sufficient to cancel the photovoltage that is generated in the tube. In the device in Figure 4.16d, the inhomogeneous character was accidental, but it should be possible to fabricate CN-FETs with two dissimilar contact metals or convert only one contact *n*-type by removing the oxygen at that contact selectively. Another interesting device is a *p-n* junction that can be fabricated by using a split gate that dopes half of the channel of a CN-FET *p*-type and the other *n*-type.<sup>97</sup> Most of the internal field then drops between the *n*- and *p*-type segments in the middle of the device, rather than at the contacts, which might increase the efficiency. An overall limit for the photovoltage is given by the band gap of the material used, which means that a photovoltage of 1 V might be achievable with a single carbon nanotube.

### 4.3 Outlook and challenges

During the last few years there has been significant progress in understanding conduction through carbon nanotube electronic devices, and this understanding has directly translated into the fabrication of significantly improved CN-FETs. Many of the performance parameters of these CN-FETs are now better than projections for scaled silicon MOSFETs. In addition, there have been first steps toward integration of CN-FETs into logic circuits. That said, there are large challenges to overcome for carbon nanotubes if they should eventually pose a threat to silicon: self-assembly of tubes into large-scale arrays is not yet realized; chirality control will be necessary because the nanotube band gap depends on chirality; and a killer application for carbon nanotubes in an electronic device that does not require large-scale integration is required to get enough research going.

The first obstacle is shared by most bottom-up approaches that rely on some kind of self-assembly of small particles over large areas. It is very difficult to make defect-free patterns over large scales this way. The top-down approach used so far by the semiconductor industry has proven amazingly robust with photolithography and pattern transfer methods into silicon, achieving extremely high yields of working devices. There has been some initial success in growing carbon nanotubes by CVD from prepatterned catalyst islands in defined directions<sup>98,99</sup> and in assembling carbon nanotubes on functionalized surfaces,<sup>100,101</sup> but both methods will need to improve their reliability and yield tremendously.

The problem of chirality control is specific to carbon nanotubes because they derive their structure from graphene, a zero-gap semiconductor. This leads to metallic and semiconducting tubes, which is great for research, but can be a showstopper for applications where either one or the other is



required. Until now, there is insufficient specificity in the nanotube diameter, let alone chirality that is grown in any of the available growth processes. In the case of CN-FETs, it might be feasible to employ semiconducting nanotubes with slightly different band gaps in one transistor technology, but it is certainly not tolerable to include metallic carbon nanotubes. Selective burning of metallic tubes in bundles<sup>102</sup> cannot seriously be considered as a solution to the problem, because scaled-down devices will require single tubes or arrays of tubes separated by at least one diameter from each other to achieve good electrostatic coupling of the gate to all tubes. Rather than growing the desired nanotube chirality exclusively, one could try to separate or enrich certain nanotubes after growth. Encouraging progress has been made recently in this area by selectively functionalizing metallic nanotubes with diazonium reagents,<sup>103</sup> and by the chirality-dependent enrichment of DNA-wrapped tubes,<sup>104</sup> and at least for small-diameter nanotubes deposited from solution, a good chirality control might be achievable in the future.

The lack of a killer application so far for carbon nanotube electronics is arguably the most serious issue. Being just slightly better than a well-established technology is simply not enough to warrant the enormous R&D spending associated with bringing a completely novel technology to market. There has to be some compelling reason for a company or industry to embark with full might on this journey. Usually this means a much better performance than could previously be achieved, or a totally new application, which happened, for example, when the early transistor found its killer application as a hearing aid and only later replaced the vacuum tube in computers.

Perhaps carbon nanotubes will first be used in rather low-tech ways to enhance conductive properties of composites. The areas where they could really shine are certainly the ones that require the tiny channels or extreme aspect ratios that carbon nanotubes naturally provide. Maybe their ballistic transport can make ultra-high-frequency applications possible. It will be fascinating to see which application will eventually emerge. The field of carbon nanotube electronics has provided many surprises in the past, and it will continue doing so for the foreseeable future.

## References

1. R.F. Peierl, *Quantum Theory of Solids*, Clarendon, Oxford, p. 108 (1955).
2. R. Landauer, *IBM J. Res. Dev.* 1, 223 (1957); R. Landauer, *IBM J. Res. Dev.* 32, 306 (1988); D.S. Fisher and P.A. Lee, *Phys. Rev. B* 23, 6851 (1981); M. Büttiker, Y. Imry, R. Landauer, and S. Pinhas, *Phys. Rev. B* 31, 6207 (1985); M. Büttiker, *Phys. Rev. Lett.* 57, 1761 (1986); Y. Imry, *Physics of mesoscopic systems*, in *Directions in Condensed Matter Physics*, edited by G. Grinstein and G. Mazenko, World Scientific Press, Singapore (1986); M. Büttiker, *IBM J. Res. Dev.* 32, 317 (1988); R. Landauer, *Physica Scripta* T42, 110 (1992).
3. S. Datta, *Electronic Transport in Mesoscopic Systems*, Cambridge University Press, Cambridge, U.K. (1995).
4. R. Saito, G. Dresselhaus, and M.S. Dresselhaus, *Physical Properties of Carbon Nanotubes*, Imperial College Press, London (1998).

5. Z. Yao, C.L. Kane, and C. Dekker, *Phys. Rev. Lett.* 84, 2941 (2000).
6. S.J. Tans, M.H. Devoret, H. Dai, A. Thess, R.E. Smalley, L.J. Geerlings, and C. Dekker, *Nature* 386, 474 (1997).
7. A. Javey, J. Guo, Q. Wang, M. Lundstrom, and H. Dai, *Nature* 424, 654 (2003).
8. D. Mann, A. Javey, J. Kong, et al., *Nano Lett.* 3, 1541 (2003).
9. J.Y. Park, S. Rosenblatt, Y. Yaish, et al., *Nano Lett.* 4, 517 (2004).
10. M. Freitag, Local Electronic Functionality in Carbon Nanotube Devices, thesis, University of Pennsylvania, Philadelphia (2002).
11. C.L. Kane, E.J. Mele, R.S. Lee, et al., *Europhys. Lett.* 41, 683 (1998).
12. L.M. Woods and G.D. Mahan, *Phys. Rev. B* 61, 10651 (2000).
13. M. Bockrath, W. Liang, D. Bozovic, et al., *Science* 291, 283 (2001).
14. V.H. Crespi, M.L. Cohen, and A. Rubio, *Phys. Rev. Lett.* 79, 2093 (1997).
15. A. Javey, J. Guo, M. Paulsson, et al., *Phys. Rev. Lett.* 92, 106804 (2004).
16. W. Shockley and G.L. Pearson, *Phys. Rev.* 74, 232 (1948).
17. D. Hahng and M.M. Atalla, Silicon-Silicon Dioxide Field Induced Surface Devices, IRE Solid-State Device Research Conference, Carnegie Institute of Technology, Pittsburgh, PA (1960).
18. S.J. Tans, A.R.M. Verschueren, and C. Dekker, *Nature* 393, 49 (1998).
19. R. Martel, T. Schmidt, H.R. Shea, et al., *Appl. Phys. Lett.* 73, 2447 (1998).
20. S.M. Sze, *Physics of Semiconductor Devices*, 2nd ed., Wiley, New York (1981).
21. Y. Taur and T.H. Ning, *Fundamentals of Modern VLSI Devices*, Cambridge University Press, Cambridge, U.K. (1998).
22. R.S. Muller and T.I. Kamins, *Device Electronics for Integrated Circuits*, 2nd ed., Wiley, New York (1986).
23. E.H. Nicollian and J.R. Brews, *MOS (Metal Oxide Semiconductor) Physics and Technology*, Wiley, New York (1982).
24. A. Thess, R. Lee, P. Nikolaev, et al., *Science* 273, 483 (1996).
25. R. Martel, V. Derycke, C. Lavoie, et al., *Phys. Rev. Lett.* 87, 256805 (2001).
26. A. Bachtold, P. Hadley, T. Nakanishi, and C. Dekker, *Science* 294, 1317 (2001).
27. J. Appenzeller, J. Knoch, V. Derycke, et al., *Phys. Rev. Lett.* 89, 126801 (2002).
28. A. Javey, H. Kim, M. Brink, et al., *Nat. Mat.* 1, 241 (2002).
29. B.M. Kim, T. Brintlinger, E. Cobas, M.S. Fuhrer, et al., *Appl. Phys. Lett.* 84, 1946 (2004).
30. S. Maruyama, R. Kojima, Y. Miyauchi, et al., *Chem. Phys. Lett.* 360, 229 (2002).
31. Y. Li, D. Mann, M. Rolandi, et al., *Nano Lett.* 4, 317 (2004).
32. N.R. Franklin, Q. Wang, T.W. Tombler, et al., *Appl. Phys. Lett.* 81, 913 (2002).
33. J. Cao, Q. Wang, D. Wang, and H. Dai, *Small* 1, 138 (2005).
34. J. Tersoff, M. Freitag, J.C. Tsang, and Ph. Avouris, cond-mat/0411537 (2004).
35. M.S. Fuhrer, B.M. Kim, T. Dürkop, and T. Brintlinger, *Nano Lett.* 2, 755 (2002).
36. T. Dürkop, S.A. Getty, E. Cobas, and M.S. Fuhrer, *Nano Lett.* 4, 35 (2004).
37. F. Leonard and J. Tersoff, *Phys. Rev. Lett.* 83, 5174 (1999).
38. F. Leonard and J. Tersoff, *Phys. Rev. Lett.* 84, 4693 (2000).
39. A.A. Odintsov, *Phys. Rev. Lett.* 85, 150 (2000).
40. S. Heinze, J. Tersoff, R. Martel, et al., *Phys. Rev. Lett.* 89, 106801 (2002).
41. T. Nakanishi, A. Bachtold, and C. Dekker, *Phys. Rev. B* 66, 073307 (2002),
42. G.D.J. Smit, S. Rogge, and T.M. Klapwijk, *Appl. Phys. Lett.* 81, 3852 (2002).
43. M.S. Fuhrer, J. Nygard, L. Shih, et al., *Science* 288, 494 (2000).
44. M. Freitag, M. Radosavljevic, Y. Zhou, et al., *Appl. Phys. Lett.* 79, 3326 (2001).
45. V. Derycke, R. Martel, J. Appenzeller, and Ph. Avouris, *Appl. Phys. Lett.* 80, 2773 (2002).

46. N.D. Lang and Ph. Avouris, *Phys. Rev. B* 64, 125323 (2001).
47. K.W. Hipps, *Science* 294, 536 (2001).
48. J. Bardeen, *Phys. Rev.* 71, 717 (1947).
49. V. Heine, *Phys. Rev.* 138, 1689 (1965).
50. P.G. Collins, K. Bradley, M. Ishigami, and A. Zettl, *Science* 287, 1801 (2000).
51. X. Cui, M. Freitag, R. Martel, L. Brus, and Ph. Avouris, *Nano Lett.* 3, 783 (2003).
52. M. Freitag, A.T. Johnson, S.V. Kalinin, and D.A. Bonnell, *Phys. Rev. Lett.* 89, 216801 (2002).
53. M. Freitag, unpublished results.
54. M.P. Anantram, *Phys. Rev. B* 62, R4837 (2000).
55. M. Radosavljevic, S. Heinze, J. Tersoff, and Ph. Avouris, *Appl. Phys. Lett.* 83, 2435 (2003).
56. D.L. John, L.C. Castro, J. Clifford, and D.L. Pulfrey, *IEEE Trans. Nano.* 2, 175 (2003).
57. S. Heinze, J. Tersoff, and Ph. Avouris, *Appl. Phys. Lett.* 83, 5038 (2003).
58. S. Heinze, M. Radosavljevic, J. Tersoff, and Ph. Avouris, *Phys. Rev. B* 68, 235418 (2003).
59. Y.M. Lin, J. Appenzeller, and Ph. Avouris, *Nano Lett.* 4, 947 (2004).
60. S.J. Wind, J. Appenzeller, and Ph. Avouris, *Phys. Rev. Lett.* 91, 058301 (2003).
61. J. Guo, A. Javey, H. Dai, S. Datta, and M. Lundstrom, *cond-mat/0309039* (2003).
62. A. Javey, J. Guo, D.B. Farmer, et al., *Nano Lett.* 4, 447 (2004).
63. Y.M. Lin, J. Appenzeller, and Ph. Avouris, *IEEE DRC Dig.* 62, 133 (2004).
64. J. Chen, C. Klinke, A. Afzali, et al., *IEDM Technol. Digest* 695 (2004).
65. P. Horowitz and W. Hill, *The Art of Electronics*, Cambridge University Press, Cambridge, U.K. (1980).
66. M. Terrones, S. Jorio, M. Endo, et al., *New Direction in Nanotube Science, Materials Today* 7, 30 (2004).
67. J. Kong, C. Zhou, E. Yenilmez, and H. Dai, *Appl. Phys. Lett.* 77, 3977 (2000).
68. B.W. Smith, M. Monthieux, and D.E. Luzzi, *Nature* 396, 323 (1998).
69. D.J. Hornbaker, S.J. Kahng, S. Misra, et al., *Science* 295, 828 (2002).
70. M. Radosavljevic, J. Appenzeller, Ph. Avouris, and J. Knoch, *Appl. Phys. Lett.* 84, 3693 (2004).
71. K. Bradley, J.C.P. Gabriel, M. Briman, et al. *Phys. Rev. Lett.* 91, 218301 (2003).
72. M. Shim, A. Javey, N.W.S. Kam, and H. Dai, *J. Am. Chem. Soc.* 123, 11512 (2001).
73. J. Chen, C. Klinke, A. Afzali, and Ph. Avouris, *IEEE DRC Dig.* 62, 137 (2004).
74. C. Klinke, J. Chen, A. Afzali, and Ph. Avouris, *Nano Lett.* 5, 555 (2005).
75. S. Peng, K. Cho, P. Qi, and H. Dai, *Chem. Phys. Lett.* 387, 271 (2004).
76. S.J. Wind, J. Appenzeller, R. Martel, et al., *Appl. Phys. Lett.* 80, 3817 (2002).
77. V. Derycke, R. Martel, J. Appenzeller, and Ph. Avouris, *Nano Lett.* 1, 453 (2001).
78. A. Javey, Q. Wang, A. Ural, Y. Li, and H. Dai, *Nano Lett.* 2, 929 (2002).
79. D.J. Frank and J. Appenzeller, *IEEE Electr. Dev. Lett.* 25, 34 (2004).
80. J.A. Misewich, R. Martel, Ph. Avouris, et al., *Science* 300, 783 (2003).
81. M. Freitag, V. Perebeinos, J. Chen, et al., *Nano Lett.* 4, 1063 (2004).
82. V. Perebeinos, J. Tersoff, and Ph. Avouris, *cond-mat* 0411021 (2004).
83. S.M. Bachilo, M.S. Strano, C. Kittrell, et al., *Science* 298, 2361 (2002).
84. S. Lebedkin, F. Hennrich, T. Skipa, and M.M. Kappes, *J. Phys. Chem. B* 107, 1949 (2003).
85. J. Lefebvre, Y. Homma, and P. Finnie, *Phys. Rev. Lett.* 90, 217401 (2003).
86. V. Perebeinos, J. Tersoff, and Ph. Avouris, *Phys. Rev. Lett.* 92, 257402 (2004).

87. H. Zhao and S. Mazumdar, *Phys. Rev. Lett.* 93, 157402 (2004).
88. M. Freitag, J. Chen, J. Tersoff, et al., *Phys. Rev. Lett.* 93, 076803 (2004).
89. M. Radosavljevic, M. Freitag, K.V. Thadani, and A.T. Johnson, *Nano Lett.* 2, 761 (2002).
90. W. Kim, A. Javey, O. Vermesh, et al., *Nano Lett.* 3, 193 (2003).
91. R.J. Chen, N.R. Franklin, J. Kong, et al., *Appl. Phys. Lett.* 79, 2258 (2001).
92. A. Fujiwara, Y. Matsuoka, H. Suematsu, et al., *Jpn. J. Appl. Phys.* 40, L1229 (2001).
93. Y. Kamada, N. Naka, N. Nagasawa, et al., *Physica B* 323, 239 (2002).
94. M. Freitag, Y. Martin, J.A. Misewich, et al., *Nano Lett.* 3, 1067 (2003).
95. G.N. Ostojic, S. Zaric, J. Kono, et al., *Phys. Rev. Lett.* 92, 117402 (2004).
96. K. Balasubramanian, Y. Fan, M. Burghard, et al., *Appl. Phys. Lett.* 84, 2400 (2004).
97. J.U. Lee, P.P. Gipp, and C.M. Heller, *Appl. Phys. Lett.* 85, 145 (2004).
98. E. Joselevich and C.M. Lieber, *Nano Lett.* 2, 1137 (2002).
99. S. Huang, X. Cai, and J. Liu, *J. Am. Chem. Soc.* 125, 5636 (2003).
100. E. Valentin, S. Auvray, J. Goethals, et al., *Microelectron Eng.* 61/62, 491 (2002).
101. S. Auvray, Thesis, Universite de Paris Sud UFR Scientifique d'Orsay (2004).
102. P.G. Collins, M.S. Arnold, and Ph. Avouris, *Science* 292, 706 (2001).
103. M.S. Strano, C.A. Dyke, M.L. Usrey, et al., *Science* 301, 1519 (2003).
104. M. Zheng, A. Jagota, M.S. Strano, et al., *Science* 302, 1545 (2003).

## chapter five

---

# Magnetic properties

*Junichiro Kono*

*Rice University*

*Stephan Roche*

*Commissariat à l'Énergie Atomique*

### Contents

5.1	Introduction .....	119
5.2	Theoretical perspectives.....	120
5.2.1	Band structure in magnetic fields .....	120
5.2.1.1	Parallel field: the Aharonov–Bohm effect.....	122
5.2.1.2	Perpendicular field: Landau quantization .....	125
5.2.2	Magnetic susceptibilities .....	126
5.2.3	Magnetotransport phenomena.....	129
5.2.3.1	Fermi's golden rule and mean free path.....	129
5.2.3.2	Aharonov–Bohm phenomena: ballistic vs. diffusive regimes .....	131
5.2.3.3	Persistent currents .....	133
5.3	Experimental results.....	138
5.3.1	Magnetization .....	138
5.3.2	Magneto-optics .....	140
5.3.3	Magnetotransport.....	144
	Acknowledgments .....	147
	References.....	147

## 5.1 Introduction

One of the unique properties of carbon nanotubes is that their metallicity can be controlled by an external magnetic field applied parallel to the tube axis. Namely, a carbon nanotube can be either semiconducting or metallic,



depending on the strength of the applied field, and its band gap is predicted to be an oscillatory function of magnetic field with period  $\phi_0 = h/e$ , i.e., the magnetic flux quantum.<sup>1–9</sup> Thus, metallic tubes can be made semiconducting by applying a (even infinitesimally small) magnetic field parallel to the tube axis, and semiconducting tubes can become metallic in ultrahigh magnetic fields. These exotic magnetic effects are related to the modulation of the electronic wavefunction along the tube circumference by the Aharonov–Bohm phase.<sup>10</sup>

Some of the predictions have been directly verified by a recent interband optical study on single-walled carbon nanotubes (SWNTs).<sup>11</sup> In addition, signatures of novel phenomena, lacking background in conventional theories of mesoscopic transport, seem to have been clearly evidenced in a number of recent magnetotransport studies on carbon nanotubes.<sup>12–19</sup> Indeed, while some studies on large-diameter multiwalled carbon nanotubes (MWNTs) have revealed some signatures of weak localization, with negative magnetoresistance and  $\phi_0/2$  periodic Aharonov–Bohm oscillations, other studies have given more importance to the field-modulated band structure effects, assuming a negligible contribution from the quantum interference effects. The possibility of superimposed contributions to the Aharonov–Bohm effect of both band structure and transport phenomena has created a rich and challenging research subject.

In this chapter, we review theoretical and experimental studies on the magnetic properties of carbon nanotubes, including both SWNTs and MWNTs. We first discuss the main effects of an external magnetic field on the electronic properties of carbon nanotubes, with the main focus on how the Aharonov–Bohm phase alters the electronic band structure, density of states, magnetic susceptibility, persistent currents, and magnetotransport properties of carbon nanotubes. A discussion about transport length scales will further elucidate the regimes in which quantum interference effects also affect the transport properties. In the second part, we will describe experimental studies on carbon nanotubes in magnetic fields. In particular, the recent magneto-optical and magnetotransport measurements that have challenged the theoretical predictions will be detailed.

## 5.2 Theoretical perspectives

### 5.2.1 Band structure in magnetic fields

The electronic spectrum of metallic or semiconducting carbon nanotubes is characterized by a set of van Hove singularities (VHSs) that reflects the quantized momentum component along the circumferential direction. Their precise locations can be analytically derived from the dispersion relations. As an illustration, if we consider armchair metallic tubes with chirality  $(N,N)$  and restrict ourselves to the  $\pi$  and  $\pi^*$  bands, the dispersions are given by

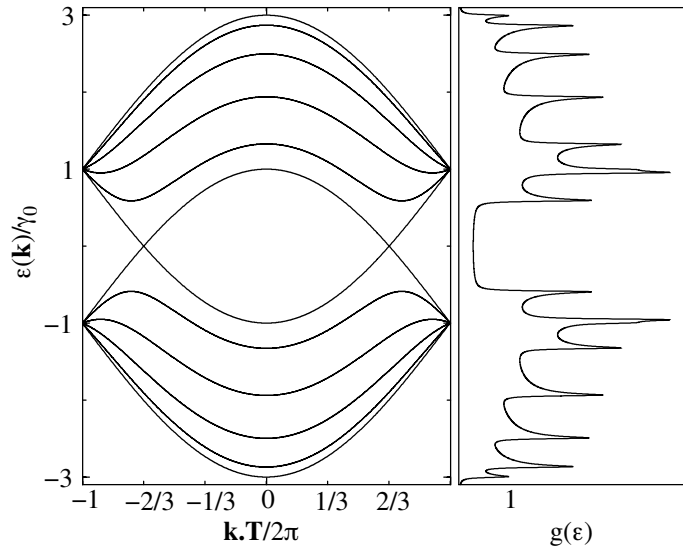


Figure 5.1 Dispersion relations and density of states for the (5, 5) metallic nanotube.

$$E_q^\pm(k) = \pm \gamma_0 \sqrt{1 \pm 4 \cos \frac{ka}{2} \cos \frac{q\pi}{N} + 4 \cos^2 \frac{ka}{2}}, \quad (5.1)$$

where  $q(= 1, 2, \dots, 2N)$  specifies the discrete part of the wavevector perpendicular to the tube axis (i.e., the band index), while  $k$  is the continuous component that describes eigenstates in a given subband ( $-\pi < ka < \pi$ );  $a = 2.46 \text{ \AA}$  and  $\gamma_0 \sim 2.7 \text{ eV}$ . The dispersion relations of the (5, 5) tube and the (10, 0) zigzag tube are shown in Figure 5.1 and Figure 5.2, respectively, together with the corresponding densities of states (DoSs),  $g(\epsilon)$ . The VHS positions are derived from the condition  $\partial E_q(k)/\partial k = 0$ , which, for the armchair tubes, yields  $\epsilon_q = \pm \gamma_0 \sin(q\pi/N)$ .

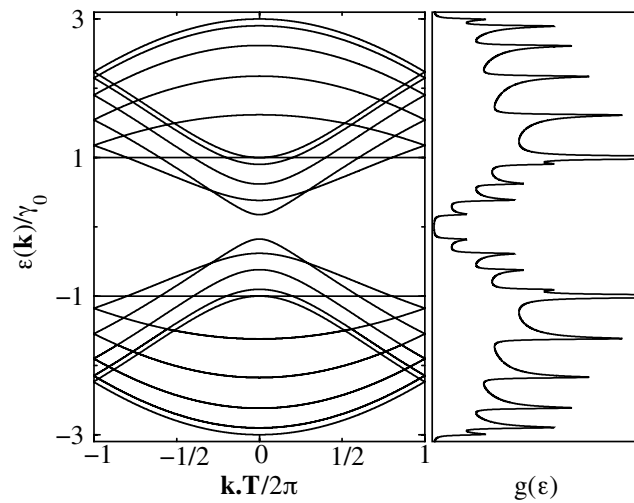


Figure 5.2 Dispersion relations and density of states for the (10, 0) semiconducting nanotube.

### 5.2.1.1 Parallel field: the Aharonov–Bohm effect

Given the specific electronic structure of a carbon nanotube, it is relatively straightforward to show that the application of an external magnetic field modifies the band structure in a truly unique manner. When applied parallel to the tube axis, the magnetic field has a direct impact on the phase of the corresponding electronic wavefunctions, under the Aharonov–Bohm effect. As a consequence, all the VHSs shift either upward or downward in energy, resulting in an apparent VHS splitting. An intriguing consequence is the opening of an energy gap in a metallic tube, which oscillates with magnetic field. A magnetic field can thus transform a metallic system into a semiconducting one and vice versa.<sup>1,5–7</sup>

More precisely, in the presence of a magnetic field, the modifications of wavefunction quantum phases are determined by the vector potential  $\vec{A}$ . Within the basis  $\{ \vec{C}_h / | \vec{C}_h |, \vec{T} / | \vec{T} | \}$  defined by the chiral vector  $\vec{C}_h$  and the unit cell vector  $\vec{T}$  of the nanotube,<sup>20</sup> the vector potential in the Landau gauge reads  $\vec{A} = (\phi / | \vec{C}_h |, 0)$  ( $\phi$  is the magnetic flux through the tube cross section). The phase factor appears in the electronic coupling factors between

site  $\vec{r} = (x, y)$  and  $\vec{r}' = (x', y')$  and can be written as<sup>1,5–7,20</sup>,  $\Delta\varphi_{\vec{r},\vec{r}'} = \int_0^1 (\vec{r}' - \vec{r}) \cdot (\vec{A}(\vec{r} + \lambda[\vec{r}' - \vec{r}]))d\lambda$ , so that  $\Delta\varphi_{\vec{r},\vec{r}'} = i(x - x')\phi / | \vec{C}_h |$ . This yields a new expression for the quantization relation of the corresponding wavevector component  $\vec{\delta}k(\phi) \cdot \vec{\kappa}_\perp = \vec{\delta}k(0) \cdot \vec{\kappa}_\perp + 2\pi\phi / (\phi_0 | \vec{C}_h |)$ , with  $\vec{\kappa}_\perp$ , the unit vector of reciprocal space, associated with  $\vec{C}_h$ . Such modulation in turn will shift the VHS positions, as illustrated in Figure 5.3.

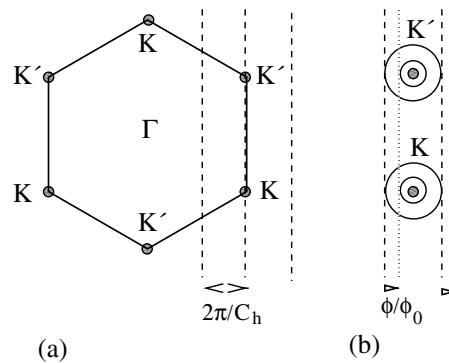


**Figure 5.3** (a) Representation of the first Brillouin zone of a graphene sheet together with allowed states for an armchair tube (dashed lines) at zero flux. (b) Modifications of allowed states in the vicinity of  $\vec{K}$ -points, under the effect of a magnetic field applied parallel to the tube axis (circles give the equipotentials close to the Fermi energy).

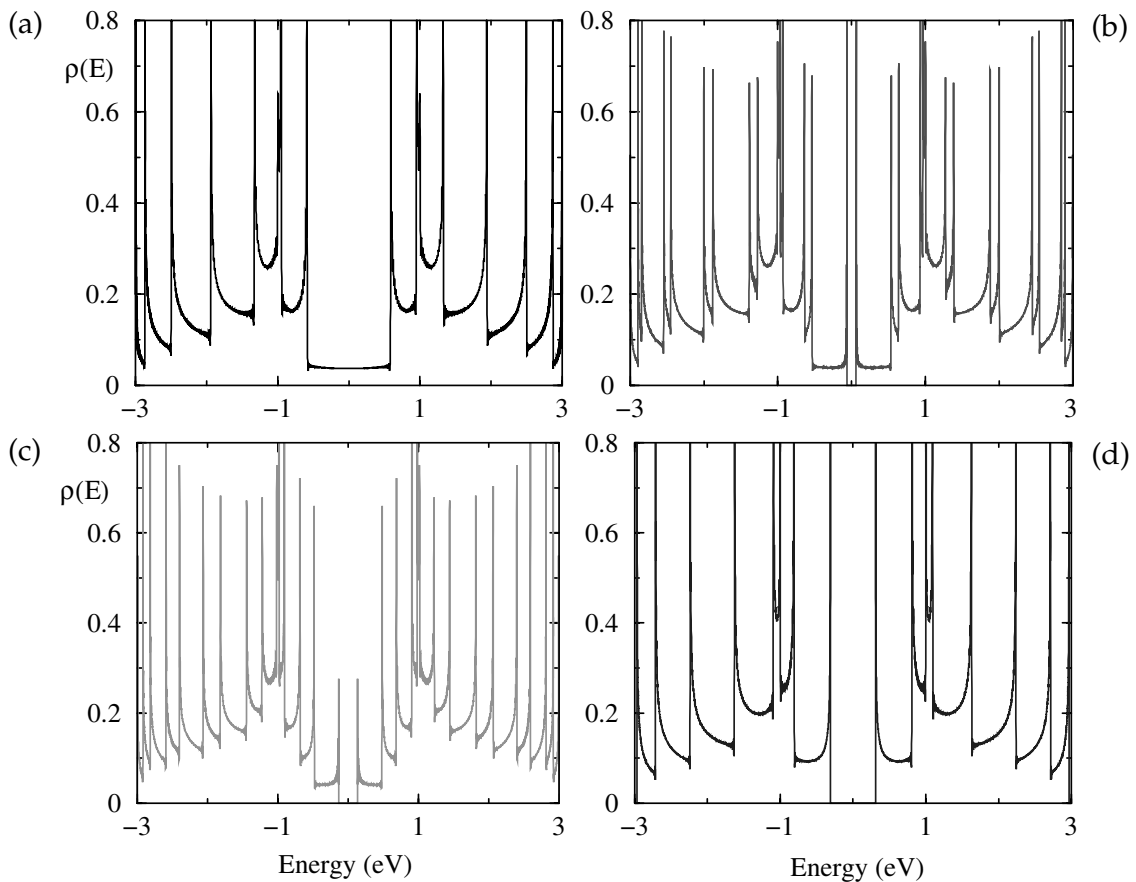


**Figure 5.4** Density of states of the (5, 5) carbon nanotube for several magnetic flux values: (a)  $\phi/\phi_0 = 0$ , (b)  $\phi/\phi_0 = 0.1$ , (c)  $\phi/\phi_0 = 0.2$ , and (d)  $\phi/\phi_0 = 0.5$ . This is a metallic tube at zero magnetic flux, but a gap opens up once a finite flux is applied, and it increases with the flux. The calculations were performed following the algorithm established in Roche.<sup>21</sup>

The magnetic flux thus modulates the band structure in a  $\phi_0$ -periodic fashion, with a band gap opening and closing. Such phenomena are illustrated in the DoS plots for the (5, 5) tube and (10, 10) tube in Figure 5.4 and Figure 5.5, respectively. Note that both tubes are metallic at zero magnetic field, but a band gap opens up once a finite magnetic flux  $\phi$  threads the tube, and the induced band gap increases linearly with  $\phi$ , and reaches a maximum value at half quantum flux. The traces (a) to (e) in Figure 5.5 are the DoSs for the (10, 10) tube at  $\phi/\phi_0 =$  (a) 0, (b) 0.125, (c) 0.25, (d) 0.375, and (e) 0.5. For  $\phi/\phi_0 = 0.125$  (trace (b)), one notices that in the vicinity of the charge neutrality point (i.e.,  $\varepsilon = 0$ ), a new VHS appears, indicating the gap opening. In traces (c) to (e), the gap is seen to increase and reach its maximum value at  $\phi/\phi_0 = 0.5$ . The evolution of VHSs is then reversed and the gap closes again at  $\phi/\phi_0 = 1$ . For VHSs at higher energies (e.g., that located at  $\varepsilon_{q=1}$ ), the oscillatory behavior is slightly more involved: at low fields a splitting is observed for each VHS, which is followed by crossing at higher flux, and finally all the VHSs return to the original positions when  $\phi/\phi_0 = 1$  (see the inset of Figure 5.5).

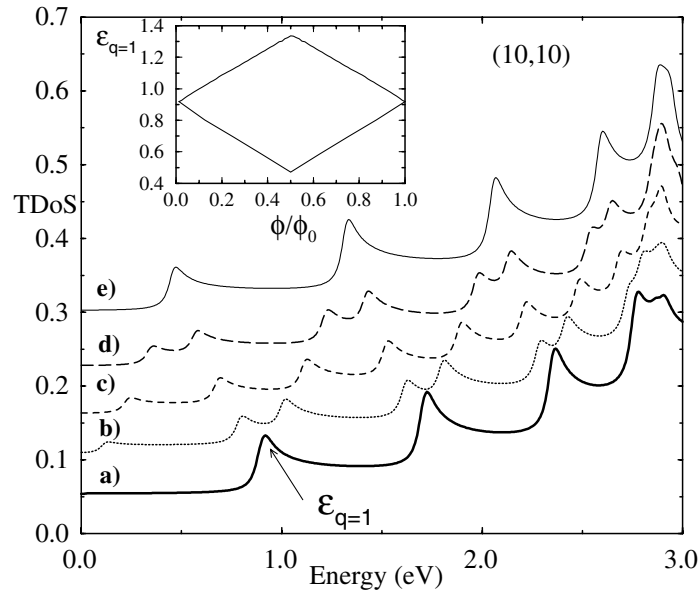


**Figure 5.5** Density of states of the (10, 10) metallic tube as a function of energy for several magnetic flux values (see text). The curves have been vertically offset for clarity. Inset: evolution of one VHS with magnetic flux.

An analytic expression for the gap evolution for  $(n, m)$  tubes with  $n - m = 3M$  ( $M$ : integer) can be derived easily as

$$\Delta_g = \begin{cases} 3\Delta_0 \frac{\phi}{\phi_0} & \text{if } 0 \leq \phi \leq \frac{\phi_0}{2}, \\ 3\Delta_0 \left| 1 - \frac{\phi}{\phi_0} \right| & \text{if } \frac{\phi_0}{2} \leq \phi \leq \phi_0, \end{cases} \quad (5.2)$$

where  $\Delta_0 = 2\pi a_{cc}\gamma_0 / |\bar{C}_h|$  and  $a_{cc} = 1.421 \text{ \AA}$ . Numerically,  $\Delta_g \approx 75 \text{ meV}$  at 50 T for the (22, 22) tube (diameter  $\approx 3 \text{ nm}$ ). The van Hove singularity splitting, which can be investigated by spectroscopic experiments (cf. Section 5.2), can be also derived analytically. For instance, in the case of armchair tubes, the magnitude of the field-dependent splitting of the  $q$ -th VHS is given by

$$\Delta_B(\varepsilon_q, \phi/\phi_0) = 2\gamma_0 \left[ \sin \frac{\pi}{q} \left( \cos \frac{\pi\phi}{q\phi_0} - 1 \right) - \cos \frac{\pi}{q} \sin \frac{\pi\phi}{q\phi_0} \right] \quad (5.3)$$

For instance,  $\Delta_B \approx 40 \text{ meV}$  at 60 T for the (10, 10) tube (diameter = 1.4 nm). In this parallel configuration, let us note that to obtain a field equivalent to  $\phi = \phi_0$  in nanotubes with diameters of 1, 10, 20, and 40 nm, one would need magnetic fields of 5325, 53, 13, and 3 T, respectively.

Semiconducting tubes [i.e.,  $(n, m)$  tubes with  $n - m = 3M \pm 1$  ( $M$ : integer)] are affected in a similar way, but the gap expression is slightly different:



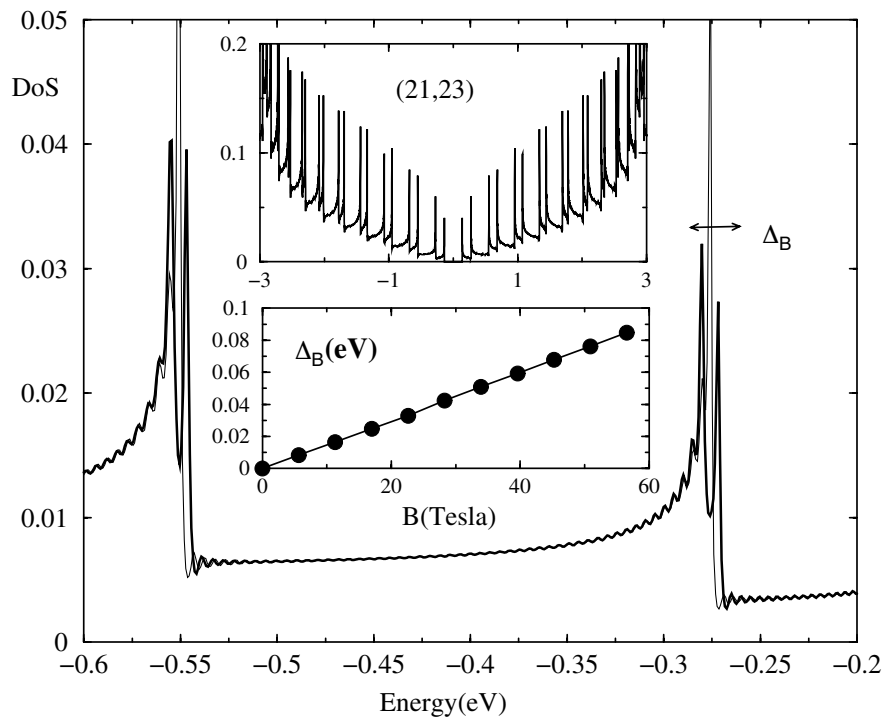


**Figure 5.6** Density of states of the (21, 23) tube at zero and finite flux. Top inset: expanded plot of the DoS. Bottom inset: evolution of the VHS splitting  $\Delta_B$  as a function of magnetic field.

$$\Delta_g = \begin{cases} \Delta_0 \left| 1 - \frac{3\phi}{\phi_0} \right| & \text{if } 0 \leq \phi \leq \frac{\phi_0}{2}, \\ \Delta_0 \left| 2 - \frac{3\phi}{\phi_0} \right| & \text{if } \frac{\phi_0}{2} \leq \phi \leq \phi_0. \end{cases} \quad (5.4)$$

Thus, the energy gap, which is  $\Delta_0$  at zero field, continuously decreases with increasing  $\phi$  and becomes zero at  $\phi = \phi_0/3$ , where the tube is metallic. The gap then changes in an intriguing way as  $\phi$  increases from  $\phi_0/3$ , reaching a local maximum ( $\Delta_0/2$ ) at  $\phi = \phi_0/2$ , becoming zero again at  $\phi = 2\phi_0/3$ , and finally recovering  $\Delta_0$  at  $\phi = \phi_0$ . In Figure 5.6, we show the case of a 3-nm-diameter semiconducting single-walled nanotube.

### 5.2.1.2 Perpendicular field: Landau quantization

The application of a magnetic field perpendicular to the tube axis leads to completely different effects. In this configuration, the zero-field band structure with characteristic one-dimensional VHSs is gradually modified into a Landau-level spectrum as the field increases. The relevant dimensionless parameter that allows us to quantify the appearance of Landau levels is given by  $\nu = |\vec{C}_h| 2\pi\ell_m$ , where  $\ell_m = \sqrt{\pi/eB}$  is the magnetic length (first cyclotron orbit radius). The vector potential  $\vec{A}$  within the Landau gauge is now

given by  $\vec{A} = \left(0, \frac{|\vec{C}_h|B}{2\pi} \sin\left(\frac{2\pi x}{|\vec{C}_h|}\right)\right)$  in the basis  $\{\vec{C}_h/|\vec{C}_h|, \vec{T}/|\vec{T}|\}$ . Seri and

Ando have demonstrated that close to the  $\vec{K}$ -points the electronic eigenstates can be analytically written as<sup>22,23</sup>

$$\Psi_{nsk}(\vec{r}) = \frac{1}{\sqrt{2L_{tube}}} \begin{pmatrix} \pm i s \Psi_{-}(x) \\ \Psi_{+}(x) \end{pmatrix} e^{iky}, \quad (5.5)$$

$$\Psi_{\pm}(x) = \frac{1}{\sqrt{|\vec{C}_h| I_0(2v^2)}} e^{\pm v^2 \cos\left(\frac{2\pi x}{|\vec{C}_h|}\right)}, \quad (5.6)$$

where  $I_0(2v^2)$  is the modified Bessel function of the first kind. One can also find the dispersion relation and the DoS in the vicinity of the Fermi level

(charge neutrality point) as  $E_{q=0}^{\pm} = \pm \gamma_0 |\vec{k}| / I_0(2v^2)$  and  $\rho(E_F) \sim \frac{I_0(2v^2)}{\pi \gamma_0} \sim \frac{e v^2}{\sqrt{4\pi} v^2}$

( $v \gg 1$ ), respectively. As a result, the DoS at the charge neutrality point diverges exponentially with increasing magnetic field. This effect is shown in Figure 5.7 for the (10, 10) tube for several magnetic field strengths. The remaining part of the DoS (VHSs) also progressively degrades as the Landau-level structure starts dominating the spectrum. Given the obvious scaling properties, the larger the tube diameter, the smaller the value of the magnetic field required to form and observe Landau levels.

As soon as  $v = |\vec{C}_h| / 2\pi \ell_m \geq 1$  is satisfied, the DoS spectrum is totally dominated by Landau levels. One finds that for tubes with diameters of 1, 10, 20, and 40 nm, the condition  $v = 1$  corresponds to magnetic field strengths of 2635, 26, 6.6, and 1.6 T, respectively. In each case,  $\ell_m \ll \ell_e$  (or  $w_c \tau_e \gg 1$ ) has to be further satisfied for clear observation of Landau quantization, where  $\ell_e$  is the mean free path,  $w_c = eB/m$  is the cyclotron frequency, and  $\tau_e$  is the scattering time (this condition is easily met at such high magnetic fields in carbon nanotubes since  $\ell_e$  can be as long as 1  $\mu\text{m}$ ). Such Landau-level formation was first reported by Kanda et al.<sup>15</sup>

### 5.2.2 Magnetic susceptibilities

The strong magnetic field dependence of the band structure suggests a large orbital magnetic susceptibility,  $\chi$ . Calculations demonstrate that the orbital component of  $\chi$  is indeed several orders of magnitude larger than the paramagnetic (or Pauli) contribution due to the electron spin.<sup>4,24–27</sup> At zero temperature, the orbital part of  $\chi$  can be computed from the second derivative of the free energy, which is in turn related to the band dispersion, i.e.,

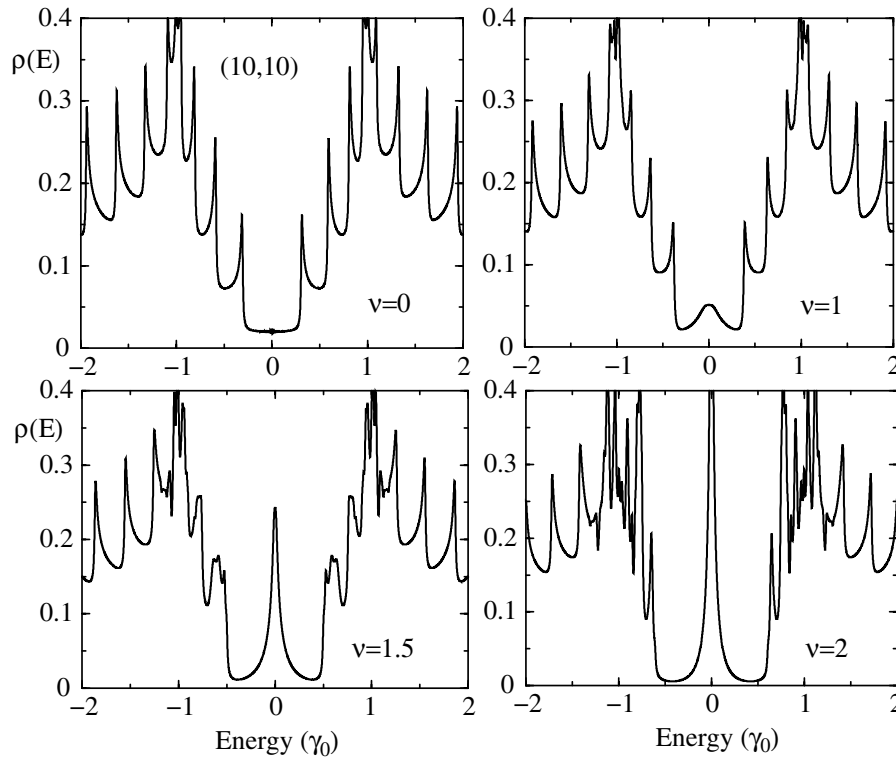


**Figure 5.7** Density of states of the (10, 10) tube in a perpendicular magnetic field for several field strengths. The field strengths are expressed in terms of the dimensionless parameter  $v = |\vec{C}_h| / 2\pi\ell_m$ , where  $\ell_m = \sqrt{\hbar / eB}$  is the magnetic length.

$$\chi = k_B T \frac{\partial^2}{\partial B^2} \sum_{nk} \ln \left[ 1 + \exp \left( - \frac{\varepsilon_n(k, \phi) - \mu}{k_B T} \right) \right] \quad (5.7)$$

Calculations have been performed for isolated single-walled carbon nanotubes<sup>4,24,25</sup> as well as for ensembles (bundles) of nanotubes,<sup>27</sup> in which averaging occurs in conjunction with the effect of intertube coupling on individual signatures.

An interesting aspect concerns the magnetic anisotropy, i.e., the difference between  $\chi_{\parallel}$  and  $\chi_{\perp}$ , which can be computed for magnetic fields parallel or perpendicular to the tube axis (Figure 5.8). It is found theoretically that for undoped metallic tubes (for which the Fermi energy is exactly at the charge neutrality point),  $\chi_{\parallel}$  is positive (paramagnetic), whereas  $\chi_{\perp}$  is negative (diamagnetic);  $\chi_{\parallel}$  rapidly decreases as the Fermi energy deviates from the charge neutrality point, exhibiting logarithmic divergence, while  $\chi_{\perp}$  remains almost constant as a function of Fermi energy near the charge neutrality point (Figure 5.8b and c). For undoped semiconducting tubes, both  $\chi_{\parallel}$  and  $\chi_{\perp}$  are negative (diamagnetic) and  $|\chi_{\perp}| > |\chi_{\parallel}|$  (Figure 5.9). As the Fermi energy is varied in a semiconducting tube, both  $\chi_{\parallel}$  and  $\chi_{\perp}$  remain constant as long as the Fermi energy lies within the band gap; however, square root-like divergence appears in  $\chi_{\parallel}$  when the Fermi energy enters the band

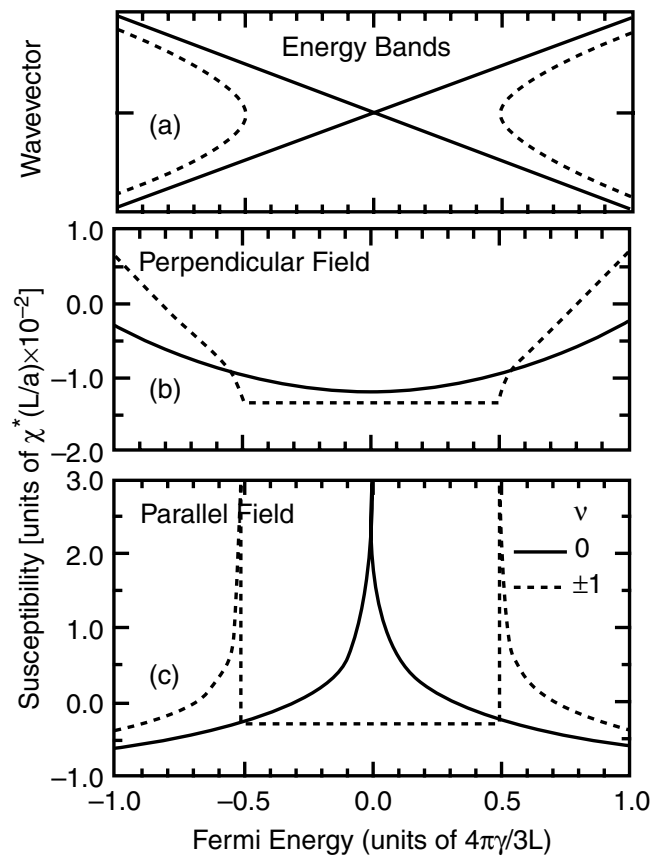


**Figure 5.8** The (a) band structure, (b)  $\chi_{\perp}$ , and (c)  $\chi_{\parallel}$  of metallic (solid lines) and semiconducting (dashed lines) SWNTs calculated by Ajiki and Ando. (Adopted from H. Ajiki and T. Ando, *J. Phys. Soc. Jpn.*, 64, 4382, 1995.)

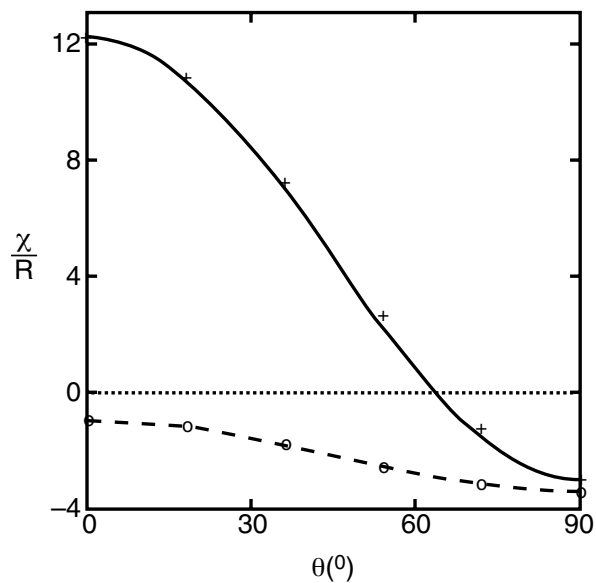


**Figure 5.9** The scaled magnetic susceptibility as a function of the angle between the tube axis and the applied magnetic field for metallic (pluses and dotted line) and semiconducting (open circles and dashed line) SWNTs calculated by Lu.  $R$  is the tube diameter. (Adopted from J. P. Lu, *Phys. Rev. Lett.*, 74, 1123, 1995.)

edges, as shown in Figure 5.8c. In contrast,  $\chi_{\perp}$  does not exhibit any divergence and is diamagnetic around the charge neutrality point region for both metallic and semiconducting tubes. In all cases, the susceptibility increases linearly with the tube radius, which makes it possible to define universal relations for  $\chi_{\perp}$  and  $\chi_{\parallel}$ . With increasing temperature,  $\chi_{\parallel}$  is predicted to decrease (increase) for metallic (semiconducting) tubes, while  $\chi_{\perp}$  is predicted to increase for both metallic and semiconducting nanotubes.<sup>27</sup> Experimental studies of magnetic susceptibilities are discussed in Section 5.3.1.

Recent experiments<sup>16</sup> have demonstrated that states near the energy gap have a magnetic moment much larger than the Bohr magneton — results that confirm that the electronic motion around the tube circumference plays an important role in the magnetic susceptibility.

### 5.2.3 Magnetotransport phenomena

#### 5.2.3.1 Fermi's golden rule and mean free path

Disorder in carbon nanotubes may come from several different origins — chemical impurities, topological defects, Stone–Wales, and vacancies. These lattice imperfections induce departure from ballistic transport, and yet preserve quantum interference effects, which can be profoundly affected by magnetic fields. Unlike strictly one-dimensional systems, disorder effects in nanotubes are strongly energy dependent, as pointed out in early theoretical studies<sup>1,5–7,28–30</sup> and recently confirmed for chemically doped (with boron and nitrogen) nanotubes.<sup>31</sup> A crucial transport length scale is the so-called elastic mean free path  $\ell_e$ , i.e., the free propagation length of coherent wavepackets before a collision occurs on the defect, an event that alters momentum without changing the energy of incident electrons.

Within Fermi's golden rule (FGR), the scattering time  $\tau$  as well as the mean free path  $\ell_e = v_F \tau$  can be analytically derived. FGR writes

$$\frac{1}{2\tau_e(E_F)} = \frac{2\pi}{\hbar} \left| \langle \Psi_{n1}(k_F) | \hat{U} | \Psi_{n2}(-k_F) \rangle \right|^2 \rho(E_F) \times N_c N_{Ring} \quad (5.8)$$

where  $N_c$  and  $N_{Ring}$  are the numbers of atomic pairs along the circumference and the total number of crowns within a unit cell (case of armchair tubes), respectively, whereas  $\hat{U}$  is the potential describing the elastic collision processes, and the DoS per carbon atom at the charge neutrality point

$\rho(E_F) = \frac{2\sqrt{3}a_{cc}}{\pi v_{0l}|\tilde{c}_h|}$ .<sup>32</sup> Thus, rewriting the eigenstates as

$$|\Psi_{n1,n2}(k_F)\rangle = \frac{1}{\sqrt{N_{Ring}}} \sum_{m=1, N_{Ring}} e^{imk_F} |\alpha_{n1,n2}(m)\rangle \quad (5.9)$$



with

$$|\alpha_{n1}(m)\rangle = \frac{1}{\sqrt{2N_c}} \sum_{n=1}^{N_c} e^{\frac{2i\pi n}{N_c}} \left( |p_{\perp}^A(mn)\rangle + |p_{\perp}^B(mn)\rangle \right) \quad (5.10)$$

$$|\alpha_{n2}(m)\rangle = \frac{1}{\sqrt{2N_c}} \sum_{n=1}^{N_c} e^{\frac{2i\pi n}{N_c}} \left( |p_{\perp}^A(mn)\rangle - |p_{\perp}^B(mn)\rangle \right) \quad (5.11)$$

and taking as an effective disorder model the so-called Anderson-type disorder with white noise statistics, i.e.,

$$\langle p_{\perp}^A(mn) | \hat{U} | p_{\perp}^A(m'n') \rangle = \varepsilon_A(m, n) \delta_{mm'} \delta_{nn'} \quad (5.12)$$

$$\langle p_{\perp}^B(mn) | \hat{U} | p_{\perp}^B(m'n') \rangle = \varepsilon_B(m, n) \delta_{mm'} \delta_{nn'} \quad (5.13)$$

$$\langle p_{\perp}^A(mn) | \hat{U} | p_{\perp}^A(m'n') \rangle = 0 \quad (5.14)$$

where  $\varepsilon_B(m, n)$  and  $\varepsilon_A(m, n)$  are the site energies on  $\pi$ -orbitals located on A and B atoms, which are taken at random within  $[-W/2, W/2]$  (probability density  $\mathcal{P} = 1/W$ ), one then finally gets

$$\frac{1}{2\tau_e(E_F)} = \frac{2\pi}{\hbar} \frac{1}{4} \left( \frac{1}{\sqrt{N_c N_{Ring}}} \sum_{N_c N_{Ring}} \varepsilon_A^2 + \frac{1}{\sqrt{N_c N_{Ring}}} \sum_{N_c N_{Ring}} \varepsilon_B^2 \right) \rho(E_F). \quad (5.15)$$

Hence, an analytical expression for the mean free path is<sup>7,28</sup>

$$\ell_e = \frac{18a_{cc}\gamma_0^2}{W^2} \sqrt{n^2 + m^2 + nm}. \quad (5.16)$$

The mean free path thus increases with diameter at fixed disorder, a property that is totally unconventional for usual mesoscopic systems. For a metallic tube (5, 5) with  $W = 0.2$ ,  $\ell_e \sim 500$  nm, which turns out to be larger than the circumference. Numerical results obtained via an order  $N$  computational approach have confirmed some specific scaling law for  $\ell_e$  that restricts to some interval around the charge neutrality point, which decreases with increasing diameter. The dependence of  $\ell_e$  on the Fermi

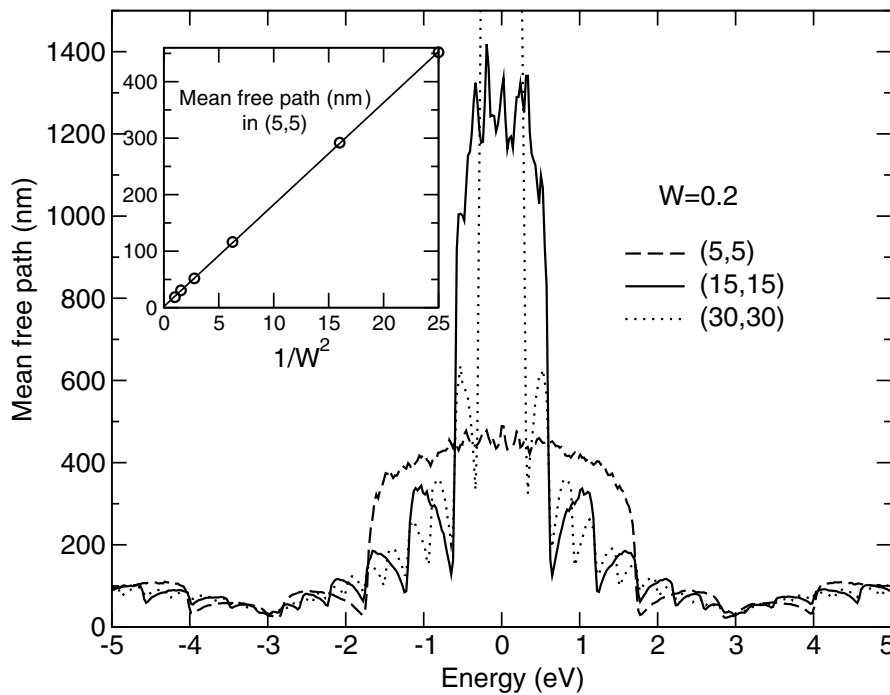


**Figure 5.10** Energy-dependent mean free paths for metallic armchair nanotubes with varying diameters. Inset:  $1/W^2$  law in agreement with FGR.<sup>33</sup>

energy and  $1/W^2$  is illustrated for three armchair tubes with different diameters in Figure 5.10.<sup>33</sup> As soon as the Fermi level is upshifted/downshifted out of the vicinity of the charge neutrality point, the  $1/\ell_e$  law is invalidated while the  $1/W^2$  law remains applicable. It is interesting to note that these properties remain valid for more realistic disorder as demonstrated in Latil et al.<sup>31</sup> for nitrogen- or boron-doped metallic tubes, in full agreement with experimental estimates.<sup>34,35</sup>

### 5.2.3.2 Aharonov–Bohm phenomena: ballistic vs. diffusive regimes

Applying a magnetic field is a powerful tool for unveiling quantum interference effects. In the presence of elastic disorder, the weak localization scheme can be illustrated for metallic nanotubes. The magnetoresistance depends on the probability  $\mathcal{P}$  for an electronic wavepacket to go from one site  $|P\rangle$  to another  $|Q\rangle$ , which can be written as

$$\mathcal{P}_{|P\rangle \rightarrow |Q\rangle} = \sum_i |\mathcal{A}_i|^2 + \sum_{i \neq j} \mathcal{A}_i \mathcal{A}_j e^{i(\alpha_i - \alpha_j)} \quad (5.17)$$

where  $\mathcal{A}_i e^{i\alpha_i}$  is the probability amplitude to go from  $|P\rangle$  to  $|Q\rangle$  via the  $i$ -path. Most of the terms in the summation vanish when averaged over disorder. In the special case of a cylinder or a nanotube, two paths returning back to the origin yield constructive contribution of quantum interference, reducing the conductance (weak localization). Switching on a magnetic field jeopardizes the

time-reversal symmetry of these paths, resulting in an increase of conductance or decrease of resistance (negative magnetoresistance).

Another magnetic field-induced quantum interference effect in a ring or cylinder geometry is the modulation of resistance with period  $\phi_0/2$ . The phase factor can then be written as ( $\vec{A}$  = the vector potential)

$$\alpha_{\pm} = \pm \frac{e}{\hbar c} \oint \vec{A} \cdot d\vec{r} = \pm \frac{2\pi}{\phi_0} \oint \vec{A} \cdot d\vec{r} , \quad (5.18)$$

and so the amplitude is given by  $|\mathcal{A}|^2 |1 + e^{i(\alpha_+ - \alpha_-)}|^2$ , resulting in a modulation factor  $\cos(2\pi\phi/\phi_0)$ . Below, the behaviors of field-dependent diffusion coefficients are shown for the (9, 0) nanotube as a function of mean free path evaluated through analytical formulas.<sup>36,37</sup> By using the Anderson-type disorder, the value of the mean free path can be tuned by the disorder strength  $W$ , so that several situations of interest can be explored.

First, the weak localization regime<sup>38</sup> is analyzed under the condition  $\ell_e < |\vec{C}_h| < L(\tau_\phi)$ . Figure 5.11 shows that the diffusivity increases at low fields (negative magnetoresistance) and that the periodic Aharonov–Bohm oscillations are dominated by a  $\phi_0/2$  period, i.e.,  $\mathfrak{D}(\tau_\phi, \phi + \phi_0/2) = \mathfrak{D}(\tau_\phi, \phi)$ , in agreement with weak localization theory. In contrast, when  $\ell_e < |\vec{C}_h|$ ,  $L(\tau_\phi) < 2\ell_e$ , the system exhibits a *positive magnetoresistance* associated with  $\mathfrak{D}(\tau_\phi, \phi + \phi_0) = \mathfrak{D}(\tau_\phi, \phi)$ . For the case  $\ell_e < |\vec{C}_h|$ ,  $L(\tau_\phi) > 2\ell_e$ , negative magnetoresistance and Aharonov–Bohm oscillations with period  $\phi_0$  are obtained. Note that with

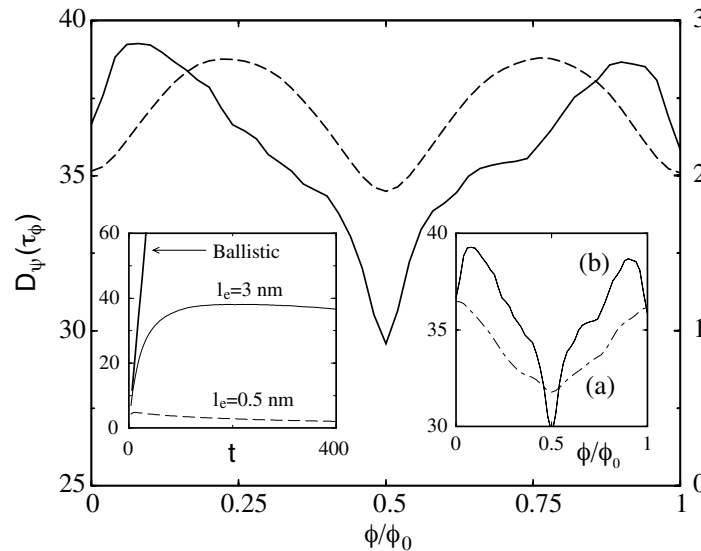


**Figure 5.11** Diffusion coefficient  $\mathfrak{D}(\tau_\phi, \phi/\phi_0)$  (in units of  $\text{\AA}^2\gamma_0/\hbar$ ) for the (9, 0) nanotube evaluated at time  $\tau_\phi \gg \tau_e$ , for two disorder strengths,  $W/\gamma_0 = 3$  and 1, such that the mean free path ( $\ell_e \sim 0.5$  and 3 nm, respectively) is either shorter (dashed line) or larger (solid line) than the nanotube circumference ( $|\vec{C}_h| \sim 2.3$  nm). The right y-axis is for the dashed line and the left y-axis is for the solid line. Inset:  $\mathfrak{D}(\tau_\phi, \phi/\phi_0)$  for  $\ell_e = 3$  nm and  $L(\tau_\phi) < 2\ell_e$ .

the analytical formula for the mean free path and estimates of disorder values, we get  $\ell_e \approx 10^4 \times |\tilde{C}_h|$  ( $|\tilde{C}_h|$  is the circumference of the outer nanotube in the experiment of Bachtold et al.<sup>12</sup>). The apparent inconsistency between the value of the mean free path and the observation of the  $\phi_0/2$  Aharonov–Bohm oscillations demonstrates that the interpretation of the experiments might be delicate since the precise position of the Fermi level and contribution of inner shells remain unclear.<sup>36,37</sup>

In fact, in the case of multiwalled carbon nanotubes, the situation is complicated. First, each shell has a different diameter, with approximately a difference of 3 Å between neighboring shells.<sup>39,40</sup> This might bring intricate contributions of Aharonov–Bohm phases with no clear overall oscillation period. In addition, in most cases, neighboring shells are incommensurate, in one respect to another. This produces an underlying aperiodic potential for  $\pi$ -electron scattering, which can give rise to unusual energy-dependent magnetotransport fingerprints.<sup>33</sup>

### 5.2.3.3 Persistent currents

The theoretical prediction and further experimental observation of persistent currents ( $I_{pc}$ ) in isolated mesoscopic rings have been one of the cornerstones of mesoscopic physics.<sup>41,42</sup> Such nondissipative currents result from inductive phenomena when a magnetic field is applied perpendicular to the ring. The Aharonov–Bohm effect modulates the boundary conditions of the quantum phase in a similar fashion as described in Section 5.2.1. Persistent currents can be observed if the electrons preserve their quantum coherent phase at least over the length of the ring.

Recently, Martel et al.<sup>43</sup> have synthesized carbon nanotube-based rings by combining chemical and ultrasonic treatments. The obtained rings formed by small bundles of single-walled nanotubes were further contacted to metallic electrodes, and a magnetotransport study was performed.<sup>44</sup> The authors conclude that electronic transport could be described by the conventional localization theory, and data were consistent with a phase coherence length smaller than the ring length, with no sign of periodic Aharonov–Bohm oscillations.<sup>44</sup> A very important issue is to investigate to which extent intrinsic properties of  $I_{pc}$  can be related to the intrinsic conduction mechanisms (ballistic vs. diffusive or localized), which can depend on the structural quality of individual tubes as well as intertube interactions in bundles.

Let us start with the basics of persistent current theory. Within the Fermi liquid framework,  $I_{pc} = -\frac{1}{\phi_0} \sum_n \partial \varepsilon_n / \partial \phi$  where  $\phi$  is the flux through the ring in units of  $\phi_0$  and the sum has to be done over all occupied states. In the case of ballistic rings (e.g., semiconducting heterostructures), the predicted average value of persistent current has been confirmed experimentally, in contrast with metallic rings with low mean free paths, for which a quantitative disagreement between theory and experiments remains controversial (typically  $I_{pc}^{\text{theor.}} \sim 10^{-2} I_{pc}^{\text{expts.}}$ ).  $I_{pc}(\phi)$  being an odd and periodic function of  $\phi$ , it

can be expanded in Fourier series as<sup>45</sup>  $I_{pc}(\phi) = \sum_{n=0}^{\infty} I_n \sin(2\pi n\phi)$ , where  $I_n$  is the  $n$ -th harmonic, which is given by  $\frac{2I_0}{n\pi} \cos(nk_F L_{ring})$ , where  $I_0 \sim e v_F / L_{ring}$ ,  $L_{ring}$  is the ring length. To represent the average value of persistent current, it is useful to compute  $J_{quad} = \sqrt{\int_{-1/2}^{+1/2} I_{pc}^2(\phi) d\phi}$ , or  $J_{\phi=1/4} = |I_{pc}(\frac{1}{4})|$ , which is dominated by the first harmonic.

In conventional mesoscopic systems, the mean free path  $\ell_e$  can be used to distinguish between the ballistic and diffusive regimes, thereby enabling one to understand the evolution of persistent currents with disorder as far as their amplitude and oscillation period are concerned. Different regimes can be defined whether  $\ell_e \gg L_{ring}$  (ballistic regime),  $\ell_e < L_{ring}$  (diffusive regime), or  $\xi \simeq N_c \ell_e < L_{ring}$  (localized regime where  $\xi$  is the localization length).<sup>45</sup> The first regime is associated with an average persistent current given by  $\sim e v_F / L_{ring}$ . In Figure 5.12, such a case is shown for (6, 6)-based tori of different lengths (Figure 5.13).<sup>46</sup> The persistent current maximum intensity for a defect-free (6, 6) tube with 82 unit cells ( $L_{ring} \simeq 20$  nm) is then found to be  $I_0 = 2e v_F / L_{ring} \simeq 15 \mu A$ .

In the diffusive regime, the average persistent current on a single eigenstate  $J_n^{typ}$  (average performed on torus length, disorder configurations, and magnetic flux) is expected to be given by the law

$\sqrt{\langle J_n^2(\phi) \rangle} \sim \sqrt{\Delta E_c} / \phi_0$  (where  $\Delta = \hbar v_F / L_{ring}$  is the average distance between eigenstates), whereas the total typical current writes  $J_{typ} =$

$$\sum_n J_n^{typ} \sim \frac{E_c}{\phi_0} = \frac{e v_F \ell_e}{L_{ring}^2} \quad (\text{where } E_c = \hbar v_F \ell_e / L_{ring}^2 \text{ is the Thouless energy}).^{45,47,48}$$

However, for weak enough disorder such that  $\ell_e \leq L_{ring}$ , the average behavior of persistent currents is much more difficult to anticipate analytically. Whenever  $\ell_e < L_{ring}$ ,<sup>49</sup> one could expect that the law  $\sim e v_F \ell_e / L_{ring}^2$  should still be satisfied to some extent so that the amplitude should remain reduced roughly by a  $\sim \ell_e / L_{ring}$  factor with respect to the ballistic case.

Assuming an Anderson-type disorder, such a law will suppose some  $(\gamma_0 / W)^2$  dependence in the quasi-ballistic regime. In Figure 5.14, the typical persistent current is plotted as a function of  $\ell_e$  for a (6, 6) tube (radius  $\simeq 258$  nm) with length in the order of  $L_{ring} \simeq 18.4$  nm ( $\Delta \sim 0.205$  eV). Results obtained for  $J_{1/4}$  and  $J_{quad}$  clearly demonstrate that the  $1/W^2$  law is not satisfied while  $2\ell_e > L_{ring}$ . Actually, a simple criterion can be found to describe the damping of persistent currents in the quasi-ballistic regime. For a given disorder strength (and corresponding  $\ell_e$ ), harmonics of rank  $n$ , such that  $\ell_e > n L_{ring}$ , will remain insensitive to disorder (as in the ballistic case), whereas others will be exponentially damped. A qualitative trend of persistent current evolutions with disorder can thus be extracted thanks to the knowledge of the dependence of  $\ell_e$  with disorder. As shown in Section 5.2.3, strong



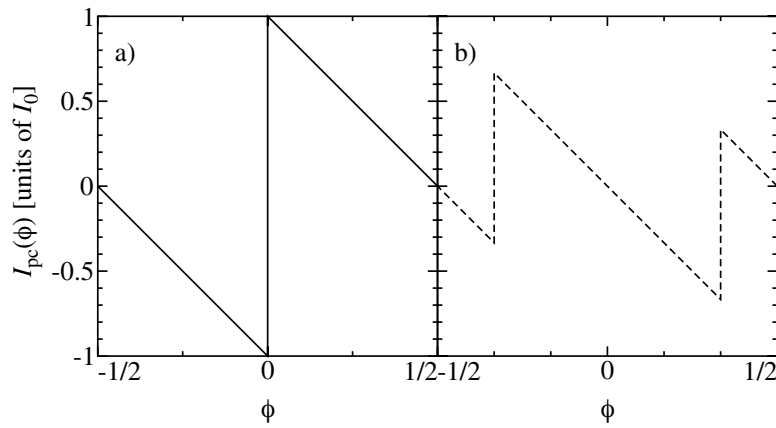


**Figure 5.12** Magnetic flux dependence of persistent currents for two (6, 6) nanotube-based torii (Figure 5.13) of different lengths.<sup>46</sup>

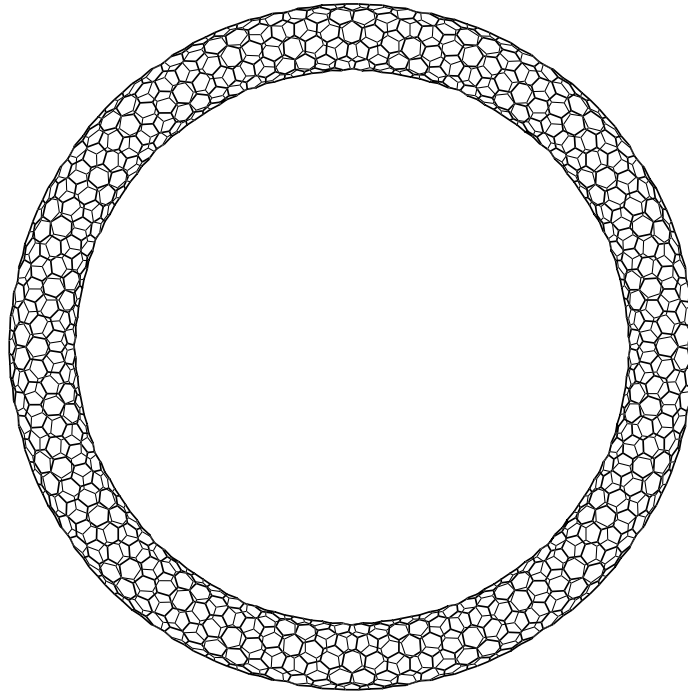


**Figure 5.13** Carbon nanotube-based torus, closed by covalent bonding.

fluctuations of  $\ell_e$  occur for small Fermi level shifts, so that *giant fluctuations of persistent currents are predicted theoretically*.

We now discuss the case of more complex geometry, in which boundary conditions of the rings are driven by noncovalent bonding (Figure 5.15, left). This case is important since synthesized nanotube-based rings are not closed by covalent bonds. The Hamiltonian of the ring is now written

$$H = -\gamma_0 \sum_{p_i, p_j(i)} |p_i\rangle \langle p_j| \exp(i\varphi_{ij}) - \gamma_1 \sum_{\langle p_i, p_k \rangle} (|p_i\rangle \langle p_k| + |p_k\rangle \langle p_i|) \exp(i\varphi_{ik}) \quad (5.19)$$

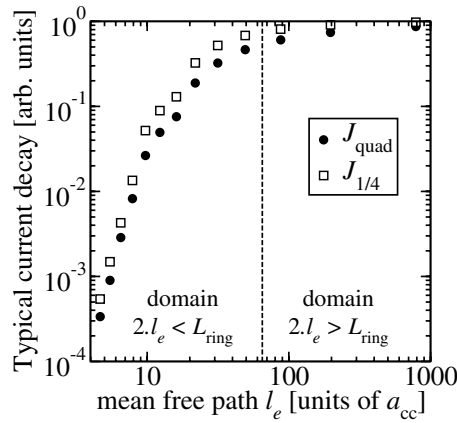


**Figure 5.14** Evolution of the typical persistent current intensity with  $\ell_e$  computed with the analytical form defined in Section 5.2.3.

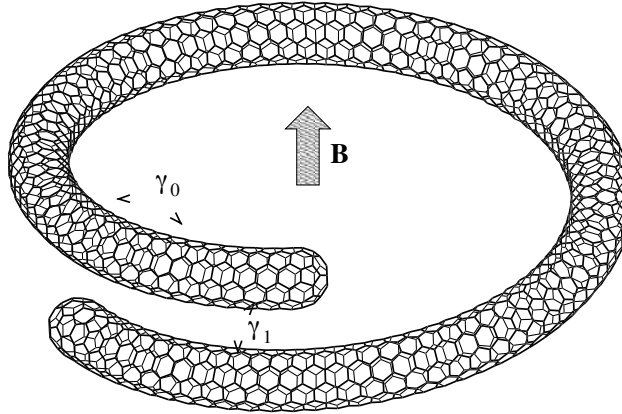


**Figure 5.15** Carbon nanotube-based coil that exhibits some weak noncovalent self-interaction at the boundaries.

where  $\phi_{ij} = 2\pi \left( \frac{z_j - z_i}{L_{\text{ring}}} \right) \phi$ , and  $|p_i\rangle$  and  $|p_j\rangle$  define the  $\pi$ -orbitals localized at sites  $z_i$  and  $z_j$  ( $\phi = \phi/\phi_0$ ),  $\gamma_1 = V_{\text{int}} \exp\left(\frac{d-\delta}{l}\right)$ , and  $d$  denotes the relative distance between the two orbitals. Remaining parameters are  $V_{\text{int}} = 0.36$  eV,  $\delta = 3.34$  Å, and  $l = 0.45$  Å (site energies are given in units of  $\gamma_0$ ).

Results show that in most cases, intertube interaction has little effect on persistent currents if two torii are considered, and if they are not commensurate. Commensurability between torii (i.e., translation invariance of tube–tube interaction, with a unit cell much smaller than torus length) might, however, significantly affect persistent currents because of degeneracy splitting induced by intertube coupling (see Latil et al.<sup>46</sup>). For noncovalent torii, as described in Figure 5.15, a pronounced damping of current amplitude is found (Figure 5.16), and the damping will be dependent on  $L_{\text{stick}}$ , the length of the self-interacting region of the coil, whereas  $d_{\text{stick}}$  gives the spacing

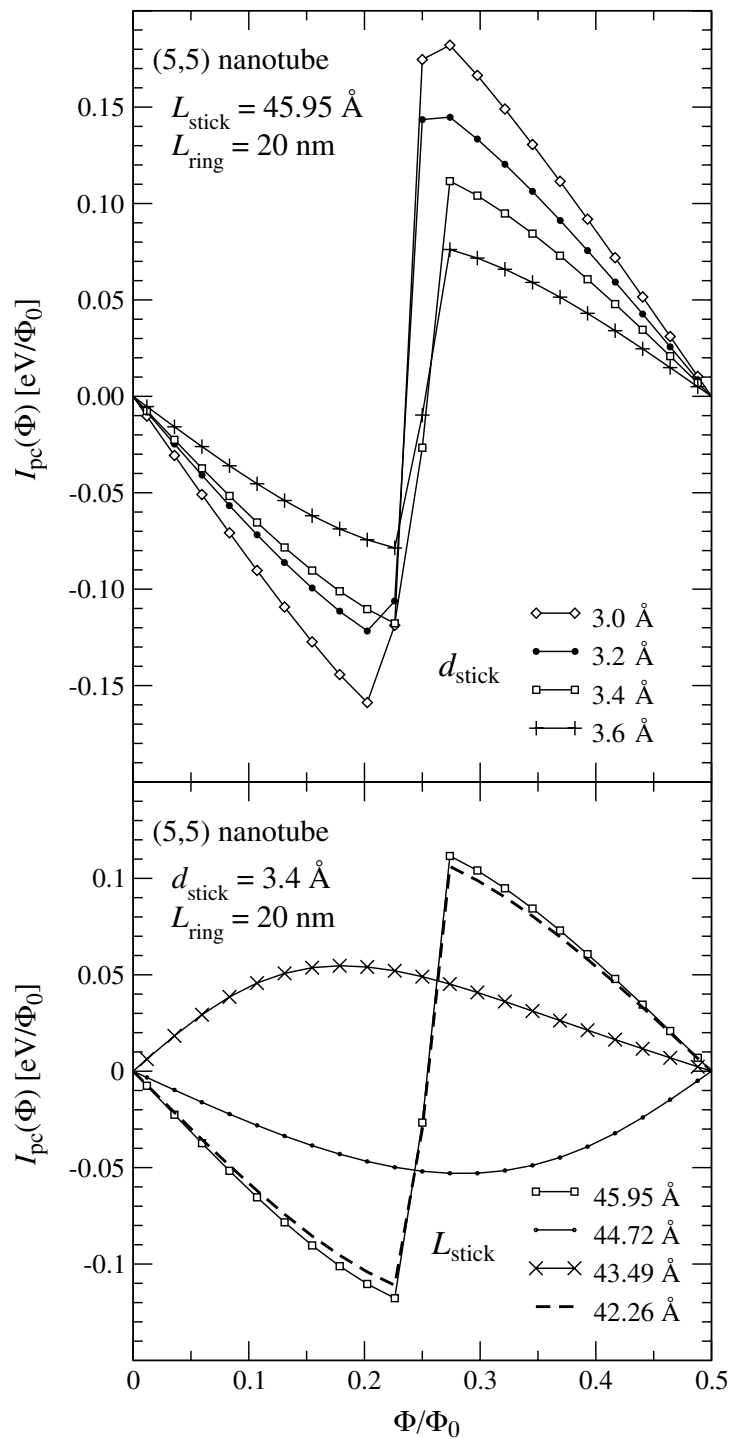


**Figure 5.16** Flux-dependent persistent currents as a function of stick length ( $L_{stick}$ ) along with the interaction between nearest neighboring orbitals come from noncovalent bonding, whereas  $d_{stick}$  denotes their relative interspacing.

distance between frontier orbitals. Typical intensity is reduced by roughly one to two orders of magnitude, compared to the case of covalent bonding (Figure 5.12).

## 5.3 Experimental results

As discussed in the previous sections, carbon nanotubes, either metallic or semiconducting, are predicted to possess novel magnetic properties. The remaining sections of this chapter review experimental studies of carbon nanotubes performed to date, which have confirmed or challenged some of the predictions, including magnetic (Section 5.3.1), magneto-optical (Section 5.3.2), and magnetotransport (Section 5.3.3) properties.

### 5.3.1 Magnetization

One of the earliest experimental studies on magnetic properties of carbon nanotubes was performed by Wang et al.<sup>50,51</sup> Through magnetic susceptibility measurements on a bulk sample of buckybundles, they concluded that these bundles are diamagnetic and  $|\chi_{\parallel}/\chi_{\perp}| \approx 1.1$ . (This anisotropy is opposite of the prediction that  $|\chi_{\parallel}| < |\chi_{\perp}|$ .) Heremans and coworkers<sup>52</sup> and Issi et al.<sup>53</sup> reported results of a systematic study on the magnetic susceptibilities of diamond, graphite, C<sub>60</sub>, and multiwalled carbon nanotubes as functions of temperature and magnetic field. It was found that the  $\chi$  of nanotubes was about half of that of graphite, which is known to be very large ( $\approx -3 \times 10^5$  emu/g for  $H \parallel$  c-axis below 100 K) due to the existence of the aromatic-like  $\pi$ -electrons that are absent in diamond; it showed similar temperature and field dependences to graphite (Figure 5.17). Ramirez et al.<sup>54</sup> reported that the  $\chi$  of carbon nanotube bundles is even larger than that of graphite on a per carbon basis. Results of these early studies are basically consistent with the notion that carbon nanotubes are rolled-up cylinders of graphene sheets that should show large diamagnetism associated with the ring currents flowing along the hexagonal rings of carbon,<sup>55</sup> but the samples studied were randomly oriented bundles and only average magnetic properties were probed.

Chauvet et al. studied magnetic properties of *aligned* multiwalled carbon nanotubes in films at various temperatures and magnetic field orientations.<sup>57</sup> They found that the nanotubes were diamagnetic and anisotropic. However, the results indicated that  $|\chi_{\parallel}| < |\chi_{\perp}|$  at all temperatures (similar to the work on buckybundles<sup>51</sup>). It was claimed<sup>55,57</sup> that the large diamagnetic susceptibility parallel to the tube axis may be due to the additional ring current along the circumference, but this behavior was clearly in contradiction with the predictions by Ajiki and Ando<sup>25,27</sup> and Lu,<sup>4</sup> described in detail in the previous section. More recent experimental studies on aligned multiwalled carbon nanotubes<sup>56,58,59</sup> unanimously showed behavior in agreement with  $|\chi_{\parallel}| > |\chi_{\perp}|$  (see, e.g., Figure 5.18). Kotosonov<sup>56</sup> argues that the confusion might have been because of inaccurate estimation of nanotube orientations in the samples used in earlier studies.

An interesting consequence of anisotropic magnetic susceptibilities is *magnetic alignment*. It has been demonstrated that paramagnetic<sup>60</sup> and diamagnetic<sup>61</sup> molecules with anisotropic susceptibilities as well as proteins can be effectively aligned by external magnetic fields if the magnetic energy

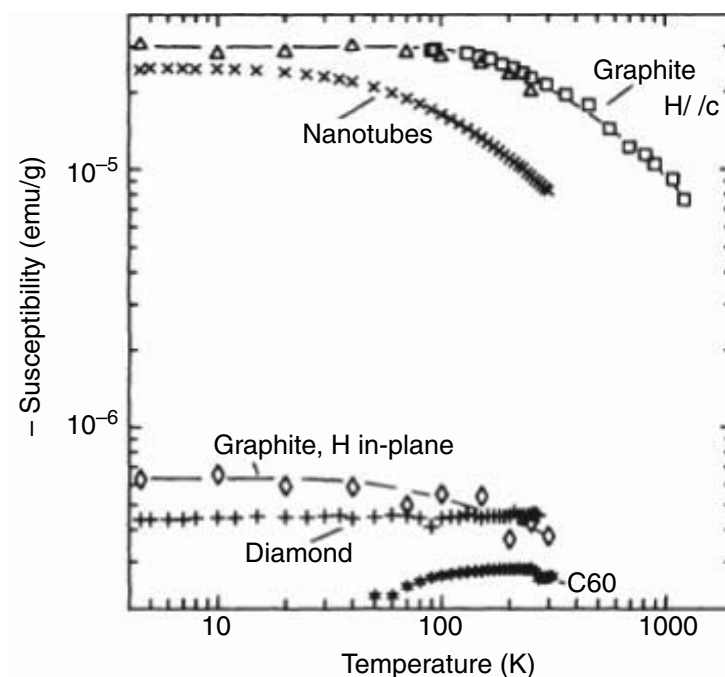


**Figure 5.17** Temperature dependence of the magnetic susceptibility of various carbon materials, including bundles of multiwalled carbon nanotubes. (Adopted from J. Heremans et al., *Phys. Rev. B*, 49, 15122, 1994.)

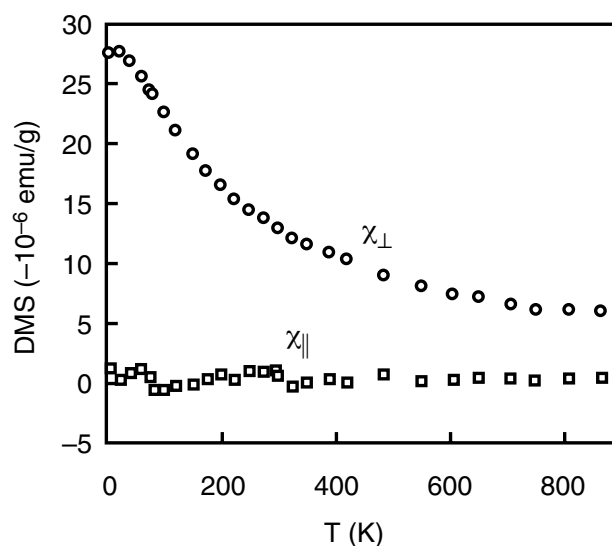


**Figure 5.18** The parallel and perpendicular magnetic susceptibilities of aligned multiwalled carbon nanotubes. (Adopted from A. S. Kotosonov, *JETP Lett.*, 70, 476, 1999.)

dominates the thermal energy. A. Fujiwara and coworkers were the first to succeed in fabricating magnetically aligned multiwalled nanotube films by drying nanotubes dispersed in methanol in a 7-T field.<sup>58</sup> Kimura et al. used a similar technique (in a 10-T field) to obtain electrically and mechanically



anisotropic multiwalled carbon nanotube/polymer composites.<sup>62</sup> Furthermore, M. Fujiwara et al.<sup>63,64</sup> succeeded in magnetically aligning *individual* multiwalled carbon nanotubes and estimated the degree of diamagnetic anisotropy to be  $\chi_{\parallel} - \chi_{\perp} \sim (9 \pm 5) \times 10^{-6}$  emu/mol ( $\chi_{\parallel} < \chi_{\perp} < 0$ ).

More recently, single-walled carbon nanotubes have been magnetically aligned.<sup>65–67</sup> Walters et al. produced thin membranes comprised of highly aligned single-walled nanotubes by producing a SWNT suspension, placing the suspension in magnetic fields as high as 25 T, and filtering the suspension in the magnetic field.<sup>65,66</sup> Zaric et al. demonstrated magnetic alignment of SWNTs of specific chiralities using micelle-suspended SWNTs in aqueous solutions.<sup>11,67</sup> Through analysis of the photoluminescence (PL) and absorption spectra in magnetic fields, in conjunction with atomic force microscopy (AFM) measurements to determine the length distribution of the nanotubes, they were able to estimate the diamagnetic anisotropy  $\chi_{\parallel} - \chi_{\perp}$  to be  $\sim 1.4 \times 10^{-5}$  emu/mol for 1-nm-diameter semiconducting nanotubes. This value is similar to the predicted values, i.e.,  $1.9 \times 10^{-5}$  emu/mol<sup>25</sup> and  $1.5 \times 10^{-5}$  emu/mol.<sup>4</sup> Furthermore, the extracted degree of alignment showed that tubes of larger diameters  $d$  align better, which is in qualitative agreement with the prediction, i.e.,  $|\chi_{\parallel} - \chi_{\perp}| \propto d$ .<sup>4,25</sup> See Section 5.3.2 for more data and analyses by Zaric et al.

### 5.3.2 Magneto-optics

As described in Section 5.2.1, when a SWNT is threaded by a magnetic flux  $\phi$ , its band structure is predicted to depend on  $\phi/\phi_0$ : the band gap oscillates with period  $\phi_0$ , and  $\phi/\phi_0$ -dependent splitting occurs. Consequences of these effects are expected to appear in various quantities, but most prominently in interband optical spectra as peak shifts and splittings.<sup>2,7,8</sup> The Aharonov–Bohm-induced VHS splittings are due to degeneracy lifting between the K and K' points, and for semiconducting nanotubes, the amount of splitting is given by  $\Delta_{KK'} = 6\Delta_g\phi/\phi_0$  (where  $\Delta_g$  is the zero-field band gap) when  $\phi/\phi_0 < 1/6$ . For a typical semiconducting SWNT with 1 nm diameter, this yields  $\Delta_{KK'} \sim 1$  meV/T.

Recent success in preparing individually suspended SWNTs in aqueous solutions led to the observation of chirality-dependent peaks in absorption and photoluminescence spectra<sup>68</sup> and to complete chirality assignments.<sup>69</sup> This has opened ways to perform spectroscopy of SWNTs of specific chiralities. Zaric et al.<sup>11,67</sup> recently utilized such samples in a series of high-field magneto-optical studies, directly verifying some of the predicted band structure modifications due to the Aharonov–Bohm effect. We summarize some of the highlights of their work in this section.

Zaric and coworkers measured absorption and PL in micelle-suspended SWNTs at magnetic fields ( $B$ ) up to 45 T. The observed peaks exhibited significant changes with increasing  $B$ . In absorption they observed splittings in some of the first subband transition peaks. The amount of splittings (30 to 40 meV at 45 T) was consistent with the expected splitting. Splittings were

not resolvable in the second subband transitions due to their larger line widths ( $\sim 100$  meV). Magneto-PL showed red shifts with increasing  $B$  for all observed peaks, the amount of which was diameter dependent in a predicted way. Detailed PL simulations, taking into account  $B$ -induced alignment of nanotubes, thermal population, and Aharonov–Bohm-induced splittings, successfully reproduced the observed spectra, supporting their interpretation. However, it is important to point out that 45 T is not high enough to reveal a full period of the Aharonov–Bohm effect. For a typical nanotube diameter of 1 nm, 45 T corresponds to  $\phi/\phi_0 \sim 10^{-2}$ .

Figure 5.19a shows polarization ( $\vec{P}$ )-dependent magnetoabsorption for the first subband ( $E_1H_1$ ) transitions. The solid and dashed lines are for parallel ( $\vec{B} \parallel \vec{P}$ ) and perpendicular ( $\vec{B} \perp \vec{P}$ ) polarizations, respectively. The field induces drastic changes in the spectrum. First, note that no traces are intentionally offset, so the  $P$ -dependent vertical shifts are real; i.e., the  $B$  increases (decreases) the absorption in the parallel (perpendicular) case, resulting in large optical anisotropy. At 45 T, the absorption coefficient ratio ( $\alpha_{\parallel}/\alpha_{\perp}$ ) is  $\sim 4$ . The optical anisotropy, defined as  $(\alpha_{\parallel} - \alpha_{\perp})/(\alpha_{\parallel} + \alpha_{\perp})$ , is plotted vs. energy for 0, 20, and 45 T in Figure 5.19b, where the dotted lines are raw data and the solid lines are polynomial fits. At a given  $B$ , the anisotropy is larger for lower energies (corresponding to larger diameters). Since perpendicularly polarized light is not absorbed,<sup>2</sup> this indicates that larger-diameter tubes align better. The field also induces spectral modifications. Each absorption peak is seen to become broader with increasing  $B$ , and finally, some of the peaks split in the highest field range, i.e., 30 to 45 T, only in the  $\vec{B} \parallel \vec{P}$  case (Figure 5.19c).

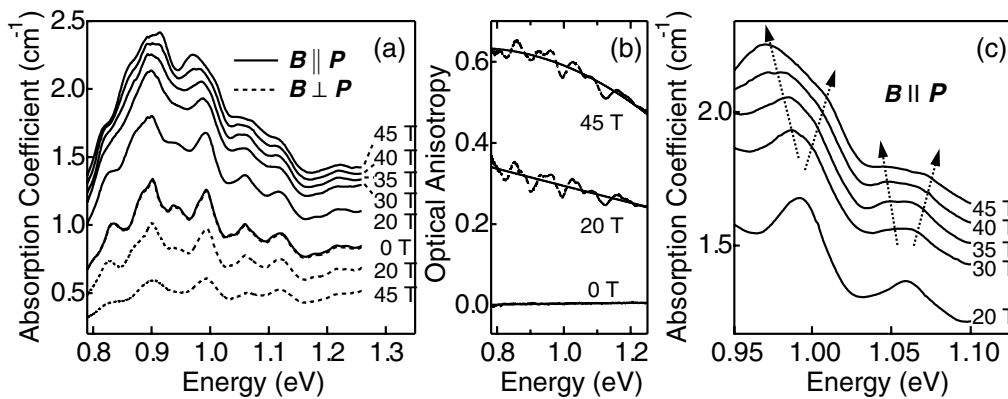


**Figure 5.19** (a) Polarization-dependent magnetoabsorption spectra for micelle-suspended SWNTs in  $D_2O$  in the spectral range of the first subband ( $E_1H_1$ ) transitions. Solid and dashed lines are for parallel ( $\vec{B} \parallel \vec{P}$ ) and perpendicular ( $\vec{B} \perp \vec{P}$ ) polarizations, respectively. No traces are offset. (b) Optical anisotropy, defined as  $(\alpha_{\parallel} - \alpha_{\perp})/(\alpha_{\parallel} + \alpha_{\perp})$ , vs. photon energy. For a given field, the larger the nanotube diameter, the larger the optical anisotropy. (c) An expanded plot of data for the  $\vec{B} \parallel \vec{P}$  case from 20 to 45 T, showing field-induced splitting of two absorption peaks.

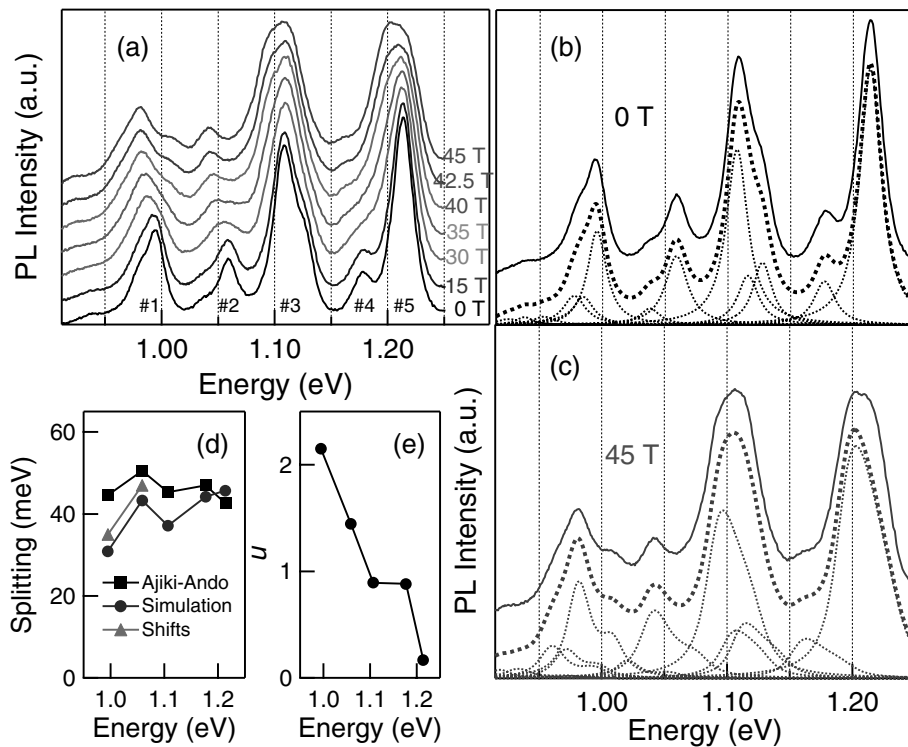


**Figure 5.20** (a) Magneto-PL spectra for micelle-suspended SWNTs in  $D_2O$ , excited with a 633-nm beam. The traces are shifted vertically for clarity. The chiralities of the most visible peaks are #1, (10, 3); #2, (8, 6); #3, (7, 6); #4, (10, 2); and #5, (7, 5). As the field increases, all peaks red shift. (b, c) Measured (solid line) and theoretical (thick dotted line) PL spectra at (b) 0 T and (c) 45 T. Individual theoretical PL peaks are also plotted as thin dotted lines. (d) Ajiki-Ando splittings obtained from predictions (solid line), simulations (solid circles), and peak shifts (solid triangles). (e) The values of the alignment parameter  $u$  (see the text for definition) at 45 T for the five main PL peaks, obtained from data analyses and simulations. Significant spectral changes are expected only when  $u > 0.707$  (see text).

Figure 5.20a shows magneto-PL spectra up to 45 T, excited by a 633-nm He-Ne laser. The chiralities ( $n, m$ ) of the main five peaks, numbers 1 to 5, are indicated in the caption. It can be seen that all PL peaks exhibit interesting spectral evolution with  $B$ . Specifically, all peaks shift to lower energy, and the shift is more obvious for lower-energy peaks (i.e., numbers 1 and 2) or larger-diameter tubes. The 0 and 45 T data are replotted as solid lines in Figure 5.20b and c, respectively, together with the simulated total (thick dotted lines) and individual (thin dotted lines) PL peaks. Magnetic field-induced red shifts, peak broadenings, and splittings are clearly visible.

These observations can be explained in terms of the Aharonov-Bohm effect only if we take into account the magnetic alignment of nanotubes. Unlike Zeeman splitting, the amount of Aharonov-Bohm-induced splitting depends on the angle between the tube and the field and can reach the predicted value,  $\Delta_{KK'} = 6\Delta_g\phi/\phi_0$ , only when the tube is completely aligned with  $B$ . This explains why significant spectral changes were observed in absorption only for  $\vec{P}$  parallel to  $\vec{B}$ . The nanotubes align due to their highly

anisotropic magnetic susceptibilities (see Section 5.2.2). Using Maxwell–Boltzmann statistics, the probability density that a given nanotube, consisting of  $N$  moles of carbon atoms, is at an angle between  $\theta$  and  $\theta + d\theta$  relative to the field is (see, e.g., Walters et al.<sup>65</sup>):

$$P(\theta)d\theta = \frac{\exp(-u^2 \sin^2 \theta)d\theta}{\int_0^{\pi/2} \exp(-u^2 \sin^2 \theta)d\theta}, \quad (5.20)$$

where  $[B^2N(\chi_{\parallel} - \chi_{\perp})/k_B T]^{1/2}$ ,  $k_B$  is the Boltzmann constant, and  $T$  is the temperature. The quantity  $u$  is a dimensionless measure of alignment, containing the ratio of the alignment energy to the thermal energy and completely determines the angular distribution for a given chirality at given  $B$  and  $T$ . As  $B$  increases,  $u$  increases and, consequently, the probability that the tube is at a small  $\theta$  increases. The existence of angle distribution prevents the full amount of red shift,  $\Delta E_{PL}^{\text{theory}} = \Delta_{KK'}/2 = 3\Delta_g\phi/\phi_0$ ; instead, the observed PL shift is given by  $\Delta E_{PL}^{\text{experiment}} = \Delta E_{PL}^{\text{theory}} \cos \theta^*$ . Here  $\theta^*$  is the angle at which  $P(\theta)$  is maximum and can be expressed in terms of  $u$ :

$$\theta^* = \begin{cases} \pi/2 & \text{for } u \leq \frac{1}{\sqrt{2}} \\ \arcsin(1/\sqrt{2}u) & \text{for } u > \frac{1}{\sqrt{2}} \end{cases}. \quad (5.21)$$

Equation 5.21 suggests that absorption and PL will not show significant shifts until  $u$  reaches the critical value ( $1/\sqrt{2} \approx 0.707$ ). In addition, since  $u$  is expected to increase with the tube diameter<sup>4,27</sup> (Section 5.2.2), one can expect stronger alignment for larger-diameter tubes, and lower-energy peaks should start showing  $B$  dependence at lower  $B$ , consistent with the data.

In order to use the experimentally determined values of  $u$  to estimate the magnetic susceptibility anisotropy through using  $u = [B^2N(\chi_{\parallel} - \chi_{\perp})/k_B T]^{1/2}$ , the length distribution of the nanotubes was measured. The nanotubes were deposited onto a SiO<sub>2</sub>-covered wafer by simply dipping the wafer into the sample solution 5 to 10 times. The wafer was then rinsed and imaged using an atomic force microscopy. The obtained length histogram had a maximum at about 300 nm. Taking into account that, for all the five peaks, the diameter of the corresponding nanotube was  $\sim 1$  nm, Zaric et al.<sup>11,67</sup> obtained  $\chi_{\parallel} - \chi_{\perp} \sim 1.4 \times 10^{-5}$  emu/mol, similar to the predicted values, i.e.,  $1.9 \times 10^{-5}$  emu/mol<sup>27</sup> and  $1.5 \times 10^{-5}$  emu/mol.<sup>4</sup>

### 5.3.3 Magnetotransport

As shown in the theoretical part, the application of a magnetic field is a precious tool for clarifying the role of quantum interferences in magnetotransport.<sup>38</sup> The first experimental magnetotransport study on carbon nanotubes was performed by Langer et al.<sup>70</sup> on large-diameter MWNTs, for fields applied perpendicular to the tube axis. The observation of negative magnetoresistance, together with universal conductance fluctuations, was compatible with the contribution of quantum interference effects in the diffusive regime and in the weak localization framework. A few years later, Bachtold et al.<sup>12</sup> provided additional evidence of such a scenario when measuring negative magnetoresistance superimposed onto  $\phi_0/2$  periodic Aharonov–Bohm oscillations, by applying a field parallel to the tube axis.

In that study, the conduction regime was extrapolated to be diffusive with  $\ell_e$  in the order of the tube circumference, while the coherence length was a few times larger and was attributed to Coulomb dephasing effects in the perturbative regime. In the same paper,<sup>12</sup> the authors also presented superimposed oscillations of a much smaller period ( $\phi_0/10$ ), which did not find any conclusive understanding.

Similarly, other groups<sup>13,14,71</sup> reported on different oscillation periods as well as changes from positive to negative magnetoresistance. The authors proposed an interpretation contradictory to Bachtold et al.<sup>12</sup> in the sense that the magnetoresistance modulations were ascribed to band structure effects, (Section 5.2.1) and the transport mechanism remained ballistic, with no quantum interference contributions. An intriguing switching effect from positive to negative magnetoresistance was also observed by changing the orientation of the magnetic field with respect to the tube axis (see Figure 5.21).<sup>13</sup>

Let us discuss with simple arguments the scenario outlined so far. The experiments performed by Bachtold et al.<sup>12</sup> on MWNTs with a diameter in the order of 20 nm appear to be well described by conventional weak localization theory (Figure 5.22). In this work, four-probe resistance was measured on two samples. First, sample 1 (diameter = 17 nm, or  $|C_h| \approx 53$  nm, and interelectrode spacing = 170 nm) was found to display negative magnetoresistance together with  $\phi_0/2$  periodic oscillations. The zero-flux resistance was given by  $R_{4c} \approx 30k\Omega$ . As usual in the theory of diffusive systems, the resistance can be written as  $R_{4c} (h/N_{\perp} 2e^2) (1 - T)/T$ . By further assuming that  $N_{\perp} = 2$  and given  $h/2e^2 = 13k\Omega$ , the transmission coefficient is found to be  $T \sim 0.174$ , so that the mean free path  $\ell_e \sim 35$  nm  $\leq |C_h|$ . This short derivation consistently shows that the obtained value for mean free path agrees with weak localization requirements. Following the same argument for sample 2 (diameter = 13 nm, or  $|C_h| \approx 40$  nm, and interelectrode spacing = 170 nm), and given that  $R_{4c} \approx 2.4k\Omega$  at zero flux, we can deduce (by still assuming  $N_{\perp} = 2$ ) a transmission coefficient  $T \approx 0.728$ . In this case,  $\ell_e \sim 450$  nm, or  $\ell_e \sim 10 |C_h|$ . It thus appears that the extrapolated transport length scale does not allow us to strictly apply conventional weak localization



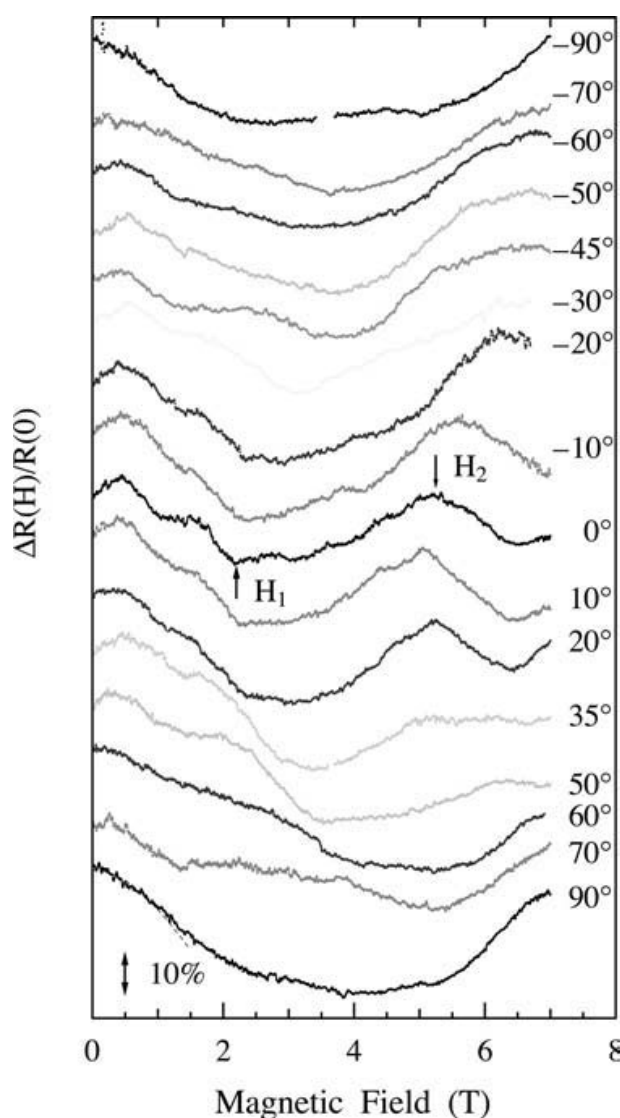


**Figure 5.21** Magnetoresistance of an MWNT as a function of magnetic field orientation with respect to tube axis. (From A. Fujiwara et al., *Phys. Rev. B*, 60, 13492, 1999.)

theory. Amazingly, sample 2 shows a much smaller oscillation period,  $\phi_0/10$ , seemingly superimposed onto the  $\phi_0/2$  oscillations, whose convincing interpretation is still lacking.

By the same argument, one can verify that other seemingly contradictory experiments (or interpretations)<sup>13</sup> are indeed achieved in a regime out of the strict applicability conditions of weak localization theory. In addition, it has to be noticed that if  $\phi_0/2$  oscillations are observed in a magnetotransport experiment, one cannot disregard the modifications of the band structure, as detailed in Section 5.2.1, and thus the whole theory should simultaneously account for both magnetic effects on electronic structure and quantum interference effects on transport, as discussed in Roche and Saito.<sup>72</sup>

Very recently, three groups have further performed novel magnetotransport experiments on carbon nanotubes. Ferorov et al. have measured magnetotransport on *double-walled* nanotubes with 3 nm diameter while varying the magnetic field orientation and applied gate voltage.<sup>73</sup> With an estimated

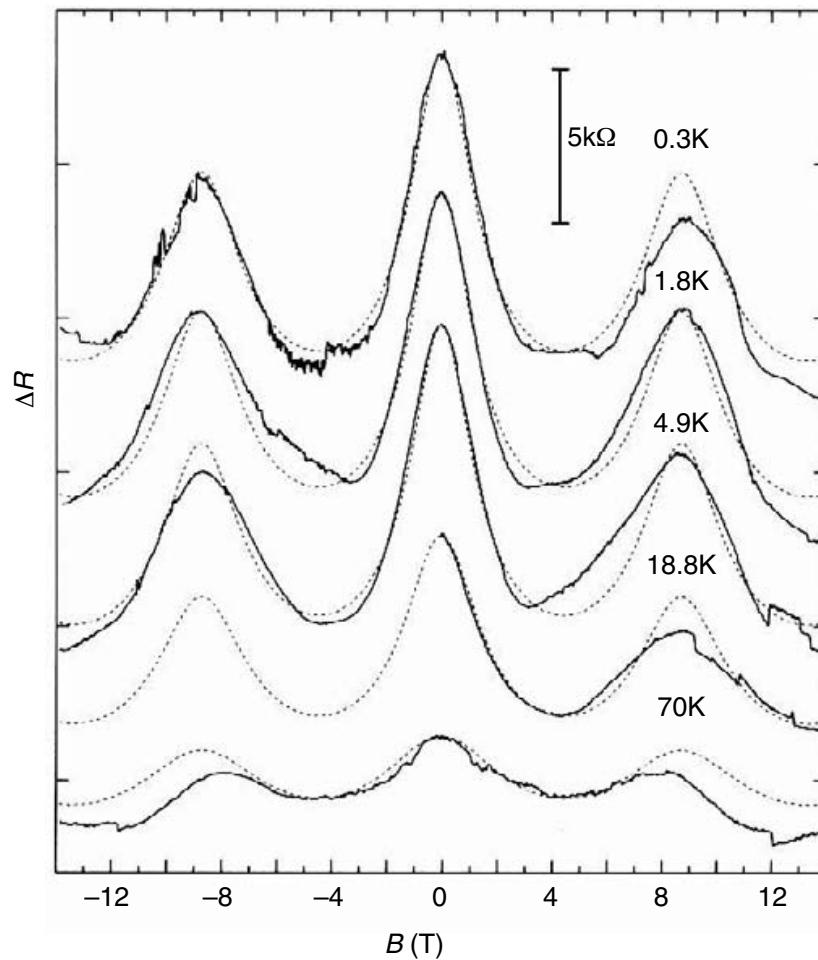


**Figure 5.22** Magnetoresistance of a MWNT measured in the parallel configuration. (From Bachtold, A. et al., *Nature*, 397, 673, 1999.)

modulation of the position of the Fermi level by about 50 meV, the magnetotransport fingerprints were shown to switch from a regime fully dominated by weak localization (negative magnetoresistance) to a more complex regime where both weak localization and band structure effects contribute. Coskun et al. have studied magnetotransport in the coulomb blockade regime, where evidence for  $\phi_0$  periodic oscillations of the energy gap was given for large-diameter multiwalled nanotubes weakly coupled to Au/Cr metallic contacts.<sup>18</sup> Furthermore, most recently, by achieving a good ohmic contact between the single-walled metallic nanotube and Pt electrodes, Cao et al. have observed  $B$ -dependent modulations of the Fabry–Perot interference patterns in single-walled carbon nanotubes in the ballistic transport regime.<sup>19</sup>

All these experimental studies confirm the subtle interplay between quantum interference phenomena and magnetic field-dependent band structure in carbon nanotubes. However, despite these results, several unanswered questions remain, such as the relation between magnetotransport oscillations and elastic and inelastic scattering in carbon nanotubes, the contribution of intershell coupling, and the superposition of various Aharonov–Bohm phases of different origins. The physics of excitons in carbon

nanotubes subjected to external magnetic fields also appears as an interesting problem to consider.<sup>74,75</sup>

## Acknowledgments

J.K. thanks the National Science Foundation (grants DMR-0134058 and DMR-0325474) and the Robert A. Welch Foundation (grant C-1509) for support and T. Ando for valuable discussions. S.R. acknowledges F. Triozon and S. Latil for valuable discussions and the research grant from the French Ministry of Research under ACI project *TransNanoFils*.

## References

1. H. Ajiki and T. Ando, Electronic states of carbon nanotubes, *J. Phys. Soc. Jpn.* 62, 1255 (1993).
2. H. Ajiki and T. Ando, Aharonov-Bohm effect in carbon nanotubes, *Physica B* 201, 349 (1994).
3. W. Tian and S. Datta, Aharonov-Bohm-type effect in graphene tubules: a Landauer approach, *Phys. Rev. B* 49, 5097 (1994).
4. J. P. Lu, Novel magnetic properties of carbon nanotubes, *Phys. Rev. Lett.* 74, 1123 (1995).
5. H. Ajiki and T. Ando, Energy bands of carbon nanotubes in magnetic fields, *J. Phys. Soc. Jpn.* 65, 505 (1996).
6. J. Jiang, J. Dong, and D. Y. Xing, Zeeman effect on the electronic spectral properties of carbon nanotubes in an axial magnetic field, *Phys. Rev. B* 62, 13209 (2000).
7. S. Roche, G. Dresselhaus, M. S. Dresselhaus, and R. Saito, Aharonov-Bohm spectral features and coherence lengths in carbon nanotubes, *Phys. Rev. B* 62, 16092 (2000).
8. F. L. Shyu, C. P. Chang, R. B. Chen, C. W. Chiu, and M. F. Lin, Magnetoelectronic and optical properties of carbon nanotubes, *Phys. Rev. B* 67, 045405 (2003).
9. T. Ando, Excitons in carbon nanotubes revisited: dependence on diameter, Aharonov-Bohm flux, and strain, *J. Phys. Soc. Jpn.* 73, 3351 (2004).
10. Y. Aharonov and D. Bohm, Significance of electromagnetic potentials in the quantum theory, *Phys. Rev.* 115, 485 (1959).
11. S. Zaric, G. N. Ostojic, J. Kono, J. Shaver, V. C. Moore, M. S. Strano, R. H. Hauge, R. E. Smalley, and X. Wei, Optical signatures of the Aharonov-Bohm phase in single-walled carbon nanotubes, *Science* 304, 1129 (2004).
12. A. Bachtold, C. Strunk, J.-P. Salvetat, J.-M. Bonard, L. Forró, T. Nussbaumer, and C. Schönenberger, Aharonov-Bohm oscillations in carbon nanotubes, *Nature* 397, 673 (1999).
13. A. Fujiwara, K. Tomiyama, H. Suematsu, M. Yumura, and K. Uchida, Quantum interference of Electrons in multiwall carbon nanotubes, *Phys. Rev. B* 60, 13492 (1999).
14. J.-O. Lee, J.-R. Kim, J.-J. Kim, J. Kim, N. Kim, J. W. Park, and K.-H. Yoo, Observation of magnetic-field-modulated energy gap in carbon nanotubes, *Solid State Commun.* 115, 467 (2000).

15. A. Kanda, S. Uryu, K. Tsukagoshi, Y. Ootuka, and Y. Aoyagi, Magnetic field dependence of coulomb oscillations in metal/multi-wall carbon nanotube/metal structures, *Physica B* 323, 246 (2002).
16. E. D. Minot, Y. Yaish, V. Sazonova, and P. L. McEuen, Determination of electron orbital magnetic moments in carbon nanotubes, *Nature* 428, 536 (2004).
17. P. Jarillo-Herrero, S. Sapmaz, C. Dekker, L. P. Kouwenhoven, and H. S. J. van der Zant, Electron-hole symmetry in a semiconducting carbon nanotube quantum dot, *Nature* 429, 389 (2004).
18. U. C. Coskun, T.-C. Wei, S. Vishveshwara, P. M. Goldbart, and A. Bezryadin,  $h/e$  magnetic flux modulation of the energy gap in nanotube quantum dots, *Science* 304, 1132 (2004).
19. J. Cao, Q. Wang, M. Rolandi, and H. Dai, Aharonov-Bohm interference and beating in single-walled carbon-nanotube interferometers, *Phys. Rev. Lett.* 93, 216803 (2004).
20. R. Saito, G. Dresselhaus, and M. S. Dresselhaus, *Physical Properties of Carbon Nanotubes*, Imperial College Press, London (1998).
21. S. Roche, Quantum transport by means of  $O(N)$  real-space methods, *Phys. Rev. B* 59, 2284 (1999).
22. T. Seri and T. Ando, Boltzmann conductivity of a carbon nanotube in magnetic fields, *J. Phys. Soc. Jpn.* 66, 169 (1997).
23. T. Ando and T. Seri, Quantum transport in a carbon nanotube in magnetic fields, *J. Phys. Soc. Jpn.* 66, 3558 (1997).
24. L. Wang, P. S. Davids, A. Saxena, and A. R. Bishop, Quasiparticle energy spectra and magnetic response of certain curved graphitic geometries, *Phys. Rev. B* 46, 7175 (1992).
25. H. Ajiki and T. Ando, Magnetic properties of carbon nanotubes, *J. Phys. Soc. Jpn.* 62, 2470 (1993).
26. P. S. Davids, L. Wang, A. Saxena, and A.R. Bishop, Magnetic ordering transition of electrons on mesoscopic tubes, *Phys. Rev. B* 48, 17545 (1993).
27. H. Ajiki and T. Ando, Magnetic properties of ensembles of carbon nanotubes, *J. Phys. Soc. Jpn.* 64, 4382 (1995).
28. C. T. White and T. N. Todorov, Carbon nanotubes as long ballistic conductors, *Nature* 393, 240 (1998).
29. T. Ando and T. Nakanishi, Impurity scattering in carbon nanotubes: absence of back scattering, *J. Phys. Soc. Jpn.* 67, 1704 (1998).
30. T. Ando, T. Nakanishi, and R. Saito, Berry's phase and absence of back scattering in carbon nanotubes, *J. Phys. Soc. Jpn.* 67, 2857 (1998).
31. S. Latil, S. Roche, D. Mayou, and J.-C. Charlier, Mesoscopic transport in chemically doped carbon nanotubes, *Phys. Rev. Lett.* 92, 256805 (2004).
32. J. W. Mintmire and C. T. White, Universal density of states for carbon nanotubes, *Phys. Rev. Lett.* 81, 2506 (1998).
33. F. Triozon, S. Roche, A. Rubio, and D. Mayou, Electrical transport in carbon nanotubes: role of disorder and helical symmetries, *Phys. Rev. B* 69, 121410(R) (2004).
34. K. Liu, P. Avouris, R. Martel, and W. K. Hsu, Electrical transport in doped multiwalled carbon nanotubes, *Phys. Rev. B* 63, 161404(R) (2001).
35. V. Krsti, S. Blumentritt, J. Muster, S. Roth, and A. Rubio, Role of disorder on transport in boron-doped multiwalled carbon nanotubes, *Phys. Rev. B* 67, 041401(R) (2003).

36. S. Roche, F. Triozon, A. Rubio, and D. Mayou, Conduction mechanisms and magnetotransport in multiwalled carbon nanotubes, *Phys. Rev. B* 64, 121401(R) (2001).
37. S. Roche, F. Triozon, A. Rubio, and D. Mayou, Electronic conduction in multi-walled carbon nanotubes: role of intershell coupling and incommensurability, *Phys. Lett. A* 285, 94 (2001).
38. A. G. Aronov and Y. V. Sharvin, Magnetic flux effects in disordered conductors, *Rev. Mod. Phys.* 59, 755 (1987).
39. R. Saito, G. Dresselhaus, and M. S. Dresselhaus, Electronic structure of double-layer graphene tubules, *J. Appl. Phys.* 73, 494 (1993).
40. J. Charlier and J. Michenaud, Energetics of multilayered carbon tubules, *Phys. Rev. Lett.* 70, 1858 (1993).
41. M. Büttiker, Y. Imry, and R. Landauer, Josephson behavior in small normal one-dimensional rings, *Phys. Lett. A* 96, 365 (1983).
42. L. P. Lévy, G. Dolan, J. Dunsmuir, and H. Bouchiat, Magnetization of mesoscopic copper rings: evidence for persistent currents, *Phys. Rev. Lett.* 64, 2074 (1990).
43. R. Martel, H. R. Shea, and P. Avouris, Rings of single-walled carbon nanotubes, *Nature (London)* 398, 299 (1999).
44. H. R. Shea, R. Martel, and P. Avouris, Electrical transport in rings of single-wall nanotubes: one-dimensional localization, *Phys. Rev. Lett.* 84, 4441 (2000).
45. Y. Imry, *Introduction to Mesoscopic Physics*, Oxford University Press, New York (1997).
46. S. Latil, S. Roche, and A. Rubio, Persistent currents in carbon nanotube based rings, *Phys. Rev. B* 67, 165420 (2003).
47. H. Bouchiat and G. Montambaux, *J. Phys. (Paris)* 50, 2695 (1989).
48. G. Montambaux, H. Bouchiat, D. Sigeti, and R. Friesner, Persistent currents in mesoscopic metallic rings: ensemble average, *Phys. Rev. B* 42, 7647 (1990).
49. A. Altland, Y. Gefen, and G. Montambaux, What is the Thouless energy for ballistic systems?, *Phys. Rev. Lett.* 76, 11301133 (1996).
50. X. K. Wang, X. W. Lin, V. P. Dravid, J. B. Ketterson, and R. P. H. Chang, Growth and characterization of buckybundles, *Appl. Phys. Lett.* 62, 1881 (1993).
51. X. K. Wang, R. P. H. Chang, A. Patashinski, and J. B. Ketterson, Magnetic susceptibility of buckytubes, *J. Mater. Res.* 9, 1578 (1994).
52. J. Heremans, C. H. Oik, and D. T. Morelli, Magnetic susceptibility of carbon structures, *Phys. Rev. B* 49, 15122 (1994).
53. J.-P. Issi, L. Langer, J. Heremans, and C. H. Oik, Electronic properties of carbon nanotubes: experimental results, *Carbon* 33, 941 (1995).
54. A. P. Ramirez, R. C. Haddon, O. Zhou, R. M. Fleming, J. Zhang, S. M. McClure, and R. E. Smalley, Magnetic susceptibility of molecular carbon: nanotubes and fullerite, *Science* 265, 84 (1994).
55. R. C. Haddon, Magnetism of the carbon allotropes, *Nature (London)* 378, 249 (1995).
56. A. S. Kotosonov, Texture and magnetic anisotropy of carbon nanotubes in cathode deposits obtained by the electric-arc method, *JETP Lett.* 70, 476 (1999).
57. O. Chauvet, L. Forro, W. Bacsá, D. Ugarte, B. Doudin, and W.A. de Heer, Magnetic anisotropies of aligned carbon nanotubes, *Phys. Rev. B* 52, R6963 (1995).



58. A. Fujiwara, F. Katayama, K. Tomiyama, H. Ootoshi, and H. Suematsu, Electronic transport and magnetic properties of carbon nanotubes, in *Molecular Nanostructures*, H. Kuzmany, J. Fink, M. Mehring, and S. Roth, Eds., World Scientific, Singapore (1998), pp. 439–442.
59. F. Tsui, L. Jin, and O. Zhou, Anisotropic magnetic susceptibility of multiwalled carbon nanotubes, *Appl. Phys. Lett.* 76, 1452 (2000).
60. P. de Rango, M. Lees, P. Lejay, A. Sulpice, R. Tournier, M. Ingold, P. Germin, and M. Pernet, Texturing of magnetic materials at high temperature by solidification in a magnetic field, *Nature (London)* 349, 770 (1991).
61. M. Fujiwara, N. Fukui, and Y. Tanimoto, Magnetic orientation of benzophenone crystals in fields up to 80.0 kOe, *J. Phys. Chem. B* 103, 2627 (1999).
62. T. Kimura, H. Ago, M. Tobita, S. Ohshima, M. Kyotani, and M. Yumura, Polymer composites of carbon nanotubes aligned by a magnetic field, *Adv. Mater.* 14, 1380 (2002).
63. M. Fujiwara, E. Oki, M. Hamada, Y. Tanimoto, I. Mukouda, and Y. Shimomura, Magnetic orientation and magnetic properties of a single carbon nanotube, *J. Phys. Chem. A* 105, 4383 (2001).
64. M. Fujiwara, K. Kawakami, and Y. Tanimoto, Magnetic orientation of carbon nanotubes at temperatures of 231 K and 314 K, *Mol. Phys.* 100, 1085 (2002).
65. D. A. Walters, M. J. Casavant, X. C. Qin, C. B. Huffman, P. J. Boul, L. M. Ericson, E. H. Haroz, M. J. O'Connell, K. Smith, D. T. Colbert, and R. E. Smalley, In-plane-aligned membranes of carbon nanotubes, *Chem. Phys. Lett.* 338, 14 (2001).
66. M. J. Casavant, D. A. Walters, J. J. Schmidt, and R. E. Smalley, Neat macroscopic membranes of aligned carbon nanotubes, *J. Appl. Phys.* 93, 2153 (2003).
67. S. Zaric, G. N. Ostojic, J. Kono, J. Shaver, V. C. Moore, M. S. Strano, R. H. Hauge, R. E. Smalley, and X. Wei, Estimation of magnetic susceptibility anisotropy of carbon nanotubes using magneto-photoluminescence, *Nano Lett.* 4, 2219 (2004).
68. M. J. O'Connell, S. M. Bachilo, C. B. Huffman, V. C. Moore, M. S. Strano, E. H. Haroz, K. L. Rialon, P. J. Boul, W. H. Noon, C. Kittrell, J. Ma, R. H. Hauge, R. B. Weisman, and R. E. Smalley, Band gap fluorescence from individual single-walled carbon nanotubes, *Science* 297, 593 (2002).
69. S. M. Bachilo, M. S. Strano, C. Kittrell, R. H. Hauge, R. E. Smalley, and R. B. Weisman, Structure-assigned optical spectra of single-walled carbon nanotubes, *Science* 298, 2361 (2002).
70. L. Langer, V. Bayot, E. Grivei, J.-P. Issi, J. P. Heremans, C. H. Oik, L. Stockman, C. van Haesendonck, and Y. Bruynseraede, Quantum transport in a multiwalled carbon nanotube, *Phys. Rev. Lett.* 76, 479 (1996).
71. J.-O. Lee, J.-R. Kim, J.-J. Kim, J. Kim, N. Kim, J.W. Park, K.-H. Yoo, and K.-H. Park, Magnetoresistance and differential conductance in multiwalled carbon nanotubes, *Phys. Rev. B* 61, R16362 (2000).
72. S. Roche and R. Saito, Magnetoresistance of carbon nanotubes: from molecular to mesoscopic fingerprints, *Phys. Rev. Lett.* 87, 246803 (2001).
73. G. Ferorov, B. Lassagne, M. Sagnes, B. Raquet, J.-M. Broto, F. Triozon, S. Roche, and E. Flahaut, Gate-dependent magnetoresistance phenomena in carbon nanotubes, *Phys. Rev. Lett.* 94, 066801 (2005).

74. S. Zaric, G.N. Ostojic, J. Shaver, J. Kono, O. Portugall, P. H. Frings, G.L.J.A. Rikken, M. Furis, S.A. Crooker, X. Wei, V.C. Moore, R.H. Hauge, and R.E. Smalley, Excitons in carbon nanotubes with broken time-reversal symmetry, *Phys. Rev. Lett.* 96, 016406 (2006).
75. T. Ando, Effects of valley mixing and exchange on excitons in carbon nanotubes with Aharonov-Bohm flux, *J. Phys. Soc. Jpn.* 75, 024707 (2006).

## chapter six

---

# Raman spectroscopy of single-walled carbon nanotubes: probing electronic and chemical behavior

*Stephen K. Doorn*

*Los Alamos National Laboratory*

*Daniel Heller, Monica Usrey, Paul Barone, Michael S. Strano*

*University of Illinois–Urbana/Champaign*

### Contents

6.1	Introduction .....	154
6.2	Resonance Raman studies of carbon nanotubes .....	156
6.2.1	Near-infrared Raman enhancement profiling of individualized carbon nanotubes .....	156
6.2.2	Chirality dependence of the Raman cross section .....	161
6.2.3	Intertube interaction effects .....	163
6.3	Raman characterization of nanotube samples and nanotube reactivity .....	167
6.3.1	Raman evaluation of the extent of nanotube aggregation .....	169
6.3.2	Experimental Kataura plots .....	171
6.3.3	Use of Raman spectroscopy to monitor covalent chemical reactions at nanotube surfaces .....	176
6.3.3.1	Review of carbon nanotube covalent chemistry .....	176

6.3.3.2	The pyramidalization angle formalism for carbon nanotube reactivity .....	177
6.3.3.3	Selective covalent chemistry of single-walled carbon nanotubes.....	178
6.4	Conclusions.....	181
	References.....	182

## 6.1 Introduction

Raman spectroscopy is a powerful, multifaceted technique with wide-ranging applications in carbon nanotube studies. As a vibrational spectroscopy it has been demonstrated to be invaluable for characterization of nanotube diameter distributions for monitoring production methods.<sup>1–4</sup> Facile evaluation of nanotube diameters is made possible by the presence of the radial breathing mode (RBM), which appears in the low-frequency (100 to 400 cm<sup>-1</sup>) region of the nanotube Raman spectrum and has an inverse dependence on nanotube diameter.<sup>5</sup> This ease of sample characterization has made Raman attractive for real-time monitoring of nanotube processing<sup>6,7</sup> and various separation methods.<sup>8–13</sup> Raman is also capable of identifying nanotube electronic nature through analysis of the nanotube G-band, found near 1600 cm<sup>-1</sup>. Semiconducting nanotubes produce a two-peak G-band structure (G<sub>+</sub> and G<sub>-</sub> bands) with Lorentzian line shapes, while the G<sub>-</sub> peak in metallic types shows a pronounced broadening with a Breit–Wigner–Fano (BWF) line shape.<sup>14–16</sup> (This line shape is caused when the tangential phonon couples to the continuum of electronic states at the Fermi level.) Additionally, measurement of the nanotube D-band (found near 1300 cm<sup>-1</sup>) can provide an evaluation of the defect density occurring in a sample and provides a useful tool for monitoring the extent of covalent sidewall modification in nanotube functionalization chemistry.<sup>17,18</sup>

Through the resonance Raman effect,<sup>19</sup> Raman spectroscopy becomes a sensitive probe of nanotube electronic structure and coupling of phonons to electronic transitions.<sup>1,2,20–30</sup> Strong resonance enhancement is obtained from nanotubes through tuning of the excitation wavelength to overlap the van Hove singularities present in the one-dimensional density of states of different nanotube species.<sup>31</sup> Because the electronic resonances are dependent on nanotube diameter and chirality, only a subset of the total nanotube population is accessed at any given excitation wavelength. Although this may complicate its application for routine sample characterization, for some sample types it makes Raman the only practical probe of nanotube band structure. This is clearly seen for spectra of solid, roped nanotube samples. In roped systems, intertube interaction effects red shift, broaden, and suppress the van Hove transitions to the extent that the individual features of separate chiralities are not resolvable by conventional absorption spectroscopy. Resonance Raman excitation profiling becomes a useful means of mapping out transitions of different chiralities for such samples.<sup>2,32,33</sup>

Absorbance spectra of single, isolated nanotubes have yet to be demonstrated, but the strong signal enhancements generated by accessing the large density of states present at resonance excitation in a Raman measurement make single-nanotube detection and spectroscopy possible. Dresselhaus and coworkers have pioneered experimental methods demonstrating single-nanotube Raman spectroscopy.<sup>25–30</sup> These studies have demonstrated the utility of Raman for chirality assignments and have uncovered a variety of new nanotube photophysical behaviors (including polarization and antenna effects, double resonance processes, and chirality effects). Single-nanotube spectroscopy has also paved the way for the recent development of nanotube imaging, including both near-field and confocal imaging techniques.<sup>34–37</sup>

The single-nanotube Raman studies demonstrate well that development of new techniques and probing of new sample types will invariably lead to new insights into nanotube chemistry and physics. Another prime example is the recent discovery of a method for producing samples of individualized nanotubes suspended in aqueous sodium dodecyl sulfate solution.<sup>38</sup> The subsequent discovery of band gap emission from semiconductor nanotube types has led to a revolution in nanotube photophysics. Availability of individualized nanotube suspensions has also created new opportunities for Raman studies. Among these is the ability to study nanotube vibrational behavior free of intertube interactions, assess intertube interaction effects (although a full analysis is complicated by environmental effects; see [Section 6.2.3](#)), and provide a determination of nanotube chiralities.<sup>33,40,41</sup> Another recent advance in nanotube synthesis that has produced novel sample types for Raman investigations has been the development of ultralong nanotubes with lengths of up to several centimeters.<sup>42–45</sup> Such macroscopic lengths hold significant potential for future applications in nanoelectronics, sensors, and high-strength, lightweight materials. These nanotube types also provide a unique experimental system for probing uniformity of nanotube structure and electronic and optical properties over large length scales.<sup>45,46</sup>

This chapter presents an overview of Raman studies performed in our laboratories on solution phase and related nanotube samples. Raman enhancement profile studies of individualized nanotube suspensions have provided confirmation of fluorescence-based chirality assignments and have also led to the discovery of a strong chirality dependence in the RBM Raman scattering cross sections.<sup>40</sup> The solution phase studies have also enabled a direct experimental determination of intertube interaction effects on nanotube electronic and vibrational structure.<sup>33</sup> In addition to enabling the discovery of new photophysical behavior in nanotubes, these investigations have led to improved assignments of vibrational features observed at a wide range of specific excitation energies. These results have important consequences for evaluating chirality distributions — of significant value in probing chirality-specific reaction chemistry and separations.



## 6.2 Resonance Raman studies of carbon nanotubes

### 6.2.1 Near-infrared Raman enhancement profiling of individualized carbon nanotubes

Past efforts at assigning carbon nanotube chiralities based on a comparison of Raman spectral data for nanotubes of relatively large diameter (1 to 3 nm) to theoretically based mappings of diameter to transition energies have met with limited success.<sup>21–23,25,30</sup> More recently, patterns observed in photoluminescence excitation (PLE) spectra of semiconducting nanotubes led to a semiempirical description of nanotube transition energies. This description incorporated deviations from limited tight-binding theory as described by functional forms that address trigonal warping and curvature effects, which become more important for the smaller-diameter (0.6- to 1.3-nm) high-pressure carbon monoxide (HiPco) nanotubes studied here.<sup>39</sup> Resultant chirality assignments agreed quite well with a limited amount of nanotube RBM data used to calibrate the assignments. A more detailed confirmation of these fluorescence-based assignments provided, in part, the motivation behind our efforts at obtaining near-infrared resonance Raman excitation profiles (REP) of individualized semiconducting nanotubes.<sup>40</sup>

Solution samples of individualized HiPco-produced<sup>47,48</sup> nanotubes were prepared as published previously.<sup>38</sup> A typical preparation combines 1 wt.% of sodium dodecyl sulfate (SDS) with 40 mg of nanotubes in 200 ml of water or D<sub>2</sub>O, followed by high shear mixing for 1 h, and ultrasonication at 540 W for 10 min. Suspensions are then centrifuged for 4 h at 122,000 g using a swing bucket rotor. The resulting decants are isolated and used for subsequent Raman experiments. Efficient individualization of the nanotubes can be verified by their display of strong band-gap emission. Solid samples of bundled HiPco single-walled carbon nanotubes (SWNTs) were prepared for investigations of intertube interaction effects. A suspension of 10 mg of solid, unprocessed nanotubes in 10 ml of isopropanol was added dropwise to a microscope slide and allowed to dry to form an opaque SWNT film.

Scanning Raman spectroscopy in the near-infrared was performed on the HiPco nanotube samples with excitation from a Ti:sapphire laser operating between 695 and 985 nm. A triple monochromator and charge-coupled device (CCD) camera were used for spectral collection. Typical laser power at the sample was 15 mW. Raw spectra must be background subtracted to remove the overlapping broad emission features originating from the semiconducting SWNTs. Each Raman spectrum in the region from 125 to 400 cm<sup>-1</sup> was then fit using a summation of Lorentzian peak shapes. Spectral intensities were then corrected for instrument response and  $\nu^4$  dependence.

Resonance Raman spectra, obtained with excitation wavelengths between 695 and 985 nm, of individualized HiPco nanotubes in aqueous SDS solution are shown in Figure 6.1a and b. Excitation in this region primarily accesses the  $\nu_2$ -c<sub>2</sub> (or E<sub>22</sub>) transitions and a limited number of  $\nu_1$ -c<sub>1</sub> (or E<sub>11</sub>) transitions of semiconducting nanotubes. Variation in resonant

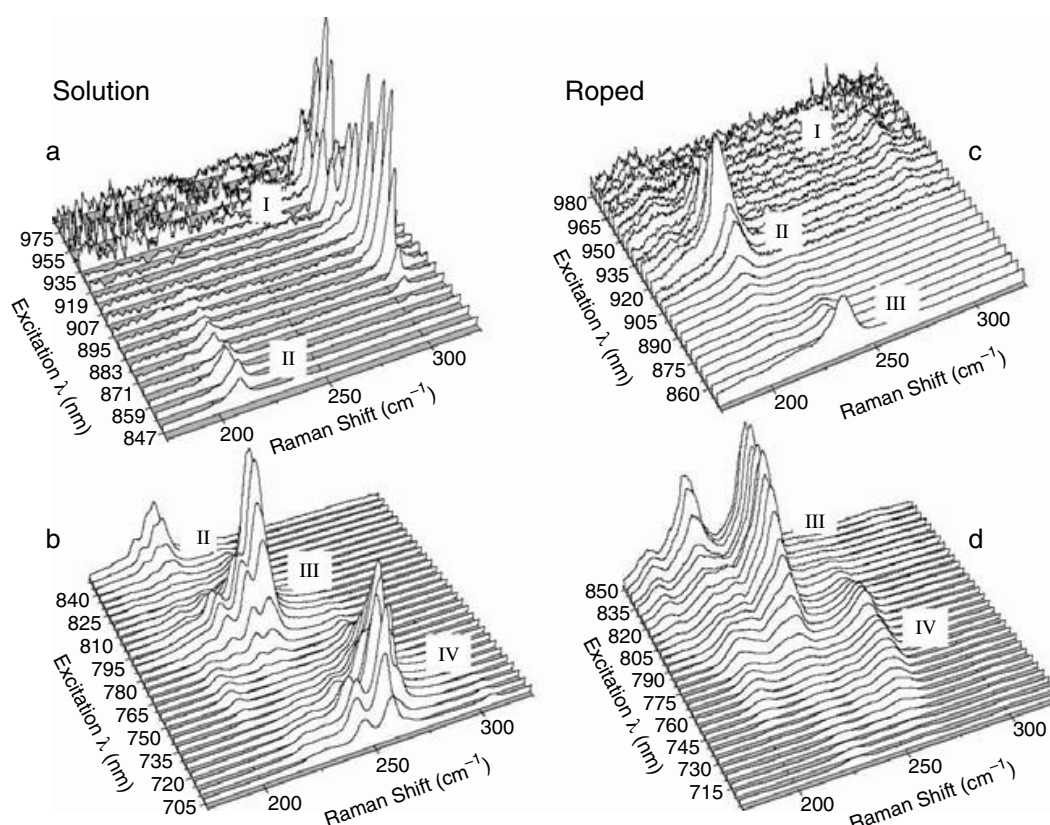


**Figure 6.1** Raman spectra of radial breathing modes for semiconducting nanotubes excited in the region of 700 to 985 nm for (a, b) individualized nanotubes in 1% SDS. (c, d) Solid bundled nanotube sample. Grouping I corresponds to E<sub>11</sub> excitation, while groupings II to IV correspond to E<sub>22</sub> excitation. (From O'Connell, M.J. et al., *Phys. Rev. B*, 69, 235415, 2004. With permission.)

excitation wavelength with nanotube chirality and diameter results in the four periodic groupings of RBMs observed in Figure 6.1a and b, and allows the resolution of a large number of nanotube chiralities, including those with identical RBM frequency, but separated by large resonant energy differences. This effective two-dimensional spectral separation allowed the observation of 22 individual semiconductor types with RBM frequencies ranging from 183 to 373 cm<sup>-1</sup>, corresponding to diameters of 1.3 to 0.6 nm.

The groupings observed in Figure 6.1 are a natural consequence of the nanotube chiralities being well described as families with  $2n + m = 3p + r$  ( $p$  = integer;  $r = 0, 1$ , and  $2$ , corresponding to metallic, type I, and type II semiconducting nanotubes, respectively).<sup>49</sup> We note that types I and II defined here correspond to the  $(n-m) \bmod 3 = 2$  or  $1$ , respectively, used in Bachilo et al.<sup>39</sup> and Doorn et al.<sup>40</sup> Such families are easily observed in photoluminescence excitation data<sup>39</sup> and result from clustering of chiralities as energy deviations from the near-armchair axis. For E<sub>22</sub> excitation, these deviations are positive for type II and negative for type I semiconductors. This dependence inverts on going to E<sub>11</sub> excitation and is determined by which side of the K-point in the graphite Brillouin zone the respective electronic states originate. Deviations from the near-armchair energy become larger as

the chirality progresses to the limit of near zigzag. At the near-zigzag terminus of a given family, transition energies and RBM frequencies switch over to the near-armchair behavior of the next set of families in the series, resulting in the apparent RBM oscillatory behavior observed here and by others.<sup>1,2</sup> Our groups labeled I, II, III, and IV (Figure 6.1) have primary contributions from  $2n + m$  families of 22 and 23, 25 and 26, 28 (and higher), and 17 and 19, respectively.

Enhancement profiles for 11 specific nanotube chiralities are shown in Figure 6.2. Relative intensities have been corrected for spectrometer response and  $\nu^4$  dependences. The enhancement profiles provide transition maxima for each individual nanotube type observed. When paired with their corresponding RBM frequency ( $\omega_{\text{RBM}}$  in  $\text{cm}^{-1}$ ), and thus nanotube diameter ( $d_t$  in nm) through Equation 6.1,<sup>39</sup> the Raman profile data can in many cases uniquely identify a single-nanotube chirality.

$$\omega_{\text{RBM}} = 223.5/d_t + 12.5 \quad (6.1)$$

Table 6.1 summarizes the results for all observed semiconducting RBMs, showing the assigned chiralities and comparing both the predicted and observed frequencies for each  $(n, m)$  feature. Raman excitation maxima are also compared to predicted or observed fluorescence maxima.<sup>39</sup> The standard deviation of differences between predicted and measured RBM frequencies is  $1.23 \text{ cm}^{-1}$ , while for the excitation the value is  $13.3 \text{ meV}$ . The close agreement in these values provides confidence in the chirality assignments and supports the use of the fluorescence-based, semiempirical model for the determination and assignment of nanotube chiralities.<sup>39</sup>

Recently completed Raman studies have now also probed the full range of  $E_{22}$  excitation (from  $1.51$  to  $2.71 \text{ eV}$ ).<sup>50,51</sup> These new results are in excellent agreement with both the fluorescence-based predictions<sup>39</sup> and our observed positions for excitation maxima (within an average deviation of  $11 \text{ meV}$ ). This deviation is consistently positive and arises from two Raman profile maxima being expected for incident and scattered photon resonances (see Equation 6.2). The individual peaks are masked by the broadened profile. The true transition energy results from a correction of the experimental  $E_{\text{max}}$  listed in Table 6.1 by subtracting  $1/2\omega_{\text{RBM}}$ . This results in nearly exact agreement among the three independent Raman studies. The results of Telg et al.<sup>50</sup> and Fantini et al.<sup>51</sup> also detail the  $2n + m$  family behavior that is observed in photoluminescence (PL) excitation plots.<sup>39</sup>

Thus, a growing body of experimental results supports the initial fluorescence-based chirality assignments of Bachilo et al.<sup>39</sup> PL studies on larger-diameter ( $1.2$ - to  $1.4$ -nm) laser vaporization-grown nanotubes are also in agreement with these semiempirical models.<sup>52</sup> The combined Raman and PL evidence demonstrates a need for further refinement of theoretical models of nanotube electronic structure. In fact, recent advances in extended tight-binding approaches,<sup>49,53</sup> which now include such parameters as long-range orbital interactions and detailed curvature effects, do an excellent

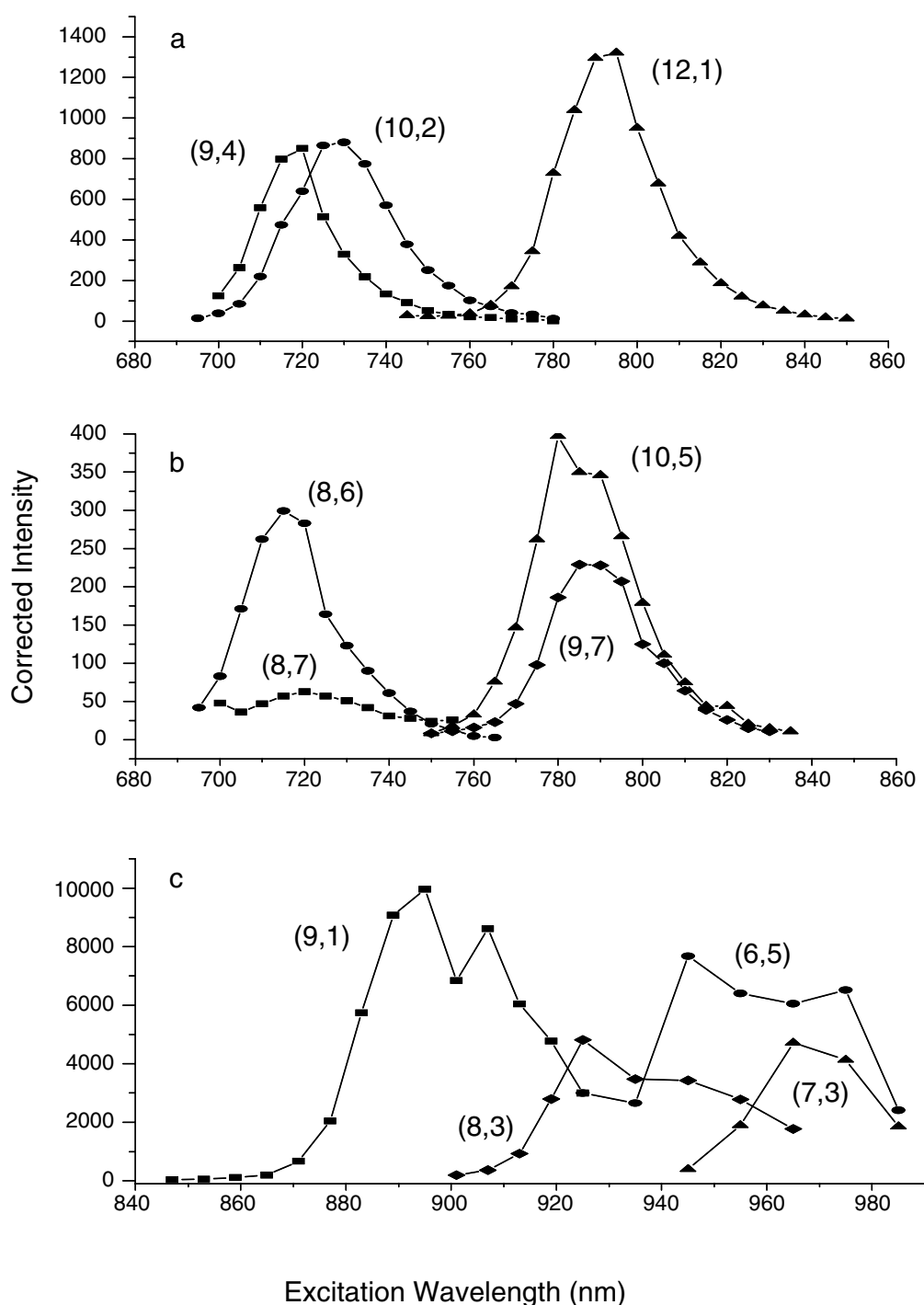


**Figure 6.2** Raman excitation profiles for several RBM frequencies/tube types: (a)  $256.4\text{ cm}^{-1}/(9, 4)$ ,  $264\text{ cm}^{-1}/(10, 2)$ , and  $236\text{ cm}^{-1}/(12, 1)$ ; (b)  $244\text{ cm}^{-1}/(8, 6)$ ,  $229\text{ cm}^{-1}/(8, 7)$ ,  $225\text{ cm}^{-1}/(10, 5)$ , and  $215\text{ cm}^{-1}/(9, 7)$ ; (c)  $304\text{ cm}^{-1}/(9, 1)$ ,  $307\text{ cm}^{-1}/(6, 5)$ ,  $296\text{ cm}^{-1}/(8, 3)$ , and  $327\text{ cm}^{-1}/(7, 3)$ . (From Doorn, S.K. et al., *Appl. Phys. A Mater. Sci. Proc.*, 78, 1147, 2004. With permission.)

job of reproducing the observed  $2n + m$  family behaviors. With the addition of contributions from many-body effects, nearly quantitative results are now obtained. These developments illustrate a useful convergence of experiment and theory. One future challenge will be to extend both modeling and

**Table 6.1** Comparison of Experimentally Observed and Predicted Raman Shifts and Transition Maxima for Semiconducting Nanotubes

Semiconductor	$d_t$ (nm)	$\nu_{\text{RBM}}$ ( $\text{cm}^{-1}$ )	Predicted <sup>a</sup>	$\lambda_{\text{exc}}^{\text{max}}$ (nm)	$\lambda_{\text{u}}$ (nm) <sup>b</sup>
(5, 4)	0.6201	373	372.7	826	833 <sup>c</sup>
(6, 4)	0.6921	—	335.4	—	874 <sup>c</sup>
(7, 3)	0.7056	327	329.2	969	—
(6, 5)	0.7573	307	307.4	970	975 <sup>c</sup>
(9, 1)	0.7573	304	307.4	905	912 <sup>c</sup>
(8, 3)	0.7819	296	298.1	944	952 <sup>c</sup>
(10, 2)	0.8841	264	265.1	729	734 <sup>d</sup>
(9, 4)	0.9156	256	256.4	718	720 <sup>d</sup>
(8, 6)	0.9658	244	243.7	716	716 <sup>d</sup>
(12, 1)	0.9948	236	237.0	792	797 <sup>d</sup>
(8, 7)	1.0321	229	228.9	720	728 <sup>d</sup>
(10, 5)	1.0503	225	225.1	785	786 <sup>d</sup>
(11, 4)	1.0681	221	221.5	713	714 <sup>d</sup>
(9, 7)	1.1029	215	214.9	789	790 <sup>d</sup>
(13, 2)	1.1200	211	211.9	857	859 <sup>d</sup>
(12, 4)	1.1450	206	207.5	855	857 <sup>d</sup>
(13, 3)	1.1700	205	203.4	754	760 <sup>d</sup>
(9, 8)	1.1700	203	203.4	794	809 <sup>d</sup>
(11, 6)	1.1856	200	200.8	866	858 <sup>d</sup>
(11, 7)	1.2477	193	191.4	850	838 <sup>e,d</sup>
(15, 2)	1.2777	188	187.2	833	825 <sup>e,d</sup>
(14, 4)	1.2997	183	184.3	845	846 <sup>e,d</sup>

<sup>a</sup> Using Equation 6.1 and assuming a C–C bond distance of 0.144 nm.

<sup>b</sup> Observed from fluorescence data.<sup>39</sup>

<sup>c</sup> ii = 11.

<sup>d</sup> ii = 22.

<sup>e</sup> Obtained from extrapolation of fluorescence results.<sup>39</sup>

Source: Doorn, S.K. et al., *Appl. Phys. A Mater. Sci. Proc.*, 78, 1147, 2004. With permission.

experimental determination of transitions to provide accurate assignments for  $E_{33}$  and  $E_{44}$  transitions in semiconductors and the  $E_{22}$  region of metallics. This information will be particularly useful for visible excitation studies of large-diameter nanotubes ( $>1.4$  nm).

Finally, we note the structure observed in the profiles in Figure 6.2c. The multiple peak structure is reproducible, with peak separations on the order of the frequency of the RBMs. We therefore assign these features to vibronic structure and use the lowest-energy feature to approximate the electronic transition energy used in Table 6.1. Although these features are clearly present for the  $E_{11}$  profiles, they are not observed in the  $E_{22}$  region. Whether this behavior originates from simple differences in transition line widths between the two excitation regions or results from varying electron–phonon coupling behavior or other effects remains an open question currently under study.



### 6.2.2 Chirality dependence of the Raman cross section

Shown in Figure 6.3 is a plot of intensity (corrected for instrument and  $\nu^4$  response) of the observed RBMs as a function of nanotube diameter. An interesting trend is observed: with  $E_{22}$  excitation, the mod  $(n-m, 3) = 2$  types (mod 2) generally have a larger intensity than mod  $(n-m, 3) = 1$  types (mod 1). Superposition of a plausible diameter-based concentration distribution (with center at 0.93 nm and standard deviation of 0.12 nm)<sup>2</sup> suggests that the intensity trend is an intrinsic property of the mod 1 vs. mod 2 classification, and does not result from differing populations of the respective chiralities. Additionally, the observed chirality dependence reverses on going from  $E_{11}$  to  $E_{22}$  excitation. For example, we find the mod 2 (6, 4) chirality to be very weak in  $E_{11}$  excitation, while it is observed quite strongly in the  $E_{22}$  region.<sup>41</sup> Conversely, the mod 1 (8, 4) tube occurs only weakly (in comparison to mod 2 types) with  $E_{22}$  excitation.<sup>41</sup>

The two classes of semiconductor types are known to have fundamental differences in electronic structure arising from trigonal warping effects.<sup>39,54</sup> As noted earlier, for the  $E_{11}$  region, the effect is to push mod 2 transitions to higher, and mod 1 transitions to lower, energy relative to the near-armchair curve expectation. The behavior is reversed on going to  $E_{22}$  excitation. Similar

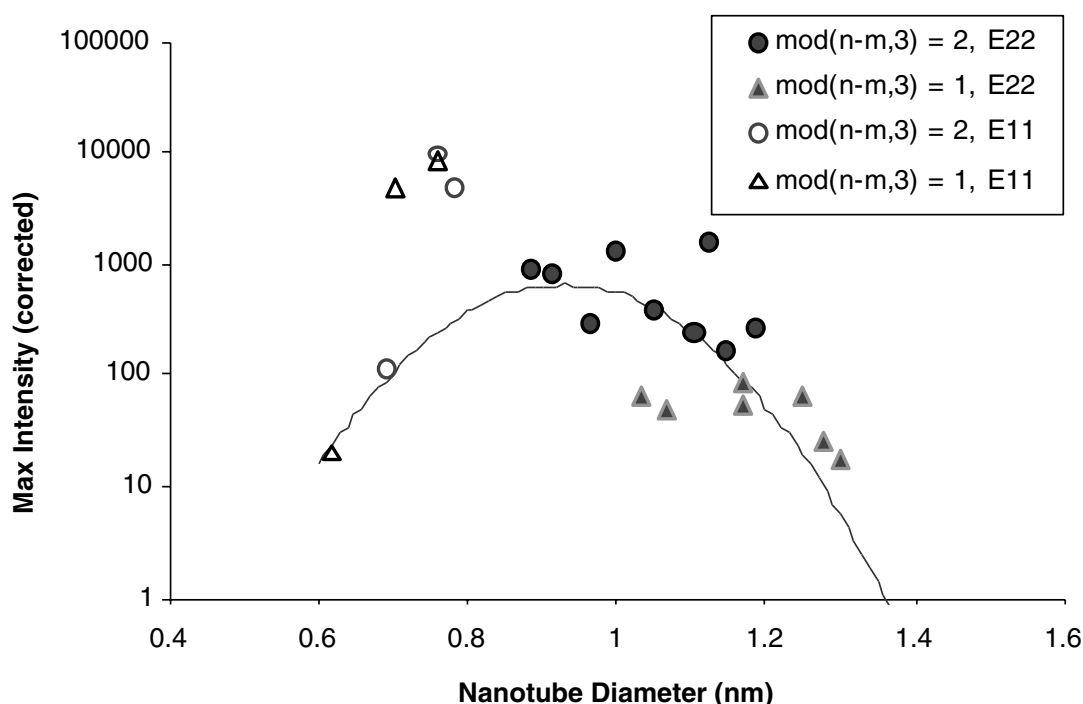


**Figure 6.3** REP-corrected intensity maxima vs. diameter for mod 1 and mod 2 semiconductors for  $E_{11}$  and  $E_{22}$  excitation. Dotted curve is an approximate diameter abundance distribution for use as a guide. (From Doorn, S.K. et al., *Appl. Phys. A Mater. Sci. Proc.*, 78, 1147, 2004. With permission.)

results are predicted for the effects of trigonal warping on absorption matrix elements and, by analogy, to the electron–photon coupling elements in Raman scattering.<sup>55</sup> Mod 2 types are predicted to have larger optical matrix elements in  $E_{11}$  than are expected for mod 1 types, with reverse behavior predicted in the  $E_{22}$  region. Although a mod 1 vs. mod 2 effect is predicted, with the expectation of a dependence reversal on switching excitation regions, the trend in Gruneis et al.<sup>55</sup> is the reverse of our observations.

The difference in predicted vs. observed behavior might be explained by the chirality dependence of the electron–phonon coupling. As seen in Equation 6.2, the Raman polarizability tensor ( $\alpha$ ) is dependent on both electron–photon ( $M_{ee}$ ) and electron–phonon ( $M_{ep}$ ) matrix elements.

$$\alpha = \sum_{ij} \frac{M_{ee}^{gi} M_{ee}^{ig} M_{ep}^{ij}}{(E_{\text{laser}} - E - i\Gamma_r)(E_S - E - i\Gamma_r)} \quad (6.2)$$

It will be important to determine experimentally the relative contributions of the two different matrix elements and to probe their chiral dependences. In particular, the electron–phonon coupling elements may be obtained through a comparison of RBM fundamental and overtone excitation behavior. Overtone data may be readily obtained for nanotubes with resonance excitation. For example, shown in Figure 6.4 is an RBM spectrum obtained at 770 nm excitation, with both fundamental and overtone regions displayed. The overtone features appear at very close to two times the frequency of the observed fundamental modes, indicating a low anharmonicity. We are currently obtaining more extensive overtone data and modeling relative excitation behavior of RBM fundamentals and overtones to explore further the chirality dependence of electron–phonon coupling.

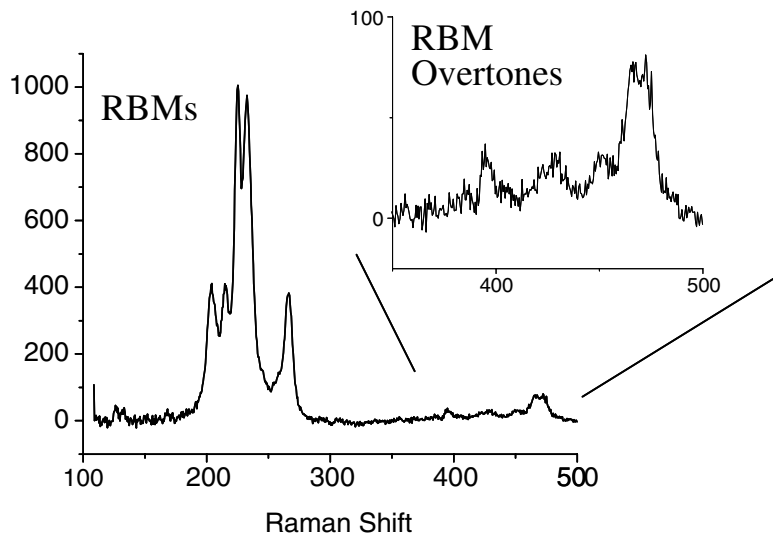


**Figure 6.4** Raman spectrum of RBM fundamental region obtained at 770 nm excitation and (inset) RBM overtone region.

Recent results have confirmed our observation that, for  $E_{22}$  excitation, Raman intensities for mod 2 chiralities will generally be more intense than for mod 1.<sup>50,56</sup> New theoretical studies confirm our expectation that this behavior originates in the electron–phonon coupling matrix element.<sup>56–59</sup> Both the contrasting mod 1 vs. mod 2 response and the reversal of their intensity behavior on changing excitation region ( $E_{11}$  vs.  $E_{22}$ ) are predicted. Additionally, chiral angle ( $\theta$ ) effects should be most easily observed within a given  $2n + m$  family, for which intensities should decrease significantly on going from near zigzag to near armchair. Explicit theoretical values of  $M_{ep}$  for several chiralities now exist.<sup>58</sup>

Inspection of Figure 6.2 demonstrates well the expected Raman intensity dependence on  $\theta$  within a given  $2n + m$  family. As seen for the  $2n + m = 25$ , 22, and 19 families, a steady decrease in intensity is observed on going from near-zigzag to near-armchair angles. This dependence on  $\theta$  also explains the seemingly contradictory behavior of the (9, 1) (mod 2 type) and the (6, 5) (mod 1 type) nanotubes shown in Figure 6.2c. Since the profiles shown are for  $E_{11}$  excitation, the (6, 5) intensity ought to be significantly more intense. Because of the  $\theta$  dependence, however, the intensities are comparable. By contrast, the (6, 4) (mod 2, with similar  $\theta$ ) intensity is a factor of 100 less than found for the (6, 5).

With the recent availability of calculated  $M_{ep}$  values,<sup>58</sup> direct comparison to experimentally determined values using the overtone data described above and other approaches will be valuable. With this new recognition of the chirality dependence found in  $M_{ep}$ , evaluation of its significance in other optical phenomena, such as photoluminescence excitation,<sup>60</sup> and in transport processes will be important.

### 6.2.3 Intertube interaction effects

Because of the strong van der Waals interactions between individual nanotubes, understanding intertube interaction effects on nanotube electronic and vibrational structure will have important implications for transport properties and potential nanoelectronics and materials applications, as well as for accurate interpretation of Raman analysis for process control. Although extensive theoretical studies of intertube interaction effects have been undertaken,<sup>61–64</sup> there have been few opportunities to directly measure this experimentally, due to the lack of appropriate sample types on which direct comparisons of interacting and noninteracting nanotube properties could be measured. Our ability to perform resonance Raman excitation profiles both on the newly developed solution phase, individualized nanotubes, and on analogous roped solid samples allow a direct evaluation of intertube interaction effects on electronic and vibrational properties.<sup>33</sup>

Near-infrared resonance Raman spectra of the RBM region for a roped nanotube sample are shown in Figure 6.1c and d. The four spectral groupings observed in the individualized nanotube spectra (Figure 6.1a and b) are clearly preserved in the roped data. The one-to-one correspondence of these

groups between the two sample types allows a direct tracking and comparison of the behavior of identical RBMs. For the bundled nanotubes, all spectral features are shifted to the red by 30 to 50 nm. Additionally, the bundled nanotube spectral regions appear blurred together, with individual RBM features appearing less well resolved. This is due to broadening of the electronic transitions. A comparison of enhancement profiles obtained for individualized and roped samples (Figure 6.5) allows a quantification of these effects. Results for the 13 chiralities observed in both data sets are directly compared in Table 6.2. A pronounced red shift (ranging from 54 to 157 meV) of transitions for all chiralities is clearly observed on going from individualized to bundled nanotubes. Additionally, transition widths are found to double and even triple (with an average factor of 2.4) on bundling for all chiralities.

Solvation/surfactant structure and sample processing effects can complicate analysis of the bundling effects. Environmental interactions can result in different degrees of stabilization of the nanotube electronic structure,<sup>65</sup> resulting in varying shifts in transition energy that may mask the total magnitude of the bundling effects. Nevertheless, our results compare well to theoretical expectations.

A number of theoretical studies predict a bundling-induced red shift in transition energies.<sup>61–64</sup> In particular, Reich et al.<sup>64</sup> have incorporated curvature-induced hybridization effects into their bundling studies. They find changes in the electronic dispersion along  $k_z$  that result in a red shift on the order of 100 meV for bundled nanotubes. A dispersion perpendicular to  $k_z$  is also found, resulting in broadening on the order of 200 meV. These results are in good agreement with our findings of an average shift of 86 meV and broadening of 77 to 120 meV.

A comparison of RBM frequencies observed for the individualized and bundled samples (Table 6.3) shows that bundling has no significant effect for 17 different chiralities. Our results demonstrate the significance of performing a direct comparison of experimental results for bundled and non-interacting systems. Previous experimental results<sup>1,2</sup> suggested that bundling can induce as much as an 8 to 10% upshift in RBM frequency, a change that we do not observe. These previous results, however, relied on comparing experimental results from bundled systems to theoretical predictions for noninteracting nanotubes. Our results suggest that the previous claims of an upshift in RBM frequency are actually only *apparent* frequency shifts resulting from the bundling-induced red shifting of the electronic transitions. We note that recent work has now both reproduced the bundling-induced red shifting we observe here and demonstrated the lack of significant change in semiconductor RBM frequencies.<sup>51</sup>

Figure 6.6 demonstrates that the differing resonance conditions between individualized and bundled nanotubes can result in markedly different RBM spectra for the two sample types observed at identical excitation wavelengths. A closer examination of Figure 6.1 reveals how the red-shifted electronic transitions affect the observed frequency of the RBM, and can result

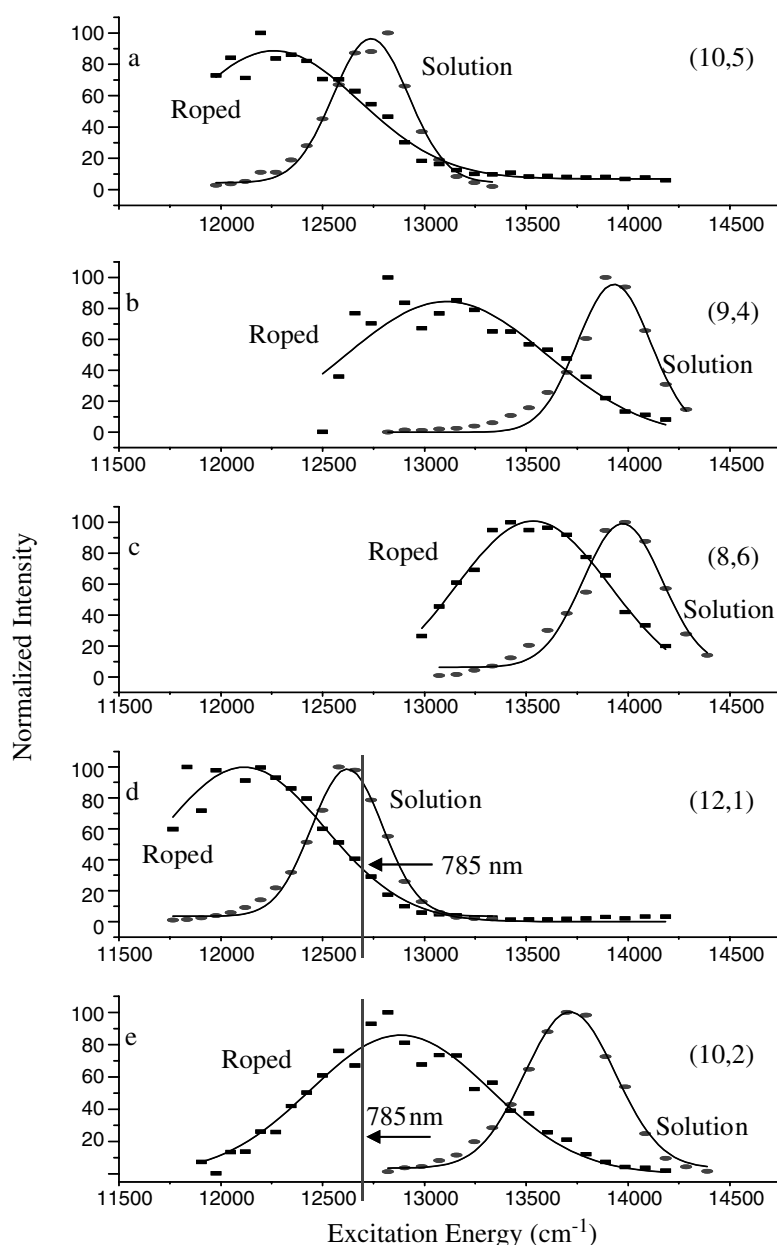


**Figure 6.5** Comparison of Raman excitation profiles for individualized and bundled nanotubes for (a) (10, 5), (b) (9, 4), (c) (8, 6), (d) (12, 1), and (e) (10, 2) chiralities (rectangles = roped data, ovals = individualized solution data). The vertical line in d and e designates the 785-nm-excitation line position.

in an apparent upshift in frequency. If the behavior at 785 nm excitation is observed, for example, as bundling occurs, the transition energies for group III are moved out of resonance and into the vicinity of transitions found for group II as isolated individuals. Similarly, the group IV transition energy region moves into resonance with the 785-nm excitation. As a result, one would expect the frequencies for group III (centered around  $225\text{ cm}^{-1}$ ) to undergo an apparent upshift to the group IV frequencies (centered around  $260\text{ cm}^{-1}$ ). The same behavior will occur at lower excitation energies, with the group II RBM frequencies (centered around  $200\text{ cm}^{-1}$ ) undergoing an apparent upshift to those of the group III frequencies.



**Table 6.2** A Comparison of Raman Enhancement Profile Energy Maxima and Transition Widths (Full Width at Half Maximum) for Individualized (Solution) and Roped Nanotube Samples

(n, m)	Diameter (nm)	E (pred) <sup>a</sup> (cm <sup>-1</sup> )	E (solution) <sup>b</sup> (cm <sup>-1</sup> )	E (roped) (cm <sup>-1</sup> )	$\Delta E^c$ (cm <sup>-1</sup> /meV)	Width (solution) (cm <sup>-1</sup> /meV)	Width (roped) (cm <sup>-1</sup> /meV)
(9, 1) <sup>d</sup>	0.7573	10,964	11,050	10,492	558 (69)	369 (46)	622 (77)
(9, 1) <sup>d</sup>	0.7573	14,466	14,430	13,804	626 (78)	—	964 (120)
(8, 3)	0.7819	15,029	—	14,286	743 (92)	—	—
(10, 2)	0.8841	13,574	13,717	12,883	834 (103)	446 (55)	883 (109)
(9, 4)	0.9156	13,843	13,928	13,105	823 (102)	333 (41)	952 (118)
(8, 6)	0.9658	13,928	13,967	13,534	433 (54)	432 (54)	763 (95)
(12, 1)	0.9948	12,516	12,626	12,115	511 (63)	350 (43)	793 (98)
(10, 5)	1.0503	12,695	12,739	12,209	530 (66)	370 (46)	936 (116)
(9, 7)	1.1029	12,658	12,674	12,200	474 (59)	380 (47)	—
(13, 2)	1.120	11,661	11,669	10,830	839 (104)	112 (14)	363 (45)
(12, 4)	1.145	11,693	11,696	10,874	822 (102)	278 (34)	757 (94)
(13, 3)	1.170	13,095	13,263	12,708	555 (69)	466 (58)	724 (90)
(11, 6)	1.1856	11,661	11,547	10,875	672 (83)	—	—
(11, 7)	1.2477	11,968	11,765	10,498	1267 (157)	—	713 (88)

<sup>a</sup> Predicted values obtained from Bachilo et al.<sup>39</sup>

<sup>b</sup> Experimental transition maxima for individualized solution samples obtained from Doorn et al.<sup>40</sup>

<sup>c</sup>  $\Delta E = E(\text{solution}) - E(\text{roped})$ , except for (8, 3) nanotube, for which  $\Delta E = E(\text{pred}) - E(\text{roped})$ .

<sup>d</sup> Note that both v1-c1 (first row) and v2-c2 (second row) results are shown for the (9, 1) nanotube.

Source: From O'Connell, M.J. et al., *Phys. Rev. B*, 69, 235415, 2004. With permission.

**Table 6.3** A Comparison of Measured RBM Frequencies for Individualized and Roped Samples

(n, m)	Diameter (nm)	$\nu$ (pred.) <sup>a</sup> (cm <sup>-1</sup> )	$\nu$ (solution) <sup>b</sup> (cm <sup>-1</sup> )	$\nu$ (roped) (cm <sup>-1</sup> )	$\Delta\nu^c$ (cm <sup>-1</sup> )
(8, 0)	0.6350	364.4	—	364	0
(6, 4)	0.6921	335.4	—	333	-2
(6, 5)	0.7573	307.6	307	307	0
(9, 1)	0.7573	307.6	304	304	0
(8, 3)	0.7819	298.3	296	296	0
(7, 5)	0.8290	282.1	—	282	0
(10, 2)	0.8841	265.3	264	266	2
(9, 4)	0.9156	256.6	256	261	5
(8, 6)	0.9658	243.9	244	244	0
(12, 1)	0.9948	237.2	236	236	0
(10, 5)	1.0503	225.3	225	227	2
(9, 7)	1.1029	215.1	215	214	-1
(13, 2)	1.120	212.1	211	213	2
(12, 4)	1.145	207.7	206	209	3
(13, 3)	1.170	203.6	205	203	-2
(11, 6)	1.1856	201.0	200	201	1
(11, 7)	1.2477	191.6	193	192	-1

<sup>a</sup> Predicted values obtained from Bachilo et al.<sup>39</sup><sup>b</sup> Experimental  $\nu_{\text{RBM}}$  for individualized solution samples obtained from Doorn et al.<sup>40</sup><sup>c</sup>  $\Delta\nu = \nu$  (roped) -  $\nu$  (solution), except for (8, 0), (6, 4), and (7, 5) nanotubes, for which  $\Delta\nu = \nu$  (roped) -  $\nu$  (pred).Source: From O'Connell, M.J. et al., *Phys. Rev. B*, 69, 235415, 2004. With permission.

Figure 6.6g and h demonstrate a striking consequence of the red shifting of transitions, bringing into resonance new chiralities not observed at the same excitation wavelength in individualized samples. Red shifting moves the high-frequency modes (near 300 cm<sup>-1</sup>) of the (9, 1) and (8, 3) chiralities out of resonance and brings into resonance the low-frequency modes (near 210 cm<sup>-1</sup>) of the (13, 2) and (12, 4) species — a significant *apparent* downshift in frequency. The actual RBM frequency for any given chirality, however, remains the same, regardless of nanotube environment or aggregation state.<sup>6,9,33</sup>

### 6.3 Raman characterization of nanotube samples and nanotube reactivity

The results of the preceding section underscore the importance of understanding the effects of electronic perturbation on observed RBMs and other vibrational features. This is particularly relevant to the use of Raman for characterization of separation processes. Care must be taken to ensure that observed changes in relative RBM intensities are not incorrectly attributed

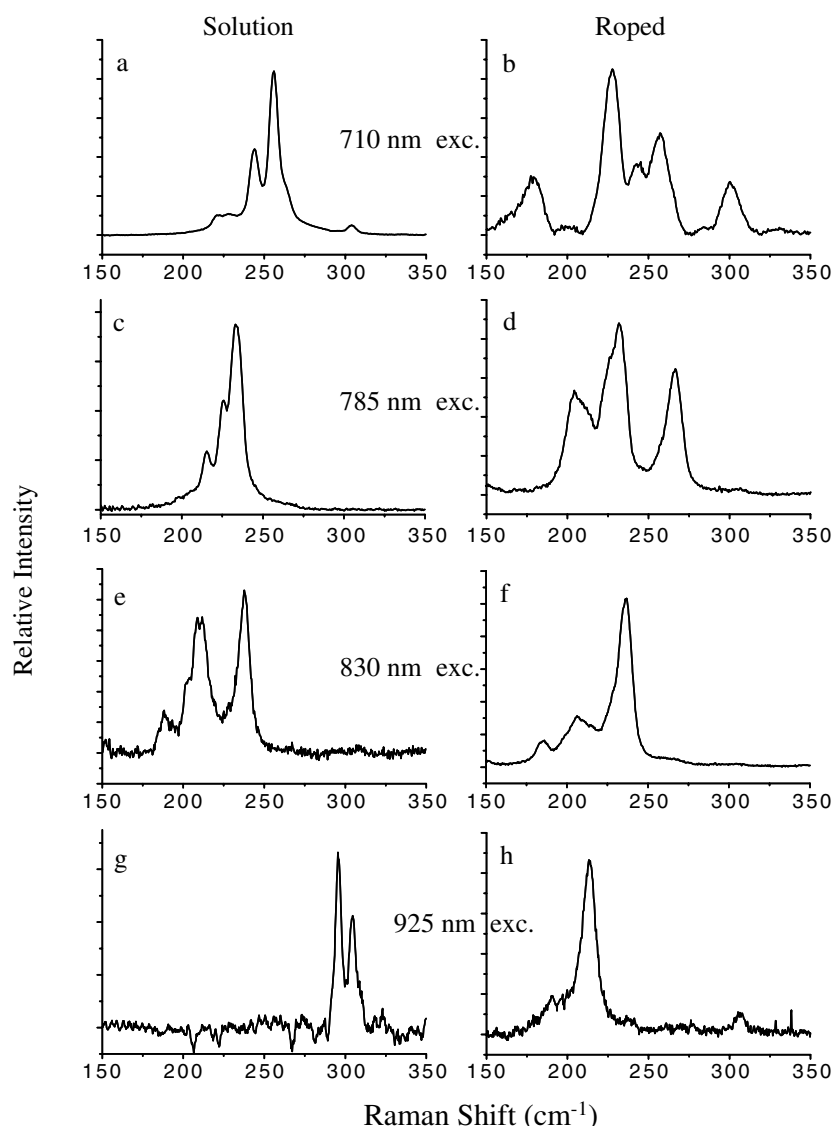


**Figure 6.6** Comparison of radial breathing mode spectra for individualized (solution) and roped (solid) nanotubes at four specific excitation wavelengths: 710 nm, (a) solution, (b) roped; 785 nm, (c) solution, (d) roped; 830 nm, (e) solution, (f) roped; 925 nm, (g) solution, (h) roped. (From O'Connell, M.J. et al., *Phys. Rev. B*, 69, 235415, 2004. With permission.)

to changes in relative populations of their corresponding chiralities when the cause may instead be a shift in electronic transition energies that brings a different set of chiralities into resonance with a specific excitation wavelength. Thus, despite the valuable information concerning SWNT sample composition, which Raman spectra provide, environmental conditions in the sample may alter the spectra, complicating use of the technique. The strong resonant enhancement and concomitant coupling between strength and energy of nanotube interband transitions cause spectral changes as physical<sup>38</sup> or chemical<sup>67</sup> conditions perturb the sample. Raman scattering can be resonantly enhanced or shifted out of resonance by nanotube bundling. Such cases are not limited to behavior of the RBM region. For instance, the

tangential G-mode at  $1593\text{ cm}^{-1}$  increases in intensity during sonication of a sample of nanotubes.<sup>6</sup> In addition, the aforementioned BWF feature may shift to become indistinguishable from the Lorentzian component of the tangential mode with decreasing pH.<sup>67</sup> In the following sections, we describe examples of practical uses of Raman spectroscopy for sample evaluation and monitoring of nanotube reaction chemistry.

### 6.3.1 Raman evaluation of the extent of nanotube aggregation

As noted in Section 6.2.3, nanotube aggregation can have a profound effect on the observed RBM spectrum. These effects have been found to vary according to the degree of aggregation in a particular sample. These intermediate effects of aggregation are illustrated on the RBMs of three different HiPco SWNT samples, excited at 785 nm, as shown in Figure 6.7. Figure 6.7a shows nanotubes in a 1% SDS/H<sub>2</sub>O solution at pH 10. Figure 6.7b shows solid HiPco SWNTs used as received and containing 28.5% Fe catalyst by weight. Figure 6.7c contains material from Figure 6.7a, which was deposited on a glass slide and heated until the water evaporated. Illustrations beside the spectra depict the believed aggregation state of the material, which increases from Figure 6.7a to Figure 6.7c. The spectra reveal a substantial decrease in the  $234\text{-cm}^{-1}$  mode and simultaneous increase in the  $267\text{-cm}^{-1}$  mode.

Thus, the use of 785 nm excitation can be a practical means for probing the extent of nanotube aggregation. Bundling of nanotubes results in increased enhancement of the (10, 2) RBM at  $264\text{ cm}^{-1}$ , relative to nearby RBMs (in particular the [12, 1] mode at  $236\text{ cm}^{-1}$ ), producing the so-called roping peak.<sup>6,9,33</sup> It is interesting to note that while the (10, 2) RBM at  $264\text{ cm}^{-1}$  is only strongly observed in the bundled samples with 785 nm excitation, the (12, 1) RBM at  $236\text{ cm}^{-1}$  appears strongly enhanced in both sample types (Figure 6.7a to c). This behavior can be understood as arising from the different resonant excitation conditions experienced by the two chiralities. As seen in Figure 6.7, 785-nm excitation is near the peak of the enhancement profile for the individualized (12, 1) nanotubes, but is well away from the resonant window for the (10, 2) in solution; thus, the (12, 1) RBM is observed but not the (10, 2). Bundling-induced red shifting places the 785-nm excitation near the peak of the (10, 2) transition, while significant intensity in the tail of the (12, 1) profile still remains. Therefore, for bundled samples, both the (12, 1) and (10, 2) chiralities will be observed. Recognizing that the relative intensities of the (12, 1) and (10, 2) RBMs will vary over the range of aggregation possibilities has led to a semiquantitative description of the extent of aggregation based on modeling of RBM spectra.<sup>66</sup>

The aggregation process can be modeled by using the spectral assignments of the six nanotubes present,<sup>66</sup> and a simple Gaussian distribution in nanotube diameters  $d_t$  ( $\sigma = 0.2\text{ nm}$ ,  $d_{\text{mean}} = 0.93\text{ nm}$ ) (Figure 6.8). We assume that interband transitions can be simplified as a delta function at energy  $E_{(n,m)}$  and that each spectral feature is Lorentzian, with shift given by  $223.5/d_t + 25.5$ .

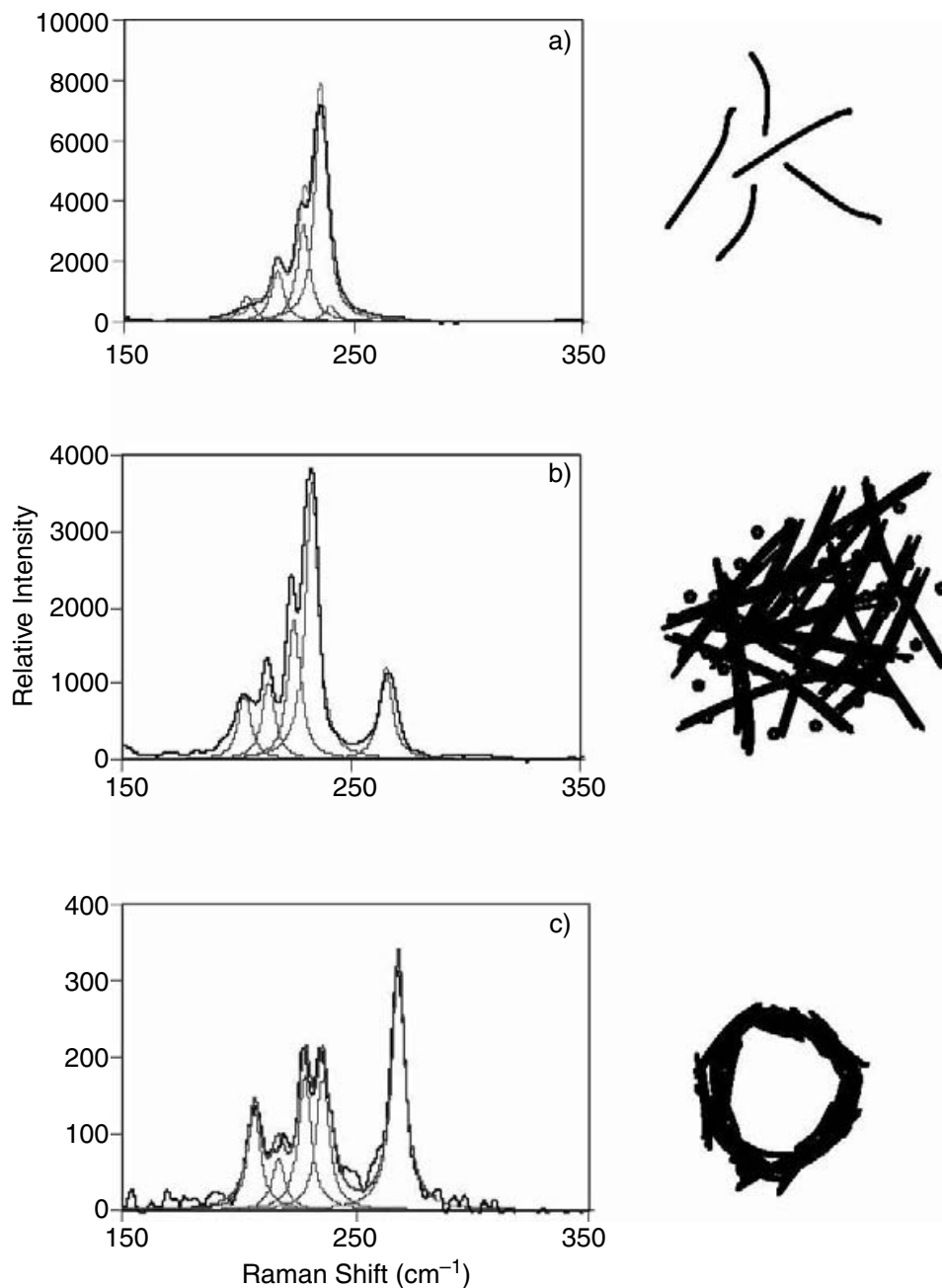


**Figure 6.7** Radial breathing modes of HiPco carbon nanotubes taken at three different states of aggregation: (a) individual tubes suspended in SDS, (b) raw HiPco material as received, (c) dry SDS-suspended tubes heated on a hot plate.

$$I(E_{\text{laser}}) \propto \frac{\frac{C_o}{\sigma\sqrt{4\pi}} \exp\left[-\frac{(d_t - d_{\text{mean}})^2}{4\sigma^2}\right]}{\left(\left(E_{\text{Laser}} - E_{(n,m)} + \Delta E\right)^2 + \frac{\Gamma^2}{4}\right) \left(\left(E_{\text{Laser}} - E_{\text{Phonon}} - E_{(n,m)} + \Delta E\right)^2 + \frac{\Gamma^2}{4}\right)} \quad (6.3)$$



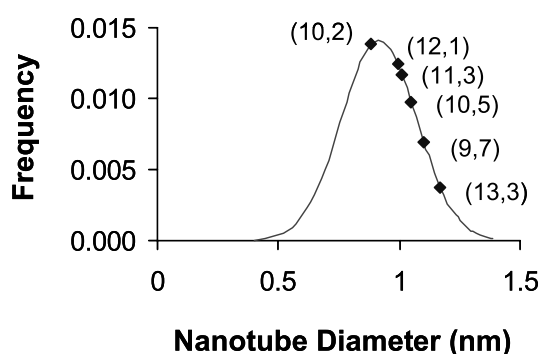


**Figure 6.8** Gaussian distribution of nanotube diameters highlighting the relative frequencies of six species.

In this expression,  $E_{\text{laser}}$  is the excitation energy while  $\Delta E$  and  $\Gamma$  are the energy shift upon roping and peak broadening due to environmental conditions surrounding the nanotube. We assume that  $\Delta E$  is the same for all transitions. Using Equation 6.3, we can simulate the Raman spectra observed in Figure 6.7. These simulated changes reflect those observed experimentally. For example, the  $267\text{-cm}^{-1}$  mode, which is the (10, 2) tube, is initially off-resonance with the 785-nm excitation laser. The transitions shift to lower energy with increasing aggregation state, as modeled by progressively larger  $\Delta E$ s and  $\Gamma$ s.

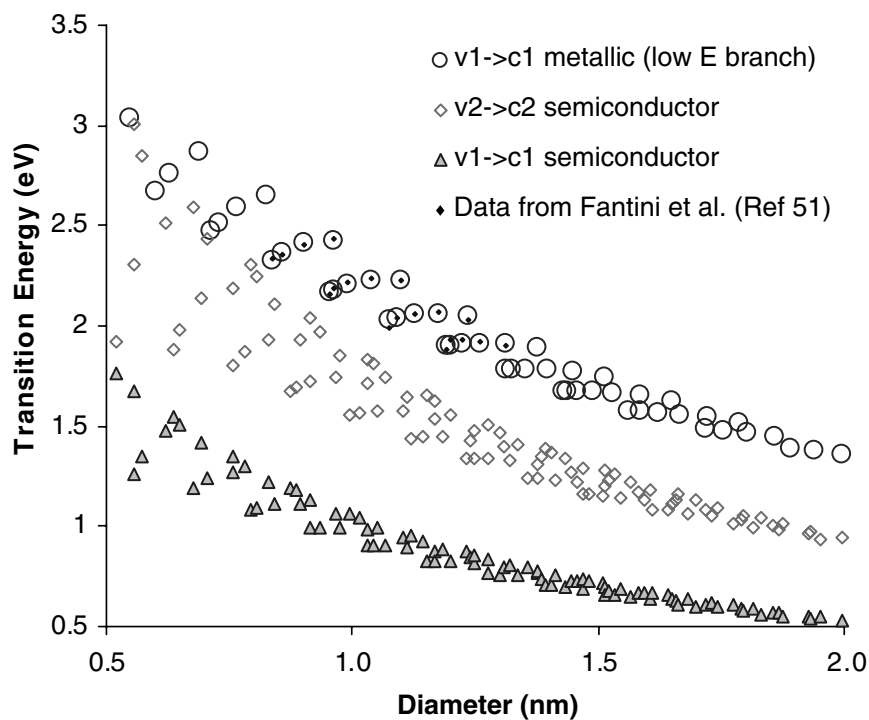
### 6.3.2 Experimental Kataura plots

Keeping in mind the need to be aware of the significant resonance effects discussed above, Raman is clearly a valuable tool for characterization of chirality distributions that result from different synthesis and processing techniques. Of significant interest is the potential that monitoring of RBMs has for tracking how specific chiralities respond to covalent and noncovalent reaction chemistries, and for evaluating the development of chirality-specific separation methods. For example, how may specific sidewall reactions and pathways be linked to the unique electronic structure of the nanotubes? This can be done by probing the radial breathing modes (and to some extent through monitoring G-band structure) of the nanotube populations that have electronic transitions in resonance with the excitation laser wavelength. Specific chirality tracking requires an accurate mapping of carbon nanotube electronic transitions as a function of diameter.<sup>16</sup> Of particular utility is the generation of plots specific to commonly accessible Raman excitation wavelengths (such as 830- and 785-nm diodes, 633-nm He-Ne, and 514-nm Ar-ion or 532-nm Nd:YAG excitation) that may be used conveniently for routine sample characterization. Even for cases in which there is a known strong electronic perturbation, such plots of ideal solution phase behavior serve as valuable reference points to which spectra can be compared.

The solution phase results discussed earlier have led to more accurate chirality assignments for subsequent organization into maps of transition energy vs. diameter. The first organization of this kind is attributed to

Kataura, using single-electron theory.<sup>16</sup> Using the tight-binding approximation, the electronic structure was described as a graphene sheet with electronic wavevectors quantized into unique integers.<sup>68</sup> This predicts the assignment of metallic and semiconducting electronic transitions based upon the chirality vector. However, the actual nanotube structure is more complicated than this simple formalism due to several effects, including trigonal warping and the warping of the Brillouin zone due to curvature.<sup>69</sup> Finally, as discussed above, single-electron models cannot include multiple electron/many-body effects, such as exciton interactions. This complicates the direct comparison of experimental results and theoretical predictions.<sup>70,71</sup>

In response to this problem, an experimentally based Kataura plot (Figure 6.9) has been generated.<sup>72</sup> All experiments were conducted using surfactant-suspended single-walled carbon nanotubes to avoid the perturbation of electronic transitions caused by nanotube ropes. Spectrofluorimetry has been utilized to map the electronic transitions of the semiconductors, denoted  $v_n \rightarrow c_n$ , where  $n$  denotes  $E_{11}$  ( $n = 1$ ) or  $E_{22}$  ( $n = 2$ ) transition. This mapping illustrated considerable deviations from the conventional Kataura plot.<sup>16</sup> Raman excitation profiles, using metallic absorbing excitations, have been used to map the  $v_1 \rightarrow c_1$  transitions for the metallic nanotube.<sup>41</sup> All experimental transitions were correlated using semiempirical models derived from asymptotic diameter expansions in the graphene dispersion relation.



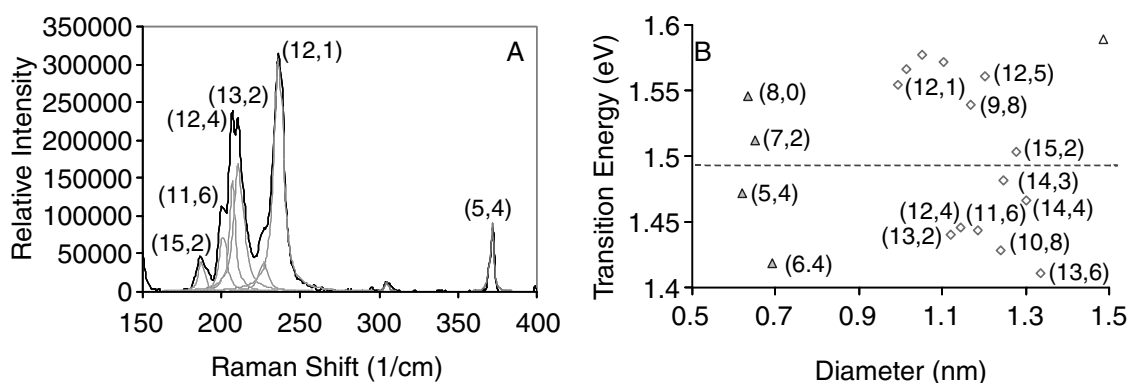
**Figure 6.9** Experimental mapping of transition energy vs. diameter for metallic and semiconducting single-walled carbon nanotubes. Metallic transitions are observed for only the low-energy transitions.

Figure 6.9 is a compilation of these results for carbon nanotubes up to 2 nm in diameter for the first and second semiconductor transitions and the first metallic and semimetallic transitions. The metallic transitions split into low- and high-energy transitions for nonarmchair ( $n \neq m$ ) metallic nanotubes, with the low-energy branch having an observable Raman cross section.<sup>51,68</sup> These nonarmchair species are actually semimetallic due to curvature-induced electronic gaps. This experimental mapping allows the interpretation of optical experiments involving single-walled carbon nanotubes.

When compared to the theoretically based Kataura plot, this experimental mapping shows an increased deviation from the armchair curve. This curve is a limiting inverse diameter curve providing the limit of the transition energy as the diameter approaches infinity. Specifically, small-diameter transitions show a notable dispersion in energy rather than an adherence to an inverse diameter relationship, in strong contrast to the single-electron theory. It is this dispersion that allows the probing of selective reaction chemistries using Raman spectroscopy.

The experimental Kataura plot (Figure 6.9) can be used to determine which nanotube diameters are in resonance with a particular excitation wavelength utilized in Raman spectroscopy. In turn, the coordinating Raman radial breathing modes can be calculated from this derived relationship using Equation 6.1. It is important to note that the values for the constants in Equation 6.1 are valid for HiPco samples under these conditions. Figure 6.10 to Figure 6.13 represent determinations of Raman RBM features from the experimental mapping for four distinct excitation wavelengths: 830, 785, 633, and 532 nm, respectively.

In Figure 6.10a, the low-wavenumber Raman shift spectrum for an aqueous solution of single-walled carbon nanotubes is given. At 830 nm, the Kataura plot predicts resonance with the  $v_1 \rightarrow c_1$  transition of the small-diameter (5, 4) species, as well as with the  $v_2 \rightarrow c_2$  transitions of a cluster of



**Figure 6.10** (a) Low-wavenumber Raman spectrum at 830-nm excitation. (b) Expanded view of Figure 6.9 comparing laser excitation energy (1.50 eV) to experimentally predicted transition energies.

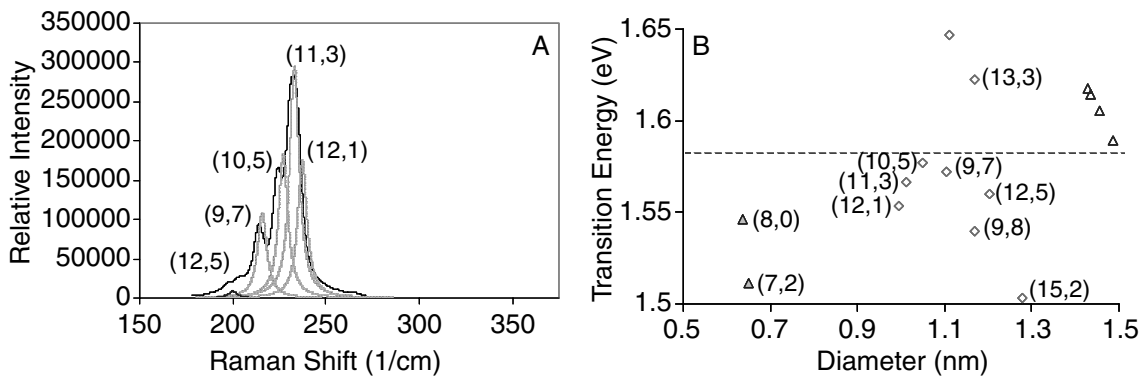


**Figure 6.11** (a) Low-wavenumber Raman spectrum at 785-nm excitation. (b) Expanded view of Figure 6.9 comparing laser excitation energy (1.58 eV) to experimentally predicted transition energies.

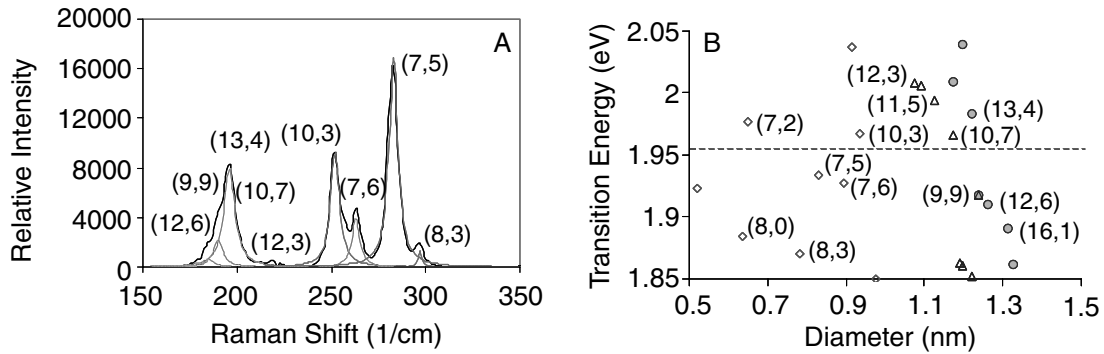


**Figure 6.12** (a) Low-wavenumber Raman spectrum at 633-nm excitation. (b) Expanded view of Figure 6.9 comparing laser excitation energy (1.96 eV) to experimentally predicted transition energies.

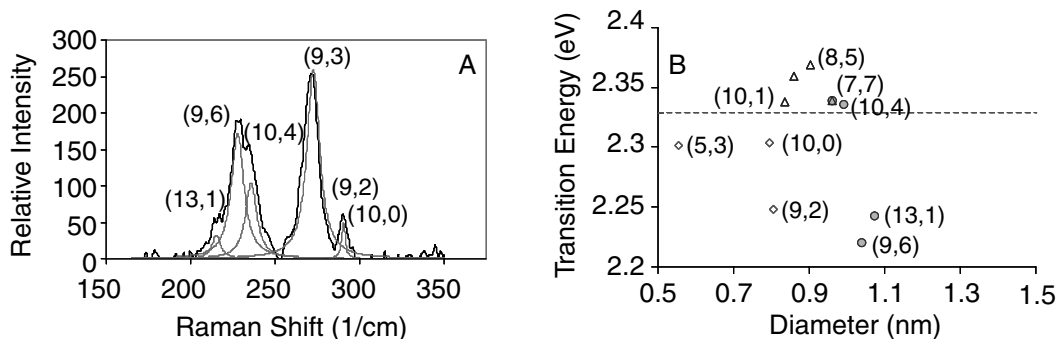


**Figure 6.13** (a) Low-wavenumber Raman spectrum at 532-nm excitation. (b) Expanded view of Figure 6.9 comparing laser excitation energy (2.33 eV) to experimentally predicted transition energies.

semiconducting nanotubes. Figure 6.10b shows an expanded version of Figure 6.9 surrounding the laser excitation energy. This shows that the mapping is able to predict the Raman RBM shift associated with each nanotube species with a transition within the resonance window (40 meV) of the laser excitation energy.<sup>40</sup>

Figure 6.11a and b show a similar comparison for a Raman excitation wavelength of 785 nm. At this wavelength,  $v_2 \rightarrow c_2$  semiconducting transitions are exclusively visible. This comparison shows an excellent agreement between theoretical prediction and experimental mapping. Figure 6.12a and b illustrates the experimental predictions for a Raman spectrum at 633 nm. At this excitation, both large-diameter metallic nanotubes and small-diameter semiconducting nanotubes are resonant. Consequently, this excitation wavelength provides a unique view for researchers interested in metallic/semiconductor separation<sup>10,73,74</sup> or electronic structure-selective chemistries. The experimental mapping is able to describe this transition region with excellent accuracy. Figure 6.13a and b at 532 nm probes mainly the  $v_1 \rightarrow c_1$  transitions for metallic nanotubes, with only one or two small-diameter semiconductors present, (9, 2) and (10, 10). The latter two species have been shown, in previous selective protonation work,<sup>67</sup> to actually be large band-gap semiconductors. In this case, the comparison between theoretical and experimental predictions is acceptable, although several metallic species are only partially resonant.

As described in the previous section, this experimental mapping of nanotube transition energies can be used to monitor selective nanotube surface chemistries. Specifically, Raman spectroscopy at 633-nm excitation is ideal for probing electronic structure-selective pathways because of its resonance with a collection of both metallic and semiconducting nanotubes, for material produced by the HiPco method.<sup>47</sup>

In conclusion, Raman spectroscopy can be a valid tool for correlating the single-walled carbon nanotube transition energies with the radial breathing modes of unique, chiral nanotubes. These results are compiled in an experimental mapping (Figure 6.9) that replaces theoretically based plots widely used in the interpretation of nanotube experiments. This revised Kataura plot allows researchers to probe electronic structure-selective chemistries of particular nanotube species for the first time. Thus, the development of solution-phase dispersion methods, spectroscopic identification and monitoring, and spectral assignments of single-walled carbon nanotubes<sup>38,39</sup> allows carbon nanotube surface chemistries to be probed and studied in great detail. Examples of reaction chemistries that benefit from this more effective gauge are surface oxidations that favor smaller diameters<sup>75</sup> or nitric acid treatments.<sup>76</sup> This has been further demonstrated with the reaction of 4-chlorobenzene-diazonium with an aqueous nanotube solution.

We conclude with an overview of nanotube covalent chemistry and a detailed description of the use of Raman spectroscopy for monitoring a specific class of sidewall reaction chemistry: functionalization with diazonium reagents.



### 6.3.3 Use of Raman spectroscopy to monitor covalent chemical reactions at nanotube surfaces

#### 6.3.3.1 Review of carbon nanotube covalent chemistry

The chemistries described here focus on the exohedral (outside wall) functionalization of single-walled carbon nanotubes and can be divided into two main classifications. First, oxidation or ozonation is used to generate defect sites in the nanotube sidewall or at the open tube ends, and then functionalize those sites.<sup>77–84</sup> These oxygenated functional groups can be converted into other derivatives, including amides. The next classification focuses on the direct chemical modification of the nanotube sidewall using addition reactions. This classification includes fluorination<sup>83</sup> and aryl diazonium salt addition.<sup>84,85</sup>

The first successful covalent chemistry was conducted under oxidizing conditions, involving sonication in either sulfuric acid–nitric acid or sulfuric acid–hydrogen peroxide mixtures.<sup>77,78</sup> These procedures not only purified the nanotube material of carbon impurities, but also reduced their lengths. Following this process, a variety of oxygenated functional groups are found on the tube ends or at highly reactive defect sites along the nanotube sidewall.<sup>86,87</sup> These groups include carboxylic acids, esters, quinones, and anhydrides. Most often, carboxylic acid groups are activated by treatment with thionyl chloride and then converted to derivative functionalities, such as amides. Carboxylic acid functional groups also provide access to peptide chemistry.

Although this chemistry is useful for some applications, including chemical force microscopy,<sup>93</sup> the restriction of the moieties to the tube ends and a limited number of defect sites do not change the bulk properties of the nanotube material. For example, the spectroscopic signatures of material functionalized in this manner do not differ significantly from unreacted nanotube material.<sup>79,80</sup>

More extensive sidewall reaction was first found by the direct fluorination of a single-walled carbon nanotube bucky paper, as reported by Mickelson et al. in 1998.<sup>83</sup> In this case, a variety of spectroscopic techniques were utilized to confirm widespread covalent functionalization.<sup>83</sup> Infrared spectroscopy confirmed the presence of covalently bound fluorine. More importantly, the signature Raman spectrum of unreacted nanotubes was found to be drastically altered following functionalization. [Section 6.3.3.3](#) below describes the analysis of covalent functionalization using Raman spectroscopy in more detail.

Furthermore, it was found that the fluorine moieties could be removed using treatment in hydrazine and the spectroscopic properties of the nanotubes almost completely restored. Conversely, the fluorine moieties can be displaced by strong nucleophiles, such as metal alkoxides and Grignard reagents.<sup>83</sup>

Other chemistries providing functionalization of single-walled carbon nanotubes include reaction with dichlorocarbene,<sup>88</sup> or carbene derivatives,<sup>89,90</sup> and reaction with nitrenes.<sup>90,91</sup> These chemistries report low degrees of functionalization, and therefore do not affect the spectroscopic signatures, similar to oxidation functionalization above.

In conclusion, the covalent chemistry of single-walled carbon nanotubes is an incredibly promising field that exhibits great potential for the applications described above. However, this field has been limited to the functionalization of carbon nanotube ropes and bundles. For many of the desired applications, the covalent modification of individually dispersed carbon nanotubes in solution is important. In the following section, such reaction chemistry is further investigated. Future applications might also require covalent reactions to be conducted on only nanotube species with a particular diameter or length.

### 6.3.3.2 *The pyramidalization angle formalism for carbon nanotube reactivity*

Fullerene chemistry has shown that the reactivity of these molecules with respect to addition chemistries is strongly dependent on the curvature of the carbon framework. In comparison, single-walled carbon nanotubes consist only of graphite-like sidewalls and are only moderately curved.<sup>92,93</sup> Consequently, nanotubes are expected to be less reactive than most fullerene molecules due to smaller curvature, but more reactive than a graphene sheet due to pyramidalization and misalignment of the  $\pi$ -orbitals.<sup>93–98</sup>

In any case, the strain of the carbon framework is reflected in the pyramidalization angle,  $\theta_p$ , of the carbon constituents. This angle equals the difference between the  $\pi$ -orbital axis vector of a conjugated carbon atom and a normal right angle ( $90^\circ$ ). This vector is defined as one that makes equal angles ( $\theta_{\sigma\pi}$ ) to the three  $\sigma$ -bonds of a conjugated carbon. Trigonal carbon atoms ( $sp^2$  hybridized) prefer a planar orientation with  $\theta_p = 0^\circ$ . Tetragonal carbon atoms ( $sp^3$  hybridized) possess a pyramidalization angle of  $19.47^\circ$  due to a larger relative  $\pi$ -orbital axis vector angle. By comparing  $\theta_p$  of a particular carbon atom with these values, it can be estimated which geometry is more appropriate for that atom. All carbons in the fullerene  $C_{60}$  have  $\theta_p = 11.6^\circ$ , which indicates a  $sp^3$ -hybridized state is more appropriate for these atoms.<sup>94</sup>

The (5, 5) single-walled carbon nanotube has  $\theta_p \approx 6^\circ$  for the sidewall and  $\theta_p \approx 11.6^\circ$  for the end cap.<sup>94</sup> Values for other distinct (n, n) nanotube species show a trend of increasing  $\theta_p$  (sidewall) with decreasing n. Therefore, it can be inferred that chemical reactivity in covalent additions is directly related to nanotube diameter. Furthermore, following the reaction of a single carbon atom, the reactivity of the remaining atoms is increased.<sup>94</sup> This occurs because as the strain is relaxed at one point on the nanotube sidewall, the total strain is divided among the remaining  $sp^2$ -hybridized carbons. Therefore, this so-called strain relief can increase the rate of addition reactions in single-walled carbon nanotubes.<sup>97–100</sup>

### 6.3.3.3 Selective covalent chemistry of single-walled carbon nanotubes

The main barrier to the extensive application of single-walled carbon nanotubes is the inability to manipulate according to electronic structure. All standard preparative techniques produce polydisperse mixtures of metallic, semimetallic, and semiconducting fractions.<sup>101</sup> In this section, novel nanotube chemistry is presented that provides electronic structure selectivity in the covalent functionalization of single-walled carbon nanotubes.

As discussed above, most developed mechanisms for nanotube selectivity in covalent reactions are based upon the carbon pyramidalization angle.<sup>93,94</sup> This indicates that nanotube diameter is the reaction index. Therefore, there is no direct evidence of the existence of covalent reaction pathways utilizing nanotube band gap as a reaction index. However, previous experimentation displayed that protonation of single-walled carbon nanotubes dispersed in solution is highly selective, depending upon the nanotube band gap. This noncovalent, reversible interaction allows the possibility for covalent, irreversible reactions to also demonstrate selectivity based upon electronic structure.

The selective pathways described here offer a unique method for the manipulation of nanotubes of distinct electronic structures by selective reaction of metallic nanotubes. This method of control should allow the separation of metallic nanotubes with high selectivity and scalability. Separation will allow the manufacture of electronic devices with specific electronic properties.

Water-soluble diazonium salts<sup>102</sup> have been shown to react with carbon nanotubes<sup>84,103,104</sup> via charge transfer, extracting electrons and forming a covalent aryl bond. During reaction, the diazonium reagent becomes part of a charge transfer complex at the surface, with electron donation from the nanotube stabilizing the transition state.

Recently, it was found that under certain controlled conditions, a reaction pathway exists in which the diazonium salt reacts selectively with the metallic nanotubes to the near exclusion of the semiconductors.<sup>7</sup> The covalent bond forms with high affinity for electrons with energies near the Fermi level ( $E_F$ ). Figure 6.14 shows the density of states for semiconducting and metallic nanotubes, as well as the region of interest at  $E_F$ . Since metallic nanotubes have a greater electron density near  $E_F$ , this translates into higher reactivity for these over semiconducting nanotubes. This reactivity is amplified once the bond symmetry of the nanotube is initially disrupted by the formation of the defect, causing adjacent carbons to increase in reactivity. This trend continues as the whole nanotube is reacted.

Spectroscopic evidence of selective functionalization can be found from ultraviolet–visible–near-infrared (UV-vis-NIR) absorption spectra. Figure 6.15 shows steady-state absorption spectra of aqueous individually dispersed nanotubes following successive, equal additions of 4-chlorobenzene-diazonium tetrafluoroborate. These spectra monitor the valence

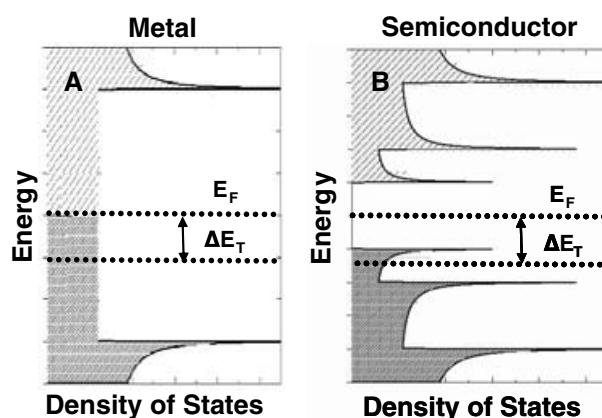


**Figure 6.14** Electron transfer extent depends on the density of states in the electron density within  $\Delta E_T$  of  $E_F$ . This leads to higher reactivity of metallic and semimetallic species.

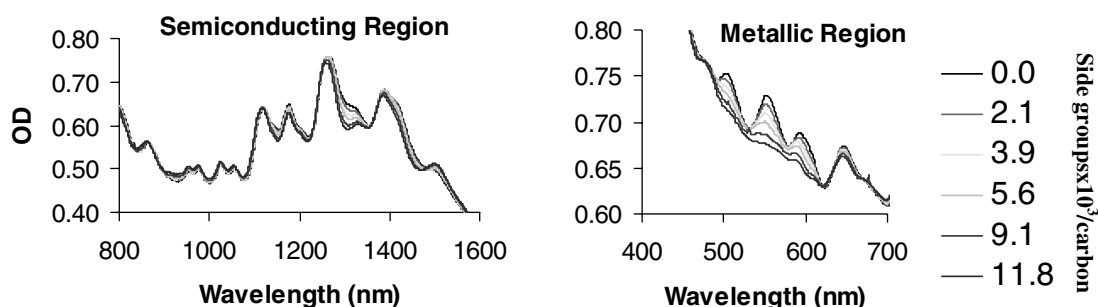


**Figure 6.15** UV-vis-NIR absorption spectra of SDS-suspended single-walled carbon nanotubes at various steady-state points in the 4-chlorobenzene-diazonium-selective reaction. Comparison indicates high selectivity for metallic species over semiconducting species, under controlled conditions.

(v)-to-conduction (c) electronic transitions, denoted  $E_{nn}$ , where  $n$  is the band index. The  $E_{11}$  transitions for the metallic and semimetallic nanotubes occur from approximately 440 to 645 nm. The  $E_{11}$  and  $E_{22}$  transitions for the semiconducting nanotubes are found from 830 to 1600 nm and 600 to 800 nm, respectively. Since individual peaks in an absorption spectrum represent a distinct, identifiable collection of nanotubes, this allows the direct monitoring of the valence electrons for each collection. As covalent bonds are formed, electrons along the nanotube are localized and the absorption maxima decay. Therefore, a relative decrease in metallic absorption features over semiconducting features represents a highly preferential functionalization of the metallic nanotubes. Selectivity is also verified by the preservation of band-gap fluorescence of the semiconducting nanotubes, which is known to be highly sensitive to chemical defects in the nanotube sidewall. Also worthy of note is that this selective decay is distinct from the similar, reversible behavior observed in band-gap-selective protonation.<sup>67</sup>

Raman spectroscopy offers another method of monitoring the selective reaction. Functionalization increases the intensity of the D peak, a phonon

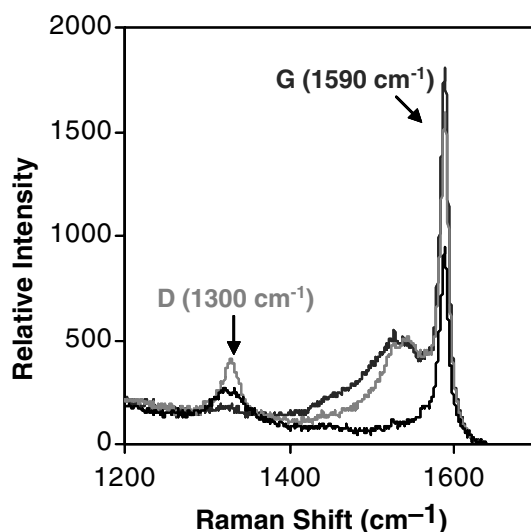


**Figure 6.16** Raman spectrum at 785-nm excitation, showing the increase in the D peak (or disorder mode) with increasing functionalization.

mode at  $1330\text{ cm}^{-1}$ , also known as the disorder mode. This mode corresponds to the conversion of a  $\text{sp}^2$ -hybridized carbon to a  $\text{sp}^3$ -hybridized carbon on the surface during the formation of the aryl-nanotube bond.<sup>101</sup> Essentially, the integrated intensity of the D peak measures covalent bonds made with the nanotube surface. Figure 6.16 illustrates the Raman spectrum at 785-nm excitation, showing the growth of the D peak with increasing reaction. This feature does not increase as a result of surfactant<sup>68</sup> or hydronium ion<sup>67</sup> adsorption on the nanotube surface. As the disorder mode increases due to functionalization, the C–C tangential mode decreases due to the loss of electronic resonance. Thus, analysis of steady-state Raman spectra during selective reaction allows correlation between the number of sidewall functionalization events and the intensity of the disorder mode.

Covalent functionalization of the nanotube sidewall disrupts the symmetry of the Raman radial breathing mode (RBM), and this  $(n, m)$ -specific feature decays with increasing reaction.<sup>84,103,104</sup> Again, analogous behavior is not observed with surface adsorption, which decreases the Raman resonance enhancement without eliminating the RBM.<sup>76</sup> Figure 6.17 shows the low-wavenumber solution-phase Raman spectra of the reaction mixture at 532 nm at three distinct steady-state points during reaction. The relative rates of decay for the features in Figure 6.17 show unprecedented reactivity differences among semimetallic species. The complete decay of all metallic modes, as seen in Figure 6.17, leaves only one low-wavenumber RBM, which has been previously assigned to the (9, 2) semiconductor RBM. This is in agreement with Figure 6.15, as complete decay of all metallic and semimetallic absorption features leaves one semiconducting feature, also belonging to the (9, 2).

The reacted material was thermally treated at  $300^\circ\text{C}$  in an atmosphere of inert gas. This cleaves the aryl chloride moieties from the nanotube sidewall and restores the spectroscopic features of pristine nanotubes.<sup>103</sup> Raman



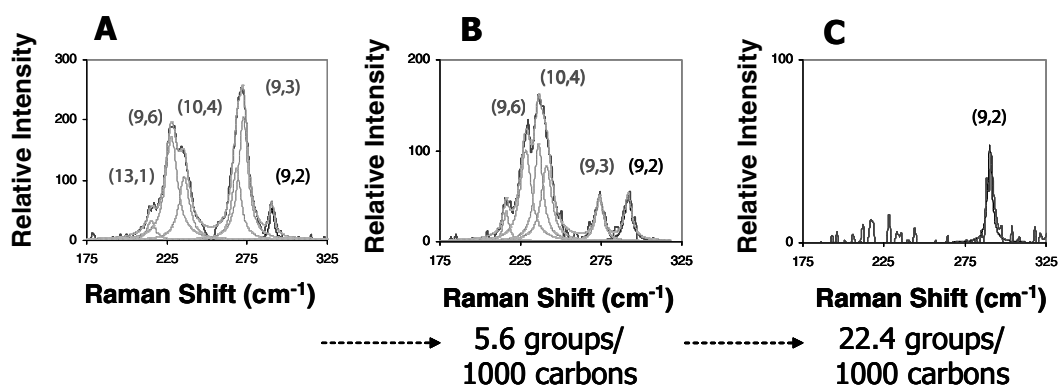


**Figure 6.17** Low-wavenumber Raman spectra at 532-nm excitation at three steady-state points during selective 4-chlorobenzene-diazonium reaction. (a) Initial solution, shows four metallic nanotube species (gray) and one semiconducting nanotube species (black) probed at this wavelength. (b) Following attachment of 5.6 groups per 1000 carbon atoms, decay of the metallic species is evident, while the (9, 2) semiconductor mode is unchanged. (c) Following attachment of 22.4 groups per 1000 carbons, all metallic modes have completely decayed, leaving only the single semiconductor. This supports the UV-vis-NIR data displayed in Figure 6.15.

spectra taken before reaction (black line) and following thermal treatment (gray line) at 633 nm are shown in Figure 6.18. This excitation wavelength was chosen because it probes both semiconducting and metallic features. The radial breathing modes are nearly completely restored, indicating the chemistry is reversible. In addition, the corresponding absorption features are recovered, signifying the restoration of the intrinsic electronic structure of the pristine nanotube. This result shows that this covalent, selective chemistry can be utilized as a reversible route to manipulate nanotubes of a particular electronic structure, and then allow the recovery of the initial optical and electronic properties.

## 6.4 Conclusions

The individualized nanotubes discussed here represent only a subset of new nanotube sample types that are emerging, which have allowed new experimental approaches to nanotube optical studies and are creating a current revolution in nanotube photophysics. Raman studies on individualized nanotubes are helping to pin down the important chirality assignments and are uncovering a variety of new chiral-dependent phenomena. Studies of individualized nanotubes will continue to provide a firm basis for understanding intertube interactions as well. Of specific future interest will be the development of a consistent model that unifies the description of large- and small-diameter nanotubes grown via different methods and studied under different environmental conditions. Although accurate assignments for small-diameter tubes now appear feasible, it remains a problem for large diameters in optically accessible regions. New experimental results that probe the  $E_{33}$  and  $E_{44}$  transition regions for both large and small diameters,

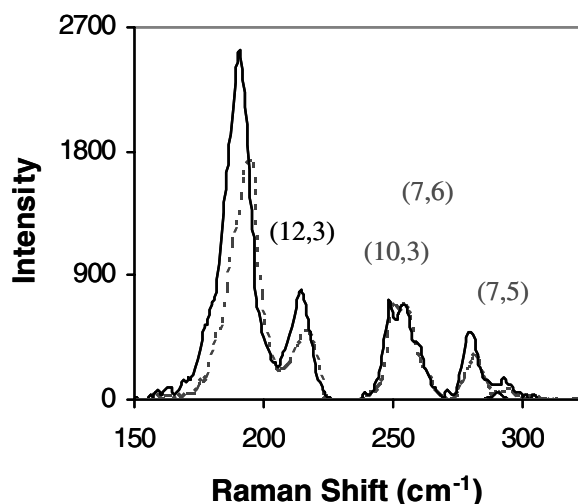


**Figure 6.18** Low-wavenumber Raman spectra at 633-nm excitation, which probes both metallic (black) and semiconducting (gray) species, before functionalization (solid line) and after recovery and thermal pyrolysis (dotted line). Restoration of RBM features indicates the chemistry is reversible and optical features can be recovered.

plus theoretical modeling efforts to accurately describe nanotube electronic structure in this region, are needed. Further studies of new photophysical phenomena in general, and specifically of Raman behavior enabled by these and other new nanotube types, will continue to provide new insight into nanotube properties. Such fundamental studies are proving themselves invaluable in characterizing nanotube processing effects, functionalization chemistry, and separation processes.

## References

1. H. Kuzmany, W. Plank, M. Hulman, C. Kramberger, A. Gruneis, T. Pichler, H. Peterlik, H. Kataura, Y. Achiba, *Eur. Phys. J. B* 22, 207 (2001).
2. A. Kukovecz, C. Kramberger, V. Georgakilas, M. Prato, H. Kuzmany, *Eur. Phys. J. B* 28, 223 (2002).
3. G. Chen, G. U. Sumanasekera, B. K. Pradhan, R. Gupta, R. C. Eklund, M. J. Bronikowski, R. E. Smalley, *J. Nanosci. Nanotechnol.* 2, 621 (2002).
4. S. Bandow, S. Asaka, Y. Saito, A. M. Rao, L. Grigorian, E. Richter, P. C. Eklund, *Phys. Rev. Lett.* 80, 3779 (1998).
5. M. S. Dresselhaus, P. C. Eklund, *Adv. Phys.* 49, 705 (2000).
6. M. S. Strano, V. C. Moore, M. K. Miller, M. J. Allen, E. H. Haroz, C. Kittrell, R. H. Hauge, R. E. Smalley, *J. Nanosci. Nanotechnol.* 3, 81 (2003).
7. M. S. Strano, C. A. Dyke, M. L. Usrey, P. W. Barone, M. J. Allen, H. Shan, C. Kittrell, R. H. Hauge, J. M. Tour, R. E. Smalley, *Science* 301, 1519 (2003).
8. S. K. Doorn, R. E. Fields, H. Hu, M. A. Hamon, R. C. Haddon, J. P. Selegue, V. Majidi, *J. Am. Chem. Soc.* 124, 3169 (2002).
9. S. K. Doorn, M. S. Strano, M. J. O'Connell, E. H. Haroz, K. L. Rialon, R. H. Hauge, R. E. Smalley, *J. Phys. Chem. B* 107, 6063 (2003).
10. R. Krupke, F. Hennrich, H. v. Lohneysen, M. M. Kappes, *Science* 301, 344 (2003).

11. M. Zheng, A. Jagota, E. D. Semke, B. A. Diner, R. S. Mclean, S. R. Lustig, R. E. Richardson, N. G. Tassi, *Nat. Mater.* 2, 338 (2003).
12. G. G. Samsonidze, S. G. Chou, A. P. Santos, V. W. Brar, G. Dresselhaus, M. S. Dresselhaus, A. Selbst, A. K. Swan, M. S. Unlu, B. B. Goldberg, D. Chattopadhyay, S. N. Kim, F. Papadimitrakopoulos, *Appl. Phys. Lett.* 85, 1006 (2004).
13. M. S. Strano, M. Zheng, A. Jagota, G. B. Onoa, D. A. Heller, P. W. Barone, M. L. Usrey, *Nano Lett.* 4, 543 (2004).
14. S. D. M. Brown, A. Jorio, P. Corio, M. S. Dresselhaus, G. Dresselhaus, R. Saito, K. Kneipp, *Phys. Rev. B* 63, 155414 (2001).
15. M. A. Pimenta, A. Marucci, S. A. Empedocles, M. G. Bawendi, E. B. Hanlon, A. M. Rao, P. C. Eklund, R. E. Smalley, G. Dresselhaus, M. S. Dresselhaus, *Phys. Rev. B* 58, R16016 (1998).
16. H. Kataura, Y. Kumazawa, Y. Maniwa, I. Umez, S. Suzuki, Y. Ohtsuka, Y. Achiba, *Synth. Met.* 103, 2555 (1999).
17. M. S. Strano, C. A. Dyke, M. L. Usrey, P. W. Barone, M. J. Allen, H. Shan, C. Kittrell, R. H. Hauge, J. M. Tour, R. E. Smalley, *Science* 301, 1519 (2003).
18. S. Banerjee, S. S. Wong, *Nano Lett.* 4, 1445 (2004).
19. R. M. Martin, L. M. Falicov, Resonant Raman scattering, chap. 3 in *Light Scattering in Solids I*, M. Cardona, Ed., Springer, Berlin (1983).
20. A. M. Rao, E. Richter, S. Bandow, B. Chase, P. C. Eklund, K. A. Williams, S. Fang, K. R. Subbaswamy, M. Menon, A. Thess, R. E. Smalley, G. Dresselhaus, M. S. Dresselhaus, *Science* 275, 187 (1997).
21. M. Canonico, G. B. Adams, C. Poweleit, J. Menendez, J. B. Page, G. Harris, H. P. van der Meulen, J. M. Calleja, J. Rubio, *Phys. Rev. B* 65, 201402 (2002).
22. L. Alvarez, A. Righi, T. Guillard, S. Rols, E. Anglaret, D. Laplaze, J. L. Sauvajol, *Chem. Phys. Lett.* 316, 186 (2000).
23. L. Alvarez, A. Righi, S. Rols, E. Anglaret, J. L. Sauvajol, *Chem. Phys. Lett.* 320, 441 (2000).
24. M. A. Pimenta, A. Marucci, S. D. M. Brown, M. J. Matthews, A. M. Rao, P. C. Eklund, R. E. Smalley, G. Dresselhaus, M. S. Dresselhaus, *J. Mater. Res.* 13, 2396 (1998).
25. A. Jorio, R. Saito, J. H. Hafner, C. M. Lieber, M. Hunter, T. McClure, G. Dresselhaus, M. S. Dresselhaus, *Phys. Rev. Lett.* 86, 1118 (2001).
26. R. Saito, A. Jorio, J. H. Hafner, C. M. Lieber, M. Hunter, T. McClure, G. Dresselhaus, M. S. Dresselhaus, *Phys. Rev. B* 64, 085312 (2001).
27. A. Jorio, C. Fantini, M. S. S. Dantas, M. A. Pimenta, A. G. Souza, G. G. Samsonidze, V. W. Brar, G. Dresselhaus, M. S. Dresselhaus, A. K. Swan, M. S. Unlu, B. B. Goldberg, R. Saito, *Phys. Rev. B* 66, 115411 (2002).
28. A. Jorio, A. G. Souza, G. Dresselhaus, M. S. Dresselhaus, A. K. Swan, M. S. Unlu, B. B. Goldberg, M. A. Pimenta, J. H. Hafner, C. M. Lieber, R. Saito, *Phys. Rev. B* 65, 155412 (2002).
29. M. S. Dresselhaus, G. Dresselhaus, A. Jorio, A. G. Souza, R. Saito, *Carbon* 40, 2043 (2002).
30. A. G. Souza Filho, S. G. Chou, G. G. Samsonidze, G. Dresselhaus, M. S. Dresselhaus, L. An, J. Liu, A. K. Swan, M. S. Unlu, B. B. Goldberg, A. Jorio, A. Gruneis, R. Saito, *Phys. Rev. B* 69, 115428 (2004).
31. R. Saito, G. Dresselhaus, M. S. Dresselhaus, *Physical Properties of Carbon Nanotubes*, Imperial College Press, London (1998).
32. M. Milnera, J. Kurti, M. Hulman, H. Kuzmany, *Phys. Rev. Lett.* 84, 1324 (2000).
33. M. J. O'Connell, S. Sivaram, S. K. Doorn, *Phys. Rev. B* 69, 235415 (2004).

34. A. Hartschuh, E. J. Sanchez, X. S. Xie, L. Novotny, *Phys. Rev. Lett.* 90, 95503 (2003).
35. A. Mews, F. Koberling, T. Basche, G. Philipp, G. S. Duesberg, S. Roth, M. Burghard, *Adv. Mater.* 12, 1210 (2000).
36. C. Jiang, J. Zhao, H. A. Therese, M. Friedrich, A. Mews, *J. Phys. Chem. B* 107, 8742 (2003).
37. V. G. Hadjiev, S. Arepalli, S. Jandl, L. Yowell, *Nanotechnology* 15, 562 (2004).
38. M. J. O'Connell, S. M. Bachilo, C. B. Huffman, V. C. Moore, M. S. Strano, E. H. Haroz, K. L. Rialon, P. J. Boul, W. H. Noon, C. Kittrell, J. P. Ma, R. H. Hauge, R. B. Weisman, R. E. Smalley, *Science* 297, 593 (2002).
39. S. M. Bachilo, M. S. Strano, C. Kittrell, R. H. Hauge, R. E. Smalley, R. B. Weisman, *Science* 298, 2361 (2002).
40. S.K. Doorn, D. A. Heller, P. W. Barone, M. L. Usrey, M. S. Strano, *Appl. Phys. A Mater. Sci. Proc.* 78, 1147 (2004).
41. M. S. Strano, S. K. Doorn, E. H. Haroz, C. Kittrell, R. H. Hauge, R. E. Smalley, *Nano Lett.* 3, 1091 (2003).
42. S. Huang, X. Cai, J. Liu, *J. Am. Chem. Soc.* 125, 5636 (2003).
43. S. Huang, B. Maynor, X. Cai, J. Liu, *Adv. Mater.* 15, 1651 (2003).
44. L. Zheng, M. J. O'Connell, S. K. Doorn, X. Liao, Y. Zhao, E. A. Akhadow, M. A. Hoffbauer, B. J. Roop, Q. Jia, R. C. Dye, D. E. Peterson, S. Hung, J. Liu, Y. T. Zhu, *Nat. Mater.* 3, 673 (2004).
45. S. K. Doorn, M. J. O'Connell, L. Zheng, Y. T. Zhu, S. Huang, J. Liu, *Phys. Rev. Lett.* 94, 016802 (2005).
46. S. K. Doorn, L. Zheng, M. J. O'Connell, Y. T. Zhu, S. Huang, J. Liu, *J. Phys. Chem. B* 109, 3751 (2005).
47. M. J. Bronikowski, P. A. Willis, D. T. Colbert, K. A. Smith, R. E. Smalley, *J. Vac. Sci. Technol. A* 19, 1800 (2001).
48. Y. Li, J. Liu, Y. Wang, Z. L. Wang, *Chem. Mater.* 13, 1008 (2001).
49. G. G. Samsonidze, R. Saito, N. Kobayashi, A. Gruneis, J. Jiang, A. Horio, S. G. Chou, G. Dresselhaus, M. S. Dresselhaus, *Appl. Phys. Lett.* 85, 5703 (2004).
50. H. Telg, J. Maultzsch, S. Reich, F. Hennrich, C. Thomsen, *Phys. Rev. Lett.* 93, 177401 (2004).
51. C. Fantini, A. Jorio, M. Souza, M. S. Strano, M. S. Dresselhaus, M. A. Pimenta, *Phys. Rev. Lett.* 93, 147406 (2004).
52. S. Lebedkin, F. Hennrich, T. Skipa, M. M. Kappes, *J. Phys. Chem. B* 107, 1949 (2003).
53. V. N. Popov, L. Henrard, *Phys. Rev. B* 70, 115407 (2004).
54. S. Reich, C. Thomsen, *Phys. Rev. B* 62, 4273 (2000).
55. A. Gruneis, R. Saito, G. G. Samsonidze, T. Kimura, M. A. Pimenta, A. Jorio, A. G. Souza, G. Dresselhaus, M. S. Dresselhaus, *Phys. Rev. B* 67, 165402 (2003).
56. A. Jorio, C. Fantini, M. A. Pimenta, R. B. Capaz, G. G. Samsonidze, G. Dresselhaus, M. S. Dresselhaus, J. Jiang, N. Kobayashi, A. Gruneis, R. Saito, *Phys. Rev. B* 71, 075401 (2005).
57. V. N. Popov, L. Henrard, P. Lambin, *Nano Lett.* 4, 1795 (2004).
58. M. Machon, S. Reich, H. Telg, J. Maultzsch, P. Ordejon, C. Thomsen, *Phys. Rev. B* 71, 035416 (2005).
59. S. Goupalov, *Phys. Rev. B* 71, 153404 (2005).
60. H. Htoon, M. J. O'Connell, S. K. Doorn, V. I. Klimov, *Phys. Rev. Lett.* 94, 127403 (2005).
61. Y. K. Kwon, S. Saito, D. Tomanek, *Phys. Rev. B* 58, R314 (1998).

62. P. Delaney, H. J. Choi, J. Ihm, S. G. Louie, M. L. Cohen, *Phys. Rev. B* 60, 7899 (1999).
63. A. A. Maarouf, C. L. Kane, E. J. Mele, *Phys. Rev. B* 61, 156 (2000).
64. S. Reich, C. Thomsen, P. Ordejon, *Phys. Rev. B* 65, 155411 (2002).
65. V. C. Moore, M. S. Strano, E. H. Haroz, R. H. Hauge, R. E. Smalley, *Nano Lett.* 3, 1379 (2003).
66. D. A. Heller, P. W. Barone, J. P. Swanson, R. M. Mayrhofer, M. S. Strano, *J. Phys. Chem. B* 108, 6905 (2004).
67. M. S. Strano, C. B. Huffman, V. C. Moore, M. J. O'Connell, E. H. Haroz, J. Hubbard, M. Miller, K. Rialon, C. Kittrell, S. Ramesh, R. H. Hauge, R. E. Smalley, *J. Phys. Chem. B* 107, 6979–6985 (2003).
68. J. W. Mintmire, C. T. White, *Phys. Rev. Lett.* 81, 2506–2509 (1998).
69. R. Saito, G. Dresselhaus, M. S. Dresselhaus, *Phys. Properties Carbon Nanotubes*, Imperial College Press, London (1998).
70. T. Ando, *J. Phys. Soc. Jpn.* 66, 1066–1073 (1997).
71. C. L. Kane, E. J. Mele, *Phys. Rev. Lett.* 90, 207401 (2003).
72. M. S. Strano, *J. Am. Chem. Soc.* 125, 16148–16153 (2003).
73. M. Zheng, A. Jagota, M. S. Strano, A. P. Santos, P. Barone, S. G. Chou, B. A. Diner, M. S. Dresselhaus, R. S. McLean, G. B. Onoa, G. G. Samsonidze, E. D. Semke, M. Usrey, D. J. Walls, *Science* 302, 1545–1548 (2003).
74. D. Chattopadhyay, L. Galeska, F. Papadimitrakopoulos, *J. Am. Chem. Soc.* 125, 3370–3375 (2003).
75. W. Zhou, Y. H. Ooi, R. Russo, P. Papanek, D. E. Luzzi, J. E. Fischer, M. J. Bronikowski, P. A. Willis, R. E. Smalley, *Chem. Phys. Lett.* 350, 6–14 (2001).
76. M. E. Itkis, S. Niyogi, M. E. Meng, M. A. Hamon, H. Hu, R. C. Haddon, *Nano Lett.* 2, 155–159 (2002).
77. J. Liu, A. G. Rinzler, H. J. Dai, J. H. Hafner, R. K. Bradley, P. J. Boul, A. Lu, T. Iverson, K. Shelimov, C. B. Huffman, F. Rodriguez-Macias, Y. S. Shon, T. R. Lee, D. T. Colbert, R. E. Smalley, *Science* 280, 1253–1256 (1998).
78. A. G. Rinzler, J. Liu, H. Dai, P. Nikolaev, C. B. Huffman, F. J. Rodriguez-Macias, P. J. Boul, A. H. Lu, D. Heymann, D. T. Colbert, R. S. Lee, J. E. Fischer, A. M. Rao, P. C. Eklund, R. E. Smalley, *Appl. Phys. A* 67, 29–37 (1998).
79. D. B. Mawhinney, V. Naumenko, A. Kuznetsova, J. T. Yates, J. Liu, R. E. Smalley, *Chem. Phys. Lett.* 324, 213–216 (2000).
80. D. B. Mawhinney, V. Naumenko, A. Kuznetsova, J. T. Yates, J. Liu, R. E. Smalley, *J. Am. Chem. Soc.* 122, 2383–2384 (2000).
81. A. Kuznetsova, I. Popova, J. T. Yates, M. J. Bronikowski, C. B. Huffman, J. Liu, R. E. Smalley, H. H. Hwu, J. G. G. Chen, *J. Am. Chem. Soc.* 123, 10699–10704 (2001).
82. J. P. Deng, C. Y. Mou, C. C. Han, *Fullerene Sci. Technol.* 5, 1033–1044 (1997).
83. E. T. Mickelson, C. B. Huffman, A. G. Rinzler, R. E. Smalley, R. H. Hauge, J. L. Margrave, *Chem. Phys. Lett.* 296, 188–194 (1998).
84. J. L. Bahr, J. P. Yang, D. V. Kosynkin, M. J. Bronikowski, R. E. Smalley, J. M. Tour, *J. Am. Chem. Soc.* 123, 6536–6542 (2001).
85. J. L. Bahr, J. M. Tour, *Chem. Mater.* 13, 3823 (2001).
86. Y. Chen, R. C. Haddon, S. Fang, A. M. Rao, W. H. Lee, E. C. Dickey, E. A. Grulke, J. C. Pendergrass, A. Chavan, B. E. Haley, R. E. Smalley, *J. Mater. Res.* 13, 2423–2431 (1998).
87. S. S. Wong, A. T. Woolley, E. Joselevich, C. L. Cheung, C. M. Lieber, *J. Am. Chem. Soc.* 120, 8557–8558 (1998).



88. H. Hu, B. Zhao, M. A. Hamon, K. Kamaras, M. E. Itkis, R. C. Haddon, *J. Am. Chem. Soc.* 125, 14893–14900 (2003).
89. J. Chen, M. A. Hamon, H. Hu, Y. S. Chen, A. M. Rao, P. C. Eklund, R. C. Haddon, *Science* 282, 95–98 (1998).
90. M. Holzinger, O. Vostrowsky, A. Hirsch, F. Hennrich, M. Kappes, R. Weiss, F. Jellen, *Angew. Chem.-Int. Ed.* 40, 4002 (2001).
91. M. Holzinger, J. Abraha, P. Whelan, R. Graupner, L. Ley, F. Hennrich, M. Kappes, A. Hirsch, *J. Am. Chem. Soc.* 125, 8566–8580 (2003).
92. A. Hirsch, *Angew. Chem.-Int. Ed.* 41, 1853–1859 (2002).
93. Z. F. Chen, W. Thiel, A. Hirsch, *ChemPhysChem* 4, 93–97 (2003).
94. S. Niyogi, M. A. Hamon, H. Hu, B. Zhao, P. Bhowmik, R. Sen, M. E. Itkis, R. C. Haddon, *Accounts Chem. Res.* 35, 1105–1113 (2002).
95. M.A. Hamon, M. E. Itkis, S. Niyogi, T. Alvaraez, C. Kuper, M. Menon, R. C. Haddon, *J. Am. Chem. Soc.* 123, 11292–11293 (2001).
96. R. C. Haddon, *J. Am. Chem. Soc.* 112, 3385–3389 (1990).
97. R. C. Haddon, *Science* 261, 1545–1550 (1993).
98. R. C. Haddon, *J. Phys. Chem. A* 105, 4164–4165 (2001).
99. R. Taylor, D. R. M. Walton, *Nature* 363, 685–693 (1993).
100. A. Hirsch, *The Chemistry of the Fullerenes*, Thieme, Stuttgart (1994).
101. M. S. Dresselhaus, G. Dresselhaus, P. C. Eklund, *Science of Fullerenes and Carbon Nanotubes*, Academic Press, San Diego (1996).
102. C. Bravo-Diaz, M. Soengas-Fernandez, M. J. Rodriguez-Sarabia, E. Gonzalez-Romero, *Langmuir* 14, 5098–5105 (1998).
103. J. L. Bahr, J. M. Tour, *J. Mater. Chem.* 12, 1952–1958 (2002).
104. C. A. Dyke, J. M. Tour, *J. Am. Chem. Soc.* 125, 1156–1157 (2003).

## *chapter seven*

---

# *Electromechanical properties and applications of carbon nanotubes*

*Randal J. Grow  
Stanford University*

### *Contents*

7.1	Introduction .....	187
7.2	Piezoresistance.....	189
7.3	Theory of strain-induced band-gap changes in carbon nanotubes .....	190
7.4	Electrical measurements of strain-induced band-gap changes in suspended tubes .....	194
7.5	Electrical measurements of strain-induced band-gap changes in tubes on a surface.....	198
7.6	Conclusion of piezoresistance of nanotubes .....	201
7.7	Electrostatic actuation .....	202
7.8	Nanoelectromechanical systems.....	205
7.9	Conclusion.....	207
	References.....	207

## *7.1 Introduction*

Carbon nanotubes have evoked much interest since their discovery in 1991<sup>1</sup> because of their remarkable electronic, mechanical, and thermal properties.<sup>2-4</sup> Many different applications have been proposed to exploit these unique properties.<sup>5</sup>

In terms of mechanical properties, nanotubes are among the stiffest (Young's modulus) and strongest (yield strength) materials yet measured. Their Young's modulus is 0.64 TPa,<sup>6-8</sup> roughly five times greater than steel, which matches theoretical predictions.<sup>9</sup> Authors report inconsistent Young's modulus values in the literature because some of them use the entire cross-sectional area that the nanotube occupies (as have I), while others use a ring of the thickness of graphene interlayer spacing (3.4 Å). Nanotubes are expected to withstand large strains of up to 6 to 10%.<sup>10</sup> Some have been shown to survive up to 5.8%, which corresponds to a yield strength of 37 GPa,<sup>11</sup> compared with ~300 MPa for steel. They are also quite flexible and can return to their original shape after bending and buckling.<sup>12</sup> These exceptional properties can be explained by the strength of the carbon-carbon bond. They have led to interesting applications, including using a nanotube as a flexible, durable, high-aspect-ratio atomic force microscope (AFM) tip<sup>13</sup> and electromechanical memories<sup>14</sup> being developed by Nantero.\* Some have even proposed that the unprecedented stiffness and strength could enable a space elevator,<sup>15</sup> in which a nanotube-based cable would link a platform in geosynchronous orbit to the surface of the Earth, allowing transport to and from orbit via an elevator traversing the cable. Chapter 10 discusses nanotube mechanical properties in more detail.

In this chapter, I focus primarily on the electromechanical properties and applications of nanotubes. Unless otherwise noted, I will assume that the nanotubes I am discussing are single walled. As with most materials, there is a strong relationship between the structure and electronic properties of a nanotube.<sup>16</sup> However, unlike many other materials, nanotubes come in a great variety of structures. A nanotube can be thought of as a rolled-up graphene sheet (Figure 7.1), and the orientation of the crystal lattice with regard to the axis of the tube, known as the chirality, determines the electronic band structure, and therefore the conductance.<sup>3</sup> In terms of the nanotube unit vector indices ( $n, m$ ), which indicate the chirality,  $n = m$  tubes have no band gap and are therefore metallic, and  $n \neq m$  have some band gap and are semiconducting, though the subset where  $n - m = 3q$  (where  $q$  is an integer) has only a small band gap induced by the curvature of the graphene sheet and is called semimetallic, quasi-metallic, or small-gap semiconducting (SGS). Within the semiconducting and SGS groups, the band gap of the specific tube varies inversely with the diameter or the square of the diameter, respectively.<sup>17</sup>

The dependence of the electronic properties on the structure implies that mechanical deformations can alter the band structure. This results in electromechanical effects such as piezoresistance and electrostatic actuation, which, together with the mechanical properties, may lead to nanotube-based mechanical sensors and actuators as well as more complex applications, such as oscillators or electromechanical switches.

\* Nantero, Inc., Woburn, MA, [www.nantero.com](http://www.nantero.com).

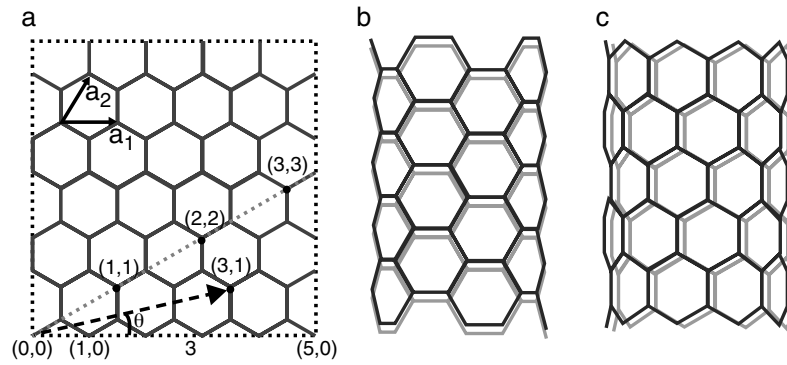


**Figure 7.1** (a) Schematic of the graphene sheet with lattice unit vectors  $a_1$  and  $a_2$ . The indices show how many unit cells to move along each vector before rolling that point back to the origin to form the nanotube.  $\theta$  shows the chiral angle of the (3, 1) tube. (b) A (5, 5) armchair tube, so called because of the shape of the lattice at the end of the tube. (c) A (9, 0) zigzag tube, again so called because of the zigzag shape at the end. (Reprinted from Maiti, A., *Nat. Mater.*, 2, 440–442, 2003. With permission. Copyright © 2003 by the Nature Publishing Group.)

## 7.2 Piezoresistance

Piezoresistance is the tendency of a material to change its resistivity under strain. As a force deforms a crystal and changes the lattice spacing, the electronic band structure changes, which changes the resistivity. This effect is well understood in bulk semiconductors like silicon and germanium,<sup>18–20</sup> and it has led to a decades-old, multibillion-dollar industry that makes piezoresistive mechanical sensors such as strain gauges, pressure sensors, and accelerometers from silicon.<sup>21</sup>

The resistivity  $\rho$  of a semiconductor is given by<sup>22</sup>

$$\rho = \frac{1}{qn\mu_n + qp\mu_p} \quad (7.1)$$

where  $q$  is the carrier charge,  $n$  and  $p$  are the carrier densities, and  $\mu_n$  and  $\mu_p$  are the carrier mobilities. The mobility is given by  $\mu = 1/m\tau$ , where  $m$  is the effective mass of the carrier and  $\tau$  is the scattering time. In silicon, piezoresistance is explained primarily by strain in a particular direction breaking the symmetry and splitting degenerate bands, which causes a shift in the population of carriers between subbands with different mobilities. In addition, the splitting suppresses band–band scattering because there are no longer phonons available with the correct energy and momentum. Another, smaller effect is a change in the overall band gap, which changes the number of carriers in the entire conduction band. The overall change in resistivity tends to be linear with strain.

In nanotubes, on the other hand, the second-lowest subband of the conduction band is typically  $\sim 1$  eV above the lowest subband,<sup>3</sup> so it is too

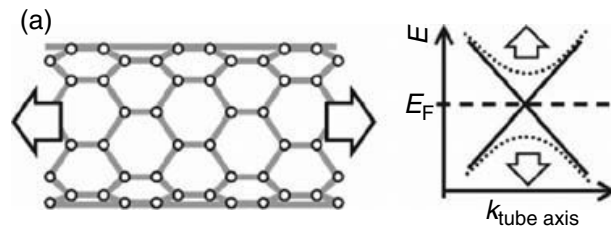


**Figure 7.2** A zigzag nanotube being stretched along its length and the resultant change in the dispersion relation (and therefore the band gap) near  $E_F$  (Reprinted from Minot, E.D. et al., *Phys. Rev. Lett.*, 90, 156401, 2003. With permission. Copyright © 2003 by the American Physical Society.)

high in energy to have any substantial carrier population. Only the lowest subband plays a role, allowing a change in the band gap to be the dominant reason for a change in resistance (Figure 7.2). If the band gap changes, that changes the overall number of carriers in the nanotube, changing the resistance.

In nanotubes, piezoresistance may be useful for mechanical sensors as well as electromechanical switches.<sup>23</sup> It may also be possible to use this effect to tune the electronic and optical properties of nanotube devices, much like piezoresistance in silicon is used to increase the carrier mobility in transistors.<sup>24</sup>

### 7.3 Theory of strain-induced band-gap changes in carbon nanotubes

Researchers have used both analytical and computational methods (tight-binding approximations) to model the electronic structure of nanotubes under uniaxial strain and torsion as well as many other deformations.<sup>17,25–29</sup>

The electronic structure of a nanotube is that of a graphene sheet with an additional periodic boundary condition imposed by having been rolled into a cylinder, which quantizes the electron wavefunctions around the tube. Graphene is a zero-band-gap semiconductor in which the conduction and valence bands meet at two points in  $k$ -space (Figure 7.3). The dispersion is linear about each of these points and so forms a cone. When rolled into a nanotube, the additional quantization condition causes a cut through the cones to define the band structure. This cut is in the direction in which electrons can travel, i.e., along the tube. Strain changes the bond lengths, which shifts the periodicity of the quantization, and that changes the conic section that defines the band structure, which increases or decreases the band gap.

As mentioned earlier, the band gap  $E_g$  of a semiconducting tube is inversely proportional to the diameter  $d$ :<sup>2</sup>



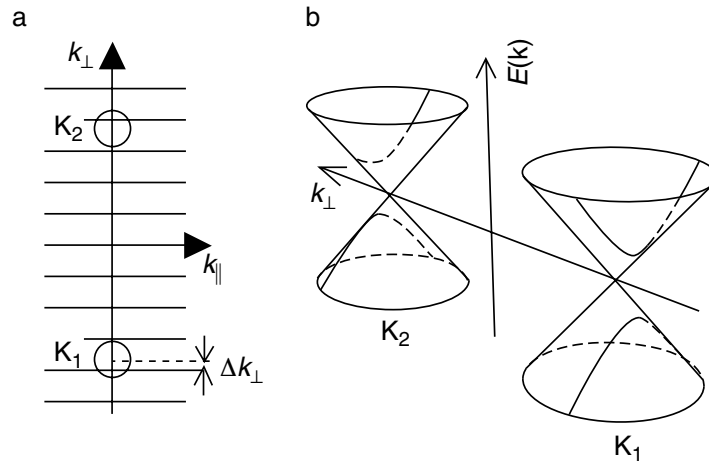


**Figure 7.3** (a) The electronic structure of the graphene sheet is described by the two points  $K_1$  and  $K_2$  in k-space, each of which has a cone-shaped dispersion around it. The periodic boundary condition quantizes the possible perpendicular states, effectively taking cuts through the dispersion cones. (b) This three-dimensional view shows the dispersion cones and how the cuts through them form the nanotube band structure. (Reprinted from Minot, E.D. et al., *Nature*, 428, 536–539, 2004. With permission. Copyright © 2004 by the Nature Publishing Group.)

$$E_g = \frac{2\gamma a}{\sqrt{3}d} \quad (7.2)$$

and is  $\sim 0.1$  to  $2$  eV for typical tubes.  $\gamma$  is the tight-binding overlap integral ( $\sim 2.6$  eV) and  $a$  is the graphene lattice unit vector length ( $\sim 2.49$  Å). A metallic tube has no band gap in its unstrained state.

For uniaxial strain and torsion, researchers have predicted chirality-dependent band-gap changes of up to  $\sim 100$  meV/% strain.<sup>25,27</sup> Yang and Han<sup>28</sup> generalized these results into an analytical expression relating the change in the band gap of both semiconducting and metallic tubes to the strain and torsion:

$$\Delta E_g = \text{sgn}(2p + 1)3\gamma \left[ (1 + \nu)\epsilon \cos 3\alpha + \xi \sin 3\alpha \right] \quad (7.3)$$

The sign depends on  $p$ , where  $n - m = 3q + p$ , and  $n$  and  $m$  are the indices of the nanotube.  $\nu$  is the Poisson's ratio of the tube ( $\sim 0.20$ ),  $\epsilon$  is the axial strain,  $\xi$  is the torsional strain, and  $\alpha$  is the chiral angle. This change is plotted for various chiralities in Figure 7.4. From this, we can see that metallic nanotubes ( $n = m$  and  $\alpha = 30^\circ$ ) show no band gap even under uniaxial strain, yet they do develop one under a twist. Zigzag nanotubes ( $[n, 0]$  and  $\alpha = 0^\circ$ ), a subset of the nonmetallic tubes, show the opposite. All other tubes show some response to both strain and torsion. Depending on the chirality of the semiconducting tube, the band gap can either increase or decrease with

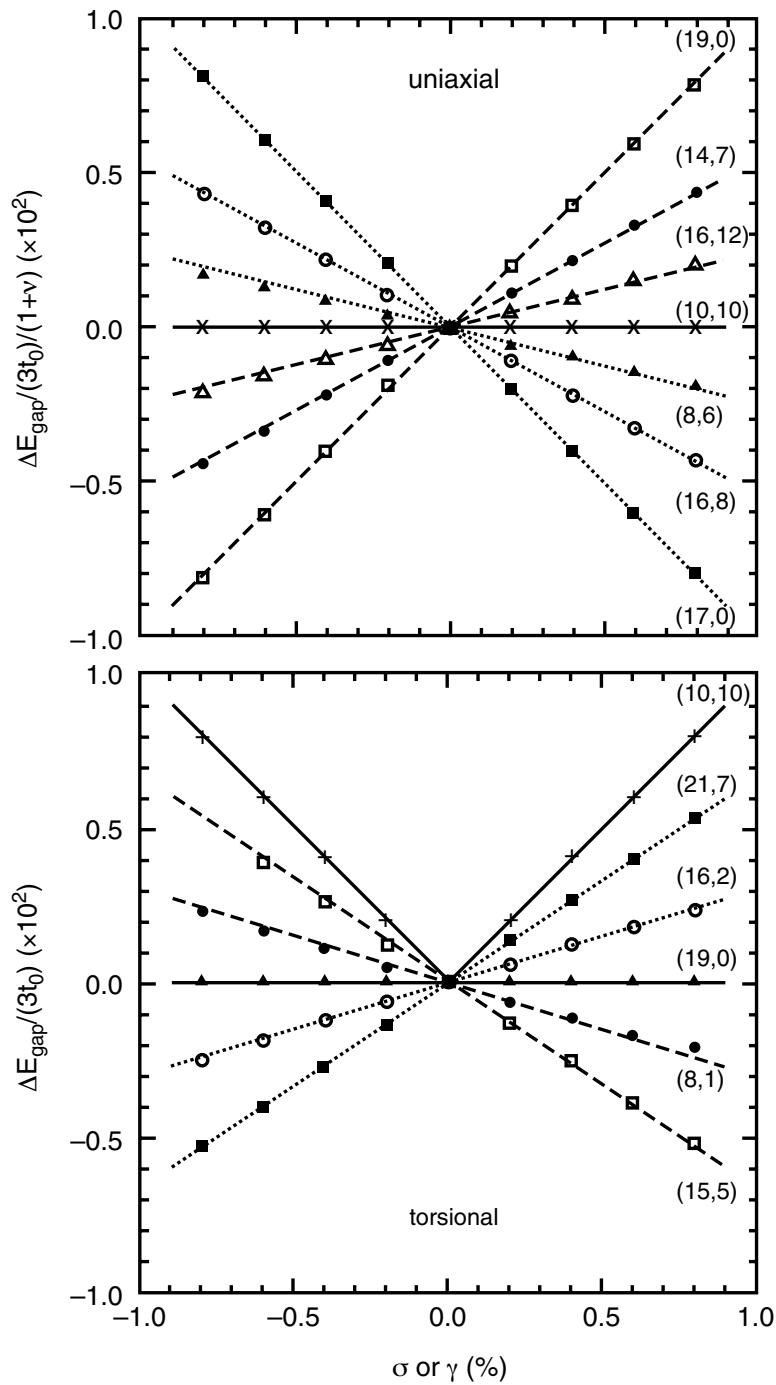


**Figure 7.4** The change in band gap vs. strain or torsion for several different chiralities. The lines are analytical results, and the points are the results of numerical modeling. (Reprinted from Yang, L. and Han, J., *Phys. Rev. Lett.*, 85, 154, 2000. With permission. Copyright © 2000 by the American Physical Society.)

strain. This change in the band gap is linear with strain, and the maximum value is ~94 meV/% strain.

This theory, however, models the nanotube as an unrolled graphene sheet with an imposed boundary condition and does not take into account the curvature-induced band gap (<50 meV) of SGS tubes, so they are not

distinguished from other semiconducting tubes. Kleiner and Eggert refined the electromechanical theory to include the effects of curvature in SGS tubes,<sup>29</sup> and they found this expression for the unperturbed SGS band gap and the changes in it with strain and torsion:

$$E_g = \left| \left( \frac{\gamma a^2}{4d^2} - \frac{ab\sqrt{3}}{2} \varepsilon \right) \cos 3\alpha - \frac{ab\sqrt{3}}{2} \xi \sin 3\alpha \right| \quad (7.4)$$

where  $b$  ( $\sim 3.5$  eV/Å) is  $d\gamma/da$ . According to this, SGS tubes should show an initial decrease in their band gap when stretched down to no band gap at  $\sim 0.2\%$  strain, followed by an increase beyond that. Again, the dependence on the strain is linear, and the maximum value is  $\sim 75$  meV/% strain.

Others have further refined the theory to include electron–electron interactions and found that even an armchair tube ( $n = m$ ) should have a small unstrained band gap of several meV,<sup>30,31</sup> as well as an increase in band gap with strain of a few meV/% strain.<sup>32</sup>

As the band gap changes according to Equations 7.3 and 7.4, that changes the activation energy necessary to get an electron from the Fermi level in the contact metal up to the nanotube conduction band (Figure 7.5). That changes the number of carriers that populate the conduction band at a given temperature, which changes the resistance of the tube, giving rise to the piezoresistive effect. Assuming the Fermi level matches the valence band of the nanotube, the number of electrons in the nanotube available for conduction is related to the band gap  $E_g$  by  $1/[1 + \exp(E_g/kT)]$ . Therefore, the conductance of the NT changes exponentially with the band gap.

I have only discussed in detail the effects expected for the uniaxial strain and torsion. Of these, only uniaxial strain has been explored well experimentally, which I discuss in the next section.

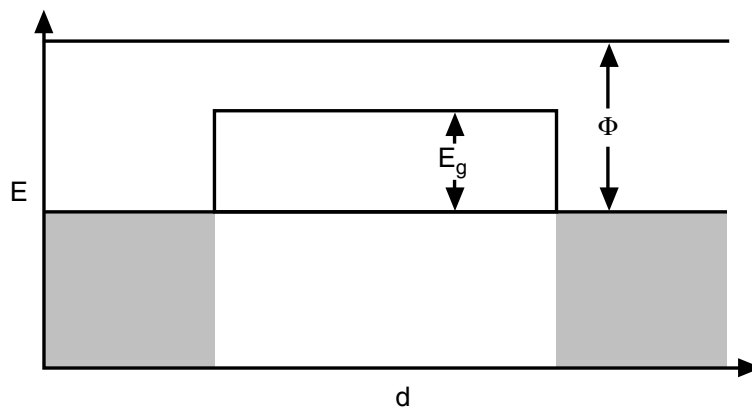


**Figure 7.5** This is the flat-band structure of a nanotube with band gap  $E_g$  contacted on both ends by a high-work-function ( $\Phi$ ) metal, so that the metal's Fermi level is the same as the valence band of the nanotube.

## 7.4 Electrical measurements of strain-induced band-gap changes in suspended tubes

In an early experiment, Tombler et al.<sup>33</sup> used an AFM tip to stretch a metallic nanotube suspended across a 600-nm trench in a silicon oxide substrate while measuring the current through the nanotube (Figure 7.6). They determined that the tube was metallic by monitoring its gate dependence at room and low temperature. During the stretching, they found a two-order-of-magnitude conductance decrease at a maximum applied strain of  $\sim 3\%$ , which was unexpected since a metallic tube should not respond strongly to either uniaxial strain<sup>28,32</sup> or bending,<sup>17</sup> the two relevant deformations. In order to explain the large change, they simulated local deformation of the tube at the tip–tube contact and found that it causes hybridization of  $sp^2$  bonding to  $sp^3$ , which sharply increases  $\sigma$ -electrons and decreases  $\pi$ -electrons, leading to the drop in conductance.<sup>33–35</sup>

Some later suggested, based on further simulations, that such a deformation of the tube at the tip–tube contact point was unlikely, and that if the tube had actually been SGS rather than metallic, the conductance change could be explained by a band-gap change induced by the axial strain alone.<sup>36</sup> Metallic and SGS tubes are often difficult to distinguish experimentally because of contact resistance or thermal effects. Also, the very sensitivity to mechanical deformation that I am discussing provides several avenues for a metallic tube to have a small band gap opened up or for an SGS tube to have the band gap closed. The diameter of the tube in question was 3.1 nm, which, if SGS, should have a band gap of only 4 meV,<sup>29</sup> which could be closed by a small twist in the tube.

Using a method similar to Tombler's, Minot et al.<sup>37</sup> measured all three types of suspended tubes under strain and extracted the initial band gaps ( $E_g$ ) and the rates of change of the band gap with strain ( $dE_g/d\epsilon$ ). Using the AFM tip as a local gate, they distinguished between metallic (metallic and SGS) and semiconducting tubes by their gate dependence. Then, they varied the gate voltage while straining the tubes, measuring  $I$ - $V_g$  curves at strains up to 2% (Figure 7.7). Of seven tubes, two semiconducting tubes showed increased conductance under strain, one semiconducting and two metallic tubes showed decreased conductance, and two metallic tubes showed no significant change.

They do not distinguish between metallic and SGS tubes, so presumably the metallic tubes that showed no change under strain were metallic in the  $n = m$  sense, while those that showed significant band-gap change under strain were SGS. Equation 7.4 predicts that SGS tubes under uniaxial strain should initially have a band-gap decrease (up to  $\sim 0.2\%$  strain) followed by an increase. They apparently did not see the band gap of the SGS tube at room temperature, nor therefore any initial decrease in it. They simply saw decreases in the conductance, corresponding to increased band gaps. Perhaps the band gap had been mechanically perturbed to zero or was lost in thermal effects and the only discernible change was once the

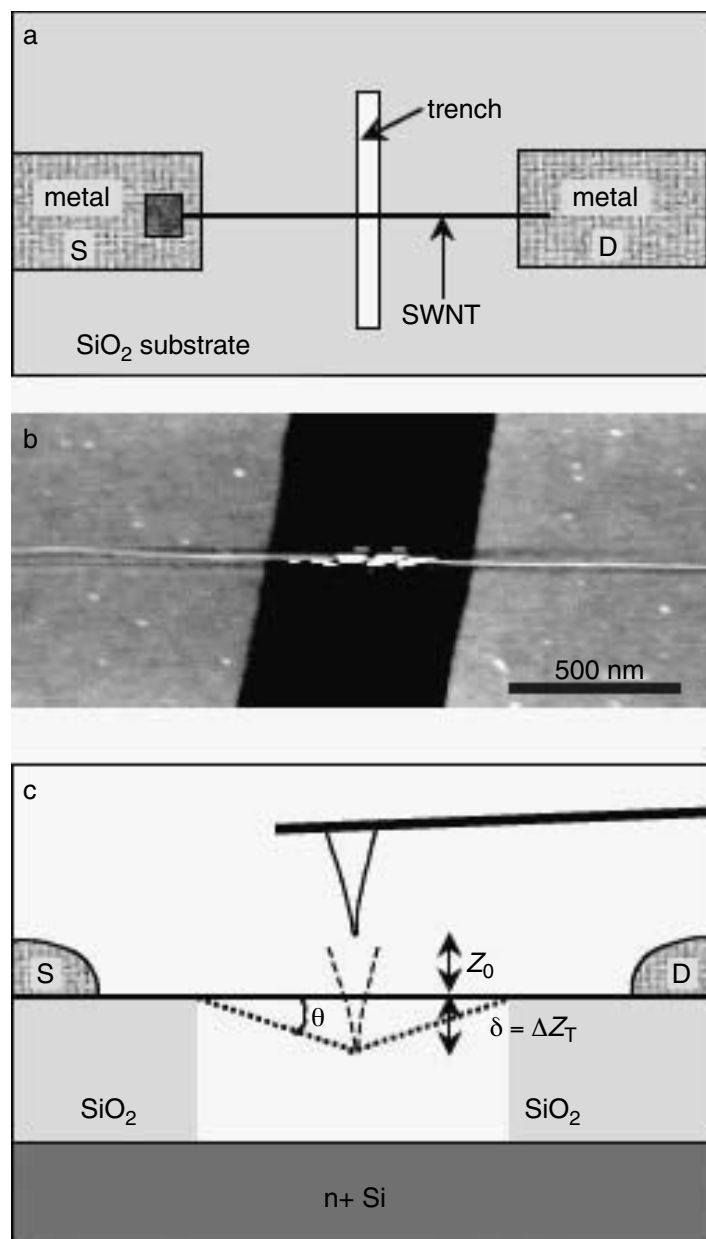


**Figure 7.6** (a) Schematic of a suspended nanotube grown across a trench by patterned chemical vapor deposition (CVD) growth and then contacted by evaporated metal electrodes. (b) Atomic force microscope (AFM) image of a suspended nanotube. (c) Schematic of the AFM stretching measurements. (Reprinted from Tombler, T.W. et al., *Nature*, 405, 769–772, 2000. With permission. Copyright © 2000 by the Nature Publishing Group.)

band gap increased. The semiconducting tubes they measured showed both increases and decreases in the band gap, which comports well with the theory (Equation 7.3).

Using the band-gap model shown in Figure 7.8 for their devices, they derived this equation to describe the low-bias off-state resistance  $R_{\text{max}}$ :



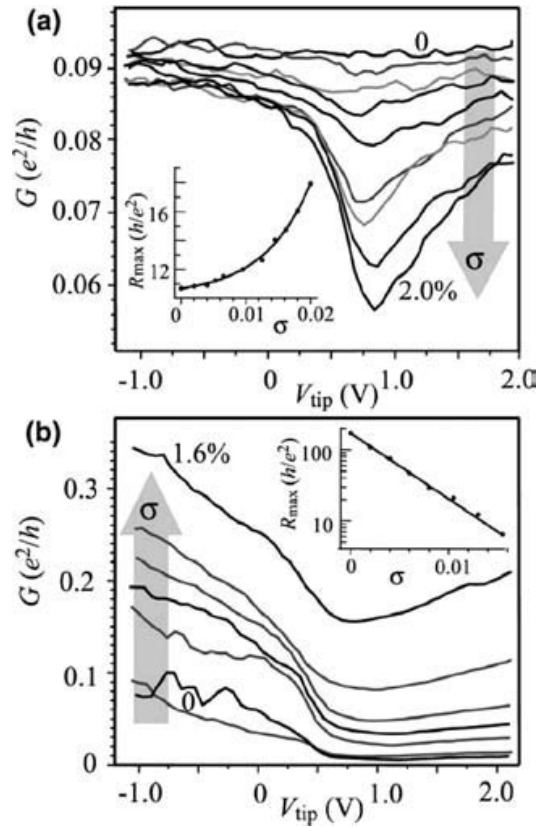


**Figure 7.7** (a)  $I$ - $V_g$  vs. strain for a metallic nanotube that shows a conductance decrease with strain. Inset: resistance in the OFF state vs. strain. (b) The same as (a) for a semiconducting tube that shows a conductance increase with strain. (Reprinted from Minot, E.D. et al., *Phys. Rev. Lett.*, 90, 156401, 2003. With permission. Copyright © 2003 by the American Physical Society.)

$$R_{\max} = R_S + \frac{1}{|t|^2} \frac{h}{8e^2} (1 + \exp(\frac{E_g}{kT})) \quad (7.5)$$

where  $R_S$  is the contact resistance, the factor before the parentheses is the quantum resistance for two channels divided by a transmission coefficient  $|t|^2$ , and the rest is the exponential dependence on energy of the carrier population.

They used this model to extract from their data  $E_g$  and  $dE_g/d\epsilon$ . The two devices they reported showed  $E_g = 160$  meV and  $dE_g/d\epsilon = -53$  meV/% for the semiconducting tube and  $E_g = 0$  and  $dE_g/d\epsilon = +35$  meV/% for the metallic tube (Figure 7.7). These values fall in the middle of the range of the theoretical predictions. In future experiments, this information about the band gaps and their responses to strain could be correlated with diameter measurements from Raman spectroscopy and AFM to determine uniquely the chirality of a tube.

Around the same time as Minot's work, Cao et al.<sup>38</sup> devised a new experiment that removed the AFM tip–nanotube interaction. They fabricated a surface-micromachined cantilever and platform, grew suspended tubes

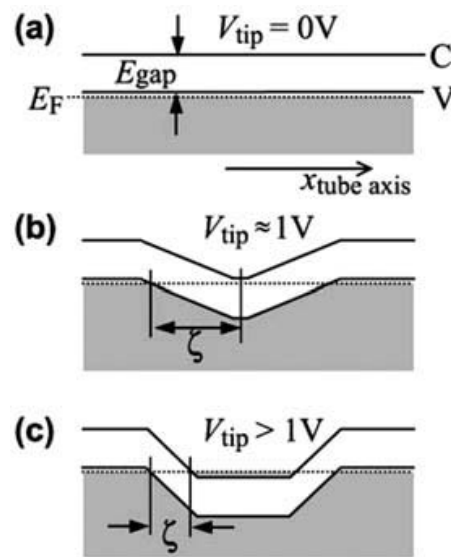


**Figure 7.8** (a) The flat-band structure for a suspended nanotube with a local tip gate at  $V_g = 0$  V. (b) The band structure in the OFF state. At  $V_g = 1$  V, the band has been pulled down to the point that minimizes the current from both holes and electrons. (c) As  $V_g$  is increased further, the tunneling barrier shrinks, so the contribution of tunneling and therefore the overall conductance increase. (Reprinted from Minot, E.D. et al., *Phys. Rev. Lett.*, 90, 156401, 2003. With permission. Copyright © 2003 by the American Physical Society.)

between the two, and used an AFM tip to press down on the cantilever, thereby controllably straining the suspended nanotube (Figure 7.9). They were able to distinguish metallic, semiconducting, and SGS tubes from each other by gating the tube from the backside of the silicon chip, and they observed conductance decreases in all three types for strains up to about 1%. The gauge factor, the change in resistance divided by the strain ( $\Delta R/R/\epsilon$ ), is the engineering metric typically used to characterize piezoresistance for silicon, in which the response is linear with strain. In silicon, the achievable gauge factor range is typically 80 to 200.<sup>21</sup> For two SGS tubes, they found gauge factors of 600 and 1000 for strains up to 0.2%, where the response was reasonably linear. For one semiconducting tube, they found a gauge factor of 150 (<0.15% strain), and for two metallic tubes, they found gauge factors of 40 and 60 (<0.15% strain). The SGS tubes show decreased conductance, even though they are expected to have a decreased band gap for the first 0.2% strain.<sup>29</sup> The responses for all three types of tubes were stronger than the theory would predict. This may be attributed to local deformations at the edges of the cantilever and platform, though that seems unlikely at these low strains.

To summarize the results of these three major experiments on suspended nanotubes, SGS tubes have shown decreased conductance over both small and large strain ranges, which contradicts the theoretical prediction that the conductance should increase and then decrease (Equation 7.4). Semiconducting tubes have shown both increases and decreases, which agrees with Equation 7.3. Metallic tubes have shown both no response, as predicted by

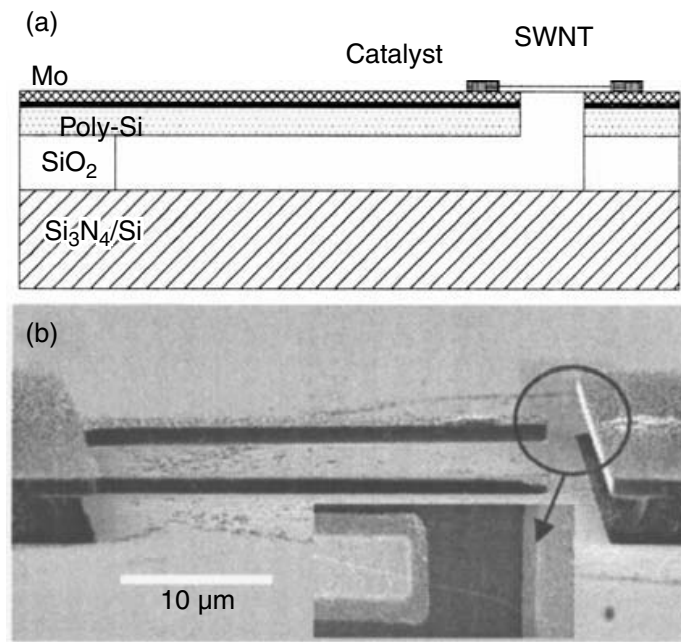


**Figure 7.9** (a) Schematic of a cantilever and a solid platform with a suspended nanotube between them. (b) Scanning electron microscope (SEM) images of the structure. (Reprinted from Cao, J. et al., *Phys. Rev. Lett.*, 90, 157601, 2003. With permission. Copyright © 2003 by the American Physical Society.)

theory, and strong responses, depending on the experiment. Under some circumstances, all three types of tubes showed responses much stronger than expected. Interpreting these measurements is complicated by the possibility that small mechanical deformations and thermal effects may mask the difference between metallic and SGS tubes, and that local deformations may play a large role at the tube–tip and tip–edge interfaces.

## 7.5 Electrical measurements of strain-induced band-gap changes in tubes on a surface

Up to this point, the work I have discussed was on suspended tubes. However, a practical approach to a mechanical sensor would more likely involve using tubes on surfaces because they are easier to fabricate and less fragile. Measuring tubes on surfaces also alleviates the uncertainties about tip–tube and edge–tube interactions that may have played a role in the suspended experiments. In work conducted by myself and others in Hongjie Dai's group,<sup>39</sup> we grew nanotubes on the surface of a deformable thin membrane of silicon nitride and then strained them by deforming the membrane with gas pressure (Figure 7.10).

We measured several semiconducting and SGS tubes and found no metallic tubes. Much like Minot et al., we measured conductance changes under strains of up to 0.2% and their dependence on the gate voltage, in our case a metal back gate applied to the back of the 1- $\mu\text{m}$ -thick membrane (Figure 7.11). The several SGS tubes we measured showed conductance

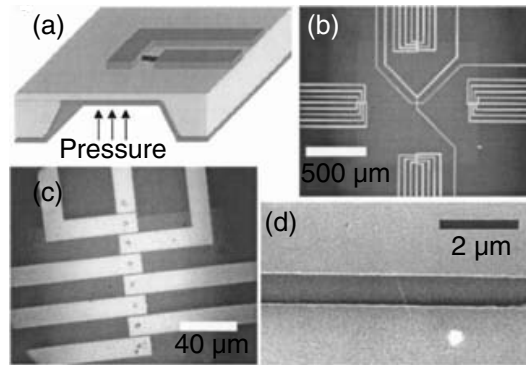


**Figure 7.10** (a) Schematic of a nanotube device on a membrane. The bottom layer is the gate electrode. (b) Optical microscope image of a membrane (~1 mm on a side) with electrodes. (c) Zoomed-in image of devices (14 μm apart) near the edge of the membrane. (d) SEM image of a nanotube crossing the gap (~800 nm) between two electrodes. (Reprinted from Grow, R.J. et al., *Appl. Phys. Lett.*, 86, 093104, 2005. With permission. Copyright © 2005 by the American Institute of Physics.)

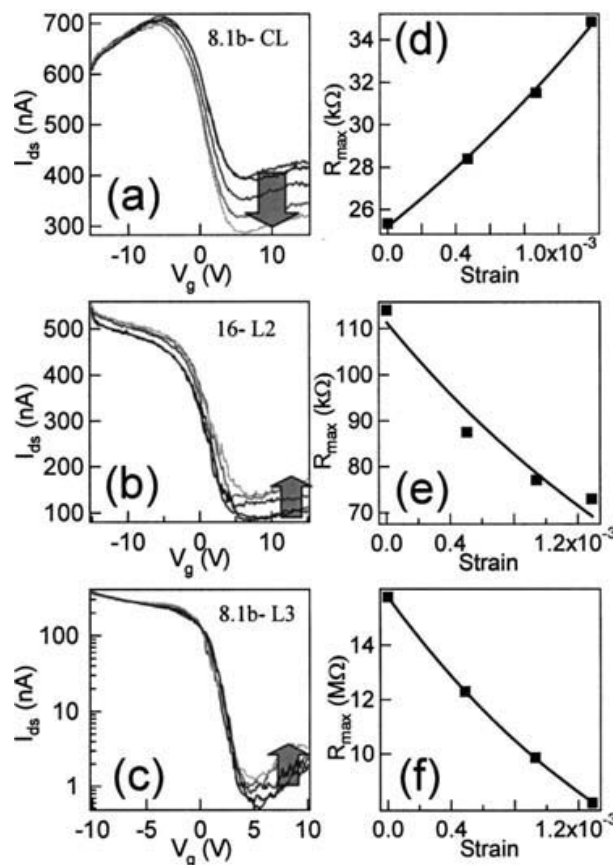


**Figure 7.11** (a–c)  $I_{ds}$ - $V_g$  curves for nanotube devices on the membrane at 0, 5, 10, 15, and 0 psi ( $V_{ds} = 10$  mV). The arrows show which way the curves moved as the pressure increased. The first two devices are SGS tubes, and the third one is semi-conducting. (d–f)  $R_{max}$  values of the  $I_{ds}$ - $V_g$  curves vs. strain and a fit to an exponential. (Reprinted from Grow, R.J. et al., *Appl. Phys. Lett.*, 86, 093104, 2005. With permission. Copyright © 2005 by the American Institute of Physics.)

changes in both directions, in opposition to Equation 7.4, as did the four semiconducting tubes (three increases and one decrease). Using a simple model of the band structure (Figure 7.12), we understand the physics of the device in the low-bias-regime OFF state to also be governed by Equation 7.5, and it is clear that the change in band gap of the nanotube with strain is the dominant effect, because the observed conductance change is largest near the threshold voltage, where the Fermi level of the contacts falls in the band gap. We used Equation 7.5 to extract the band gap and band-gap changes for most of the tubes, which I have plotted in Figure 7.13. Some of the band-gap changes clearly exceed the theoretical predictions. In addition, the initial unstrained band gaps for the SGS tubes appear larger than one would expect given the diameters we measured with AFM (Figure 7.14).

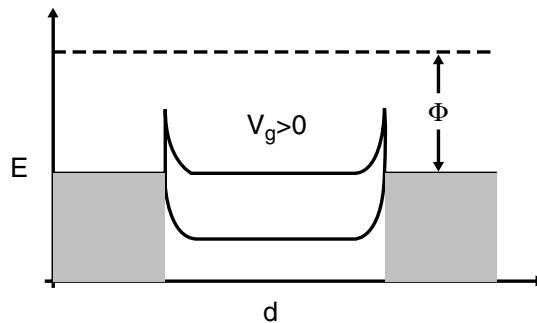


**Figure 7.12** The band structure of the same nanotube device shown in Figure 7.5, but this time in the OFF state.

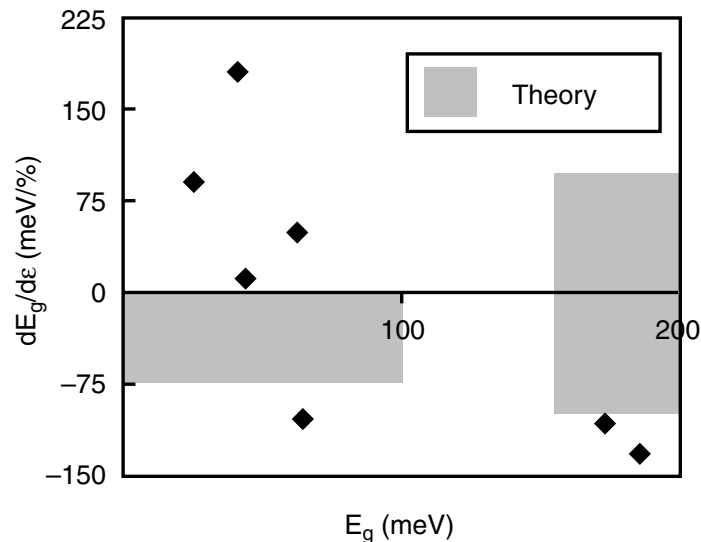


**Figure 7.13** The 10 tubes we measured plotted by their band gap vs. the change in band gap with strain. The gray regions show the predicted response strength and direction for the two types of tubes.



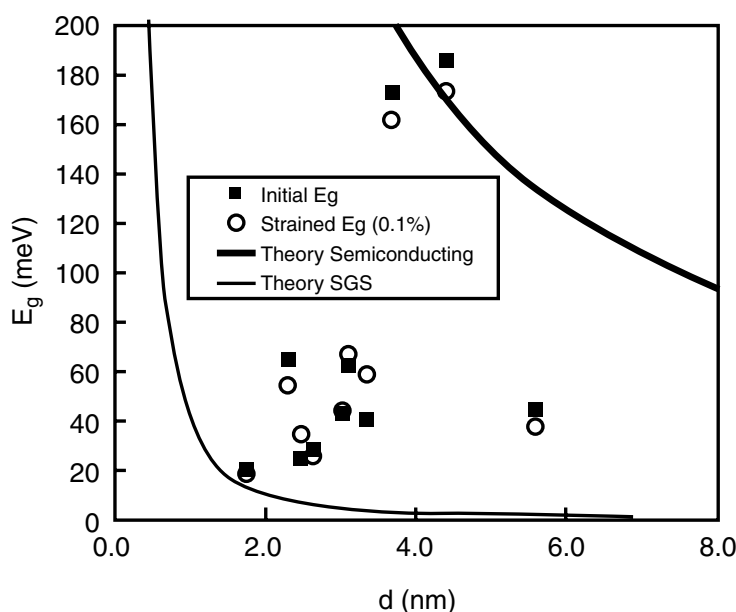


**Figure 7.14** The 10 tubes we measured plotted by their band gap at 0 and 0.1% strain vs. the AFM-measured tube diameter along with theory curves. (Reprinted from Grow, R.J. et al., *Appl. Phys. Lett.*, 86, 093104, 2005. With permission. Copyright © 2005 by the American Institute of Physics.)

We attribute both of these discrepancies to interactions with the rather rough ( $\sim 1$ -nm root-mean-square [RMS]) silicon nitride surface. Given the nanotube's strong interaction with the surface, it likely conforms to the rough surface by twisting around or flattening itself over obstacles, creating local perturbations to the nanotube structure, which would induce local band-gap changes. Local deformations, including uniaxial strain, torsion, squashing,<sup>40</sup> or adhering to the surface,<sup>41</sup> can increase the band gap of a metallic or SGS tube. The larger tubes could actually be double walled<sup>42</sup> or two bundled together,<sup>43</sup> which would perturb the band structure as well. This pre-perturbed state probably also accounts for the anomalously large responses to strain. The fact that SGS tubes changed conductance in both directions is more puzzling. Perhaps the perturbations are making metallic tubes look SGS, and then they show an increase rather than a decrease in band gap.

In conclusion, except for SGS tubes changing conductance in both directions, the measurements yield data much like the suspended systems that others have measured, but perturbations from interaction with the surface can change the behavior. This means that smooth surfaces would be important for reproducibility in applications, or that stress concentration features might be useful for engineering the band gap of a nanotube for an electronic device or a mechanical sensor.

## 7.6 Conclusion of piezoresistance of nanotubes

Analytical and computational studies of the effects of mechanical deformations on the band structure of nanotubes have predicted that uniaxial strain,

torsion, bending, and squashing all have effects that depend on the chirality of the nanotube. Nanotubes have only been studied in detail experimentally under uniaxial strain, and they have shown behavior reasonably close to theory, although responses stronger than the theory predicts have regularly been observed and not explained well, and the behavior of SGS and metallic tubes does not seem to match the theory. Most likely, that comes from difficulties distinguishing the two, and future experiments to make a direct determination of the chirality are needed to sort the behavior out completely.

In considering nanotubes vs. silicon for practical mechanical sensor applications, there are a number of advantages and disadvantages. Nanotubes clearly show stronger responses than silicon over a practical strain range for silicon ( $<0.2\%$ ). This would lead to higher sensitivity, if a less linear response, since nanotubes respond exponentially. They also have a lower temperature coefficient of resistivity, by about five times, than a typical silicon piezoresistor.<sup>44</sup> This means that temperature compensation circuitry, which makes up a significant part of the cost of silicon sensors, might be able to be eliminated in some cases. The difficulties with nanotube sensors, on the other hand, are similar to the difficulties in making any type of electronic devices with nanotubes. The piezoresistive effect depends strongly on the chirality, and the strain the tube is under depends on the placement and the alignment of the nanotube, none of which are very easily controlled. In addition, single nanotubes tend to be noisy.<sup>45,46</sup> One great advantage that nanotubes have is that they do not have to be fabricated on silicon. One group has done electronic and optical measurements of nanotube films on other surfaces and found responses.<sup>47,48</sup> It may be possible to make piezoresistive composites of polymers mixed with nanotubes that could withstand a much greater range of strains than silicon could. This ensemble approach would have noise advantages as well.

## 7.7 Electrostatic actuation

While piezoresistance is useful for the detection of motion, the production of motion requires a material capable of electromechanical actuation. Typical actuator materials are piezoelectric. The piezoelectric effect differs from the piezoresistive effect in that the mechanical deformation, rather than changing the resistance, induces a voltage across the material, which can be used for sensing. This effect can also be reversed so that putting a voltage across the material induces a change in shape, which can be used for actuation. Some examples of piezoelectric materials are quartz, zinc oxide, and ceramics such as lead zirconate titanate (PZT).

Carbon nanotubes are not piezoelectric, but an effect has been demonstrated that should be useful for actuation. Baughman and colleagues have shown that a two-dimensional film of nanotubes immersed in an electrolyte solution can function as an electromechanical actuator.<sup>5,49</sup> When a voltage is applied to the nanotube film, charge is injected into the nanotubes. The electrolyte solution provides a source of oppositely charged ions, which form

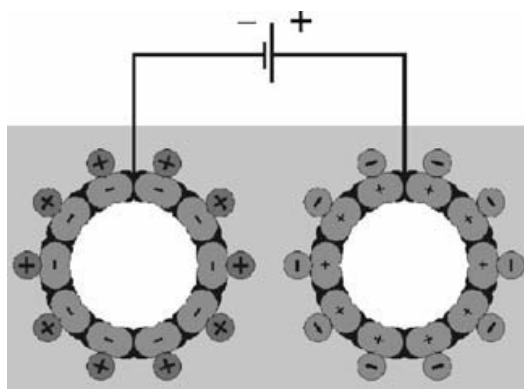


**Figure 7.15** Schematic of two nanotubes with a voltage between them in an electrolyte solution. The injected charges are matched by ions in the electrolyte, forming double layers of charge and allowing large amounts of charge to be injected. These charges then actuate the nanotubes by making them elongate or shrink, depending on the polarities and the charge densities. (Reprinted from Baughman, R.H. et al., *Science*, 284, 1340–1344, 1999. With permission. Copyright © 1999 by the American Association for the Advancement of Science.)

a double layer with the injected charges at the surface of the nanotubes (Figure 7.15). This additional charge causes the nanotubes to elongate and the film stretches out. Additional modeling has been done to explain the mechanisms in more detail.<sup>50,51</sup> At small numbers of injected carriers, the response is quantum mechanical in nature. At larger numbers, the response becomes coulombic, i.e., the carriers all repel each other.

Nanotubes using this effect have many advantages over piezoelectric and other types of electrically actuated materials. They operate at a few volts, in contrast to hundreds. They can achieve strains greater than 1% (10 times larger than piezoelectrics), and they can operate at high temperatures (up to 350°C demonstrated, possibly up to 1000°C). They have already achieved stresses of 26 MPa, which is 100 times greater than that achievable by animal muscle and on par with top piezoelectric materials (40 MPa), but it is still 100 times lower than the theoretical maximum that could be achieved with good separation between well-aligned single-walled nanotubes, which would allow for better penetration of the electrolyte and direct all the motion in one direction. The one major disadvantage is that their response time is limited by the diffusion of ions in the electrolyte, which might limit some applications.

A different electrostatic actuation method was demonstrated by Kim and Lieber<sup>52</sup> in the operation of nanotube nanotweezers (Figure 7.16). They started with a tapered glass filament, deposited metal on both sides of it to create two conducting electrodes, and attached one nanotube to each of the metal sides. When they applied a voltage of 0 to 8.3 V across the nanotubes, they saw reversible deformations of the nanotubes toward each other. At about 8.5 V, the two nanotubes suddenly snapped together, and then stayed together even when the voltage had been removed, because of the attractive van der Waals forces between the tubes. However, the two tubes could be separated again

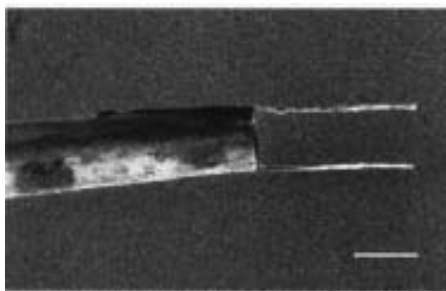


**Figure 7.16** SEM image of the nanotube nanotweezers. The scale bar is 2  $\mu\text{m}$ . (Reprinted from Kim, P. and Lieber, C.M., *Science*, 286, 2148–2150, 1999. With permission. Copyright © 1999 by the American Association for the Advancement of Science.)

by putting a voltage on them and bringing them near a grounded counter-electrode. The mechanism for this is the electrostatic attraction of two oppositely charged nanotubes overcoming the resistance of their natural mechanical stiffness. They used these tweezers to trap and move some nanoscale objects such as SiC nanoclusters ( $\sim 500$  nm) and GaAs nanowires.

Also from Lieber's group, Rueckes et al.<sup>14</sup> have shown a concept for a nanotube-based nonvolatile random-access memory (NRAM), which has since been developed further for commercial application by the start-up company Nantero. The basic NRAM cell concept consists of a nanotube suspended above another nanotube running perpendicular to it (Figure 7.17). This device can store a bit of information because it is bistable. In the OFF position, the nanotubes are separated. Their dynamic operation is much like the nanotube nanotweezers. In order to change the device to the ON position, the two nanotubes are attracted electrostatically by applying a voltage between them, so the top nanotube stretches downward and comes into contact with the bottom nanotube. Once there, it sticks because of the van der Waals interaction between the tubes. Readout consists of applying a voltage between the two tubes and seeing if a current flows between them. The memory cell can be reverted to the OFF state by applying the same voltage to both tubes, which causes them to separate and return to their initial positions.

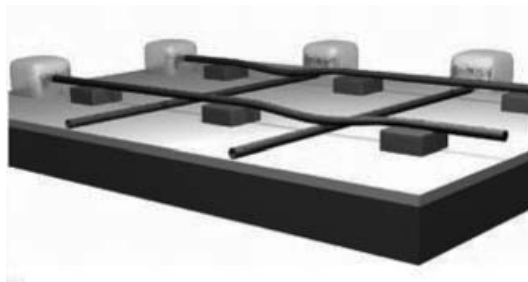


**Figure 7.17** Schematic of an array of nanotube-based nonvolatile random-access memory (NRAM) cells. (Reprinted from Rueckes, T. et al., *Science*, 289, 94, 2000. With permission. Copyright © 2000 by the American Association for the Advancement of Science.)

Nantero has refined this concept to using films of nanotubes suspended above metal bottom electrodes, probably for ease of fabrication and operational reliability. After nanotube AFM tips, this may turn out to be the next major product that takes advantage of the mechanical properties of nanotubes.

Cummings and Zettl and Fennimore et al. have developed interesting structures that take advantage of the interactions between the shells of multiwalled nanotubes. They have made linear bearings<sup>53</sup> and rotational bearings and motors<sup>54</sup> by allowing one nanotube shell to slide within another. Graphite has well-known lubricating properties caused by the low friction between graphene sheets as they slip past each other, and nanotube shell-shell interactions should be similar. The first structure they developed was a linear bearing,<sup>53</sup> in which they used a nanoscale probe to slide an inner shell of a multiwalled nanotube back and forth smoothly within an uncapped outer shell. They found a restoring force caused by the van der Waals interaction between the two shells that tended to pull the inner shell back in, and very low friction forces. They also observed no wear after many cycles, as they did this inside a transmission electron microscope (TEM), which allowed atomic resolution imaging.

In a second experiment,<sup>54</sup> they fabricated a structure in which the outer shell of a multiwalled tube was cut so it could slide freely on an inner shell. A piece of metal was connected to this outer shell, and they were able to rotate the outer shell as an electric motor would by electrostatics from other electrodes. This work evokes Drexler's<sup>55,56</sup> vision of atomically precise mechanical components, such as gears, bearings, and motors.

## 7.8 *Nanoelectromechanical systems*

The unique mechanical and electromechanical properties of nanotubes may well find application in the emerging field of nanoelectromechanical systems (NEMS). Beginning in the 1970s, microelectromechanical systems (MEMS) leveraged silicon processing knowledge from the integrated circuit industry to make three-dimensional silicon structures with integrated sensing and actuation elements.<sup>21</sup> Common MEMS products today include AFM cantilevers, inkjet print heads, Texas Instruments' Digital Light Processor,\* and myriad mechanical sensors, such as accelerometers, pressure sensors, gyroscopes, and strain gauges. Most of these structures have features no smaller than a few microns, but as the microelectronics industry has continued to follow Moore's law, advances in photolithography and electron-beam lithography have made much smaller feature sizes possible by top-down fabrication, down to 90 and ~5 nm, respectively. Recent innovations in the bottom-up synthesis of nanoscale structures also make it possible to build up similar structures chemically. Together, these techniques make it possible to take MEMS down to the nanoscale, resulting in NEMS.<sup>57,58</sup>

\* Texas Instruments, Inc., Dallas, TX, [www.ti.com](http://www.ti.com).



NEMS researchers are exploring the mechanical aspects of nanoscale structures for sensing applications such as magnetic resonance force microscopy (MRFM) and mass spectrometry,<sup>59</sup> radiofrequency (RF) resonators for RF generation and filtering, and fundamental measurements of structures as they reach the length scale at which quantum effects become visible.<sup>60</sup> People have measured the quantum of heat conductance,<sup>61</sup> observed single electrons interacting with nanoscale oscillators, and attempted to observe the quantization of mechanical motions at the appropriate length scale. The nanostructures typically used in these experiments include top-down fabricated semiconductors, bottom-up fabricated semiconductor nanowires, and carbon nanotubes.

Most of these proposed applications involve exciting a nanoscale oscillator, detecting its motion, and then noting changes in the frequency or amplitude of the motion in response to changes in the environment or excitation signal. One of the great challenges in this area is that the quality factor  $Q$  of a resonator seems to trend downward with size in the same material, typically silicon or another crystalline semiconductor. Possible mechanisms for this include increased effects of surface defects or adsorbates and thermoelastic damping. Carbon nanotubes may be the ultimate material for NEMS oscillators because their extremely small size and structural perfection may solve this  $Q$  problem. Since they can function as transistors, they can also sense their own motion as they move with respect to a charged gate.

A number of groups have worked to realize nanotube-based oscillators. Researchers in Paul McEuen's group had a recent major breakthrough when they succeeded in making self-detecting electromechanical oscillators from suspended nanotubes.<sup>62</sup> They fabricated an electrically contacted nanotube suspended across a  $\sim 1\text{-}\mu\text{m}$  trench with a back gate (Figure 7.18). Then, they

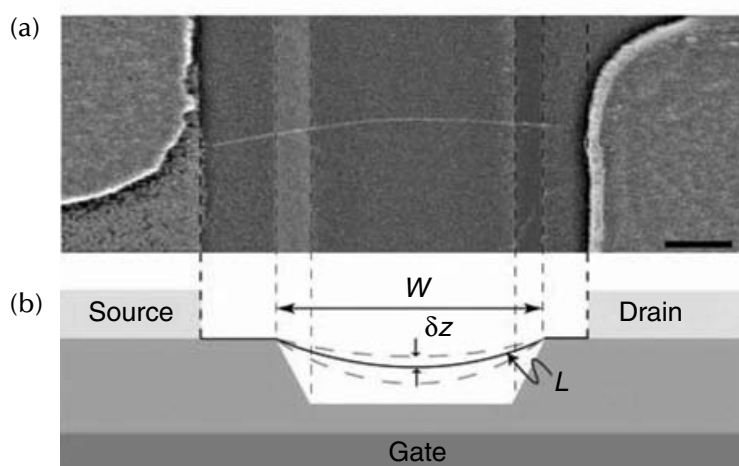


**Figure 7.18** (a) SEM image of a suspended nanotube operated as an oscillator. (b) Schematic of the suspended nanotube and structure. (Reprinted from Sazonova, V. et al., *Nature*, 431, 284–287, 2004. With permission. Copyright © 2004 by the Nature Publishing Group.)

excited the nanotube electrostatically by putting a voltage between it and the gate with both direct current (DC) and alternating current (AC) components. The AC component excited the oscillation, and the DC component varied the tension in the tube. They were able to read out the motion of the nanotube by also measuring an AC going through it. If the nanotube is moving because the drive frequency is on the nanotube's resonance, the gate efficiency changes as the nanotube moves in relation to the gate. This changes the conductance of the nanotube. Detecting this small current change, given the nanotube's generally large resistance and the complication of large capacitive currents to the gate, required using the nanotube as a mixer and demodulating the desired signal. This neatly solved the major problems that had plagued earlier experiments. They were able to extract the current through the nanotube with a lock-in amplifier. They operated the oscillator from 3 to 200 MHz and were able to excite different modes of the nanotube. They also varied the DC component of the gate voltage to change the tension in the tube and were able to distinguish different mechanical regimes. In addition, they varied the amplitude of the AC component of the driving gate voltage and were therefore able to push the oscillator to a nonlinear regime. Despite the hopes of high Qs, they did not achieve a Q higher than about 200. The experiments were conducted at  $10^{-4}$  Torr. At about 10 Torr, the ambient gases damped out the motions completely. It is possible that the low Qs came from surface adsorbates or clamping losses, which could be addressed in future experiments. The force sensitivities they measured were about 1 fN/SQRT(Hz), which is within a factor of 10 of the highest sensitivity achieved at room temperature by any method. Even with no improvements in Q, the force sensitivity achievable at low temperature should be as good as 5 aN/SQRT(Hz), which is also comparable to the highest measured. The combination of high operating frequency, high force sensitivity, and tunability along multiple parameters promises to make nanotubes very useful as oscillators.

## 7.9 Conclusion

Nanotubes have remarkable mechanical and electromechanical properties: stiffness, strength, piezoresistance, the capability of electrostatic actuation, and few structural defects. These properties are being modeled and explored and are starting to find uses. They provide the building blocks for motion detection and actuation, novel memory architectures, nanoscale precision manipulation, low-friction bearings, and even oscillators. While the potential for these applications has been demonstrated, many challenges remain for researchers to tackle. These are exciting times for the applications of nanotubes, and they offer much promise for electromechanical applications.

## References

1. Iijima, S., Helical microtubules of graphitic carbon, *Nature* 354, 56, 1991.

[www.iran-mavad.com](http://www.iran-mavad.com)

مرجع دانشجویان و مهندسين مواد

2. Dresselhaus, M. S., Dresselhaus, G., and Eklund, P. C., *Science of Fullerenes and Carbon Nanotubes*, Academic Press, San Diego, 1996.
3. Saito, R., Dresselhaus, G., and Dresselhaus, M. S., *Physical Properties of Carbon Nanotubes*, Imperial College Press, London, 1998.
4. Dresselhaus, M. S., Dresselhaus, G., and Avouris, P., Carbon nanotubes: synthesis, structure, properties, and applications, in *Topics in Applied Physics*, Springer, Berlin, 2001.
5. Baughman, R. H., Zakhidov, A. A., and de Heer, W. A., Carbon nanotubes: the route toward applications, *Science* 297, 787–792, 2002.
6. Treacy, M. M. J., Ebbesen, T. W., and Gibson, J. M., Exceptionally high Young's modulus observed for individual carbon nanotubes, *Nature* 381, 678–680, 1996.
7. Krishnan, A., Dujardin, E., Ebbesen, T. W., Yianilos, P. N., and Treacy, M. M. J., Young's modulus of single-walled nanotubes, *Physical Review B* 58, 14013–14019, 1998.
8. Yu, M.-F., Files, B. S., Arepalli, S., and Ruoff, R. S., Tensile loading of ropes of single-wall nanotubes and their mechanical properties, *Physical Review Letters* 84, 5552, 2000.
9. Gao, G., Agin, T., and III, Goddard, W. A., Energetics, structure, mechanical and vibrational properties of single-walled carbon nanotubes, *Nanotechnology* 3, 184, 1998.
10. Nardelli, M. B. and Bernholc, J., Mechanical deformations and coherent transport in carbon nanotubes, *Physical Review B (Condensed Matter)* 60, R16338–41, 1999.
11. Walters, D. A., Ericson, L. M., Casavant, M. J., Liu, J., Colbert, D. T., Smith, K. A., and Smalley, R. E., Elastic strain of freely suspended single-wall carbon nanotube ropes, *Applied Physics Letters* 74, 3803–3805, 1999.
12. Falvo, M. R., Clary, G. J., Taylor, R. M., Chi, V., Brooks, F. P., Washburn, S., and Superfine, R., Bending and buckling of carbon nanotubes under large strain, *Nature* 389, 582–584, 1997.
13. Dai, H. J., Hafner, J. H., Rinzler, A. G., Colbert, D. T., and Smalley, R. E., Nanotubes as nanoprobe in scanning probe microscopy, *Nature* 384, 147–150, 1996.
14. Rueckes, T., Kim, K., Joselevich, E., Tseng, G. Y., Cheung, C. L., and Lieber, C. M., Carbon nanotube-based nonvolatile random access memory for molecular computing, *Science* 289, 94, 2000.
15. Yakobson, B. I. and Smalley, R. E., Fullerene nanotubes: C1,000,000 and beyond, *American Scientist* 85, 324–337, 1997.
16. Mintmire, J. W., Dunlap, B. I., and White, C. T., Are fullerene tubules metallic? *Physical Review Letters* 68, 631, 1992.
17. Kane, C. L. and Mele, E. J., Size, shape, and low energy electronic structure of carbon nanotubes, *Physical Review Letters* 78, 1932–1935, 1997.
18. Smith, C. S., Piezoresistance effect in germanium and silicon, *Physical Review* 94, 42, 1954.
19. Herring, C. and Vogt, E., Transport and deformation: potential theory for many-valley semiconductors with anisotropic scattering, *Physical Review* 101, 944–961, 1956.
20. Kanda, Y., Piezoresistance effect of silicon, *Sensors and Actuators A* 28, 83–91, 1991.

21. Kovacs, G. T. A., *Micromachined Transducers Sourcebook*, McGraw-Hill, New York, 1998.
22. Pierret, R. F., *Semiconductor Device Fundamentals*, Addison-Wesley Publishing Company, Reading, MA, 1996.
23. Maiti, A., Carbon nanotubes: bandgap engineering with strain, *Nature Materials* 2, 440–442, 2003.
24. Welser, J., Hoyt, J. L., and Gibbons, J. F., Electron mobility enhancement in strained-Si n-type metal-oxide-semiconductor field-effect transistors, *Electron Device Letters, IEEE* 15, 100, 1994.
25. Heyd, R., Charlier, A., and McRae, E., Uniaxial-stress effects on the electronic properties of carbon nanotubes, *Physical Review B (Condensed Matter)* 55, 6820–6824, 1997.
26. Rochefort, A., Avouris, P., Lesage, F., and Salahub, D. R., Electrical and mechanical properties of distorted carbon nanotubes, *Physical Review B (Condensed Matter)* 60, 13824–13830, 1999.
27. Yang, L., Anantram, M. P., Han, J., and Lu, J. P., Band-gap change of carbon nanotubes: effect of small uniaxial and torsional strain, *Physical Review B* 60, 13874–13878, 1999.
28. Yang, L. and Han, J., Electronic structure of deformed carbon nanotubes, *Physical Review Letters* 85, 154–157, 2000.
29. Kleiner, A. and Eggert, S., Band gaps of primary metallic carbon nanotubes, *Physical Review B (Condensed Matter)* 63, 073408-4, 2001.
30. Balents, L. and Fisher, M. P. A., Correlation effects in carbon nanotubes, *Physical Review B* 55, R11973–R11976, 1997.
31. Gloor, T. A. and Mila, F., Correlation gap in armchair carbon nanotubes, *Europhysics Letters* 61, 513–519, 2003.
32. Gloor, T. A. and Mila, F., Strain induced correlation gaps in carbon nanotubes, *European Physical Journal B: Condensed Matter* 38, 9, 2004.
33. Tombler, T. W., Zhou, C. W., Alexseyev, L., Kong, J., Dai, H. J., Lei, L., Jayanthi, C. S., Tang, M. J., and Wu, S. Y., Reversible electromechanical characteristics of carbon nanotubes under local-probe manipulation, *Nature* 405, 769–772, 2000.
34. Liu, L., Jayanthi, C. S., Tang, M. J., Wu, S. Y., Tombler, T. W., Zhou, C. W., Alexseyev, L., Kong, J., and Dai, H. J., Controllable reversibility of an sp(2) to sp(3) transition of a single wall nanotube under the manipulation of an AFM tip: a nanoscale electromechanical switch?, *Physical Review Letters* 84, 4950–4953, 2000.
35. Maiti, A., Mechanical deformation in carbon nanotubes: bent tubes vs. tubes pushed by atomically sharp tips, *Chemical Physics Letters* 331, 21–25, 2000.
36. Maiti, A., Svizhenko, A., and Anantram, M. P., Electronic transport through carbon nanotubes: effects of structural deformation and tube chirality, *Physical Review Letters* 88, 126805-4, 2002.
37. Minot, E. D., Yaish, Y., Sazonova, V., Park, J. Y., Brink, M., and McEuen, P. L., Tuning carbon nanotube band gaps with strain, *Physical Review Letters* 90, 156401-4, 2003.
38. Cao, J., Wang, Q., and Dai, H. J., Electromechanical properties of metallic, quasimetallic, and semiconducting carbon nanotubes under stretching, *Physical Review Letters* 90, 157601, 2003.

39. Grow, R. J., Wang, Q., Cao, J., Wang, D., and Dai, H., Piezoresistance of carbon nanotubes on deformable thin-film membranes, *Applied Physics Letters* 86, 093104, 2005.
40. Lammert, P. E., Zhang, P. H., and Crespi, V. H., Gapping by squashing: metal-insulator and insulator-metal transitions in collapsed carbon nanotubes, *Physical Review Letters* 84, 2453–2456, 2000.
41. Hertel, T., Walkup, R. E., and Avouris, P., Deformation of carbon nanotubes by surface van der Waals forces, *Physical Review B (Condensed Matter)* 58, 13870–13873, 1998.
42. Kwon, Y.-K. and Tomanek, D., Electronic and structural properties of multi-wall carbon nanotubes, *Physical Review B (Condensed Matter)* 58, R16001-4, 1998.
43. Reich, S., Thomsen, C., and Ordejon, P., Electronic band structure of isolated and bundled carbon nanotubes, *Physical Review B (Condensed Matter and Materials Physics)* 65, 155411-11, 2002.
44. Kane, C. L., Mele, E. J., Lee, R. S., Fischer, J. E., Petit, P., Dai, H., Thess, A., Smalley, R. E., Verschuere, A. R. M., Tans, S. J., and Dekker, C., Temperature-dependent resistivity of single-wall carbon nanotubes, *Europhysics Letters* 41, 683–688, 1998.
45. Collins, P. G., Fuhrer, M. S., and Zettl, A., 1/f noise in carbon nanotubes, *Applied Physics Letters* 76, 894–896, 2000.
46. Snow, E. S., Novak, J. P., Lay, M. D., and Perkins, F. K., 1/f noise in single-walled carbon nanotube devices, *Applied Physics Letters* 85, 4172, 2004.
47. Li, Z. L., Dharap, P., Nagarajaiah, S., Barrera, E. V., and Kim, J. D., Carbon nanotube film sensors, *Advanced Materials* 16, 640, 2004.
48. Dharap, P., Li, Z. L., Nagarajaiah, S., and Barrera, E. V., Nanotube film based on single-wall carbon nanotubes for strain sensing, *Nanotechnology* 15, 379–382, 2004.
49. Baughman, R. H., Cui, C., Zakhidov, A. A., Iqbal, Z., Barisci, J. N., Spinks, G. M., Wallace, G. G., Mazzoldi, A., De Rossi, D., Rinzler, A. G., Jaschinski, O., Roth, S., and Kertesz, M., Carbon nanotube actuators, *Science* 284, 1340–1344, 1999.
50. Gartstein, Y. N., Zakhidov, A. A., and Baughman, R. H., Charge-induced anisotropic distortions of semiconducting and metallic carbon nanotubes, *Physical Review Letters* 89, 045503, 2002.
51. Gartstein, Y. N., Zakhidov, A. A., and Baughman, R. H., Mechanical and electromechanical coupling in carbon nanotube distortions, *Physical Review B (Condensed Matter and Materials Physics)* 68, 115415, 2003.
52. Kim, P. and Lieber, C. M., Nanotube nanotweezers, *Science* 286, 2148–2150, 1999.
53. Cumings, J. and Zettl, A., Low-friction nanoscale linear bearing realized from multiwall carbon nanotubes, *Science* 289, 602–604, 2000.
54. Fennimore, A. M., Yuzvinsky, T. D., Han, W.-Q., Fuhrer, M. S., Cumings, J., and Zettl, A., Rotational actuators based on carbon nanotubes, *Nature* 424, 408–410, 2003.
55. Drexler, K. E., *Engines of Creation: The Coming Era of Nanotechnology*, Anchor Books, New York, 1986.
56. Drexler, K. E., *Nanosystems: Molecular Machinery, Manufacturing, and Computation*, John Wiley & Sons, New York, 1992.



57. Roukes, M., Nanoelectromechanical systems face the future, *Physics World* 14, 25–31, 2001.
58. Schwab, K. and Roukes, M., Putting Mechanics into Quantum Mechanics, *Physics Today* 2005, pp. 36–42.
59. Roukes, M., Plenty of Room Indeed, *Scientific American* 2001, p. 48.
60. Cho, A., Researchers race to put the quantum into mechanics, *Science* 299, 36, 2003.
61. Schwab, K., Henriksen, E. A., Worlock, J. M., and Roukes, M. L., Measurement of the quantum of thermal conductance, *Nature* 404, 974, 2000.
62. Sazonova, V., Yaish, Y., Ustunel, H., Roundy, D., Arias, T. A., and McEuen, P. L., A tunable carbon nanotube electromechanical oscillator, *Nature* 431, 284–287, 2004.

## *chapter eight*

---

# *Carbon nanotube-enabled materials*

*Han Gi Chae, Jing Liu, Satish Kumar*  
*Georgia Institute of Technology*

### *Contents*

8.1	Introduction .....	214
8.2	Dispersion and processing issues .....	214
8.3	Characterization of polymer/CNT composites .....	218
8.4	CNT films and fibers .....	223
8.5	Polymer/CNT composite films and fibers .....	228
8.5.1	Mechanical properties .....	228
8.5.1.1	PAN/CNT .....	229
8.5.1.2	PBO/CNT .....	234
8.5.1.3	PVA/CNT .....	234
8.5.1.4	PMMA/CNT .....	235
8.5.1.5	PS/CNT .....	240
8.5.2	Thermal properties .....	241
8.5.3	Electrical properties .....	242
8.5.4	Optical properties .....	244
8.5.5	Miscellaneous properties .....	246
8.6	Crystallization, wrapping, interaction, and intercalation .....	247
8.7	Concluding remarks .....	250
	Acknowledgment .....	252
	References .....	252

## 8.1 Introduction

Carbon nanotubes (CNTs), developed in the 1990s, are available with single wall (SWNT),<sup>1,2</sup> double wall (DWNT),<sup>3,4</sup> and multiwall (MWNT)<sup>5</sup>. By comparison, carbon fibers (typical diameter = 5 to 10  $\mu\text{m}$ ) for composite applications were developed in the 1960s,<sup>6</sup> while vapor-grown carbon nanofibers (VGCNFs) were developed in the 1980s.<sup>6-9</sup> The major synthetic routes to form CNTs are arc discharge,<sup>1</sup> laser ablation,<sup>10</sup> gas phase catalytic growth from carbon monoxide (high-pressure carbon monoxide, or HiPco),<sup>11</sup> and chemical vapor deposition (CVD).<sup>12,13</sup> Due to their exceptional mechanical, electrical, thermal, and optical properties,<sup>14,15</sup> CNTs are sometimes heralded as the ultimate reinforcing systems. The theoretical properties of CNTs have been compared with the properties of selected commercial high-performance fibers in Table 8.1. A comparison of these properties suggests that there is a significant potential for producing composites with much higher tensile strength than the current state-of-the-art composites.

Significant developments have been reported in processing CNTs<sup>16-25</sup> and polymer/CNT composite films<sup>26-34</sup> and fibers.<sup>35-40</sup> Composite studies include semicrystalline<sup>41,42</sup> and amorphous<sup>43,44</sup> thermoplastics, thermosetting<sup>45-47</sup> resins, water-soluble polymers,<sup>48</sup> liquid crystalline polymers,<sup>38,49</sup> and conjugated polymers.<sup>50-52</sup> Furthermore, CNTs are also being used to reinforce ceramics<sup>41,53</sup> and metal matrices.<sup>54-56</sup> As a result of interaction between nanotube and polymer, property improvements with CNTs include enhanced tensile modulus,<sup>36,57,58</sup> tensile strength,<sup>36,59,60</sup> torsional modulus,<sup>61</sup> compressive strength,<sup>62,63</sup> fatigue behavior,<sup>64,65</sup> toughness,<sup>35,36</sup> glass transition temperature,<sup>36,66,67</sup> electrical conductivity,<sup>68,69</sup> thermal conductivity,<sup>31,70</sup> solvent resistance,<sup>36,71</sup> and reduction in thermal shrinkage,<sup>36,62,72</sup> as well as anisotropic optical properties.<sup>36,73</sup> CNT-based materials are also being evaluated for their functional characteristics, such as flame-retardant performance,<sup>74</sup> charge storage device,<sup>75-77</sup> field emission,<sup>78-80</sup> and sensors of chemicals,<sup>81,82</sup> stress,<sup>83,84</sup> and temperature.<sup>85,86</sup>

General considerations in polymer/carbon nanotube composite research are also addressed. The field of polymer/CNT composites is only about a decade old. In this period, more than 1000 referred publications have appeared on this subject, while more than 10,000 publications have appeared on CNTs. Selected CNT films, fibers, and composites studies are summarized in this chapter.

## 8.2 Dispersion and processing issues

SWNTs agglomerate into 5- to 100-nm-diameter bundles<sup>87</sup> and form hexagonal lattices within the bundle, with binding energy between the tubes being of the order of 900 meV/nm.<sup>88</sup> The SWNT length typically ranges from 200 to >10  $\mu\text{m}$ . Therefore, counterbalancing the van der Waals interaction is one of the challenges for dispersing and exfoliating SWNTs. In addition, SWNT ropes/bundles have a highly entangled network structure. DWNTs,

**Table 8.1** Typical Properties of CNTs, Vapor-Grown Carbon Nanofiber (VGCNF), and Commercial High-Performance Fibers

	SWNT <sup>14,157,219,221-223</sup>			Carbon Fiber <sup>6</sup>			Kevlar 49 <sup>@232,361</sup>	
	DWNT <sup>352</sup>	MWNT <sup>225,353-355</sup>	VGCNF <sup>166,356-358</sup>	Zylon <sup>@232,359</sup>	Spectra <sup>@232,360</sup>			
Tensile strength (GPa)	23-63		3-20	4-7	5.8	3.1	3.6-4.1	
Tensile modulus (GPa)	640	1060	50-775	150-950	270	105	130	
Elongation at break (%)	5.8	28	—	0.5-2.5	2.5	2.5	2.8	
Density (g/cm <sup>3</sup> )	1.3-1.5	1.5						
Electrical conductivity (S/m)		~10 <sup>6</sup>		5.5 × 10 <sup>4</sup> to 9 × 10 <sup>5</sup>	1.56	0.97	<10 <sup>-13</sup>	
Typical diameter	1 nm	~5 nm	~20 nm	60-100 nm			5-10 μm	

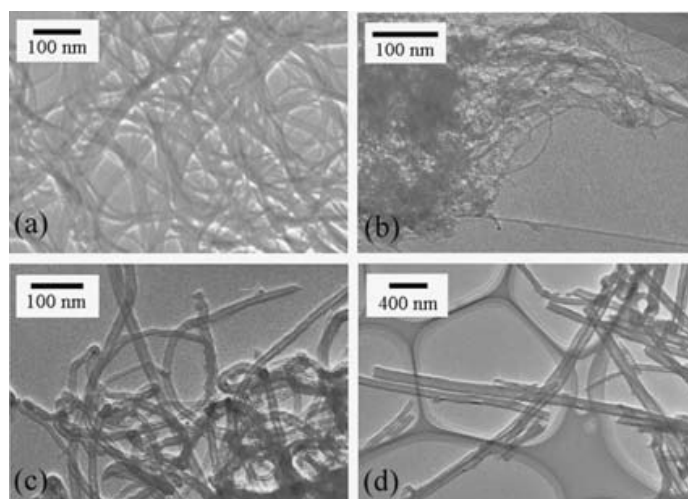


**Figure 8.1** Bright-field TEM images for (a) SWNTs, (b) DWNTs, (c) MWNTs, and (d) VGCNFs. (From ref. 163.)

MWNTs, and VGCNF generally exist as individuals and generally do not aggregate into bundles as SWNTs do (Figure 8.1). However, they can also be entangled, requiring significant effort for their dispersion. Physical and chemical approaches currently being pursued to unentangle, disperse, and exfoliate nanotubes are briefly summarized here.

Most of the polymer/CNT composite studies to date carried out in solution have employed sonication for the CNT dispersion. However, sonication introduces defects, including buckling, bending, and dislocations in the carbon structure. Prolonged sonication increases disorder, reduces nanotube length, and ultimately leads to the formation of amorphous carbon.<sup>88</sup> In addition, high shear mixing, in the presence of selected polymers, has also been used to unentangle ropes, yielding homogeneous dispersion. If the sonication is carried out in the presence of polymer, then it is also important to understand the effect of sonication on polymer molecular weight.

CNTs have been dispersed using *in situ* polymerization in a number of polymers, including polyaniline, poly(p-phenylene benzobisoxazole), poly(methyl methacrylate) (PMMA), polypyrrole, and so on. Well-dispersed SWNT/polyaniline composite films have been prepared by electrochemical polymerization.<sup>52</sup> A homogeneous SWNT/polyimide composite has been obtained by *in situ* polymerization, exhibiting electrical percolation at 0.1 vol% SWNT.<sup>89</sup> Successful *in situ* polymerization studies have also been reported on SWNT/PMMA<sup>90</sup> and SWNT/poly(p-phenylene benzobisoxazole) (PBO).<sup>38</sup> A CNT/polypyrrole (PPy) composite processed by electrochemical polymerization<sup>91</sup> revealed remarkably uniform PPy coating on individual nanotubes, indicating nanotube wetting by the continuous polymer phase. The *in situ* polymerization of caprolactam in the presence of SWNTs allowed the continuous spinning of single-walled carbon nanotubes (SWNTs)-nylon 6 (PA6) fibers.<sup>92</sup> In addition, caprolactam is an excellent solvent for carboxylic acid-functionalized SWNTs (SWNTs-COOH). This allows the efficient dispersion of the SWNTs and subsequent grafting of PA6



chains to the SWNTs-COOH through condensation reaction. The presence of the graft copolymer increases the polymer/SWNT compatibility while strengthening the interfacial interaction between the nanotube and matrix. The Young's modulus, tensile strength, and thermal stability of the SWNT-reinforced composite fibers produced by this process are significantly improved.<sup>92</sup>

Solvents such as 1,2-dichlorobenzene, chloroform, N,N-dimethylformamide (DMF), and N-methylpyrrolidone (NMP)<sup>93</sup> are examples of good nanotube solvents/dispersants, while acetone, ethanol, and toluene are examples of poor solvents. Ausman et al.<sup>94</sup> investigated the room temperature solubility of SWNTs in a variety of solvents. Good SWNT solvents are characterized by high electron pair donicity, high solvatochromic parameter, and negligible hydrogen bonding.<sup>94</sup> Higher polar solvent helps to get better SWNT dispersion in the PMMA matrix.<sup>95</sup> Other studies correlating the solubility parameters of solvents with the CNTs' solubility have also been reported.<sup>96,97</sup>

CNTs can be dispersed in water using anionic, cationic, and nonionic surfactants.<sup>98–101</sup> The size of the hydrophilic group of nonionic surfactant or polymer is claimed to be the major factor for suspending nanotubes. Di- and triblock copolymers can also be used. For example, a diblock copolymer of poly(propylene oxide)-co-poly(ethylene oxide) (PPO-co-PEO), where PPO is hydrophobic and PEO is hydrophilic, can be used to disperse nanotubes in water.<sup>100</sup> A poly(acrylic acid)-hexadecyltrimethylammonium bromide (CTAB)-MWNT complex can help micrometer-length MWNTs dissolve in water by forming a lamellar structure.<sup>102</sup> Transmission electron microscopy (TEM) studies show that sodium dodecyl sulfate (SDS) is absorbed on the SWNT surface in an extremely ordered manner.<sup>103</sup> Molecular dynamics simulation results suggest that several-tens-of-nanometers-thick layers of surfactant can wrap around the SWNT.<sup>104–110</sup> While the removal of the surfactant from the end product, such as processed composite, may be problematic, the intrinsic CNT structure, for example, the electronic structure, is preserved in this approach.

Oxidation, for example, in nitric acid or in a mixture of sulfuric and nitric acids, can introduce oxygen-containing functional groups such as -OH and -COOH on the nanotube surface.<sup>23,98</sup> Nanotube ends can be opened in the oxidizing media. Oxidized tubes can form a well-dispersed electrostatically stabilized colloid in water as well as in ethanol.<sup>111</sup> It has been suggested that SWNT bundles form intercalation compounds with HNO<sub>3</sub> and individual SWNTs can be exfoliated from the bundles after longer exposure to HNO<sub>3</sub>.<sup>112,113</sup> The presence of oxidizing groups helps the attachment of organic<sup>114–117</sup> or inorganic materials to the surface that is important for solubilizing nanotubes, for self-assembly, or for chemical sensors.<sup>118–122</sup> SWNT films<sup>18</sup> and fibers<sup>16</sup> have been processed from oleum or fuming sulfuric acid.

CNTs can be functionalized at end caps or at the sidewall<sup>123,124</sup> to enhance their dispersion in solvents and in polymer matrices. SWNTs dissolved in organic solutions have been derivatized with thioylchloride

and octadecylamine. Reaction of soluble SWNTs with dichlorocarbene led to functionalization of the nanotubes. For instance, nanotubes could be solubilized by functionalizing the end caps with long aliphatic amines.<sup>97</sup> SWNTs have been solubilized by functionalizing their sidewalls by nitrene,<sup>97,125</sup> fluorination,<sup>126,127</sup> alkylation,<sup>128</sup> arylation,<sup>129,130</sup> and 1,3-dipolar cycloaddition.

The polymer-grafted CNTs are particularly important for processing polymer/CNT nanocomposites.<sup>72,131,132</sup> CNT-bound carboxylic acids can be used to attach aminopolymers via the formation of amide linkages.<sup>133</sup> Functionalization of both SWNT and MWNT with poly(styrene-co-p-[4-(4'-vinylphenyl)-3-oxabutanol]) has been reported.<sup>134</sup> The polymer-bound CNTs can be formed by covalently attaching nanotubes to highly soluble linear polymers, such as poly(propionylethylenimine-co-ethylenimine) (PPEI-EI) via amide linkages or poly(vinyl acetate-co-vinyl alcohol) (PVA-VA) via ester linkages.<sup>135</sup> The samples of polymer-bound nanotubes are soluble in both organic solvents and water, and highly homogenous solutions are formed.<sup>135</sup> Nitric acid-functionalized SWNTs with carboxylic groups allow broader solvent selection.<sup>96</sup> They are not soluble in xylene, but exhibit good solubility in an ethanol/xylene mixture, providing a route for their dispersion in polymers such as polypropylene.

CNTs are also being dispersed and exfoliated using various salts.<sup>136–138</sup> The idea is that positive ions will have good affinity to electron-rich nanotubes.

### 8.3 Characterization of polymer/CNT composites

Optical microscopy, scanning electron microscopy (SEM), TEM, and atomic force microscopy (AFM) are often used for characterizing nanocomposite morphology. Cryo-TEM is also used for observing the exfoliation state of CNTs in solution. Dynamic mechanical analysis (DMA) has often been used to characterize mechanical properties as a function of temperature. Differential scanning calorimetry (DSC), thermal gravimetric analysis (TGA), and thermomechanical analyzer (TMA) have been used to characterize thermal properties. Rheology has also been used to characterize the viscoelastic behavior of CNT dispersions and polymer/CNT composite melts or solutions.<sup>7,111,139–154</sup> CNTs show highly anisotropic electrical,<sup>155</sup> optical,<sup>156</sup> mechanical,<sup>157</sup> and thermal properties.<sup>158</sup> Physical properties of CNT fibers and films and their composites strongly depend upon the CNT orientation in the bulk sample. Therefore, for good understanding of the properties of CNT-based materials, accurate orientation determination is necessary. Orientation of SWNT and DWNT can be determined from Raman spectroscopy, and the orientation of MWNT and VGCNF can be determined from wide-angle x-ray diffraction.

Intensity of the Raman G band in the oriented systems depends on the polarization direction. The Raman spectra can be measured in the VV or VH mode. In the VV mode, the polarizer and analyzer are parallel to each other,

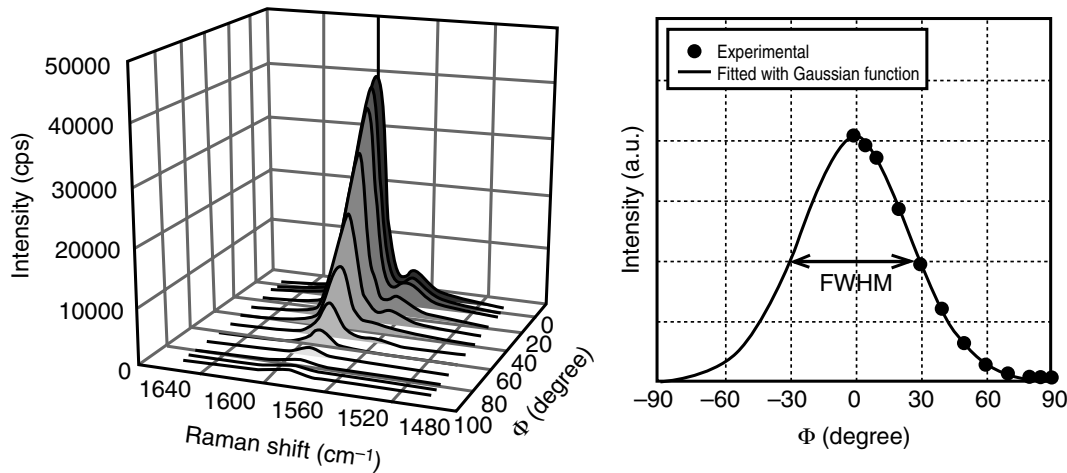


**Figure 8.2** (a) Angular dependence of Raman G band intensity with respect to angle  $\Phi$  (angle between polarization direction and composite fiber axis). (b) The experimental Raman G band intensity as a function of angle  $\Phi$  and the fitted result with Gaussian distribution function.

while in the VH mode, the polarizer is perpendicular to the analyzer. As an example, the G band Raman spectra (VV) and the maximum G band intensity in an oriented composite fiber as a function of polarization angle are plotted in Figure 8.2. By fitting with a Gaussian or Lorentzian distribution function, one can obtain the full-width-at-half-maximum (FWHM) intensity.<sup>22,159,160</sup> The FWHM can be taken as a measure of the nanotube orientation in the sample.

A more rigorous approach is based on determining the nanotube orientation distribution function (ODF). Here we consider the case of uniaxial orientation, possessing cylindrical symmetry. The orientation distribution function is given by<sup>161,162</sup>

$$f(\theta) = \sum_{i=0}^{i=\infty} \frac{2i+1}{2} \langle P_i \cos \theta \rangle P_i(\cos \theta)$$

where  $P_i(\cos \theta)$  is the Legendre polynomials of degree  $i$  and the average is

$$\langle P_i(\cos \theta) \rangle = \frac{\int_0^\pi P_i(\cos \theta) f(\theta) \sin \theta d\theta}{\int_0^\pi f(\theta) \sin \theta d\theta}$$

The average values of  $P_i(\cos \theta)$  are also defined as the orientation order parameter. Specifically,  $\langle P_2(\cos \theta) \rangle$  is the so-called Herman's orientation factor  $[(3\langle \cos^2 \theta \rangle - 1)/2]$ . The expressions for the polarized Raman scattering intensity of CNT fiber with respect to the angle  $\Phi$  (angle between the polarization direction and the fiber axis) are given by

[www.iran-mavad.com](http://www.iran-mavad.com)

مرجع دانشجویان و مهندسين مواد

$$I_{Fiber}^{VV}(\Phi) \propto \left( \cos^4 \Phi - \frac{6}{7} \cos^2 \Phi + \frac{3}{35} \right) \langle P_4(\cos \theta) \rangle + \left( \frac{6}{7} \cos^2 \Phi - \frac{2}{7} \right) \langle P_2(\cos \theta) \rangle + \frac{1}{5}$$

$$I_{Fiber}^{VH}(\Phi) \propto \left( -\cos^4 \Phi + \cos^2 \Phi - \frac{4}{35} \right) \langle P_4(\cos \theta) \rangle + \frac{2}{21} \langle P_2(\cos \theta) \rangle + \frac{1}{15}$$

Therefore, the orientation order parameter terms  $P_2(\cos \theta)$  and  $P_4(\cos \theta)$  can be determined by fitting the experimentally determined polarized Raman scattering intensity (Figure 8.2b). Alternatively,  $P_2(\cos \theta)$  and  $P_4(\cos \theta)$  can also be determined by solving the following equations:

$$\frac{I_{Fiber}^{VV}(\Phi = 0)}{I_{Fiber}^{VH}(\Phi = 0)} = \frac{I_{Fiber}^{VV}(\Phi = 0)}{I_{Fiber}^{VH}(\Phi = 90)} = -\frac{24 \langle P_4(\cos \theta) \rangle + 60 \langle P_2(\cos \theta) \rangle + 21}{12 \langle P_4(\cos \theta) \rangle - 5 \langle P_2(\cos \theta) \rangle - 7}$$

$$\frac{I_{Fiber}^{VV}(\Phi = 90)}{I_{Fiber}^{VH}(\Phi = 0)} = \frac{I_{Fiber}^{VV}(\Phi = 90)}{I_{Fiber}^{VH}(\Phi = 90)} = -\frac{-9 \langle P_4(\cos \theta) \rangle + 30 \langle P_2(\cos \theta) \rangle - 21}{12 \langle P_4(\cos \theta) \rangle - 5 \langle P_2(\cos \theta) \rangle - 7}$$

where  $I_{VV}(\Phi = 0)$ ,  $I_{VV}(\Phi = 90)$ ,  $I_{VH}(\Phi = 0)$ , and  $I_{VH}(\Phi = 90)$  are the experimentally measured values. In order to obtain correct  $I_{VV}/I_{VH}$ , the instrumental polarization factor should be considered. DWNT orientation can also be determined using Raman spectroscopy by this approach.<sup>163</sup>

The orientation of MWNTs and that of the vapor-grown carbon nanofibers (VGCNFs) can be determined using wide angle x-ray diffraction (WAXD). MWNTs and VGCNFs have a layered graphitic structure. The diffraction from the graphite (002) plane with a  $d$ -spacing of 3.34 Å for graphite and 3.4 to 3.44 Å for turbostratic graphite is relatively prominent. The integrated scan and WAXD patterns of polyacrylonitrile (PAN) and PAN/MWNT composite fibers are shown in Figure 8.3, indicating the presence of graphite (002) peak in the composite fiber. From the graphite (002) azimuthal scan (not shown), the orientation of the axis perpendicular to the (002) plane (i.e., the  $c$ -axis) is given by

$$f_c = \frac{3 \langle \cos^2 \theta_{002} \rangle - 1}{2}$$

where

$$\langle \cos^2 \theta_{002} \rangle = \frac{\int_0^{\pi/2} I(\theta_{002}) \cos^2 \varphi \sin \varphi d\varphi}{\int_0^{\pi/2} I(\theta_{002}) \sin \varphi d\varphi}$$

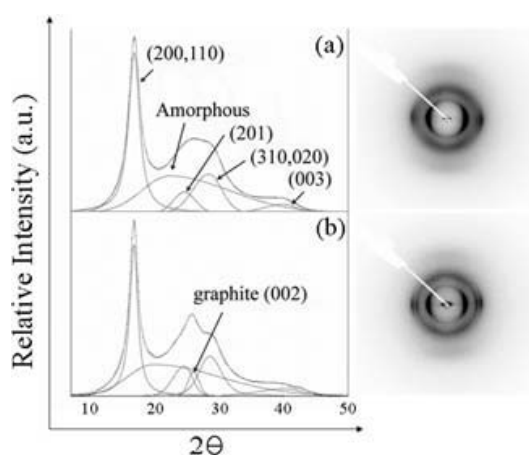


**Figure 8.3** WAXD patterns for (a) PAN and (b) PAN/MWNT composite fibers. (From ref. 163.)

where  $I(\theta_{002})$  is the intensity distribution of the (002) plane with respect to the azimuthal angle ( $\phi$ ). Based on the orthogonality condition, the orientation of the MWNT would then be given by the equation<sup>164,165</sup>

$$f_{MWNT} = -2f_c$$

**Figure 8.4** exhibits the TEM image and WAXD pattern of VGCNFs and a polymer/VGCNF composite fiber. As can be seen from the TEM image, graphite planes are not parallel to the fiber axis. The WAXD pattern of the composite fiber shows a four-point pattern corresponding to the graphite (002) peak, which is consistent with the graphite plane orientation with respect to the nanofiber axis. One can fit the WAXD pattern with a Gaussian or Lorentzian distribution function (**Figure 8.5**). Any one of the four peaks can be used for determining the orientation of VGCNF in a method similar to the one described above for the MWNT. The detailed calculation procedure is reported elsewhere.<sup>166</sup>

The typical Raman spectrum of SWNT includes four main features: the tangential G band (near  $1600\text{ cm}^{-1}$  and derived from the graphite in-plane vibration mode), the disorder-induced D band (around  $1300\text{ cm}^{-1}$ ), the  $G^*$  band (at about  $2600\text{ cm}^{-1}$ , and generally considered to be the overtone of the D band), and the radial breathing mode (RBM) (generally in the  $150 \sim 500\text{ cm}^{-1}$  range), which corresponds to the collective out-of-plane radial displacement of the carbon atoms.<sup>167</sup> The position of RBM is inversely proportional to the nanotube diameter and is frequently used to characterize the diameter distribution in a given SWNT sample. More than one laser excitation wavelength is generally required to identify both the metallic and semiconducting tubes in a given batch, which may typically contain 20 different types of tubes.<sup>168</sup>

Raman spectroscopy is also very effective for monitoring CNT deformation. The position of both G and  $G^*$  bands downshifts under tensile stress and upshifts upon the application of compression or with pressure<sup>169</sup> (G band



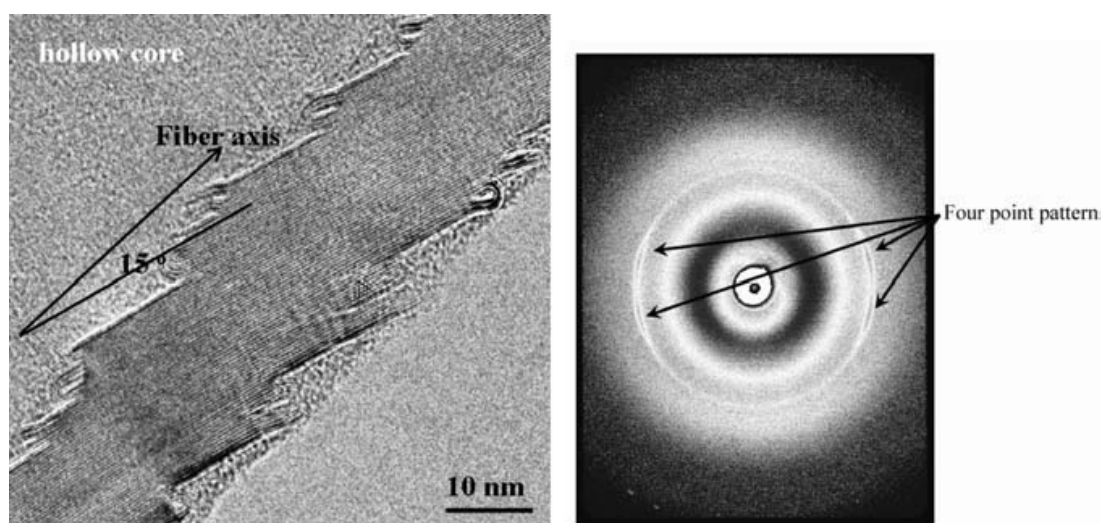


**Figure 8.4** (a) TEM image of VGCNF. (b) WAXD pattern for PMMA/VGCNF composite fiber. (From ref. 166.)

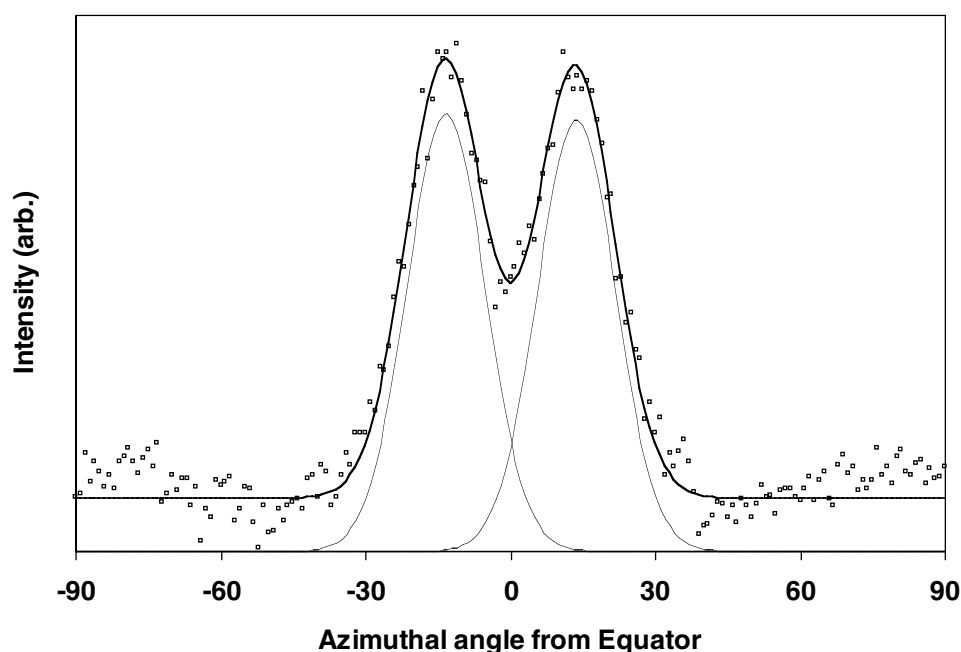


**Figure 8.5** The azimuthal scan of the graphite (002) plane at  $2\theta = 26.5^\circ$  ( $\lambda = 1.54 \text{ \AA}$ ) for PMMA/VGCNF composite fiber. (From ref. 166.)

shift constant is between 5 and  $8.7 \text{ cm}^{-1}/\text{GPa}^{170}$  and  $G^*$  band shift constant is about  $23 \text{ cm}^{-1}/\text{GPa}^{171}$ ). The charge transfer also affects SWNT Raman spectra;<sup>172</sup> n doping causes Raman bands to downshift, and p doping results in the upshifting of Raman bands. SWNT Raman modes shift to lower wave numbers with increasing temperature due to the decrease in carbon-carbon bond force constant.<sup>173</sup> The temperature coefficient of the G band ( $\sim -0.038 \text{ cm}^{-1}/\text{K}$ ) is higher than that of the RBM band ( $\sim -0.013 \text{ cm}^{-1}/\text{K}$ ).<sup>174</sup> Recently, the relative intensity of the Raman radial breathing mode at  $267 \text{ cm}^{-1}$  using

785-nm laser excitation has also been shown to relate to the SWNT aggregation state.<sup>175</sup>

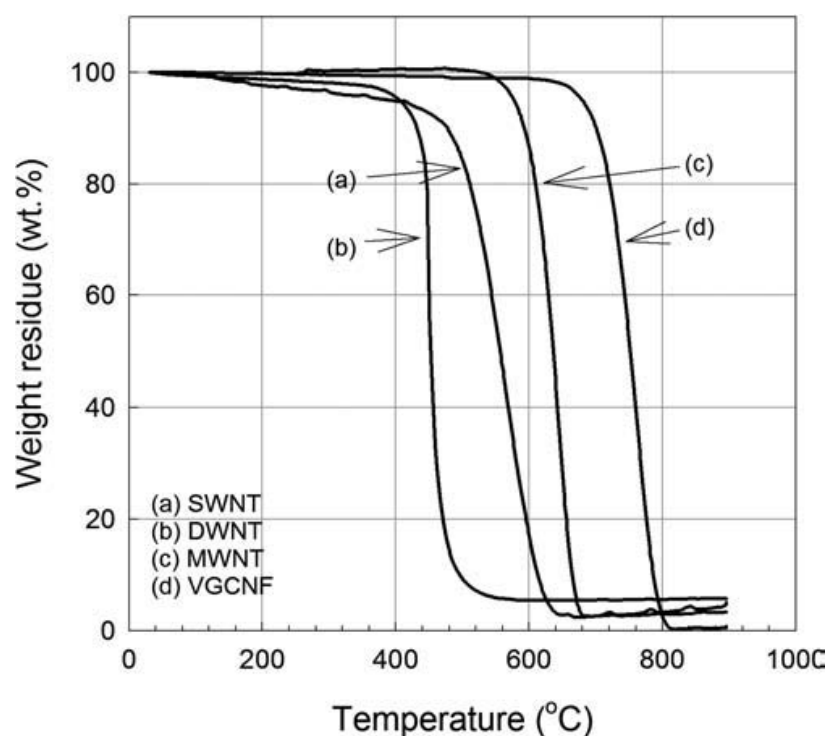
Individual or exfoliated SWNTs exhibit van Hove singularities in the ultraviolet–visible–near-infrared (UV-vis-NIR) range.<sup>176–180</sup> However, van Hove transitions are quenched in the bundles or ropes. Therefore, optical spectra are used to assess the SWNT exfoliation state. The selective functionalization and interaction between solvent/CNT or polymer/CNT can also be monitored using van Hove transitions in the optical spectra.<sup>181–183</sup> In the fully exfoliated semiconducting SWNTs, the absorbed energy is reemitted as fluorescence, which can be used to characterize their chirality and diameter.<sup>184</sup>

## 8.4 CNT films and fibers

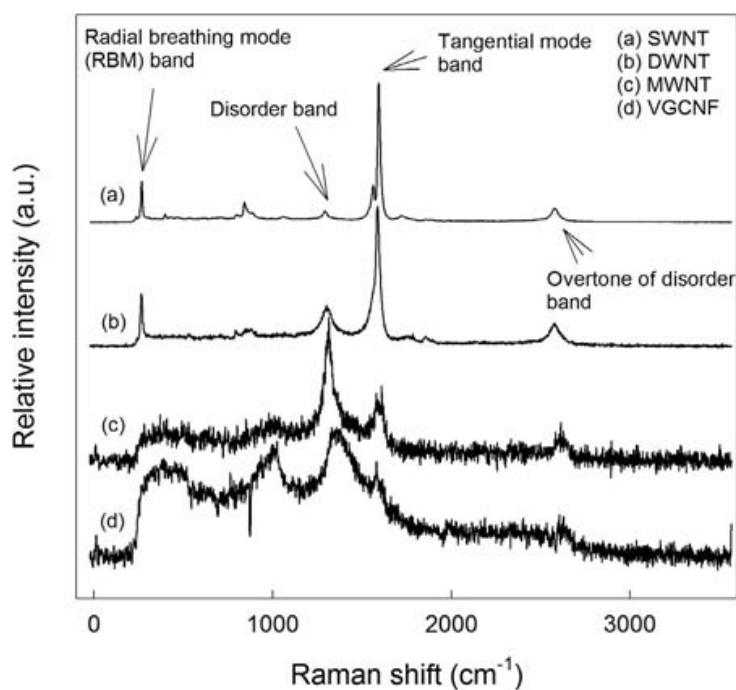
As indicated in Figure 8.1, SWNTs show 5- to 50-nm-diameter bundles or ropes, with an average diameter of about 30 nm. Diameters of DWNTs were about 5 nm, and they mostly existed as highly entangled individual tubes. The average diameter of MWNTs was about 20 nm, and these also existed as mostly individuals, though entangled. The diameter of VGCNFs was about 60 nm, and they appeared to be relatively free of entanglements. TGA results for these CNTs showed that DWNT, SWNT, MWNT, and VGCNF degradation peaks in air at about 440, 500, 600, and 700°C, respectively (Figure 8.6). Raman spectra (Figure 8.7) show that the intensity of the disorder band (ca. 1300 cm<sup>-1</sup>) in MWNTs and in VGCNFs is quite high, suggesting a highly defective graphitic structure in these two cases. Among the four types of tubes, based on the Raman disorder band, SWNTs appear to have the highest perfection, followed by DWNTs.

SWNT film,<sup>18</sup> also referred to as bucky paper, can be made without polymer matrix or any other binder by filtering SWNT dispersion in aqueous or organic media and then peeling off the nanotube paper from the filter paper. SWNT films with mechanical properties higher than the bucky paper processed from aqueous or organic media have been processed from oleum as well as from nitric acid. Typical properties of the SWNT films (bucky paper) processed from dimethyl formamide (DMF), nitric acid, and oleum are given in Table 8.2. Optically transparent thin films can also be processed from SWNT/oleum dispersion (Figure 8.8). Mechanical properties of the SWNT bucky paper can be enhanced by reinforcing it with polymers such as PVA, poly(vinyl pyrrolidone) (PVP), and polystyrene (PS).<sup>185</sup> This can be done by simply soaking the nanotube sheets in polymer solutions. The bucky paper density increased after soaking in the polymer solution, and the SEM shows that polymer fills the pores in between the SWNT ropes. Mechanical properties of PAN/SWNT composite films were also substantially higher than either the PAN film or the SWNT bucky paper (Table 8.2).<sup>71</sup>

X-ray diffraction of the SWNT powder along with the  $d_{11}$  and  $d_{10}$  spacings in the SWNT rope are shown in Figure 8.9.  $d_{11}$  and  $d_{10}$  can be used to calculate the average tube diameter. Both the  $d_{10}$  and  $d_{11}$  spacing increased (Figure 8.10) when nanotubes were treated with increasing concentration of nitric



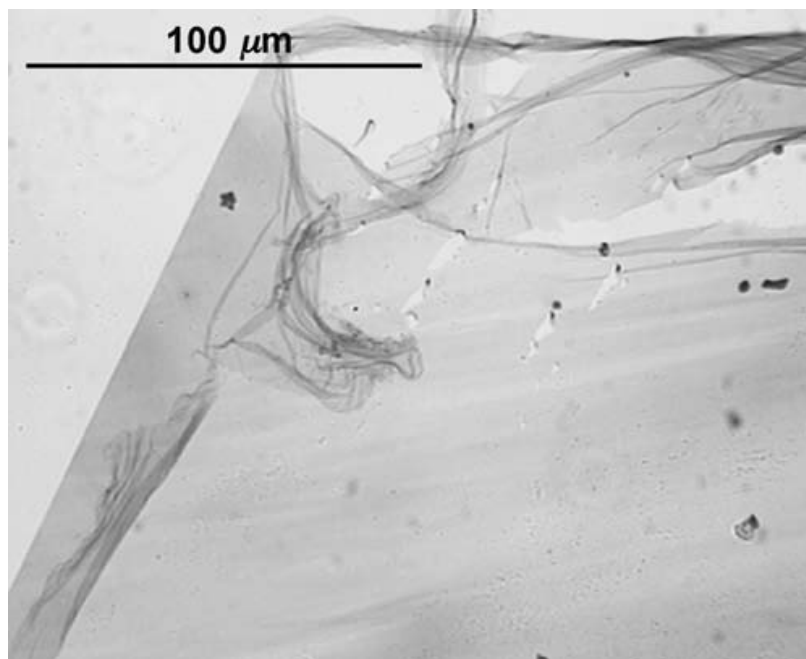
**Figure 8.6** Thermogravimetric analysis results for pristine CNTs: (a) SWNTs, (b) DWNTs, (c) MWNTs, and (d) VGCNFs. (From ref. 163.)



**Figure 8.7** Raman spectra for pristine CNTs: (a) SWNTs, (b) DWNTs, (c) MWNTs, and (d) VGCNFs. (From ref. 163.)

**Table 8.2** Typical Properties of the SWNT Film (Bucky Paper), Control PAN, and PAN/SWNT (60/40) Film

	SWNT Film from Oleum <sup>18</sup>	SWNT Film from Nitric Acid <sup>23</sup>	SWNT Film from DMF <sup>71</sup>	Control PAN Film <sup>71</sup>	PAN/SWNT (60/40) Film <sup>71</sup>
Tensile strength (MPa)	30	70	1.1	57	103
Tensile modulus (GPa)	8	5	7.6	2.7	10.9
Elongation at break (%)	0.5	3	0.6	22.3	1.6
Electrical conductivity (S/m)	$1.3 \times 10^5$	$1.2 \times 10^4$	$3 \times 10^4$	—	$1.5 \times 10^4$

**Figure 8.8** Optical micrograph of transparent SWNT thin film.

acid.<sup>23</sup> At low nitric acid concentration, smaller-diameter SWNTs were damaged and ultimately converted to amorphous carbon; thus, average tube diameter increased. The degradation of the small-diameter tubes was also confirmed by the Raman radial breathing mode.<sup>23</sup>

Aqueous SWNT dispersions stabilized by the surfactant SDS were extruded in the PVA solution to yield 15-μm-diameter SWNT fiber with a tensile strength and modulus of 0.15 and 15 GPa, respectively,<sup>20</sup> with the subsequent drawing fiber modulus improved by a factor of 4.<sup>186</sup> Continuous well-aligned macroscopic SWNT fibers<sup>16</sup> have been solution spun from fuming sulfuric acid with a tensile strength and modulus of 116 MPa and 120 GPa, respectively. CNT yarns with tensile strength as high as 1 GPa have

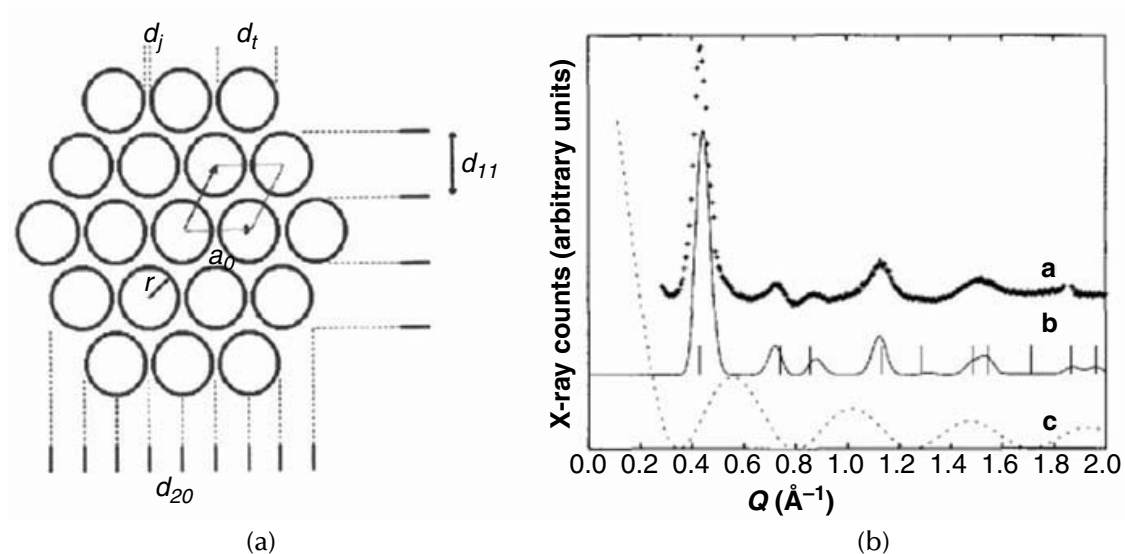


**Figure 8.9** Schematic description of (a) SWNTs' bundle and (b) simulated WAXD pattern.<sup>15</sup>  $Q$  in (b) is the scattering vector, which can be defined as  $Q = \frac{4\pi \sin \theta}{\lambda}$ , where  $\theta$  is Bragg's angle and  $\lambda$  is the wavelength of the incident x-ray ( $\lambda = 1.54 \text{ \AA}$  for  $\text{CuK}\alpha$  radiation).

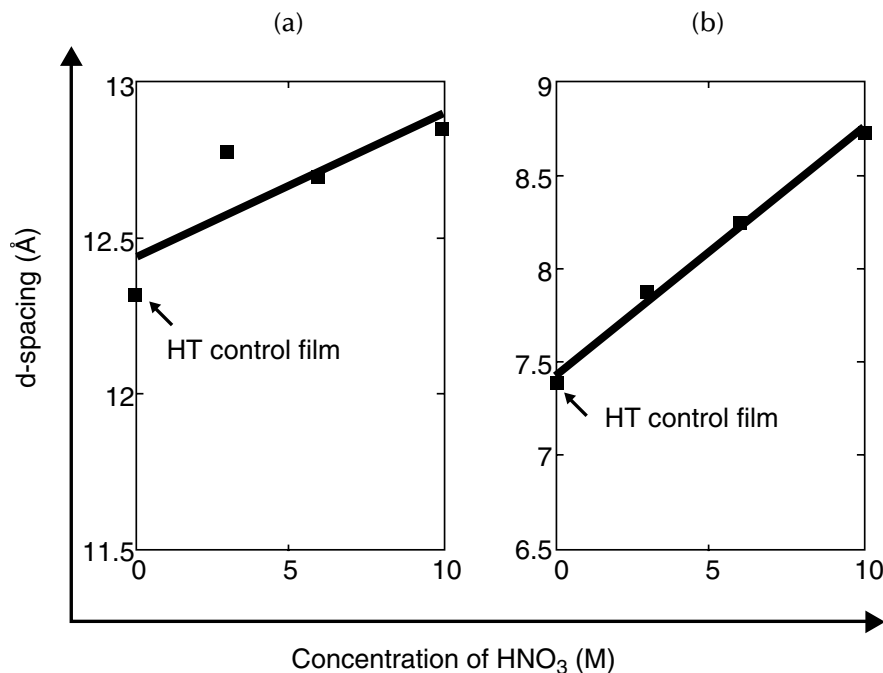


**Figure 8.10** d-spacing of SWNT diffraction peaks in films processed from nitric acid. Diffraction planes (a) (1, 0) and (b) (1, 1). (From ref. 23.)

been drawn directly from the CVD reaction chamber (Figure 8.11).<sup>187</sup> CNT yarns of 2 to 10  $\mu\text{m}$  diameter, with a tensile strength of 460 MPa, electrical conductivity of  $3 \times 10^4 \text{ S/m}$ , and Poisson's ratio in the range of 2 to 4.2, have been made by simultaneous drawing and twisting of tubes from an MWNT forest (Figure 8.12 and Figure 8.13).<sup>17</sup> The yarn strength can be further increased by polymer infiltration. Tensile strength of the yarn can be as high as the tensile strength of the staple fiber from which the yarn is made. Factors that affect yarn strength are nanotube–nanotube friction, nanotube migration



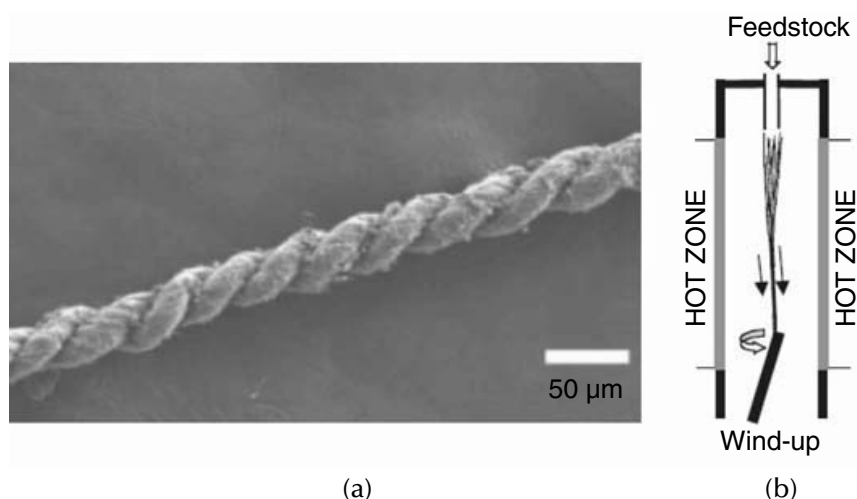


**Figure 8.11** (a) SEM image of twisted yarn from the reactor. (b) Schematic description of direct producing CNT yarn from the reactor. (From ref. 187.)

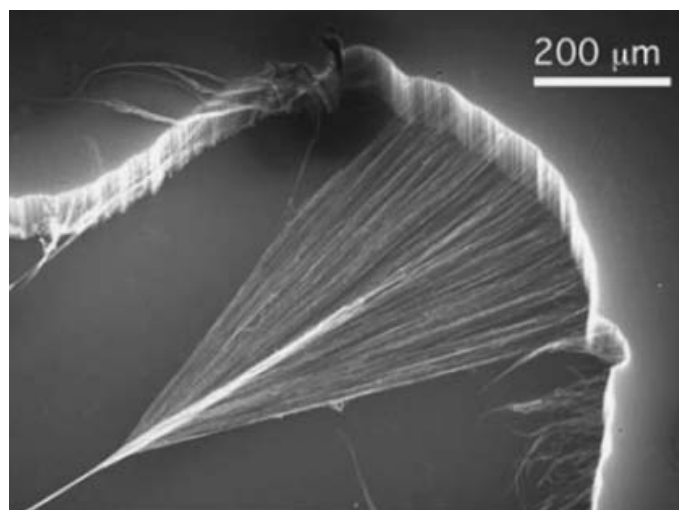


**Figure 8.12** SEM image of direct yarn formation from MWNT forest. (From ref. 17.)

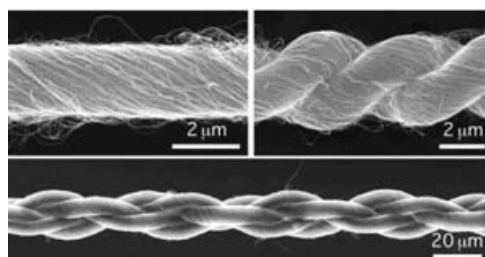


**Figure 8.13** SEM image of twisted yarn from MWNT forest. (From ref. 17.)

in the transverse direction in the yarn, and the nanotube length.<sup>188</sup> Once their parameters are optimized, nanotube yarn with a tensile strength close to the nanotube tensile strength can be expected.

The tensile strength of polymers and polymeric fibers increases with increasing molecular weight, and hence with increasing length of the polymer molecule.<sup>189–192</sup> Similarly, the tensile strength of 100% carbon nanotube films and fibers, as well as of composites containing carbon nanotubes, is expected to increase with increasing nanotube length. Therefore, long, continuous nanotubes are of interest for mechanical properties. In addition, long, continuous nanotubes are also of interest for microelectromechanical applications.<sup>14,25</sup> Progress toward synthesizing long nanotubes continues. A 4-cm-long SWNT with a growth rate of 11  $\mu\text{m}/\text{sec}$  produced by the catalytic CVD process has already been reported.<sup>162</sup>

## 8.5 Polymer/CNT composite films and fibers

A wide range of polymer matrices have been employed with carbon nanotubes, including poly(3-octylthiophene) (P3OT),<sup>193,194</sup> poly(m-phenylenevinylene-co-2,5-dioctyloxy-p-phenylenevinylene) (PmPV), poly(vinyl alcohol) (PVA),<sup>26,27,37</sup> poly(methyl methacrylate) (PMMA),<sup>28,29,62,195,196</sup> polypropylene (PP),<sup>30,63,197</sup> epoxy,<sup>31–33,45,46,64,139</sup> polyimide,<sup>198,199</sup> polycarbonate (PC),<sup>34,200</sup> polystyrene (PS),<sup>66,201</sup> polyaniline,<sup>202</sup> polypyrrole,<sup>77,203,204</sup> alkoxy-silane-terminated amide acid (ASTAA),<sup>205</sup> polyacrylonitrile (PAN),<sup>36,39,40,71,75,141,206–212</sup> poly(p-phenylene benzobisoxazole) (PBO),<sup>38</sup> polyethylene (PE),<sup>213</sup> nylon,<sup>214</sup> poly(phenylene sulfide),<sup>215</sup> phenolic resin,<sup>216</sup> poly(ethylene terephthalate) (PET),<sup>61</sup> poly(p-phenylene benzobisthiazole) (PBZT),<sup>217</sup> and so on. Here we discuss nanotube composites in several polymer matrices, with a focus toward resulting property enhancement.

### 8.5.1 Mechanical properties

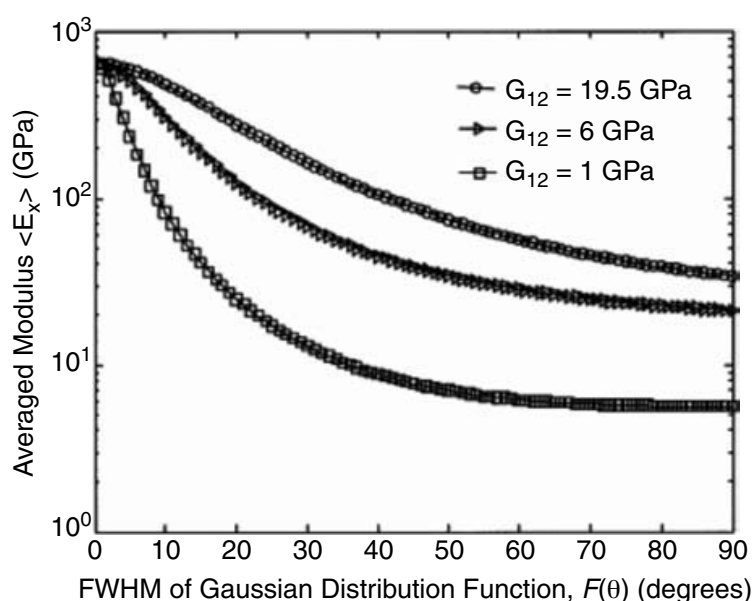
The modulus of SWNT films and fibers calculated using the following continuum mechanics equation is consistent with the experimentally measured moduli of these products:<sup>36,163,218</sup>

$$\begin{aligned}\frac{1}{(E_{CNT})_{II}} &= \frac{1}{E_1} \langle \cos^4 \theta \rangle + \frac{1}{E_2} \langle \sin^4 \theta \rangle + \left( \frac{1}{G_{12}} - \frac{2\nu_{12}}{E_1} \right) \langle \sin^2 \theta \cos^2 \theta \rangle \\ &= \frac{1}{E_1} + \left( \frac{1}{G_{12}} - \frac{2\nu_{12}}{E_1} - \frac{2}{E_2} \right) \langle \cos^2 \theta \rangle + \left( \frac{1}{E_1} + \frac{1}{E_2} - \frac{1}{G_{12}} + \frac{2\nu_{12}}{E_1} \right) \langle \cos^4 \theta \rangle\end{aligned}$$

where  $(E_{CNT})_{II}$  is the effective modulus of CNT along the composite fiber axis;  $E_1$ ,  $E_2$ , and  $G_{12}$  are the longitudinal, transverse, and in-plane shear moduli, respectively;  $\nu_{12}$  is Poisson's ratio; and  $\theta$  is the angle between the composite fiber axis and CNT axis. Carbon nanotube elastic constants are listed in Table 8.3.<sup>157,219–225</sup> For SWNT, the axial tensile modulus of large-diameter ropes drops precipitously with orientation, while the smaller-diameter rope modulus exhibits lower orientation dependence (Figure 8.14). Therefore, in

**Table 8.3** The Elastic Constants of SWNTs and MWNTs<sup>163</sup>

	SWNTs			MWNTs
	1 nm	4.5 nm	20 nm	
$E_1$ (GPa)		640 <sup>157,221–223</sup>		1060 <sup>224,225</sup>
$E_2$ (GPa)		15 <sup>157</sup>		50 <sup>220,362</sup>
$G_{12}$ (GPa)	19.5 <sup>219</sup>	6 <sup>219</sup>	1 <sup>219</sup>	4 <sup>225</sup>
$\nu_{12}$		0.17 <sup>157</sup>		0.14 <sup>224</sup>

**Figure 8.14** Effect of SWNT rope orientation on the modulus of SWNT fiber.<sup>218</sup>  $G_{12}$  for 20-nm-diameter rope is 1 GPa, and that for a 4-nm-rope is 6 GPa. (From ref. 218.)

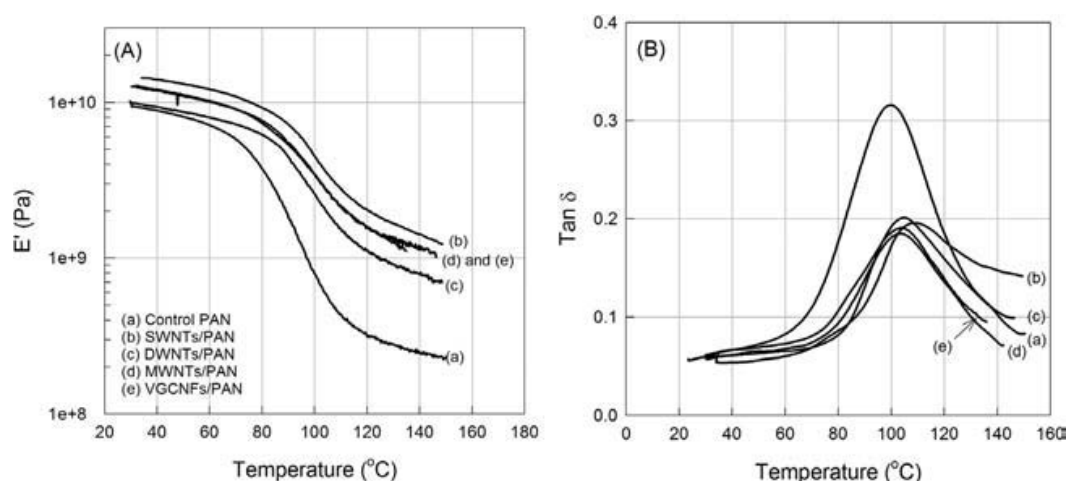
addition to orientation, for the ropes composed of SWNT with varying diameters and chirality, exfoliation is also important for achieving high-modulus SWNT or SWNT/polymer films and fibers. Theoretical calculations also suggest that polymer/MWNT composites can also yield an extremely high modulus at high orientations (orientation factor  $> 0.99$ ).<sup>163</sup>

### 8.5.1.1 PAN/CNT

Polyacrylonitrile (PAN) is a commercially important polymer and is the predominant precursor for carbon fibers.<sup>226,227</sup> PAN/CNT composites<sup>36,40,75,141,163,206–212,228,229</sup> are of significant current interest. These composites are processed using solvents such as N,N-dimethylacetamide (DMAc), N,N-dimethylformamide (DMF), or dimethylsulfoxide (DMSO), using conventional solution spinning, gel spinning, or electrospinning. Limited oxidative stabilization and carbonization studies have also been reported on PAN/CNT composites.<sup>210</sup> Continuous PAN/CNT composite fibers containing SWNTs, DWNTs, MWNTs, and VGCNFs have been processed from DMAc.<sup>163</sup> Due to a

**Table 8.4** Mechanical Properties and Structural Parameters of PAN and PAN/CNT Composite Fibers<sup>163</sup>

	Control PAN	PAN/SWNTs	PAN/DWNTs	PAN/MWNTs	PAN/VGCNFs
Modulus (GPa)	7.8 ± 0.3	13.6 ± 0.5	9.7 ± 0.5	10.8 ± 0.4	10.6 ± 0.2
Strength at break (MPa)	244 ± 12	335 ± 9	316 ± 15	412 ± 23	335 ± 13
Strain to failure (% strain)	5.5 ± 0.5	9.4 ± 0.3	9.1 ± 0.7	11.4 ± 1.2	6.7 ± 0.3
Toughness (MPa)	8.5 ± 1.3	20.4 ± 0.8	17.8 ± 1.7	28.3 ± 3.3	14.0 ± 1.0
Shrinkage at 160°C (%)	13.5	6.5	11.5	8.0	11.0
T <sub>g</sub> <sup>a</sup> (°C)	100	109	105	103	103
f <sub>PAN</sub>	0.52	0.62	0.53	0.60	0.57
f <sub>CNT</sub>	—	0.98	0.88	0.91	0.91
Crystal size (nm)	3.7	5.0	4.1	5.0	4.4
Crystallinity (%)	58	54	57	55	55

**Figure 8.15** Dynamic mechanical analysis results of PAN and PAN/CNT composite fibers: (A) storage modulus and (B) loss factor as a function of temperature. (From ref. 163.)

high degree of entanglements, DWNTs did not disperse well. Mechanical property improvements were observed in all cases (Table 8.4), and the low-strain properties (modulus and thermal shrinkage) were most improved by SWNT (Figure 8.15 and Figure 8.16), while the high-strain properties (tensile strength and toughness) were most improved by MWNT (Table 8.4). As mentioned earlier, the modulus improvement with SWNTs, MWNTs, and VGCNFs was consistent with the theoretical predictions (Table 8.5).<sup>163</sup> The improvement in thermal shrinkage exhibited a strong dependence on the nanotube surface area (Table 8.5, Figure 8.16). The length of SWNTs and well-dispersed DWNTs was in the 200- to 300-nm range, while MWNTs and VGCNFs of  $>1 \mu\text{m}$  length could be observed in the composite fibers (Figure 8.17). However, due to stacked-cup

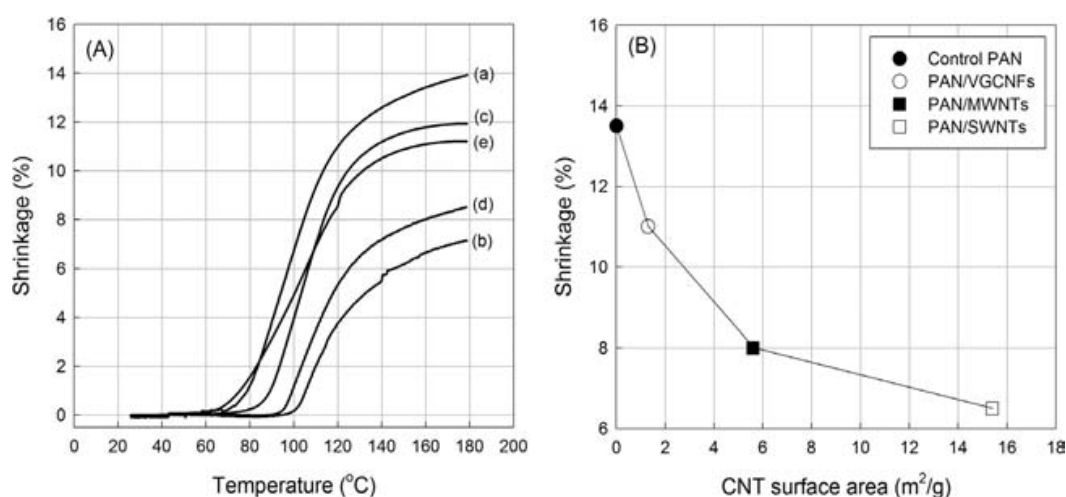


**Figure 8.16** Thermomechanical analysis results of PAN and PAN/CNT composite fibers: (A) shrinkage vs. temperature ((a) control PAN, (b) PAN/SWNT, (c) PAN/DWNT, (d) PAN/MWNT, and (e) PAN/VGCNF composite fibers) and (B) shrinkage vs. CNT surface area. (From ref. 163.)

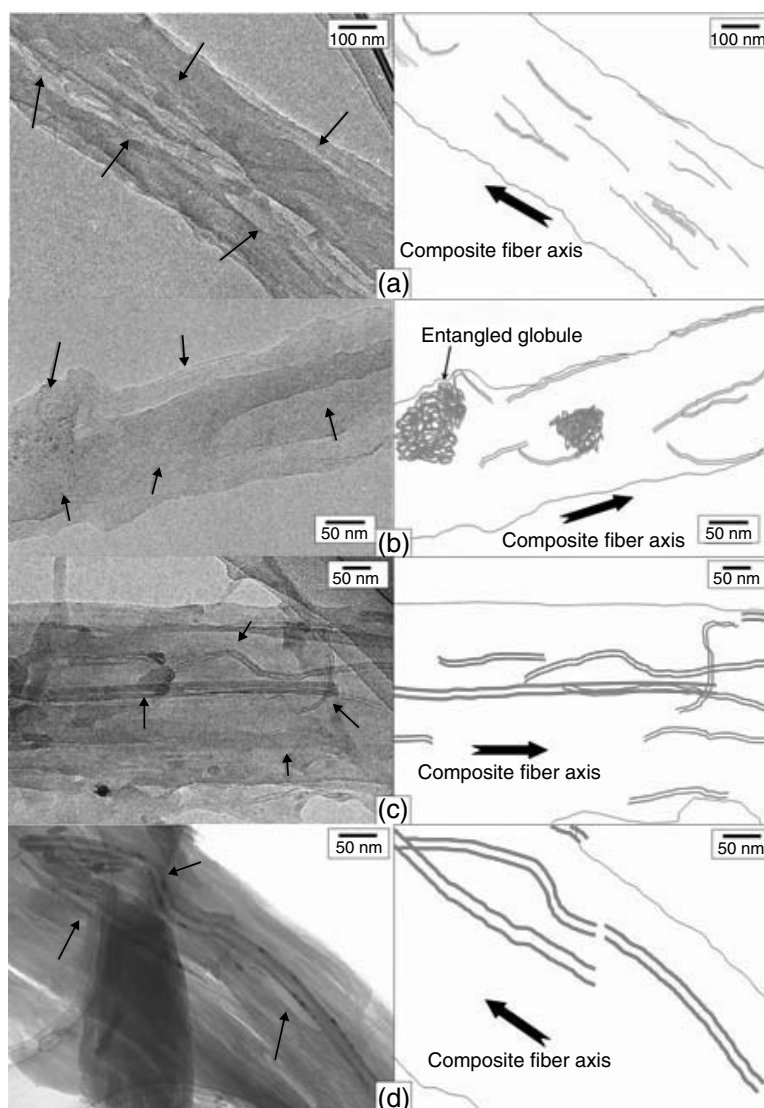
geometry, the tensile strength of the VGCNFs is expected to be relatively low. The largest improvements in tensile strength and toughness in MWNT-containing composite fibers are attributed to the average longer-length MWNTs, rather than the average SWNT and DWNT lengths.  $\tan \delta$  peak temperature, PAN and CNT orientation, and PAN (110, 200) crystal size and crystallinity for various composite fibers are also listed in Table 8.4. PAN/SWNT fibers containing 10 wt% nanotubes exhibit an order of magnitude increase in modulus at 150°C, significant reduction in polymer solubility, and 40°C increase in glass transition temperature, compared to the control PAN fiber.<sup>36</sup> In the composite fiber, CNTs exhibit higher orientation than polyacrylonitrile.<sup>36,163</sup>

PAN/SWNT composite films<sup>71</sup> have been processed with a unique combination of tensile strength (103 MPa), modulus (10.9 GPa), electrical conductivity ( $1.5 \times 10^4$  S/m), dimensional stability (coefficient of thermal expansion  $1.7 \times 10^{-6}/^\circ\text{C}$ ), low density (1.08 g/cm<sup>3</sup>), solvent resistance, and thermal stability. PAN molecular motion above the glass transition temperature ( $T_g$ ) in the composite film is significantly suppressed. As a result, the storage modulus of the PAN/SWNT (60/40) film above  $T_g$  is 40 times the PAN film storage modulus. Rope diameter in the SWNT powder was 26 nm, while in 60/40 PAN/SWNT film, the rope diameter was 40 nm, suggesting that the PAN molecules either cover the nanotube bundles or intercalate them, or both (Figure 8.18). The PAN crystallite sizes from the (110) plane in the PAN and PAN/SWNT films were 5.3 and 2.9 nm, respectively. This study suggests good interaction between PAN and SWNT. PAN/MWNT (95/5) composite gel films<sup>211</sup> have a Young's modulus of 8 GPa and electrical conductivity of  $10^{-1}$  S/m. After stabilization (in air at 330°C) and carbonization (at 1000°C), the Young's modulus was 30 GPa and electrical conductivity reached  $10^4$  S/m. Improved property PAN/CNT nanofiber sheets have been processed by electrospinning (Table 8.6).<sup>209</sup>

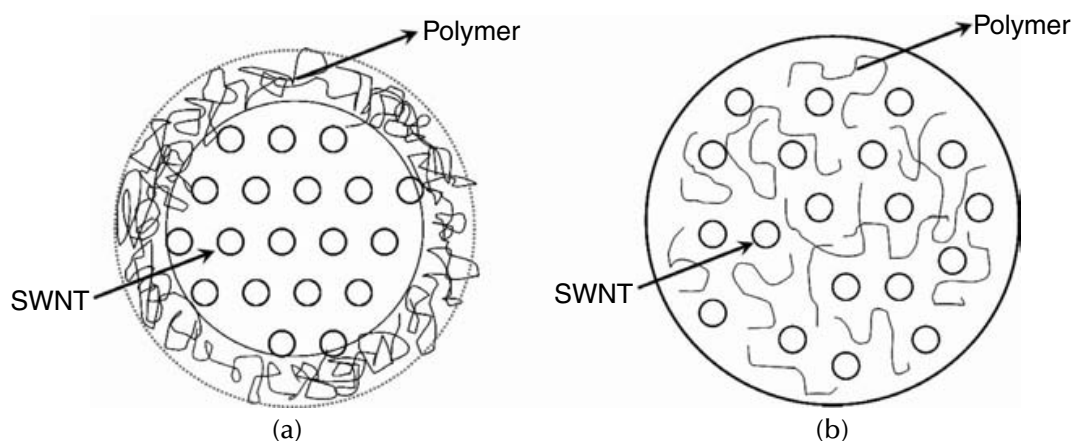


**Table 8.5** Physical Carbon Nanotube Parameters, as well as Theoretical and Experimental Moduli of the Various Composite Fibers<sup>163</sup>

	Diameter (nm)	CNT density (g/cm <sup>3</sup> )	CNT wt%	CNT vol%	PAN/CNT interface area in the composite fiber at 5 wt% loading (m <sup>2</sup> /g)	PAN/CNT composite fiber tensile modulus (GPa)	
						Theoretical	Experimental
VGCNF	60	1.95		3.1	1.3	9.7	10.6
MWNT	20	1.8		3.3	5.6	10.7	10.8
SWNT bundle	20	1.3		4.6	7.7	11.9	—
	10		5.0		15.4	—	13.6
	4.5				34.2	21.4	—
DWNT	5	1.5		4.0	26.6	—	10.8
Exfoliated SWNT	1	1.3		4.6	154	29.7	—



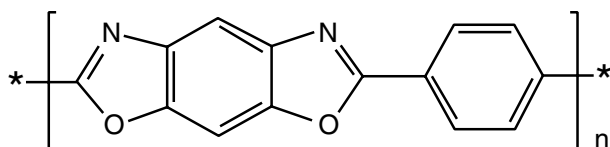
**Figure 8.17** Bright-field TEM images and schematic descriptions for (a) PAN/SWNT, (b) PAN/DWNT, (c) PAN/MWNT, and (d) PAN/VGCNF composite fibers. (From ref. 163.)



**Figure 8.18** Schematic description for (a) polymer wrapping and (b) polymer intercalation in SWNT bundles.

**Table 8.6** Mechanical Properties of PAN and PAN/MWNT Nanofiber Sheets<sup>209</sup>

	PAN/MWNT				
	100/0	97/3	95/5	90/10	80/20
Diameter (nm)	50 ~ 300				
Tensile strength (MPa)	265	312	366	370	285
Tensile modulus (GPa)	4.5	6.4	9.8	10.9	14.5
Elongation at break (%)	17.8	12.8	9.9	8.2	4.4

**Figure 8.19** Chemical structure of poly(p-phenylene benzobisoxazole) (PBO).

### 8.5.1.2 PBO/CNT

Poly(p-phenylene benzobisoxazole) (PBO) (Figure 8.19) is a high-temperature, high-strength polymeric fiber initially processed at the U.S. Air Force Research Laboratory at Wright Patterson Air Force Base in Dayton, OH, in the 1970s.<sup>230,231</sup> The fiber was commercialized in 1998 under the trade name Zylon® (Table 8.1). PBO tensile strength can be enhanced by incorporating nanotubes in the fiber. PBO was synthesized in the presence of SWNT in polyphosphoric acid (PPA) using typical PBO polymerization conditions.<sup>38</sup> PBO and SWNT/PBO lyotropic liquid crystalline solutions in PPA were spun into fibers using dry-jet wet spinning. The tensile strength of the SWNT/PBO fiber containing 10 wt% SWNT was over 50% higher than that of the control PBO fiber (Table 8.7) processed under the same conditions. Similar improvements in commercial PBO fiber (Zylon®) would lead to a fiber with a tensile strength of more than 8 GPa.

### 8.5.1.3 PVA/CNT

Poly(vinyl alcohol) (PVA) is playing an important role<sup>26</sup> in the development of carbon nanotube-based materials, including the processing of the first continuous single-wall carbon nanotube fiber,<sup>20</sup> as well as a super-tough PVA/SWNT composite fiber.<sup>35</sup> Numerous other studies report increased mechanical properties in PVA films and fibers with the addition of less than 10 wt% nanotubes.<sup>27,232,233</sup> PVA composite films using PVP- and SDS-covered, well-dispersed SWNTs exhibit improvement in tensile strength and modulus, compared to the control PVA and PVA/PVP/SDS films (Table 8.8). The evidence of load transfer to the nanotubes in the composite film was obtained from the shift of the SWNT Raman D\* band position (Figure 8.20).<sup>27</sup> Using the D\* band stress coefficient

**Table 8.7** Mechanical Properties of PBO and PBO/SWNT Composite Fibers<sup>38</sup>

	PBO	PBO/SWNT (95/5)	PBO/SWNT (90/10)
Tensile strength (GPa)	2.6	3.2	4.2
Tensile modulus (GPa)	138	156	167
Elongation at break (%)	2.0	2.3	2.8
Compressive strength (GPa)	0.35	0.4	0.5
Fiber diameter ( $\mu\text{m}$ )	22	25	25

**Table 8.8** Tensile Properties of Various PVA Films<sup>27</sup>

	PVA	PVA/PVP/SDS	PVA/PVP/SDS/SWNT (5 wt% SWNT)
Tensile strength (MPa)	83	50	148
Tensile modulus (GPa)	1.9	2.5	4.0
Elongation at break (%)	45	207	48

value of  $23 \text{ cm}^{-1}/\text{GPa}^{171}$ , based on the maximum shift reported in Figure 8.21, average local stress on SWNT was calculated to be as much as 0.7 GPa. In another study, SWNTs dispersed in a DMSO/H<sub>2</sub>O mixture in the presence of PVA were gel spun into composite fiber.<sup>37</sup> The glass transition peak in the composite fiber is broader and shifts to higher temperatures than the control PVA (Figure 8.22). In the control sample, the glass transition peak is at 62°C, while in the composite fiber, the peak is significantly broader and centers at ~75°C, suggesting interaction between SWNTs and amorphous PVA. The transition peak at 170°C is attributed to the subcrystal transition. Temperature shift in this transition suggests SWNT interaction with PVA in the crystalline regions. Mechanical properties of the control and the composite gel-spun fibers are listed in Table 8.9. Super-tough SWNT/PVA composite fiber containing 60 wt% SWNTs, with a breaking energy of 570 J/g, has been reported.<sup>35</sup> By comparison, the breaking energies of existing tough materials, spider silk, Kevlar, and Zylon fibers are about 165, 34, and 70 J/g, respectively. More recently, the tensile strength of SWNT/PVA composite fiber near 3 GPa was reported by the same research group.<sup>234</sup>

#### 8.5.1.4 PMMA/CNT

Significant research efforts have been invested in dispersing carbon nanotubes in PMMA in solution,<sup>82,142,195,235,236</sup> in melt,<sup>28,62,196,237–239</sup> as well as via *in*

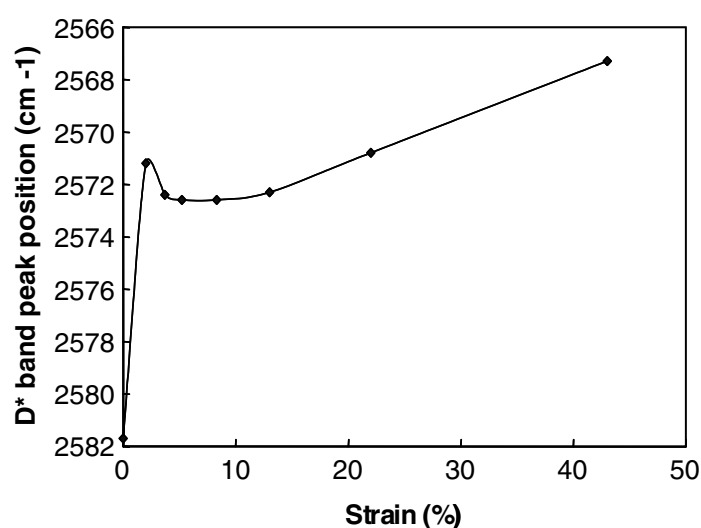


**Figure 8.20** Raman D\* band peak position as a function of strain for PVA/PVP/SDS/SWNT composite films containing 5 wt% SWNTs. The excitation laser wavelength is 785 nm and the laser power is 1.5 mW. (From ref. 27.)

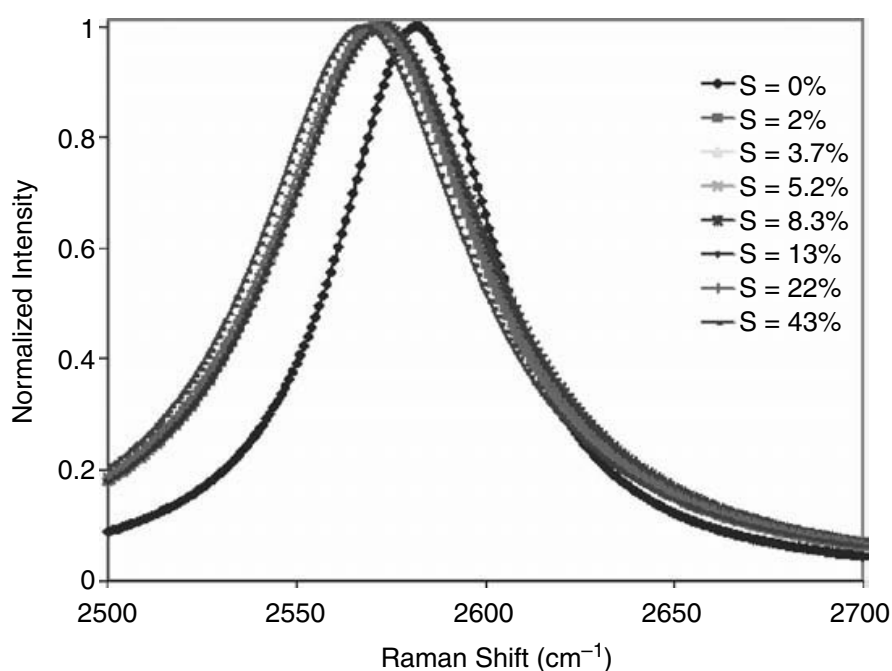


**Figure 8.21** The shifting behavior of the D\* band of PVA/PVP/SDS/SWNT composite films containing 5 wt% SWNTs at various strains, as indicated.

*situ* polymerization.<sup>44,90,240–242</sup> Most studies report property improvements in one or more categories, that is, mechanical, thermal, and electrical properties. For example, *in situ* polymerized PMMA containing 7 wt% MWNT show increased tensile strength (from 55 to 72 MPa), hardness (from 19 to 28 kg/m<sup>2</sup>), and heat deflection temperature (from 388 to 429 K). It was suggested that the bonds in CNT open with azobisisobutyronitrile (AIBN) and react with PMMA to form covalent bonds. A PMMA/CNT composite exhibited



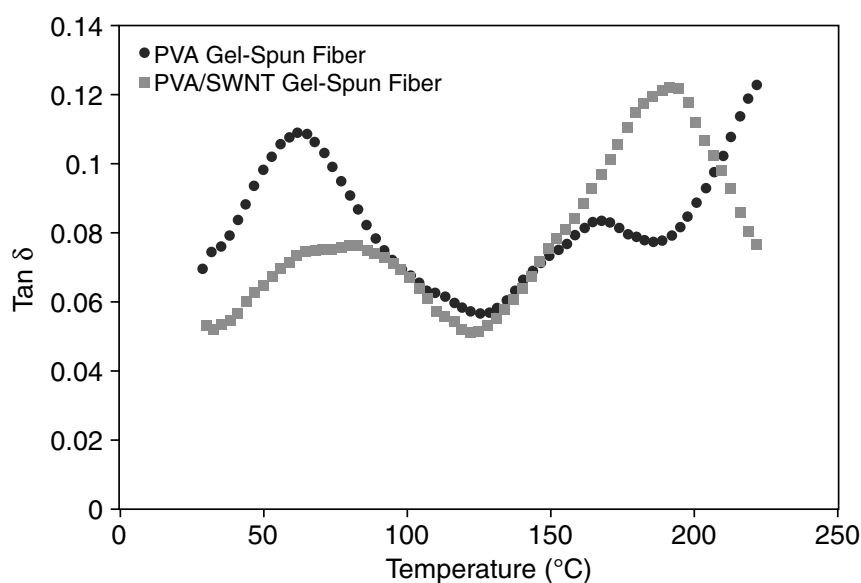


**Figure 8.22** Dynamic mechanical analysis results of gel-spun PVA and PVA/SWNT composite fibers. (From ref. 37.)

**Table 8.9** Mechanical Properties of PVA and PVA/SWNT Gel-Spun Fibers<sup>37</sup>

	PVA	PVA/SWNT (97/3)
Tensile strength (GPa)	0.9	1.1
Tensile modulus (GPa)	25.6	35.8
Elongation at break (%)	7.5	8.8
Fiber diameter (μm)	26.5	27.0

a new infrared absorption peak at  $1665\text{ cm}^{-1}$  and was proposed to be due to shift in the carbonyl PMMA peak resulting from the PMMA/CNT reaction (Figure 8.23).<sup>44,240,241</sup>

In another study it has been suggested that PMMA intercalates SWNT bundles, and as a result, distance between SWNTs increases.<sup>90,171,195,243,244</sup> However, no direct evidence of the increased intertube distance has so far been reported. The Raman G band was analyzed by fitting up to five peaks. With the incorporation of PMMA in SWNTs, the widths of all the G bands decreased, irrespective of the excitation wavelength. The decreased G band width was attributed to the reduced nanotube–nanotube interaction, resulting from increased intertube distance due to polymer intercalation. With the incorporation of PMMA, RBM upshifted. The upshift of the RBMs and their recovery after annealing to high temperature was cited as the evidence of PMMA intercalation into SWNT bundles, as PMMA would be burned out at high temperature. It was suggested that at low SWNT content, SWNT bundles may be fully exfoliated. The relative area of  $1553\text{-}$ ,  $1568\text{-}$ , and  $1573\text{-cm}^{-1}$  peaks in the composite to that of the control SWNT is shown as the

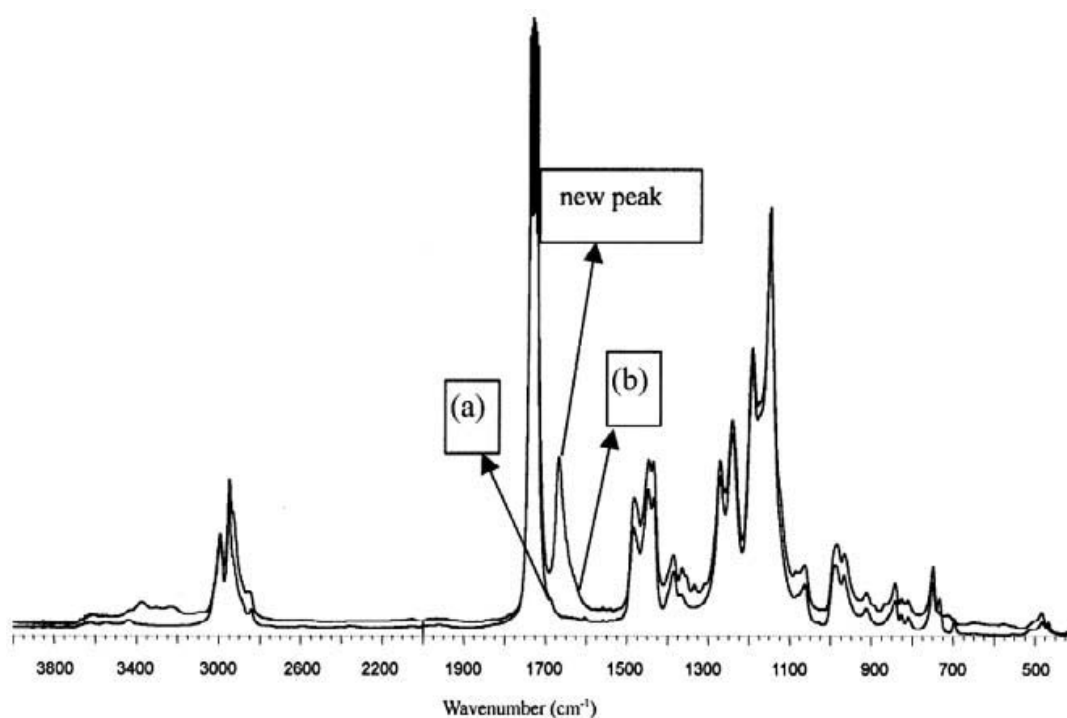


**Figure 8.23** Fourier-transformed infrared spectra for (a) PMMA and (b) PMMA/CNT (80/20) composites. (From ref. 44.)

evidence for exfoliation/intercalation at low SWNT content.<sup>195,243</sup> SWNT intercalation by PMMA has also been discussed in other studies.<sup>90,171,195,243,244</sup>

There are wide-ranging reports of mechanical property improvements in PMMA. Storage modulus increased from 3.1 to 6 GPa at 8 wt% SWNT loading.<sup>196</sup> By incorporating 26 wt% MWNTs,  $T_g$  increased by more than 15°C and composite modulus increased by a factor of 2 (from 0.7 to 1.4 GPa) at room temperature and by a factor of 27 (from about 20 to above 540 MPa) at 120°C, compared to the control specimen.<sup>237</sup> At 2 wt% SWNTs, the composite fiber modulus increased from about 3.5 to 6.3 GPa.<sup>236</sup> The orientation of MWNTs in PMMA proved to be an effective way to substantially toughen the composite; 1 wt% MWNT in PMMA (oriented composite) exhibited a 170% increase in tensile toughness over the oriented PMMA. This was attributed to MWNT being perpendicular to the direction of craze propagation.<sup>239</sup> Thermal stability of an optically homogeneous PMMA/SWNT containing a 0.5 wt% SWNT composite was reportedly enhanced by 80°C as measured by thermogravimetric analysis.<sup>90</sup> The addition of less than 0.1 wt% SWNTs in PMMA increased the low-temperature (−150°C) modulus from 5 to 7 GPa, while the  $T_g$  and high-temperature modulus essentially remained unchanged. These changes were attributed to PMMA/SWNT cohesive interactions at low temperature and not to any morphological changes in PMMA. The modulus improvement is much more than expected from the rule of mixtures. With the presence of 1.5 wt% MWNTs, the modulus of PMMA at 50°C increased from 1.2 to 2.2 GPa when 0.5 wt% polyvinylidene difluoride (PVDF) was added.<sup>238</sup> The increased properties were attributed to PMMA/MWNT

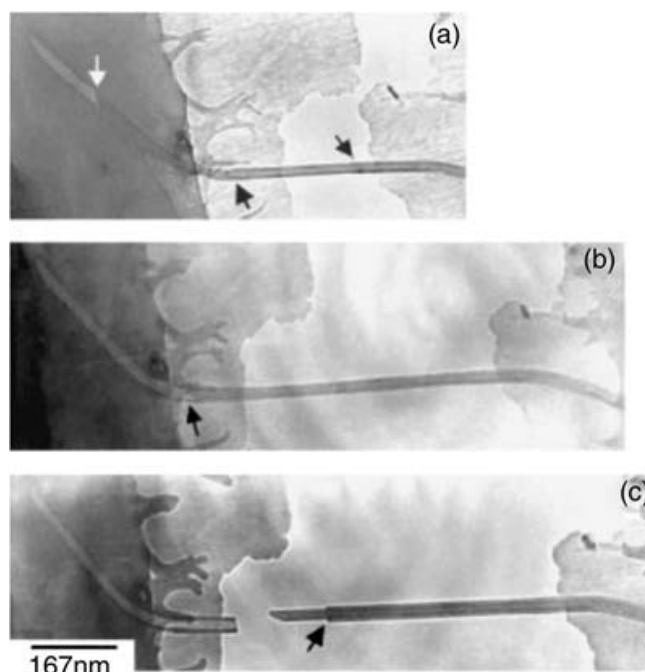


**Figure 8.24** TEM images of a MWNT-containing PMMA thin film taken at different times: (a)  $t = 0$ , (b)  $t = 4$ , and (c)  $t = 10$  min. (From ref. 242.)

interaction assisted by PVDF. However, no spectroscopic evidence of the interaction was provided. PMMA-grafted MWNTs were synthesized using cetyltrimethylammonium bromide aqueous solution and potassium persulfate ( $K_2S_2O_8$ ). Evidence of an efficient load transfer was observed in PMMA/MWNT. The telescopic effect in the MWNT pullout was also observed (Figure 8.24).<sup>242</sup> SWNTs (1 wt%) containing drawn PMMA fiber exhibited a dramatic 700% increase in the strain failure compared to the PMMA fiber of a similar draw ratio.<sup>245</sup> In this case, SWNTs were dispersed in a solution of hydroxylamine hydrochloric acid salt  $[(NH_2OH)(HCl)]$ .

PMMA/SWNT fibers were electrospun with a SWNT core and PMMA shell (Figure 8.25).<sup>246</sup> The sheath core fibers can be used as joints, bearings,

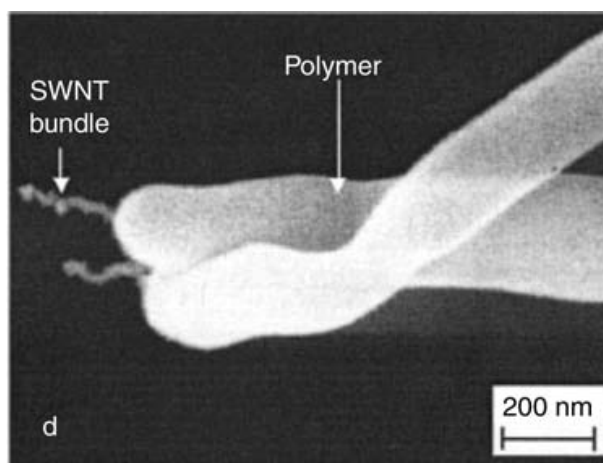


**Figure 8.25** SEM image of a SWNT bundle's core polymer shell nanofibers. (From ref. 246.)

and shafts in microdevices if the core can slip and slide inside the sheath. These can also be used as electrically conductive nanowires and optical wave guides, as well as nanoelectrodes in electrochemical devices where the nanotube core is used for conduction and the shell polymer as an insulator. Another important application is the AFM probe tip, where the individual SWNT or small SWNT bundles can be used for achieving high resolution, while the larger-diameter shell provides rigidity and ease of handling. The core diameter is the diameter of the individual nanotube or that of the nanotube bundle, depending on the extent of exfoliation. Use of chemically or biologically functionalized tips, as well as tips with electrical and thermal conductivity, provides additional capability to AFM. The electrospun fibers can typically be processed in the 100-nm- to 2- $\mu$ m-diameter range by controlling solution characteristics (the type of polymer, solution concentration, and polarity and surface tension of the solvent) and processing parameters (the strength of the applied electric field, the distance between spinneret and collector, and the solution feeding rate).<sup>246</sup>

In addition, VGCNFs were also incorporated in a PMMA matrix exhibiting a 62% increase in tensile modulus and 160% increase in compressive strength (Table 8.10)<sup>62</sup>. In the case of PP, adding VGCNFs resulted in increased tensile strength and modulus (Table 8.10).<sup>63</sup>

#### 8.5.1.5 PS/CNT

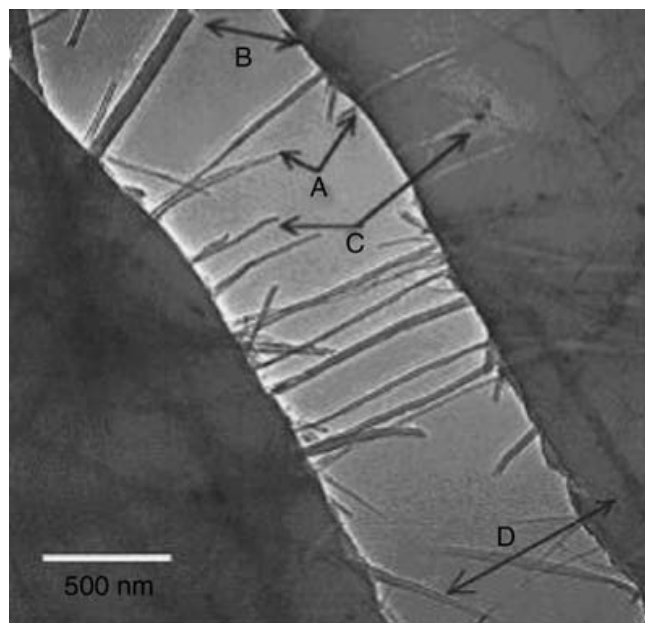
MWNTs were dispersed in polystyrene using toluene. *In situ* TEM study shows that the external load can be effectively transmitted from the matrix to the nanotubes.<sup>247</sup> The cracks tend to nucleate at low-nanotube-density areas and then propagate along weak MWNT/PS interfaces or relatively low MWNT density regions. The MWNTs align perpendicular to the crack direction and bridge the crack faces. When the crack opening displacement exceeds ~800 nm, the nanotubes begin to break or pull out of the matrix. Figure 8.26 shows that about half of the aligned nanotubes have broken and subsequently pulled out of the matrix. Mechanical properties of PS/MWNT composites for various MWNT loading (1 to 5 wt%) processed from toluene

**Table 8.10** Mechanical Properties of Control Polymer and Polymer/VGCNF Composite Fibers

	Tensile Strength (GPa)	Tensile Modulus (GPa)	Elongation at Break (%)	Compressive Strength (GPa)
PMMA <sup>62</sup>	0.2 $\pm$ 0.04	4.7 $\pm$ 1.5	16 $\pm$ 3	28 $\pm$ 2
PMMA/VGCNF <sup>62</sup> (90/10)	0.15 $\pm$ 0.01	7.6 $\pm$ 0.9	9 $\pm$ 4	73 $\pm$ 11
PP <sup>63</sup>	0.49 $\pm$ 0.06	4.6 $\pm$ 0.7	23 $\pm$ 5	25 $\pm$ 1
PP/VGCNF <sup>63</sup> (95/5)	0.57 $\pm$ 0.07	7.1 $\pm$ 0.9	16 $\pm$ 2	48 $\pm$ 10

**Table 8.11** Mechanical Properties of PS and PS/MWNT Composite Films<sup>140</sup>

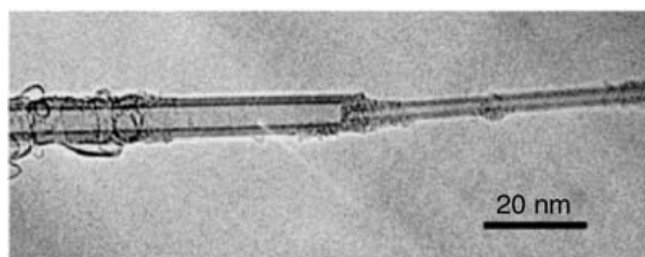
	Control PS	PS/MWNT (99/1)	PS/MWNT (98/2)	PS/MWNT (95/5)
Tensile strength (MPa)	20	25	26	31
Elastic modulus (GPa)	1.5	2.1	2.7	3.4

**Figure 8.26** TEM image of the fractured PS/MWNT composite film. (From ref. 247.)

exhibiting increased tensile strength and modulus are listed in Table 8.11.<sup>140</sup> The telescopic behavior of MWNTs has been reported (Figure 8.27).<sup>248</sup>

### 8.5.2 Thermal properties

Thermal conductivity of an isolated SWNT has been predicted to be as high as 6600 W/mK at room temperature,<sup>249</sup> and an experimental value of 3000 W/mK has been reported for a single MWNT.<sup>250</sup> Theoretical calculations also suggest that the thermal conductivity of SWNTs is not only related to their

**Figure 8.27** Telescopic behavior of MWNTs. (From ref. 248.)



radii and the temperature, but also to their chirality.<sup>251</sup> The zigzag nanotube has the highest value, while the chiral nanotube has the lowest value,<sup>251</sup> with the armchair nanotubes exhibiting intermediate behavior. The thermal conductivity of the three types of nanotubes shows similar temperature dependence.

Thermal conductivities of the commercial continuous carbon fibers are in the range of 8 to 1100 W/mK.<sup>6</sup> Thermal conductivity of the SWNT film aligned in the magnetic field is about 220 W/mK at room temperature along the alignment direction.<sup>252</sup> The room temperature axial thermal conductivity of the annealed SWNT fiber spun from sulfuric acid suspension was reported to be about 19 W/mK.<sup>24</sup> The relatively low thermal conductivity of the sulfuric acid-processed fiber was attributed to poor nanotube alignment and porosity. The thermal conductivity of the nanotube-based composites has been predicted based on the conventional effective-medium theory,<sup>253</sup> suggesting that the dispersion of a small amount of CNTs can result in a remarkable enhancement in the effective thermal conductivity of the composites. The thermal conductivity of epoxy with 1 wt% SWNT is about 0.5 W/mK at room temperature, while the thermal conductivity of the control epoxy without SWNT was about 0.2 W/mK.<sup>31</sup> With magnetic field (25 T) alignment,<sup>254</sup> the thermal conductivity of epoxy with 3 wt% SWNTs was reported to be 6.5 W/mK. Improved thermal conductivity behavior has also been reported in polypropylene/carbon nanotubes,<sup>255</sup> as well as in carbon-carbon nanotube composites.<sup>256</sup> A structure-property relationship study shows that the thermal conductivity improves with increasing nanotube alignment, while the absolute values are limited by the disorder network of finite-length individual tubes and tube bundles.<sup>257</sup> High-thermal-conductivity materials are quite attractive for thermal management applications.<sup>258</sup>

### 8.5.3 Electrical properties

The high aspect ratio and high conductivity make CNTs excellent candidates for conducting composites. According to the percolation theory,  $\sigma_c \propto (V - V_c)^\beta$ , where  $\sigma_c$  is the composite conductivity,  $V$  is the CNT volume fraction,  $V_c$  is the CNT volume fraction at the percolation threshold, and  $\beta$  is the critical exponent. The electrical conductivity of SWNT films and fibers has been reported<sup>16,18</sup> to be in the range of  $10^4$  to  $10^5$  S/m, while the conductivity of the individual nanotubes and nanotube ropes has been measured<sup>14</sup> to be on the order of  $10^6$  S/m.

Different systems give percolation values within a wide range, even the same system, such as epoxy/SWNTs, still results in various percolation values due to different preparation methods, resulting in different morphologies (Table 8.12, Figure 8.28). A percolation threshold well below 0.1 wt% has been demonstrated when gum arabic-stabilized SWNTs were combined with a PVA emulsion.<sup>68</sup> Homogeneous polymer/SWNT composites were fabricated using noncovalently functionalized soluble SWNT. These composites showed a percolation threshold at 0.05 to 0.1 wt% SWNTs.<sup>201</sup> The

**Table 8.12** Electrical Conductivity of CNT-Enabled Materials

	$V_c$ (vol%) <sup>a</sup>	$\beta$	Maximum Conductivity <sup>b</sup> (S/m)
Ceramic/SWNT <sup>363</sup>	0.64	1.7	$8.5 \times 10^2$ (25 vol%)
PPE/PS/SWNT <sup>201</sup>	0.045	1.5	10 (10 wt%)
PPE/PC/SWNT <sup>201</sup>	0.11	2.8	$4.8 \times 10^2$ (10 wt%)
P3OT/SWNT <sup>194</sup>	11	2.0	$\sim 10^{-3}$ (35 wt%)
Epoxy/SWNT <sup>32</sup>	0.074	1.3	$1.2 \times 10^{-3}$ (0.2 wt%)
Epoxy/MWNT-1 <sup>33</sup>	0.01	—	$5 \times 10^{-1}$ (0.1 wt%)
Epoxy/MWNT-2 <sup>33</sup>	0.0025	1.2	2 (1 wt%)

<sup>a</sup>  $V_c$  is the critical volume fraction at percolation threshold and  $\beta$  is the critical exponent.  $\beta = 1$  to 1.3 in two dimensions,  $\beta = 1.6$  to 2 in three dimensions, and  $\beta > 2$  has been observed in anisotropic systems.

<sup>b</sup> Nanotube loading at which maximum conductivity is reported in parentheses.

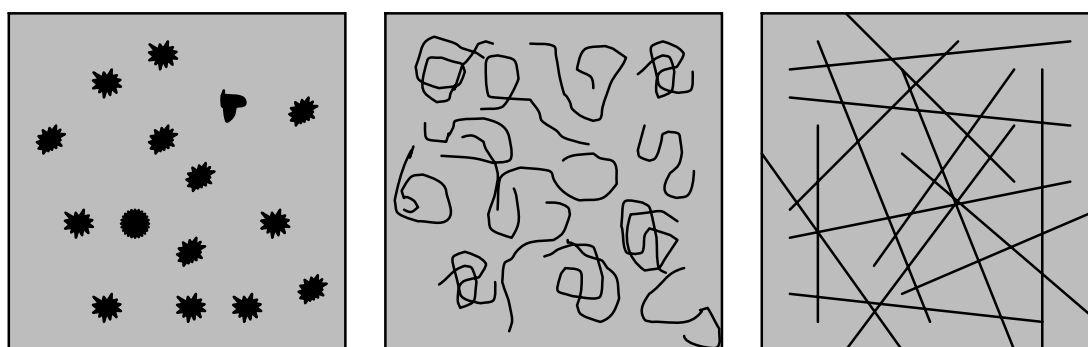


**Figure 8.28** Schematics of various CNT morphologies in polymer matrix (a) CNT globules, (b) well-dispersed coiled CNTs, and (c) well-dispersed extended CNTs.

percolation threshold for PP/MWNT composites was between 1 and 2 wt% MWNT.<sup>151</sup> Epoxy/MWNT composites with weight fractions ranging from as low as 0.001 up to 1 wt% were produced with the percolation threshold at 0.04 wt%.<sup>33</sup> Electrical conductivity of the PMMA/SWNT composite film increased from 0.118 to 11.5 S/m as the SWNT content increased from 1.3 to 6.6 wt%.<sup>196</sup> When PMMA/MWNT nanocomposites with the same MWNT concentrations were electrospun in DMF into nanofibrous membrane (the diameter of the electrospun fibers ranged between  $120 \pm 30$  and  $710 \pm 20$  nm), the conductivity was reduced to  $\sim 10^{-8}$  S/m. The dispersion of the MWNTs in the electrospun nanofibers was superior to the conventional CNT/polymer composites, and MWNTs in the electrospun nanofibers were found to be embedded in the polymer matrix and to align along the fiber axis, which decreases the contact points between MWNTs, resulting in low electrical conductivity.<sup>241</sup> The electrical conductivity of the composites strongly depends not only on the dispersion, exfoliation, and orientation of CNTs, but also on the length of the CNTs. Figure 8.28 shows schematic descriptions of three different states of nanotube dispersion and orientation

in polymer matrix, where nanotube loading required for electrical percolation would be highest in Figure 8.28a and lowest in Figure 8.28c. Electrically conducting composites can be used for electrostatic painting, antistatic shielding on airplanes, electromagnetic interference (EMI) shielding, and as a transparent conductor.<sup>259</sup>

#### 8.5.4 Optical properties

Carbon nanotubes exhibit intrinsic anisotropic optical properties. As described earlier, using the resonance-enhanced Raman spectra as a function of polarization direction, the orientation of single- and double-wall carbon nanotubes can be determined.<sup>30,36,159,161,163</sup> The absorbance due to SWNT van Hove transitions has also been shown to be dependent on the polarization direction.<sup>73</sup> For example, the absorption corresponding to the first- and second-order van Hove transitions ( $S_{11}$  and  $S_{22}$ ) in the semiconducting tubes and the first-order transition ( $M_{11}$ ) in the metallic tubes observed at  $\sim 0.8$ ,  $\sim 1.4$ , and  $\sim 2.0$  eV, respectively, in highly stretched polystyrene show a strong dependence on the polarization direction (Figure 8.29). The absorbance is maximum when the polarization direction is parallel to the stretching direction and minimum when it is perpendicular. Anisotropic absorption in the infrared region for highly oriented polyacrylonitrile fibers containing 1 wt% SWNT is shown in Figure 8.30.<sup>36</sup> PAN fiber spectra for the two polarization directions are comparable, while the composite fiber spectra show significant absorbance differences in the two polarization directions. The carbon nanotube optical properties can be calculated based on the Maxwell–Garnett (MG) effective-medium approximation,<sup>260</sup> as well as based on an improved equivalent dielectric function.<sup>261</sup> The polarized absorption coefficient of SWNT has

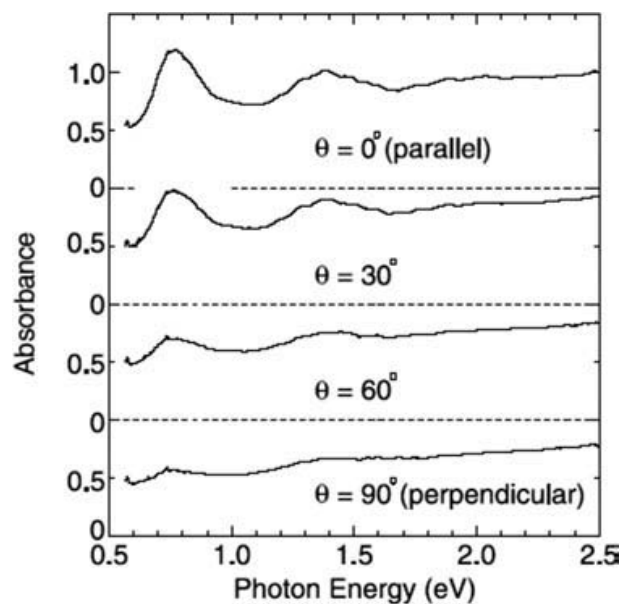


**Figure 8.29** Optical anisotropic behavior of highly stretched PS/SWNT film. (From ref. 73.)

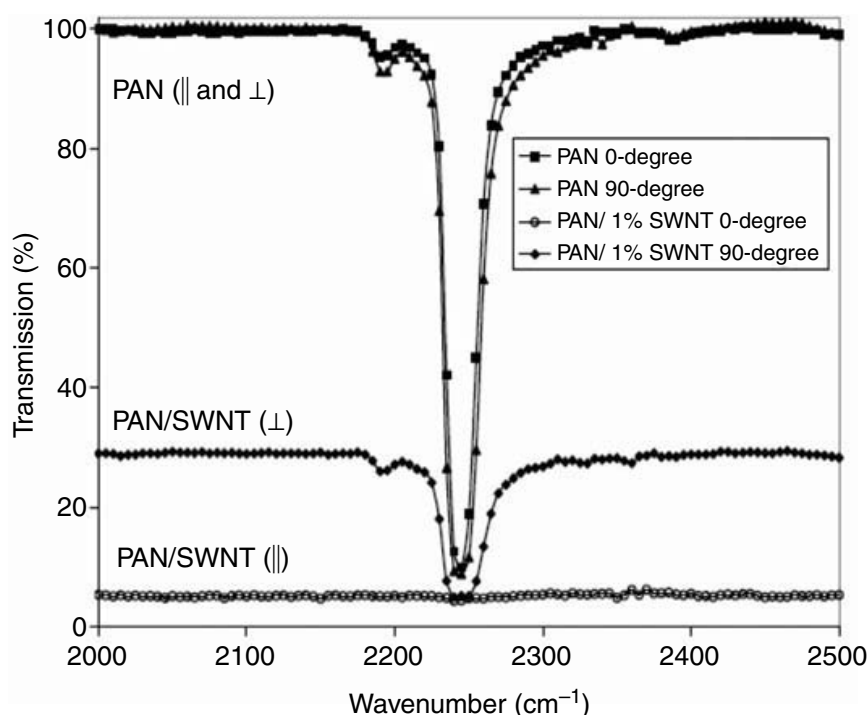


**Figure 8.30** Polarized infrared spectra of PAN and PAN/SWNT (99/1) composite fibers. (From ref. 36.)

been calculated from measured polarized absorption of PMMA/SWNT (1 wt% SWNT) composite fiber.<sup>262</sup> The optical properties of SWNT/poly(3-octylthiophenes) (P3OT) composite film were studied as a function of the nanotube volume fraction.<sup>263</sup> Results demonstrate that the Maxwell–Garnett effective-medium theory can explain the observed results. These studies suggest that the optical properties of the composites can be tailored in a predetermined manner by controlling the nanotube content and orientation, thus opening a pathway for developing optically functional materials.

Composites of  $\pi$ -conjugated polymers and CNTs are of interest for applications in photovoltaic devices.<sup>50,264</sup> It has been shown that the quantum efficiency of a MWNT/poly(p-phenylene vinylene) (PPV) hole-collecting photovoltaic device is twice that of the device employing the standard indium tin oxide (ITO) electrode.

The nonlinear optical properties of several polymer-coated or polymer-grafted MWNTs have been investigated.<sup>102</sup> Nonlinear optical extinction of nanosecond laser pulses by a set of conjugated copolymer/MWNT composites dispersed in solution has also been reported.<sup>265</sup> The optical properties of PmPV/MWNT composites varied according to nanotube content. Either the MWNT or the polymer dominates the nonlinear response of the composite, depending on the relative mass of the polymer and the nanotube. At 10 J/cm<sup>2</sup>, the sample with 3.6 wt% MWNTs has a normalized nonlinear extinction of 12%, while the sample with 5.9 wt% MWNT mass has a normalized extinction of 41%. The other three samples (0, 1.3, and 2.5 wt%

MWNTs) have no nonlinear extinction at this energy density. Thus, the materials displayed a dramatic improvement in the optical-limiting performance when the MWNT mass content increased from 1.3 to 3.6%.

### 8.5.5 Miscellaneous properties

Carbon nanotube bucky paper and polymer/CNT composites are being developed for electrochemical supercapacitor electrodes.<sup>75,266,267</sup> Capacitance values depend on CNT purity and electrolyte,<sup>268–273</sup> as well as on specimen treatment such as CO<sub>2</sub> physical activation,<sup>274</sup> KOH chemical activation,<sup>275,276</sup> or exposure to nitric acid,<sup>266,267,277–279</sup> fluorine,<sup>280</sup> or ammonia plasma.<sup>281</sup> The requirements for a carbon-based electrochemical supercapacitor are high electrical conductivity, high specific surface area with appropriate pore size control, and stability in the presence of electrolyte. The specific capacitance, as well as the power and energy densities of the carbonized and activated PAN/SWNT composite films, is higher than that of the SWNT bucky paper.<sup>75</sup> The Ragone plot, comparing the power and energy densities of the SWNT bucky paper and carbonized and activated SWNT/PAN composite films, is given in Figure 8.31. Electrospun fiber mats of CNT/PAN and many other carbonizing polymers composed of fibers of tens to hundreds of nanometers in diameter are also expected to be quite attractive for supercapacitor application.<sup>282</sup> Conducting polymers, such as polyacetylene, polypyrrole, polyaniline, and polythiophene, are also common electrode materials for supercapacitors.<sup>283–285</sup> Composites of electrically conducting polymers with carbon nanotubes are also being evaluated for supercapacitors.<sup>77,204,268,286–293</sup> The capacitance of MWNT/polypyrrole (PPy) was reported to be 163 F/g, while that for the pristine nanotubes was 50 F/g.<sup>287</sup> In a recent study,<sup>294</sup> supercapacitor electrodes based on pyrrole-treated functionalized SWNTs exhibited

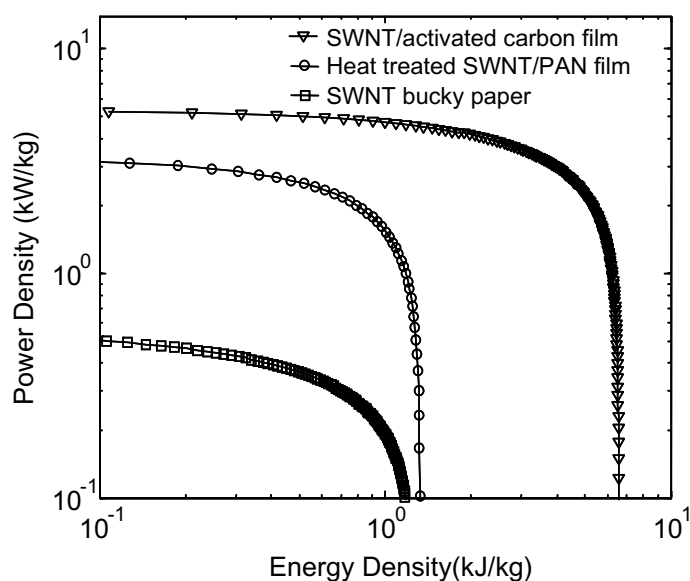


**Figure 8.31** Ragone plot for various electrodes evaluated at a discharging current of 0.01 A. (From ref. 75.)



a capacitance of 350 F/g, power density of 4.8 kW/kg, and energy density of 3.3 kJ/kg. Literature reports<sup>295</sup> suggest that the mesopores (dimension = 2 to 50 nm) are important for the electrochemical supercapacitor; however, the study on pyrrole-treated functionalized SWNTs showed that the contribution of macropores (pores with dimensions of >50 nm) is also important.<sup>294</sup> The double-layer capacity of the pyrrole-treated films was 154  $\mu\text{F}/\text{cm}^2$ , while the double-layer capacity of the classical porous carbons was reported to be in the range of 10 to 70  $\mu\text{F}/\text{cm}^2$ .

CNTs are also being studied for application as actuators.<sup>296–307</sup> Uniform dispersion of 1 ~ 5 vol% of CNTs in a thermoplastic elastomer can store and subsequently release, through remote means, up to 50% more recovery stress than the pristine resin.<sup>308</sup> The nanotubes also increased the matrix modulus by a factor of 5 and improved shape fixity by enhancing strain-induced crystallization. The infrared absorption of CNTs affords remote actuation, providing new opportunities for the design and fabrication of stimuli-responsive polymers.

Carbon nanotube-based materials are being studied for a variety of sensor applications.<sup>82,118–122,301–307,309–337</sup> MWNT/PMMA composite thin films have been studied for gas and chemical sensors by monitoring the change in the film resistance when exposed to vapors of dichloromethane, chloroform, acetone, methanol, ethyl acetate, toluene, and hexane.<sup>235</sup> The resistance of functionalized MWNT/PMMA, compared to an unfunctionalized MWNT/PMMA composite, increased by two to three orders of magnitude when exposed to various chemical vapors. The sensing mechanism is explained on the basis of volume expansion caused by PMMA swelling and polar interaction of the various vapors on the MWNT surface.

## 8.6 Crystallization, wrapping, interaction, and intercalation

Carbon nanotubes can be used as a template for crystallization of polymers and of low-molecular-weight compounds. Crystallization of polypropylene on CNTs has been studied by several groups.<sup>30,51,338–340</sup> The addition of 1 wt% MWNTs into polypropylene resulted in an increased crystallization rate and fibrillar morphology rather than the spherulitic morphology.<sup>51</sup> Crystallization and orientation behavior of polypropylene in the presence of SWNTs has also been studied.<sup>30</sup> The spherulite size in pure PP is much larger than that in PP/SWNT composites (Figure 8.32), indicating that SWNTs act as nucleating sites for PP crystallization. Based on the half crystallization time as a function of isothermal crystallization temperature (Figure 8.33), it has been shown that the addition of 0.8 wt% SWNTs increases the PP crystallization rate by as much as an order of magnitude or higher. Thus, both SWNTs and MWNTs can nucleate polypropylene crystallization. The SWNT has also been shown to nucleate PVA crystallization.<sup>338</sup> MWNTs also resulted in enhanced crystallization of a semiconjugated host polymer PmPV,<sup>339</sup> where

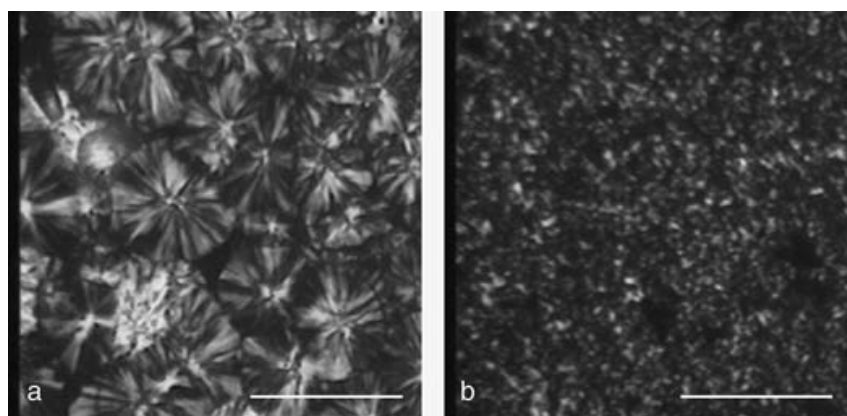


**Figure 8.32** Polarized optical micrographs for (a) PP and (b) PP/SWNT (99.2/0.8) composites. (From ref. 30.)

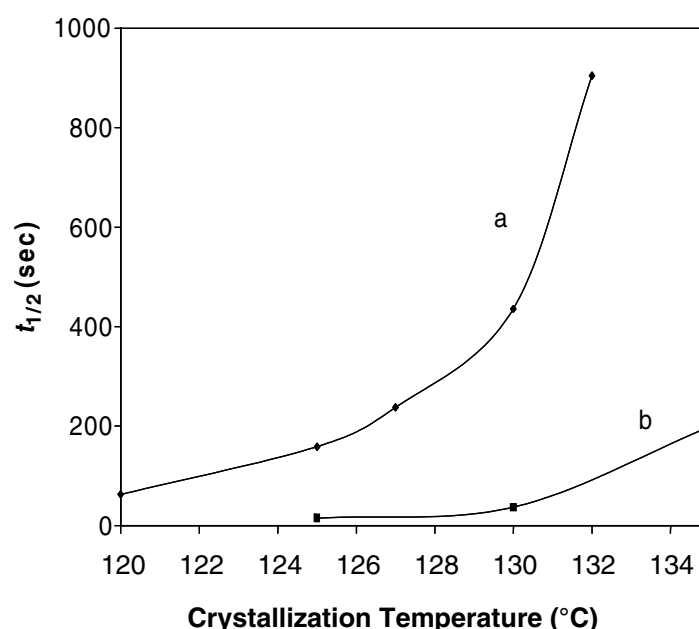


**Figure 8.33** Crystallization half-time ( $t_{1/2}$ ) of (a) PP and (b) PP/SWNT (99.2/0.8) as a function of crystallization temperature. (From ref. 30.)

crystallinity increased from 20% in PmPV to approximately 55% in the 3 vol% MWNTs containing the PmPV composite. Ultra-high-molecular-weight poly(vinyl alcohol) fibers self-assemble while stirring the solution. The fibers are unoriented amorphous when no nanotubes are present. However, in the presence of SWNTs, self-assembled PVA fibers exhibited significant orientation and crystallinity, providing further proof of nanotube-templated crystallization.<sup>341</sup>

Anhydrous liquid sulfuric acid has been shown to be partially ordered in the presence of SWNTs.<sup>342</sup> The x-ray diffraction pattern of the dried SWNT fiber shows SWNT orientation with diffraction peaks arising from the SWNT ropes (Figure 8.34a). The SWNT fiber swollen with sulfuric acid shows a peak corresponding to the ordered sulfuric acid, while the liquid sulfuric

acid is amorphous and unoriented (Figure 8.34b). The azimuthal spread of the sulfuric acid WAXD peak was the same as that for the SWNTs. It is suggested that the acid interacting with SWNTs represents a new phase different from the bulk acid.<sup>342</sup> Differential scanning calorimetry shows a sharp crystallization peak for the sulfuric acid (enthalpy  $\sim 114$  J/g). With increasing SWNT content in the sulfuric acid, both the crystallization temperature and the enthalpy decrease (Figure 8.35). This was interpreted to be due to the presence of two types of acid: free acid, which can crystallize, and the acid interacting with the nanotubes, which does not crystallize in the temperature range investigated.<sup>343</sup> The x-ray diffraction pattern of the oriented sulfuric acid crystal and the hypothesized structure of sulfuric acid in the vicinity of the nanotube are shown in Figure 8.36.

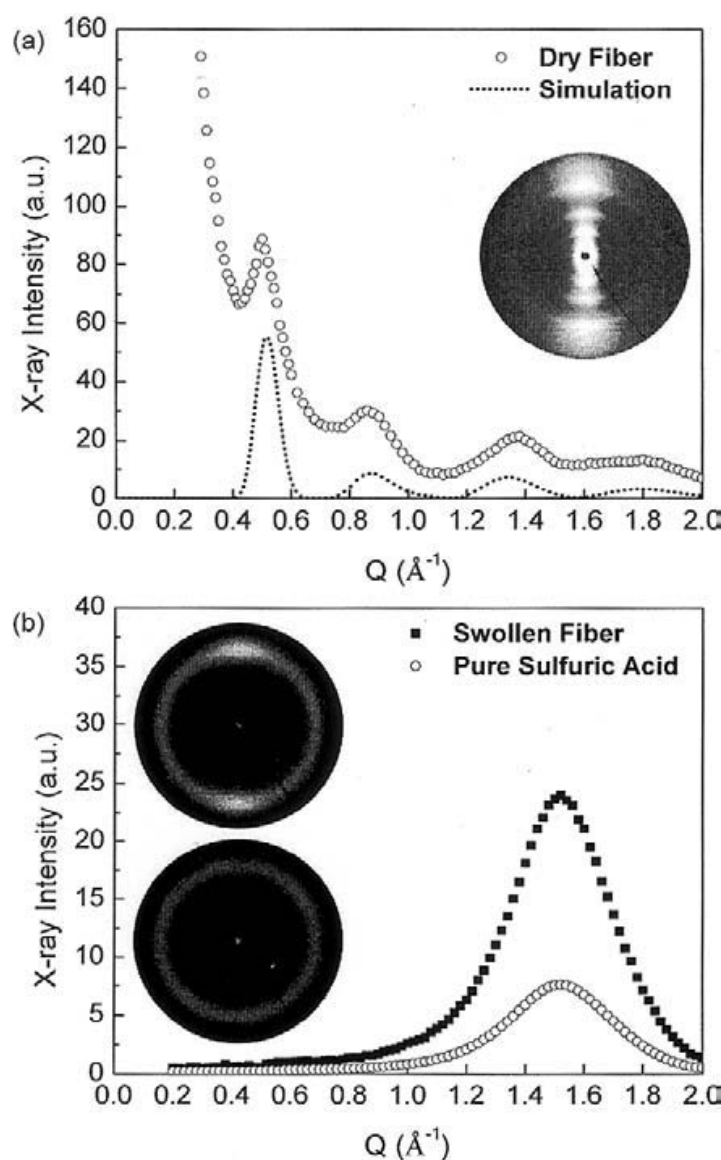


**Figure 8.34** X-ray scattering data. (a) Integrated scattering profile (empty circle) of dry annealed SWNT fibers. (b) Swollen SWNT fiber (solid squares) and pure sulfuric acid (empty circles). (From ref. 342.)

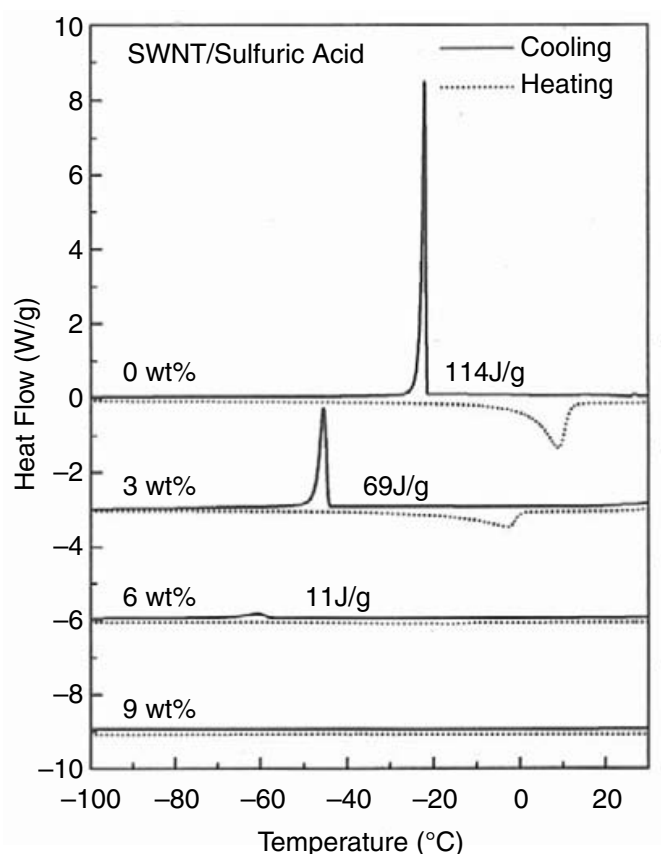


**Figure 8.35** Differential scanning calorimetry data of SWNT dispersion in sulfuric acid. (From ref. 342.)

PVP can wrap around the SWNTs, rendering them soluble in aqueous media.<sup>344</sup> Similar behavior has been reported in the PmPV/SWNT system, as described by scanning tunneling microscopy (STM). The PmPV-wrapped SWNT can be dissolved in organic solvents. It has also been reported that PPV covers the surface of MWNTs and forms a well-mixed composite as observed by AFM.<sup>50</sup> Polymer wrapping and intercalation have also been suggested in the case of the PAN/SWNT system (Figure 8.18).<sup>71</sup> A number of research papers have discussed the possibility of PMMA intercalation in SWNT bundles.<sup>91,171,195,243,244</sup>

## 8.7 Concluding remarks

A summary of the research work presented in this chapter shows that carbon nanotubes are promising candidates for developing high-performance functional materials. CNTs have been dispersed in a variety of polymer matrices using melt processing, solution processing, or *in situ* polymerization using pristine, functionalized, or polymer-grafted nanotubes. Nanotubes are dispersed using strong acids, organic solvents, electrolytes, and surfactants in aqueous media. Carbon nanotube composites with more than 25 different polymers, including semicrystalline, amorphous, liquid crystalline, conjugated, and solvent-processable polymers, as well as thermosetting resins,

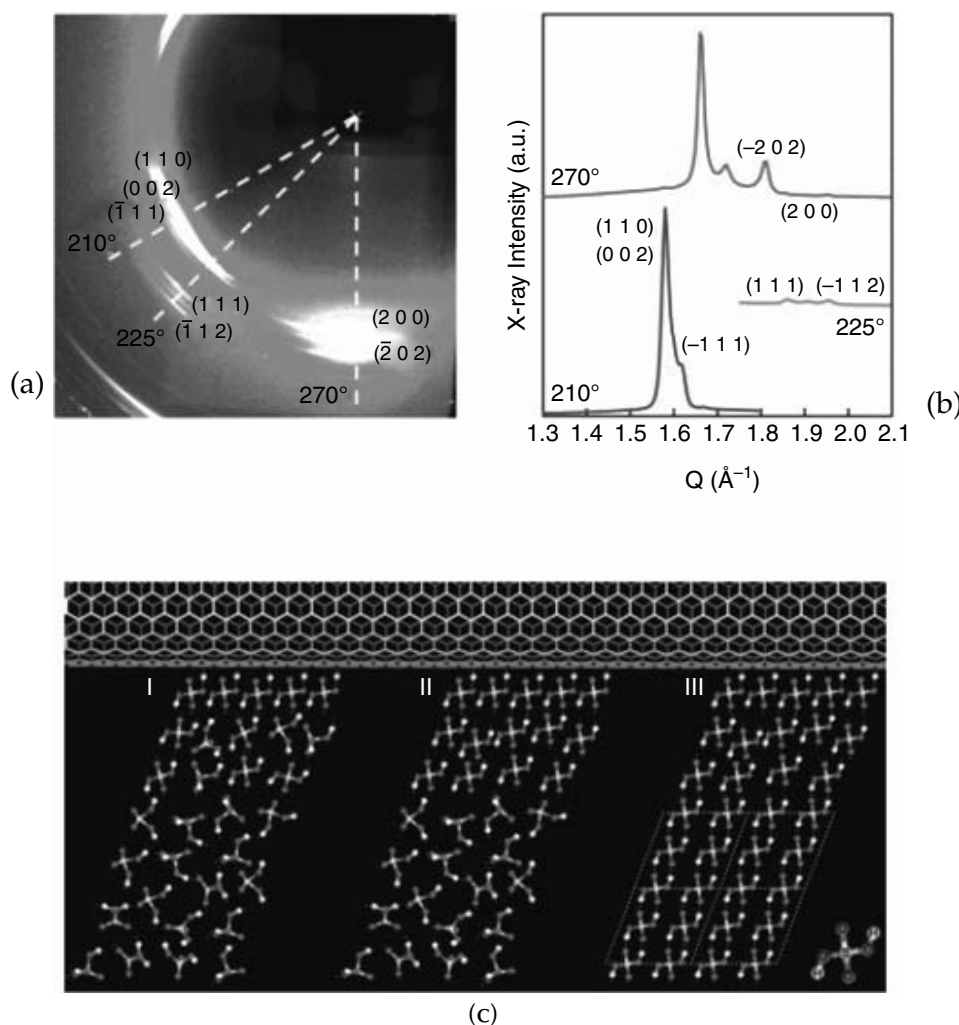


**Figure 8.36** (a) X-ray scattering and integrated patterns for swollen SWNT fiber by sulfuric acid at 200 K. (b) Schematic description for crystallization  $\text{H}_2\text{SO}_4$  templated by SWNT or SWNT rope. (c) (I) Liquid phase of  $\text{H}_2\text{SO}_4$ . Two or three layers of structured acid wrapped around nanotubes possess both positional order and orientational order, with the inside layer being most ordered. Outside layers interact with the first layer via hydrogen bonding. Outside the two or three layers of semiordered acid is free bulk acid. (II) Molecular orientations in the semiordered region become ordered upon cooling, with their positional order remaining unchanged. It represents a purely hypothetical but reasonable intermediate state. (III) Crystallization of free acid with its crystal orientation determined by the molecular orientation in the structured acid. (From ref. 343.)

have been processed. Property enhancements include strength, stiffness, thermal stability, solvent resistance, glass transition temperature, crystallization time, crystallinity, electrical conductivity, reduced thermal shrinkage, and optical anisotropy. Though many highly successful studies have been reported, the dispersion of nanotubes and fabrication of homogenous polymer composites, while maintaining nanotube length, remain the main technical challenges in processing bulk nanotube-based materials. Polymer tensile strength increases with increasing molecular weight.<sup>189–192</sup> Similarly, the



strength of the polymer/CNT composites is expected to depend on the CNT length.

Potential CNT-enabled materials applications include chemical and physical sensors, probe tips for the AFM, electrically and thermally conducting fibers for functional textiles, nanowires, quantum wires, nanoscopic levers, and other components in molecular motors and molecular devices. Other major promising applicable directions lie in the biomedical field, including scaffolds for tissue growth,<sup>345–347</sup> substrate for neuron growth, actuators,<sup>202,273,296–307,310,348</sup> novel micro- and mesoporous carbon structures for filtration,<sup>349</sup> and other applications.<sup>350</sup> Carbon nanotube material applications in field emission display devices,<sup>80,193,351</sup> photovoltaic materials,<sup>50,76,263,264</sup> electromagnetic interference shielding, packaging materials for thermal management, and supercapacitors as charge storage devices are also being actively investigated.

## Acknowledgment

The authors' work on carbon nanotubes is funded by the Air Force Office of Scientific Research (F49620-03-1-0124), Office of Naval Research (N00014-01-1-0657), and Carbon Nanotechnologies, Inc. The assistance of Huina Guo in preparing this chapter is gratefully acknowledged.

## References

1. Iijima, S., Ichihashi, T., Single-shell carbon nanotubes of 1-nm diameter, *Nature* 1993, 363, 603–605.
2. Bethune, D.S., Kiang, C.H., Devries, M.S., Gorman, G., Savoy, R., Vazquez, J., Beyers, R., Cobalt-catalyzed growth of carbon nanotubes with single-atomic-layerwalls, *Nature* 1993, 363, 605–607.
3. Sugai, T., Yoshida, H., Shimada, T., Okazaki, T., Shinohara, H., New synthesis of high-quality double-walled carbon nanotubes by high-temperature pulsed arc discharge, *Nano Letters* 2003, 3, 769–773.
4. Bandow, S., Takizawa, M., Hirahara, K., Yudasaka, M., Iijima, S., Raman scattering study of double-wall carbon nanotubes derived from the chains of fullerenes in single-wall carbon nanotubes, *Chemical Physics Letters* 2001, 337, 48–54.
5. Iijima, S., Helical microtubules of graphitic carbon, *Nature* 1991, 354, 56–58.
6. Minus, M.L., Kumar, S., The processing, properties, and structure of carbon fibers, *JOM* 2005, 57, 52–58.
7. Carneiro, O.S., Covas, J.A., Bernardo, C.A., Caldeira, G., Van Hattum, F.W.J., Ting, J.M., Alig, R.L., Lake, M.L., Production and assessment of polycarbonate composites reinforced with vapour-grown carbon fibres, *Composites Science and Technology* 1998, 58, 401–407.
8. Singh, C., Quested, T., Boothroyd, C.B., Thomas, P., Kinloch, I.A., Abou-Kandil, A.I., Windle, A.H., Synthesis and characterization of carbon nanofibers produced by the floating catalyst method, *Journal of Physical Chemistry B* 2002, 106, 10915–10922.

9. Maruyama, B., Alam, H., Carbon nanotubes and nanofibers in composite materials, *SAMPE Journal* 2002, 38, 59–70.
10. Guo, T., Nikolaev, P., Thess, A., Colbert, D.T., Smalley, R.E., Catalytic growth of single-walled nanotubes by laser vaporization, *Chemical Physics Letters* 1995, 243, 49–54.
11. Nikolaev, P., Bronikowski, M.J., Bradley, R.K., Rohmund, F., Colbert, D.T., Smith, K.A., Smalley, R.E., Gas-phase catalytic growth of single-walled carbon nanotubes from carbon monoxide, *Chemical Physics Letters* 1999, 313, 91–97.
12. Joseyacaman, M., Mikiyoshida, M., Rendon, L., Santiesteban, J.G., Catalytic growth of carbon microtubules with fullerene structure, *Applied Physics Letters* 1993, 62, 657–659.
13. Huang, S.M., Woodson, M., Smalley, R., Liu, J., Growth mechanism of oriented long single walled carbon nanotubes using “fast-heating” chemical vapor deposition process, *Nano Letters* 2004, 4, 1025–1028.
14. Baughman, R.H., Zakhidov, A.A., de Heer, W.A., Carbon nanotubes — the route toward applications, *Science* 2002, 297, 787–792.
15. Thess, A., Lee, R., Nikolaev, P., Dai, H.J., Petit, P., Robert, J., Xu, C.H., Lee, Y.H., Kim, S.G., Rinzler, A.G., Colbert, D.T., Scuseria, G.E., Tomanek, D., Fischer, J.E., Smalley, R.E., Crystalline ropes of metallic carbon nanotubes, *Science* 1996, 273, 483–487.
16. Ericson, L.M., Fan, H., Peng, H.Q., Davis, V.A., Zhou, W., Sulpizio, J., Wang, Y.H., Booker, R., Vavro, J., Guthy, C., Parra-Vasquez, A.N.G., Kim, M.J., Ramesh, S., Saini, R.K., Kittrell, C., Lavin, G., Schmidt, H., Adams, W.W., Billups, W.E., Pasquali, M., Hwang, W.F., Hauge, R.H., Fischer, J.E., Smalley, R.E., Macroscopic, neat, single-walled carbon nanotube fibers, *Science* 2004, 305, 1447–1450.
17. Zhang, M., Atkinson, K.R., Baughman, R.H., Multifunctional carbon nanotube yarns by downsizing an ancient technology, *Science* 2004, 306, 1358–1361.
18. Sreekumar, T.V., Liu, T., Kumar, S., Ericson, L.M., Hauge, R.H., Smalley, R.E., Single-wall carbon nanotube films, *Chemistry of Materials* 2003, 15, 175–178.
19. Jiang, K.L., Li, Q.Q., Fan, S.S., Nanotechnology: Spinning continuous carbon nanotube yarns — carbon nanotubes weave their way into a range of imaginative macroscopic applications, *Nature* 2002, 419, 801–801.
20. Vigolo, B., Penicaud, A., Coulon, C., Sauder, C., Pailler, R., Journet, C., Bernier, P., Poulin, P., Macroscopic fibers and ribbons of oriented carbon nanotubes, *Science* 2000, 290, 1331–1334.
21. Endo, M., Muramatsu, H., Hayashi, T., Kim, Y.A., Terrones, M., Dresselhaus, N.S., “Buckypaper” from coaxial nanotubes, *Nature* 2005, 433, 476–476.
22. Fischer, J.E., Zhou, W., Vavro, J., Llaguno, M.C., Guthy, C., Haggenueller, R., Casavant, M.J., Walters, D.E., Smalley, R.E., Magnetically aligned single wall carbon nanotube films: preferred orientation and anisotropic transport properties, *Journal of Applied Physics* 2003, 93, 2157–2163.
23. Zhang, X.F., Sreekumar, T.V., Liu, T., Kumar, S., Properties and structure of nitric acid oxidized single wall carbon nanotube films, *Journal of Physical Chemistry B* 2004, 108, 16435–16440.
24. Zhou, W., Vavro, J., Guthy, C., Winey, K.I., Fischer, J.E., Ericson, L.M., Ramesh, S., Saini, R., Davis, V.A., Kittrell, C., Pasquali, M., Hauge, R.H., Smalley, R.E., Single wall carbon nanotube fibers extruded from super-acid suspensions: Preferred orientation, electrical, and thermal transport, *Journal of Applied Physics* 2004, 95, 649–655.

25. Zhu, H.W., Xu, C.L., Wu, D.H., Wei, B.Q., Vajtai, R., Ajayan, P.M., Direct synthesis of long single-walled carbon nanotube strands, *Science* 2002, 296, 884–886.
26. Shaffer, M.S.P., Windle, A.H., Fabrication and characterization of carbon nanotube/poly(vinyl alcohol) composites, *Advanced Materials* 1999, 11, 937–941.
27. Zhang, X.F., Liu, T., Sreekumar, T.V., Kumar, S., Moore, V.C., Hauge, R.H., Smalley, R.E., Poly(vinyl alcohol)/SWNT composite film, *Nano Letters* 2003, 3, 1285–1288.
28. Cooper, C.A., Ravich, D., Lips, D., Mayer, J., Wagner, H.D., Distribution and alignment of carbon nanotubes and nanofibrils in a polymer matrix, *Composites Science and Technology* 2002, 62, 1105–1112.
29. Benoit, J.M., Corraze, B., Chauvet, O., Localization, Coulomb interactions, and electrical heating in single-wall carbon nanotubes/polymer composites, *Physical Review B* 2002, 65, 241405.
30. Bhattacharyya, A.R., Sreekumar, T.V., Liu, T., Kumar, S., Ericson, L.M., Hauge, R.H., Smalley, R.E., Crystallization and orientation studies in polypropylene/single wall carbon nanotube composite, *Polymer* 2003, 44, 2373–2377.
31. Biercuk, M.J., Llaguno, M.C., Radosavljevic, M., Hyun, J.K., Johnson, A.T., Fischer, J.E., Carbon nanotube composites for thermal management, *Applied Physics Letters* 2002, 80, 2767–2769.
32. Kim, B., Lee, J., Yu, I.S., Electrical properties of single-wall carbon nanotube and epoxy composites, *Journal of Applied Physics* 2003, 94, 6724–6728.
33. Sandler, J.K.W., Kirk, J.E., Kinloch, I.A., Shaffer, M.S.P., Windle, A.H., Ultralow electrical percolation threshold in carbon-nanotube-epoxy composites, *Polymer* 2003, 44, 5893–5899.
34. Sennett, M., Welsh, E., Wright, J.B., Li, W.Z., Wen, J.G., Ren, Z.F., Dispersion and alignment of carbon nanotubes in polycarbonate, *Applied Physics B-Lasers and Optics* 2003, 76, 111–113.
35. Dalton, A.B., Collins, S., Munoz, E., Razal, J.M., Ebron, V.H., Ferraris, J.P., Coleman, J.N., Kim, B.G., Baughman, R.H., Super-tough carbon-nanotube fibres — these extraordinary composite fibres can be woven into electronic textiles, *Nature* 2003, 423, 703–703.
36. Sreekumar, T.V., Liu, T., Min, B.G., Guo, H., Kumar, S., Hauge, R.H., Smalley, R.E., Polyacrylonitrile single-walled carbon nanotube composite fibers, *Advanced Materials* 2004, 16, 58–61.
37. Zhang, X.F., Liu, T., Sreekumar, T.V., Kumar, S., Hu, X.D., Smith, K., Gel spinning of PVA/SWNT composite fiber, *Polymer* 2004, 45, 8801–8807.
38. Kumar, S., Dang, T.D., Arnold, F.E., Bhattacharyya, A.R., Min, B.G., Zhang, X.F., Vaia, R.A., Park, C., Adams, W.W., Hauge, R.H., Smalley, R.E., Ramesh, S., Willis, P.A., Synthesis, structure, and properties of PBO/SWNT composites, *Macromolecules* 2002, 35, 9039–9043.
39. Ko, F., Gogotsi, Y., Ali, A., Naguib, N., Ye, H.H., Yang, G.L., Li, C., Willis, P., Electrospinning of continuous carbon nanotube-filled nanofiber yarns, *Advanced Materials* 2003, 15, 1161–1165.
40. Weisenberger, M.C., Grulke, E.A., Jacques, D., Rantell, T., Andrews, R., Enhanced mechanical properties of polyacrylonitrile/multiwall carbon nanotube composite fibers, *Journal of Nanoscience and Nanotechnology* 2003, 3, 535–539.
41. Wu, M., Shaw, L.L., "On the improved properties of injection-molded, carbon nanotube-filled PET/PVDF blends, *Journal of Power Sources* 2004, 136, 37–44.

42. Mylvaganam, K., Zhang, L.C., Chemical bonding in polyethylene-nanotube composites: a quantum mechanics prediction, *Journal of Physical Chemistry B* 2004, 108, 5217–5220.
43. Sen, R., Zhao, B., Perea, D., Itkis, M.E., Hu, H., Love, J., Bekyarova, E., Haddon, R.C., Preparation of single-walled carbon nanotube reinforced polystyrene and polyurethane nanofibers and membranes by electrospinning, *Nano Letters* 2004, 4, 459–464.
44. Jia, Z.J., Wang, Z.Y., Xu, C.L., Liang, J., Wei, B.Q., Wu, D.H., Zhu, S.W., Study on poly(methyl methacrylate)/carbon nanotube composites, *Materials Science and Engineering a-Structural Materials Properties Microstructure and Processing* 1999, 271, 395–400.
45. Martin, C.A., Sandler, J.K.W., Windle, A.H., Schwarz, M.K., Bauhofer, W., Schulte, K., Shaffer, M.S.P., Electric field-induced aligned multi-wall carbon nanotube networks in epoxy composites, *Polymer* 2005, 46, 877–886.
46. Pecastaings, G., Delhaes, P., Derre, A., Saadaoui, H., Carmona, F., Cui, S., Role of interfacial effects in carbon nanotube/epoxy nanocomposite behavior, *Journal of Nanoscience and Nanotechnology* 2004, 4, 838–843.
47. Sandler, J., Shaffer, M.S.P., Prasse, T., Bauhofer, W., Schulte, K., Windle, A.H., Development of a dispersion process for carbon nanotubes in an epoxy matrix and the resulting electrical properties, *Polymer* 1999, 40, 5967–5971.
48. Zhao, B., Hu, H., Haddon, R.C., Synthesis and properties of a water-soluble single-walled carbon nanotube-poly(m-aminobenzene sulfonic acid) graft copolymer, *Advanced Functional Materials* 2004, 14, 71–76.
49. Mrozek, R.A., Kim, B.S., Holmberg, V.C., Taton, T.A., Homogeneous, coaxial liquid crystal domain growth from carbon nanotube seeds, *Nano Letters* 2003, 3, 1665–1669.
50. Ago, H., Petritsch, K., Shaffer, M.S.P., Windle, A.H., Friend, R.H., Composites of carbon nanotubes and conjugated polymers for photovoltaic devices, *Advanced Materials* 1999, 11, 1281–1285.
51. Assouline, E., Lustiger, A., Barber, A.H., Cooper, C.A., Klein, E., Wachtel, E., Wagner, H.D., Nucleation ability of multiwall carbon nanotubes in polypropylene composites, *Journal of Polymer Science Part B-Polymer Physics* 2003, 41, 520–527.
52. Huang, J.E., Li, X.H., Xu, J.C., Li, H.L., Well-dispersed single-walled carbon nanotube/polyaniline composite films, *Carbon* 2003, 41, 2731–2736.
53. Lupo, F., Kamalakaran, R., Scheu, C., Grobert, N., Ruhle, M., Microstructural investigations on zirconium oxide-carbon nanotube composites synthesized by hydrothermal crystallization, *Carbon* 2004, 42, 1995–1999.
54. Laurent, C., Peigney, A., Rousset, A., Synthesis of carbon nanotube Fe-Al<sub>2</sub>O<sub>3</sub> nanocomposite powders by selective reduction of different Al<sub>1.8</sub>Fe<sub>0.2</sub>O<sub>3</sub> solid solutions, *Journal of Materials Chemistry* 1998, 8, 1263–1272.
55. Kuzumaki, T., Ujiie, O., Ichinose, H., Ito, K., Mechanical characteristics and preparation of carbon nanotube fiber-reinforced Ti composite, *Advanced Engineering Materials* 2000, 2, 416–418.
56. Flahaut, E., Peigney, A., Laurent, C., Marliere, C., Chastel, F., Rousset, A., Carbon nanotube-metal-oxide nanocomposites: Microstructure, electrical conductivity and mechanical properties, *Acta Materialia* 2000, 48, 3803–3812.



57. Velasco-Santos, C., Martinez-Hernandez, A.L., Fisher, F.T., Ruoff, R., Castano, V.M., Improvement of thermal and mechanical properties of carbon nanotube composites through chemical functionalization, *Chemistry of Materials* 2003, 15, 4470–4475.
58. Thostenson, E.T., Chou, T.W., Aligned multi-walled carbon nanotube-reinforced composites: processing and mechanical characterization, *Journal of Physics D-Applied Physics* 2002, 35, L77–L80.
59. Coleman, J.N., Cadek, M., Blake, R., Nicolosi, V., Ryan, K.P., Belton, C., Fonseca, A., Nagy, J.B., Gun'ko, Y.K., Blau, W.J., High-performance nanotube-reinforced plastics: understanding the mechanism of strength increase, *Advanced Functional Materials* 2004, 14, 791–798.
60. Mamedov, A.A., Kotov, N.A., Prato, M., Guldi, D.M., Wicksted, J.P., Hirsch, A., Molecular design of strong single-wall carbon nanotube/polyelectrolyte multilayer composites, *Nature Materials* 2002, 1, 190–194.
61. Ma, H.M., Zeng, J.J., Realff, M.L., Kumar, S., Schiraldi, D.A., Processing, structure, and properties of fibers from polyester/carbon nanofiber composites, *Composites Science and Technology* 2003, 63, 1617–1628.
62. Zeng, J.J., Saltysiak, B., Johnson, W.S., Schiraldi, D.A., Kumar, S., Processing and properties of poly(methyl methacrylate)/carbon nano fiber composites, *Composites Part B-Engineering* 2004, 35, 173–178.
63. Kumar, S., Doshi, H., Srinivasarao, M., Park, J.O., Schiraldi, D.A., Fibers from polypropylene/nano carbon fiber composites, *Polymer* 2002, 43, 1701–1703.
64. Ren, Y., Fu, Y.Q., Liao, K., Li, F., Cheng, H.M., Fatigue failure mechanisms of single-walled carbon nanotube ropes embedded in epoxy, *Applied Physics Letters* 2004, 84, 2811–2813.
65. Ren, Y., Li, F., Cheng, H.M., Liao, K., Tension-tension fatigue behavior of unidirectional single-walled carbon nanotube reinforced epoxy composite, *Carbon* 2003, 41, 2177–2179.
66. Pham, J.Q., Mitchell, C.A., Bahr, J.L., Tour, J.M., Krishnamoorti, R., Green, P.F., Glass transition of polymer/single-walled carbon nanotube composite films, *Journal of Polymer Science Part B-Polymer Physics* 2003, 41, 3339–3345.
67. Gong, X.Y., Liu, J., Baskaran, S., Voise, R.D., Young, J.S., Surfactant-assisted processing of carbon nanotube/polymer composites, *Chemistry of Materials* 2000, 12, 1049–1052.
68. Grunlan, J.C., Mehrabi, A.R., Bannon, M.V., Bahr, J.L., Water-based single-walled-nanotube-filled polymer composite with an exceptionally low percolation threshold, *Advanced Materials* 2004, 16, 150–153.
69. Benoit, J.M., Corraze, B., Lefrant, S., Blau, W.J., Bernier, P., Chauvet, O., Transport properties of PMMA-carbon nanotubes composites, *Synthetic Metals* 2001, 121, 1215–1216.
70. Shenogin, S., Xue, L.P., Ozisik, R., Keblinski, P., Cahill, D.G., Role of thermal boundary resistance on the heat flow in carbon-nanotube composites, *Journal of Applied Physics* 2004, 95, 8136–8144.
71. Guo, H., Sreekumar, T.V., Liu, T., Minus, M., Kumar, S., Structure and properties of polyacrylonitrile/single wall carbon nanotube composite films, *Polymer* 2005, 46, 3001–3005.
72. Baek, J.B., Lyons, C.B., Tan, L.S., Grafting of vapor-grown carbon nanofibers via in situ polycondensation of 3-phenoxybenzoic acid in poly(phosphoric acid), *Macromolecules* 2004, 37, 8278–8285.



73. Ichida, M., Mizuno, S., Kataura, H., Achiba, Y., Nakamura, A., Anisotropic optical properties of mechanically aligned single-walled carbon nanotubes in polymer, *Applied Physics a-Materials Science & Processing* 2004, 78, 1117–1120.
74. Kashiwagi, T., Grulke, E., Hilding, J., Harris, R., Awad, W., Douglas, J., "Thermal degradation and flammability properties of poly(propylene)/carbon nanotube composites, *Macromolecular Rapid Communications* 2002, 23, 761–765.
75. Liu, T., Sreekumar, T.V., Kumar, S., Hauge, R.H., Smalley, R.E., SWNT/PAN composite film-based supercapacitors, *Carbon* 2003, 41, 2440–2442.
76. Kymakis, E., Alexandrou, I., Amaratunga, G.A.J., High open-circuit voltage photovoltaic devices from carbon-nanotube-polymer composites, *Journal of Applied Physics* 2003, 93, 1764–1768.
77. Xiao, Q.F., Zhou, X., The study of multiwalled carbon nanotube deposited with conducting polymer for supercapacitor, *Electrochimica Acta* 2003, 48, 575–580.
78. Wang, Q.H., Setlur, A.A., Lauerhaas, J.M., Dai, J.Y., Seelig, E.W., Chang, R.P.H., A nanotube-based field-emission flat panel display, *Applied Physics Letters* 1998, 72, 2912–2913.
79. Kim, J.Y., Kim, M., Choi, J.H., Characterization of light emitting devices based on a single-walled carbon nanotube-polymer composite, *Synthetic Metals* 2003, 139, 565–568.
80. Park, J.H., Choi, J.H., Moon, J.S., Kushinov, D.G., Yoo, J.B., Park, C.Y., Nam, J.W., Lee, C.K., Park, J.H., Choe, D.H., Simple approach for the fabrication of carbon nanotube field emitter using conducting paste, *Carbon* 2005, 43, 698–703.
81. Sayago, I., Terrado, E., Lafuente, E., Horrillo, M.C., Maser, W.K., Benito, A.M., Navarro, R., Urriolabeitia, E.P., Martinez, M.T., Gutierrez, J., Hydrogen sensors based on carbon nanotubes thin films, *Synthetic Metals* 2005, 148, 15–19.
82. Abraham, J.K., Philip, B., Witchurch, A., Varadan, V.K., Reddy, C.C., A compact wireless gas sensor using a carbon nanotube/PMMA thin film chemiresistor, *Smart Materials & Structures* 2004, 13, 1045–1049.
83. Zhao, Q., Frogley, M.D., Wagner, H.D., Direction-sensitive stress measurements with carbon nanotube sensors, *Polymers for Advanced Technologies* 2002, 13, 759–764.
84. Zhao, Q., Frogley, M.D., Wagner, H.D., The use of carbon nanotubes to sense matrix stresses around a single glass fiber, *Composites Science and Technology* 2001, 61, 2139–2143.
85. Wood, J.R., Zhao, Q., Frogley, M.D., Meurs, E.R., Prins, A.D., Peijs, T., Dunstan, D.J., Wagner, H.D., Carbon nanotubes: From molecular to macroscopic sensors, *Physical Review B* 2000, 62, 7571–7575.
86. Raravikar, N.R., Keblinski, P., Rao, A.M., Dresselhaus, M.S., Schadler, L.S., Ajayan, P.M., Temperature dependence of radial breathing mode Raman frequency of single-walled carbon nanotubes, *Physical Review B* 2002, 66, 235424.
87. Monthieux, M., Smith, B.W., Berteaux, B., Claye, A., Fischer, J.E., Luzzi, D.E., Sensitivity of single-wall carbon nanotubes to chemical processing: an electron microscopy investigation, *Carbon* 2001, 39, 1251–1272.
88. Girifalco, L.A., Hodak, M., Lee, R.S., Carbon nanotubes, buckyballs, ropes, and a universal graphitic potential, *Physical Review B* 2000, 62, 13104–13110.

89. Park, C., Ounaies, Z., Watson, K.A., Crooks, R.E., Smith, J., Lowther, S.E., Connell, J.W., Siochi, E.J., Harrison, J.S., Clair, T.L.S., Dispersion of single wall carbon nanotubes by in situ polymerization under sonication, *Chemical Physics Letters* 2002, 364, 303–308.
90. Putz, K.W., Mitchell, C.A., Krishnamoorti, R., Green, P.F., Elastic modulus of single-walled carbon nanotube/poly(methyl methacrylate) nanocomposites, *Journal of Polymer Science Part B-Polymer Physics* 2004, 42, 2286–2293.
91. Chen, G.Z., Shaffer, M.S.P., Coleby, D., Dixon, G., Zhou, W.Z., Fray, D.J., Windle, A.H., Carbon nanotube and polypyrrole composites: Coating and doping, *Advanced Materials* 2000, 12, 522–526.
92. Gao, J.B., Itkis, M.E., Yu, A.P., Bekyarova, E., Zhao, B., Haddon, R.C., Continuous spinning of a single-walled carbon nanotube-nylon composite fiber, *Journal Of The American Chemical Society* 2005, 127, 3847–3854.
93. Liu, J., Casavant, M.J., Cox, M., Walters, D.A., Boul, P., Lu, W., Rimberg, A.J., Smith, K.A., Colbert, D.T., Smalley, R.E., Controlled deposition of individual single-walled carbon nanotubes on chemically functionalized templates, *Chemical Physics Letters* 1999, 303, 125–129.
94. Ausman, K.D., Piner, R., Lourie, O., Ruoff, R.S., Korobov, M., Organic solvent dispersions of single-walled carbon nanotubes: Toward solutions of pristine nanotubes, *Journal of Physical Chemistry B* 2000, 104, 8911–8915.
95. Liu, J., Liu, T., Kumar, S., Effect of solvent solubility parameter on SWNT dispersion in PMMA, *Polymer* 2005, 46, 3419–3424.
96. Lee, G.W., Kumar, S., Dispersion of nitric acid-treated SWNTs in organic solvents and solvent mixtures, *Journal of Physical Chemistry B* 2005, 109, 17128–17133.
97. Bahr, J.L., Mickelson, E.T., Bronikowski, M.J., Smalley, R.E., Tour, J.M., Dissolution of small diameter single-wall carbon nanotubes in organic solvents? *Chemical communications* 2001, 193–194.
98. Rinzler, A.G., Liu, J., Dai, H., Nikolaev, P., Huffman, C.B., Rodriguez-Macias, F.J., Boul, P.J., Lu, A.H., Heymann, D., Colbert, D.T., Lee, R.S., Fischer, J.E., Rao, A.M., Eklund, P.C., Smalley, R.E., Large-scale purification of single-wall carbon nanotubes: process, product, and characterization, *Applied Physics a-Materials Science & Processing* 1998, 67, 29–37.
99. Duesberg, G.S., Muster, J., Krstic, V., Burghard, M., Roth, S., Chromatographic size separation of single-wall carbon nanotubes, *Applied Physics a-Materials Science & Processing* 1998, 67, 117–119.
100. Moore, V.C., Strano, M.S., Haroz, E.H., Hauge, R.H., Smalley, R.E., Schmidt, J., Talmon, Y., Individually suspended single-walled carbon nanotubes in various surfactants, *Nano Letters* 2003, 3, 1379–1382.
101. Islam, M.F., Rojas, E., Bergey, D.M., Johnson, A.T., Yodh, A.G., High weight fraction surfactant solubilization of single-wall carbon nanotubes in water, *Nano Letters* 2003, 3, 269–273.
102. Jin, Z.X., Huang, L., Goh, S.H., Xu, G.Q., Ji, W., Characterization and nonlinear optical properties of a poly(acrylic acid)-surfactant-multi-walled carbon nanotube complex, *Chemical Physics Letters* 2000, 332, 461–466.
103. Richard, C., Balavoine, F., Schultz, P., Ebbesen, T.W., Mioskowski, C., Supramolecular self-assembly of lipid derivatives on carbon nanotubes, *Science* 2003, 300, 775–778.

104. Takahashi, T., Tsunoda, K., Yajima, H., Ishii, T., Isolation of single-wall carbon nanotube bundles through gelatin wrapping and unwrapping processes, *Chemistry Letters* 2002, 690–691.
105. Zheng, M., Jagota, A., Semke, E.D., Diner, B.A., McLean, R.S., Lustig, S.R., Richardson, R.E., Tassi, N.G., DNA-assisted dispersion and separation of carbon nanotubes, *Nature Materials* 2003, 2, 338–342.
106. Zheng, M., Jagota, A., Strano, M.S., Santos, A.P., Barone, P., Chou, S.G., Diner, B.A., Dresselhaus, M.S., McLean, R.S., Onoa, G.B., Samsonidze, G.G., Semke, E.D., Usrey, M., Walls, D.J., Structure-based carbon nanotube sorting by sequence-dependent DNA assembly, *Science* 2003, 302, 1545–1548.
107. Chou, S.G., Ribeiro, H.B., Barros, E.B., Santos, A.P., Nezich, D., Samsonidze, G.G., Fantini, C., Pimenta, M.A., Jorio, A., Plentz, F., Dresselhaus, M.S., Dresselhaus, G., Saito, R., Zheng, M., Onoa, G.B., Semke, E.D., Swan, A.K., Unlu, M.S., Goldberg, B.B., Optical characterization of DNA-wrapped carbon nanotube hybrids, *Chemical Physics Letters* 2004, 397, 296–301.
108. Jin, W.J., Sun, X.F., Wang, Y., Solubilization and functionalization of carbon nanotubes, *New Carbon Materials* 2004, 19, 312–318.
109. Satake, A., Miyajima, Y., Kobuke, Y., Porphyrin-carbon nanotube composites formed by noncovalent polymer wrapping, *Chemistry of Materials* 2005, 17, 716–724.
110. Xie, Y.H., Soh, A.K., Investigation of noncovalent association of single-walled carbon nanotube with amylose by molecular dynamics simulation, *Materials Letters* 2005, 59, 971–975.
111. Shaffer, M.S.P., Fan, X., Windle, A.H., Dispersion and packing of carbon nanotubes, *Carbon* 1998, 36, 1603–1612.
112. Kim, H.J., Jeon, K.K., An, K.H., Kim, C., Heo, J.G., Lim, S.C., Bae, D.J., Lee, Y.H., Exfoliation of single-walled carbon nanotubes by electrochemical treatment in a nitric acid, *Advanced Materials* 2003, 15, 1757–1760.
113. Bower, C., Kleinhammes, A., Wu, Y., Zhou, O., Intercalation and partial exfoliation of single-walled carbon nanotubes by nitric acid, *Chemical Physics Letters* 1998, 288, 481–486.
114. Chen, J., Hamon, M.A., Hu, H., Chen, Y.S., Rao, A.M., Eklund, P.C., Haddon, R.C., Solution properties of single-walled carbon nanotubes, *Science* 1998, 282, 95–98.
115. Hamon, M.A., Chen, J., Hu, H., Chen, Y.S., Itkis, M.E., Rao, A.M., Eklund, P.C., Haddon, R.C., Dissolution of single-walled carbon nanotubes, *Advanced Materials* 1999, 11, 834.
116. Chen, J., Rao, A.M., Lyuksyutov, S., Itkis, M.E., Hamon, M.A., Hu, H., Cohn, R.W., Eklund, P.C., Colbert, D.T., Smalley, R.E., Haddon, R.C., Dissolution of full-length single-walled carbon nanotubes, *Journal of Physical Chemistry B* 2001, 105, 2525–2528.
117. Hamon, M.A., Hui, H., Bhowmik, P., Itkis, H.M.E., Haddon, R.C., Ester-functionalized soluble single-walled carbon nanotubes, *Applied Physics a-Materials Science & Processing* 2002, 74, 333–338.
118. Xu, Z., Chen, X., Qu, X.H., Jia, J.B., Dong, S.J., Single-wall carbon nanotube-based voltammetric sensor and biosensor, *Biosensors & Bioelectronics* 2004, 20, 579–584.
119. An, K.H., Jeong, S.Y., Hwang, H.R., Lee, Y.H., Enhanced sensitivity of a gas sensor incorporating single-walled carbon nanotube-polypyrrole nanocomposites, *Advanced Materials* 2004, 16, 1005.

120. Jang, Y.T., Moon, S.I., Ahn, J.H., Lee, Y.H., Ju, B.K., A simple approach in fabricating chemical sensor using laterally grown multi-walled carbon nanotubes, *Sensors and Actuators B-Chemical* 2004, 99, 118–122.
121. Star, A., Han, T.R., Joshi, V., Stetter, J.R., Sensing with Nafion coated carbon nanotube field-effect transistors, *Electroanalysis* 2004, 16, 108–112.
122. Kong, J., Franklin, N.R., Zhou, C.W., Chapline, M.G., Peng, S., Cho, K.J., Dai, H.J., Nanotube molecular wires as chemical sensors, *Science* 2000, 287, 622–625.
123. Niyogi, S., Hamon, M.A., Hu, H., Zhao, B., Bhowmik, P., Sen, R., Itkis, M.E., Haddon, R.C., Chemistry of single-walled carbon nanotubes, *Accounts of Chemical Research* 2002, 35, 1105–1113.
124. Zhou, O., Fleming, R.M., Murphy, D.W., Chen, C.H., Haddon, R.C., Ramirez, A.P., Glarum, S.H., Defects in carbon nanostructures, *Science* 1994, 263, 1744–1747.
125. Holzinger, M., Vostrowsky, O., Hirsch, A., Hennrich, F., Kappes, M., Weiss, R., Jellen, F., Sidewall functionalization of carbon nanotubes, *Angewandte Chemie-International Edition* 2001, 40, 4002–4005.
126. Mickelson, E.T., Chiang, I.W., Zimmerman, J.L., Boul, P.J., Lozano, J., Liu, J., Smalley, R.E., Hauge, R.H., Margrave, J.L., Solvation of fluorinated single-wall carbon nanotubes in alcohol solvents, *Journal of Physical Chemistry B* 1999, 103, 4318–4322.
127. Mickelson, E.T., Huffman, C.B., Rinzler, A.G., Smalley, R.E., Hauge, R.H., Margrave, J.L., Fluorination of single-wall carbon nanotubes, *Chemical Physics Letters* 1998, 296, 188–194.
128. Boul, P.J., Liu, J., Mickelson, E.T., Huffman, C.B., Ericson, L.M., Chiang, I.W., Smith, K.A., Colbert, D.T., Hauge, R.H., Margrave, J.L., Smalley, R.E., Reversible sidewall functionalization of buckytubes, *Chemical Physics Letters* 1999, 310, 367–372.
129. Bahr, J.L., Yang, J.P., Kosynkin, D.V., Bronikowski, M.J., Smalley, R.E., Tour, J.M., Functionalization of carbon nanotubes by electrochemical reduction of aryl diazonium salts: a bucky paper electrode, *Journal of the American Chemical Society* 2001, 123, 6536–6542.
130. Bahr, J.L., Tour, J.M., Highly functionalized carbon nanotubes using in situ generated diazonium compounds, *Chemistry of Materials* 2001, 13, 3823–3824.
131. Jin, Z.X., Sun, X., Xu, G.Q., Goh, S.H., Ji, W., Nonlinear optical properties of some polymer/multi-walled carbon nanotube composites, *Chemical Physics Letters* 2000, 318, 505–510.
132. Philip, B., Xie, J.N., Chandrasekhar, A., Abraham, J., Varadan, V.K., A novel nanocomposite from multiwalled carbon nanotubes functionalized with a conducting polymer, *Smart Materials & Structures* 2004, 13, 295–298.
133. Lin, Y., Rao, A.M., Sadanadan, B., Kenik, E.A., Sun, Y.P., Functionalizing multiple-walled carbon nanotubes with aminopolymers, *Journal of Physical Chemistry B* 2002, 106, 1294–1298.
134. Hill, D.E., Lin, Y., Rao, A.M., Allard, L.F., Sun, Y.P., Functionalization of carbon nanotubes with polystyrene, *Macromolecules* 2002, 35, 9466–9471.
135. Riggs, J.E., Guo, Z.X., Carroll, D.L., Sun, Y.P., Strong luminescence of solubilized carbon nanotubes, *Journal of the American Chemical Society* 2000, 122, 5879–5880.



136. Penicaud, A., Poulin, P., Derre, A., Anglaret, E., Petit, P., Spontaneous dissolution of a single-wall carbon nanotube salt, *Journal of the American Chemical Society* 2005, 127, 8–9.
137. Petit, P., Mathis, C., Journet, C., Bernier, P., Tuning and monitoring the electronic structure of carbon nanotubes, *Chemical Physics Letters* 1999, 305, 370–374.
138. Jouguelet, E., Mathis, C., Petit, P., Controlling the electronic properties of single-wall carbon nanotubes by chemical doping, *Chemical Physics Letters* 2000, 318, 561–564.
139. Ajayan, P.M., Stephan, O., Colliex, C., Trauth, D., Aligned Carbon Nanotube Arrays Formed by Cutting a Polymer Resin-Nanotube Composite, *Science* 1994, 265, 1212–1214.
140. Safadi, B., Andrews, R., Grulke, E.A., Multiwalled carbon nanotube polymer composites: Synthesis and characterization of thin films, *Journal of Applied Polymer Science* 2002, 84, 2660–2669.
141. Wang, B., Li, J.W., Wang, H.P., Jiang, J.M., Liu, Y.Q., Rheological behavior of spinning dope of multiwalled carbon nanotube/polyacrylonitrile composites, *Macromolecular Symposia* 2004, 216, 189–194.
142. Du, F.M., Scogna, R.C., Zhou, W., Brand, S., Fischer, J.E., Winey, K.I., Nanotube networks in polymer nanocomposites: rheology and electrical conductivity, *Macromolecules* 2004, 37, 9048–9055.
143. Covas, J.A., Bernardo, C.A., Carneiro, O.S., Maia, J.M., van Hattum, F.W.J., Gaspar-Cunha, A., Biro, L.P., Horvath, Z.E., Kiricsi, I., Konya, Z., Niesz, K., Continuous production of polycarbonate-carbon nanotube composites, *Journal of Polymer Engineering* 2005, 25, 39–57.
144. Choi, Y.J., Hwang, S.H., Hong, Y.S., Kim, J.Y., Ok, C.Y., Huh, W., Lee, S.W., Preparation and characterization of PS/multi-walled carbon nanotube nanocomposites, *Polymer Bulletin* 2005, 53, 393–400.
145. Davis, V.A., Ericson, L.M., Parra-Vasquez, A.N.G., Fan, H., Wang, Y.H., Prieto, V., Longoria, J.A., Ramesh, S., Saini, R.K., Kittrell, C., Billups, W.E., Adams, W.W., Hauge, R.H., Smalley, R.E., Pasquali, M., Phase behavior and rheology of SWNTs in superacids, *Macromolecules* 2004, 37, 154–160.
146. Potschke, P., Fornes, T.D., Paul, D.R., Rheological behavior of multiwalled carbon nanotube/polycarbonate composites, *Polymer* 2002, 43, 3247–3255.
147. Lee, Y.S., Cho, T.H., The rheological behavior of carbon nanotube-dispersed mesophase pitches, *Journal of Industrial and Engineering Chemistry* 2004, 10, 631–635.
148. Chang, T.E., Jensen, L.R., Kisliuk, A., Pipes, R.B., Pyrz, R., Sokolov, A.P., Microscopic mechanism of reinforcement in single-wall carbon nanotube/polypropylene nanocomposite, *Polymer* 2005, 46, 439–444.
149. Kinloch, I.A., Roberts, S.A., Windle, A.H., A rheological study of concentrated aqueous nanotube dispersions, *Polymer* 2002, 43, 7483–7491.
150. Kharchenko, S.B., Douglas, J.F., Obrzut, J., Grulke, E.A., Migler, K.B., Flow-induced properties of nanotube-filled polymer materials, *Nature Materials* 2004, 3, 564–568.
151. Seo, M.K., Park, S.J., Electrical resistivity and rheological behaviors of carbon nanotubes-filled polypropylene composites, *Chemical Physics Letters* 2004, 395, 44–48.



152. Potschke, P., Abdel-Goad, M., Alig, I., Dudkin, S., Lellinger, D., Rheological and dielectrical characterization of melt mixed polycarbonate-multiwalled carbon nanotube composites, *Polymer* 2004, 45, 8863–8870.
153. Song, Y.S., Youn, J.R., Modeling of rheological behavior of nanocomposites by Brownian dynamics simulation, *Korea-Australia Rheology Journal* 2004, 16, 201–212.
154. Raravikar, N.R., Schadler, L.S., Vijayaraghavan, A., Zhao, Y.P., Wei, B.Q., Ajayan, P.M., Synthesis and characterization of thickness-aligned carbon nanotube-polymer composite films, *Chemistry of Materials* 2005, 17, 974–983.
155. Bae, D.J., Kim, K.S., Park, Y.S., Suh, E.K., An, K.H., Moon, J.M., Lim, S.C., Park, S.H., Jeong, Y.H., Lee, Y.H., Transport phenomena in an anisotropically aligned single-wall carbon nanotube film, *Physical Review B* 2001, 64, 233401.
156. Bozovic, I., Bozovic, N., Damjanovic, M., Optical dichroism in nanotubes, *Physical Review B* 2000, 62, 6971–6974.
157. Popov, V.N., Van Doren, V.E., Balkanski, M., Elastic properties of crystals of single-walled carbon nanotubes, *Solid State Communications* 2000, 114, 395–399.
158. Che, J.W., Cagin, T., Goddard, W.A., Thermal conductivity of carbon nanotubes, *Nanotechnology* 2000, 11, 65–69.
159. Anglaret, E., Righi, A., Sauvajol, J.L., Bernier, P., Vigolo, B., Poulin, P., Raman resonance and orientational order in fibers of single-wall carbon nanotubes, *Physical Review B* 2002, 65, 165426.
160. Brown, S.D.M., Jorio, A., Corio, P., Dresselhaus, M.S., Dresselhaus, G., Saito, R., Kneipp, K., Origin of the Breit–Wigner–Fano lineshape of the tangential G-band feature of metallic carbon nanotubes, *Physical Review B* 2001, 6315, art. no.-155414.
161. Liu, T., Kumar, S., Quantitative characterization of SWNT orientation by polarized Raman spectroscopy, *Chemical Physics Letters* 2003, 378, 257–262.
162. Zheng, L.X., O'Connell, M.J., Doorn, S.K., Liao, X.Z., Zhao, Y.H., Akhadow, E.A., Hoffbauer, M.A., Roop, B.J., Jia, Q.X., Dye, R.C., Peterson, D.E., Huang, S.M., Liu, J., Zhu, Y.T., Ultralong single-wall carbon nanotubes, *Nature Materials* 2004, 3, 673–676.
163. Chae, H.G., Sreekumar, T.V., Uchida, T., Kumar, S., A comparison of reinforcement efficiency of various types of carbon nanotubes in polyacrylonitrile fiber, *Polymer* 2005, 46, 10925–10935.
164. Wilchinsky, Z.W., Measurement of Orientation in Polypropylene Film, *Journal of Applied Physics* 1960, 31, 1969–1972.
165. Samuels, R.J. Structured Polymer Properties. John Wiley & Sons, Inc., New York, 1974, pp. 28–41.
166. Uchida, T., Anderson, D.P., Minus, M.L., Kumar, S., Morphology and modulus of vapor grown carbon nano fiber, *Journal of Materials Science*, in press.
167. Dresselhaus, M.S., Dresselhaus, G., Jorio, A., Souza, A.G., Saito, R., Raman spectroscopy on isolated single wall carbon nanotubes, *Carbon* 2002, 40, 2043–2061.
168. Kataura, H., Kumazawa, Y., Maniwa, Y., Umezue, I., Suzuki, S., Ohtsuka, Y., Achiba, Y., Optical properties of single-wall carbon nanotubes, *Synthetic Metals* 1999, 103, 2555–2558.

169. Sandler, J., Shaffer, M.S.P., Windle, A.H., Halsall, M.P., Montes-Moran, M.A., Cooper, C.A., Young, R.J., Variations in the Raman peak shift as a function of hydrostatic pressure for various carbon nanostructures: a simple geometric effect, *Physical Review B* 2003, 67, 035417.
170. Venkateswaran, U.D., Gosselin, M.E., Postek, B., Masica, D.L., Chen, G., Gupta, R., Eklund, P.C., Radial and tangential vibrational modes of HiPco-derived carbon nanotubes under pressure, *Physica Status Solidi B-Basic Research* 2003, 235, 364–368.
171. Cooper, C.A., Young, R.J., Halsall, M., Investigation into the deformation of carbon nanotubes and their composites through the use of Raman spectroscopy, *Composites Part a-Applied Science and Manufacturing* 2001, 32, 401–411.
172. Souza, A.G., Jorio, A., Samsonidze, G.G., Dresselhaus, G., Saito, R., Dresselhaus, M.S., Raman spectroscopy for probing chemically/physically induced phenomena in carbon nanotubes, *Nanotechnology* 2003, 14, 1130–1139.
173. Huang, F.M., Yue, K.T., Tan, P.H., Zhang, S.L., Shi, Z.J., Zhou, X.H., Gu, Z.N., Temperature dependence of the Raman spectra of carbon nanotubes, *Journal of Applied Physics* 1998, 84, 4022–4024.
174. Li, H.D., Yue, K.T., Lian, Z.L., Zhan, Y., Zhou, L.X., Zhang, S.L., Shi, Z.J., Gu, Z.N., Liu, B.B., Yang, R.S., Yang, H.B., Zou, G.T., Zhang, Y., Iijima, S., Temperature dependence of the Raman spectra of single-wall carbon nanotubes, *Applied Physics Letters* 2000, 76, 2053–2055.
175. Heller, D.A., Barone, P.W., Swanson, J.P., Mayrhofer, R.M., Strano, M.S., Using Raman spectroscopy to elucidate the aggregation state of single-walled carbon nanotubes, *Journal of Physical Chemistry B* 2004, 108, 6905–6909.
176. Wildoer, J.W.G., Venema, L.C., Rinzler, A.G., Smalley, R.E., Dekker, C., Electronic structure of atomically resolved carbon nanotubes, *Nature* 1998, 391, 59–62.
177. Dresselhaus, M.S., Nanotechnology — new tricks with nanotubes, *Nature* 1998, 391, 19–20.
178. White, C.T., Mintmire, J.W., Density of states reflects diameter in nanotubes, *Nature* 1998, 394, 29–30.
179. Saito, R., Dresselhaus, G., Dresselhaus, M.S., Trigonal warping effect of carbon nanotubes, *Physical Review B* 2000, 61, 2981–2990.
180. Kim, P., Odom, T.W., Huang, J.L., Lieber, C.M., Electronic density of states of atomically resolved single-walled carbon nanotubes: Van Hove singularities and end states, *Physical Review Letters* 1999, 82, 1225–1228.
181. Strano, M.S., Dyke, C.A., Usrey, M.L., Barone, P.W., Allen, M.J., Shan, H.W., Kittrell, C., Hauge, R.H., Tour, J.M., Smalley, R.E., Electronic structure control of single-walled carbon nanotube functionalization, *Science* 2003, 301, 1519–1522.
182. Hagen, A., Hertel, T., Quantitative analysis of optical spectra from individual single-wall carbon nanotubes, *Nano Letters* 2003, 3, 383–388.
183. Itkis, M.E., Niyogi, S., Meng, M.E., Hamon, M.A., Hu, H., Haddon, R.C., Spectroscopic study of the Fermi level electronic structure of single-walled carbon nanotubes, *Nano Letters* 2002, 2, 155–159.
184. Bachilo, S.M., Strano, M.S., Kittrell, C., Hauge, R.H., Smalley, R.E., Weisman, R.B., Structure-assigned optical spectra of single-walled carbon nanotubes, *Science* 2002, 298, 2361–2366.

185. Coleman, J.N., Blau, W.J., Dalton, A.B., Munoz, E., Collins, S., Kim, B.G., Razal, J., Selvidge, M., Vieiro, G., Baughman, R.H., Improving the mechanical properties of single-walled carbon nanotube sheets by intercalation of polymeric adhesives, *Applied Physics Letters* 2003, 82, 1682–1684.
186. Vigolo, B., Poulin, P., Lucas, M., Launois, P., Bernier, P., Improved structure and properties of single-wall carbon nanotube spun fibers, *Applied Physics Letters* 2002, 81, 1210–1212.
187. Li, Y.L., Kinloch, I.A., Windle, A.H., Direct spinning of carbon nanotube fibers from chemical vapor deposition synthesis, *Science* 2004, 304, 276–278.
188. Wang, Y.J., School of Polymer, Textile, & Fiber Engineering, Georgia Institute of Technology, *Personal Communication*, 2005.
189. Ledbetter, H.D., Rosenberg, S., Hurtig, C.W. In Materials Research Society *Symposium Proceedings*, 1989, p. 253.
190. Donald, A.M., Windle, A.H. *Liquid Crystalline Polymers*. Cambridge University Press, Cambridge, U. K., 1992, p. 250.
191. Zimmerman, J., Kohan, M.I., Nylon-selected topics, *Journal of Polymer Science Part a-Polymer Chemistry* 2001, 39, 2565–2570.
192. Luo, S., Grubb, D.T., Netravali, A.N., The effect of molecular weight on the lamellar structure, thermal and mechanical properties of poly(hydroxybutyrate-co-hydroxyvalerates), *Polymer* 2002, 43, 4159–4166.
193. Alexandrou, I., Kymakis, E., Amaratunga, G.A.J., Polymer-nanotube composites: Burying nanotubes improves their field emission properties, *Applied Physics Letters* 2002, 80, 1435–1437.
194. Kymakis, E., Alexandou, I., Amaratunga, G.A.J., Single-walled carbon nanotube-polymer composites: electrical, optical and structural investigation, *Synthetic Metals* 2002, 127, 59–62.
195. Stephan, C., Nguyen, T.P., de la Chapelle, M.L., Lefrant, S., Journet, C., Bernier, P., Characterization of single-walled carbon nanotubes-PMMA composites, *Synthetic Metals* 2000, 108, 139–149.
196. Haggenueller, R., Gommans, H.H., Rinzler, A.G., Fischer, J.E., Winey, K.I., Aligned single-wall carbon nanotubes in composites by melt processing methods, *Chemical Physics Letters* 2000, 330, 219–225.
197. Lozano, K., Barrera, E.V., Nanofiber-reinforced thermoplastic composites. I. Thermoanalytical and mechanical analyses, *Journal of Applied Polymer Science* 2001, 79, 125–133.
198. Chen, Y.C., Raravikar, N.R., Schadler, L.S., Ajayan, P.M., Zhao, Y.P., Lu, T.M., Wang, G.C., Zhang, X.C., Ultrafast optical switching properties of single-wall carbon nanotube polymer composites at 1.55  $\mu\text{m}$ , *Applied Physics Letters* 2002, 81, 975–977.
199. Lillehei, P.T., Park, C., Rouse, J.H., Siochi, E.J., Imaging carbon nanotubes in high performance polymer composites via magnetic force microscopy, *Nano Letters* 2002, 2, 827–829.
200. Carneiro, O.S., Maia, J.M., Rheological behavior of (Short) carbon fiber/thermoplastic composites. Part 1: The influence of fiber type, processing conditions and level of incorporation, *Polymer Composites* 2000, 21, 960–969.
201. Ramasubramaniam, R., Chen, J., Liu, H.Y., Homogeneous carbon nanotube/polymer composites for electrical applications, *Applied Physics Letters* 2003, 83, 2928–2930.

202. Tahhan, M., Truong, V.T., Spinks, G.M., Wallace, G.G., Carbon nanotube and polyaniline composite actuators, *Smart Materials & Structures* 2003, 12, 626–632.
203. Ferrer-Anglada, N., Kaempgen, M., Skakalova, V., Dettlaff-Weglikowska, U., Roth, S., Synthesis and characterization of carbon nanotube-conducting polymer thin films, *Diamond and Related Materials* 2004, 13, 256–260.
204. Hughes, M., Shaffer, M.S.P., Renouf, A.C., Singh, C., Chen, G.Z., Fray, J., Windle, A.H., Electrochemical capacitance of nanocomposite films formed by coating aligned arrays of carbon nanotubes with polypyrrole, *Advanced Materials* 2002, 14, 382–385.
205. Smith, J.G., Connell, J.W., Delozier, D.M., Lillehei, P.T., Watson, K.A., Lin, Y., Zhou, B., Sun, Y.P., Space durable polymer/carbon nanotube films for electrostatic charge mitigation, *Polymer* 2004, 45, 825–836.
206. Pirlot, C., Mekhalif, Z., Fonseca, A., Nagy, J.B., Demortier, G., Delhalle, J., Surface modifications of carbon nanotube/polyacrylonitrile composite films by proton beams, *Chemical Physics Letters* 2003, 372, 595–602.
207. Pirlot, C., Willems, I., Fonseca, A., Nagy, J.B., Delhalle, J., Preparation and characterization of carbon nanotube/polyacrylonitrile composites, *Advanced Engineering Materials* 2002, 4, 109–114.
208. Ye, H.H., Lam, H., Titchenal, N., Gogotsi, Y., Ko, F., Reinforcement and rupture behavior of carbon nanotubes-polymer nanofibers, *Applied Physics Letters* 2004, 85, 1775–1777.
209. Ge, J.J., Hou, H.Q., Li, Q., Graham, M.J., Greiner, A., Reneker, D.H., Harris, F.W., Cheng, S.Z.D., Assembly of well-aligned multiwalled carbon nanotubes in confined polyacrylonitrile environments: electrospun composite nanofiber sheets, *Journal of the American Chemical Society* 2004, 126, 15754–15761.
210. Min, B.G., Sreekumar, T.V., Uchida, T., Kumar, S., Oxidative stabilization of PAN/SWNT composite fiber, *Carbon* 2005, 43, 599–604.
211. Koganemaru, A., Bin, Y., Agari, Y., Matsuo, M., Composites of polyacrylonitrile and multiwalled carbon nanotubes prepared by gelation/crystallization from solution, *Advanced Functional Materials* 2004, 14, 842–850.
212. Kim, S.H., Min, B.G., Lee, S.C., Park, S.B., Lee, T.D., Park, M., Kumar, S., Morphology and properties of polyacrylonitrile/single wall carbon nanotube composite films, *Fibers and Polymers* 2004, 5, 198–203.
213. Bin, Y.Z., Kitanaka, M., Zhu, D., Matsuo, M., Development of highly oriented polyethylene filled with aligned carbon nanotubes by gelation/crystallization from solutions, *Macromolecules* 2003, 36, 6213–6219.
214. Pogue, R.T., Ye, J., Klosterman, D.A., Glass, A.S., Chartoff, R.P., Evaluating fiber-matrix interaction in polymer-matrix composites by inverse gas chromatography, *Composites Part a-Applied Science and Manufacturing* 1998, 29, 1273–1281.
215. Patton, R.D., Pittman, C.U., Wang, L., Hill, J.R., Vapor grown carbon fiber composites with epoxy and poly(phenylene sulfide) matrices, *Composites Part a-Applied Science and Manufacturing* 1999, 30, 1081–1091.
216. Patton, R.D., Pittman, C.U., Wang, L., Hill, J.R., Day, A., Ablation, mechanical and thermal conductivity properties of vapor grown carbon fiber/phenolic matrix composites, *Composites Part a-Applied Science and Manufacturing* 2002, 33, 243–251.



217. Uchida, T., Dang, T., Min, B.G., Zhang, X.F., Kumar, S., Processing, structure, and properties of carbon nano fiber filled PBZT composite fiber, *Composites Part B-Engineering* 2005, 36, 183–187.
218. Liu, T., Kumar, S., Effect of orientation on the modulus of SWNT films and fibers, *Nano Letters* 2003, 3, 647–650.
219. Salvétat, J.P., Briggs, G.A.D., Bonard, J.M., Bacsá, R.R., Kulik, A.J., Stockli, T., Burnham, N.A., Forro, L., Elastic and shear moduli of single-walled carbon nanotube ropes, *Physical Review Letters* 1999, 82, 944–947.
220. Koerner, H., Liu, W.D., Alexander, M., Mirau, P., Dowty, H., Vaia, R.A., Deformation-morphology correlations in electrically conductive carbon nanotube thermoplastic polyurethane nanocomposites, *Polymer* 2005, 46, 4405–4420.
221. Lu, J.P., "Elastic properties of carbon nanotubes and nanoropes, *Physical Review Letters* 1997, 79, 1297–1300.
222. Gao, G.H., Cagin, T., Goddard, W.A., Energetics, structure, mechanical and vibrational properties of single-walled carbon nanotubes, *Nanotechnology* 1998, 9, 184–191.
223. Sinnott, S.B., Shenderova, O.A., White, C.T., Brenner, D.W., Mechanical properties of nanotubule fibers and composites determined from theoretical calculations and simulations, *Carbon* 1998, 36, 1–9.
224. Shen, L.X., Li, J., Transversely isotropic elastic properties of multiwalled carbon nanotubes, *Physical Review B* 2005, 71, Art. No. 035412.
225. Johnson, W. The Structure of PAN Based Carbon Fibers and Relationship to the Physical Properties. Handbook of Composites 1. Strong Fibers. Watt, W., Perov, B. V., Eds., Elsevier Science Publisher, New York, 1988, p. 393.
226. Masson, J.C. Acrylic Fiber Technology and Applications. Marcel Dekker, New York, 1995.
227. Bahl, O.P., Shen, Z., Lavin, J.G., Ross, R.A. Carbon Fibers. Marcel Dekker, New York, 1998.
228. Petrov, P., Lou, X.D., Pagnoulle, C., Jerome, C., Calberg, C., Jerome, R., Functionalization of multi-walled carbon nanotubes by electrografting of polyacrylonitrile, *Macromolecular Rapid Communications* 2004, 25, 987–990.
229. Oya, A., Yokoyama, T., Yamamoto, M., Hulicova, D., A novel preparation method of carbon nanotubes by spinning core/shell polymer particles, *Euro Ceramics VIII, Pts 1–3* 2004, 264–268, 2275–2278.
230. Hu, X.D., Jenkins, S.E., Min, B.G., Polk, M.B., Kumar, S., Rigid-rod polymers: synthesis, processing, simulation, structure, and properties, *Macromolecular Materials and Engineering* 2003, 288, 823–843.
231. Chae, H.G., Kumar, S., Rigid-rod polymeric fibers, *Journal of Applied Polymer Science* 2006, 100, 791–802.
232. Cadek, M., Coleman, J.N., Barron, V., Hedicke, K., Blau, W.J., Morphological and mechanical properties of carbon-nanotube-reinforced semicrystalline and amorphous polymer composites, *Applied Physics Letters* 2002, 81, 5123–5125.
233. Cadek, M., Coleman, J.N., Ryan, K.P., Nicolosi, V., Bister, G., Fonseca, A., Nagy, J.B., Szostak, K., Beguin, F., Blau, W.J., "Reinforcement of polymers with carbon nanotubes: The role of nanotube surface area, *Nano Letters* 2004, 4, 353–356.



234. Dalton, A.B., Collins, S., Razal, J., Munoz, E., Ebron, V.H., Kim, B.G., Coleman, J.N., Ferraris, J.P., Baughman, R.H., Continuous carbon nanotube composite fibers: properties, potential applications, and problems, *Journal of Materials Chemistry* 2004, 14, 1–3.
235. Philip, B., Abraham, J.K., Chandrasekhar, A., Varadan, V.K., Carbon nanotube/PMMA composite thin films for gas-sensing applications, *Smart Materials & Structures* 2003, 12, 935–939.
236. Du, F.M., Fischer, J.E., Winey, K.I., Coagulation method for preparing single-walled carbon nanotube/poly(methyl methacrylate) composites and their modulus, electrical conductivity, and thermal stability, *Journal of Polymer Science Part B-Polymer Physics* 2003, 41, 3333–3338.
237. Jin, Z., Pramoda, K.P., Xu, G., Goh, S.H., Dynamic mechanical behavior of melt-processed multi-walled carbon nanotube/poly(methyl methacrylate) composites, *Chemical Physics Letters* 2001, 337, 43–47.
238. Jin, Z.X., Pramoda, K.P., Goh, S.H., Xu, G.Q., Poly(vinylidene fluoride)-assisted melt-blending of multi-walled carbon nanotube/poly(methyl methacrylate) composites, *Materials Research Bulletin* 2002, 37, 271–278.
239. Gorga, R.E., Cohen, R.E., Toughness enhancements in poly(methyl methacrylate) by addition of oriented multiwall carbon nanotubes, *Journal of Polymer Science Part B-Polymer Physics* 2004, 42, 2690–2702.
240. Park, S.J., Cho, M.S., Lim, S.T., Cho, H.J., Jhon, M.S., Synthesis and dispersion characteristics of multi-walled carbon nanotube composites with poly(methyl methacrylate) prepared by in situ bulk polymerization, *Macromolecular Rapid Communications* 2003, 24, 1070–1073.
241. Sung, J.H., Kim, H.S., Jin, H.J., Choi, H.J., Chin, I.J., Nanofibrous membranes prepared by multiwalled carbon nanotube/poly(methyl methacrylate) composites, *Macromolecules* 2004, 37, 9899–9902.
242. Hwang, G.L., Shieh, Y.T., Hwang, K.C., Efficient load transfer to polymer-grafted multiwalled carbon nanotubes in polymer composites, *Advanced Functional Materials* 2004, 14, 487–491.
243. de la Chapelle, M.L., Stephan, C., Nguyen, T.P., Lefrant, S., Journet, C., Bernier, P., Munoz, E., Benito, A., Maser, W.K., Martinez, M.T., de la Fuente, G.F., Guillard, T., Flamant, G., Alvarez, L., Laplaze, D., Raman characterization of singlewalled carbon nanotubes and PMMA-nanotubes composites, *Synthetic Metals* 1999, 103, 2510–2512.
244. Zhang, M.F., Yudasaka, M., Koshio, A., Iijima, S., Effect of polymer and solvent on purification and cutting of single-wall carbon nanotubes, *Chemical Physics Letters* 2001, 349, 25–30.
245. Sabba, Y., Thomas, E.L., High-concentration dispersion of single-wall carbon nanotubes (vol 37, pg 4815, 2004), *Macromolecules* 2004, 37, 6662–6662.
246. Liu, J., Wang, T., Uchida, T., Kumar, S., Carbon nanotube core-polymer shell nanofibers, *Journal of Applied Polymer Science* 2005, 96, 1992–1995.
247. Qian, D., Dickey, E.C., In situ transmission electron microscopy studies of polymer-carbon nanotube composite deformation, *Journal of Microscopy-Oxford* 2001, 204, 39–45.
248. Cumings, J., Zettl, A., Low-friction nanoscale linear bearing realized from multiwall carbon nanotubes, *Science* 2000, 289, 602–604.
249. Berber, S., Kwon, Y.K., Tomanek, D., Unusually high thermal conductivity of carbon nanotubes, *Physical Review Letters* 2000, 84, 4613–4616.

250. Kim, P., Shi, L., Majumdar, A., McEuen, P.L., Thermal transport measurements of individual multiwalled nanotubes, *Physical Review Letters* 2001, 87, Art. No. 215502.
251. Zhang, W., Zhu, Z.Y., Wang, F., Wang, T.T., Sun, L.T., Wang, Z.X., Chirality dependence of the thermal conductivity of carbon nanotubes, *Nanotechnology* 2004, 15, 936–939.
252. Hone, J., Llaguno, M.C., Nemes, N.M., Johnson, A.T., Fischer, J.E., Walters, D.A., Casavant, M.J., Schmidt, J., Smalley, R.E., Electrical and thermal transport properties of magnetically aligned single wall carbon nanotube films, *Applied Physics Letters* 2000, 77, 666–668.
253. Nan, C.W., Shi, Z., Lin, Y., A simple model for thermal conductivity of carbon nanotube-based composites, *Chemical Physics Letters* 2003, 375, 666–669.
254. Choi, E.S., Brooks, J.S., Eaton, D.L., Al-Haik, M.S., Hussaini, M.Y., Garmestani, H., Li, D., Dahmen, K., Enhancement of thermal and electrical properties of carbon nanotube polymer composites by magnetic field processing, *Journal of Applied Physics* 2003, 94, 6034–6039.
255. Kashiwagi, T., Grulke, E., Hilding, J., Groth, K., Harris, R., Butler, K., Shields, J., Kharchenko, S., Douglas, J., Thermal and flammability properties of polypropylene/carbon nanotube nanocomposites, *Polymer* 2004, 45, 4227–4239.
256. Gong, Q.M., Li, Z., Bai, X.D., Li, D., Zhao, Y., Liang, J., Thermal properties of aligned carbon nanotube/carbon nanocomposites, *Materials Science and Engineering a-Structural Materials Properties Microstructure and Processing* 2004, 384, 209–214.
257. Badaire, S., Pichot, V., Zakri, C., Poulin, P., Launois, P., Vavro, J., Guthy, C., Chen, M., Fischer, J.E., Correlation of properties with preferred orientation in coagulated and stretch-aligned single-wall carbon nanotubes, *Journal of Applied Physics* 2004, 96, 7509–7513.
258. Hone, J., Batlogg, B., Benes, Z., Johnson, A.T., Fischer, J.E., Quantized phonon spectrum of single-wall carbon nanotubes, *Science* 2000, 289, 1730–1733.
259. Robertson, J., *Materials Today* 2004, October, 46–52.
260. Levy, O., Stroud, D., Maxwell Garnett theory for mixtures of anisotropic inclusions: application to conducting polymers, *Physical Review B* 1997, 56, 8035–8046.
261. Wu, X.H., Pan, L.S., Fan, X.J., Xu, D., Li, H., Zhang, C.X., A semi-analytic method for studying optical properties of aligned carbon nanotubes, *Nanotechnology* 2003, 14, 1180–1186.
262. Hwang, J., Gommans, H.H., Ugawa, A., Tashiro, H., Haggenueller, R., Winney, K.I., Fischer, J.E., Tanner, D.B., Rinzler, A.G., Polarized spectroscopy of aligned single-wall carbon nanotubes, *Physical Review B* 2000, 62, R13310–R13313.
263. Kymakis, E., Amaratunga, G.A.J., Optical properties of polymer-nanotube composites, *Synthetic Metals* 2004, 142, 161–167.
264. Kymakis, E., Amaratunga, G.A.J., Single-wall carbon nanotube/conjugated polymer photovoltaic devices, *Applied Physics Letters* 2002, 80, 112–114.
265. O'Flaherty, S.M., Hold, S.V., Brennan, M.E., Cadek, M., Drury, A., Coleman, J.N., Blau, W.J., Nonlinear optical response of multiwalled carbon-nanotube dispersions, *Journal of the Optical Society of America B-Optical Physics* 2003, 20, 49–58.

266. Niu, C.M., Sichel, E.K., Hoch, R., Moy, D., Tennent, H., High power electrochemical capacitors based on carbon nanotube electrodes, *Applied Physics Letters* 1997, 70, 1480–1482.
267. Ma, R.Z., Liang, J., Wei, B.Q., Zhang, B., Xu, C.L., Wu, D.H., Study of electrochemical capacitors utilizing carbon nanotube electrodes, *Journal of Power Sources* 1999, 84, 126–129.
268. Frackowiak, E., Jurewicz, K., Delpeux, S., Beguin, F., Nanotubular materials for supercapacitors, *Journal of Power Sources* 2001, 97–8, 822–825.
269. Barisci, J.N., Wallace, G.G., Baughman, R.H., Electrochemical quartz crystal microbalance studies of single-wall carbon nanotubes in aqueous and non-aqueous solutions, *Electrochimica Acta* 2000, 46, 509–517.
270. Barisci, J.N., Wallace, G.G., Baughman, R.H., Electrochemical characterization of single-walled carbon nanotube electrodes, *Journal of the Electrochemical Society* 2000, 147, 4580–4583.
271. Barisci, J.N., Wallace, G.G., Chattopadhyay, D., Papadimitrakopoulos, F., Baughman, R.H., Electrochemical properties of single-wall carbon nanotube electrodes, *Journal of the Electrochemical Society* 2003, 150, E409–E415.
272. Shiraishi, S., Kurihara, H., Okabe, K., Hulicova, D., Oya, A., Electric double layer capacitance of highly pure single-walled carbon nanotubes (HiPco (TM) Buckytubes (TM)) in propylene carbonate electrolytes, *Electrochemistry Communications* 2002, 4, 593–598.
273. Barisci, J.N., Wallace, G.G., MacFarlane, D.R., Baughman, R.H., Investigation of ionic liquids as electrolytes for carbon nanotube electrodes, *Electrochemistry Communications* 2004, 6, 22–27.
274. Li, C.S., Wang, D.Z., Liang, T.X., Li, G.T., Wang, X.F., Cao, M.S., Liang, J., Oxidation behavior of CNTs and the electric double layer capacitor made of the CNT electrodes, *Science in China Series E-Technological Sciences* 2003, 46, 349–354.
275. Jiang, Q., Qu, M.Z., Zhou, G.M., Zhang, B.L., Yu, Z.L., A study of activated carbon nanotubes as electrochemical super capacitors electrode materials, *Materials Letters* 2002, 57, 988–991.
276. Frackowiak, E., Delpeux, S., Jurewicz, K., Szostak, K., Cazorla-Amoros, D., Beguin, F., Enhanced capacitance of carbon nanotubes through chemical activation, *Chemical Physics Letters* 2002, 361, 35–41.
277. Lee, Y.H., An, K.H., Lim, S.C., Kim, W.S., Jeong, H.J., Doh, C.H., Moon, S.I., Applications of carbon nanotubes to energy storage devices, *New Diamond and Frontier Carbon Technology* 2002, 12, 209–228.
278. Frackowiak, E., Metenier, K., Bertagna, V., Beguin, F., Supercapacitor electrodes from multiwalled carbon nanotubes, *Applied Physics Letters* 2000, 77, 2421–2423.
279. Frackowiak, E., Beguin, F., Carbon materials for the electrochemical storage of energy in capacitors, *Carbon* 2001, 39, 937–950.
280. Lee, J.Y., An, K.H., Heo, J.K., Lee, Y.H., Fabrication of supercapacitor electrodes using fluorinated single-walled carbon nanotubes, *Journal of Physical Chemistry B* 2003, 107, 8812–8815.
281. Yoon, B.J., Jeong, S.H., Lee, K.H., Kim, H.S., Park, C.G., Han, J.H., Electrical properties of electrical double layer capacitors with integrated carbon nanotube electrodes, *Chemical Physics Letters* 2004, 388, 170–174.
282. Wang, T., Kumar, S., Electrospun polyacrylonitrile/carbon nanotube composite fibers for supercapacitor electrode, in preparation.

283. Belanger, D., Ren, X.M., Davey, J., Uribe, F., Gottesfeld, S., Characterization and long-term performance of polyaniline-based electrochemical capacitors, *Journal of the Electrochemical Society* 2000, 147, 2923–2929.
284. Ryu, K.S., Wu, X.L., Lee, Y.G., Chang, S.H., Electrochemical capacitor composed of doped polyaniline and polymer electrolyte membrane, *Journal of Applied Polymer Science* 2003, 89, 1300–1304.
285. Lota, K., Khomenko, V., Frackowiak, E., Capacitance properties of poly(3,4-ethylenedioxythiophene)/carbon nanotubes composites, *Journal of Physics and Chemistry of Solids* 2004, 65, 295–301.
286. Sun, Y., Wilson, S.R., Schuster, D.I., High dissolution and strong light emission of carbon nanotubes in aromatic amine solvents, *Journal of the American Chemical Society* 2001, 123, 5348–5349.
287. Jurewicz, K., Delpeux, S., Bertagna, V., Beguin, F., Frackowiak, E., Supercapacitors from nanotubes/polypyrrole composites, *Chemical Physics Letters* 2001, 347, 36–40.
288. An, K.H., Jeon, K.K., Heo, J.K., Lim, S.C., Bae, D.J., Lee, Y.H., High-capacitance supercapacitor using a nanocomposite electrode of single-walled carbon nanotube and polypyrrole, *Journal of the Electrochemical Society* 2002, 149, A1058–A1062.
289. Hughes, M., Chen, G.Z., Shaffer, M.S.P., Fray, D.J., Windle, A.H., Electrochemical capacitance of a nanoporous composite of carbon nanotubes and polypyrrole, *Chemistry of Materials* 2002, 14, 1610–1613.
290. Downs, C., Nugent, J., Ajayan, P.M., Duquette, D.J., Santhanam, S.V., Efficient polymerization of aniline at carbon nanotube electrodes, *Advanced Materials* 1999, 11, 1028–1031.
291. Snook, G.A., Chen, G.Z., Fray, D.J., Hughes, M., Shaffer, M., Studies of deposition of and charge storage in polypyrrole-chloride and polypyrrole-carbon nanotube composites with an electrochemical quartz crystal microbalance, *Journal of Electroanalytical Chemistry* 2004, 568, 135–142.
292. Frackowiak, E., Jurewicz, K., Szostak, K., Delpeux, S., Beguin, F., Nanotubular materials as electrodes for supercapacitors, *Fuel Processing Technology* 2002, 77, 213–219.
293. Zhou, Y.K., He, B.L., Zhou, W.J., Li, H.L., Preparation and Electrochemistry of SWNT/PANI composite films for electrochemical capacitors, *Journal of the Electrochemical Society* 2004, 151, A1052–A1057.
294. Zhou, C.F., Kumar, S., Doyle, C.D., Tour, J.M., Functionalized single wall carbon nanotubes treated with pyrrole for electrochemical supercapacitor membranes, *Chemistry of Materials* 2005, 17, 1997–2002.
295. Conway, B.E. *Electrical Supercapacitors, Scientific Fundamental and Technological Applications*. Plenum Publishers, New York, 1999.
296. Baughman, R.H., Cui, C.X., Zakhidov, A.A., Iqbal, Z., Barisci, J.N., Spinks, G.M., Wallace, G.G., Mazzoldi, A., De Rossi, D., Rinzler, A.G., Jaschinski, O., Roth, S., Kertesz, M., Carbon nanotube actuators, *Science* 1999, 284, 1340–1344.
297. Landi, B.J., Raffaele, R.P., Heben, M.J., Alleman, J.L., VanDerveer, W., Gennett, T., Single wall carbon nanotube-Nafion composite actuators, *Nano Letters* 2002, 2, 1329–1332.
298. Spinks, G.M., Wallace, G.G., Fifield, L.S., Dalton, L.R., Mazzoldi, A., De Rossi, D., Khayrullin, II, Baughman, R.H., Pneumatic carbon nanotube actuators, *Advanced Materials* 2002, 14, 1728.



299. Fennimore, A.M., Yuzvinsky, T.D., Han, W.Q., Fuhrer, M.S., Cumings, J., Zettl, A., Rotational actuators based on carbon nanotubes, *Nature* 2003, 424, 408–410.
300. Barisci, J.N., Spinks, G.M., Wallace, G.G., Madden, J.D., Baughman, R.H., Increased actuation rate of electromechanical carbon nanotube actuators using potential pulses with resistance compensation, *Smart Materials & Structures* 2003, 12, 549–555.
301. Gupta, S., Hughes, M., Windle, A.H., Robertson, J., Charge transfer in carbon nanotube actuators investigated using in situ Raman spectroscopy, *Journal of Applied Physics* 2004, 95, 2038–2048.
302. Gupta, S., Hughes, M., Windle, A.H., Robertson, J., In situ Raman spectro-electrochemistry study of single-wall carbon nanotube mat, *Diamond and Related Materials* 2004, 13, 1314–1321.
303. Kang, J.W., Hwang, H.J., Gigahertz actuator of multiwall carbon nanotube encapsulating metallic ions: molecular dynamics simulations, *Journal of Applied Physics* 2004, 96, 3900–3905.
304. Madden, J.D.W., Vandesteeg, N.A., Anquetil, P.A., Madden, P.G.A., Takshi, A., Pytel, R.Z., Lafontaine, S.R., Wieringa, P.A., Hunter, I.W., Artificial muscle technology: physical principles and naval prospects, *Ieee Journal of Oceanic Engineering* 2004, 29, 706–728.
305. Kyokane, J., Tsujimoto, N., Ishida, M., Fukuma, M., Space charge characteristics of fullerene and carbon nanotube doped polyurethane elastomer (PUE) actuators, *Ieice Transactions on Electronics* 2004, E87C, 2125–2128.
306. Landi, B.J., Raffaele, R.P., Heben, M.J., Alleman, J.L., VanDerveer, W., Gennett, T., Development and characterization of single wall carbon nanotube-Nafion composite actuators, *Materials Science and Engineering B-Solid State Materials for Advanced Technology* 2005, 116, 359–362.
307. Deshpande, S.D., Kim, J., Yun, S.R., New electro-active paper actuator using conducting polypyrrole: actuation behaviour in LiClO<sub>4</sub> acetonitrile solution, *Synthetic Metals* 2005, 149, 53–58.
308. Koerner, H., Price, G., Pearce, N.A., Alexander, M., Vaia, R.A., Remotely actuated polymer nanocomposites - stress-recovery of carbon-nanotube-filled thermoplastic elastomers, *Nature Materials* 2004, 3, 115–120.
309. Chopra, S., Pham, A., Gaillard, J., Parker, A., Rao, A.M., Carbon-nanotube-based resonant-circuit sensor for ammonia, *Applied Physics Letters* 2002, 80, 4632–4634.
310. Liu, P.F., Hu, J.H., Carbon nanotube powder microelectrodes for nitrite detection, *Sensors and Actuators B-Chemical* 2002, 84, 194–199.
311. Valentini, L., Armentano, I., Kenny, J.M., Cantalini, C., Lozzi, L., Santucci, S., Sensors for sub-ppm NO<sub>2</sub> gas detection based on carbon nanotube thin films, *Applied Physics Letters* 2003, 82, 961–963.
312. Cai, H., Cao, X.N., Jiang, Y., He, P.G., Fang, Y.Z., Carbon nanotube-enhanced electrochemical DNA biosensor for DNA hybridization detection, *Analytical and Bioanalytical Chemistry* 2003, 375, 287–293.
313. Peng, S., Cho, K.J., Ab initio study of doped carbon nanotube sensors, *Nano Letters* 2003, 3, 513–517.
314. Modi, A., Koratkar, N., Lass, E., Wei, B.Q., Ajayan, P.M., Miniaturized gas ionization sensors using carbon nanotubes, *Nature* 2003, 424, 171–174.
315. Valentini, L., Lozzi, L., Cantalini, C., Armentano, I., Kenny, J.M., Ottaviano, L., Santucci, S., Effects of oxygen annealing on gas sensing properties of carbon nanotube thin films, *Thin Solid Films* 2003, 436, 95–100.



316. Li, J., Lu, Y.J., Ye, Q., Cinke, M., Han, J., Meyyappan, M., Carbon nanotube sensors for gas and organic vapor detection, *Nano Letters* 2003, 3, 929–933.
317. Wohlstadter, J.N., Wilbur, J.L., Sigal, G.B., Biebuyck, H.A., Billadeau, M.A., Dong, L.W., Fischer, A.B., Gudibande, S.R., Jamieson, S.H., Kenten, J.H., Leginus, J., Leland, J.K., Massey, R.J., Wohlstadter, S.J., Carbon nanotube-based biosensor, *Advanced Materials* 2003, 15, 1184.
318. Chopra, S., McGuire, K., Gothard, N., Rao, A.M., Pham, A., Selective gas detection using a carbon nanotube sensor, *Applied Physics Letters* 2003, 83, 2280–2282.
319. Dharap, P., Li, Z.L., Nagarajaiah, S., Barrera, E.V., Nanotube film based on single-wall carbon nanotubes for strain sensing, *Nanotechnology* 2004, 15, 379–382.
320. Peng, S., Cho, K.J., Qi, P.F., Dai, H.J., Ab initio study of CNT NO<sub>2</sub> gas sensor, *Chemical Physics Letters* 2004, 387, 271–276.
321. Li, Z.L., Dharap, P., Nagarajaiah, S., Barrera, E.V., Kim, J.D., Carbon nanotube film sensors, *Advanced Materials* 2004, 16, 640.
322. Mateiu, R., Davis, Z.J., Madsen, D.N., Molhave, K., Boggild, P., Rassmusen, A.M., Brorson, M., Jacobsen, C.J.H., Boisen, A., An approach to a multi-walled carbon nanotube based mass sensor, *Microelectronic Engineering* 2004, 73–74, 670–674.
323. Lu, Y.J., Li, J., Han, J., Ng, H.T., Binder, C., Partridge, C., Meyyappan, M., Room temperature methane detection using palladium loaded single-walled carbon nanotube sensors, *Chemical Physics Letters* 2004, 391, 344–348.
324. Xu, Y., Jiang, Y., Cai, H., He, P.G., Fang, Y.Z., Electrochemical impedance detection of DNA hybridization based on the formation of M-DNA on polypyrrole/carbon nanotube modified electrode, *Analytica Chimica Acta* 2004, 516, 19–27.
325. Ahn, K.S., Kim, J.H., Lee, K.N., Kim, C.O., Hong, J.P., Multi-wall carbon nanotubes as a high-efficiency gas sensor, *Journal of the Korean Physical Society* 2004, 45, 158–161.
326. Salimi, A., Compton, R.G., Hallaj, R., Glucose biosensor prepared by glucose oxidase encapsulated sol-gel and carbon-nanotube-modified basal plane pyrolytic graphite electrode, *Analytical Biochemistry* 2004, 333, 49–56.
327. Koratkar, N., Modi, A., Lass, E., Ajayan, P., Temperature effects on resistance of aligned multiwalled carbon nanotube films, *Journal of Nanoscience and Nanotechnology* 2004, 4, 744–748.
328. Langlet, R., Arab, M., Picaud, F., Devel, M., Girardet, C., Influence of molecular adsorption on the dielectric properties of a single wall nanotube: A model sensor, *Journal of Chemical Physics* 2004, 121, 9655–9665.
329. Katz, H.E., Chemically sensitive field-effect transistors and chemiresistors: New materials and device structures, *Electroanalysis* 2004, 16, 1837–1842.
330. Chen, H.W., Wu, R.J., Chan, K.H., Sun, Y.L., Su, P.G., The application of CNT/Nafion composite material to low humidity sensing measurement, *Sensors and Actuators B-Chemical* 2005, 104, 80–84.
331. Lee, J.W., Choi, Y.M., Kong, K.J., Lee, J.O., Chang, H.J., Ryu, B.H., Fabrication of a single-walled carbon nanotube (SWCNT) device using a novel barricade-confronting electrode (BCE) pattern for gas sensor applications, *Sensors and Materials* 2004, 16, 357–365.
332. Roman, C., Ciontu, F., Courtois, B., Nanoscopic modeling of a carbon nanotube force-measuring biosensor, *Molecular Simulation* 2005, 31, 123–133.

333. Deo, R.P., Wang, J., Block, I., Mulchandani, A., Joshi, K.A., Trojanowicz, M., Scholz, F., Chen, W., Lin, Y.H., Determination of organophosphate pesticides at a carbon nanotube/organophosphorus hydrolase electrochemical biosensor, *Analytica Chimica Acta* 2005, 530, 185–189.
334. Fei, S.D., Chen, J.H., Yao, S.Z., Deng, G.H., He, D.L., Kuang, Y.F., Electrochemical behavior of L-cysteine and its detection at carbon nanotube electrode modified with platinum, *Analytical Biochemistry* 2005, 339, 29–35.
335. Li, G., Liao, J.M., Hu, G.Q., Ma, N.Z., Wu, P.J., Study of carbon nanotube modified biosensor for monitoring total cholesterol in blood, *Biosensors & Bioelectronics* 2005, 20, 2140–2144.
336. Suehiro, J., Zhou, G.B., Hara, M., Detection of partial discharge in SF<sub>6</sub> gas using a carbon nanotube-based gas sensor, *Sensors and Actuators B-Chemical* 2005, 105, 164–169.
337. Kerman, K., Morita, Y., Takamura, Y., Tamiya, E., Escherichia coli single-strand binding protein-DNA interactions on carbon nanotube-modified electrodes from a label-free electrochemical hybridization sensor, *Analytical and Bioanalytical Chemistry* 2005, 381, 1114–1121.
338. Probst, O., Moore, E.M., Resasco, D.E., Grady, B.P., Nucleation of polyvinyl alcohol crystallization by single-walled carbon nanotubes, *Polymer* 2004, 45, 4437–4443.
339. Ryan, K.P., Lipson, S.M., Drury, A., Cadek, M., Ruether, M., O'Flaherty, S.M., Barron, V., McCarthy, B., Byrne, H.J., Blau, W.J., Coleman, J.N., Carbon-nanotube nucleated crystallinity in a conjugated polymer based composite, *Chemical Physics Letters* 2004, 391, 329–333.
340. Valentini, L., Biagiotti, J., Kenny, J.M., Santucci, S., Effects of single-walled carbon nanotubes on the crystallization behavior of polypropylene, *Journal of Applied Polymer Science* 2003, 87, 708–713.
341. Minus, M., Chae, H.G., Kumar, S., Single-wall carbon nanotube templated oriented crystallization of poly(vinyl alcohol), *Polymer*, submitted.
342. Zhou, W., Fischer, J.E., Heiney, P.A., Fan, H., Davis, V.A., Pasquali, M., Smalley, R.E., Single-walled carbon nanotubes in superacid: X-ray and calorimetric evidence for partly ordered H<sub>2</sub>SO<sub>4</sub>, *Physical Review B* 2005, 72, Art. No. 045440.
343. Zhou, W., Heiney, P.A., Fan, H., Smalley, R.E., Fischer, J.E., Single-walled carbon nanotube-templated crystallization of H<sub>2</sub>SO<sub>4</sub>: Direct evidence for protonation, *Journal of the American Chemical Society* 2005, 127, 1640–1641.
344. O'Connell, M.J., Boul, P., Ericson, L.M., Huffman, C., Wang, Y.H., Haroz, E., Kuper, C., Tour, J., Ausman, K.D., Smalley, R.E., Reversible water-solubilization of single-walled carbon nanotubes by polymer wrapping, *Chemical Physics Letters* 2001, 342, 265–271.
345. Britto, P.J., Santhanam, K.S.V., Ajayan, P.M., Carbon nanotube electrode for oxidation of dopamine, *Bioelectrochemistry and Bioenergetics* 1996, 41, 121–125.
346. Tamura, K., Takashi, N., Akasaka, T., Roska, I.D., Uo, M., Totsuka, Y., Watari, F., Effects of micro/nano particle size on cell function and morphology. In *Bioceramics*, Vol 16, 2004; Vol. 254–2, pp. 919–922.
347. Correa-Duarte, M.A., Wagner, N., Rojas-Chapana, J., Morscheck, C., Thie, M., Giersig, M., Fabrication and biocompatibility of carbon nanotube-based 3D networks as scaffolds for cell seeding and growth, *Nano Letters* 2004, 4, 2233–2236.

348. Gartstein, Y.N., Zakhidov, A.A., Baughman, R.H., Mechanical and electromechanical coupling in carbon nanotube distortions, *Physical Review B* 2003, 68, Art. No. 115415.
349. Viswanathan, G., Kane, D.B., Lipowicz, P.J., High efficiency fine particulate filtration using carbon nanotube coatings, *Advanced Materials* 2004, 16, 2045.
350. Dillon, A.C., Jones, K.M., Bekkedahl, T.A., Kiang, C.H., Bethune, D.S., Heben, M.J., Storage of hydrogen in single-walled carbon nanotubes, *Nature* 1997, 386, 377–379.
351. Rinzler, A.G., Hafner, J.H., Nikolaev, P., Lou, L., Kim, S.G., Tomanek, D., Nordlander, P., Colbert, D.T., Smalley, R.E., Unraveling nanotubes — field-emission from an atomic wire, *Science* 1995, 269, 1550–1553.
352. Li, Y.J., Wang, K.L., Wei, J.Q., Gu, Z.Y., Wang, Z.C., Luo, J.B., Wu, D.H., Tensile properties of long aligned double-walled carbon nanotube strands, *Carbon* 2005, 43, 31–35.
353. Yu, M.F., Lourie, O., Dyer, M.J., Moloni, K., Kelly, T.F., Ruoff, R.S., Strength and breaking mechanism of multiwalled carbon nanotubes under tensile load, *Science* 2000, 287, 637–640.
354. Pan, Z.W., Xie, S.S., Lu, L., Chang, B.H., Sun, L.F., Zhou, W.Y., Wang, G., Zhang, D.L., Tensile tests of ropes of very long aligned multiwall carbon nanotubes, *Applied Physics Letters* 1999, 74, 3152–3154.
355. Liew, K.M., He, X.Q., Wong, C.H., On the study of elastic and plastic properties of multi-walled carbon nanotubes under axial tension using molecular dynamics simulation, *Acta Materialia* 2004, 52, 2521–2527.
356. Gaier, J.R., Hambourger, P.D., Slabe, M.E., Effect of heat-treatment temperature of vapor-grown graphite fibers 1. Properties of their bromine intercalation compounds, *Synthetic Metals* 1989, 31, 229–240.
357. Gaier, J.R., Slabe, M.E., Stahl, M., Effect of heat-treatment temperature of vapor-grown graphite fibers 2. Stability of their bromine intercalation compounds, *Synthetic Metals* 1989, 31, 241–249.
358. Subramoney, S., Novel nanocarbons— structure, properties, and potential applications, *Advanced Materials* 1998, 10, 1157.
359. Toyobo, Inc. (<http://www.toyobo.co.jp/e/seihin/kc/pbo/menu>).
360. Honeywell, Inc. (<http://www.spectrafiber.com>).
361. Dupont, Inc. (<http://www.dupont.com/kevlar>).
362. Yakobson, B.I., Avouris, P.H. Carbon Nanotubes. Dresselhaus, M. S., Avouris, P. H., Eds., Springer-Verlag, Berlin, 2001, p. 297.
363. Rul, S., Lefevre-schlick, F., Capria, E., Laurent, C., Peigney, A., Percolation of single-walled carbon nanotubes in ceramic matrix nanocomposites, *Acta Materialia* 2004, 52, 1061–1067.

## chapter nine

---

# Functionalized carbon nanotubes in composites\*

Christopher A. Dyke  
NanoComposites, Inc.

James M. Tour  
Rice University

### Contents

9.1	Introduction .....	276
9.2	SWNT preparation and characterization .....	277
9.3	Functionalized SWNTs .....	278
9.3.1	Functionalization methodologies .....	278
9.3.2	Selective functionalization and separation .....	283
9.4	Carbon nanotube-modified composites .....	286
9.5	Conclusions .....	290
	Acknowledgments .....	291
	References .....	291

**Abstract** Covalent functionalization of single-walled carbon nanotubes (SWNTs) has significantly expanded the utility of the nanotube structure. Covalent sidewall functionalization has been employed to increase the solubility of these materials, allowing for the manipulation and processing of these otherwise insoluble nanotubes. Increased solubility leads to better dispersion in polymeric systems. Also, functionalization can be performed selectively, wherein the metallic SWNTs react faster than the semiconductors. This has allowed a separation of

\* Much of this review was adapted from a text that we recently prepared on a similar topic for the *Journal of Physical Chemistry*.

carbon nanotubes by type. Covalent sidewall functionalization also allows nanotube-based composite formation where the functional group is well mixed with the polymer matrix. This has led to dramatic increases in the modulus of elastomers while retaining their elongation-at-break properties.

## 9.1 Introduction

The National Nanotechnology Initiative (NNI) has defined nine thrusts called grand challenges aimed at rapidly converting scientific discoveries into innovative technology. SWNTs could potentially be useful in several of the research and development areas directed toward composite structural and electronic materials. Covalent functionalization of SWNTs has given scientists and engineers the ability to manipulate these astonishing structures in ways that would otherwise be unattainable.<sup>1,2</sup> SWNTs consist of only carbon and can be considered theoretically as a graphene sheet rolled into a seamless cylinder.<sup>3,4</sup> SWNTs, the strongest material known, are ladder polymers; i.e., more than one bond needs to be broken to cleave the backbone. Typical ladder polymers are fully joined by only two repeating bonds. However, depending on the tube type, SWNTs have 10 to 20 carbon–carbon bonds per repeat unit that would need to be broken for polymer strand rupture to occur. Furthermore, each of those 10 to 20 carbon–carbon bonds has a bond order of ca. 1.3, and since the carbon–carbon bond is among the strongest bonds in the universe, it is unlikely that we will ever find more robust polymeric chains. Beyond their amazing mechanical properties, they also exhibit extraordinary optical, electrical, and thermal properties,<sup>5</sup> as nanotubes can be either carbon-based metals or semiconductors,<sup>6,7</sup> and have been used in the construction of nanotube-based transistors,<sup>2,8</sup> as well as serving as interconnects in a small integrated circuit.<sup>9</sup> Furthermore, nanotube-based composites show tremendous promise; the lightweight yet strong, flexible,<sup>10</sup> and resilient<sup>11</sup> nanotubes can add fortification to many polymeric structural materials. Unfortunately, much of the optical, electrical, and thermal properties are extended pi-conjugation dependent, and therefore, covalent functionalization causes a loss in these qualities.

SWNTs are synthesized in a variety of ways with the two most prevalent being laser ablation of a metal-doped graphite target (laser oven)<sup>12</sup> and gas phase catalytic growth from carbon monoxide (high-pressure carbon monoxide, or HiPco)<sup>13</sup> or other carbon sources, such as methane or mixed carbon/H<sub>2</sub> sources. All known preparations of SWNTs give mixtures of nanotube chiralities, diameters, and lengths. The diameter and vector of a carbon nanotube is defined by two integers,  $n$  and  $m$ . When  $n - m = 3q$ , where  $q$  is an integer that does not equal 0, the nanotube is semimetallic with a band gap on the order of meVs; when  $n - m = 0$ , the nanotube is metallic with a band gap of 0 eV and referred to as an armchair-type nanotube. All other nanotubes ( $n - m \neq 3q$ ) are semiconductors with a band gap of ca. 0.5 to 1 eV. Prepared lengths of carbon nanotubes can vary anywhere from 50 nm



to 2 cm long.<sup>14</sup> Carbon nanotubes are highly polarizable, smooth-sided compounds with attractive interactions of 0.5 eV/nm of tube-to-tube contact. Due to these extreme cohesive forces, SWNTs exist as bundled structures that are often referred to as ropes.<sup>15</sup> This bundling or roping phenomenon contributes to the bulk materials having limited solubility and poor dispersion in polymers.<sup>16,17</sup> In fact, pristine carbon nanotubes tend to agglomerate in polymer hosts, which often weakens the mechanical strength of these composite materials.<sup>18–20</sup> Another problem associated with pristine nanotubes in composites and blends is the lack of interfacial bonding (SWNTs to matrix material), which leads to fiber pullout during stress, followed by catastrophic failure. Bundling also convolutes the optical and electronic property characterizations. Covalent functionalization can provide “handles” for dispersion in host polymers, and also provide exfoliation of the bundles, ultimately paving the way for important discoveries that would be unrealized without functionalization.

Strategies for noncovalent<sup>21</sup> and covalent<sup>22–24</sup> functionalization of SWNTs have been reviewed. Noncovalent functionalization of SWNTs, such as wrapping of the nanotubes with surfactants,<sup>25</sup> led to the discovery of carbon nanotube fluorescence-based identification,<sup>26</sup> and in turn led to the optical assignment of the semiconductors by their *n* and *m* values.<sup>27</sup> Several covalent functionalization strategies exist, such as defect site creation and functionalization from the defects,<sup>28</sup> creating carboxylic acids on the end caps of carbon nanotubes and subsequent derivatization from the acids,<sup>29,30</sup> and covalent sidewall functionalization.<sup>24</sup> This chapter focuses on covalent sidewall functionalization of SWNTs and discusses how this methodology generates the ability to solubilize and disperse these nanotubes into polymer matrices.<sup>17</sup> Covalent sidewall functionalization can even be performed selectively; i.e., metallic nanotubes can be modified without affecting the semiconductors.<sup>31</sup> Functionalized SWNTs also lead to the creation of novel composite materials and elastomers, where the issues of fiber pullout and interfacial bonding are addressed.<sup>32,33</sup>

## 9.2 SWNT preparation and characterization

SWNTs prepared from laser ablation,<sup>34</sup> HiPco,<sup>35</sup> or related gas phase growth methods are typically contaminated with amorphous carbon and metal particles. The as-prepared material, in general, is purified by an oxidative treatment to remove amorphous carbon and an acid treatment to remove metal particles. Functionalization can be performed on the raw or purified material as well as material individualized in aqueous surfactants (*vide infra*). Covalently functionalized SWNTs are characterized by several analytical techniques that we recently reviewed.<sup>36</sup> Absorption and resonance Raman spectroscopy are employed to ensure that the functionalization is covalent and occurs at the sidewalls, not at merely defect sites or at the ends of the SWNTs. Once covalent sidewall functionalization is confirmed, thermogravimetric analysis (TGA) and x-ray photoelectron spectroscopy (XPS) are used to

determine the degree of functionalization. Use of these techniques is difficult unless the modified carbon nanotubes are purified. Imaging techniques such as atomic force microscopy (AFM), scanning electron microscopy (SEM), and transmission electron microscopy (TEM) are used to analyze the diameter of the bundles or individuals, and AFM gives a good indication of average lengths of the nanotubes.

## 9.3 Functionalized SWNTs

### 9.3.1 Functionalization methodologies

Several SWNT sidewall functionalization methodologies now exist, and they all have one thing in common: a highly reactive intermediate is necessary to attack the carbon nanotubes. Table 9.1 lists common functionalization protocols available to researchers who desire modified carbon nanotubes. The first methodology developed by the authors is functionalization of carbon nanotubes with substituted benzene diazonium salts. This can be performed in several ways, including electrochemical reduction of the salt,<sup>37</sup> as well as treating surfactant-wrapped nanotubes<sup>26,38–40</sup> with the salt in aqueous solution.<sup>41,42</sup> The arene diazonium species can be used directly or formed *in situ* by mixing an aniline and isoamyl nitrite (or sodium nitrite) with the SWNTs in organic solvents,<sup>43</sup> oleum ( $\text{H}_2\text{SO}_4$  with dissolved  $\text{SO}_3$ ),<sup>44</sup> or without any solvent.<sup>45</sup> The solvent-free process is particularly attractive for large-scale functionalizations because previously developed procedures required ca. 2 l of solvent per gram of SWNTs due to the poor dispersion of SWNTs. Additionally, the solvent-free process could be performed in the same blending equipment used for polymer blending, thereby streamlining the overall functionalization/blending protocol.

The methodology that gives the most highly functionalized SWNTs is functionalization by adding preformed aryl diazonium salts to micelle-coated carbon nanotubes at pH 10, the micelle most often being generated from the surfactant sodium dodecyl sulfate (SDS).<sup>41</sup> The micelle-coated material generated according to the published procedure gives noncovalently wrapped SWNTs as individuals (unbundled). Functionalization of this material is rapid according to ultraviolet–visible–near-infrared (UV-vis-NIR) (Table 9.1), and the material is heavily functionalized according to Raman spectroscopy (Figure 9.1) and TGA. In fact, SWNTs functionalized in this way have approximately 1 in 10 carbons on the sidewalls bearing an aryl moiety; this ratio varies slightly, depending on the substituent on the arene ring of the diazonium salt. After only 10 min, all of the van Hove singularities in the absorption spectra are lost (Figure 9.2), and after purification of this reaction, Raman analysis shows carbon nanotubes with the disorder mode (D band,  $1290\text{ cm}^{-1}$ ) higher in intensity than the tangential mode ( $1590\text{ cm}^{-1}$ ), which is some of the most heavily functionalized material known. Analysis by AFM (Figure 9.3) of the functionalized material, dispersed from *N,N*-dimethyl formamide (DMF), shows the carbon nanotubes with a dramatic decrease in the ability to bundle;

**Table 9.1** Common SWNT Sidewall Functionalization Methodologies

Methodology	Addend	Characterization Techniques	Degree of Functionalization	Highest Solubility
Diazonium <sup>37,41,43,45</sup>	Aryl	UV-vis-NIR, Raman, TGA, XPS, ATR-IR, AFM, TEM	1 addend in every 10 carbons in SDS/water and 1 addend in every 25 carbons in organic solvent or neat	0.8 mg/ml in DMF
Diazonium in oleum <sup>44</sup>	Aryl	UV-vis-NIR, Raman, TGA, XPS, ATR-IR, AFM, TEM	1 addend in every 20 carbons	0.25 mg/ml in H <sub>2</sub> O
Fluorination <sup>47</sup>	Fluorine	ATR-IR, AFM, STM, VTP-EIMS, UV-vis-NIR, Raman, TGA	1 addend in every 2 carbons	1 mg/ml in 2-propanol
Radical chemistry <sup>50</sup>	Alkyl	Raman, ATR-IR, UV-vis-NIR, TGA	1 addend in every 6 carbons	Not given
Dissolving metal reduction (Billups reaction) <sup>51</sup>	Alkyl, aryl	TEM, AFM, Raman, ATR-IR, TGA-MS	1 addend in every 17 carbons	Not given
Azomethine ylides (Prato reaction) <sup>52</sup>	Pyrrolidine	UV-vis-NIR, Raman, TEM	1 addend in every 100 carbons	50 mg/ml in CHCl <sub>3</sub>
Nitrene <sup>53</sup>	Aziridene	XPS, AFM, TEM, NMR, UV-vis-NIR, Raman	1 addend in every 50 carbons	1.2 mg/ml in DMSO
Bingel reaction <sup>54</sup>	Cyclopropane	AFM, <sup>19</sup> F-NMR, XPS	1 addend in every 50 carbons	Not given
Dichlorocarbene <sup>55</sup>	Cyclopropane	Mid-IR, Raman, EDS, UV-vis-NIR, AFM, thermal	1 addend in every 25 carbons	Not given

therefore, SWNTs functionalized as individuals tend to disperse as individuals in organic solvent. This gives a profound increase in solubility in DMF of functionalized carbon nanotubes (0.8 mg/ml),<sup>41</sup> compared to pristine carbon nanotubes (0.07 mg/ml).<sup>16</sup> This increase in solubility allows the functionalized material to be solvent blended into host polymers. For comparison, micelle-coated carbon nanotubes that are not functionalized but washed to remove the surfactant are rapidly rebundled (Figure 9.4). Analysis by TEM (Figure 9.5) confirms that the functionalized SWNTs are predominately dispersed as individuals in organic solvent, and they are not prone to rebundling,

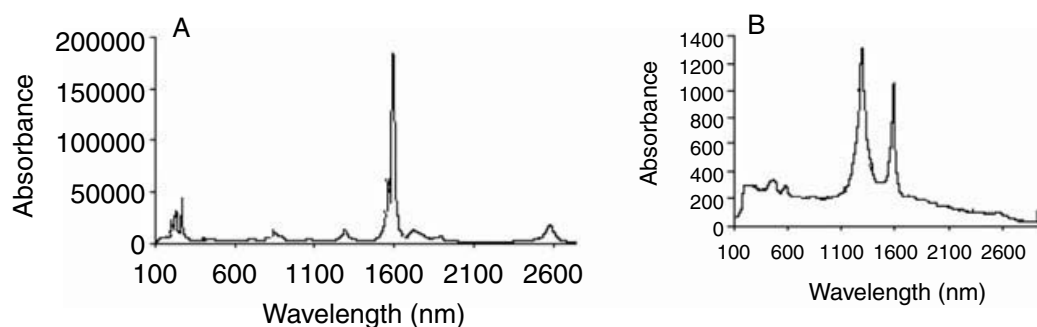


**Figure 9.1** Raman (780-nm excitation) of (A) pristine SWNTs and (B) heavily functionalized individual carbon nanotubes. (Reproduced from Dyke, C. A. and Tour, J. M. Feature article: covalent functionalization of single-walled carbon nanotubes for materials applications, *J. Phys. Chem. A.*, 108, 11151–11159, 2004. Copyright © 2004 American Chemical Society. With permission.)

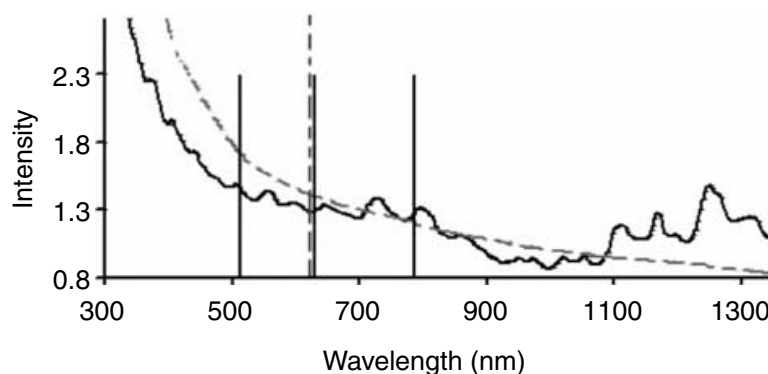


**Figure 9.2** Absorption spectra of SDS-coated SWNTs (black) and heavily functionalized carbon SWNTs (dashed gray). Hence, functionalization causes loss of the van Hove singularities in the absorption spectra that is a key tool for verification of functionalization. (Reproduced from Dyke, C. A. and Tour, J. M. Feature article: covalent functionalization of single-walled carbon nanotubes for materials applications, *J. Phys. Chem. A.*, 108, 11151–11159, 2004. Copyright © 2004 American Chemical Society. With permission.)

thus overcoming the original 0.5-eV/nm attractive interactions. Also note in [Figure 9.5](#) that the roughened SWNT surface is due to arene functionalities.

There is a significant downside to the SDS-wrapping protocol, however. The procedure for obtaining individual SDS-wrapped SWNTs is laborious due to multiple sonications and centrifugations being required. A day's work can afford only about 15 mg of the SDS-wrapped SWNTs. Nonetheless, until recently, wrapping SWNTs with surfactants was the only means of obtaining unbundled nanotubes.

Interestingly, oleum, a super acid medium, has recently been used by Davis and coworkers to spin SWNT fibers.<sup>46</sup> Using this protocol, the SWNTs are dispersed as individuals and there is no need to sonicate or centrifuge the mixtures. Following that lead, we showed that functionalization of SWNTs in oleum ([Table 9.1](#)) provides nanotubes that are individualized.<sup>44</sup>

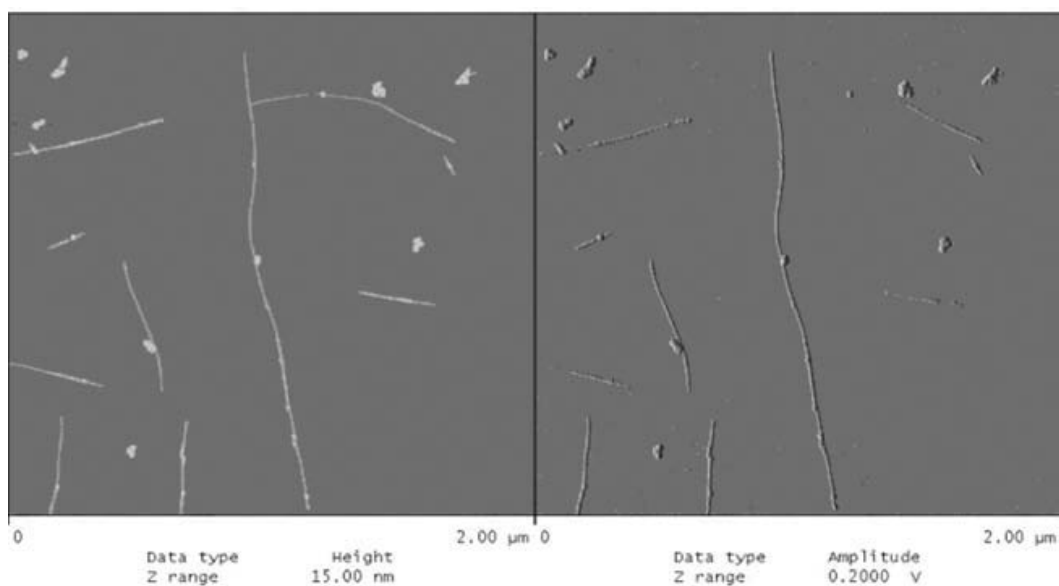


**Figure 9.3** AFM analysis (spin coated onto freshly cleaved mica) by (left) height and (right) amplitude of 4-*tert*-butyl benzene functionalized individual SWNTs that had been treated as SDS-wrapped SWNTs in water. These functionalized SWNTs were washed free of their SDS wrapping prior to imaging, yet they remain unbundled throughout their entire lengths. (Reproduced from Dyke, C. A. and Tour, J. M. Feature article: covalent functionalization of single-walled carbon nanotubes for materials applications, *J. Phys. Chem. A.*, 108, 11151–11159, 2004. Copyright © 2004 American Chemical Society. With permission.)

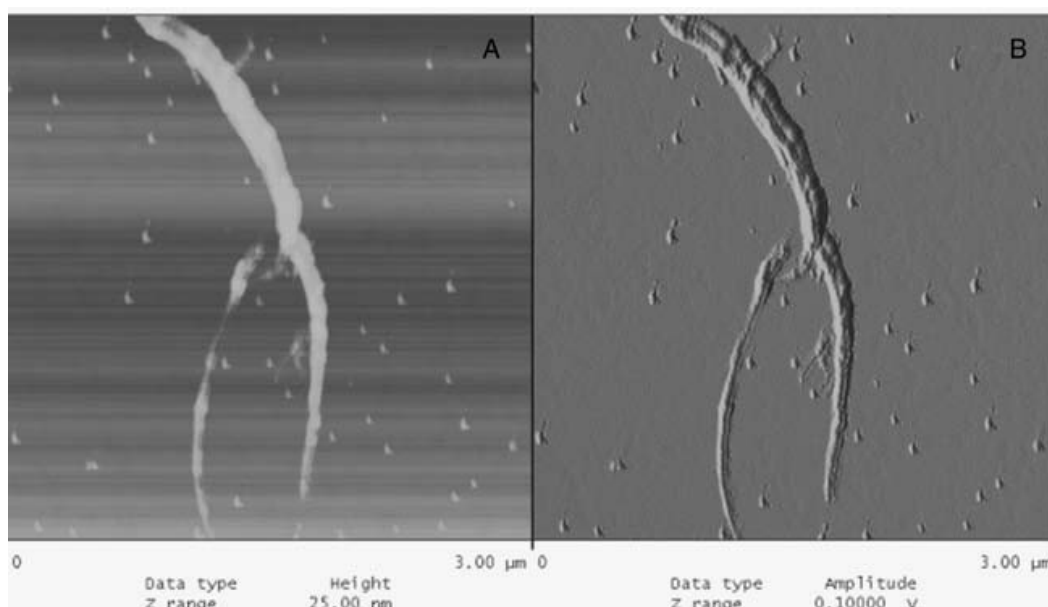


**Figure 9.4** AFM analysis (spin coated onto freshly cleaved mica) by (A) height and (B) amplitude of unfunctionalized SWNTs that were washed free of their SDS wrappings. Notice their tendency to rebundle, unlike the functionalized SWNTs in Figure 9.3. (Reproduced from Dyke, C. A. and Tour, J. M. Feature article: covalent functionalization of single-walled carbon nanotubes for materials applications, *J. Phys. Chem. A.*, 108, 11151–11159, 2004. Copyright © 2004 American Chemical Society. With permission.)



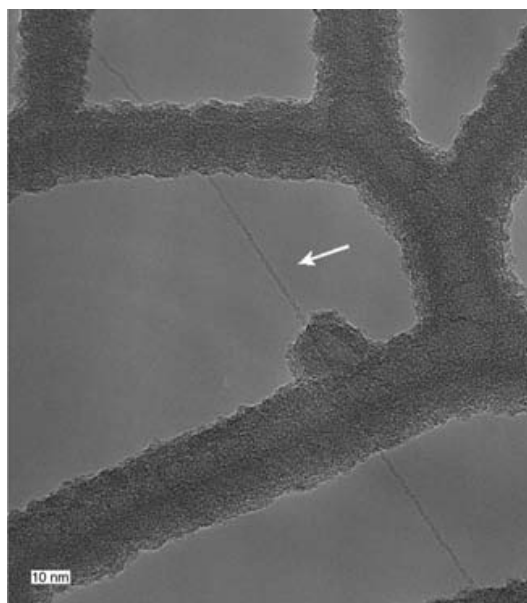


**Figure 9.5** TEM of a functionalized carbon nanotube (arrow) on a lacey carbon grid. There is no tendency to rebundle for the 4-*tert*-butyl benzene functionalized SWNTs. (Reproduced from Dyke, C. A. and Tour, J. M. Feature article: covalent functionalization of single-walled carbon nanotubes for materials applications, *J. Phys. Chem. A.*, 108, 11151–11159, 2004. Copyright © 2004 American Chemical Society. With permission.)

The functionalized nanotubes show little tendency to rebundle. Moreover, the products are even soluble in water due to concomitant arene sulfonic acid formation.

Fluorination of carbon nanotubes was developed by Mickelson and coworkers.<sup>47</sup> Typically, purified carbon nanotubes are added to a reactor and treated with fluorine gas to provide highly fluorinated SWNTs, and this material is also sold commercially. The methodology gives heavily functionalized carbon nanotubes according to Raman analysis and TGA with increased solubility in organic solvents.<sup>48</sup> Fluorine appended to the sidewall can be displaced with various nucleophiles, such as organolithium and Grignard reagents, to give nanotubes functionalized with organic moieties.<sup>49</sup>

Another radical process was developed<sup>50</sup> where highly reactive alkyl radicals are generated by the addition of a radical source in the presence of an alkyl iodide, typically to form the alkyl radical that reacts with carbon nanotubes. This gives highly functionalized material as well.

More excitingly, the Billups reaction, involving treatment of SWNTs with lithium metal in liquid ammonia — a modified Birch-type protocol — was recently disclosed to generate ultra-highly lithiated SWNTs (ca. 1 lithium atom per 2.2 carbon atoms) that can be further treated with numerous electrophiles, including alkyl halides, aryl halides, and even vinyl monomers.<sup>51</sup> A most interesting feature of the Billups reaction is that it affords predominantly individualized SWNTs, since the lithium intercolates between the SWNTs of the bundles. Therefore, the rule of thumb is that if the SWNTs are dispersed as individuals in the reaction medium (as in oleum or Li/NH<sub>3</sub>),

they will react as individuals and remain unbundled. Finally, the Billups reaction could be a predecessor to a new form of unprecedented ultra-highly lithiated carbon materials for battery and related storage applications.

A functionalization methodology developed by Georgakilas and coworkers<sup>52</sup> affords SWNTs that, albeit lightly functionalized relative to the above protocols, are reported to be exceedingly soluble in organic solvents (50 mg/ml; Table 9.1). This methodology involves a 1,3-dipolar cycloaddition of an azomethine ylide generated *in situ* from an amino acid and aldehyde. Three other methods that use highly reactive intermediates to functionalize carbon nanotubes are nitrene decomposition, the Bingel reaction, and dichlorocarbene formation, as developed by Holzinger,<sup>53</sup> Coleman,<sup>54</sup> and Kamaras,<sup>55</sup> respectively (Table 9.1). These are the same reagents that were developed for reactions on C<sub>60</sub>; therefore, there is some commonality of reactive patterns between SWNTs and C<sub>60</sub>. The characterization tools and the reported solubility values for the functionalized SWNTs are summarized in Table 9.1.

### 9.3.2 Selective functionalization and separation

Another aspect of functionalization chemistry is that there are covalent and noncovalent functionalization protocols that show preferential reactivity toward the metallic nanotubes over the semiconductor SWNTs. Such selective reactions include diazonium chemistry,<sup>31</sup> dichlorocarbene reactions,<sup>55</sup> and osmylation<sup>56</sup> for covalent functionalization, and selective absorption of bromine,<sup>57</sup> amines,<sup>58</sup> and DNA<sup>59</sup> for selective noncovalent methodologies. This is important because it now gives researchers the ability to manipulate carbon nanotubes by band gap, and thus begin to separate the metallic from the semiconducting SWNTs.<sup>57–60</sup>

SWNTs that are SDS wrapped as individuals in aqueous solutions and titrated with a benzene diazonium salt show a profound difference between the rate of functionalization of the metallic and semimetallic SWNTs over the functionalization rate of semiconductor SWNTs. Under carefully controlled conditions, the selective functionalization with benzene diazonium salt even shows differences in the rate of reaction between the metallic and semimetallic nanotubes.<sup>61</sup> The selective nature of the functionalization reaction is apparent from the absorption spectra (Figure 9.6). The three peaks grouped in the region from 480 to 680 nm correspond to metallic and semimetallic nanotubes; the rest of the transitions correspond to semiconductors. After the addition of 12 equivalent of diazonium salt for every 1000 C atoms on the nanotube, these transitions are lost and the semiconductor transitions are unaffected. Raman spectra also show the same trend, wherein metallic carbon nanotubes react at a much faster rate than the semiconductors (Figure 9.7). The selective functionalization reaction was monitored by Raman excitation at 532 nm. This wavelength probes the metallics and one semiconductor, the (9, 2) SWNT (recall, as described above,  $9 - 2 = 7$ , which is not a

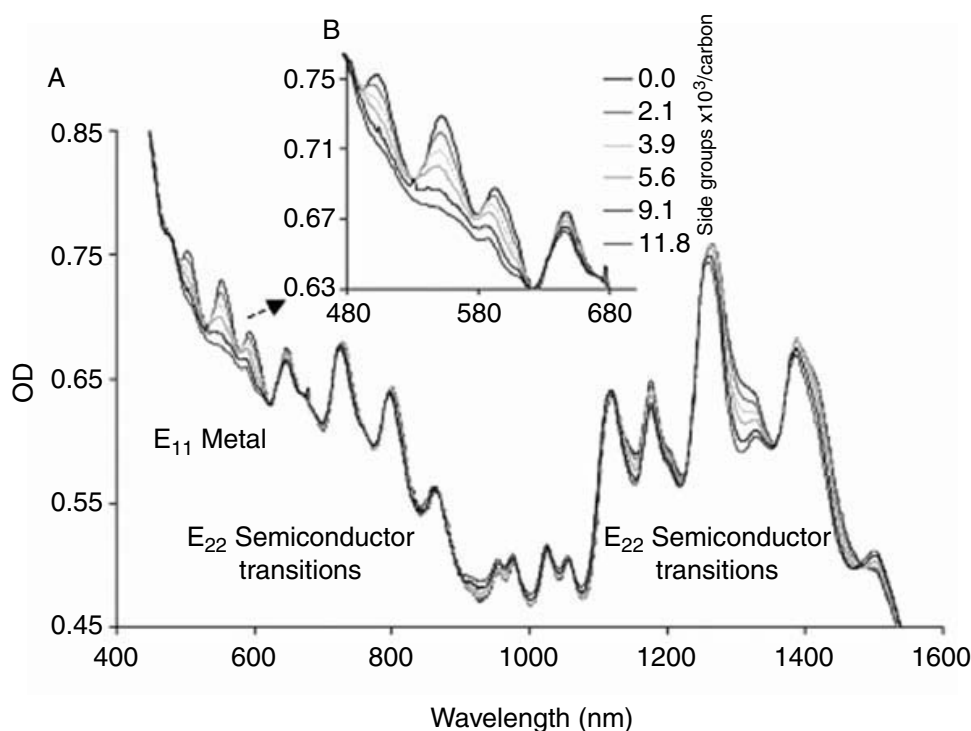


**Figure 9.6** Progressive loss of the van Hove absorption bands of the three metallic/semimetallic peaks in the region from 480 to 600 nm during slow addition of an aryl diazonium salt. The semiconducting SWNTs' bands remain largely unaffected. (Reproduced from Dyke, C. A. and Tour, J. M. Feature article: covalent functionalization of single-walled carbon nanotubes for materials applications, *J. Phys. Chem. A*, 108, 11151–11159, 2004. Copyright © 2004 American Chemical Society. With permission.)

multiple of 3; therefore, the (9, 2) tube is a semiconductor). Even upon loss of all of the radial breathing modes for the metallic SWNTs, the (9, 2) semiconducting SWNT remains largely unaffected.

The selective functionalization was recently used to possibly separate the metallic nanotubes from the semiconductors.<sup>60</sup> This was realized by selectively reacting a nonpolar addend onto the sidewall of the metallic carbon nanotubes, then reacting the semiconductors with a polar aryl moiety. Silica gel column chromatography was performed on the now chemically distinguished SWNT types, and the nonpolar component was collected, thermalized (which has been shown to remove the addends to regenerate the pristine SWNTs),<sup>42</sup> and analyzed. The thermolysis is typically performed with TGA by heating to 750°C in an inert atmosphere such as nitrogen or argon.<sup>31,36,37</sup> Raman analysis of the regenerated material showed that this separation did, in fact, give a SWNT sample enriched in the metallic nanotubes. This is most apparent by comparing the Raman spectra (at 633-nm excitation) of the starting mixture (Figure 9.8) against the enriched component (Figure 9.9). This wavelength of excitation probes both the metallic and semiconducting nanotubes; therefore, of the common Raman excitation wavelengths, 633-nm excitation gives valuable information about both

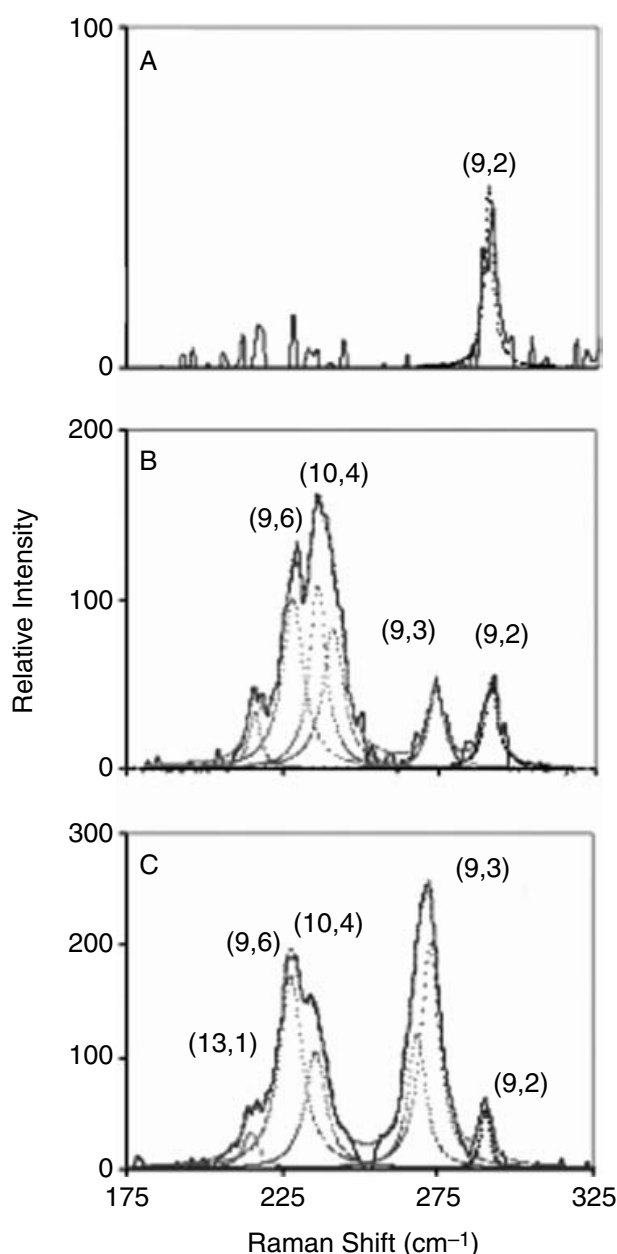


**Figure 9.7** Raman (532-nm excitation) (A) of radial breathing modes of the starting SWNTs, (B) after the addition of 6 equiv of 4-chlorobenzene diazonium salt, and (C) after the addition of 25 equiv of the diazonium salt. Only the semiconductor transition ( $n - m = 7 \neq 3q$ ) remains, while the semimetallic transitions ( $n - m = 3q$ ) are lost. (Reproduced from Dyke, C. A. and Tour, J. M. Feature article: covalent functionalization of single-walled carbon nanotubes for materials applications, *J. Phys. Chem. A.*, 108, 11151–11159, 2004. Copyright © 2004 American Chemical Society. With permission.)

nanotube types. Clearly, the separated material is enriched in the (13, 4) semimetallic carbon nanotube and the (9, 9) metallic species.<sup>36</sup> Thus, selective functionalization and separation offers prospects for interesting electronic and optoelectronic applications of SWNTs once the covalent functionalities are removed by thermolysis.

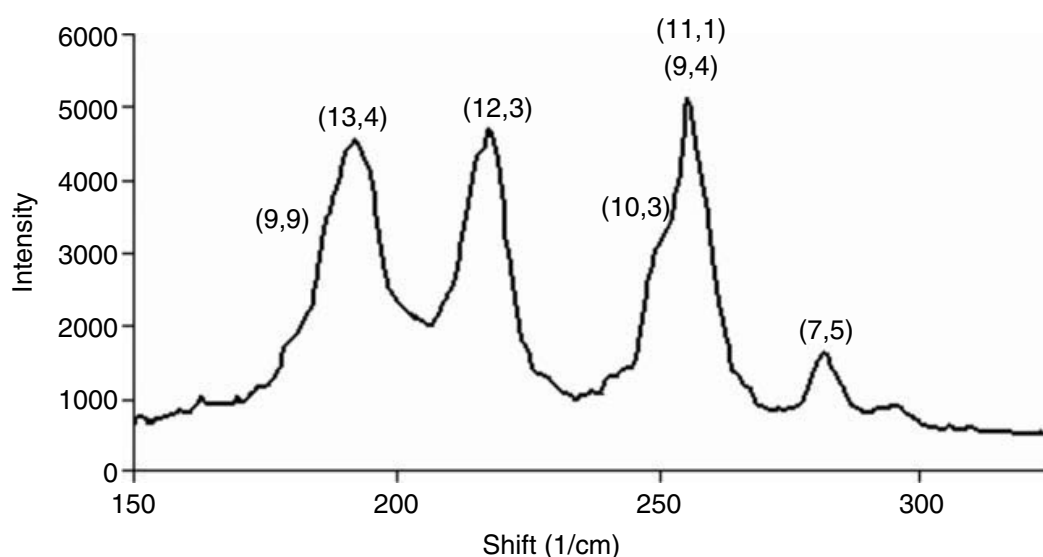


**Figure 9.8** Raman (633-nm excitation) of the starting SWNTs with the radial breathing modes assigned to specific tube types. (Reproduced from Dyke, C. A. and Tour, J. M. Feature article: covalent functionalization of single-walled carbon nanotubes for materials applications, *J. Phys. Chem. A.*, 108, 11151–11159, 2004. Copyright © 2004 American Chemical Society. With permission.)

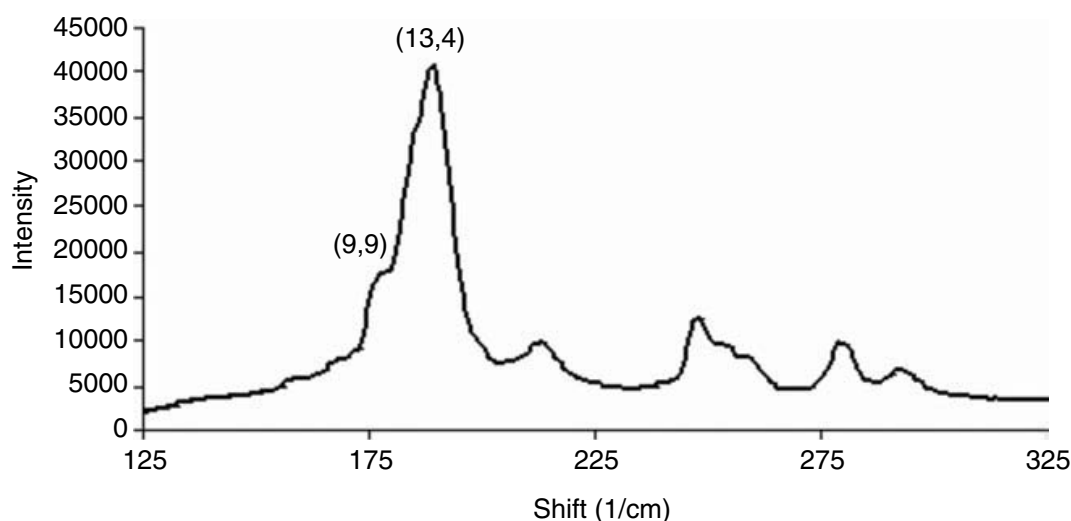


**Figure 9.9** Raman (633-nm excitation) analysis of the separated SWNT material enriched in metallics after functionalization, chromatography on silica gel, and thermolysis. (Reproduced from Dyke, C. A. and Tour, J. M. Feature article: covalent functionalization of single-walled carbon nanotubes for materials applications, *J. Phys. Chem. A.*, 108, 11151–11159, 2004. Copyright © 2004 American Chemical Society. With permission.)

## 9.4 Carbon nanotube-modified composites

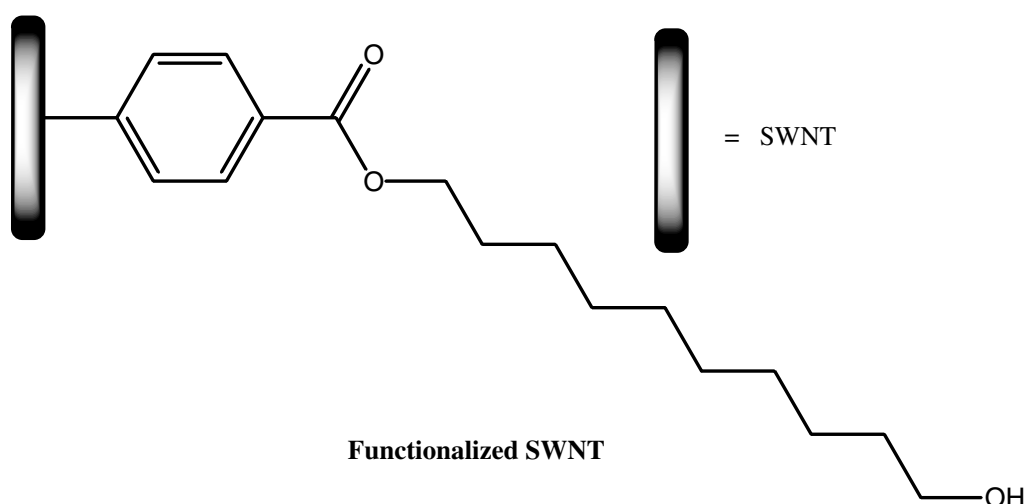
Polymer-based composites and blends, where polymers serve as the matrices for inorganic, organic, or carbon fillers, have had enormous impact as engineering materials, and they are widely used in commercial products. Often



carbon black, glass fibers, and phenolic resins are incorporated into the polymer hosts, resulting in significant improvements in mechanical properties, including impact strength and tensile and compressive moduli (stiffness) over that of the nonfilled polymer. As stated previously, SWNTs exhibit extraordinary mechanical properties,<sup>1,62,63</sup> such as tensile strengths of 50 to 200 GPa, estimated Young's moduli of 1 to 5 TPa, and high strains (ca. 5 to 6%) at break.<sup>64</sup> Further, when released from strain, bent SWNTs recover their original form without direct fracture.<sup>65</sup> On the basis of these extraordinary mechanical properties and the large aspect ratio (typically ~500 to 1000) associated with individual tubes, SWNTs are excellent candidates for the development of nano-reinforced polymer composite materials,<sup>17,66</sup> complementing or substituting the traditional carbon black and glass fiber fillers. Moreover, the functionalized SWNTs show further promise because their miscibility at >1 wt% levels in the polymer host is often enhanced relative to the unfunctionalized SWNTs.

Research on nanotube composites has concentrated, for the most part, on polymer-MWNT-based materials,<sup>67-70</sup> wherein they exhibit mechanical properties that are superior to conventional polymer-based composites due to their considerably higher intrinsic strengths and moduli, and the fact that the stress transfer efficiency can be 10 times higher than that of traditional additives.<sup>69</sup> However, polymer-SWNT composites show even more promise than the MWNT-based nanocomposites as potential high-performance engineering materials.<sup>71,72</sup> For instance, dynamic mechanical analysis (DMA) studies of *in situ* polymerized poly(methyl methacrylate) (PMMA)-SWNTs demonstrated that the tensile modulus increased by more than a factor of 2 with only 0.1 wt% SWNTs added.<sup>73</sup> These improvements are far in excess of that observed in the PMMA-MWNT nanocomposites. Independent experiments on PMMA-SWNTs at low nanotube concentrations (<1 wt%) indicate that the polymer is intimately mixed with the nanotubes. Furthermore, measurements of the melt rheology of polystyrene-SWNT nanocomposites indicate a substantial increase in the viscosity and elasticity of the system at low shear rates, even at 1 wt% SWNT loadings.<sup>17,66</sup> The low-frequency linear oscillatory shear moduli for polystyrene functionalized-SWNT nanocomposites demonstrate a transition from liquid-like to solid-like behavior associated with the formation of a percolated network structure, while that for the unfunctionalized SWNT and polystyrene remains liquid-like for nanocomposites with 3 wt% SWNT.<sup>17,66</sup> The formation of such a percolated nanoparticle network structure is a consequence of the dispersion of the functionalized SWNTs, the effective aspect ratio of the SWNTs, and, perhaps most importantly, the strength of the polymer-functionalized SWNT interaction. Thus, functionalization greatly increases the dispersion of SWNTs in polymer matrices, and the functional moiety increases the interfacial bonding or entanglement. This is in sharp contrast to unfunctionalized SWNTs, where dispersion and interfacial bonding or entanglement are minimal.

Elastomers are another class of composites that could be profoundly influenced by SWNT additions. Elastomers are used commercially in a wide



**Scheme 9.1** Functionalized carbon nanotubes used to make the SWNT–PDMS composite. (Reproduced from Dyke, C. A. and Tour, J. M. Feature article: covalent functionalization of single-walled carbon nanotubes for materials applications, *J. Phys. Chem. A.*, 108, 11151–11159, 2004. Copyright © 2004 American Chemical Society. With permission.)

range of applications in market segments, including rubber tires, which are the largest consumer of natural and synthetic rubbers. The North American synthetic rubber industry had a volume of 2.2 million metric tons in 2002.<sup>74</sup> Traditionally, additives are applied within elastomers to make them have a higher tensile modulus (stiffness), but the result is generally a concomitant large reduction in the strain at break (the stretch point at which the polymer will break). For the sake of illustration, polyisoprene shows a strain at break of ca. 10 (i.e., 1000%) or higher, meaning that it can stretch to 10 times its original length with nearly complete return to its original state upon release. By adding 30 to 50 wt% carbon black, the tensile modulus could increase 10-fold, but the strain at break could fall to 1.25 (125%); hence, it would no longer respond as an elastomer, but as a thermoplastic in dynamic mechanical properties. The development of high-strength elastomers with high breaking strains and low densities is crucial in many applications, including tires, belts, hoses, seals, O-rings, etc., that affect industries such as automotive, engine, aerospace, and oil drilling and refining. Therefore, to be able to stiffen elastomers while retaining the strain-at-break properties is highly desirable.

We have recently developed model functionalized SWNT reinforced networks of an amine-terminated poly(dimethylsiloxane) (PDMS) (Scheme 9.1) that typifies the extraordinary effects of functionalized SWNT-filled elastomeric composites.<sup>75</sup> Typical data for the tensile stress vs. strain for one such nanocomposite, along with a comparable PDMS network with roughly the same cross-link density (based on solvent swelling), are shown in Figure 9.10. Comparison of the tensile modulus and the elongation at break for a series of nanocomposites is shown in Figure 9.11. Note that the functionalized SWNT material (Scheme 9.1) was prepared by the dry functionalization

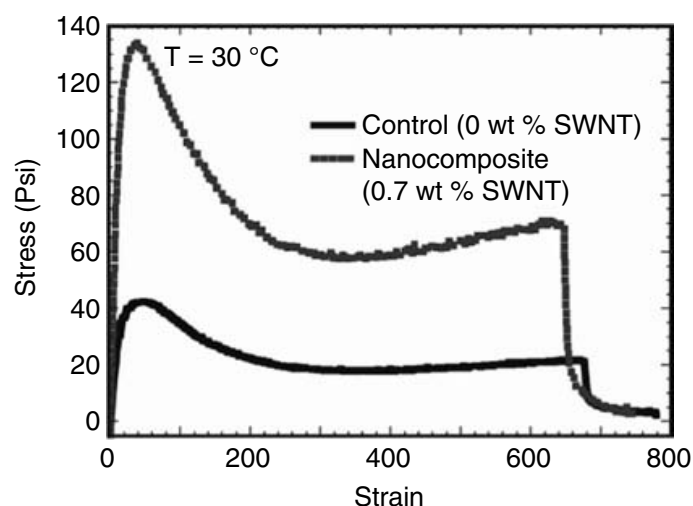


**Figure 9.10** Tensile testing of a 0.7 wt% functionalized SWNT-filled PDMS nanocomposite compared to a similarly cross-linked PDMS network that contains no nanotubes. The sample was stretched at a rate of 2 mm/min in a mini-Instron tester. (Reproduced from Dyke, C. A. and Tour, J. M. Feature article: covalent functionalization of single-walled carbon nanotubes for materials applications, *J. Phys. Chem. A.*, 108, 11151–11159, 2004. Copyright © 2004 American Chemical Society. With permission.)

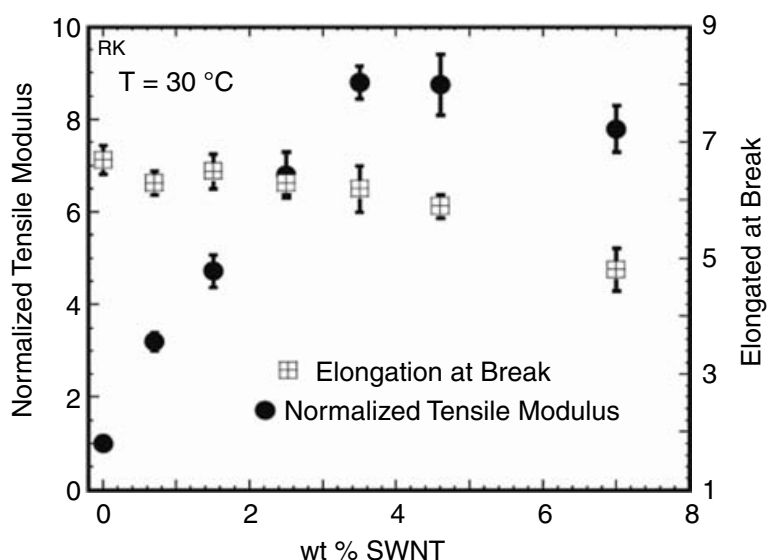


**Figure 9.11** Composition dependence and elongation at break for the functionalized PDMS nanocomposite shown in Figure 9.10. (Reproduced from Dyke, C. A. and Tour, J. M. Feature article: covalent functionalization of single-walled carbon nanotubes for materials applications, *J. Phys. Chem. A.*, 108, 11151–11159, 2004. Copyright © 2004 American Chemical Society. With permission.)

process that produces small bundles,<sup>45</sup> and even greater enhancement is expected with unbundled, functionalized SWNTs. These results are remarkable because the tensile modulus and strength are considerably increased while the strain at break is largely unchanged. The area under the curves in

Figure 9.10 is proportional to the energy needed to cause polymer failure. Further, the data suggest an optimal network structure at 3 to 4 wt% addition of the functionalized SWNTs (Figure 9.11). There is no other elastomer additive system known that can so dramatically increase the tensile modulus with so little effect on the strain at break, underscoring the applicability of functionalized SWNT composites. One only needs a compatibilizing nanotube functionalization pendant for efficient polymer blending and miscibility, and it should be readily extendable to a wide range of elastomers and network-forming polymers, including high-temperature epoxies.<sup>33</sup> Considering polymeric pendants emanating from the functionalized SWNTs (and in the extreme, every polymer chain in the composite bound to a nanotube), pendants may be required to have molecular weights similar to the molecular weight of the polymer, or else miscibility will be disfavored due to an unfavorable entropy of mixing. However, this could be overcome enthalpically by using polymeric pendants that are known to mix well with the polymer host.

In light of the above considerations, for their full potential to be realized, SWNT sidewall functionalization must be achieved, thereby generating reinforced polymer and composite material.<sup>17,66,75</sup> Not only does functionalization give nanotubes with increased solubility in organic solvent, but these modified nanotubes disperse far better in polymers than the unfunctionalized SWNTs. Agglomeration must be overcome to give well-dispersed material, and since the organic moieties prevent bundling, agglomeration is lessened and dispersion is increased. Also, functionalization with an appropriate handle gives carbon nanotubes with increased interfacial bonding to the polymer, thereby lessening fiber pullout during mechanical stress. In multicomponent, cross-linked composite material, such as elastomers, carbon nanotubes with an appropriate addend can be covalently attached to the host, thereby creating greatly fortified, novel nanocomposite structures that maintain elongation to break with increased modulus.

## 9.5 Conclusions

Covalent functionalization of carbon nanotubes gives researchers the ability to manipulate these entities in typical organic solvents or even in solvent-free conditions. Functionalization can be done on the as-generated SWNT bundles to afford functionalized SWNT bundles. However, using protocols that disperse the SWNTs as individuals in the reaction medium (such as wrapping with surfactants, using oleum or Li/liquid ammonia), functionalization can ensure individual unbundled SWNTs. These unbundled entities should prove to be the optimal additives for nanocomposites. Since selective reaction chemistries are now available that can react preferentially with SWNTs based on nanotube type ( $n$ ,  $m$  value), functionalization allows the manipulation and separation of highly enriched SWNT fractions. Covalent sidewall functionalization also overcomes the issues of poor interfacial bonding and dispersion in host polymeric matrices, and thus routes to unprecedented

ultra-high-performance blends and composites are being realized. For all of these reasons, functionalization of carbon nanotubes allows scientists to manipulate these incredible materials in ways unimagined previous to the development of this technology, and should give researchers material for use in most or all of NNI's grand challenge areas.

## Acknowledgments

Much of the composite and rheological work described here was done in collaboration with Professor Ramanan Krishnamoorti at the University of Houston, to whom we are greatly indebted. We thank the National Aeronautics and Space Administration (NASA), the Office of Naval Research (ONR), the Defense Advanced Research Projects Agency (DARPA), and the National Science Foundation (NSF) for their gracious support of our SWNT research program, and the late Professor Richard Smalley of Rice University for the generous supply of HiPco SWNTs.

## References

1. Saito, R., Dresselhaus, G., and Dresselhaus, M. S. *Physical Properties of Carbon Nanotubes*, Imperial College Press, London, 1998.
2. Javey, A. et al. Ballistic carbon nanotube field-effect transistors, *Nature*, 424, 654, 2003.
3. Iijima, S. Helical microtubules of graphitic carbon, *Nature*, 354, 56, 1991.
4. Dresselhaus, M., Dresselhaus, G., and Avouris, P. *Carbon Nanotubes: Synthesis, Structure, Properties and Applications*, Springer-Verlag, Berlin, 2001.
5. de Heer, W. A. Nanotubes and the pursuit of applications, *MRS Bull.*, 29, 281, 2004.
6. Zheng, M. et al. DNA-assisted dispersion and separation of carbon nanotubes, *Nat. Mater.*, 2, 338, 2003.
7. Krupke, R. et al. Separation of metallic from semiconducting single-walled carbon nanotubes, *Science*, 301, 344, 2003.
8. Misewich, J. A. et al. Electrically induced optical emission from a carbon nanotube FET, *Science*, 300, 783, 2003.
9. Li, J., et al. Bottom-up approach for carbon nanotube interconnects, *Appl. Phys. Lett.*, 82, 2491, 2003.
10. Yu, M.-F., Dyer, M. J., and Ruoff, R. S. Structure and mechanical flexibility of carbon nanotube ribbons: an atomic-force microscopy study, *J. Appl. Phys.*, 89, 4554, 2001.
11. Buongiorno Nardelli, M., Yakobson, B. I., and Bernholc, J. Mechanism of strain release in carbon nanotubes, *Phys. Rev. B*, 57, R4277, 1998.
12. Thess, A. et al. Crystalline ropes of metallic carbon nanotubes, *Science*, 273, 483, 1996.
13. Nikolaev, P. et al. Gas-phase catalytic growth of single-walled carbon nanotubes from carbon monoxide, *Chem. Phys. Lett.*, 313, 91, 1999.
14. Huang, S., Cai, X., and Liu, J. Growth of millimeter-long and horizontally aligned single-walled carbon nanotubes on flat substrates, *J. Am. Chem. Soc.*, 125, 5636, 2003.



15. O'Connell, M. J. et al. Reversible water-solubilization of single-walled carbon nanotubes by polymer wrapping, *Chem. Phys. Lett.*, 342, 265, 2001.
16. Bahr, J. L. et al. Dissolution of small diameter single-wall carbon nanotubes in organic solvents?, *Chem. Comm.*, 193, 2001.
17. Mitchell, C. A. et al. Dispersion of functionalized carbon nanotubes in polystyrene, *Macromolecules*, 35, 8825, 2002.
18. Lourie, O. and Wagner, H. D. Transmission electron microscopy observations of fracture of single-wall carbon nanotubes under axial tension, *Appl. Phys. Lett.*, 73, 3527, 1998.
19. Peigney, A. et al. Aligned carbon nanotubes in ceramic-matrix nanocomposites prepared by high-temperature extrusion, *Chem. Phys. Lett.*, 352, 20, 2002.
20. Hadjiev, V. G. et al. Raman scattering test of single-wall carbon nanotube composites, *Appl. Phys. Lett.*, 78, 3193, 2001.
21. Banerjee, S., Kahn, M. G. C., and Wong, S. S. Rational chemical strategies for carbon nanotube functionalization, *Chem. Eur. J.*, 9, 1898, 2003.
22. Niyogi, S. et al. Chemistry of single-walled carbon nanotubes, *Acc. Chem. Res.*, 35, 1105, 2002.
23. Hirsch, A. Functionalization of single-walled carbon nanotubes, *Angew. Chem. Int. Ed. Engl.*, 41, 1853, 2002.
24. Bahr, J. L. and Tour, J. M. Covalent chemistry of single-wall carbon nanotubes: a review, *J. Mater. Chem.*, 12, 1952, 2002.
25. Strano, M. S. et al. The role of surfactant adsorption during ultrasonication in the dispersion of single-walled carbon nanotubes, *J. Nanosci. Nanotechnol.*, 3, 81, 2003.
26. O'Connell, M. J. et al. Band gap fluorescence from individual single-walled carbon nanotubes, *Science*, 297, 593, 2002.
27. Bachilo, S. M. et al. Structure-assigned optical spectra of single-walled carbon nanotubes, *Science*, 5602, 2361, 2002.
28. Fu, K. et al. Defunctionalization of functionalized carbon nanotubes, *Nano Lett.*, 1, 439 2001.
29. Hamon, M. A. et al. Ester-functionalized soluble single-walled carbon nanotubes, *Appl. Phys. A*, 74, 333, 2002.
30. Wong, S. S. et al. Covalently functionalized nanotubes as nanometer-sized probes in chemistry and biology, *Nature*, 394, 52, 1998.
31. Strano, M. S. et al. Electronic structure control of single walled carbon nanotube functionalization, *Science*, 301, 1519, 2003.
32. Tour, J. M. and Krishnamoorti, R. Unpublished data.
33. Zhu, J. et al. Improving the dispersion and integration of single-walled carbon nanotubes in epoxy composites through functionalization, *Nano Lett.*, 3, 1107, 2003.
34. Hennrich, F. et al. Preparation, characterization, and applications of free-standing single walled carbon nanotube thin films, *Phys. Chem. Chem. Phys.*, 4, 2273, 2002.
35. Chiang, I. W. et al. Purification and characterization of single-wall carbon nanotubes (SWNTs) obtained from the gas-phase decomposition of CO (HiP-co process), *J. Phys. Chem. B*, 105, 8297, 2001.
36. Dyke, C. A. and Tour, J. M. Overcoming the insolubility of carbon nanotubes through high degrees of sidewall functionalization, *Chem.-Eur. J.*, 10, 813, 2004.

37. Bahr, J. L. et al. Functionalization of carbon nanotubes by electrochemical reduction of aryl diazonium salts: a bucky paper electrode, *J. Am. Chem. Soc.*, 123, 6536, 2001.
38. Islam, M. F. et al. High weight fraction surfactant solubilization of single-wall carbon nanotubes in water, *Nano Lett.*, 3, 269, 2003.
39. Shim, M. et al. Functionalization of carbon nanotubes for biocompatibility and biomolecular recognition, *Nano Lett.*, 2, 285, 2002.
40. Moore, V. C. et al. Individually suspended single-walled carbon nanotubes in various surfactants, *Nano Lett.*, 3, 1379, 2003.
41. Dyke, C. A. and Tour, J. M. Unbundled and highly functionalized carbon nanotubes from aqueous reactions, *Nano Lett.*, 3, 1215, 2003.
42. Dyke, C. A. et al. Diazonium-based functionalization of carbon nanotubes: XPS and GC-MS analysis and mechanistic implications, *Synlett*, 155, 2004.
43. Bahr, J. L. and Tour, J. M. Highly functionalized carbon nanotubes using *in situ* generated diazonium compounds, *Chem. Mater.*, 13, 3823, 2001.
44. Hudson, J. L., Casavant, M. J., and Tour, J. M. Water-soluble, exfoliated, nonroping single-wall carbon nanotubes, *J. Am. Chem. Soc.*, 126, 11158, 2004.
45. Dyke, C. A. and Tour, J. M. Solvent-free functionalization of carbon nanotubes, *J. Am. Chem. Soc.*, 125, 1156, 2003.
46. Davis, V. A. et al. Phase behavior and rheology of SWNTs in superacids, *Macromolecules*, 37, 154, 2004.
47. Mickelson, E. T. et al. Fluorination of single-wall carbon nanotubes, *Chem. Phys. Lett.*, 296, 188, 1998.
48. Mickelson, E. T. et al. Solvation of fluorinated single-wall carbon nanotubes in alcohol solvents, *J. Phys. Chem. B*, 103, 4318, 1999.
49. Khabashesku, V. N., Billups, W. E., and Margrave, J. L. Fluorination of single-wall carbon nanotubes and subsequent derivatization reactions, *Acc. Chem. Res.*, 35, 1087, 2002.
50. Ying, Y. et al. Functionalization of carbon nanotubes by free radicals, *Org. Lett.*, 5, 1471, 2003.
51. Liang, F. et al. A convenient route to functionalized carbon nanotubes, *Nano Lett.*, 4, 1257, 2004.
52. Georgakilas, V. et al. Organic functionalization of carbon nanotubes, *J. Am. Chem. Soc.*, 124, 760, 2002.
53. Holzinger, M. et al. Functionalization of single-walled carbon nanotubes with (R-)oxycarbonyl nitrenes, *J. Am. Chem. Soc.*, 125, 8566, 2003.
54. Coleman, K. S. et al. Functionalization of single-walled carbon nanotubes via the Bingel reaction, *J. Am. Chem. Soc.*, 125, 8722, 2003.
55. Kamaras, K. et al. Covalent bond formation to a carbon nanotube metal, *Science*, 301, 1501, 2003.
56. Banerjee, S. and Wong, S. S. Selective metallic tube reactivity in the solution-phase osmylation of single-walled carbon nanotubes, *J. Am. Chem. Soc.*, 126, 2073, 2004.
57. Chen, Z. H. et al. Bulk separative enrichment in metallic or semiconducting single-walled carbon nanotubes, *Nano Lett.*, 3, 1245, 2003.
58. Chattopadhyay, D., Galeska, I., and Papadimitrakopoulos, F. A route for bulk separation of semiconducting from metallic single-wall carbon nanotubes, *J. Am. Chem. Soc.*, 125, 3370, 2003.
59. Zheng, M. et al. Structure-based carbon nanotube sorting by sequence-dependent DNA assembly, *Science*, 302, 1545, 2003.

60. Dyke, C. A., Stewart, M. P., Tour, J. M. Separation of single-walled carbon nanotubes on silica gel. Materials morphology and Raman excitation wavelength affect data interpretation, *J. Am. Chem. Soc.*, 127, 4497, 2005.
61. Strano, M. S. Probing chiral selective reactions using a revised Kataura plot for the interpretation of single-walled carbon nanotube spectroscopy, *J. Am. Chem. Soc.*, 125, 16148, 2003.
62. Yakobson, B. I., Brabec, C. J., and Bernholc, J. Nanomechanics of carbon tubes: instabilities beyond linear response, *Phys. Rev. Lett.*, 76, 2511, 1996.
63. Walters, D. A. et al. Elastic strain of freely suspended single-wall carbon nanotube ropes, *Appl. Phys. Lett.*, 74, 3803, 1999.
64. Yu, M.-F. et al. Tensile loading of ropes of single wall carbon nanotubes and their mechanical properties, *Phys. Rev. Lett.*, 84, 5552, 2000.
65. Cooper, C. A., Young, R. J., and Halsall, M. Investigation into the deformation of carbon nanotubes and their composites through the use of Raman spectroscopy, *Composites A Appl. Sci. Mfg.*, 32, 401, 2001.
66. Barraza, H. J. et al. SWNT-filled thermoplastic and elastomeric composites prepared by miniemulsion polymerization, *Nano Lett.*, 2, 797, 2002.
67. Qian, D. et al. Load transfer and deformation mechanisms in carbon nanotube-polystyrene composites, *Appl. Phys. Lett.*, 76, 2868, 2000.
68. Wagner, H. D. et al. Stress-induced fragmentation of multiwall carbon nanotubes in a polymer matrix, *Appl. Phys. Lett.*, 72, 188, 1998.
69. Schadler, L. S., Giannaris, S. C., and Ajayan, P. M. Load transfer in carbon nanotube epoxy composites, *Appl. Phys. Lett.*, 73, 3842, 1998.
70. Cooper, C. A. and Young, R. J. Investigation of structure/property relationships in particulate composites through the use of Raman spectroscopy, *J. Raman Spectrosc.*, 30, 929, 1999.
71. Steuerman, D. W. et al. Interactions between conjugated polymers and single-walled carbon nanotubes, *J. Phys. Chem. B*, 106, 3124, 2002.
72. Wei, C. Y., Srivastava, D., and Cho, K. J. Thermal expansion and diffusion coefficients of carbon nanotube-polymer composites, *Nano Lett.*, 2, 647, 2002.
73. Stephan, C. et al. Characterization of single-walled carbon nanotube-PMMA composites. *Synth. Met.*, 108, 139, 2000.
74. Tullo, A. H. Synthetic rubber, *Chem. Eng. News*, 81, 23, 2003.
75. Krishnamoorti, R., Dyke, C. A., and Tour, J. M. Unpublished work.

## *chapter ten*

---

# *Carbon nanotube tips for scanning probe microscopy*

*C. Patrick Collier*

*California Institute of Technology*

### *Contents*

10.1 Carbon nanotubes as AFM probes.....	295
10.2 Fabrication of nanotube probe tips.....	297
10.3 AFM imaging with nanotube probes .....	299
10.4 Applications of carbon nanotube probes.....	303
10.4.1 Applications in structural biology .....	303
10.4.2 Nanolithography .....	304
10.4.3 SWNT probe functionalization .....	304
10.4.4 Nanoelectrode scanning probes.....	305
10.5 Future directions .....	308
Acknowledgments .....	309
References.....	309

## *10.1 Carbon nanotubes as AFM probes*

Atomic force microscopy (AFM) has become an indispensable tool due to its ability to image and manipulate matter at the nanometer scale in air, liquid, or vacuum. The AFM uses a micromachined silicon or silicon nitride probe mounted on a flexible cantilever that can sense or generate forces between the probe tip and a sample surface. The AFM can thus be used as either an imaging instrument or a manipulation device.<sup>1</sup> Because it can acquire high-resolution topographical images in physiologically relevant aqueous environments, AFM has become especially important for structural biology and biophysics.<sup>2</sup>

AFM is distinct from other highly sensitive techniques for measuring intermolecular forces, such as the surface force apparatus and optical tweezers, due to the high spatial resolution possible and the capability to dynamically measure and control time-dependent forces.<sup>3</sup> In addition to obtaining topographic images of biological structures, AFM can probe dynamic processes in solution, such as chemically and mechanically induced unfolding mechanisms in proteins<sup>4</sup> and DNA.<sup>5</sup> In chemical force microscopy, chemically functionalized tips have been used to map the spatial arrangement of chemical functional groups on a macromolecule, and to measure the interactions between different functional groups from changes in adhesive forces as a function of pH.<sup>6</sup> Van der Waals, hydrogen-bond, and electrostatic interactions can be measured this way.

The level of resolution possible in AFM for both single-molecule imaging and force transduction is ultimately limited by the structure of the tip. Commercially available silicon probe tips have radii of curvature of 5 to 15 nm and cone angles of 20° to 30°. These tips make imaging large, isolated macromolecules, such as proteins with high resolution, difficult.<sup>7</sup> In addition, the variations in tip-to-tip properties are often substantial, which leads to uncertainty in interpreting image or force data due to poorly characterized tip-sample interactions.<sup>8</sup>

Carbon nanotubes are, in many respects, ideal high-resolution probe tips for AFM.<sup>7</sup> Carbon nanotubes are hollow cylinders formed from rolled-up graphene sheets that can be up to microns in length. A single-walled nanotube (SWNT) consists of a single graphene sheet, one atom thick, rolled up seamlessly into a cylinder with a diameter ranging from 0.7 to 6 nm. SWNTs can be used as high-aspect-ratio probes with radii comparable to molecular-scale dimensions. Individual SWNTs can bundle together, driven by attractive van der Waals forces, to form SWNT ropes containing up to hundreds of nanotubes each. Multiwalled nanotubes (MWNTs) consist of concentric graphene cylinders and can have diameters ranging from 6 to 100 nm.

Carbon nanotubes are chemically and mechanically robust. Both single-walled and multiwalled nanotubes are the stiffest material known, with Young's moduli of about 1.25 to 1.3 TPa,<sup>9,10</sup> which limits the noise due to thermal vibrations from degrading the ultimate obtainable resolution. Unlike other materials, carbon nanotubes can buckle and bend elastically under large loads, limiting damage to both the tips and the sample.<sup>11</sup> Because nanotubes have well-defined molecular structures, the tip-sample interaction is better characterized and more reproducible than with conventional probes. This combination of mechanical properties and repeatable small size of SWNT probe tips makes them uniquely suited for robust AFM resolution at the molecular scale.

AFM probes fabricated with individual SWNTs vs. MWNTs or SWNT bundles have different imaging characteristics and properties. There are trade-offs between various figures of merit for each type of nanotube probe, and the choice of which one to use will be different depending on the intended application. For example, AFM probes assembled using MWNTs



or SWNT bundles having diameters greater than 5 to 10 nm are ideally suited for imaging rough terrain, such as narrow, deep recesses and other high-aspect-ratio features that are inaccessible to conventional microfabricated probes. Probes fabricated with *individual* SWNTs represent the ultimate in resolution, but are more susceptible to lateral bending and other deformation modes that can impact image quality.

The state of the art in fabrication methods and applications of carbon nanotube AFM probe tips up to 2001 has been published in review articles.<sup>7,12</sup> In this chapter, we will summarize the earlier results and present developments that have occurred in the intervening 3 years, from both experimental and theoretical viewpoints. These recent advances have enriched the field and increased our understanding of the capabilities of carbon nanotube AFM tips, as well as some of their limitations. Although carbon nanotubes were initially intended as high-resolution topographical imaging probes, their unique mechanical, electrical, and chemical properties have been exploited for more than just conventional AFM, impacting virtually every field in the scanning probe microscopy family, including scanning tunneling microscopy (STM), near-field scanning optical microscopy (NSOM), and scanning conductive probe microscopy, permitting a broad array of applications, from microelectronics to structural biology.

## 10.2 Fabrication of nanotube probe tips

Smalley's group reported the first example of the use of carbon nanotubes as scanning probe tips in 1996.<sup>13</sup> They manually attached multiwalled carbon nanotubes and ropes of individual SWNTs to the apex of silicon pyramidal tips using tape adhesive and a micromanipulator in an optical microscope. The attached nanotube tips were usually too long to be useful for high-resolution topographical imaging due to thermal vibrations. The length of the nanotube could be shortened *in situ* in the AFM by electrical pulse etching of the probe tip on a conductive surface. The drawbacks to this method were that the mounting process was slow and painstaking, and larger nanotube structures like MWNTs that could be imaged by the optical microscope were more likely to be attached. Nevertheless, this study was the first to demonstrate several important advantages that nanotube probes have in general over conventional AFM tips. The high aspect ratio of the nanotubes enabled more accurate imaging of the sidewalls of deep silicon trenches. Strong adhesive forces between the sample surface and an AFM tip that complicate imaging with conventional probes were greatly reduced in the case of nanotube tips, due to their small size and cylindrical geometry. Finally, this study demonstrated that the nanotube probes elastically buckled at higher contact forces.

Since then, several reports have described manual assembly of nanotube probes, using optical microscopes as well as inside scanning electron microscopes (SEMs) for the fabrication of AFM tips,<sup>14–21</sup> STM tips,<sup>13,22–26</sup> and even near-field optical probes.<sup>27</sup> Nanotube AFM probes manually assembled from

MWNTs with this method are available commercially (e.g., [www.npoint.com](http://www.npoint.com)). In addition to the use of adhesives, other methods for bonding probes have been developed, including spot welding the attachment site of the nanotube on the tip support and deposition of amorphous carbon from the electron beam in the SEM. The ability to visualize the mounting of the probe and its morphology during fabrication allows one to optimize the characteristics of the probe almost in real time. Examples include controlling the length of individual MWNTs on support tips by Joule heating or application of mechanical force,<sup>26,28</sup> sharpening a nanotube probe via extraction of an inner shell from an attached MWNT<sup>29</sup> or by stripping away outer layers locally at the tip,<sup>30</sup> and tuning the projection angle of attached SWNT bundles by repeated AFM scanning of the probe across an array of tall pillars.<sup>31</sup> Of course, the degree of control possible will depend on the imaging resolution of the microscope employed. Ultimate resolution requires *individual* SWNT tips. Wong and coworkers manually attached bundles of SWNTs to AFM tips that were approximately 10 nm in diameter and contained up to hundreds of SWNTs each, but occasionally the electrical etching procedure would result in the exposure of one or a few SWNTs at the tip apex to give a high-resolution probe.<sup>32,33</sup>

Lieber's group<sup>34</sup> and Cooper et al.<sup>35</sup> were the first to show that individual single-wall carbon nanotubes could be directly grown by chemical vapor deposition (CVD) on the silicon tips themselves by first precoating the tip with a metal catalyst. Direct-growth techniques were later applied to electrochemically etched tungsten tips for STM.<sup>36</sup> Unlike manual assembly methods, CVD can be potentially applied to massively parallel fabrication of nanotube probe tips on a wafer scale.<sup>37–39</sup> In the CVD synthesis of carbon nanotubes, metal catalyst nanoparticles are heated in the presence of a hydrocarbon gas or carbon monoxide; the gas molecules dissociate on the catalyst surface and carbon is absorbed into the particle. As the carbon precipitates, a carbon nanotube is grown with a diameter similar to that of the catalyst particle. Varying the concentration of the catalyst on the tip controls the distribution of MWNTs to SWNTs, and the particle diameter controls the diameter of the tube.

Early work with direct CVD growth involved creating nanopores, by etching the silicon tip in hydrofluoric acid; the nanopores could then have catalyst particles deposited inside them.<sup>40</sup> The CVD growth of the carbon nanotubes from pores located at the flattened apex of the silicon tip had the correct geometry for AFM imaging. Now, individual SWNT tips could be prepared, but the preparation of the porous layer in the silicon was still time-consuming, and often placement of the nanotube at the optimal location near the tip apex was not achieved. Later, direct surface growth of SWNTs by CVD on silicon tips was demonstrated, without the use of pores.<sup>41,35</sup> Individual SWNT tips could be prepared this way by lowering the catalyst density coating the silicon tip, although this also reduced the tip yield.<sup>42</sup> [Figure 10.1](#) is a schematic of CVD nanotube tip growth methods.

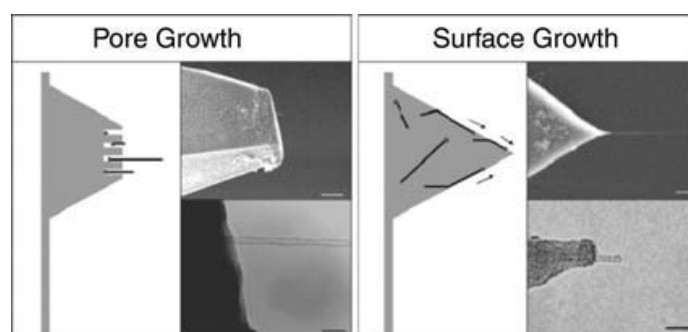


**Figure 10.1** CVD nanotube tip growth methods. (From Odom, T.W. et al., *Top. Appl. Phys.*, 80, 200, 2001, Figure 20. Copyright © 2001 Springer-Verlag, Berlin-Heidelberg. With permission.)

Hafner et al. devised a hybrid CVD/assembly approach, known as the pickup technique, which significantly increased the yield of high-resolution AFM probes fabricated from individual SWNTs.<sup>43</sup> When SWNTs are grown by CVD on a flat substrate, some fraction of the tubes are oriented vertically and can be picked up when the AFM tip scans across the surface in tapping (intermittent contact) mode.<sup>44,45</sup> The nanotube binds to the side of the AFM tip via attractive van der Waals forces and can remain attached firmly enough that it can be repeatedly pressed into and scanned across the substrate surface. Pickup SWNT tips can be shortened to useful lengths by a combination of push shortening (incrementally pushing the nanotube up the side of the AFM tip during successive force calibrations) and electrical pulse etching. Imaging in liquids with SWNT tips was made possible by coating the silicon tip pyramid with a thin layer of a UV-curable adhesive before pickup. The pickup technique was an important milestone in carbon nanotube AFM probe manufacture because of the increased tip yield compared to either manual assembly or direct-growth methods described earlier. In exceptional cases, production of high-quality SWNT tips at rates as high as several per hour over the course of several consecutive hours has been reported.<sup>45</sup>

Liquid phase deposition techniques for assembling nanotube probes are also being explored, such as magnetophoretic<sup>46</sup> and dielectrophoretic<sup>47</sup> attachment of MWNTs onto gold-coated AFM tips from liquid suspensions, dip-coating tips in a sol-gel containing nanotubes,<sup>48</sup> and covalent attachment of chemically functionalized SWNTs to self-assembled monolayers on gold AFM<sup>49</sup> and STM tips.<sup>50</sup>

### 10.3 AFM imaging with nanotube probes

To determine the performance capabilities and obtainable resolution for carbon nanotube probes, a more quantitative understanding of tip-sample interactions is needed. These interactions will, of course, be dependent on the type of scanned probe microscopy performed (e.g., tapping-mode vs. noncontact mode AFM), the environment, the type of nanotube tip

employed, and the intended application. In a simple geometric model for the nanotube tip-sample interaction, the ultimate resolution possible will be determined solely by the size of the tip. However, carbon nanotube probes have unique properties compared to conventional tips that can strongly affect imaging fidelity in AFM, sometimes in unexpected ways.

Colloidal gold nanoparticles are useful imaging standards to characterize nanotube tip resolution, because of their monodispersity in size and shape, and their incompressibility.<sup>51</sup> The effective tip size can be calculated from images of the particles based on the two-sphere model of Bustamante and coworkers.<sup>52</sup> Using this characterization method, Wong et al. reported that manually assembled MWNT probes had limiting tip radii of about 6 nm,<sup>14</sup> while manually assembled SWNT probes, which consisted of bundles of 1.4-nm-diameter SWNTs, had effective imaging radii of about 3.5 nm.<sup>14,33</sup> Direct-CVD-growth MWNTs from porous silicon AFM tips had limiting radii ranging from 3.5 to 6 nm.<sup>34</sup> Both pore growth<sup>40</sup> and surface growth<sup>41,42</sup> SWNT bundles had effective radii in the 2- to 4-nm range. An effective radius of just 1 nm was reported for a pickup SWNT AFM tip.<sup>43</sup> In some cases, comparable results have been reported for silicon or silicon nitride probes,<sup>53</sup> but in those cases, high resolution was likely due to fragile tip asperities, which were not well defined. Notably, the range of limiting nanotube tip radii calculated from high-resolution AFM images of colloidal gold nanoparticles were reported to agree with transmission electron microscopy (TEM) measurements of the probes.<sup>7,12</sup>

Simple models of AFM resolution assume that the probe is a rigid, incompressible cylinder with a flat or hemispherical end. In practice, this is not the case. While nanotubes have exceptional longitudinal stiffness,<sup>9,10</sup> radially they are far more compliant, especially SWNTs, a characteristic that renders these tubes susceptible to bending or localized deformations of the nanotube walls. Snow et al. have shown that image artifacts and snap-to-contact behavior can result from tubes that exceed either a critical length or a critical angle relative to the substrate surface normal.<sup>54,55</sup> High-magnification TEM images show that the nanotube probe ends are open due to ablation from the electrical pulse etching procedure used to shorten the tubes to useful lengths. The likelihood of deformation is further increased due to structural discontinuities at the open end of the nanotube probe.

Our group has carried out a rigorous examination of the influence of nanotube probe morphology on AFM image resolution and quality by directly correlating scans taken with several pickup SWNT probes operating in tapping-mode AFM in air with TEM images taken of these probes.<sup>45</sup> The sample in this study consisted of individual SWNTs lying flat on the same silicon oxide growth substrate used to fabricate the nanotube AFM tips. By correlating probe structure and orientation seen in the TEM images with topographic AFM imaging performance, we have provided direct experimental evidence consistent with the mechanical modeling studies carried out by Snow et al.<sup>54,55</sup> Other artifacts in addition to tip broadening can affect imaging. For example, we found that a SWNT projecting from the AFM tip

at a  $40^\circ$  angle produced an image containing a positive height shadowing artifact approximately 10 nm in width parallel to each sample nanotube, due to the nonideal orientation of the probe. Additionally, the TEM image for that probe showed that the nanotube was buckled near the silicon tip apex. Previous reports have described reversible *elastic* buckling of the nanotube, which did not have a serious impact on image quality.<sup>10,40,43</sup> Our TEM correlations indicated, however, that buckling can, under some circumstances, be inelastic, resulting in irreversible structural changes.

We found that images taken with high-quality SWNT probes (i.e., those that were not too long and were oriented close to perpendicular with respect to the substrate) showed no sign of artifacts. By comparing the observed AFM resolution with the diameter of the nanotube probe measured from the corresponding TEM image, it was found that the lateral resolution was, on average, 1.2 times the nanotube probe diameter, a value that approached the ideal ratio of unity in the absence of thermal vibrations and bending effects of the probe.

Surprisingly, we found that for some cases, the apparent lateral resolution was actually *better* than expected on the basis of the probe diameter, as determined by TEM. The nanotube tip in Figure 10.2 is one such case. The lateral resolution from this 5.5-nm-diameter probe was 1.2 nm, which is only 22% of the probe diameter. Here, the lateral resolution of the probe is defined as the difference between the measured height of a sample, which can be determined to high precision with AFM, and the measured diameter (full width at the noise floor).

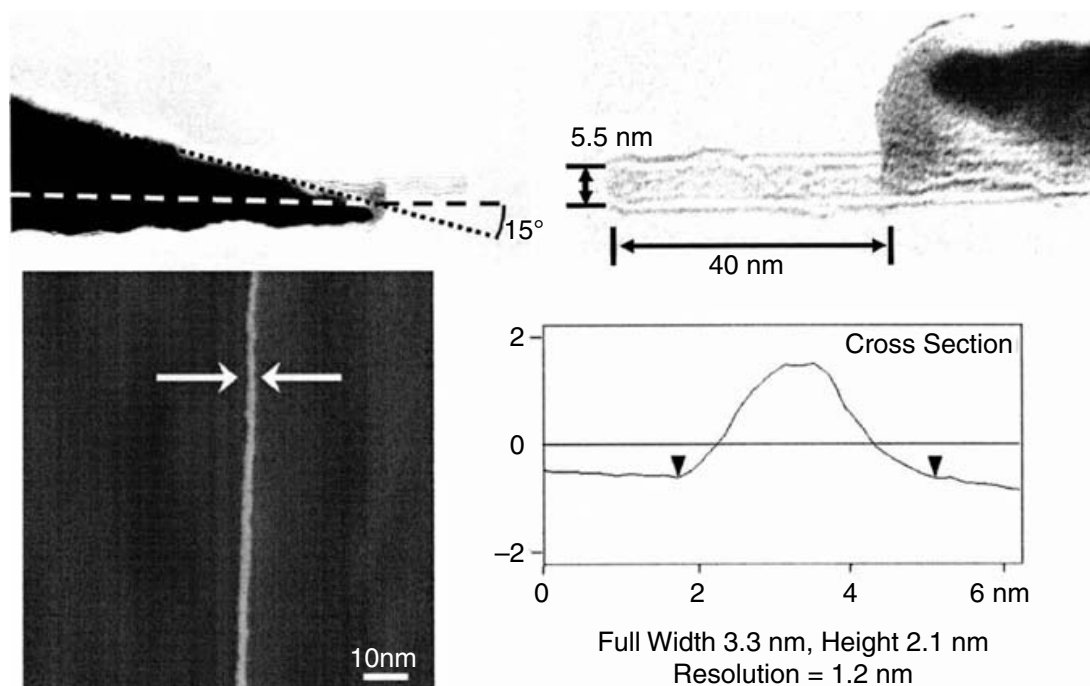


**Figure 10.2** TEM-AFM correlation of a SWNT tip that demonstrated sub-probe-diameter resolution. (Reprinted from Wade, L.A. et al., *Nano Lett.*, 4, 725, 2004. Copyright © 2004 American Chemical Society. With permission.)



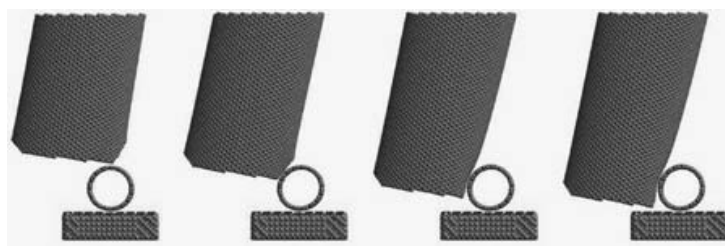


**Figure 10.3** Illustration of SWNT probe slipping past SWNT sample. (Reprinted from Shapiro, I.R. et al., *J. Phys. Chem. B*, 108, 13613, 2004. Copyright © 2004 American Chemical Society. With permission.)

To elucidate the tip–sample interactions that were responsible for this phenomenon, the TEM-AFM correlation data were used to construct realistic molecular models of an open-ended SWNT probe interacting with a prone SWNT sample on a flat hydroxyl-terminated silicon surface.<sup>56</sup> These models were used to generate accurate potential curves at different positions of the probe relative to the sample. Integration of the resultant forces into the equation of motion for an oscillating cantilever operating in the tapping mode yielded simulated topographic cross-section profiles that agreed with the experimental results. The simulations indicated that both elastic probe bending and localized deformations of the probe and sample SWNTs resulted in reduction of the apparent width of the sample tube. This phenomenon is illustrated in Figure 10.3. The result is an ostensive improvement of the lateral resolution, to the extent that the resolution appeared to be better than expected from the measured diameter of the nanotube probe. This phenomenon is the result of the unique elastic properties of both the sample and probe nanotubes under the relatively high driving forces employed in tapping-mode AFM. Nevertheless, it is important to determine under what circumstances this phenomenon may result in a net loss of information when SWNT probes are used to scan soft biological samples. Carbon nanotubes are remarkably resilient; the deformations seen in the simulations were completely elastic and reversible. On the other hand, tapping-mode AFM imaging with the forces employed here (several nano-Newtons [nN]) using conventional probes has been shown to irreversibly damage biomolecules.<sup>57</sup>

From both experimental measurement and numerical simulations of conventional AFM probes, García and San Paulo have shown that an atomic force microscope operating in the tapping mode can have two coexisting tip–sample interaction regimes, known as attractive and repulsive regimes.<sup>57,58</sup> Image quality and resolution differ significantly between these two regimes. In the attractive regime, the AFM cantilever is oscillating in the absence of actual tip–sample contact. This attractive regime (noncontact mode) generally results in lowered resolution due to long-range attractive tip–sample interactions. In the repulsive regime, the tip comes into physical contact with the sample intermittently. It is also possible to have bistable switching of the cantilever oscillation between the two regimes, which manifests itself as sudden changes in the observed sample height and width.<sup>59</sup>

These amplitude instabilities and associated imaging artifacts can be avoided by operating the cantilever exclusively in the repulsive regime. However, the transient forces generated at the tip–sample interface can be high enough to damage soft samples (nN). For this reason, García and San Paulo recommended imaging biological molecules only in the attractive mode.<sup>57</sup>

Quantitative understanding of the effects these tip–sample interaction regimes have on tapping-mode AFM image resolution is not possible for microfabricated silicon tips due to ambiguities discussed earlier in terms of tip size and shape. Chen and coworkers<sup>60</sup> carried out an analysis similar to that of García and San Paulo's, but for well-characterized SWNT AFM tips, operating either in ambient air or in fluid. In contrast to García and San Paulo, these authors suggested that SWNT AFM tapping-mode imaging is actually best performed in the repulsive regime for accurate results. However, for soft biological molecules, the repulsive regime in air is not desirable due to possible irreversible deformation. Interestingly, the simulations of Chen et al. suggest that the repulsive regime is dominant in aqueous tapping-mode AFM imaging, even at the much smaller oscillation amplitudes, due to hydrodynamic damping of the cantilever. These authors predicted that tapping-mode imaging in fluids with active Q-control (where the quality factor of the resonance peak of the cantilever is adjusted to control the degree of damping) can lead to tip-limited resolution for SWNT probes, with an order of magnitude less force imparted on the sample than tapping-mode imaging in air.

## 10.4 Applications of carbon nanotube probes

### 10.4.1 Applications in structural biology

The use of carbon nanotube AFM tips for structural biology applications has been well described in earlier review articles from Lieber's group<sup>7,12</sup> and will thus only be summarized here. One of the first types of samples to be imaged with carbon nanotube AFM probes after their introduction in 1996 was DNA. Several groups reported imaging DNA and DNA–protein complexes with manually assembled MWNT tips in air,<sup>16–18,61–63</sup> in fluids,<sup>64</sup> and in vacuum.<sup>65</sup> The resolution reported for SWNT tip imaging of a RNA polymerase–DNA complex in air was about the same as that for MWNT tips (3.5 nm),<sup>66</sup> although truly tip-limited resolution in SWNT AFM images of 2.4-nm-diameter DNA was reported by Chen et al., when imaged in aqueous solution with active Q-control, as described above.<sup>60</sup>

Lieber's group has imaged a number of isolated proteins using both MWNT and SWNT AFM probes. CVD pore growth MWNT tips were used to image immunoglobulin G (IgG)<sup>40</sup> and IgM<sup>34</sup> antibody proteins. IgG proteins are approximately 15 nm in diameter and have a characteristic Y shape. This shape had been seen previously with AFM only at cryogenic temperatures.<sup>67</sup> The IgM antibody is a pentameric association of IgG proteins. Lieber and coworkers were able to image new structures not seen before with x-ray

diffraction methods.<sup>68</sup> CVD SWNT tips were used to image the smaller (8-nm) GroES protein, with submolecular resolution.<sup>40</sup>

These initial studies demonstrated the potential power of nanotube scanned probes for structural biology studies. The Lieber group went on to publish reports of nanotube AFM probes used to characterize aggregation intermediates in fibril formation of amyloid proteins implicated in Alzheimer's disease,<sup>7</sup> the dependence of nucleosome remodeling on adenosine triphosphate (ATP),<sup>69</sup> and the detection of specific sequences in kilobase-size DNA for single-nucleotide polymorphism mapping.<sup>70</sup>

### 10.4.2 Nanolithography

The advanced imaging capabilities, well-defined morphology, and resistance to wear of nanotube AFM probes, compared to conventional tips, were technological driving forces for their rapid development into new classes of high-resolution nanolithographic tools. Dai and coworkers demonstrated the capability of MWNT probes as direct-write patterning tools by exploiting the high electrical conductivity of the tubes to fabricate oxide nanostructures on silicon.<sup>71</sup> The process relied on field-induced anodization of hydrogen-passivated Si (100) surfaces in air with a negatively biased scanning probe;<sup>72–73</sup> however, tip wear was a serious issue that had limited the development of the technique for nanolithography.<sup>74</sup> Dai et al. found that the MWNT tips did not suffer any noticeable degradation due to compressive or lateral stresses, and were able to fabricate 10-nm-wide oxide lines at a 100-nm pitch over a 100- $\mu\text{m}^2$  surface area in 100 sec while operating in the tapping mode. Later, direct-CVD-grown SWNT AFM probes were used to oxidize atomically flat titanium and achieve features as small as 8 nm in diameter at 20-nm spacing.<sup>35</sup> If this technology were to be developed for data storage, this would correspond to a bit density of 1.6 Tbits ( $10^{12}$  bits) per square inch. SWNT probes were also used to pattern 5- to 6-nm-wide lines of titanium oxide as tunnel junctions in the construction of a single-electron transistor that showed coulomb oscillations at room temperature.<sup>75,76</sup>

MWNT AFM tips have proven flexurally rigid enough to be used in contact-mode AFM,<sup>77</sup> a mode in which the tip experiences significantly higher lateral forces than in the tapping mode. Okazaki and coworkers used a negatively biased MWNT tip scanning in contact mode to etch patterns into a polysilane mask.<sup>78</sup> MWNT tips are also suitable for indentation lithography of polymer films and could be used to write bits into polycarbonate films used in DVD disks.<sup>79,80</sup>

### 10.4.3 SWNT probe functionalization

Carbon nanotubes hold great promise in many areas of science and technology due to their unique physical properties and molecular-scale dimensions. A significant technological advance for these materials has been their incorporation as specific molecular transducers in nanosensors, molecular

electronics, and as molecular manipulation tools. This potential is based on the remarkable molecular recognition capabilities of carbon nanotubes through covalent chemical bonding, surface charge transfer, or electrostatic changes when a specific molecule binds to a tube. Nanotubes can be chemically, physically, or biologically functionalized to recognize a particular target molecule and reject others in a complex environment.

Perhaps the most exciting aspect of carbon nanotubes as AFM probe tips for probing the dynamics of biomolecules is that they can be chemically functionalized uniquely at their very ends. This can be initiated by an electrical etching process, which is also used to shorten the attached SWNTs in order to achieve lengths suitable for high-resolution imaging.<sup>81</sup> When SWNT tips are etched in an oxidizing environment (for example, in ambient air), the ends become functionalized with carboxyl groups. Wong et al. measured the chemical properties of oxidized nanotube AFM tips by measuring their adhesion on hydroxyl-terminated self-assembled monolayers, and demonstrated that carboxyl groups were present by observing a decrease in the adhesion force at pH 4.5, which corresponds to the deprotonation of carboxylic acid.<sup>32</sup> The tips can be chemically modified further by coupling organic amines to the carboxylate group to form amide bonds. The use of reactive amino chemistry is a common biochemical conjugation technique, and can be exploited further to take advantage of a wide range of chemical and biological means available for attaching fluorophores, antibodies, ligands, proteins, or nucleic acids to the ends of the nanotubes with well-defined orientations. With SWNT imaging, covalent and noncovalent forces can be mapped on single macromolecules or between individual biomolecules with greater specificity than with conventional probes, due to the molecular-scale resolution of the nanotube tip. Using functionalized SWNT probes, it is easier to ensure that there is only one molecule or complex attached to the probe. The manipulation of a ligand–protein interaction with specific single molecules coupled to the nanotube tip has been measured with AFM by Wong et al.<sup>81</sup> Figure 10.4 shows quantized adhesion measurements carried out by the authors that indicate single- and double-biotin-streptavidin-binding events for nanotube tips functionalized with biotin.

#### 10.4.4 Nanoelectrode scanning probes

In addition to all the benefits of carbon nanotubes as scanning microscopy probes that we have discussed so far, carbon nanotubes have unique electrical properties. SWNTs act as remarkable one-dimensional conductors and are either semiconducting or metallic. MWNTs are metallic. Metallic nanotubes have extremely high conductivity; a single metallic SWNT can support electrical currents as high as tens of microamps.<sup>82</sup> These characteristics have expanded the capabilities of these tools beyond simple topographical imaging applications. Electrically conductive carbon nanotube AFM tips have shown great promise for conductive probe methods, such as STM<sup>22–26</sup> and electrostatic force microscopy (EFM) techniques.<sup>83–85</sup> SWNT bundles attached

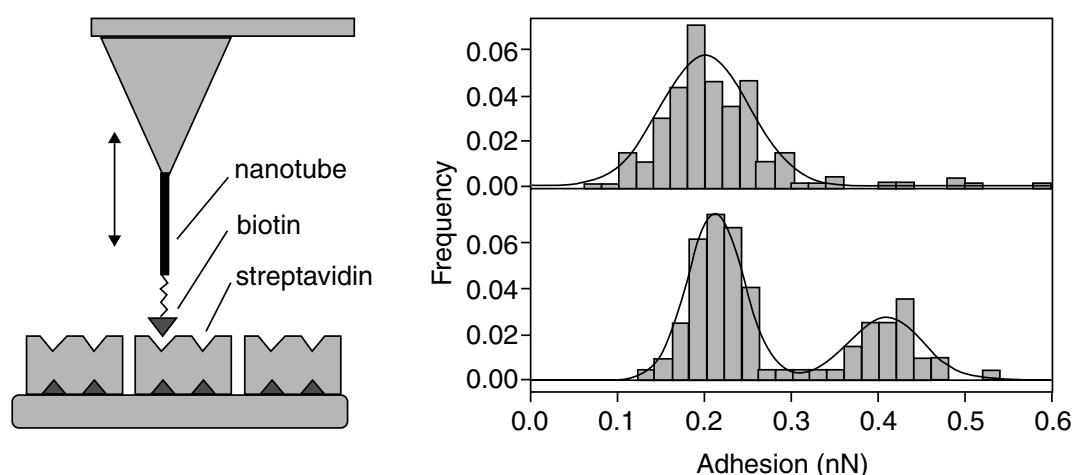


**Figure 10.4** Nanotube tips functionalized with biotin in force microscopy. (From Odom, T.W. et al., *Top. Appl. Phys.*, 80, 206, 2001, Figure 24. Copyright © 2001 Springer-Verlag, Berlin-Heidelberg. With permission.)

to AFM tips have also been used as templates for metal nanowire-conducting probes that were robust enough to function in either the tapping or contact mode.<sup>86</sup>

Wilson and coworkers characterized the conductivity of SWNT probe tips in detail by forming low-resistance electrical contacts to metal-coated AFM tips and dipping the probes into a liquid mercury (Hg) droplet.<sup>87</sup> They were able to discriminate between metallic and semiconducting SWNTs, separate the contact resistance of the nanotube on its AFM tip support from its inherent resistivity, and detect the presence of multiple tubes on the tip. This work set the stage for constructing geometrically well-defined and reproducible nanoelectrodes. The development of such nanoelectrodes will be particularly exciting for bioelectrochemical applications, including the real-time electrochemical probing of biochemical reactions in a single live cell with a minimally invasive probe.

In electrochemical experiments, carbon nanotube-based electrodes and electrode arrays have demonstrated exceptional electrocatalytic activities. The nature of this enhanced electrocatalytic performance relative to other materials is not clearly understood, but is thought to depend sensitively on defect sites along the walls and open ends of the nanotubes. These mimic reactive edge planes of highly oriented pyrolytic graphite (HOPG), allowing for more efficient electron transfer with electroactive species in solution and faster electrochemical kinetics.<sup>88</sup> Cyclic voltammetry of the  $\text{Fe}(\text{CN})_6^{3-/4-}$  reduction–oxidation (redox) couple using MWNT bundles as the electrode showed purely Nernstian behavior, with no apparent activation barrier, which was not the case for a conventional platinum electrode.<sup>89</sup> Conductive nanotube tips are therefore excellent candidates for electrochemical applications of scanning probe microscopes.

For high spatial resolution and sensitivity, the probe should be passivated and electrically insulated everywhere except at the very end of the



nanotube tip. Campbell et al. first reported the fabrication and characterization of nanoelectrodes from individual 100-nm MWNTs.<sup>90</sup> The MWNTs were coated with an insulating layer formed by electrochemical polymerization reactions of polyphenol. Removal of the coating from the nanotube tip end was accomplished by electrochemical etching or by electrical pulse etching in air. However, the authors found that consistent etching of the insulating coating without destruction of the nanotube itself was difficult to achieve.<sup>91</sup> Patil et al. described a method for coating long (2- to 3- $\mu\text{m}$ ) MWNT probes (8 nm diameter uncoated; total probe diameter,  $\sim 260$  nm) based on high-temperature vapor phase Parylene polymerization, followed by laser-induced vaporization of the coating at the nanotube end.<sup>92</sup> These authors demonstrated increased sensitivity for electrostatic force microscopy using coated MWNT probes, compared to conventional EFM probes. They also demonstrated electrochemical activity confined to the exposed tip end by detecting faradaic currents in NaCl electrolyte solutions only after the insulating coating at the tip end had been removed.

More recently, our group has developed a method to coat 5-nm-diameter SWNTs attached to AFM tips with ultrathin ( $\sim 5$ -nm) fluorocarbon (Teflon-like) polymer films formed at room temperature in an inductively coupled plasma reactor.<sup>93</sup> The maximum *total* length of these coated SWNT probes was as long as the exposed regions of the Parylene-coated MWNT probes described by Patil et al., while the total probe diameter was about an order of magnitude less ( $\sim 15$  to  $20$  nm). The fluorocarbon polymer provided a chemically inert and electrically insulating outer layer and reinforced the attachment site of the nanotube to its AFM tip support without the need for adhesives. In addition, the coatings significantly enhanced the mechanical stability of SWNT probes, as has been observed by Patil's group for MWNTs.<sup>92</sup> Finally, electrical pulse etching of the coated nanotube probe was used to expose the tip end, resulting in a nanoelectrode that could be further functionalized.

With this procedure, nanoelectrode probes consisting of both metallic and semiconducting SWNTs attached to gold-coated AFM tips have been constructed and their electrical properties characterized by contacting them to a Hg droplet, following methodology described by Wilson et al.<sup>87</sup> For these nanoelectrodes, the electrical properties of the SWNTs were not affected by the coating. Figure 10.5 shows current–voltage ( $I$ - $V$ ) scans taken for a nanoelectrode probe consisting of a metallic SWNT attached to a gold-coated AFM tip in contact with Hg both before and after applying an electrical etching pulse to the probe to selectively remove the insulating coating from the tip. The  $I$ - $V$  curve is symmetric with a low-bias resistance of  $177$  k $\Omega$ , which is consistent with measured contact resistances between uncoated metallic SWNTs and gold-coated AFM tips.<sup>87</sup> Figure 10.5c shows a subsequent TEM image of the same probe used to generate the  $I$ - $V$  data.

Some probes exhibited strongly rectifying behavior in their current–voltage ( $I$ - $V$ ) curves at *positive* potentials, reminiscent of previously reported metal–semiconducting heterojunctions in single-walled carbon

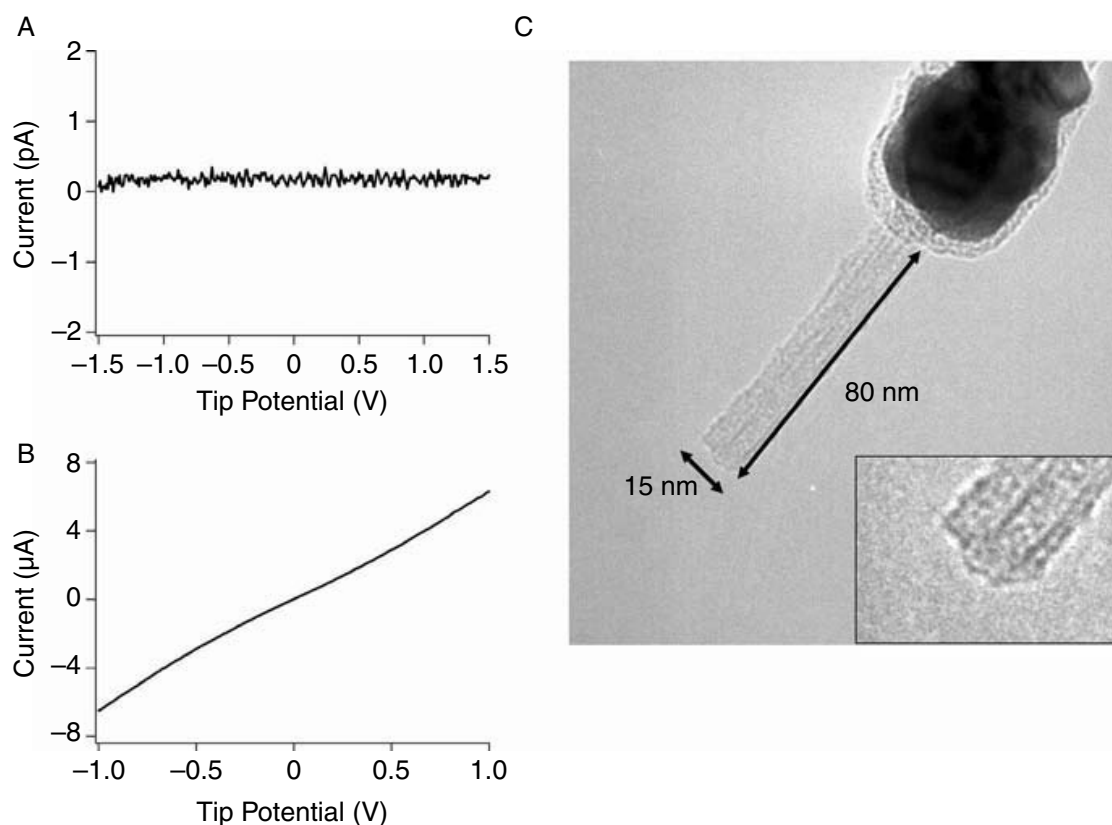


**Figure 10.5** Current–voltage ( $I$ - $V$ ) scans taken for a nanoelectrode probe consisting of a metallic SWNT attached to a gold-coated AFM tip in contact with a mercury droplet both before (a) and after (b) applying an electrical etching pulse to the probe. (c) Subsequent TEM image of the etched nanotube probe. (Adapted from Esplandiu, M.J. et al., *Nano Lett.*, 4, 1873, 2004. Copyright © 2004 American Chemical Society. With permission.)

nanotubes.<sup>94–96</sup> Nanoelectrodes consisting of individual SWNTs attached to n-type silicon AFM tips without a gold precoating were also fabricated. These nanoelectrodes displayed strongly rectifying diode behavior at *negative* potentials, due to the dominant influence of the n-type silicon to the conductive behavior. These results suggest the possibility of developing novel scanning probes that can function as nanodiodes.

## 10.5 Future directions

Improved techniques for the manufacture of carbon nanotubes as robust and well-characterized scanning probes have resulted in wider availability of these tools to research groups performing AFM imaging. In addition to numerous demonstrations of nanotube tips as high-resolution topographical and chemical imaging tools, some exciting new applications have been developed within the last few years that could significantly impact nanobiotechnology. Conductive nanotube tips attached to scanning probes can be assembled into functionalized nanoelectrodes capable of carrying out electrochemical reactions in physiologically relevant environments. For example, these probes could be used as

nanoscopic electroanalytical tools to monitor cellular signaling pathways, including neurotransmitter release at synapses.<sup>92</sup> Many signaling molecules, such as ligands, hormones, and neurotransmitters, are electrochemically active. Carbon nanotubes have been functionalized with biomolecules in numerous ways in the construction of hybrid devices, such as field effect transistors, enzyme electrodes, and other biosensors.<sup>97</sup> The integration of such a device on an AFM tip would represent the ultimate functionalized scanning probe.

## Acknowledgments

I thank Larry Wade for helpful comments. This work was supported by Caltech start-up funds, the Caltech President's Fund, NASA contract NAS7-1407, and Arrowhead Research.

## References

1. Müller, D.J., Baumeister, W., and Engel, A., Controlled unzipping of a bacterial surface layer with atomic force microscopy, *Proc. Natl. Acad. Sci. U.S.A.*, 96, 13170, 1999.
2. Hörber, J.K.H. and Miles, M.J., Scanning probe evolution in biology, *Science*, 302, 1002, 2003.
3. Bustamante, C., Macosko, J.C., and Wuite, G.J.L., Grabbing the cat by the tail: manipulating molecules one by one, *Nat. Rev. Mol. Cell Biol.*, 1, 130, 2000.
4. Carrion-Vazquez, M. et al., Mechanical and chemical unfolding of a single protein: a comparison, *Proc. Natl. Acad. Sci. U.S.A.*, 96, 3694, 1999.
5. Krauthauer, R. et al., Discriminating small molecule DNA binding modes by single molecule force spectroscopy, *FEBS Lett.*, 510, 154, 2002.
6. Vezenov, D. et al., Force titrations and ionization state sensitive imaging of functional groups in aqueous solutions by chemical force microscopy, *J. Am. Chem. Soc.*, 119, 2006, 1997.
7. Hafner, J.H. et al., Structural and functional imaging with carbon nanotube AFM probes, *Prog. Biophys. Mol. Biol.*, 77, 73, 2001.
8. Leckband, D., Measuring the forces that control protein interactions, *Annu. Rev. Biophys. Biomol. Struct.*, 29, 1, 2000.
9. Krishnan, A. et al., Young's modulus of single-walled nanotubes, *Phys. Rev. B*, 58, 14013, 1999.
10. Wong, E.W. et al. Nanobeam mechanics: elasticity, strength, and toughness of nanorods and nanotubes, *Science*, 277, 1971, 1997.
11. Larsen, T. et al., Comparison of wear characteristics of etched-silicon and carbon nanotube atomic-force microscopy probes, *Appl. Phys. Lett.*, 80, 1996, 2002.
12. Odom, T.W., Hafner, J.H., and Lieber, C.M., Scanning probe microscopy studies of carbon nanotubes, *Top. Appl. Phys.*, 80, 173, 2001.
13. Dai, H. et al., Nanotubes as nanoprobe in scanning probe microscopy, *Nature*, 384, 147, 1996.
14. Wong, S.S. et al., Carbon nanotube tips: high-resolution probes for imaging biological systems, *J. Am. Chem. Soc.*, 120, 603, 1998.

15. Nagy, G. et al., Carbon nanotube tipped atomic force microscopy for measurement of <100 nm etch morphology on semiconductors, *Appl. Phys. Lett.*, 73, 529, 1998.
16. Nishijima, H. et al., Carbon-nanotube tips for scanning probe microscopy: preparation by a controlled process and observation of deoxyribonucleic acid, *Appl. Phys. Lett.*, 74, 4061, 1999.
17. Akita, S. et al., Carbon nanotube tips for a scanning probe microscope: their fabrication and properties, *J. Phys. D*, 32, 1044, 1999.
18. Nakayama, Y. et al., Microprocess for fabricating carbon-nanotube probes of a scanning probe microscope, *J. Vac. Sci. Technol. B*, 18, 661, 2000.
19. Stevens, R.M.D. et al., Carbon nanotubes as probes for atomic force microscopy, *Nanotechnology*, 11, 1, 2000.
20. Stevens, R. et al., Improved fabrication approach for carbon nanotube probe devices, *Appl. Phys. Lett.*, 77, 3453, 2000.
21. Yasutake, M. et al., Performance of the carbon-nanotube assembled tip for surface shape characterization, *Ultramicroscopy*, 91, 57, 2002.
22. Yamashita, J. et al., Growth of a single-wall carbon nanotube in the gap of scanning tunneling microscope, *Appl. Phys. Lett.*, 74, 2450, 1999.
23. Shimizu, T. et al., Stable atomic imaging of Si(111)- $7 \times 7$  surface by scanning tunneling microscope with carbon nanotube tip, *Surf. Sci.*, 486, L455, 2001.
24. Mizutani, W. et al., Carbon nanotube tip for scanning tunneling microscope, *Jpn. J. Appl. Phys.*, 40, 4328, 2001.
25. Ikuno, T. et al., Metal-coated carbon nanotube tip for scanning tunneling microscope, *Jpn. J. Appl. Phys.*, 43, L644, 2004.
26. de Jonge, N., Lamy, Y., and Kaiser, M., Controlled mounting of individual multiwalled carbon nanotubes on support tips, *Nano Lett.*, 3, 1621, 2003.
27. Hillenbrand, R. et al., Coherent imaging of nanoscale plasmon patterns with a carbon nanotube optical probe, *Appl. Phys. Lett.*, 83, 368, 2003.
28. Akita, S. and Nakayama, Y., Length adjustment of carbon nanotube probes by electron bombardment, *Jpn. J. Appl. Phys.*, 41, 4887, 2002.
29. Akita, S. and Nakayama, Y., Extraction of inner shell from multiwall carbon nanotubes for scanning probe microscope tip, *Jpn. J. Appl. Phys.*, 42, 3933, 2003.
30. Nguyen, C. et al., High lateral resolution imaging with sharpened tip of multi-walled carbon nanotube scanning probe, *J. Phys. Chem. B*, 108, 2816, 2004.
31. Chang, Y.C. et al., Easy method to adjust the angle of the carbon nanotube probe of an atomic force microscope, *Appl. Phys. Lett.*, 82, 3541, 2003.
32. Wong, S.S. et al., Covalently-functionalized single-walled carbon nanotube probe tips for chemical force microscopy, *J. Am. Chem. Soc.*, 120, 8557, 1998.
33. Wong, S.S. et al., Single-walled carbon nanotube probes for high-resolution nanostructure imaging, *Appl. Phys. Lett.*, 73, 3465, 1998.
34. Hafner, J.H., Cheung, C.-L., and Lieber, C.M., Growth of nanotubes for probe microscopy tips, *Nature*, 398, 761, 1999.
35. Cooper, E.B. et al., Terabit-per-square-inch data storage with the atomic force microscope, *Appl. Phys. Lett.*, 75, 3566, 1999.
36. Shingaya, Y., Nakayama, T., and Aono, M., Carbon nanotube tip for scanning tunneling microscopy, *Physica B*, 323, 153, 2002.
37. Yenilmez, E. et al., Wafer scale production of carbon nanotube scanning probe tips for atomic force microscopy, *Appl. Phys. Lett.*, 80, 2225, 2002.

38. Ye, Q. et al., Large-scale fabrication of carbon nanotube probe tips for atomic force microscopy critical dimension imaging applications, *Nano Lett.*, 4, 1301, 2004.
39. Pan, F.M. et al., Selective growth of carbon nanotube on scanning probe tips by microwave plasma chemical vapor deposition, *J. Vac. Sci. Technol. B*, 22, 90, 2004.
40. Cheung, C.-L., Carbon nanotube atomic force microscopy tips: direct growth by chemical vapor deposition and application to high-resolution imaging, *Proc. Natl. Acad. Sci. U.S.A.*, 97, 3809, 2000.
41. Hafner, J.H., Cheung, C.-L., and Lieber, C.M., Direct growth of single-walled carbon nanotube scanning probe microscopy tips, *J. Am. Chem. Soc.*, 121, 9750, 1999.
42. Cheung, C.-L. et al., Growth and fabrication with single-walled carbon nanotube probe microscopy tips, *Appl. Phys. Lett.*, 76, 3136, 2000.
43. Hafner, J.H. et al., High-yield assembly of individual single-walled carbon nanotube tips for scanning probe microscopies, *J. Phys. Chem. B*, 105, 743, 2001.
44. Campbell, P.M., Snow, E.S., and Novak, J.P., Simple catalyst for the growth of small-diameter carbon nanotubes, *Appl. Phys. Lett.*, 81, 4586, 2002.
45. Wade, L.A. et al., Correlating AFM probe morphology to image resolution for single-wall carbon nanotube tips, *Nano Lett.*, 4, 725, 2004.
46. Hall, A. et al., Simple and efficient method for carbon nanotube attachment to scanning probes and other substrates, *Appl. Phys. Lett.*, 82, 2506, 2003.
47. Maeda, C. et al., Atomic force microscopy and Kelvin probe microscopy measurements of semiconductor surface using carbon nanotube tip fabricated by electrophoresis, *Jpn. J. Appl. Phys.*, 41, 2615, 2002.
48. Brioude, A. et al., Synthesis of sheathed carbon nanotube tips by the sol-gel technique, *Appl. Surf. Sci.*, 221, 4, 2004.
49. Yang, Y. et al., Toward the chemistry of carboxylic single-walled carbon nanotubes by chemical force microscopy, *J. Phys. Chem. B*, 106, 4139, 2002.
50. Nishino, T., Ito, T., and Umezawa, Y., Carbon nanotube scanning tunneling microscopy tips for chemically selective imaging, *Anal. Chem.*, 74, 4275, 2002.
51. Vesenska, J. et al., Colloidal gold particles as an incompressible atomic force microscope imaging standard for assessing the compressibility of biomolecules, *Biophys. J.*, 65, 992, 1993.
52. Bustamante, C., Keller, D., and Yang, G., Scanning force microscopy of nucleic acids and nucleoprotein assemblies, *Curr. Opin. Struct. Biol.*, 3, 363, 1993.
53. Engel, A. and Müller, D., Observing single biomolecules at work with the atomic force microscope, *Nat. Struct. Biol.*, 7, 715, 2000.
54. Snow, E.S., Campbell, P.M., and Novak, J.P., Single-wall carbon nanotube atomic force microscopy probes, *Appl. Phys. Lett.*, 80, 2002, 2002.
55. Snow, E.S., Campbell, P.M., and Novak, J.P., Atomic force microscopy using single-wall C nanotube probes, *J. Vac. Sci. Technol. B*, 20, 822, 2002.
56. Shapiro, I.R. et al., Influence of elastic deformation on single-wall carbon nanotube atomic force microscopy probe resolution, *J. Phys. Chem. B*, 108, 13613, 2004.
57. San Paulo, A. and García, R., High-resolution imaging of antibodies by tapping-mode atomic force microscopy: attractive and repulsive tip-sample interaction regimes, *Biophys. J.*, 78, 1599, 2000.
58. García, R. and San Paulo, A., Attractive and repulsive tip-sample interaction regimes in tapping-mode atomic force microscopy, *Phys. Rev. B*, 60, 4961, 1999.



59. García, R. and San Paulo, A., Dynamics of a vibrating tip near or in intermittent contact with a surface, *Phys. Rev. B*, 61, R13381, 2000.
60. Chen, L. et al., Single-walled carbon nanotube AFM probes: optimal imaging resolution of nanoclusters and biomolecules in ambient and fluid environments, *Nano Lett.*, 4, 1725, 2004.
61. Maeda, Y. et al., Reduction of long-range interactions using carbon nanotube probes in biological systems, *Jpn. J. Appl. Phys.*, 40, 1425, 2001.
62. Umemura, K. et al., Atomic force microscopy of RecA-DNA complexes using a carbon nanotube tip, *Biochem. Biophys. Res. Commun.*, 281, 390, 2001.
63. Chang, Y.C. et al., Nanoscale imaging of biomolecules by controlled carbon nanotube probes, *Jpn. J. Appl. Phys.*, 43, 4517, 2004.
64. Li, J., Cassell, A.M., and Dai, H., Carbon nanotubes as AFM tips: measuring DNA molecules at the liquid/solid interface, *Surf. Interface Anal.*, 28, 8, 1999.
65. Uchihashi, T. et al., Carbon-nanotube tip for highly-reproducible imaging of deoxyribonucleic acid helical turns by noncontact atomic force microscopy, *Jpn. J. Appl. Phys.*, 39, L887, 2000.
66. Bunch, J.S., Rhodin, T.N., and McEuen, P.L., Noncontact-AFM imaging of molecular surfaces using single-wall carbon nanotube technology, *Nanotechnology*, 15, S76, 2004.
67. Zhang, Y., Sheng, S.J., and Shao, Z., Imaging biological structures with the cryo atomic force microscope, *Biophys. J.*, 71, 2168, 1996.
68. Perkins, S.J. et al., Solution structure of human and mouse immunoglobulin M by synchrotron x-ray scattering and molecular graphics modeling: a possible mechanism for complement activation, *J. Mol. Biol.*, 221, 1345, 1991.
69. Schnitzler, G.R. et al., Direct imaging of human SWI/SNF-remodeled mono- and polynucleosomes by atomic force microscopy employing carbon nanotube tips, *Mol. Cell Biol.*, 21, 8504, 2001.
70. Woolley, A.T. et al., Direct haplotyping of kilobase-size DNA using carbon nanotube probes, *Nat. Biotechnol.*, 18, 760, 2000.
71. Dai, H., Franklin, N., and Han, J., Exploiting the properties of carbon nanotubes for nanolithography, *Appl. Phys. Lett.*, 73, 1508, 1998.
72. Dagata, J.A. et al., Modification of hydrogen-passivated silicon by a scanning tunneling microscope operating in air, *Appl. Phys. Lett.*, 56, 2001, 1990.
73. Snow, E.S. and Campbell, P.M., Fabrication of Si nanostructures with an atomic force microscope, *Appl. Phys. Lett.*, 64, 1932, 1994.
74. Minne, S.C. et al., Atomic force microscope lithography using amorphous silicon as a resist and advances in parallel operation, *J. Vac. Sci. Technol. B*, 13, 1380, 1995.
75. Gotoh, Y. et al., Experimental and theoretical results of room-temperature single-electron transistor formed by the atomic force microscope nano-oxidation process, *J. Vac. Sci. Technol. B*, 18, 1321, 2000.
76. Gotoh, Y., Matsumoto, K., and Maeda, T., Room temperature coulomb diamond characteristic of single electron transistor made by AFM nano-oxidation process, *Jpn. J. Appl. Phys.*, 41, 2578, 2002.
77. Ishikawa, M. et al., A study of friction by carbon nanotube tip, *Appl. Surf. Sci.*, 188, 456, 2002.
78. Okazaki, A., Akita, S., and Nakayama, Y., Scanning probe microscopy lithography of silicon using a combination of carbon nanotube tip and a polysilane film as a mask, *Jpn. J. Appl. Phys.*, 41, 4973, 2002.

79. Akita, S. et al., Nanoindentation of polycarbonate using carbon nanotube tip, *Jpn. J. Appl. Phys.*, 39, 7086, 2000.
80. Akita, S. and Nakayama, Y., Structural stability of carbon nanotube tips on nanoindentation of polycarbonate, *Jpn. J. Appl. Phys.*, 40, 4289, 2001.
81. Wong, S.S. et al., Covalently functionalized nanotubes as nanometer-sized probes in chemistry and biology, *Nature*, 394, 52, 1998.
82. Saito, R., Dresselhaus, G., and Dresselhaus, M.S., *Physical Properties of Carbon Nanotubes*, Imperial College Press, London, 1998.
83. Arnason, S.B. et al., Carbon nanotube-modified cantilevers for improved spatial resolution in electrostatic force microscopy, *Appl. Phys. Lett.*, 75, 2842, 1999.
84. Tzeng, S.-D. et al., Charge imaging and manipulation using carbon nanotube probes, *Appl. Phys. Lett.*, 81, 5042, 2002.
85. Wilson, N.R. and Macpherson, J.V., Enhanced resolution electric force microscopy with single-wall carbon nanotube tips, *J. Appl. Phys.*, 96, 3565, 2004.
86. Wilson, N.R. and Macpherson, J.V., Single-walled carbon nanotubes as templates for nanowire conducting probes, *Nano Lett.*, 3, 1365, 2003.
87. Wilson, N.R., Cobden, D.H., and Macpherson, J.V., Single-wall carbon nanotube conducting probe tips, *J. Phys. Chem. B*, 106, 13102, 2002.
88. Gooding, J.J. et al., Protein electrochemistry using aligned carbon nanotube arrays, *J. Am. Chem. Soc.*, 125, 9006, 2003.
89. Nugent, J.M. et al., Fast electron transfer kinetics on multiwalled carbon nanotube microbundle electrodes, *Nano Lett.*, 1, 87, 2001.
90. Campbell, J.K., Sun, L., and Crooks, R.M., Electrochemistry using single carbon nanotubes, *J. Am. Chem. Soc.*, 121, 3779, 1999.
91. Ito, T., Sun, L., and Crooks, R.M., Electrochemical etching of individual multiwall carbon nanotubes, *Electrochem. Solid-State Lett.*, 6, C4, 2003.
92. Patil, A. et al., Enhanced functionality of nanotube atomic force microscopy tips by polymer coating, *Nano Lett.*, 4, 303, 2004.
93. Esplandiu, M.J. et al., Nanoelectrode scanning probes from fluorocarbon-coated single-walled carbon nanotubes, *Nano Lett.*, articles ASAP, published on the web August 19, 2004.
94. Yao, Z. et al., Carbon nanotube intramolecular junctions, *Nature*, 402, 273, 1999.
95. Collins, P.G. et al., Nanotube nanodevice, *Science*, 278, 100, 1997.
96. Nishijima, N., Akita, S., and Nakayama, Y., Novel process for fabricating nanodevices consisting of carbon nanotubes, *Jpn. J. Appl. Phys.*, 38, 7147, 1999.
97. Katz, E. and Willner, I., Biomolecule-functionalized carbon nanotubes: applications in bioelectronics, *ChemPhysChem*, 5, 1084, 2004.